Mathematical Problems in Engineering

Chaotic Oscillators: Theory, Experiments, Control, and Applications

Lead Guest Editor: Viet-Thanh Pham
Guest Editors: Sundarapandian Vaidyanathan, Adel Ouannas, and Tomasz Kapitaniak

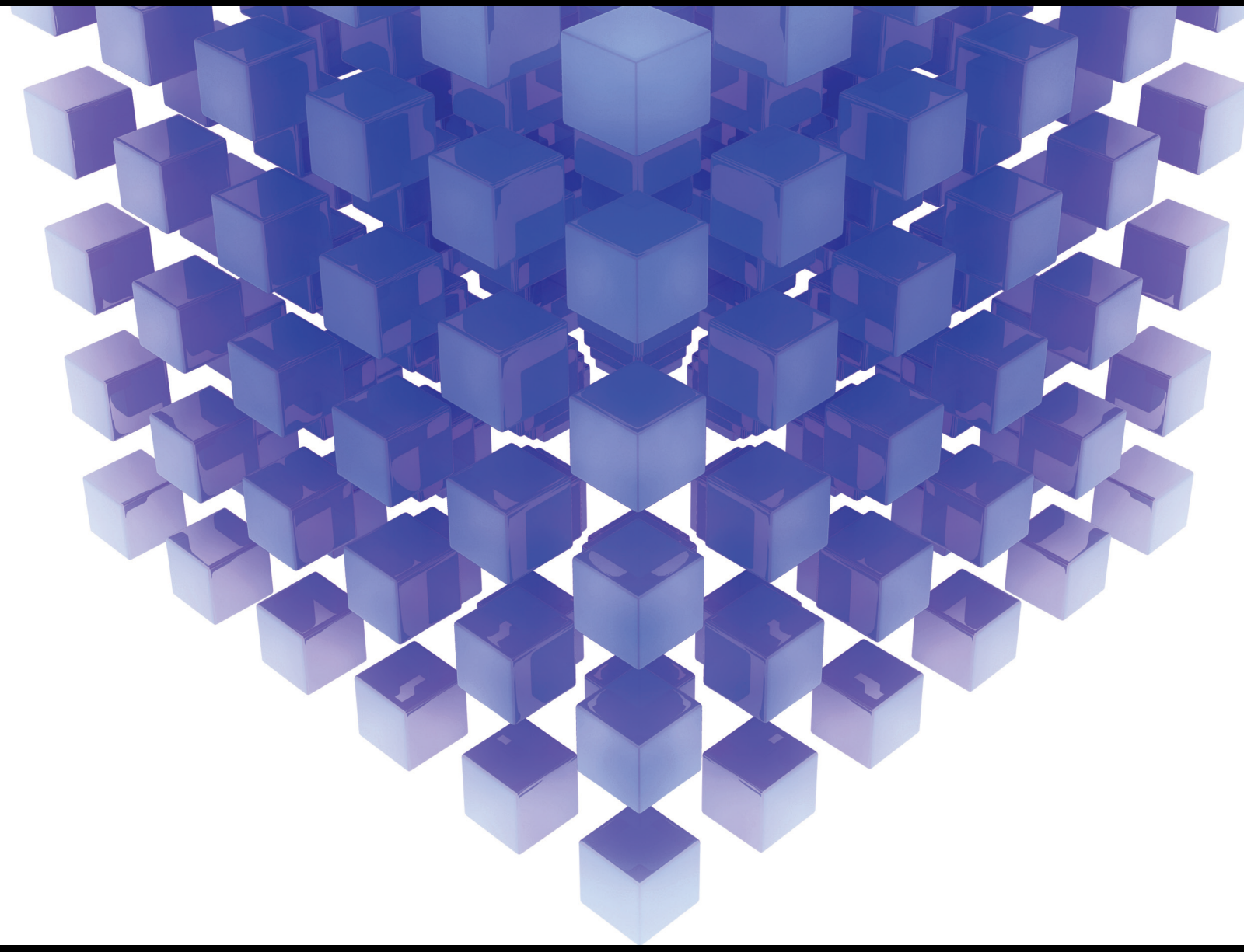

Chaotic Oscillators: Theory, Experiments, Control, and Applications

Mathematical Problems in Engineering

Chaotic Oscillators: Theory, Experiments, Control, and Applications

Lead Guest Editor: Viet-Thanh Pham
Guest Editors: Sundarapandian Vaidyanathan, Adel Ouannas, and Tomasz Kapitaniak

Contents

On the Analytical Solutions of the Forced Damping Duffing Equation in the Form of Weierstrass Elliptic Function and its Applications
S. A. El-Tantawy, Alvaro H. Salas, and M. R. Alharthi
Research Article (9 pages), Article ID 6678102, Volume 2021 (2021)

Self-Sustained Oscillation of a Photothermal-Responsive Pendulum under Steady Illumination
Dali Ge, Peibao Xu, and Kai Li
Research Article (12 pages), Article ID 5531530, Volume 2021 (2021)

A New General Decay Rate of Wave Equation with Memory-Type Boundary Control
Sheng Fan
Research Article (11 pages), Article ID 5571072, Volume 2021 (2021)

Realization of a Secure Visible Light Communication System via Chaos Synchronization
Teh-Lu Liao, Chih-Yung Chen, Hsin-Chieh Chen, Yung-Yi Chen, and Yi-You Hou
Research Article (12 pages), Article ID 6661550, Volume 2021 (2021)

On the Approximate Solutions of the Constant Forced (Un)Damping Helmholtz Equation for Arbitrary Initial Conditions
Alvaro H. Salas, Castillo H. Jairo E, and M. R. Alharthi
Research Article (10 pages), Article ID 8887566, Volume 2021 (2021)

An Improved Linear State Error Feedback Synchronization Control Criteria for a Six-Axis Duffing Chaotic System
Hao Jia and Chen Guo
Research Article (11 pages), Article ID 6681562, Volume 2021 (2021)

Finite Horizon Robust Nonlinear Model Predictive Control for Wheeled Mobile Robots
Phuong Nam Dao, Hong Quang Nguyen, Thanh Long Nguyen, and Xuan Sinh Mai
Research Article (8 pages), Article ID 6611992, Volume 2021 (2021)

Solitary Wave Diffraction with a Single and Two Vertical Circular Cylinders
Zouhair Hafsia, Saliha Nouri, Salah Mahmoud Boulaaras, Ali Allahem, Salem Alkhalaf, and Aldo Munoz Vazquez
Research Article (9 pages), Article ID 6634762, Volume 2021 (2021)

Spiral Waves in a Lattice Array of Josephson Junction Chaotic Oscillators with Flux Effects
Balamurali Ramakrishnan, Ramesh Ramamoorthy, Chunbiao Li, Akif Akgul, and Karthikeyan Rajagopal
Research Article (9 pages), Article ID 8848914, Volume 2021 (2021)

Analysis of a New Hidden Attractor Coupled Chaotic System and Application of Its Weak Signal Detection
Wenhui Luo, Qingli Ou, Fei Yu, Li Cui, and Jie Jin
Research Article (15 pages), Article ID 8849283, Volume 2020 (2020)

Stability, Chaos Detection, and Quenching Chaos in the Swing Equation System
Shun-Chang Chang
Research Article (12 pages), Article ID 6677084, Volume 2020 (2020)

Asymmetric Information on Price Can Affect Bertrand Duopoly Players with the Gradient-Based Mechanism
S. S. Askar
Research Article (12 pages), Article ID 6620570, Volume 2020 (2020)

New Chaotic Oscillator Derived from Class C Single Transistor-Based Amplifier
Jiri Petrzela
Research Article (18 pages), Article ID 2640629, Volume 2020 (2020)

Mathematical Modelling of the Sterile Insect Technique Using Different Release Strategies
Anis Ben Dhahbi, Yassine Chargui, Salah Mahmoud Boulaaras, Sana Ben Khalifa, Waleed Koko, and Faisal Alresheedi
Research Article (9 pages), Article ID 8896566, Volume 2020 (2020)

Synchronized Chaos of a Three-Dimensional System with Quadratic Terms
Ali Allahem
Research Article (4 pages), Article ID 8813736, Volume 2020 (2020)

Synchronous Behavior for Memristive Synapse-Connected Chay Twin-Neuron Network and Hardware Implementation
Quan Xu, Xiao Tan, Dong Zhu, Mo Chen, Jie Zhou, and Huagan Wu
Research Article (12 pages), Article ID 8218740, Volume 2020 (2020)

Multistability Analysis, Coexisting Multiple Attractors, and FPGA Implementation of Yu–Wang Four-Wing Chaotic System
Fei Yu, Li Liu, Hui Shen, Zinan Zhang, Yuanyuan Huang, Shuo Cai, Zelin Deng, and Qiuzhen Wan
Research Article (16 pages), Article ID 7530976, Volume 2020 (2020)

Hindawi
Mathematical Problems in Engineering
Volume 2021, Article ID 6678102, 9 pages
https://doi.org/10.1155/2021/6678102

Research Article

On the Analytical Solutions of the Forced Damping Duffing Equation in the Form of Weierstrass Elliptic Function and its Applications

S. A. El-Tantawy,[1,2] **Alvaro H. Salas**,[3] **and M. R. Alharthi**[4]

[1]*Department of Physics, Faculty of Science, Port Said University, Port Said 42521, Egypt*
[2]*Research Center for Physics (RCP), Department of Physics, Faculty of Science and Arts, Al-Baha University, Al-Mikhwah, Saudi Arabia*
[3]*Department of Mathematics, Universidad Nacional de Colombia, Universidad Nacional de Colombia-Nubia Campus Department of Mathematics and Statistics FIZMAKO Research Group, Bogota, Colombia*
[4]*Department of Mathematics and Statistics, College of Science, Taif University, P.O.Box 11099, Taif 21944, Saudi Arabia*

Correspondence should be addressed to S. A. El-Tantawy; samireltantawy@yahoo.com

Received 1 December 2020; Revised 30 January 2021; Accepted 3 February 2021; Published 16 February 2021

Academic Editor: Sundarapandian Vaidyanathan

In this study, a novel analytical solution to the integrable undamping Duffing equation with constant forced term is obtained. Also, a new approximate analytical (semianalytical) solution for the nonintegrable linear damping Duffing oscillator with constant forced term is reported. The analytical solution is given in terms of the Weierstrass elliptic function with arbitrary initial conditions. With respect to it, the semianalytical solution is constructed depending on a new ansatz and the exact solution of the standard Duffing equation (in the absence of both damping and forced terms). A comparison between the obtained solutions and the Runge–Kutta fourth-order (RK4) is carried out. Moreover, some complicated oscillator equations such as the constant forced damping pendulum equation, forced damping cubic-quintic Duffing equation, and constant forced damping Helmholtz–Duffing equation are reduced to the forced damping Duffing oscillator, in which its solution is known. As a practical application, the proposed techniques are applied to investigate the characteristics behavior of the signal oscillations arising in the RLC circuit with externally applied voltage.

1. Introduction

Since the early century until now, Duffing equation [1–3] has been devoted by many authors in order to investigate the nonlinear oscillations in engineering technology fields and in several physical systems including electrical and mechanical with nonlinear restoring force [4]. So far, this equation and its family have remained a good model in studying and explaining many nonlinear structures in the dynamic systems and various branches of sciences [5]. This family is considered an excellent example for the dynamic system that exhibits chaotic behavior. The Duffing equation with a cubic stiffness term was introduced for the first time by Duffing [6] in 1918 for describing the hardening spring effect observed in many mechanical problems. Since then, this equation has become one of the commonest examples in nonlinear oscillation texts and research articles [4, 7].

The exact analytic solutions of the standard (unforced and undamping) Duffing equation ($\ddot{x} + \alpha x + \beta x^3 = 0$) and the cubic-quintic Duffing equation ($\ddot{x} + px + qx^3 + rx^5 = 0$) have been obtained by many authors in terms of Jacobian elliptic functions [8–14]. Since most realistic physical systems are subjected to the influence of some frictional forces, these forces must be taken into account in Duffing equation to become unforced damping Duffing equation ($\ddot{x} + 2\gamma\dot{x} + \alpha x + \beta x^3 = 0$) [15–19]. The unforced undamping Duffing

equation has been solved numerically using the differential transform method, and the author found that both numerical and exact analytic solutions coincide with each other [13]. Also, the analytical solution of the unforced damping Duffing equation in terms of Jacobian elliptic functions has been derived by Johannessen [17, 18]. Moreover, Johannessen [17, 18] made a comparison between the analytical solution and the approximate numerical solution using RK4, and he found that the two solutions were largely identical.

In some physical and engineering systems, the system can be excited by an external force, and this force may be constant or a function of the time. In this case, for modeling the oscillations in these systems, the excited force must be taken into consideration in the Duffing equation which we finally obtain as the forced damping Duffing equation ($\ddot{x} + 2\gamma\dot{x} + \alpha x + \beta x^3 = F$). Some authors studied the Duffing equation solutions with (out) both damping term and driving/external force [8, 20–24]. For instance, the exact solutions of both undamped Duffing equation and forced undamped Duffing equation have been derived in the form of Jacobian elliptic functions by Hsu [8]. Furthermore, the Jacobian elliptic functions have been devoted for getting the approximate solution of the forced damped Duffing equation [20]. This new equation of motion has many applications in electrical and mechanical systems [21, 22] as well as in different branches of science such as studying the oscillations in plasma physics. For example, the forced damping Duffing equation with constant force can be used for investigating the nonlinear oscillations in RLC circuits if the circuit has DC battery. Moreover, the forced damping Duffing equation can be used for modeling the damping oscillations in different plasma models. For instance, for any plasma system having a critical value for its related parameters, we can reduce the fluid equations of the plasma species to a modified Korteweg–de Vries–Burgers (mKdVB) equation ($\partial_t\phi + A_p\phi^2\partial_x\phi + B_p\partial_x^3\phi - C_p\partial_x^2\phi$) using the reductive perturbation technique (RPT). After that the mKdVB can be transformed to the forced damping Duffing equation by means of a traveling wave transformation for studying the damping oscillations in the plasma system. It should be noted here that the last term in the mKdV equation appeared as a result of taking the kinematic viscosity of some plasma species into account. Motivated by the mentioned investigations, we restrict our attention for studying and solving the forced damping Duffing equation,

$$\left\{ \ddot{x} + 2\gamma\dot{x} + \alpha x + \beta x^3 = F, x(0) = x_0 \& x'(0) = \dot{x}_0, \right. \quad (1)$$

and some related equations using some new approaches. Thus, our study will be divided into two main goals/parts. First, we will solve the forced damping Duffing equation in the absence of the friction force ($\gamma = 0$) in order to get an exact solution in terms of Weierstrass elliptic function. In the second part, a new ansatz will be utilized with the help of some exact solution of standard Duffing equation ($\gamma = F = 0$) in order to find an approximate analytic solution for the initial value problem (1).

2. Methodology

In the beginning, we dissect the i.v.p (1) into two cases and then solve them. In the first case, the undamping Duffing equation with perturbation/excitation force, i.e., $\gamma = 0$ and $F \neq 0$, is considered. This case has several applications in plasma physics, oceans, mechanical fluid, and electronic circuits in the absence viscosity and friction forces. In the second case, the linear damping Duffing equation with perturbation force (sometimes is called the constant forced damping Duffing equation), i.e., $\gamma \neq 0$ and $F \neq 0$, is considered. Also, this case has various applications in plasma physics if the kinematic viscosity of the plasma species is taken into account or if the dust fluctuations are taken into consideration.

2.1. Case I: An Exact Analytic Solution for the Forced Undamping Duffing Equation. If the damping term in the i.v.p (1) is neglected ($\gamma = 0$), then the i.v.p (1) reduces to the following integrable i.v.p.

$$\left\{ \ddot{x} + px + qx^3 = F, x(0) = x_0 \text{ and } x'(0) = \dot{x}_0. \right. \quad (2)$$

Let us assume that the following solution satisfies the i.v.p. (2)

$$\eta(t) = \lambda + \frac{\mu}{1 + \rho\wp}, \quad (3)$$

where $\wp \equiv \wp(t + t_0; g_2, g_3)$ is the Weierstrass elliptic function and satisfies the following condition:

$$\wp'^2 = 4\wp^3 - g_2\wp - g_3. \quad (4)$$

By inserting solution (3) into equation (2) and taking relation (4) into consideration, we get

$$\sum_{j=0}^{3} W_j \wp^j = 0, \quad (5)$$

with

$$\begin{aligned} W_0 &= -2F - 4g_3\mu\rho^2 + g_2\mu\rho + 2p\lambda + 2p\mu \\ &\quad + 2q\lambda^3 + 6q\lambda^2\mu + 6q\lambda\mu^2 + 2q\mu^3, \\ W_1 &= -\rho\begin{pmatrix} 6F + 3g_2\mu\rho - 6p\lambda - 4p\mu \\ -6q\lambda^3 - 12q\lambda^2\mu - 6q\lambda\mu^2 \end{pmatrix}, \\ W_2 &= 2\rho\begin{pmatrix} -3F\rho + 3p\lambda\rho + p\mu\rho \\ +3q\lambda^3\rho + 3q\lambda^2\mu\rho - 6\mu \end{pmatrix}, \\ W_3 &= 2\rho^2\left(-F\rho + p\lambda\rho + q\lambda^3\rho + 2\mu\right). \end{aligned} \quad (6)$$

By equating the coefficients W_j to zero, a system of algebraic equations is obtained, and by solving this system, the values of μ, ρ, g_2, and g_3 are obtained as follows:

$$\mu = \frac{6\left(F - \lambda\left(p + q\lambda^2\right)\right)}{p + 3q\lambda^2},$$
$$\rho = \frac{12}{p + 3q\lambda^2},$$
$$g_2 = \frac{1}{12}\left(-3q\lambda\left(q\lambda^3 - 4F\right) + p^2 - 6pq\lambda^2\right),$$
$$g_3 = \frac{1}{216}\left(27F^2q + 9pq\lambda\left(q\lambda^3 - 4F\right) + p^3 + 18p^2q\lambda^2\right). \tag{7}$$

By applying the initial conditions given in i.v.p (2), we get

$$t_0 = \wp^{-1}\left(\frac{\lambda + \mu - x_0}{\rho\left(x_0 - \lambda\right)}; g_2, g_3\right). \tag{8}$$

The value of λ is a solution to the following quartic equation:

$$q\lambda^4 + 2p\lambda^2 - 4F\lambda + \left(4Fx_0 - 2px_0^2 - qx_0^4 - 2\dot{x}_0^2\right) = 0. \tag{9}$$

Note that the solution (3) is periodic with period

$$T = 2\int_r^{\infty} \frac{\mathrm{d}x}{\sqrt{4x^3 - g_2x - g_3}}, \tag{10}$$

where r is the greatest real root of the cubic equation: $4x^3 - g_2x - g_3 = 0$.

In equation (9), let us discuss the value of the following number:

$$\Delta = -\frac{1}{q}\left(4Fx_0 - 2px_0^2 - qx_0^4 - 2\dot{x}_0^2\right), \tag{11}$$

which is called the discriminant of the i.v.p. (2). If equation (9) has at least one real root, then all parameters that are given in equation (7) become real for real λ. On the other side, if all roots of equation (9) are complex, then $\Delta < 0$. Indeed, let $r_1, \ldots, r_4$ be the roots of equation (9), and then

$$r_1r_2r_3r_4 = \frac{1}{q}\left(4Fx_0 - 2px_0^2 - qx_0^4 - 2\dot{x}_0^2\right) = -\Delta > 0, \tag{12}$$

so that $\Delta < 0$, and in this case, we cannot obtain real values for the parameters given in equation (7). In order to obtain a solution to the i.v.p. (2) with real values to parameters (μ, ρ, g_2, g_3), we make the following substitution:

$$x(t) = s - \frac{2s}{1 + v(t)}, \tag{13}$$

where $s \neq 0$, and $v \equiv v(t)$ is a solution to the following Duffing equation:

$$\ddot{v} + Mv + Nv^3 = F_0. \tag{14}$$

Taking into account the initial conditions given in the i.v.p. (2), we obtain

$$v(0) = \frac{2s\dot{x}_0}{\left(s - x_0\right)^2},$$
$$v'(0) = \frac{s + x_0}{s - x_0}. \tag{15}$$

On the other hand, the first integration of equation (14) gives

$$v'(t)^2 = C + 2F_0v(t) - Mv(t)^2 - \frac{1}{2}Nv(t)^4, \tag{16}$$

and by applying initial condition given in the i.v.p. (2), we get

$$C = \frac{1}{2\left(s - x_0\right)^4}\left[\begin{array}{c} -4F_0\left(s - x_0\right)^3\left(s + x_0\right) + 2M\left(s^2 - x_0^2\right)^2 \\ +N\left(s + x_0\right)^4 + 8s^2\dot{x}_0^2 \end{array}\right], \tag{17}$$

with

$$N = \frac{-F + ps + qs^3}{2s},$$
$$M = \frac{3F - ps + 3qs^3}{2s},$$
$$F_0 = -\frac{F}{s}. \tag{18}$$

Inserting equations (14)–(17) into the first equation (here, $\mathbb{R} \equiv \ddot{x} + px + qx^3 - F$) of i.v.p (2), we have

$$\mathbb{R} = -\frac{8qs^3}{\left(1 + v(t)\right)^3\left(s - x_0\right)^4}\left(s^4 + \frac{2Fs}{q} + \Delta\right). \tag{19}$$

Observe that the quartic equation,

$$s^4 + \frac{2F}{q}s + \Delta = 0, \tag{20}$$

has at least one real root, since $\Delta < 0$. Thus, for $\Delta < 0$, the solution of the i.v.p. (14) and (15) expresses the solution of the i.v.p. (2), where the parameters (M, N, F_0) are given in equation (18).

Example 1. The solution of the following i.v.p. according to the relation (3)

$$\left\{\ddot{x} + x + x^3 = 1, x(0) = 1 \text{and} x'(0) = 1,\right. \tag{21}$$

reads

$$x(t) = 1.29637 - \frac{2.45792}{1 + 1.98619\wp(0.521719 - t; -0.166667, 0.171296)}. \tag{22}$$

Figure 1 illustrates the comparison between the solution (22) and the RK4 numerical solution. It is known that RK4 numerical solution to the ordinary differential equations is the best so far. Thus, our solution is compared to it, and it is found that the obtained results are completely compatible with each other. Moreover, the periodicity of solution (22) is given by $T = 4.24727$.

2.2. Case II: An Approximate Analytic Solution for the Forced Damping Duffing Equation. It is known that the forced damping Duffing equation ($\mathbb{R} = \ddot{x} + 2\gamma\dot{x} + \alpha x + \beta x^3 - F$) is not integrable unless $F = 0$ and $\alpha = (8/9)\gamma^2$. Thus, in this subsection, we seek an approximate analytic solution to (1) in the form

$$x(t) = d + \exp(-\gamma t)\eta(t), \tag{23}$$

where $\eta \equiv \eta(t)$ is a solution to standard Duffing equation ($\ddot{x} + \alpha x + \beta x^3 = 0$), and d is some constant to be determined later.

Substituting solution (23) into the forced damping Duffing equation ($\mathbb{R} \equiv \ddot{x} + 2\gamma\dot{x} + \alpha x + \beta x^3 - F = 0$), we have

$$\begin{aligned}\mathbb{R} = &\left(\beta d^3 + \alpha d - F\right)\\ &+\left(3d^2\beta e^{-t\gamma} + \alpha e^{-t\gamma} - \gamma^2 e^{-t\gamma}\right)\eta(t)\\ &+ 3\,d\beta\, e^{-2t\gamma}\eta(t)^2 + \beta e^{-3t\gamma}\eta(t)^3 + e^{-t\gamma}\eta''(t).\end{aligned} \tag{24}$$

For small $\gamma \ll 1$ and not too large t, $e^{\gamma t} \approx 1$, so that equation (24) reduces to

$$\begin{aligned}\mathbb{R} \approx &\,\eta''(t) + \left(3d^2\beta + \alpha - \gamma^2\right)\eta(t)\\ &+ 3\,d\beta\,\eta(t)^2 + \beta\eta(t)^3\\ &+\left(\beta d^3 + \alpha\, d - F\right).\end{aligned} \tag{25}$$

The value of d could be obtained by equating the last term in equation (25) to zero:

$$\beta d^3 + \alpha\, d - F = 0. \tag{26}$$

Accordingly, the following new i.v.p. needs to solve.

$$\begin{cases}\eta''(t) + \left(3d^2\beta + \alpha - \gamma^2\right)\eta(t)\\ +3\,d\beta\,\eta(t)^2 + \beta\eta(t)^3 = 0,\\ \eta(0) = \dot{x}_0 + \gamma\left(x_0 - d\right),\\ \eta'(0) = x_0 - d.\end{cases} \tag{27}$$

Inserting the hypothesis $\eta(t) = z(t) - d$ into the i.v.p. (27), we get

$$\begin{cases}z''(t) + \tilde{\alpha} z(t) + \beta z(t)^3 = \tilde{F},\\ z(0) = \dot{x}_0 + \gamma\left(x_0 - d\right)\&z'(0) = x_0,\end{cases} \tag{28}$$

where $\tilde{\alpha} = (\alpha - \gamma^2)$ and $\tilde{F} = (F - \mathrm{d}\gamma^2)$. Observe that the i.v.p. (28) refers to the constant forced undamping Duffing equation. From previous section, we already know how to solve this problem. Then, an approximate analytical solution to the constant forced damping Duffing equation (1) could be given by

$$x(t) = d + \exp(-\gamma t)(z(t) - d), \tag{29}$$

where the number d is a solution to the cubic equation (26), and $z = z(t)$ is the exact solution of the i.v.p. (28). Note that for $\gamma > 0$, the value of parameter d must be chosen according: $\lim_{t\longrightarrow\infty} x(t) = d$.

Example 2. Let us analyze the i.v.p. (1) using different values for $(\gamma, \alpha, \beta, F)$. The solutions of the i.v.p. (1) according to the relation (23) and $(\gamma, \alpha, \beta, F) = (0.1, 2.2, 1, 0.01)$ and $(\gamma, \alpha, \beta, F) = (0.1, 2.2, 1, 0)$ are, respectively, given by

$$x(t) = 0.00454541 + e^{-0.1t}\left(0.13229 - \frac{0.780732}{1 + 5.34242\wp(t + 3.15199; 0.380447, 0.0556578)}\right), \tag{30}$$

$$x(t) = e^{-0.1t}\left(0.134868 - \frac{0.796091}{1 + 5.34624\wp(t + 3.17447; 0.379675, 0.0559271)}\right). \tag{31}$$

Figures 2(a) and 2(b), respectively, demonstrate the comparison between the approximate analytical solutions (30) and (31) and the RK4 approximate solution. Also, the maximum distance error (L_D) with respect to RK4 is

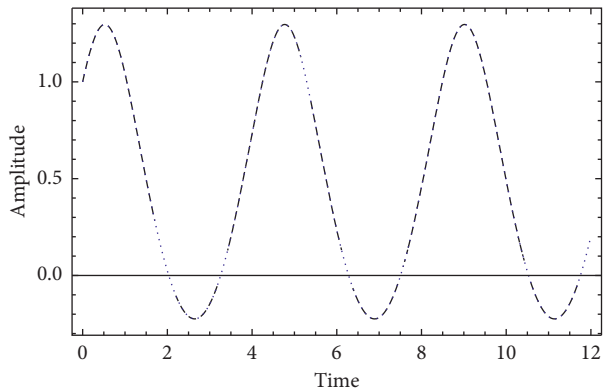

Figure 1: The comparison between the analytical solution (20) (dotted curve) and the RK4 numerical solution (dashed curve) for the forced undamping Duffing equation (21) is investigated for $(\gamma, \alpha, \beta, F) = (0, 1, 1, 1)$.

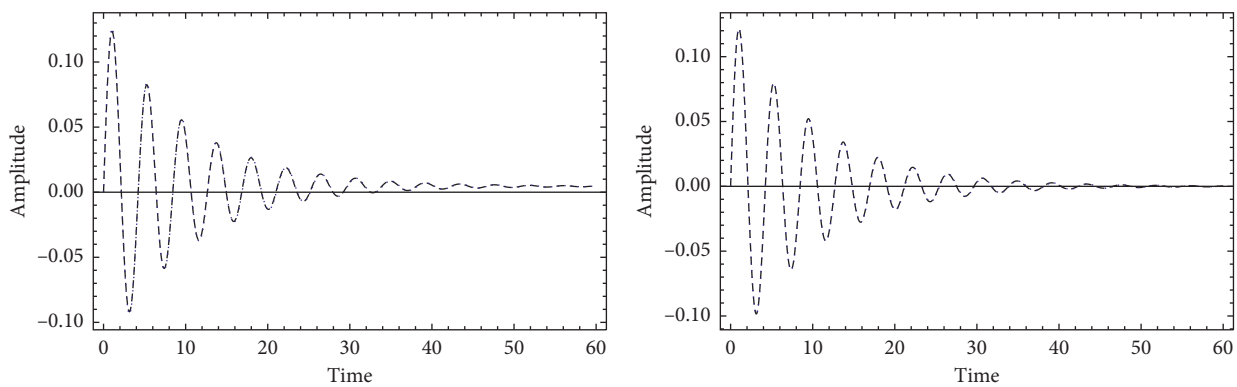

Figure 2: The comparison between the approximate analytic solutions (30) and (31) (dotted curve) and the RK4 numerical solution (dashed curve) for the forced damping Duffing equation (22) is carried out different values for $(\gamma, \alpha, \beta, F)$.

estimated for different values of the parameters $(\gamma, \alpha, \beta, F)$ as shown in Table 1.

It is noticed from Figure 2 and the values of distance error (L_D) given in Table 1 that the semianalytical solution (23) gives good results as compared to the approximate numerical solution using RK4. Also, it is seen that the distance error decreases with the enhancement of the coefficient of the damping term (γ), while the forced term (F) has an opposite effect on the distance error, i.e., increasing F leads the enhancement of the distance error L_D. Moreover, our solution gives good results for $\alpha > \beta$. Also, it is noted that the distance error (L_D) decreases as the difference between α and β is large.

Table 1: The maximum distance error (L_D) is estimated for $(\alpha, \beta) = (2.2, 1)$ and different values of (γ, F).

(γ, F)	Time range	L_D
$(0, 0)$	$0 \le t \le 60$	2.45967×10^{-6}
$(0.01, 0)$	$0 \le t \le 60$	0.00829489
$(0.1, 0)$	$0 \le t \le 60$	0.00142482
$(1, 0)$	$0 \le t \le 60$	0.000434655
$(0.1, 0.01)$	$0 \le t \le 60$	0.0021093
$(0.1, 0.1)$	$0 \le t \le 60$	0.0272933

3. Applications

Here, we try to find the link between the constant forced damping Duffing equation and some physical and engineering problems related to this equation in order to investigate the nonlinear oscillations in various fields of physics and engineering such as the oscillations in RLC circuits and plasma physics.

3.1. Forced Damping Pendulum Equation. The most popular law of motion in mechanics is $\mathsf{F} = ma$, where F is the force, m is the particle mass, and a is the particle acceleration. Thus, we have a pendulum with length l and with a ball of mass m

moving in a constant gravitational field g and under friction proportional to the particle velocity and external (un)periodic force. Accordingly, the dimensionless differential equation that can describe the pendulum motion is given by

$$\begin{cases} \ddot{\theta} + 2\gamma\dot{\theta} + \omega^2 \sin\theta = F, \\ \theta(0) = \theta_0 \& \theta'(0) = \dot{\theta}_0. \end{cases} \tag{32}$$

Note that

$$\begin{aligned} &\min_{a,b} \int_{-(\pi/2)}^{\pi/2} \left[\left(ax + bx^3\right) - \sin x\right]^2 \mathrm{d}x \\ &= \frac{-806400 + 161280\pi^2 - 8160\pi^4 + \pi^8}{2\pi^7} \\ &\approx 0.000024, \end{aligned} \tag{33}$$

for

$$\begin{aligned} a &= \frac{240\left(21 - 2\pi^2\right)}{\pi^5}, \\ b &= \frac{3360\left(\pi^2 - 10\right)}{\pi^7}. \end{aligned} \tag{34}$$

Accordingly, and by expanding $\sin\theta = \theta - (\theta^3/6) + O(\theta^5)$, the i.v.p. (32) could be replaced by the following new i.v.p.

$$\begin{cases} \ddot{\theta} + 2\gamma\dot{\theta} + \alpha\theta + \beta\theta^3 = F, \\ \theta(0) = \theta_0 \& \theta'(0) = \dot{\theta}_0, \end{cases} \tag{35}$$

with

$$\begin{aligned} \alpha &= \frac{240\left(21 - 2\pi^2\right)\omega^2}{\pi^5}, \\ \beta &= \frac{3360\left(\pi^2 - 10\right)\omega^2}{\pi^7}. \end{aligned} \tag{36}$$

Now, the i.v.p. (35) is similar to the i.v.p. (1), which we discussed as its solution in the above sections.

Example 3. The solution of the i.v.p. (32) for $(\gamma, \omega, F, \theta_0, \dot{\theta}_0) = (0.1, 1, 0.1, 0, 0)$ reads

$$\theta(t) = 0.101286 + e^{-0.1t}\left(-0.102309 + \frac{0.612929}{1 + 12.26\wp(t + 6.22606; 0.0798509, 0.0041612)}\right). \tag{37}$$

The comparison between solution (37) and the numerical solution using RK4 is displayed in Figure 3. Also, the distance error is estimated ($L_D = 0.00560317$). It is observed that the obtained results are completely compatible with each other.

3.2. Forced Damping Cubic-Quintic Duffing Equation. The idea is to replace a cubic-quintic polynomial by an odd parity cubic polynomial. Observe that

$$\min_{p,q} \int_{-A}^{A} \left[\left(\alpha x + \beta x^3 + \delta x^5\right) - \left(px + qx^3\right)\right]^2 \mathrm{d}x = \varepsilon, \tag{38}$$

for

$$\begin{aligned} p &= \alpha - \frac{5A^4\delta}{21}, \\ q &= \frac{10A^2\delta}{9} + \beta, \\ \varepsilon &= \frac{128}{43659}A^{11}\delta^2. \end{aligned} \tag{39}$$

According to the transformation (38) and (39), the following constant forced damping cubic-quintic Duffing equation

$$\left\{ \ddot{x} + 2\gamma\dot{x} + \alpha x + \beta x^3 + \delta x^5 = F, x(0) = x_0 \& x'(0) = \dot{x}_0, \right. \tag{40}$$

could be reduced to the following new i.v.p.

$$\left\{ \ddot{x} + 2\gamma\dot{x} + \tilde{\alpha}x + \tilde{\beta}x^3 = F, x(0) = x_0 \& x'(0) = \dot{x}_0, \right. \tag{41}$$

with

$$\begin{aligned} \tilde{\alpha} &= \left(\alpha - \frac{5A^4\delta}{21}\right), \\ \tilde{\beta} &= \left(\frac{10A^2\delta}{9} + \beta\right). \end{aligned} \tag{42}$$

Note that the approximation becomes good for small values of ε which can be achieved for $|\delta| \le 1$ and $0 < A \le 1$.

Example 4. The solution of the i.v.p. (41) for $(\gamma, \tilde{\alpha}, \tilde{\beta}, \delta, F, x_0, \dot{x}_0) = (0.1, 3, 0.5, 0.1, 0.1, 0, 0)$ reads

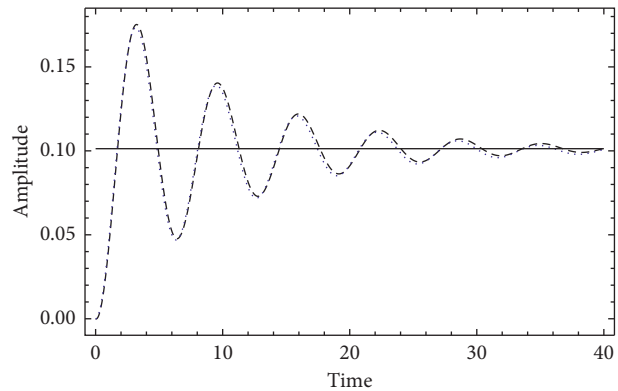

Figure 3: The comparison between the solution (37) and the numerical solution using RK4 of the i.v.p. (32) is reported for $(\gamma, \omega, F, \theta_0, \dot{\theta}_0) = (0.1, 1, 0.1, 0, 0)$.

$$x(t) = 0.0335922 + e^{-0.1t}\left(0.000091584 - \frac{0.000549507}{1 + 4.04044\wp(t + (1.82295 + 3.82875i); 0.735051, 0.121281)}\right). \tag{43}$$

In Figure 4, the comparison between solution (43) and the RK4 numerical solution is introduced. Moreover, the distance error is calculated $(L_D = 0.0304975)$.

3.3. Forced Damping Helmholtz–Duffing Equation. Let us consider the following i.v.p.

$$\left\{ \ddot{x} + 2\gamma\dot{x} + px + qx^2 + \beta x^3 = F, x(0) = x_0 \& x'(0) = \dot{x}_0. \right. \tag{44}$$

To convert the i.v.p. (44) to the i.v.p. (1), the following transformation is introduced:

$$x(t) = z(t) - \frac{q}{3\beta}, \tag{45}$$

and by substituting this transformation into the i.v.p. (44), we finally get

$$\begin{cases} z''(t) + 2\gamma z'(t) + \tilde{\alpha} z(t) + \beta z(t)^3 = \tilde{\mathsf{F}}, \\ z(0) = x_0 + \dfrac{q}{3\beta} \text{ and } z'(0) = \dot{x}_0, \end{cases} \tag{46}$$

with

$$\tilde{\alpha} = \left(p - \frac{q^2}{3r}\right), \qquad \tilde{\mathsf{F}} = F + \frac{pq}{3\beta} - \frac{2q^3}{27\beta^2}. \tag{47}$$

This is a constant forced damping Duffing equation with its initial conditions.

3.4. Nonlinear Oscillations in RLC Series Circuits with Applied External Source. In an RLC series circuits consisting of a resistor with resistance R (ohm), an inductor with inductance L (H), and ferroelectric nonlinear capacitor with capacitance C (F) as well as external applied voltage E (V), Kirchhoff's voltage law (KVL) could be written as

$$L\partial_t i'(t) + i(t)R + sq + aq^3 = E, \tag{48}$$

where the relation between the current and charge is given by $i = \partial_t q \equiv \dot{q}$, $i' \equiv \partial_t i$, the coefficients (a, s) are related to the nonlinear capacitor, and E represents the voltage of the battery which is constant. By reorganizing equation (48), the following constant forced and damped Helmholtz equation could be obtained as

$$\ddot{q} + 2\gamma\dot{q} + \alpha q + \beta q^3 = F, \tag{49}$$

with $\gamma = (R/(2L)), \alpha = (1/(LC))$, $\beta = 1/(Cq_0L)$, and $F = E/L$, where $q_0 = q(t = 0)$ is the initial charge value at $t = 0$, $\ddot{q} \equiv \partial_t^2 q$, and $\dot{q} \equiv \partial_t q$.

Let us now apply the obtained solution on equation (49) and analyze it numerically using some various values to the coefficients $(\alpha, \beta, \gamma, F)$ according to the RLC series circuit. The solution of the following i.v.p. according to the relation (23) and for $(\alpha, \beta, \gamma, F) = (4, 1, 0.1, 0.2)$ reads

$$x(t) = 0.0499688 + e^{-0.1t}\left(0.130143 - \frac{0.770662}{2.93591\wp(t + 2.55163; 1.29763, 0.318372) + 1}\right). \tag{50}$$

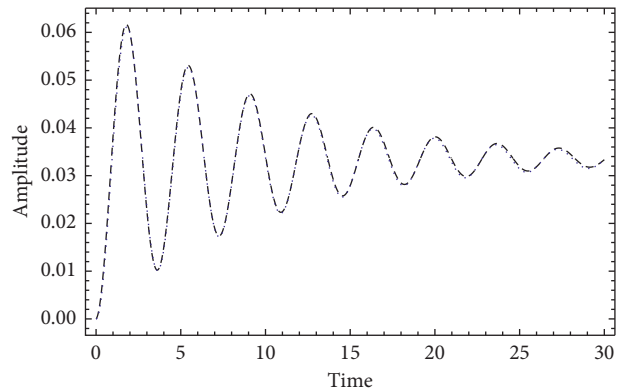

Figure 4: The comparison between the solution (43) and the RK4 numerical solution of the i.v.p. (40) is introduced for $(\gamma, \tilde{\alpha}, \tilde{\beta}, \delta, F, x_0, \dot{x}_0) = (0.1, 3, 0.5, 0.1, 0.1, 0, 0)$.

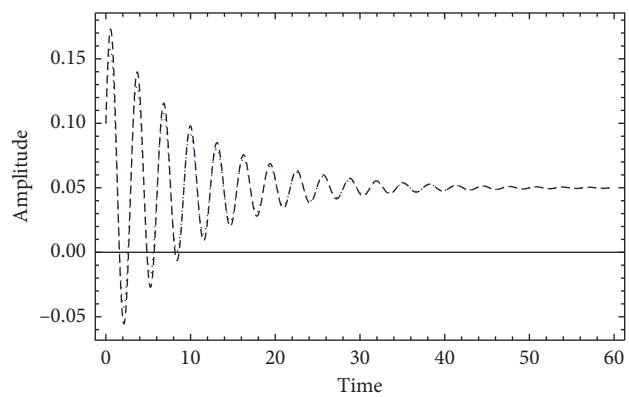

Figure 5: A comparison between the approximate analytical solution (50) (dotted curve) and the RK4 numerical solution (dashed curve) is investigated for RLC series circuits parameters (R, L, C, E), i.e., for $(\alpha, \beta, \gamma, F, q_0, \dot{q}_0) = (4, 1, 0.1, 0.2, 0.1, 0.2)$.

Figure 5 demonstrates the behavior of the damping oscillations in RLC series circuit for $(\alpha, \beta, \gamma, F, q_0, \dot{q}_0) = (4, 1, 0.1, 0.2, 0.1, 0.2)$. Also, in this figure, we make a comparison between the approximate analytical solution (50) and the approximate numerical solution using the RK4, and the distance error $L_D (= 0.0164089)$ is estimated. The harmony between two solutions has been observed, which confirms the high accuracy of the approximate analytical solutions.

4. Conclusion

Some novel solutions to the Duffing equation and its family (including the constant forced undamping Duffing equation and constant forced damping Duffing equation) have been derived in detail. First, we derived an analytical solution to the integrable constant forced undamping Duffing equation in the form of Weierstrass elliptic function with arbitrary initial conditions. Also, the periodicity of this solution has been obtained. Then, an approximate analytical (semianalytical) solution for the nonintegrable constant forced damping Duffing equation has been discussed depending on the exact solution of the unforced undamping (standard) Duffing equation. The relation between the constant forced damping Duffing equation and the constant forced damping pendulum equation, the constant forced damping cubic-quintic Duffing equation, and the constant forced damping Helmholtz–Duffing equation has been investigated. Some numerical examples have been introduced to demonstrate the obtained results and to make a comparison between the obtained solutions and RK4 numerical solutions. It was found from the results of the comparison that the semianalytical solution is compatible with the RK4 solution.

Future work: in some physical and engineering systems, the driving forces maybe a function of time and with an arbitrary circular frequency such as in the RLC circuits if the AC applied source. In this case, we obtain a new equation of motion which is called the damping Duffing equation with time-dependent driving force: $(\ddot{x} + 2\gamma\dot{x} + \alpha x + \beta x^3 = F(t))$.

This equation of motion needs to be solved in the form of Weierstrass elliptic function, but it is outside the goal of the present work.

Data Availability

The data that support the findings of this study are available from the corresponding author upon request.

Conflicts of Interest

The authors declare that they have no conflicts of interest.

Acknowledgments

This study was supported by Taif University Researchers supporting project number (TURSP-2020/275), Taif University, Taif, Saudi Arabia.

References

[1] O. N. F. Nelson, Z. Yu, B. P. Dorian, and Y. Wang, "A new method for the exact solution of duffing equation," *Journal of Applied Mathematics and Physics*, vol. 6, no. 12, pp. 2718–2726, 2018.

[2] K. Johannessen, "The Duffing oscillator with damping," *European Journal of Physics*, vol. 36, p. 13, 2015 and references in therein, Article ID 065020.

[3] S. K. Lai and C. W. Lim, "Higher-order approximate solutions to a strongly nonlinear duffing oscillator," *International Journal for Computational Methods in Engineering Science and Mechanics*, vol. 7, no. 3, pp. 201–208, 2006.

[4] I. Kovacic and M. J. Brennan, *The Duffing Equation: Nonlinear Oscillators and Their Behaviour*, John Wiley & Sons, Ltd., Hoboken, NJ, USA, 1st edition, 2011.

[5] P. S. Landa, *Nonlinear Oscillations and Waves in Dynamical Systems*, Springer, Berlin, Germany, 1996.

[6] G. Duffing, *Erzwungene Schwingungen bei Veränderlicher Eigenfrequenz*, F. Vieweg und Sohn, Braunschweig, Germany, 1918.

[7] J. Guckenheimer and P. J. Holmes, *Nonlinear Oscillations, Dynamical Systems, and Bifurcations of Vector Fields*, Springer Vrlag, Berlin, Germany, 1983.

[8] C. S. Hsu, "On the application of elliptic functions in nonlinear forced oscillations," *Quarterly of Applied Mathematics*, vol. 17, no. 4, pp. 393–407, 1960.

[9] E. T. Whittaker and G. N. Watson, *A Course of Modern Analysis*, Cambridge University Press, Cambridge, MA, USA, 4th edition, 1980.

[10] M. Abramowitz and I. Stegun, *Handbook of Mathematical Functions*, Dover, New York, NY, USA, 9th edition, 1980.

[11] A. H. Salas, E. Jairo, and H. Castillo, "Exact solutions to cubic duffing equation for a nonlinear electrical circuit," *Journal of the American Mathematical Society*, vol. 7, pp. 46–53, 2014.

[12] Ma'mon Abu Hammad, A. H. Salas, and S. A. El-Tantawy, "New method for solving strong conservative odd parity nonlinear oscillators: applications to plasma physics and rigid rotator," *AIP Advances*, vol. 10, p. 11, Article ID 085001, 2020.

[13] M. El-Shahed, "Application of differential transform method to non-linear oscillatory systems," *Communications in Nonlinear Science and Numerical Simulation*, vol. 13, no. 8, pp. 1714–1720, 2008.

[14] Y. Khan, M. Akbarzade, and A. Kargar, "Coupling of homotopy and the variational approach for a conservative oscillator with strong odd-nonlinearity," *Scientia Iranica*, vol. 19, no. 3, pp. 417–422, 2012.

[15] S. Nourazar and A. Mirzabeigy, "Approximated solution for nonlinear Duffing oscillator with damping effect using the modified differential transform method," *Scientia Iranica*, vol. 20, pp. 364–368, 2013.

[16] A. H. Salas and S. A. El-Tantawy, "On the approximate solutions to a damped harmonic oscillator with higher-order nonlinearities and its application to plasma physics: semi-analytical solution and moving boundary method," *The European Physical Journal Plus*, vol. 135, pp. 833–917, 2020.

[17] K. Johannessen, "The Duffing oscillator with damping," *The European Physical Journal Plus*, vol. 36, p. 13, Article ID 065020, 2015.

[18] K. Johannessen, "The duffing oscillator with damping for a softening potential," *International Journal of Applied and Computational Mathematics*, vol. 3, no. 4, pp. 3805–3816, 2017.

[19] J.-w. Zhu, "A new exact solution of a damped quadratic nonlinear oscillator," *Applied Mathematical Modelling*, vol. 38, no. 24, pp. 5986–5993, 2014.

[20] A. E. Zúñga, "Application of jacobianan elliptic functions to the analysis of the steady-state solution of the damped duffing equation with driving force of elliptic type," *Nonlinear Dynamics*, vol. 42, pp. 175–184, 2005.

[21] U. R. Singh, G. Purohit, A. Sharma, and V. Patidar, "An analogue circuit to study the forced and quadratically damped Duffing oscillator," *International Journal of Nonlinear Dynamics and Control*, vol. 1, no. 1, pp. 87–96, 2017.

[22] U. R. Singh and G. Purohit, "Synchronization of quadratically damped mathieu-duffing based chaotic circuits with applications to secure communications," *IJSR*, vol. 5, pp. 80–85, 2016.

[23] W. D. Iwan, "On defining equivalent systems for certain ordinary non-linear differential equations," *International Journal of Non-linear Mechanics*, vol. 4, no. 4, pp. 325–334, 1969.

[24] B. Baumann, J. Schwieger, M. Wolff, F. Manders, and J. Suijker, "Nonlinear behavior in high-intensity discharge lamps," *Journal of Physics D Applied Physics*, vol. 49, p. 10, Article ID 255201, 2015.

Hindawi
Mathematical Problems in Engineering
Volume 2021, Article ID 5531530, 12 pages
https://doi.org/10.1155/2021/5531530

Research Article

Self-Sustained Oscillation of a Photothermal-Responsive Pendulum under Steady Illumination

Dali Ge,[1,2] **Peibao Xu**,[1] **and Kai Li**[1]

[1]*Department of Civil Engineering, Anhui Jianzhu University, Hefei 230601, Anhui, China*
[2]*Institute of Advanced Technology, University of Science and Technology of China, Hefei 230001, Anhui, China*

Correspondence should be addressed to Kai Li; kli@ahjzu.edu.cn

Received 8 January 2021; Revised 28 January 2021; Accepted 3 February 2021; Published 16 February 2021

Academic Editor: Sundarapandian Vaidyanathan

Self-sustained oscillation has the advantages of harvesting energy from the environment and self-control, and thus, the development of new self-oscillating systems can greatly expand its applications in active machines. In this paper, based on conventional photothermal shrinkable material or photothermal expansive material, a simple pendulum is proposed. The light-powered self-sustained oscillation of the simple pendulum is theoretically studied by establishing a dynamic model of the photothermal-responsive pendulum. The results show that there are two motion modes of the simple pendulum, which are the static mode and the oscillation mode. Based on the photothermal-responsive model, this paper elucidates the mechanism of the self-excited oscillation. The condition for triggering self-excited oscillation is further studied. In addition, the influence of the system parameters on the amplitude and frequency is also obtained. This study may have potential applications in energy harvesting, signal monitoring, and soft machines.

1. Introduction

Photothermal-responsive materials exhibit photothermal effects under light illumination, which results in some macroscopic changes, such as shape change and color change. Due to the advantages of light stimulus, such as environmentally friendly, remote controllability, and instantaneity, photothermal-responsive materials have attracted many researchers' attention. Suzuki and Tanaka [1] introduced the photosensitive component chlorophyll in the gel and designed a light-sensitive gel. The temperature of the illuminated gel increases and the gel shrinks. Hu et al. [2] found that PNIPAM gel will reduce the transmittance of visible laser light when infrared radiation makes the gel locally heated up. Kubo et al. [3] filled silicon dioxide inverse opal with liquid crystal molecules and made a device that changes the color of reflected light caused by the light response.

Photothermal-responsive materials with reasonable design can produce photo-induced deformation and motion for a variety of flexible intelligent actuators, which have wide application prospects in the fields of artificial muscles [4], retractable optical devices [5], light-driven microbionic propellers [6–8], light-powered microfluidic pump [9], light-fueled microgenerator [10], and so on. Ikeda et al. [11] used alternating ultraviolet and visible light to achieve *cis-trans* isomer photomechanical actuation of liquid crystal elastomers containing azobenzene. Carbon nanotubes, graphene, and graphene oxide have good photothermal effects, which can convert near-infrared light and visible light into heat [12–15]. They can be used as nanoheaters to generate local heat and cause conformational modification or phase transition of elastomer matrix [15–18] to realize light-powered motions.

Self-excited oscillations have been observed in many fields of science and engineering [19–23] and can be utilized to produce periodic motions which are often required in numerous engineering applications [24–28]. Different from the forced vibration with damping dissipation, which often applies periodic stimulus to cause periodic vibration, the self-excited oscillation utilizes the nonlinear feedback within the system to result in and maintain steady-state periodic

motions, such as the flapping of leaves under the breeze, the peristalsis of the digestive tract, the periodic beating of the heart, and the beautiful music produced by the violin bow. Under the steady environment, the self-excited oscillation system takes its own motion state as the regulator to balance the input energy and the dissipated energy, so as to realize the continuous periodic motion. The characteristics of the self-excited oscillation system, such as frequency and amplitude, are often determined by the physical and geometrical parameters of the system and have nothing to do with the initial conditions. The particularity of the self-excited oscillation arouses the interest of researchers and has been applied in robots and other fields. Xu et al. [24] have carried out dynamic simulation for a woodpecker robot running under friction and collision. Ono et al. [25] studied the mechanism of achieving steady walking motion of a self-oscillating bipedal knee robot. Morazzani et al. [26] proposed a new type of self-excited three-legged walking robot. According to the principle of bionics, Li et al. [27] proposed a pipeline crawling microrobot based on the self-excited oscillation. Yamano et al. [28] constructed a multilink adaptive control swimming robot model, which can generate different self-excited oscillations according to the change of environment, so as to change the motion mode.

Recently, the self-excited oscillation of optomechanical oscillators has been extensively explored and applied in macrodevices [29], microdevices [30], and nanodevices [31]. There exist various self-excited periodic motions in systems dominated by photothermal effects [32, 33]. With the in-depth study of photothermal-responsive materials, more progress has been made in the study of self-excited oscillation based on photothermal-responsive materials. Hollander et al. [34] studied a nonlinear thermoviscoelastic cantilever coated with a light-absorbing film. The self-excited oscillation of the cantilever is triggered by the photothermal effect. Dirk J. Gelebart's research group [35] added light-absorbing dyes to liquid crystal network polymers and prepared a continuous oscillating composite film by the photothermal effect. Houri et al. [36] irradiate the graphene barrel with a red continuous wave laser beam, and it oscillates autonomously by photothermal feedback. Buks and Martin [37] studied a fully on-fiber optomechanical cavity which was formed by patterning a suspended metallic mirror near the tip of an optical fiber and by introducing a static reflector inside the fiber and characterized its performance as a sensor. Optically induced self-excited oscillation is observed above a threshold value of the injected laser power.

Although some self-excited oscillations of photothermal-responsive materials and their applications have been studied, the modes of self-excited oscillation are not enough, which limits the potential applications of self-excited oscillation. In this paper, a simple pendulum is constructed by using conventional photothermal expansive material (PEM) or photothermal shrinkable material (PSM) as a cycloid, and the governing equation of variable pendulum length is established based on the photothermal effect. Through numerical calculation, it is verified that the photothermal-responsive pendulum can realize self-excited oscillation under steady light illumination. The mechanism of self-excited oscillation is elucidated, the conditions for realizing self-excited oscillation are discussed, and the dependence of amplitude and frequency on system parameters is extensively studied.

2. Theoretical Model and Formulation

2.1. Governing Equations for Dynamics of the Simple Pendulum. The dynamic model and governing equations of a photothermal-responsive pendulum under steady illumination are established in this section. As shown in Figure 1, a simple pendulum made of photothermal-responsive materials is established and illuminated steadily. The end of the cycloid made of photothermal-responsive material with negligible mass is tied to a fixed point O. A pendulum ball with mass m is suspended by the cycloid. By establishing a polar coordinate system, the position of a simple pendulum can be expressed by pendulum length r and swing angle θ. During the motion of the pendulum, the length r and swing angle θ of the pendulum both vary with the time. In the polar coordinate system, two mutually perpendicular unit vectors $\mathbf{e}_r$ and $\mathbf{e}_\theta$ are along the directions of increasing pendulum length and pendulum angle, respectively, and they also change during the swing of the pendulum.

To obtain the self-excited motion, a PSM pendulum should be illuminated in the middle zone as shown in Figure 1(a), while a PSE pendulum should be illuminated on the two sides as shown in Figure 1(b), where the angle φ denotes the illuminated zone or dark zone in the middle. For the two pendulum systems in Figure 1, the cycloid gradually shrinks when it is in the middle zone, while gradually expands when it swings out of the middle zone. Eventually, the pendulum could swing continuously as discussed as follows.

In the polar coordinate system, the velocity and acceleration of the pendulum along the directions $\mathbf{e}_\theta$ and $\mathbf{e}_r$ are as follows:

$$\begin{aligned} v_\theta &= r\dot{\theta}, \\ a_\theta &= r\theta + 2\dot{r}\dot{\theta}, \\ v_r &= \dot{r}, \\ a_r &= r - r\dot{\theta}^2, \end{aligned} \tag{1}$$

where $\dot{r}$ and $\ddot{r}$ are the first derivative $\mathrm{d}r/\mathrm{d}t$ and the second derivative $\mathrm{d}^2r/\mathrm{d}t^2$, respectively, and $\dot{\theta}$ and $\ddot{\theta}$ are the first derivative $\mathrm{d}\theta/\mathrm{d}t$ and the second derivative $\mathrm{d}^2\theta/\mathrm{d}t^2$, respectively.

As shown in Figure 1, mg is the gravity of the pendulum, F is the tension of the cycloid, and F_θ and F_r are the components of the air damping force in $\mathbf{e}_\theta$ and $\mathbf{e}_r$ directions, respectively. Since the fiber is generally much thinner than the pendulum ball, the air damping force of the fiber is ignored for simplicity. It is assumed that the air damping force of the pendulum is proportional to the velocity of the ball, and the direction is opposite to the velocity of the ball. The governing equation for the dynamic of the pendulum can be given as

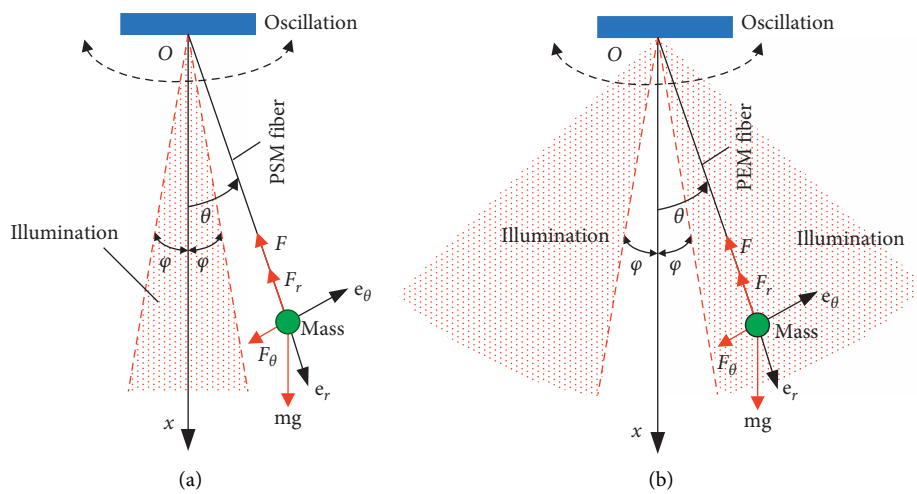

Figure 1: Schematics of the light-driven swing of a photothermal-responsive pendulum based on (a) PSM cycloid and (b) PEM cycloid.

$$m(r\ddot{\theta} + 2\dot{r}\dot{\theta}) = -\mathrm{mg}\sin\theta - \beta\dot{\theta}r,$$
$$m\left(\ddot{r} - r\dot{\theta}^2\right) = \mathrm{mg}\cos\theta - \beta\dot{r} - F, \tag{2}$$

where β is the linear air damping coefficient. To study the light-powered motion of a simple pendulum with the photothermal response and its mechanism, equation (2) is rewritten as

$$\ddot{\theta} = -\left(\frac{2\dot{r}}{r} + \frac{\beta}{m}\right)\dot{\theta} - \frac{g}{r}\sin\theta,$$
$$F = \mathrm{mg}\cos\theta - \beta\dot{r} - m\left(\ddot{r} - r\dot{\theta}^2\right). \tag{3}$$

2.2. Model of the Photothermal-Responsive Pendulum. This section mainly describes the dynamics of temperature and length of the photothermal-responsive pendulum under stable light illumination and in dark. Since the simple pendulums made with PSM and PEM in Figure 1 have the same photothermal effect, in the following, the simple pendulum of PSM in Figure 1(a) is chosen as the representative of the photothermal-responsive pendulum.

The cycloid of the pendulum has a very small radius, i.e., the well-known Biot number is very small. Therefore, heat exchange in the pendulum is assumed to be very fast and the temperature in the pendulum is homogeneous. Due to the photothermal effect, the pendulum can convert light illumination into heat. The heat converted from light per second is denoted by q. The pendulum can also exchange heat with the environment, and the heat flux is assumed to be linear to the temperature difference T between the pendulum and the environment. Under light illumination, the temperature difference T is determined by

$$\dot{T} = \frac{q - kT}{\rho_c}, \tag{4}$$

where ρ_c is the specific heat capacity and k is the heat transfer coefficient. By solving equation (4), in the illumination zone, the temperature difference T is

$$T = T_0\left(1 - e^{-t/\tau}\right), \tag{5}$$

while in the dark zone, i.e., $q = 0$, the temperature difference T is

$$T = T_0 e^{-t/\tau}, \tag{6}$$

where $T_0 = q/k$ represents the limit temperature difference of photothermal-responsive fiber under longtime illumination, $\tau = \rho_c/k$ reflects the characteristic time for heat exchange between photothermal-responsive fiber and environment, and the larger τ indicates the longer time required for attaining the limit temperature difference T_0 of the photothermal-responsive fiber.

Deformation of the photothermal-responsive pendulum can be driven by the temperature change, and the thermal strain of the fiber is assumed to be linear to the temperature change. The elastic modulus is assumed to be very large, and the elastic strain is ignored. Therefore, the length of the PSM fiber can be calculated as, in the illumination zone:

$$r = r_0\left[1 - \alpha T_0\left(1 - e^{-t/\tau}\right)\right], \tag{7}$$

in the dark zone:

$$r = r_0\left(1 - \alpha T_0 e^{-t/\tau}\right), \tag{8}$$

where r_0 is the origin length of the PSM fiber without thermal strain and α is the linear thermal contraction coefficient of the PSM fiber.

2.3. Nondimensionalization. To nondimensionalize the governing equations above, we introduce the following dimensionless parameters: $\bar{t} = t/\tau$, $\bar{T} = T/T_0$, $\bar{r} = r/r_0$, $\varepsilon_0 = \alpha T_0$, $\bar{\beta} = \beta\tau/m$, $\bar{g} = g\tau^2/r_0$, and $\bar{F} = F\tau^2/mr_0$. Here, ε_0 is the contraction strain of the photothermal-responsive cycloid at the limit temperature difference T_0, and $\bar{\beta}$ reflects the

air damping. $\overline{g}$ can be rewritten as $\overline{g} = (\tau/\tau_0)^2$ by the natural period $\tau_0 = \sqrt{r_0/g}$ of the single pendulum, so it represents the speed of heat transfer relative to natural oscillation. The larger $\overline{g}$ is, the faster the heat transfers. The dimensionless parameter $\overline{F}$ characterizes the tension of the photothermal-responsive cycloid. Then, equations (5)–(8) can also be rewritten as, in the illumination zone, i.e., $-\varphi \le \theta \le \varphi$.

$$\begin{aligned} \overline{T} &= 1 - e^{-\overline{t}}, \\ \overline{r} &= 1 - \varepsilon_0\left(1 - e^{-\overline{t}}\right). \end{aligned} \tag{9}$$

in the dark zone, i.e., $\theta < -\varphi$ or $\theta > \varphi$:

$$\begin{aligned} \overline{T} &= e^{-\overline{t}}, \\ \overline{r} &= 1 - \varepsilon_0 e^{-\overline{t}}. \end{aligned} \tag{10}$$

The following differential equation is introduced:

$$\begin{aligned} \dot{r} &= \frac{\mathrm{d}r}{\mathrm{d}t} = \frac{1}{\tau}\frac{\mathrm{d}r}{\mathrm{d}\overline{t}} = \frac{\dot{\overline{r}}}{\tau}, \\ r &= \frac{\mathrm{d}^2 r}{\mathrm{d}t^2} = \frac{\ddot{\overline{r}}}{\tau^2}. \end{aligned} \tag{11}$$

By inserting equations (9)–(11), equation (3) can be derived as, in the illumination zone, i.e., $-\varphi \le \theta \le \varphi$:

$$\begin{aligned} \frac{\mathrm{d}^2\theta}{\mathrm{d}\overline{t}^2} &= \left[\frac{2\varepsilon_0 e^{\overline{t}}}{1 - \varepsilon_0\left(1 - e^{\overline{t}}\right)} - \overline{\beta}\right]\frac{\mathrm{d}\theta}{\mathrm{d}\overline{t}} - \frac{\overline{g}}{1 - \varepsilon_0\left(1 - e^{\overline{t}}\right)}\sin\theta, \\ \overline{F} &= \overline{g}\cos\theta + \overline{\beta}\varepsilon_0 e^{-\overline{t}} - \varepsilon_0 e^{-\overline{t}} + \left[1 - \varepsilon_0\left(1 - e^{-\overline{t}}\right)\right]\left(\frac{\mathrm{d}\theta}{\mathrm{d}\overline{t}}\right)^2, \end{aligned} \tag{12}$$

in the dark zone, i.e., $\theta < -\varphi$ or $\theta > \varphi$:

$$\begin{aligned} \frac{\mathrm{d}^2\theta}{\mathrm{d}\overline{t}^2} &= \left[\frac{-2\varepsilon_0 e^{\overline{t}}}{1 - \varepsilon_0 e^{\overline{t}}} - \overline{\beta}\right]\frac{\mathrm{d}\theta}{\mathrm{d}\overline{t}} - \frac{\overline{g}}{1 - \varepsilon_0 e^{\overline{t}}}\sin\theta, \\ \overline{F} &= \overline{g}\cos\theta - \overline{\beta}\varepsilon_0 e^{-\overline{t}} + \varepsilon_0 e^{-\overline{t}} + \left(1 - \varepsilon_0 e^{-\overline{t}}\right)\left(\frac{\mathrm{d}\theta}{\mathrm{d}\overline{t}}\right)^2. \end{aligned} \tag{13}$$

2.4. Solution Method. The second-order differential equations (12) and (13) provide a complete description of the dynamics of the photothermal-responsive pendulum. The swing angle θ can be obtained by the first equation in equation (13), and then, the pendulum force $\overline{F}$ can be further obtained by the second equation in equation (13). It is very challenging to obtain an analytical solution to equation (13). In this paper, we will numerically solve the swing of the pendulum based on the well-known fourth-order Runge–Kutta method. By letting $\psi = \dot{\theta}$, the second-order ordinary differential equation (13) is transformed into a first-order differential equation system as follows:

$$\frac{\mathrm{d}\theta}{\mathrm{d}\overline{t}} = \psi, \tag{14}$$

in the illumination zone, i.e., $-\varphi \le \theta \le \varphi$:

$$\frac{\mathrm{d}\psi}{\mathrm{d}\overline{t}} = \left[\frac{2\varepsilon_0 e^{\overline{t}}}{1 - \varepsilon_0\left(1 - e^{\overline{t}}\right)} - \overline{\beta}\right]\psi - \frac{\overline{g}}{1 - \varepsilon_0\left(1 - e^{\overline{t}}\right)}\sin\theta, \tag{15}$$

in the dark zone, i.e., $\theta < -\varphi$ or $\theta > \varphi$:

$$\frac{\mathrm{d}\psi}{\mathrm{d}\overline{t}} = \left[\frac{-2\varepsilon_0 e^{\overline{t}}}{1 - \varepsilon_0 e^{\overline{t}}} - \overline{\beta}\right]\psi - \frac{\overline{g}}{1 - \varepsilon_0 e^{\overline{t}}}\sin\theta. \tag{16}$$

The initial conditions are $\theta|_{\overline{t}=0} = \theta_0$ and $\psi|_{\overline{t}=0} = \dot{\theta}_0$. Given the dimensionless parameters φ, $\overline{\beta}$, ε_0, and $\overline{g}$, the solution to equations (14)–(16) can be obtained numerically by programming in software *Matlab*. When the angle $\theta(\overline{t})$ and the angular velocity $\dot{\theta}(\overline{t})$ of the simple pendulum are obtained, $\overline{T}(\overline{t})$, $\overline{r}(\overline{t})$, and $\overline{F}(\overline{t})$ can be further calculated.

3. Two Motion Modes and Mechanism of the Self-Excited Oscillation

3.1. Two Motion Modes. By setting the parameters θ_0, $\dot{\theta}_0$, φ, $\overline{\beta}$, ε_0, and $\overline{g}$, the time histories and phase diagrams of the light-powered swing of the pendulum can be obtained. The numerical calculation shows that there exist two motion modes of the simple pendulum: static mode and oscillation mode, as shown in Figure 2. In the computation, we set $\theta_0 = 0$, $\dot{\theta}_0 = 0.2$, $\varphi = 0.1$, $\overline{\beta} = 0.12$, and $\overline{g} = 2$. For $\varepsilon_0 = 0$, the pendulum with initial angular velocity first swings, and then, the amplitude of swing gradually decreases under the air damping, as shown in Figures 2(a) and 2(b). Eventually, the pendulum comes to cease at the middle, which is named as static mode. Although the pendulum is illuminated and the cycloid temperature rises, the pendulum length for $\varepsilon_0 = 0$ will not change and cannot convert light energy into kinetic energy. For $\varepsilon_0 = 0.3$, the pendulum under light illumination can swing continuously and finally develops into self-sustained oscillation, which is named as oscillation mode (Figures 2(c) and 2(d)). Although there is damping in the system, the energy compensation from the light maintains the oscillation. In the following section, we further explore the mechanism of self-excited oscillation and in detail elucidate how the light energy converts into kinetic energy.

3.2. Mechanism of the Self-Excited Oscillation. To explore the mechanism of self-excited oscillation, the evolution laws of the temperature and length of the cycloid are first studied. Based on equations (9) and (10), Figure 3 plots the evolution law of $\overline{T}$ and $\overline{r}$ during swing in the illumination zone and the dark zone. As shown in Figure 3(a), the temperature of cycloid increases under continuous illumination, and the dimensionless temperature difference parameter $\overline{T}$ can gradually increase from 0 to nearly 1. In the dark zone, $\overline{T}$ can gradually decrease from the maximum value of 1 to 0. When the pendulum passes through the interface of the illumination and dark zones, the temperature of the cycloid will

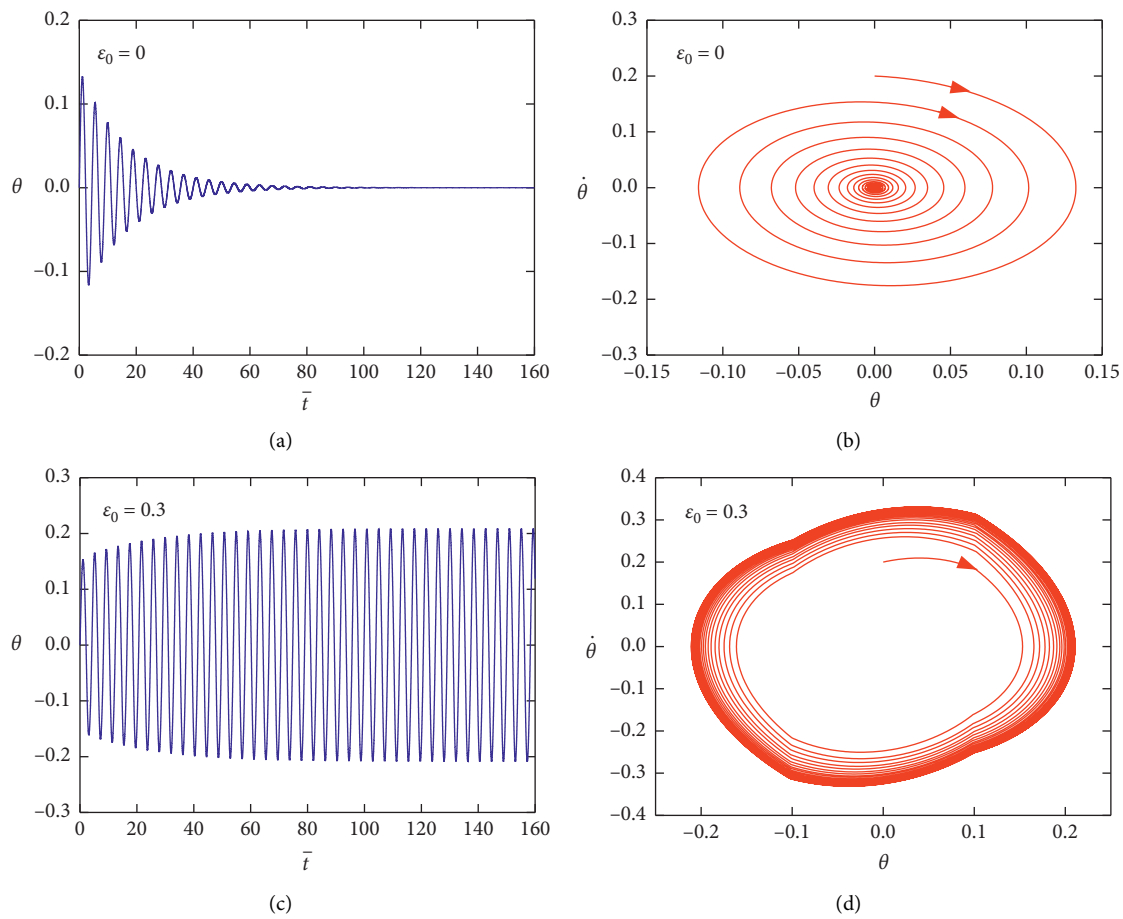

FIGURE 2: Time histories and phase diagrams of two motion modes of the pendulum: (a, b) the static mode for $\varepsilon_0 = 0$; (c, d) the oscillation mode for $\varepsilon_0 = 0.3$.

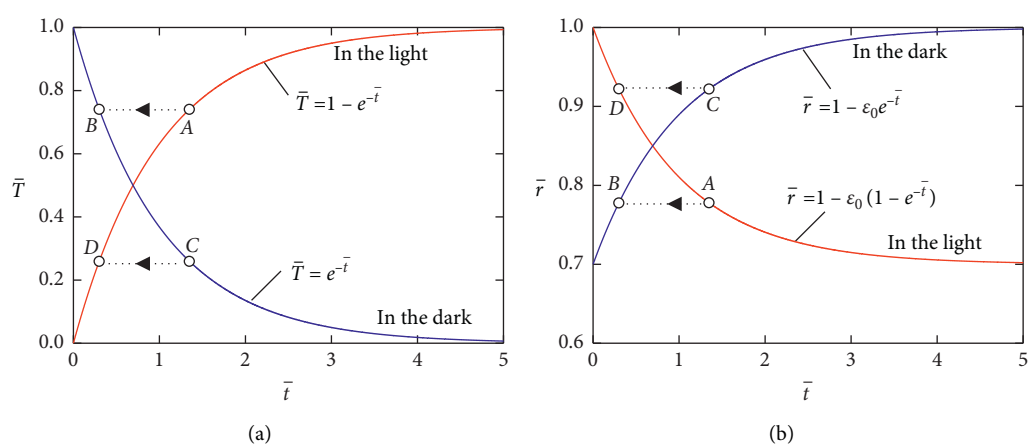

FIGURE 3: Evolution laws of (a) $\overline{T}$ and (b) $\bar{r}$ of the PSM pendulum.

switch to obeying the other evolution law, i.e., from point A to point B or from point C to point D as shown in Figure 3(a). Similarly, the evolution law of the dimensionless parameter $\bar{r}$ for $\varepsilon_0 = 0.3$ in Figure 3(b) shows that the pendulum length $\bar{r}$ contracts into $1 - \varepsilon_0$ in the illumination zone, while recovers gradually to 1 in the dark zone. The pendulum length also switches when the pendulum passes through the interface between the illumination and dark zones.

Based on the evolution law in Figure 3, the mechanism of the self-excited oscillation in Figure 2(b) can be elucidated by investigating the time histories of $\overline{T}$ and $\bar{r}$ in detail. Figure 4(a) plots the dependence of the dimensionless temperature difference parameter $\overline{T}$ on the swing angle θ.

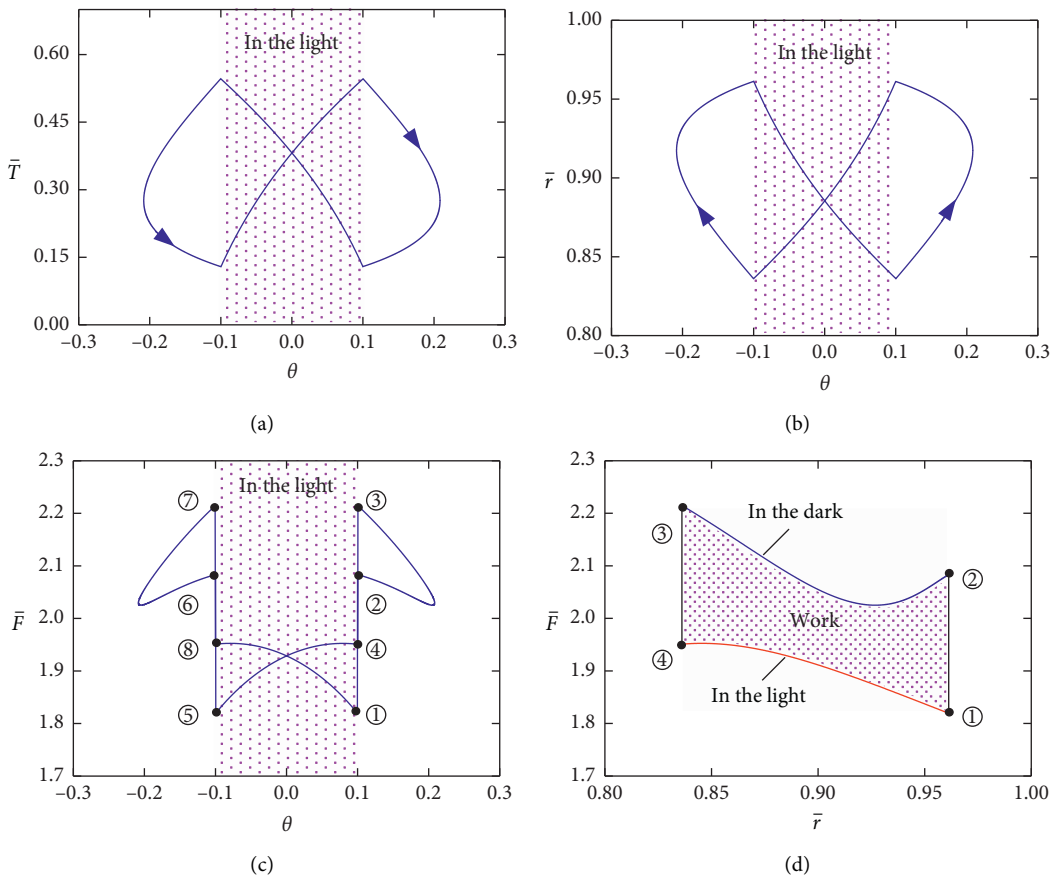

Figure 4: Mechanism of self-excited oscillation of the PSM pendulum, for $\theta_0 = 0$, $\dot{\theta}_0 = 0.2$, $\varphi = 0.1$, $\overline{\beta} = 0.12$, $\varepsilon_0 = 0.3$, and $\overline{g} = 2$. (a) $\overline{T}$ vs. θ. (b) $\overline{r}$ vs. θ. (c) $\overline{F}$ vs. θ. (d) $\overline{F}$ vs. $\overline{r}$.

For $-0.1 \le \theta \le 0.1$, the cycloid is in the illumination zone and $\overline{T}$ increases. When the pendulum swings into the dark zone, $\overline{T}$ decreases. Similarly, Figure 4(b) plots the dependence of $\overline{r}$ on θ. The length $\overline{r}$ decreases in the illumination zone, while it increases in the dark zone. Further, Figure 4(c) plots the dependence of $\overline{F}$ on θ, where $\overline{F}$ is discontinuous at some points of θ. The tension $\overline{F}$ sharply increases at the moment of swinging into the dark region (point ②) from the illumination region (point ①). This is because the temperature of the pendulum swinging into the dark zone decreases and in turn the cycloid length increases. As the pendulum swings in the dark area, $\overline{F}$ continuously varies from point ② to ③. Then, the tension $\overline{F}$ sharply decreases from point ③ to point ④ when the pendulum reenters into the illumination zone. Eventually, tension $\overline{F}$ and swing angle θ form a symmetrical closed loop according to the trajectory cycle of ①②③④⑤⑥⑦⑧① in a swing period.

Based on Figures 4(a)–4(c), Figure 4(d) plots the dependence of $\overline{F}$ with $\overline{r}$, where the shadow area enclosed by curve of $\overline{F}$ with $\overline{r}$ represents the magnitude of the work done by the tension $\overline{F}$ in a half swing period of the simple pendulum. In an oscillation period, the work done by $\overline{F}$ is twice shadow area in Figure 4(d), which is the source of self-excited oscillation. When the net work is enough for compensating the dissipation by air damping, the pendulum can oscillate continuously.

4. Influence of Systematic Parameters on the Self-Excited Oscillation

In equations (15) and (16), there are six dimensionless parameters: φ, $\overline{\beta}$, ε_0, $\overline{g}$, θ_0, and $\dot{\theta}_0$. The swing of the PSM pendulum in Figure 1(a) is controlled by the above six parameters. In this section, the influence of the six parameters on the onset, frequency, and amplitude of the self-excited oscillation is extensively investigated. Considering the parameter θ_0 can be transformed into the corresponding value $\dot{\theta}_0$ through the energy transformation between gravitational energy and kinetic energy, θ_0 is set to be zero in the calculation. The dimensionless oscillation frequency $\overline{f}$ of the simple pendulum is defined as the number of oscillations per unit time $\overline{t}$, and the angular amplitude of the self-excited oscillation of the simple pendulum is denoted by A.

4.1. Effect of Initial Angular Velocity $\dot{\theta}_0$. Figure 5 shows the influence of the initial angular velocity $\dot{\theta}_0$ on the swing of the simple pendulum, for $\theta_0 = 0$, $\varphi = 0.1$, $\overline{\beta} = 0.12$, $\varepsilon_0 = 0.3$, and $\overline{g} = 2$. Figure 5(a) plots the phase diagram of the swing angle for $\dot{\theta}_0 = 0.12$. The result shows that the simple pendulum swings with gradually attenuating amplitude and eventually comes to rest, which is static mode. The maximum swing angle $\theta_{\max}$ of simple pendulum is less than φ in the initial

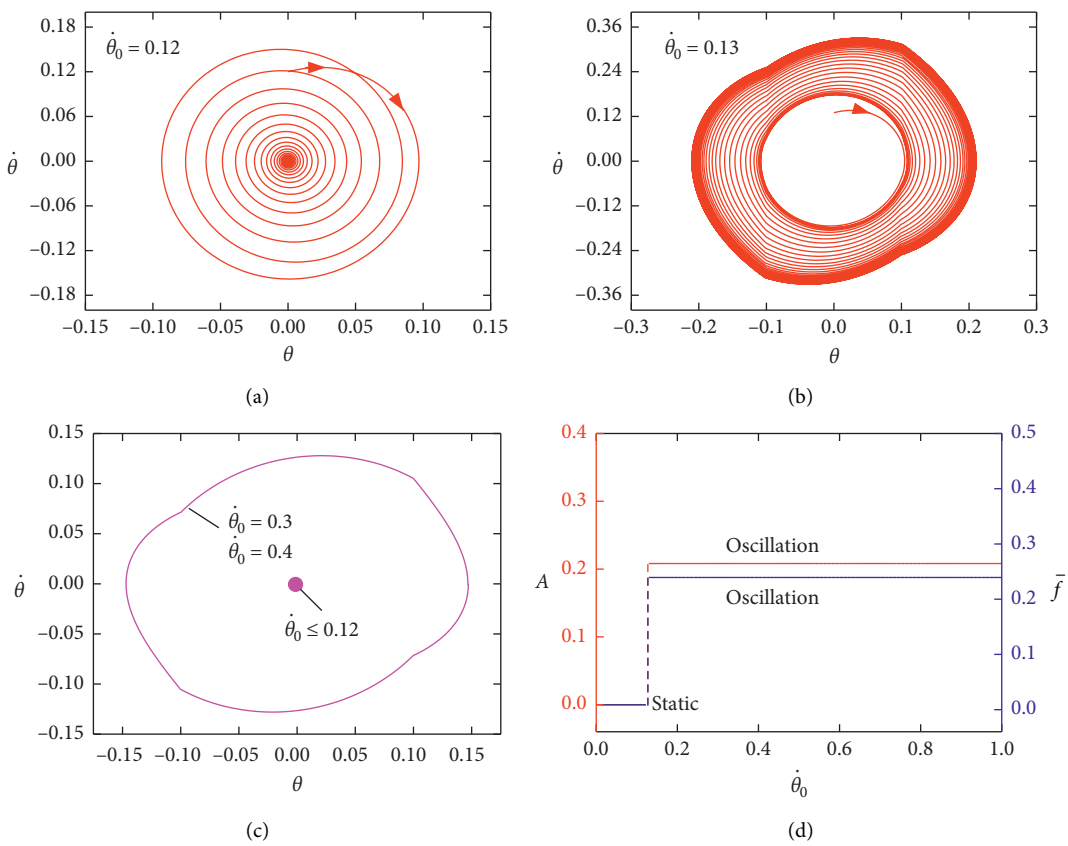

Figure 5: The effect of $\dot{\theta}_0$ on the swing of the simple pendulum, for $\theta_0 = 0$, $\varphi = 0.1$, $\overline{\beta} = 0.12$, $\varepsilon_0 = 0.3$, and $\overline{g} = 2$. (a) Phase diagram of the static mode for $\dot{\theta}_0 = 0.12$. (b) Phase diagram of the oscillation mode for $\dot{\theta}_0 = 0.13$. (c) Limit cycles. (d) Amplitude and frequency.

stage of vibration, i.e., the pendulum is always in the illumination region. Therefore, the pendulum length $\overline{r}$ decreases continuously and approaches the value of $1 - \varepsilon_0$. Figure 5(b) plots the phase diagram of the swing angle for $\dot{\theta}_0 = 0.13$. The result shows that the amplitude of the single pendulum first increases and then asymptotically approaches a fixed value, which is oscillation mode. As explained previously, the single pendulum absorbs light autonomously during alternately swinging between the illumination and dark zones, which results in self-excited oscillation of the simple pendulum. Figure 5(c) plots the limit cycles, in which there exists a critical $\dot{\theta}_0 = 0.12$ for transition between static mode and oscillation mode.

Figure 5(d) plots the frequency and amplitude of self-excited oscillation for different $\dot{\theta}_0$, respectively. For $\dot{\theta}_0 > 0.12$, the frequency and amplitude are both zero because the pendulum is in static mode. For $\dot{\theta}_0 < 0.12$, the frequency and amplitude of light-powered self-excited oscillation are the same and independent on $\dot{\theta}_0$. These results mean that the initial state affects the onset of the oscillation mode, while does not affect the frequency and amplitude of the oscillation. This is consistent with the general characteristic of self-excited motions [38].

4.2. Effect of Illumination Zone. Figure 6 shows the influence of the angle φ of the illumination zone on the swing of the simple pendulum, for $\theta_0 = 0$, $\dot{\theta}_0 = 0.2$, $\varepsilon_0 = 0.3$, $\overline{\beta} = 0.12$, and $\overline{g} = 2$. Figure 6(a) plots the phase diagram of the swing angle of the pendulum, for $\varphi = 0.154$. Initially, the maximum swing angle of the simple pendulum is larger than φ, and then, the simple pendulum swings with increasing amplitude alternately in the illuminated zone and the dark zone. The result shows that the oscillation mode of the pendulum is triggered. Figure 6(b) plots the phase diagram of the swing angle of the pendulum, for $\varphi = 0.155$. The amplitude of the simple pendulum decreases continuously and the pendulum eventually comes to cease. This is because the pendulum with φ larger than the maximum swing angle is always in the illumination zone and gradually develops into static mode. Figure 6(c) plots the limit cycles, in which there also exists a critical φ for the phase transition between static mode and oscillation mode, which is numerically determined to be 0.154.

Figure 6(d) plots the frequency and amplitude of self-excited oscillation for different φ values, respectively. For $\varphi > 0.154$, the frequency and amplitude are both zero because the pendulum is in static mode. For $\varphi < 0.154$, the frequency of light-powered self-excited oscillation is the same and independent on φ, while the amplitude is proportional to φ. These results mean that the illuminated zone affects the amplitude of the oscillation mode, while it does not affect the frequency of the oscillation. The result can be understood by the energy competition between energy input and damping dissipation. The increasing illuminated area

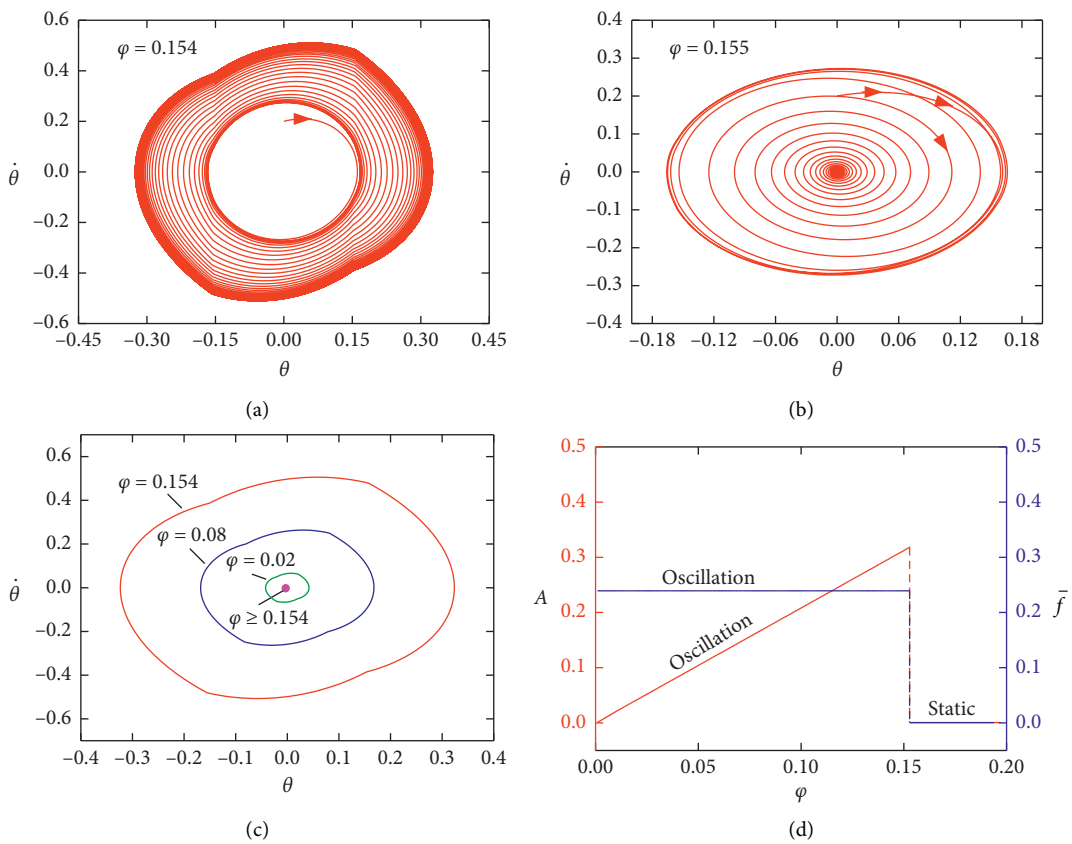

Figure 6: The effect of φ on the swing of the pendulum, for $\theta_0 = 0$, $\dot{\theta}_0 = 0.2$, $\overline{\beta} = 0.12$, $\varepsilon_0 = 0.3$, and $\overline{g} = 2$. (a) Phase diagram of the oscillation mode for $\varphi = 0.154$. (b) Phase diagram of the static mode for $\varphi = 0.155$. (c) Limit cycles. (d) Amplitude and frequency.

amplifies the energy input and in turn enlarges the amplitude of the oscillation.

4.3. Effect of Damping Coefficient $\overline{\beta}$. Figure 7 shows the influence of $\overline{\beta}$ on the swing of the simple pendulum, for $\theta_0 = 0$, $\dot{\theta}_0 = 0.2$, $\varphi = 0.1$, $\varepsilon_0 = 0.3$, and $\overline{g} = 2$. Figure 7(a) plots the phase diagram of the swing angle of the pendulum, for $\overline{\beta} = 0.15$. The result shows that the self-excited oscillation of the pendulum is triggered. For $\overline{\beta} = 0.17$, the pendulum develops into static mode, as shown in Figure 7(b). These results can be understood by the energy competition between energy input and damping dissipation. With the increase of $\overline{\beta}$, the heat exchange between pendulum and environment becomes slower, and the net energy input during the swing decreases. Once the net energy input is not enough for compensating the damping dissipation, the pendulum will come to cease. Figure 7(c) plots the limit cycles, in which there also exists a critical $\overline{\beta}$ for the transition between static mode and oscillation mode, which is numerically determined to be 0.17.

For small $\overline{\beta}$, the amplitude calculated may be larger than $\pi/2$, i.e., the simple pendulum may rotate or the tension of the cycloid is negative, which is beyond the scope of this paper. Here, $\overline{\beta}$ is chosen as $\overline{\beta} \leq 0.02$. Figure 7(d) plots the frequency and amplitude of self-excited oscillation for different $\overline{\beta}$, respectively. For $\overline{\beta} > 0.17$, the frequency and amplitude are both zero because the pendulum is in static mode. For $\overline{\beta} < 0.17$, the frequency of light-powered self-excited oscillation increases slightly, while the amplitude decreases obviously and gradually approaches the fixed value, with the increase of $\overline{\beta}$. The result can also be understood by the energy competition between energy input and damping dissipation. The increasing $\overline{\beta}$ decreases the energy input and in turn attenuates the amplitude of the oscillation. The result implies that, in order to improve the absorption of light energy by the pendulum, $\overline{\beta}$ can be appropriately reduced for large energy harvesting in engineering.

4.4. Effect of Contraction Coefficient ε_0. Figure 8 shows the influence of ε_0 on the swing of the simple pendulum, for $\theta_0 = 0$, $\dot{\theta}_0 = 0.2$, $\varphi = 0.1$, $\overline{\beta} = 0.12$, and $\overline{g} = 2$. Figure 8(a) plots the phase diagram of the swing angle of the pendulum, for $\varepsilon_0 = 0.22$. The pendulum is in static mode because the small strain of the cycloid cannot provide enough net energy input to compensate the energy dissipation by air damping. Figure 8(b) plots the phase diagram of the swing angle of the pendulum, for $\varepsilon_0 = 0.25$. The result shows that the oscillation mode of the pendulum is triggered. In this case, the light-driven strain can provide enough net energy input for the oscillation. Figure 8(c) plots the limit cycles, in which there also exists a critical ε_0 for the phase transition between static mode and oscillation mode, which is numerically determined to be 0.25.

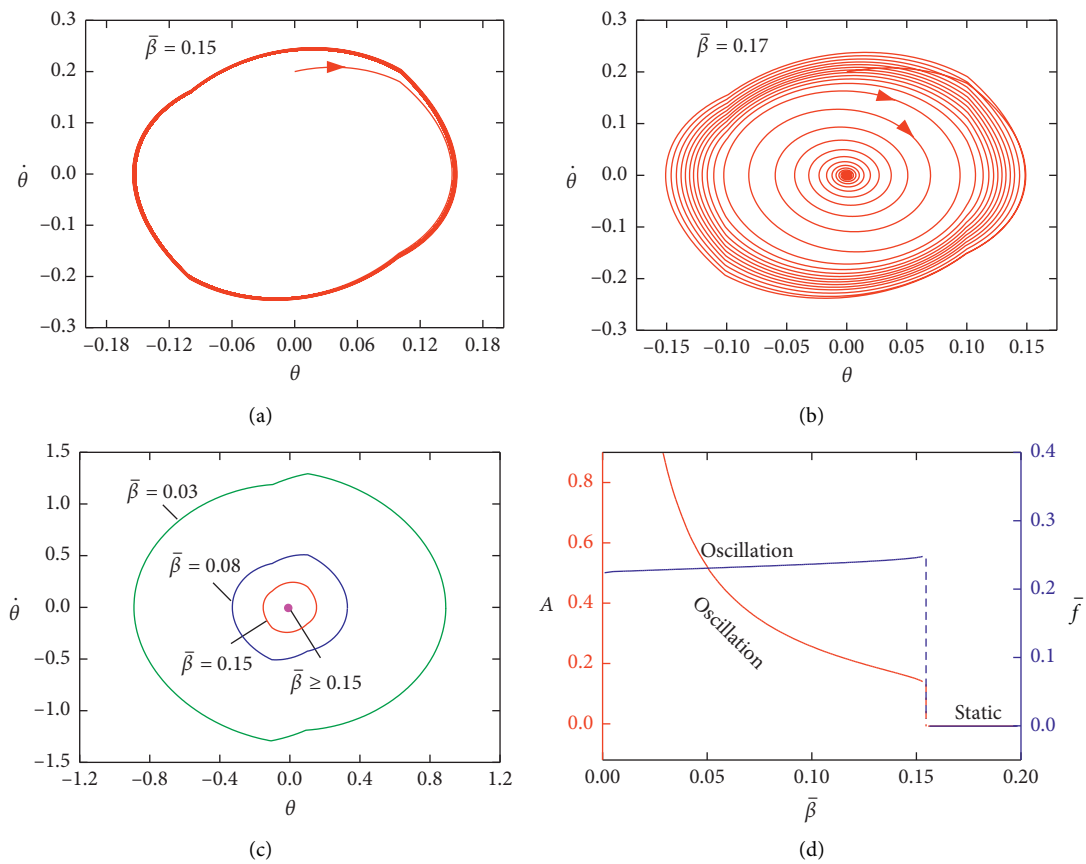

Figure 7: The effect of $\bar{\beta}$ on the swing of the pendulum for $\theta_0 = 0$, $\dot{\theta}_0 = 0.2$, $\varphi = 0.1$, $\varepsilon_0 = 0.3$, and $\bar{g} = 2$. (a) Phase diagram of the oscillation mode for $\bar{\beta} = 0.15$. (b) Phase diagram of the static mode for $\bar{\beta} = 0.17$. (c) Limit cycles. (d) Amplitude and frequency.

For larger ε_0, the pendulum can also oscillate continuously. However, according to the physical meaning of contraction strain ε_0, the maximum value should be smaller than 1. Here, ε_0 is chosen as $0.25 \le \varepsilon_0 \le 0.9$. Figure 8(d) plots the frequency and amplitude of self-excited oscillation for different ε_0, respectively. For $\varepsilon_0 < 0.25$, the frequency and amplitude are both zero because the pendulum is in static mode. For $\varepsilon_0 > 0.25$, the increase of ε_0 has no obvious effect on the self-excited oscillation frequency, while the amplitude increases dramatically with the increase of ε_0. Therefore, in order to improve the engineering application of photothermal-responsive pendulum, light-driven contractile or expansive strain of the material should be amplified for the efficient conversion of light energy to mechanical energy.

4.5. Effect of Gravitational Acceleration $\bar{g}$. Figure 9 shows the influence of $\bar{g}$ on the swing of the simple pendulum, for $\theta_0 = 0$, $\dot{\theta}_0 = 0.2$, $\varphi = 0.1$, $\bar{\beta} = 0.12$, and $\varepsilon_0 = 0.3$. Figure 9(a) plots the phase diagram of the swing angle of the pendulum for $\bar{g} = 0.4$, which is static mode. Figures 9(b) and 9(c) plot the phase diagrams of the swing angle of the pendulum, for $\bar{g} = 0.5$ and $\bar{g} = 4.7$, respectively. The result shows that the oscillation mode of the pendulum is triggered. Careful calculations show that, for $0.4 \le \bar{g} \le 4.7$, the simple pendulum is in oscillation mode. However, for $\bar{g} = 4.8$, the pendulum swings in static mode again, as shown in Figure 9(d). Figure 9(e) also plots the limit cycles of the light-powered swing of the pendulum. The results can be understood by the energy compensation between net energy input and damping dissipation. For small $\bar{g}$, i.e., the heat exchange is too fast, the cycloid rapidly deforms just only when passing through the interface between the illumination and dark zones. For large $\bar{g}$, i.e., the heat exchange is too slow, the cycloid almost does not deform during the swing. Therefore, the net work done of single pendulum by the light is too small and cannot compensate the energy dissipated by air damping to maintain the oscillation.

Figure 9(f) plots the frequency and amplitude of self-excited oscillation of the simple pendulum for $0.4 \le \bar{g} \le 4.7$, respectively. It can be seen that the oscillation frequency and amplitude of the pendulum can be significantly increased by increasing $\bar{g}$. According to the physical meaning of $\bar{g}$, reducing the heat transfer rate within a certain range can amplify the oscillation frequency and amplitude and improve the efficiency of light energy to mechanical energy in engineering application.

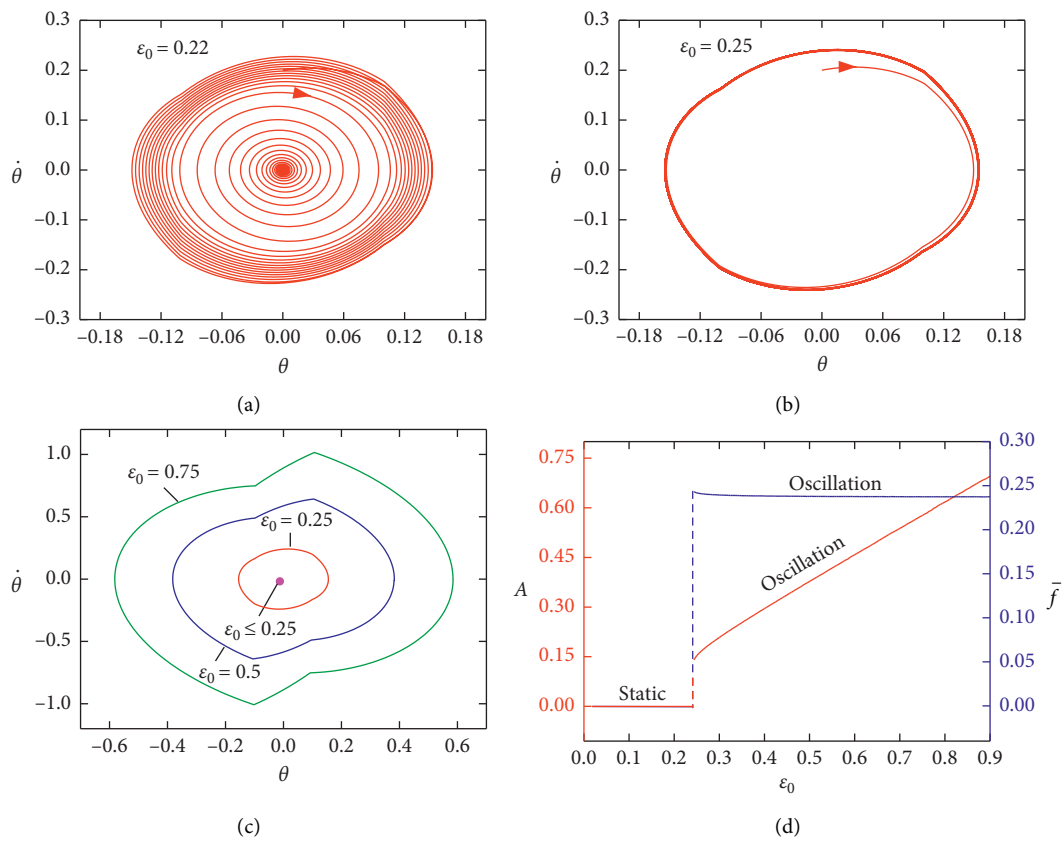

Figure 8: The effect of ε_0 on the swing of the pendulum for $\theta_0 = 0$, $\dot{\theta}_0 = 0.2$, $\varphi = 0.1$, $\overline{\beta} = 0.12$, and $\overline{g} = 2$. (a) Phase diagram of the static mode at $\varepsilon_0 = 0.22$. (b) Phase diagram of the oscillation mode at $\varepsilon_0 = 0.25$. (c) Limit cycles. (d) Amplitude and frequency.

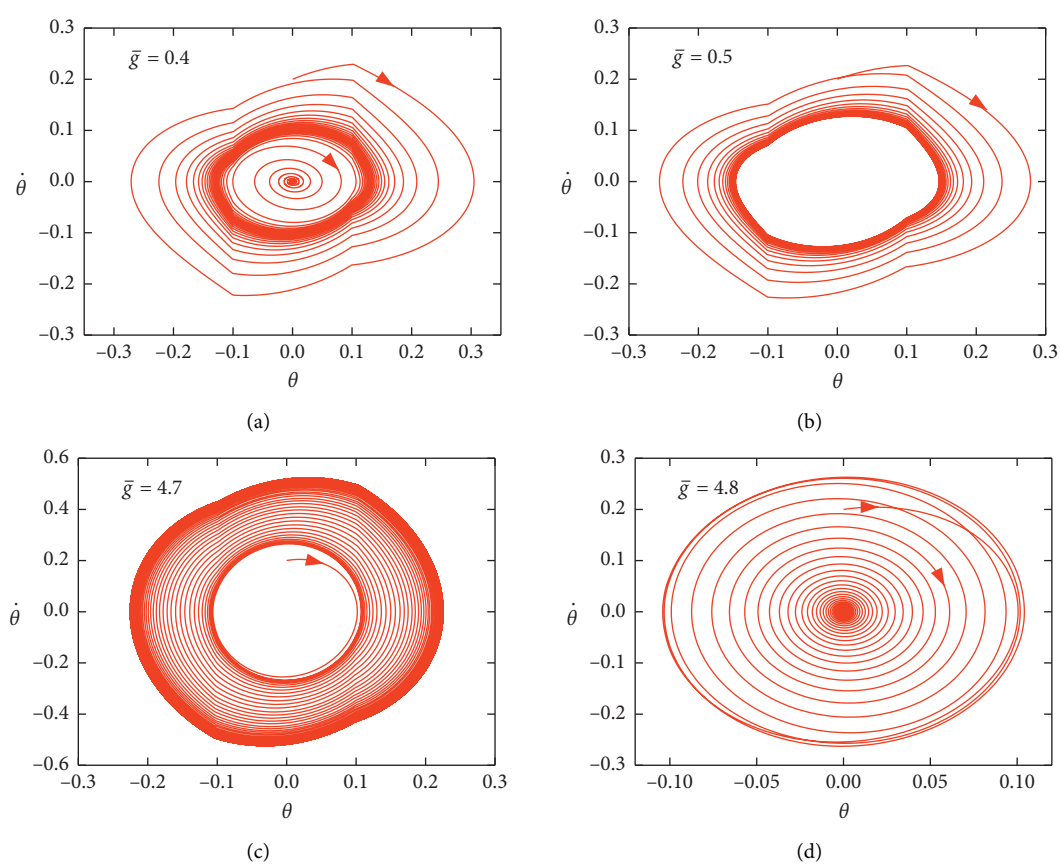

Figure 9: Continued.

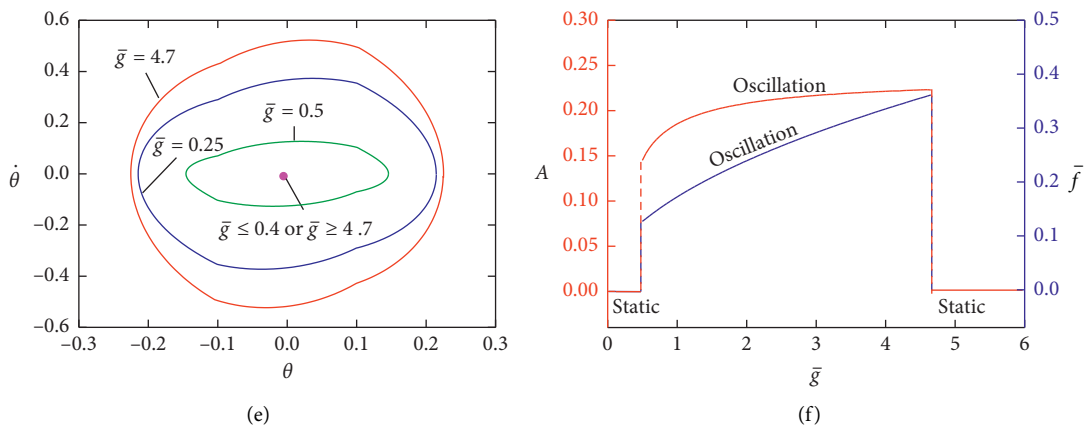

Figure 9: The effect of $\overline{g}$ on the swing of the pendulum for $\theta_0 = 0$, $\dot{\theta}_0 = 0.2$, $\varphi = 0.1$, $\overline{\beta} = 0.12$, and $\varepsilon_0 = 0.3$. (a) Phase diagram of the static mode at $\overline{g} = 0.4$. (b) Phase diagram of the oscillation mode at $\overline{g} = 0.5$. (c) Phase diagram of the oscillation mode at $\overline{g} = 4.7$. (d) Phase diagram of the static mode at $\overline{g} = 4.8$. (e) Limit cycles. (f) Amplitude and frequency.

5. Conclusions

Photothermal-responsive materials can convert light energy into mechanical energy for driving active machines. In this work, a simple pendulum capable of self-excited oscillation is innovatively constructed by using ordinary PSM or PEM as the cycloid, and the dynamic model is established for investigating the light-powered swing of the photothermal-responsive pendulum. By theoretical formulation and numerical calculation, the self-excited oscillation behaviors of the simple pendulum are extensively studied. When the PSM pendulum is irradiated in the central zone of the swing, or conversely the PEM pendulum is illuminated on the two sides of the swing, the simple pendulum could oscillate autonomously. There exist two motion modes of the pendulum, which are static mode and oscillation mode. The numerical calculation provides time histories of the cycloid length and cycloid tension in detail and in turn elucidates the mechanism of self-excited oscillation that results from the coupling of heat exchange, photothermal deformation, and swing. When the net input energy compensates the damping dissipation, the pendulum keeps swinging. This paper further investigates the influence of physical parameters on the self-excited oscillation. The results show that the amplitude of the self-excited oscillation can be effectively increased by increasing the illumination zone, reducing the air damping dissipation, increasing the limit contraction strain of the material, or decreasing the heat transfer rate of the photothermal material, while the frequency of the self-excited oscillation is almost only affected by the heat transfer coefficient of the photothermal-responsive material. Unfortunately, as far as we know, there are no experimental studies in the literature to verify our findings. Next, we do plan to carry out corresponding experiments to further confirm our results. We hope the light-powered self-excited oscillation of photothermal-responsive pendulums can not only deepen the understanding of self-excited oscillations but also have potential applications in harvesting energy, signal sensing, soft robots, and so on.

Data Availability

No data were used to support the findings of this study.

Conflicts of Interest

The authors declare no conflicts of interest.

Acknowledgments

This study was supported by the Outstanding Talents Cultivation Project of Universities in Anhui (Grant no. gxyqZD2019056) and the Key Project of Natural Science Research of Universities in Anhui (Grant nos. KJ2020A0449 and KJ2020A0452).

References

[1] A. Suzuki and T. Tanaka, "Phase transition in polymer gels induced by visible light," *Nature*, vol. 346, no. 6282, pp. 345–347, 1990.

[2] Z. Hu, Y. Li, X. Zhang, and C. L. Littler, "CO_2 laser-controlled transmission of visible light in N-isopropylacrylamide gel," *Polymer Gels and Networks*, vol. 3, no. 3, pp. 267–279, 1995.

[3] S. Kubo, Z.-Z. Gu, K. Takahashi, A. Fujishima, H. Segawa, and O. Sato, "Control of the optical properties of liquid crystal-infiltrated inverse opal structures using photo irradiation and/or an electric field," *Chemistry of Materials*, vol. 17, no. 9, pp. 2298–2309, 2005.

[4] M. H. Li and P. Keller, "Artificial muscles based on liquid crystal elastomers," *Philosophical Transactions of the Royal Society A-Mathematical Physical and Engineering Sciences*, vol. 364, no. 1847, pp. 2763–2777, 2006.

[5] N. J. Dawson, M. G. Kuzyk, J. Neal, P. Luchette, and P. Palffy-Muhoray, "Cascading of liquid crystal elastomer photomechanical optical devices," *Optics Communications*, vol. 284, no. 4, pp. 991–993, 2011.

[6] M. Camacho-Lopez, H. Finkelmann, P. Palffy-Muhoray, and M. Shelley, "Fast liquid-crystal elastomer swims into the dark," *Nature Materials*, vol. 3, no. 5, pp. 307–310, 2004.

[7] C. Huang, J. A. Lv, X. Tian, Y. Wang, Y. Yu, and J. Liu, "Miniaturized swimming soft robot with complex movement

actuated and controlled by remote light signals," *Scientific Reports*, vol. 5, Article ID 17414, 2015.

[8] L. Yu and H. Yu, "Light-powered tumbler movement of graphene oxide/polymer nanocomposites," *ACS Applied Materials & Interfaces*, vol. 7, no. 6, pp. 3834–3839, 2015.

[9] J. A. Rogers, T. Someya, and Y. Huang, "Materials and mechanics for stretchable electronics," *Science*, vol. 327, no. 5973, pp. 1603–1607, 2010.

[10] F. Cheng, R. Yin, Y. Zhang, C.-C. Yen, and Y. Yu, "Fully plastic microrobots which manipulate objects using only visible light," *Soft Matter*, vol. 6, no. 15, pp. 3447–3449, 2010.

[11] T. Ikeda, J.-i. Mamiya, and Y. Yu, "Photomechanics of liquid-crystalline elastomers and other polymers," *Angewandte Chemie International Edition*, vol. 46, no. 4, pp. 506–528, 2007.

[12] S.-H. Hu, R.-H. Fang, Y.-W. Chen, B.-J. Liao, I.-W. Chen, and S.-Y. Chen, "Photoresponsive protein-graphene-protein hybrid capsules with dual targeted heat-triggered drug delivery approach for enhanced tumor therapy," *Advanced Functional Materials*, vol. 24, no. 26, pp. 4144–4155, 2014.

[13] Y. Zeng and J. Q. Lu, "Optothermally responsive nanocomposite generating mechanical forces for cells enabled by few-walled carbon nanotubes," *ACS Nano*, vol. 8, no. 11, pp. 11695–11706, 2014.

[14] Y. Yang, W. Zhan, R. Peng et al., "Graphene-Enabled superior and tunable photomechanical actuation in liquid crystalline elastomer nanocomposites," *Advanced Materials*, vol. 27, no. 41, pp. 6376–6381, 2015.

[15] C. Li, Y. Liu, C.-w. Lo, and H. Jiang, "Reversible white-light actuation of carbon nanotube incorporated liquid crystalline elastomer nanocomposites," *Soft Matter*, vol. 7, no. 16, pp. 7511–7516, 2011.

[16] L. Q. Yang, K. Setyowati, A. Li, Sh. Q. Gong, and J. Chen, "Reversible infrared actuation of carbon nanotube–liquid crystalline elastomer nanocomposites," *Advanced Materials*, vol. 20, no. 12, pp. 2271–2275, 2010.

[17] Y. Ji, Y. Y. Huang, R. Rungsawang, and E. M. Terentjev, "Dispersion and alignment of carbon nanotubes in liquid crystalline polymers and elastomers," *Advanced Materials*, vol. 22, no. 31, pp. 3436–3440, 2010.

[18] J. E. Marshall, Y. Ji, N. Torras, K. Zinoviev, and E. M. Terentjev, "Carbon-nanotube sensitized nematic elastomer composites for ir-visible photo-actuation," *Soft Matter*, vol. 8, no. 5, pp. 1570–1574, 2012.

[19] S. C. Chang, "Stability, chaos detection, and quenching chaos in the swing equation system," *Mathematical Problems in Engineering*, vol. 2020, Article ID 6677084, 12 pages, 2020.

[20] H. Zeng, M. Lahikainen, L. Liu et al., "Light-fuelled freestyle self-oscillators," *Nature Communications*, vol. 10, no. 1, pp. 1–9, 2019.

[21] K. Li, X. Su, and S. Q. Cai, "Self-sustained rolling of a thermally responsive rod on a hot surface," *Extreme Mechanics Letters*, vol. 42, Article ID 101116, 2021.

[22] A. Chakrabarti, G. P. Choi, and L. Mahadevan, "Self-excited motions of volatile drops on swellable sheets," *Physical Review Letters*, vol. 124, no. 25, Article ID 258002, 2020.

[23] B. Ramakrishnan, R. Ramamoorthy, C. Li, A. Akgul, and K. Rajagopal, "Spiral waves in a lattice array of Josephson junction chaotic oscillators with flux effects," *Mathematical Problems in Engineering*, vol. 2021, Article ID 8848914, 9 pages, 2021.

[24] Y. Xu, W. Hu, and S. P. Zhang, "Dynamic simulation of a woodpecker robot based on self-excited vibration," *Advanced Materials Research*, vol. 753-755, pp. 2020–2024, 2013.

[25] K. Ono, T. Furuichi, and R. Takahashi, "Self-excited walking of a biped mechanism," *International Journal of Robotics Research*, vol. 23, no. 1, pp. 953–966, 2001.

[26] I. Morazzani, D. Lahr, D. Hong, P. Ren, and V. Tech, "Novel tripedal mobile robot and considerations for gait planning strategies based on kinematics," *Lecture Notes in Control and Information Sciences*, vol. 370, pp. 35–48, 2008.

[27] C. Li and X. He, "A bio-mimetic pipe crawling microrobot driven based on self-excited vibration," in *Proceedings of the IEEE International Conference on Robotics And Biomimetics*, pp. 984–988, Sanya, China, 2007.

[28] A. Yamano and H. Ijima, "Basic study of the adaptive control for the swimming robot using self-excited oscillation," *Transactions of the JSME (In Japanese)*, vol. 84, no. 864, pp. 18–00054, 2018.

[29] N. A. D. Stokes, R. M. A. Fatah, and S. Venkatesh, "Self-excitation in fibre-optic microresonator sensors," *Sensors and Actuators A Physical*, vol. 21, no. 1-3, pp. 369–372, 1990.

[30] K. Hane and K. Suzuki, "Self-excited vibration of a self-supporting thin film caused by laser irradiation," *Sensors and Actuators A: Physical*, vol. 51, no. 2-3, pp. 179–182, 1995.

[31] K. Aubin, M. Zalalutdinov, T. Alan et al., "Limit cycle oscillations in cw laser-driven nems," *Journal of Microelectromechanical Systems*, vol. 13, no. 6, pp. 1018–1026, 2004.

[32] H. Hoelscher, P. U. Zerweck, L. M. Eng, and R. Hoffmann, "The effective quality factor at low temperatures in dynamic force microscopes with Fabry–Pérot interferometer detection," *Applied Physics Letters*, vol. 94, no. 22, Article ID 223514, 2009.

[33] C. Metzger, M. C. Neuenhahn, A. Ortlieb, I. Favero, K. Karrai, and F. Marquardt, "Self-induced oscillations in an optomechanical system driven by bolometric backaction," *Physical Review Letters*, vol. 101, no. 13, Article ID 133903, 2008.

[34] E. Hollander and O. Gottlieb, "Self-excited chaotic dynamics of a nonlinear thermo-visco-elastic system that is subject to laser irradiation," *Applied Physics Letters*, vol. 101, no. 13, Article ID 133507, 2012.

[35] A. H. Gelebart, G. Vantomme, E. W. Meijer, and D. J. Broer, "Mastering the photothermal effect in liquid crystal networks: a general approach for self-sustained mechanical oscillators," *Advanced Materials*, vol. 29, no. 18, Article ID 1606712, 2017.

[36] S. Houri, S. J. Cartamil-Bueno, M. Poot, P. G. Steeneken, H. S. J. van der Zant, and W. J. Venstra, "Direct and parametric synchronization of a graphene self-oscillator," *Applied Physics Letters*, vol. 110, no. 7, Article ID 073103, 2017.

[37] E. Buks and I. Martin, "Self-excited oscillation and synchronization of an on-fiber optomechanical cavity," *Physical Review E*, vol. 100, no. 3, Article ID 032202, 2019.

[38] W. Ding, *Self-excited Vibration*, Springer, Berlin, Germany, 2010.

Hindawi
Mathematical Problems in Engineering
Volume 2021, Article ID 5571072, 11 pages
https://doi.org/10.1155/2021/5571072

Research Article

A New General Decay Rate of Wave Equation with Memory-Type Boundary Control

Sheng Fan

Department of Economic Mathematics, Southwestern University of Finance and Economics, Chengdu 611130, China

Correspondence should be addressed to Sheng Fan; fansheng@swufe.edu.cn

Received 7 January 2021; Revised 16 January 2021; Accepted 23 January 2021; Published 13 February 2021

Academic Editor: Sundarapandian Vaidyanathan

Of interest is a wave equation with memory-type boundary oscillations, in which the forced oscillations of the rod is given by a memory term at the boundary. We establish a new general decay rate to the system. And it possesses the character of damped oscillations and tends to a finite value for a large time. By assuming the resolvent kernel that is more general than those in previous papers, we establish a more general energy decay result. Hence the result improves earlier results in the literature.

1. Introduction

It is well-known that if we add a damping to a system, the amplitude of the oscillations can be reduced very fast. The memory term can be as a damping (viscoelastic damping) which is weaker than frictional damping. For viscoelastic materials, Boltzmann theory gives us that the stress-strain viscoelastic law depending on a relaxation measure, see Prüss [1] and Eden et al. [2]. Based on the Boltzmann principle, the viscoelastic stress-strain relations can be generally given by a convolution term, which can be regarded as a lower order perturbation and can also be regarded as a kind of memory effect, for instance, g^*u. And we call the function $g(t)$ memory kernel. One can find a detail derivation on some systems with memory in [3].

To motivate our work, we start with some known results on wave equation with memory-type oscillations. The general wave equation with viscoelastic term in the internal feedback

$$u_{tt} - \Delta u + \int_0^t g(t-s)\Delta u(s)\mathrm{d}s = \mathscr{F}(u). \tag{1}$$

Messaoudi and Messaoudi [4, 5] studied $\mathscr{F}(u) = 0$ and $\mathscr{F}(u) = |u|^\rho u$, by introducing the assumption $g'(t) \leq -\xi(t)g(t)$, and obtained the energy decays exponentially (polynomially) as g decays exponentially (polynomially), respectively.

Lasiecka et al. [6] considered the general assumption on g: $g'(t) \leq -H(g(t))$ to establish general decay of energy. Here H, which was introduced by Alabau-Boussouira and Cannarsa [7], is strictly convex and increasing function. Cavalcanti et al. [8, 9], Lasiecka and Wang [10], Mustafa and Messaoudi [11], and Xiao and Liang [12] also used this

assumption to obtain some general decay rates of corresponding models. In recent papers [13–15], the authors investigated three classes of viscoelastic wave equation as in [4, 5] and established optimal and explicit decay results of energy by adopting the assumption on g: $g'(t) \leq -\xi(t)H(g(t))$.

In this paper, we considered the following wave equation with boundary oscillations of memory type:

$$\begin{cases} u_{tt} - \Delta u = 0, \quad \text{in } \Omega \times \mathbb{R}^+, \\ u = 0, \quad \text{on } \Gamma_0 \times \mathbb{R}^+, \\ u + \int_0^t g(t-s)\dfrac{\partial u}{\partial \nu}(s)\mathrm{d}s = 0, \quad \text{on } \Gamma_1 \times \mathbb{R}^+, \\ u(x,0) = u_0(x), \\ u_t(x,0) = u_1(x), \quad x \in \Omega, \end{cases} \tag{2}$$

where $\Omega \subset \mathbb{R}^n (n \geq 1)$ is a bounded domain with smooth boundary Γ, $\Gamma = \Gamma_0 \cup \Gamma_1$, and Γ_0 and Γ_1 are closed and disjoint with measure $(\Gamma_0) > 0$. ν is the unit outward normal to Γ.

For wave equation with memory-type boundary oscillations, it can be regarded as a wave equation with viscoelastic damping at the boundary. Santos [16] considered a one-dimensional wave equation with memory conditions at the boundary, respectively. He proved that the energy of solutions decays exponentially (polynomially) as k and k' decay exponentially (polynomially). Here k is the resolvent kernel of $(-g'/g(0))$. Santos et al. [17] extended the results in [16] to an n-dimensional wave equation of Kirchhoff type with memory-type boundary. They proved the global existence of solutions and obtained that the energy of solution decays uniformly with the same rate of decay k under the same conditions on k and k', which improves the results in [18] by Park et al. Santos and Junior [19] obtained a similar result for plate equation with memory-type boundary. We also mention the work of Cavalcanti et al. [20], where the authors showed the global existence and the uniform decay of solutions to a semilinear wave equation with memory-type boundary condition and a nonlinear boundary source. Messaoudi and Soufyane [21] considered a general assumption on k': $k'' \geq -\xi(t)k'(t)$ and established a general decay result. Wu [22] used this assumption to study a wave Kirchhoff-type wave equation with a boundary control of memory type. For nonlinear wave equations with memory-type boundary condition, we refer to Cavalcanti and Guesmia [23], Feng [24], Feng et al. [25–27], Muñoz Rivera and Andrade [28], and Zhang [29].

Concerning the system (2), Mustafa [30], by assuming the function k: $k''(t) \geq H(-k'(t))$, where k is the resolvent kernel of $(-g'/g(0))$, established a general decay of solutions of the form

$$E(t) \leq k_3 H_1^{-1}(k_1 t + k_2), \quad \forall t \geq 0. \tag{3}$$

Here

$$\begin{aligned} H_1(t) &= \int_t^1 \frac{1}{sH_0'(\varepsilon_0 s)}\mathrm{d}s, \\ H_0(t) &= H(D(t)), \end{aligned} \tag{4}$$

and D is a positive C^1 function with $D(0) = 0$, and H_0 is strictly increasing and strictly convex C^2 function on $(0, r]$. In particular, for $H(t) = t^p$, i.e., $k'' \geq c(-k')^p$, the author proved the energy decay holds for $1 \leq p < (3/2)$. Whether can the range be extended to a more larger range? In this paper, we give a positive answer to study problem (2) and extend the result to get a more general decay rate. In particular, we obtain that the energy result holds for $H(t) = t^p$ with the full admissible range $1 \leq p < 2$. More exactly, by assuming the relaxation function k with minimal conditions on $L^1(0, \infty)$, i.e., $k''(t) \geq \eta(t)H(-k'(t))$, where H is linear or strictly increasing and strictly convex functions of class $C^2(\mathbb{R}^+)$, we establish an optimal explicit and general energy decay result. In particular, the energy result holds for $H(t) = t^p$ with the range $p \in [1, 2)$ instead of $p \in [1, (3/2))$ in [30]. Hence our results extend and improve the stability results in [30] and also in [16–18, 21]. We mainly adopt the idea of [14, 15, 31] and some properties of convex function developed in [7, 32].

The remaining of the paper is organized as follows: in Section 2, we propose some preliminaries. In Section 3, main results are given. Section 4 is devoted to proving the general decay result.

2. Preliminaries

Taking the derivative of (2) with respect to t, we shall see that

$$\frac{\partial u}{\partial \nu} = -\frac{1}{g(0)}\left[u_t + g_2' * \frac{\partial u}{\partial \nu}\right]. \tag{5}$$

We denote the resolvent kernel of $(-g'/g(0))$ by k satisfying for $t \geq 0$:

$$k(t) + \frac{1}{g(0)}\left(g'^* k\right)(t) = -\frac{1}{g(0)}g'(t). \tag{6}$$

Using Volterra's inverse operator and taking $\alpha = (1/g(0))$, we have

$$\frac{\partial u}{\partial \nu} = -\alpha\left[u_t + k_2 * u_t\right]. \tag{7}$$

Assume $u_0 = 0$ on Γ_1 in this paper, we get

$$\frac{\partial u}{\partial \nu} = -\alpha\left[u_t + k(0) + k * u\right], \quad \text{on } \Gamma_1 \times \mathbb{R}^+. \tag{8}$$

In the following, we use boundary conditions (8) instead of (2).

As in [30], we consider the following assumption:

(A1) There exists a fixed point $x_0 \in \mathbb{R}^2$ and some constant $\delta_0 > 0$ such that for $m(x) = x - x_0$,

$$\begin{aligned} \Gamma_0 &= \{x \in \Gamma\colon m(x) \cdot \nu(x) \le 0\}, \\ \Gamma_1 &= \{x \in \Gamma\colon m(x) \cdot \nu(x) \ge \delta_0\}. \end{aligned} \tag{9}$$

For the kernel k, we assume

(A2) $k\colon \mathbb{R}^+ \longrightarrow \mathbb{R}^+$ is nonincreasing and twice differentiable function satisfying for any $t \ge 0$,

$$\begin{aligned} k(0) &> 0, \\ k'(t) &\le 0. \end{aligned} \tag{10}$$

(A3) There exist a C^1 function $H\colon \mathbb{R}^+ \longrightarrow \mathbb{R}^+$, with $H(0) = H'(0) = 0$, which is linear or is strictly increasing and strictly convex function of class $C^2(\mathbb{R}^+)$ on $(0, r]$, $r \le -k'(0)$ such that

$$k''(t) \ge \eta(t) H(-k'(t)), \quad \forall t \ge 0, \tag{11}$$

where $\eta(t)$ is C^1 nonincreasing continuous function.

Remark 2.1. If assuming further $\lim_{t\longrightarrow\infty} k(t) = 0$, since $\lim_{t\longrightarrow\infty} k(t) = 0$ and $(-k'(t))$ is nonincreasing and nonnegative, we can get

$$\lim_{t\longrightarrow\infty} (-k'(t)) = 0. \tag{12}$$

Then for some $t_1 \ge 0$ large,

$$-k'(t_1) = r \Rightarrow -k'(t) \le r, \quad \forall t \ge t_1. \tag{13}$$

Noting that $(-k')$ is nonincreasing, $-k'(0) > 0$, and $-k'(t_1) > 0$, we have $-k'(t_1) > 0$ for any $t \in [0, t_1]$, and for any $t \in [0, t_1]$,

$$\begin{aligned} 0 &< -k'(t_1) \le -k'(t) \le -k'(0), \\ 0 &< \eta(t_1) \le \eta(t) \le \eta(0). \end{aligned} \tag{14}$$

Therefore we obtain that there exist two positive constants a and b such that for any $t \in [0, t_1]$,

$$a \le \eta(t) H(-k'(t)) \le b. \tag{15}$$

Then for any $t \in [0, t_1]$,

$$k''(t) \ge \eta(t) H(-k'(t)) \ge a = \frac{a}{k'(0)} k'(0) \ge \frac{a}{k'(0)} k'(t). \tag{16}$$

This implies that there exists a constant $d > 0$ such that for any $t \in [0, t_1]$,

$$k''(t) \ge -d k'(t). \tag{17}$$

The proof is done.

3. Main Results

The well-posedness result is given in [30] proved by using the Faedo–Galerkin method as in [17].

Theorem 1. *Assume that (A1) and (A2) hold. Let $(u_0, u_1) \in (H^2(\Omega) \cap V) \times V$, and then problem (2) admits a unique solution u satisfying*

$$\begin{aligned} u \in L^\infty\left(0, T; H^2(\Omega) \cap V\right) \cap W^{1,\infty}(0, T; V) \\ \cap W^{2,\infty}\left(0, T; L^2(\Omega)\right), \end{aligned} \tag{18}$$

where $V = \{v \in H^1(\Omega)\colon v = 0 \text{ on } \Gamma_0\}$.

The total energy of the system is defined by

$$\mathscr{E}(t) = \frac{1}{2}\|u_t\|^2 + \frac{1}{2}\|\nabla u\|^2 + \frac{\alpha}{2}\left[k(t)\|u\|_{\Gamma_1}^2 - \int_{\Gamma_1} k' \circ u \, d\Gamma\right], \tag{19}$$

where

$$(k \circ u)(t) = \int_0^t k(t-s)[u(t) - u(s)]^2 ds. \tag{20}$$

We can get the following stability result.

Theorem 2. *Assume k satisfies (A1)–(A3) and further $\lim_{t\longrightarrow\infty} k(t) = 0$. Then there exist $\lambda_1, \lambda_2 > 0$ such that*

$$\mathscr{E}(t) \le \lambda_2 H_4^{-1}\left(\lambda_1 \int_{K^{-1}(r)}^t \eta(s) ds\right), \quad \forall t > K^{-1}(r), \tag{21}$$

where

$$\begin{aligned} H_4(t) &= \int_t^r \frac{1}{s H_0(s)} ds, \\ H_0(t) &= H'(t), \end{aligned} \tag{22}$$

and $K(t) = -k'(t)$. In particular, if $H(t) = t^p$, then for any $t > 0$,

$$\mathscr{E}(t) \le \begin{cases} c_1 e^{-c_2 \int_0^t \eta(s) ds}, & \text{if } p = 1, \\ c_3\left(1 + \int_0^t \eta(s) ds\right)^{-(1/(p-1))}, & \text{if } 1 < p < 2, \end{cases} \tag{23}$$

where c_1, c_3, and $c_2 \le 1$ are positive constants.

Remark 3.1. From (23), the energy result holds for $H(t) = t^p$ with the full admissible range $p \in [1, 2)$ instead of $p \in [1, (3/2))$. If the viscoelastic term is as internal feedback, Lasiecka and Wang [10] provided the proof for optimal decay rates of second-order systems in the full admissible range $[1, 2)$.

At last, we show two examples to illustrate explicit formulas for the decay rates of the energy, which can be found in the studies of Mustafa and Mustafa [14, 15].

Example 1. Take $k'(t) = -e^{-t^q}$ with $0 < q < 1$, we get $k''(t) = H(-k'(t))$, where $H(t) = ((qt)/([\ln(1/t)]^{(1/q)-1}))$. Since

$$H'(t) = \frac{(1-q) + q\ln(1/t)}{[\ln(1/t)]^{(1/q)}},$$
$$H''(t) = \frac{(1-q)[\ln(1/t) + (1/q)]}{[\ln(1/t)]^{((1/q)+1)}}, \tag{24}$$

we can deduce that the function H satisfies (A3) on $(0, r]$ for any $0 < r < 1$. Then,

$$\mathscr{E}(t) \le c_1 e^{-c_2 t^q}. \tag{25}$$

Example 2. Consider $k'(t) = (-1/((t+e)[\ln(t+e)]^p))$ with $p > 1$, we get $k''(t) = ([\ln(t+e) + p]/((t+e)^2[\ln(t+e)]^{p+1}))$. Clearly,

$$k''(t) = \frac{[\ln(t+e) + p]}{(t+e)\ln(t+e)}[-k'(t)]. \tag{26}$$

By part 1 of (23), we get

$$\mathscr{E}(t) \le c_1 \exp\left(-c_2 \int_0^t \frac{[\ln(t+e) + p]}{(t+e)\ln(t+e)} \mathrm{d}s\right) = \frac{c_1}{[(t+e)(\ln(t+e))^p]^{c_2}}. \tag{27}$$

As $c_2 \le 1$, this is slower rate than $[-k'(t)]$. In addition,

$$k''(t) = \frac{[\ln(t+e) + p]}{(t+e)^{(1-(1/p))}}(-k'(t))^{(1+(1/p))}. \tag{28}$$

From part 2 of (23), we infer that for large t

$$\mathscr{E}(t) c_3 \left(1 + \int_0^t \frac{\ln(t+e) + p}{(t+e)^{1-(1/p)}} \mathrm{d}s\right)^{-p} \le \frac{c_3}{(t+e)[\ln(t+e)]^p}, \tag{29}$$

which is the same rate as $[-k'(t)]$.

4. Proof of Main Result

To prove Theorem 2, we need the following lemmas.

4.1. Technical Lemmas

Lemma 1. *The total energy functional $E(t)$ satisfies for any $t \ge 0$,*

$$\mathscr{E}'(t) \le -\frac{\alpha}{2}\left(\|u_t\|_{\Gamma_1}^2 + \int_{\Gamma_1} k'' \circ u \mathrm{d}\Gamma\right) \le 0. \tag{30}$$

Proof. See [30]. □

As in [31], for $0 < \delta < 1$, we introduce

$$C_\delta = \int_0^\infty \frac{[k'(s)]^2}{k''(s) - \delta k'(s)} \mathrm{d}s,$$
$$h(t) = k''(s) - \delta k'(s). \tag{31}$$

Lemma 2. *Define the functional $\Phi(t)$ by*

$$\Phi(t) := \int_\Omega [2m \cdot \nabla u + (n-1)u] u_t \mathrm{d}x. \tag{32}$$

Then we can get for any $t \ge t_1$,

$$\Phi'(t) \le -\|u_t\|^2 - \frac{1}{2}\|\nabla u\|^2 + c\|u_t\|_{\Gamma_1}^2 + C_\delta \int_{\Gamma_1} h \circ u \mathrm{d}\Gamma. \tag{33}$$

Proof. From the same arguments as in the study of Mustafa [30], we can obtain

$$\Phi'(t) \le -\|u_t\|^2 - \|\nabla u\|^2 - \delta_0 \|\nabla u\|_{\Gamma_1}^2 + \int_{\Gamma_1} (m \cdot \nu)|u_t|^2 \mathrm{d}\Gamma + \int_{\Gamma_1} (2m \cdot \nabla u)\frac{\partial u}{\partial \nu} \mathrm{d}\Gamma + (n-1)\int_{\Gamma_1} u \frac{\partial u}{\partial \nu} \mathrm{d}\Gamma. \tag{34}$$

It follows from Young's inequality that for any $\varepsilon > 0$,

$$\int_{\Gamma_1} (2m \cdot \nabla u)\frac{\partial u}{\partial \nu} \mathrm{d}\Gamma + (n-1)\int_{\Gamma_1} u \frac{\partial u}{\partial \nu} \mathrm{d}\Gamma \le \delta_0 \|\nabla u\|_{\Gamma_1}^2 + \varepsilon \|u\|_{\Gamma_1}^2 + c\left\|\frac{\partial u}{\partial \nu}\right\|_{\Gamma_1}^2. \tag{35}$$

Recalling $k' * u = (-k' \odot u) + [k(t) - k(0)]u$, where $k \odot u = \int_0^t k(t-s)(u(t) - u(s))\mathrm{d}s$; then we have from (8),

$$\frac{\partial u}{\partial \nu}(t) = -\alpha[u_t(t) + k(t)u(t) + (-k' \odot u)(t)]. \tag{36}$$

By using Young's inequality, we obtain

$$\left\|\frac{\partial u}{\partial \nu}(t)\right\|_{\Gamma_1}^2 \le 4\alpha^2\left[\|u_t\|_{\Gamma_1}^2 + k^2(t)\|u\|_{\Gamma_1}^2 + \int_{\Gamma_1}(-k'\odot u)^2 \mathrm{d}\Gamma\right]. \tag{37}$$

Hölder's inequality implies

$$\begin{aligned}(-k'\odot u)^2 &= \left(\int_0^t (-k'(t-s))(u(t)-u(s))\mathrm{d}s\right)^2\\ &= \left(\int_0^t \frac{-k'(t-s)}{\sqrt{k''(t-s)-\delta k'(t-s)}}\sqrt{k''(t-s)-\delta k'(t-s)}\,(u(t)-u(s))\mathrm{d}s\right)^2\\ &\le \left(\int_0^t \frac{[k'(s)]^2}{k''(s)-\delta k'(s)}\mathrm{d}s\right)\int_0^t (k''(t-s)-\delta k'(t-s))(u(t)-u(s))^2\mathrm{d}s\\ &\le C_\delta(h\circ u),\end{aligned} \tag{38}$$

which, together with (37), gives us that

$$\left\|\frac{\partial u}{\partial \nu}(t)\right\|_{\Gamma_1}^2 \le 4\alpha^2\left[\|u_t\|_{\Gamma_1}^2 + k^2(t)\|u\|_{\Gamma_1}^2 + C_\delta\int_{\Gamma_1}(h\circ u)\mathrm{d}\Gamma\right]. \tag{39}$$

Inserting (39) into (35), we obtain for any $\varepsilon > 0$,

$$\begin{aligned}&\int_{\Gamma_1}(2m\cdot\nabla u)\frac{\partial u}{\partial \nu}\mathrm{d}\Gamma + (n-1)\int_{\Gamma_1} u\frac{\partial u}{\partial \nu}\mathrm{d}\Gamma\\ &\le \delta_0\|\nabla u\|_{\Gamma_1}^2 + \left(\varepsilon + 4\alpha^2k^2(t)\right)\|u\|_{\Gamma_1}^2\\ &\quad + 4\alpha^2 c\|u_t\|_{\Gamma_1}^2 + C_\delta\int_{\Gamma_1}(h\circ u)\mathrm{d}\Gamma.\end{aligned} \tag{40}$$

Noting that

$$\|u\|_{\Gamma_1}^2 \le c\|\nabla u\|^2, \tag{41}$$

using $\lim_{t\longrightarrow\infty}k(t) = 0$ and taking $\varepsilon > 0$ small enough, we can get (33) from (34) and (40). The proof is done. □

To get the optimal energy decay, we need the following estimate.

Lemma 3. *The functional $\Psi(t)$ is defined by*

$$\Psi(t) := \int_0^t k(t-s)\|u(s)\|_{\Gamma_1}^2\mathrm{d}s, \tag{42}$$

which satisfies for any $t > 0$,

$$\Psi'(t) \le \frac{1}{2}\int_{\Gamma_1} k'\circ u\mathrm{d}\Gamma + 3k(0)\|u(t)\|_{\Gamma_1}^2. \tag{43}$$

Proof. Differentiating $\Psi(t)$ with respect to t, we get

$$\begin{aligned}\Psi'(t) &= k_2(0)\|u(t)\|_{\Gamma_1}^2 + \int_0^t k_2'(t-s)\|u(s)\|_{\Gamma_1}^2\mathrm{d}s\\ &= \int_0^t k'(t-s)\int_{\Gamma_1}[u(s)-u(t)]^2\mathrm{d}\Gamma\mathrm{d}s + k(t)\|u(t)\|_{\Gamma_2}^2\\ &\quad + 2\int_{\Gamma_1}u(t)\int_0^t k'(t-s)[u(s)-u(t)]\mathrm{d}s\mathrm{d}\Gamma.\end{aligned} \tag{44}$$

In view of Young's and Hölder's inequalities, we obtain

$$\begin{aligned}&2\int_{\Gamma_1}u(t)\int_0^t k'(t-s)\left[u(s)-u(t)\sqrt{a^2+b^2}\right]\mathrm{d}s\mathrm{d}\Gamma\\ &\le 2k(0)\int_{\Gamma_1}u^2(t)\mathrm{d}\Gamma + \frac{1}{2k(0)}\int_{\Gamma_1}\left(\int_0^t\sqrt{-k'(t-s)}\sqrt{-k'(t-s)}\,[u(s)-u(t)]\mathrm{d}s\right)^2\mathrm{d}\Gamma\\ &\le 2k(0)\|u(t)\|_{\Gamma_1}^2 + \frac{\int_0^t k'(s)\mathrm{d}s}{2k(0)}\int_0^t k'(t-s)\|u(s)-u(t)\|_{\Gamma_1}^2\mathrm{d}s.\end{aligned} \tag{45}$$

Then we can get (43) following from the fact

$$k(t) \le k(0),$$
$$\frac{\int_0^t k'(s)\mathrm{d}s}{2k(0)} \ge -\frac{1}{2}. \tag{46}$$

The proof is complete. □

4.2. Proof of Theorem 2

Proof. Define the functional $L(t)$ by

$$L(t) := N\mathscr{E}(t) + \Phi(t), \tag{47}$$

where $N > 0$ is a constant that will be taken later. Clearly we can take N a large value to get

$$L(t) \sim \mathscr{E}(t). \tag{48}$$

Recalling $k'' = \delta k' + h$, combining (30) and (33), we conclude that for any $t > t_1$,

$$\begin{aligned} L'(t) \le & -\left(\frac{\alpha}{2}N - c\right)\|u_t\|_{\Gamma_1}^2 - \|u_t\|^2 - \frac{1}{2}\|\nabla u\|^2 \\ & \cdot -\frac{\alpha}{2}N\delta\int_{\Gamma_1} k'\circ u\mathrm{d}\Gamma - \left(\frac{\alpha}{2}N - cC_\delta\right)\int_{\Gamma_1} h\circ u\mathrm{d}\Gamma. \end{aligned} \tag{49}$$

Noting $-k' > 0$ and $k'' > 0$, for each $s \in [0, \infty)$, we shall see below,

$$\begin{aligned} & \lim_{\delta\longrightarrow 0} \frac{\delta[k'(s)]^2}{k''(s) - \delta k'(s)}\mathrm{d}s = 0, \\ & \frac{\delta[k'(s)]^2}{k''(s) - \delta k'(s)} < -k'(s). \end{aligned} \tag{50}$$

It follows from Lebesgue dominated convergence theorem that

$$\lim_{\delta\longrightarrow 0} \delta C_\delta = \lim_{\delta\longrightarrow 0} l\int_0^\infty \frac{\delta[k'(s)]^2}{k''(s) - \delta k'(s)}\mathrm{d}s = 0. \tag{51}$$

Therefore there exist $0 < \gamma < 1$ such that if $\delta < \gamma$, then

$$\delta C_\delta < \frac{1}{4c}. \tag{52}$$

And then we choose N a larger value that

$$\frac{\alpha}{2}N - c > 4k(0), \tag{53}$$

and take $\delta > 0$ satisfying

$$\delta = \frac{1}{2\alpha N} < \gamma. \tag{54}$$

This implies

$$\frac{\alpha}{2}N - cC_\delta > 0. \tag{55}$$

Then there exists a positive constant β such that for large $t_1 > 0$,

$$\begin{aligned} L'(t) \le & -\beta\left(\|u_t\|^2 + \|\nabla u\|^2\right) - 4k(0)\|u_t\|_{\Gamma_1}^2 \\ & -\frac{1}{4}\int_{\Gamma_1} k'\circ u\mathrm{d}\Gamma, \quad \forall t \ge t_1. \end{aligned} \tag{56}$$

By (17) and (30), we get

$$\begin{aligned} & \int_0^{t_1} (-k'(s))\int_{\Gamma_1} [u(t) - u(t-s)]^2\mathrm{d}\Gamma\mathrm{d}s \\ & \le \frac{1}{d}\int_0^{t_1} k''(s)\int_{\Gamma_1} [u(t) - u(t-s)]^2\mathrm{d}\Gamma\mathrm{d}s \le -c\mathscr{E}'(t). \end{aligned} \tag{57}$$

Then from (56), we infer that there exists a constant $\chi > 0$ such that

$$\begin{aligned} L'(t) & \le -\chi\mathscr{E}(t) - c\int_0^t k'(s)\int_{\Gamma_1} [u(t) - u(t-s)]^2\mathrm{d}\Gamma\mathrm{d}s \\ & \le -\chi\mathscr{E}(t) - c\mathscr{E}'(t) - c\int_{t_1}^t k'(s)\int_{\Gamma_1} [u(t) - u(t-s)]^2\mathrm{d}\Gamma\mathrm{d}s. \end{aligned} \tag{58}$$

Denoting $F(t) := L(t) + c\mathscr{E}(t) \sim E(t)$, and using (58), we know that

$$F'(t) \le -\chi\mathscr{E}(t) - c\int_{t_1}^t k_2'(s)\int_{\Gamma_1} [u(t) - u(t-s)]^2\mathrm{d}\Gamma\mathrm{d}s. \tag{59}$$

In the sequel, we consider two cases.

Case 1. The particular case $H(t) = t^p$.

(I) $p = 1$.

Multiplying (59) by $\eta(t)$, and using (19) and (A2)-(A3), we have

$$\eta(t)F'(t) \le -\chi\eta(t)\mathscr{E}(t) - c\mathscr{E}'(t), \quad \forall t \ge t_1. \tag{60}$$

Since $\eta(t)$ is a nonincreasing continuous function and $\eta'(t) \le 0$ for a.e. t, then

$$\begin{aligned} (\eta F + c\mathscr{E})'(t) & \le \eta(t)F'(t) + c\mathscr{E}'(t) \\ & \le -m\eta(t)\mathscr{E}(t), \quad \text{a.e. } t \ge t_1. \end{aligned} \tag{61}$$

In view of $\eta F + c\mathscr{E} \sim \mathscr{E}$, we obtain that there exist two positive constants $c_1, c_2 > 0$,

$$\mathscr{E}(t) \le c_1 e^{-c_2\int_{t_1}^t \eta(s)\mathrm{d}s}. \tag{62}$$

(II) $1 < p < 2$.

Define $\mathscr{G}(t)$ by

$$\mathscr{G}(t) = L(t) + \Psi(t). \tag{63}$$

It follows from (43) and (56) that $\mathscr{E}(t) \ge 0$, and for any $t \ge t_1$,

$$\mathcal{G}'(t) \le -\beta\left(\|u_t\|^2 + \|\nabla u\|^2\right) - k(0)\|u_t\|_{\Gamma_1}^2 + \frac{1}{4}\int_{\Gamma_1} k' \circ u \mathrm{d}\Gamma. \tag{64}$$

Then there exists a certain constant $\beta_1 > 0$,

$$\mathcal{G}'(t) \le -\beta_1 \mathcal{E}(t), \quad \forall t \ge t_1. \tag{65}$$

This gives us

$$\beta_1 \int_{t_1}^{t} E(s)\mathrm{d}s \le \mathcal{G}(t_1) - \mathcal{G}(t) \le \mathcal{G}(t_1). \tag{66}$$

Hence

$$\int_0^\infty \mathcal{E}(s)\mathrm{d}s < \infty. \tag{67}$$

Define

$$I(t) = \int_0^t \int_{\Gamma_1} [u(t) - u(t-s)]^2 \mathrm{d}\Gamma \mathrm{d}s, \tag{68}$$

we know that

$$I(t) \le c\int_0^t \mathcal{E}(s)\mathrm{d}s. \tag{69}$$

Without loss of generality assuming t_1 so large that $I(t_1) > 0$, then

$$0 < I(t_1) \le I(t) < \infty, \quad \forall t \ge t_1. \tag{70}$$

Using Jensen's inequality and by (30) and (A2)-(A3), we can derive from (56) that for some constant $q > 0$,

$$\begin{aligned} L'(t) &\le -q\mathcal{E}(t) + \frac{cI(t)}{I(t)}\int_{\Gamma_1}\left[(-k')^{p\cdot(1/p)} \circ u\right]\mathrm{d}\Gamma \\ &\le -q\mathcal{E}(t) + cI(t)\left[\frac{1}{I(t)}\int_{\Gamma_1}(-k')^p \circ u \mathrm{d}\Gamma\right]^{(1/p)} \\ &\le -q\mathcal{E}(t) + cI^{1-(1/p)}(t)\left[\int_{\Gamma_1}\frac{k''}{\eta}\circ u \mathrm{d}\Gamma\right]^{(1/p)} \\ &\le -q\mathcal{E}(t) + \frac{c}{[\eta(t)]^{(1/p)}}\left[\int_{\Gamma_1} k'' \circ u \mathrm{d}\Gamma\right]^{(1/p)} \\ &\le -q\mathcal{E}(t) + \frac{c}{[\eta(t)]^{(1/p)}}\left[-\mathcal{E}'(t)\right]^{(1/p)}. \end{aligned} \tag{71}$$

We multiply (71) by $\mathcal{E}^{p-1}(t)$ and use (19) to deduce

$$\begin{aligned} \left(L\mathcal{E}^{p-1}\right)'(t) &\le L'(t)\mathcal{E}^{p-1}(t) \le -q\mathcal{E}^p(t) \\ &\quad + c\left[-\frac{\mathcal{E}'(t)}{\eta(t)}\right]^{(1/p)}\mathcal{E}^{p-1}(t). \end{aligned} \tag{72}$$

By Young's inequality, we have for any $\varepsilon_1 > 0$,

$$\left(L\mathcal{E}^{p-1}\right)'(t) \le -q\mathcal{E}^p(t) + \varepsilon_1\mathcal{E}^p(t) + \frac{c}{\varepsilon_1}\left[-\frac{\mathcal{E}'(t)}{\eta(t)}\right]. \tag{73}$$

Taking $\varepsilon_1 < (1/2)q$, we conclude

$$\left(L\mathcal{E}^{p-1}\right)'(t) \le -\frac{q}{2}\mathcal{E}^p(t) - c\frac{\mathcal{E}'(t)}{\eta(t)}. \tag{74}$$

Define $F(t) = \eta L\mathcal{E}^{p-1} + c\mathcal{E} \sim \mathcal{E}$. Multiplying (74) by $\eta(t)$, we have

$$F'(t) \le -\frac{q}{2}\eta(t)\mathcal{E}^p(t). \tag{75}$$

Then there exists a certain constant $q_0 > 0$ such that

$$F'(t) \le -q_0\eta(t)F^p(t), \tag{76}$$

from which we obtain

$$\mathcal{E}(t) \le c_3\left(1 + \int_0^t \eta(s)\mathrm{d}s\right)^{-(1/(p-1))}, \tag{77}$$

where c_3 is a positive constant.

Combining (**I**) and (**II**) and using the boundedness of $\eta(t)$ and $\mathcal{E}(t)$, we can get (23).

Case 2. The general case.

Define

$$I(t) := q\int_{t_1}^t \int_{\Gamma_1} [u(t) - u(t-s)]^2 \mathrm{d}\Gamma \mathrm{d}s. \tag{78}$$

In view of (67), we can take $0 < q < 1$ such that

$$I(t) < 1, \quad \forall t \ge t_1. \tag{79}$$

Without loss of generality, we assume that $I(t) > 0$ for all $t \ge t_1$. On the other hand, we define

$$\pi(t) := \int_{t_1}^t k''(s)\int_{\Gamma_1}[u(t) - u(t-s)]^2 \mathrm{d}\Gamma \mathrm{d}s. \tag{80}$$

From (30), we can easily get $\pi(t) \le -c\mathrm{E}'(t)$. As $H(t)$ is strictly convex on $(0, r]$ and $H(0) = 0$, we see that

$$H(\lambda x) \le \lambda H(x), \quad i = 1, 2, 0 \le \lambda \le 1, x \in (0, r]. \tag{81}$$

It follows from Jensen's inequality and (11) and (79) that

$$\begin{aligned}
\pi_1(t) &= \frac{1}{qI(t)} \int_{t_1}^{t} I(t)(k''(s))q \int_{\Gamma_1} [u(t) - u(t-s)]^2 \mathrm{d}\Gamma \mathrm{d}s \\
&\ge \frac{1}{qI(t)} \int_{t_1}^{t} I(t)\eta(s)H(-k'(s))q \int_{\Gamma_1} [u(t) - u(t-s)]^2 \mathrm{d}\Gamma \mathrm{d}s \\
&\ge \frac{\eta(t)}{qI(t)} \int_{t_1}^{t} H(I(t)(-k'(s)))q \int_{\Gamma_1} [u(t) - u(t-s)]^2 \mathrm{d}\Gamma \mathrm{d}s \\
&\ge \frac{\eta(t)}{q} H\left(\frac{1}{I(t)} \int_{t_1}^{t} I(t)(-k'(s))q \int_{\Gamma_1} [u(t) - u(t-s)]^2 \mathrm{d}\Gamma \mathrm{d}s\right) \\
&= \frac{\eta(t)}{q} H\left(q \int_{t_1}^{t} (-k')(s) \int_{\Gamma_1} [u(t) - u(t-s)]^2 \mathrm{d}\Gamma \mathrm{d}s\right) \\
&= \frac{\eta(t)}{q} \overline{H}\left(q \int_{t_1}^{t} (-k'(s)) \int_{\Gamma_1} [u(t) - u(t-s)]^2 \mathrm{d}\Gamma \mathrm{d}s\right),
\end{aligned} \tag{82}$$

where $\overline{H}$, which is strictly convex and increasing function on $(0, \infty)$ of class C^2, is called the extension of H. We infer from (82) that

$$\int_{t_1}^{t} (-k'(s)) \int_{\Gamma_1} [u(t) - u(t-s)]^2 \mathrm{d}\Gamma \mathrm{d}s \le \frac{1}{q} \overline{H}^{-1}\left(\frac{q\pi(t)}{\eta(t)}\right). \tag{83}$$

Then we can get from (59) that for any $t \ge t_1$,

$$F'(t) \le -\chi \mathscr{E}(t) + c\overline{H}^{-1}\left(\frac{q\pi(t)}{\eta(t)}\right). \tag{84}$$

Denote

$$H_0(t) = \overline{H}'(t). \tag{85}$$

For $r_0 < r$, we define $\mathscr{K}_1(t)$ by

$$\mathscr{K}_1(t) = H_0\left(r_0 \frac{\mathscr{E}(t)}{\mathscr{E}(0)}\right) F(t) + \mathscr{E}(t) \sim \mathscr{E}(t). \tag{86}$$

Since $E'(t) \le 0$, $\overline{H}' > 0$, and $\overline{H}'' > 0$, we get from (84) that

$$\begin{aligned}
\mathscr{K}_1'(t) &= r_0 \frac{\mathscr{E}'(t)}{\mathscr{E}(0)} H_0'\left(r_0 \frac{\mathscr{E}(t)}{\mathscr{E}(0)}\right) F(t) + H_0\left(r_0 \frac{\mathscr{E}(t)}{\mathscr{E}(0)}\right) F'(t) + \mathscr{E}'(t) \\
&\le -m\mathscr{E}(t) H_0\left(r_0 \frac{\mathscr{E}(t)}{\mathscr{E}(0)}\right) + cH_0\left(r_0 \frac{\mathscr{E}(t)}{\mathscr{E}(0)}\right) \overline{H}^{-1}\left(\frac{q\pi(t)}{\eta(t)}\right).
\end{aligned} \tag{87}$$

We denote by $\overline{H}^*$ the conjugate function of the convex function $\overline{H}$ (see Arnold [33]), and then

$$\overline{H}^*(s) = s(\overline{H}')^{-1}(s) - \overline{H}\left[(\overline{H}')^{-1}(s)\right] \tag{88}$$

satisfies Young's inequality,

$$AB \le \overline{H}^*(A) + \overline{H}(B). \tag{89}$$

Taking $A = \overline{H}_0'(r_0(\mathrm{E}(t)/\mathrm{E}(0)))$ and $B = \overline{H}^{-1}((q\pi(t))/\eta(t))$, and using $\overline{H}^*(s) \le s(\overline{H}')^{-1}(s)$ and (87), we have

$$\begin{aligned}
\mathscr{K}_1'(t) &\le -\chi\mathscr{E}(t)H_0\left(r_0\frac{\mathscr{E}(t)}{\mathscr{E}(0)}\right) + c\overline{H}^*\left(H_0\left(r_0\frac{\mathscr{E}(t)}{\mathscr{E}(0)}\right)\right) + c\frac{q\pi(t)}{\eta(t)} \\
&\le -\chi\mathscr{E}(t)H_0\left(r_0\frac{\mathscr{E}(t)}{\mathscr{E}(0)}\right) + cH_0\left(r_0\frac{\mathscr{E}(t)}{\mathscr{E}(0)}\right)(\overline{H}')^{-1}\left(H_0\left(r_0\frac{\mathscr{E}(t)}{\mathscr{E}(0)}\right)\right) + c\frac{q\pi(t)}{\eta(t)} \\
&\le -\chi\mathscr{E}(t)H_0\left(r_0\frac{\mathscr{E}(t)}{\mathscr{E}(0)}\right) + cH_0\left(r_0\frac{\mathscr{E}(t)}{\mathscr{E}(0)}\right)(\overline{H}')^{-1}\left(\overline{H}'\left(r_0\frac{\mathscr{E}(t)}{\mathscr{E}(0)}\right)\right) + c\frac{q\pi(t)}{\eta(t)} \\
&\le -(\chi\mathscr{E}(0) - cr_0)\frac{\mathscr{E}(t)}{\mathscr{E}(0)}H_0\left(r_0\frac{\mathscr{E}(t)}{\mathscr{E}(0)}\right) + cq\frac{\pi(t)}{\eta_1(t)}.
\end{aligned} \tag{90}$$

We multiply (90) by $\eta(t)$ to arrive at

$$\begin{aligned}
\eta(t)\mathscr{K}_1'(t) &\le -(\chi\mathscr{E}(0) - cr_0)\eta(t)\frac{\mathscr{E}(t)}{\mathscr{E}(0)}H_0\left(r_0\frac{\mathscr{E}(t)}{\mathscr{E}(0)}\right) + cq\pi(t) \\
&\le -(\chi\mathscr{E}(0) - cr_0)\eta(t)\frac{\mathscr{E}(t)}{\mathscr{E}(0)}H_0\left(r_0\frac{\mathscr{E}(t)}{\mathscr{E}(0)}\right) - c\mathscr{E}'(t).
\end{aligned} \tag{91}$$

The functional $\mathscr{K}_2(t)$ is defined by

$$\mathscr{K}_2(t) = \eta(t)\mathscr{K}_1(t) + c\mathscr{E}(t). \tag{92}$$

Then we can easily obtain that there exist constants $\beta_5 > 0$ and $\beta_6 > 0$ such that

$$\beta_5\mathscr{K}_2(t) \le \mathrm{E}(t) \le \beta_6\mathscr{K}_2(t). \tag{93}$$

Choosing a suitable $r_0 > 0$, and defining $H_3(t) = tH_0(r_0t)$, from (91), we infer that for a constant $\gamma > 0$,

$$\mathscr{K}_2'(t) \le -\gamma\eta(t)\frac{\mathscr{E}(t)}{\mathscr{E}(0)}H_0\left(r_0\frac{\mathscr{E}(t)}{\mathscr{E}(0)}\right) := -\gamma\eta(t)H_3\left(\frac{\mathscr{E}(t)}{\mathscr{E}(0)}\right). \tag{94}$$

It follows from $0 \le r_0(\mathscr{E}(t)/\mathscr{E}(0)) < r$ that for any $t > 0$,

$$H_0\left(r_0\frac{\mathscr{E}(t)}{\mathscr{E}(0)}\right) = \overline{H}'\left(r_0\frac{\mathscr{E}(t)}{\mathscr{E}(0)}\right) = H'\left(r_0\frac{\mathscr{E}(t)}{\mathscr{E}(0)}\right). \tag{95}$$

Using (93), we have

$$R(t) := \frac{\beta_5\mathscr{K}_2(t)}{\mathscr{E}(0)} \sim \mathscr{E}(t). \tag{96}$$

Since $H_3'(t) = H_0(r_0t) + r_0tH_0'(r_0t)$, then, noting the strict convexity of H_0 on $(0, r]$, we know $H_3'(t), H_3(t) > 0$ on $(0, 1]$. By (94), we conclude that there exists $\gamma_1 > 0$ such that for any $t \ge t_1$,

$$R'(t) \le -\gamma_1\eta(t)H_3(R(t)). \tag{97}$$

Integrating (97) over (t_1, t), we see that

$$\int_{t_1}^{t}\frac{-R'(s)}{H_3(R(s))}\mathrm{d}s \ge \gamma_1\int_{t_1}^{t}\eta(s)\mathrm{d}s \Rightarrow \int_{r_0R(t)}^{r_0R(t_1)}\frac{1}{sH_0(s)}\mathrm{d}s \ge \gamma_1\int_{t_1}^{t}\eta(s)\mathrm{d}s. \tag{98}$$

Define

$$H_4(t) = \int_t^r\frac{1}{sH_0(s)}\mathrm{d}s. \tag{99}$$

It is to verify that H_4 is strictly decreasing on $(0, r]$ and $\lim_{t\longrightarrow 0}H_4(t) = +\infty$. It follows that

$$R(t) \le \frac{1}{r_0}H_4^{-1}\left(\zeta_1\int_{t_1}^{t}\eta(s)\mathrm{d}s\right). \tag{100}$$

Combining (96) and (100), we can obtain (21). This finishes the proof of Theorem 2

Data Availability

No data were used during this study.

Conflicts of Interest

The author declares that there are no conflicts of interest regarding the publication of this paper.

Acknowledgments

This work was supported by the Fundamental Research Funds for the Central Universities (no. JBK1809025).

References

[1] J. Prüss, "Evolutionary integral equations and applications," in *Monographs in Mathematics*, vol. 87, Birkhäuser Verlag, Basel, Switzerland, 1993.

[2] A. Eden, C. Foias, B. Nicolaenko, and R. Temam, "Exponential attractors for dissipative evolution equations," in *RAM: Research in Applied Mathematics*, vol. 37, Masson, Paris, France, 1994.

[3] B. Feng, M. A. Jorge Silva, and A. H. Caixeta, "Long-time behavior for a class of semi-linear viscoelastic Kirchhoff beams/plates," *Applied Mathematics & Optimization*, vol. 82, no. 2, pp. 657–686, 2020.

[4] S. A. Messaoudi, "General decay of solutions of a viscoelastic equation," *Journal of Mathematical Analysis and Applications*, vol. 341, no. 2, pp. 1457–1467, 2008.

[5] S. A. Messaoudi, "General decay of the solution energy in a viscoelastic equation with a nonlinear source," *Nonlinear Analysis: Theory, Methods & Applications*, vol. 69, no. 8, pp. 2589–2598, 2008.

[6] I. Lasiecka, S. A. Messaoudi, and M. I. Mustafa, "Note on intrinsic decay rates for abstract wave equations with memory," *Journal of Mathematical Physics*, vol. 54, p. 31504, 2013.

[7] F. Alabau-Boussouira and P. Cannarsa, "A general method for proving sharp energy decay rates for memory-dissipative evolution equations," *Comptes Rendus Mathematique*, vol. 347, no. 15-16, pp. 867–872, 2009.

[8] M. M. Cavalcanti, V. N. Domingos Cavalcanti, I. Lasiecka, and F. A. Nascimento, "Intrinsic decay rate estimates for the wave equation with competing viscoelastic and frictional dissipative effects," *Discrete & Continuous Dynamical System _ B*, vol. 19, pp. 1987–2012, 2014.

[9] M. M. Cavalcanti, A. D. D. Cavalcanti, I. Lasiecka, and X. Wang, "Existence and sharp decay rate estimates for a von Karman system with long memory," *Nonlinear Analysis: Real World Applications*, vol. 22, pp. 289–306, 2015.

[10] I. Lasiecka and X. Wang, "Intrinsic decay rate estimates for semilinear abstract second order equations with memory," in *New Prospects in Direct, Inverse and Control Problems for Evolution Equations*, vol. 10, pp. 271–303, Springer INdAM Series, Cham, Switzerland, 2014.

[11] M. I. Mustafa and S. A. Messaoudi, "General stability result for viscoelastic wave equations," *Journal of Mathematical Physics*, vol. 53, p. 53702, 2012.

[12] T.-J. Xiao and J. Liang, "Coupled second order semilinear evolution equations indirectly damped via memory effects," *Journal of Differential Equations*, vol. 254, no. 5, pp. 2128–2157, 2013.

[13] B. Feng and A. Soufyane, "Optimal decay rates of a nonlinear time-delayed viscoelastic wave equation," *International Journal of Differential Equations*, vol. 33, pp. 43–65, 2020.

[14] M. I. Mustafa, "Optimal decay rates for the viscoelastic wave equation," *Mathematical Methods in the Applied Sciences*, vol. 41, no. 1, pp. 192–204, 2018.

[15] M. I. Mustafa, "General decay result for nonlinear viscoelastic equations," *Journal of Mathematical Analysis and Applications*, vol. 457, no. 1, pp. 134–152, 2018.

[16] M. L. Santos, "Asymptotic behavior of solutions to wave equations with a memory conditions at the boundary," *Electron. J. Differ. Equ.*vol. 73, p. 11, 2001.

[17] M. L. Santos, J. Ferreira, D. C. Pereira, and C. A. Raposo, "Global existence and stability for wave equation of Kirchhoff type with memory condition at the boundary," *Nonlinear Analysis: Theory, Methods & Applications*, vol. 54, no. 5, pp. 959–976, 2003.

[18] J. Y. Park, J. J. Bae, and I. H. Jung, "Uniform decay of solution for wave equation of Kirchhoff type with nonlinear boundary damping and memory term," *Nonlinear Analysis: Theory, Methods & Applications*, vol. 50, no. 7, pp. 871–884, 2002.

[19] M. d. L. Santos and F. Junior, "A boundary condition with memory for Kirchhoff plates equations," *Applied Mathematics and Computation*, vol. 148, no. 2, pp. 475–496, 2004.

[20] M. M. Cavalcanti, V. N. D. Cavalcanti, J. S. P. Filho, and J. A. Soriano, "Existence and uniform decay of solutions of a degenerate equation with nonlinear boundary damping and boundary memory source term," *Nonlinear Analysis: Theory, Methods & Applications*, vol. 38, no. 3, pp. 281–294, 1999.

[21] S. A. Messaoudi and A. Soufyane, "General decay of solutions of a wave equation with a boundary control of memory type," *Nonlinear Analysis: Real World Applications*, vol. 11, no. 4, pp. 2896–2904, 2010.

[22] S. T. Wu, "General decay for a wave equation of Kirchhoff type with a boundary control of memory type," *Boundary Value Problems*, vol. 2011, p. 15, 2011.

[23] M. M. Cavalcanti and A. Guesmia, "General decay rates of solutions to a nonlinear wave equation with boundary conditions of memory type," *Differential Intermediate Equations*, vol. 18, pp. 583–600, 2005.

[24] B. Feng, "General decay rates for a viscoelastic wave equation with dynamic boundary conditions and past history," *Mediterranean Journal of Mathematics*, vol. 15, p. 103, 2018.

[25] B. Feng and A. Soufyane, "New general decay results for a von Karman plate equation with memory-type boundary conditions," *Discrete & Continuous Dynamical Systems - A*, vol. 40, no. 3, pp. 1757–1774, 2020.

[26] B. Feng and A. Soufyane, "Existence and decay rates for a coupled Balakrishnan-Taylor viscoelastic system with dynamic boundary conditions," *Mathematical Methods in the Applied Sciences*, vol. 43, no. 6, pp. 3375–3391, 2020.

[27] B. Feng and A. Soufyane, "Memory-type boundary control of a laminated Timoshenko beam," *Mathematics and Mechanics of Solids*, vol. 25, no. 8, pp. 1568–1588, 2020.

[28] J. E. Muñoz Rivera and D. Andrade, "Exponential decay of non-linear wave equation with a viscoelastic boundary condition," *Mathematical Methods in the Applied Sciences*, vol. 23, no. 1, pp. 41–61, 2000.

[29] Q. Zhang, "Global existence and exponential stability for a quasilinear wave equation with memory damping at the boundary," *Journal of Optimization Theory and Applications*, vol. 139, no. 3, pp. 617–634, 2008.

[30] M. I. Mustafa, "On the control of the wave equation by memory-type boundary condition," *Discrete and Continuous Dynamical Systems Journal*, vol. 35, pp. 1179–1192, 2015.
[31] K.-P. Jin, J. Liang, and T.-J. Xiao, "Coupled second order evolution equations with fading memory: optimal energy decay rate," *Journal of Differential Equations*, vol. 257, no. 5, pp. 1501–1528, 2014.
[32] I. Lasiecka and D. Tataru, "Uniform boundary stabilization of semilinear wave equation with nonlinear boundary damping," *Differential Intermediate Equations*, vol. 8, pp. 507–533, 1993.
[33] V. I. Arnold, *Mathematical Methods of Classical Mechanics*, Springer-Verlag, New York, NY, USA, 1989.

Hindawi
Mathematical Problems in Engineering
Volume 2021, Article ID 6661550, 12 pages
https://doi.org/10.1155/2021/6661550

Research Article

Realization of a Secure Visible Light Communication System via Chaos Synchronization

Teh-Lu Liao,[1] Chih-Yung Chen,[1,2] Hsin-Chieh Chen,[3] Yung-Yi Chen,[1] and Yi-You Hou[4]

[1]*Department of Engineering Science, National Cheng Kung University, Tainan, Taiwan*
[2]*Department of Computer Science and Information Engineering, Shu-Te University, Kaohsiung, Taiwan*
[3]*Department of Biomedical Engineering, Hungkuang University, Taichung, Taiwan*
[4]*Department of Intelligent Commerce, National Kaohsiung University of Science and Technology, Kaohsiung, Taiwan*

Correspondence should be addressed to Yi-You Hou; yyhou@nkust.edu.tw

Received 3 December 2020; Revised 5 January 2021; Accepted 22 January 2021; Published 8 February 2021

Academic Editor: Viet-Thanh Pham

A novel technique for transmission of information through visible light communication (VLC) is developed in this study. A light-emitting diode is used as the light source at the transmitting side to send the encrypted information. At the receiving side, a light sensor, OPT-101, is used to receive the light signals that carry the encrypted information. The Arduino Due microcontroller board is used for digital signal processing at both the transmitting and receiving sides. Furthermore, to prevent the transmitted message from being intercepted, two chaotic systems, a master and a slave, with a synchronization controller are designed to obtain the transmitted audio signals. The design enables not only a VLC system with the light transmission path as a straight line (so that data cannot be stolen) but also the encryption of the audio signals with the chaotic system (Rössler system) to enhance data transmission security. The effectiveness of this system is then experimentally verified.

1. Introduction

Advancements in information technology have enabled the development of fast wired transmission and wireless transmission methods, such as Ethernet, serial communication, Bluetooth, and Wi-Fi, which are now commonly used in daily life. However, regardless of the communication method used, in addition to the requirements of high-speed transmission, low power consumption, strong stability, wide communication range, and other performance parameters, the focus of information transmission has shifted to communication security. Therefore, related encryption methods, such as Rivest–Shamir–Adleman encryption [1], ElGamal encryption, Paillier encryption [2], and the chaos-based encryption (Rossler system) [3], have been proposed.

Visible light communication (VLC) uses light-emitting diodes (LED) to send out high-speed light and dark flashing signals to transmit data, it can reach 500 Mbit/s, and the transmission distance can reach 1 to 2 kilometers, which can be used as a local area network technology. Nowadays, it is used in applications such as unidirectional indoor broadcasting system [4] or indoor positioning [5]. Voice signal transmission over distant places through VLC [6] is a critical topic of research.

For security considerations, in the proposed technique, the signal that carries crucial information is encrypted. A chaotic system that is characterized by a dynamic system, which is very sensitive to the initial value [7] and can only be decrypted after the system is synchronized [8], was used in the proposed system. The proposed system increases communication security. Here, the Rossler system is mainly used for secure communication [3]. The system contains a transmission device and a receiving device, which function as a master and a slave, respectively. A controller is designed to synchronize the master and slave systems and decrypt the encrypted transmitted audio signals. Many synchronization design methods are available for chaotic systems [9–13]. Different from the implementation methods proposed in other documents [14–16], the main purpose of this manuscript is to transmit through VLC. Because of the analog

transmission through the LED, the data is not easy to be stolen. In order to enhance its security, we encrypt it through a chaotic system, design a set of channel modulation methods to enable it to successfully synchronize and decrypt, and strengthen its confidentiality. In this study, we adopted the proportional integral derivative (PID) controller for synchronization [17, 18]. The state error of the master and slave systems is used as the PID input, and suitable PID parameters are used to ensure that the system quickly achieves synchronization to complete the decryption.

2. Research Methods

2.1. Simulation and Synchronization of Chaotic Systems. Because security of information is critical, the transmission signal is encrypted to increase communication security. The Rossler chaotic system is mathematically expressed as follows:

$$\begin{cases} \dfrac{\mathrm{d}x(t)}{\mathrm{d}t} = -y(t) - z(t), \\ \dfrac{\mathrm{d}y(t)}{\mathrm{d}t} = x(t) + ay(t), \\ \dfrac{\mathrm{d}z(t)}{\mathrm{d}t} = b + z(t)(x(t) - c), \\ \text{where } a = b = 0.2, c = 5.7. \end{cases} \tag{1}$$

In the matrix form, it is described as follows:

$$\begin{bmatrix} \dfrac{\mathrm{d}x(t)}{\mathrm{d}t} \\ \dfrac{\mathrm{d}y(t)}{\mathrm{d}t} \\ \dfrac{\mathrm{d}z(t)}{\mathrm{d}t} \end{bmatrix} = A \begin{bmatrix} x(t) \\ y(t) \\ z(t) \end{bmatrix} + B[0.2 + x(t)z(t)], \tag{2}$$

where $A = \begin{bmatrix} 0 & -1 & -1 \\ 1 & 0.2 & 0 \\ 0 & 0 & -5.7 \end{bmatrix}$ and $B = \begin{bmatrix} 0 \\ 0 \\ 1 \end{bmatrix}$.

Here, x, y, and z are the three states of the chaotic system. Because these states can be implemented in the transmission system, the chaotic system is then discretized. By applying a sampling time (T) of 25 ms, the discrete time system can be obtained as follows, where k is the time index:

$$G = e^{AT},\ H = (G - I_3)A^{-1}B, \tag{3}$$

where $I_3 = \begin{bmatrix} 1 & 0 & 0 \\ 0 & 1 & 0 \\ 0 & 0 & 1 \end{bmatrix}$.

$$\begin{bmatrix} x^{(k+1)} \\ y^{(k+1)} \\ z^{(k+1)} \end{bmatrix} = G \begin{bmatrix} x^{(k)} \\ y^{(k)} \\ z^{(k)} \end{bmatrix} + H\left[0.2 + x^{(k)}z^{(k)}\right], \tag{4}$$

where $G = \begin{bmatrix} 0.9997 & -0.0251 & -0.0233 \\ 0.0251 & 1.0047 & -0.0003 \\ 0 & 0 & 0.8672 \end{bmatrix}$ and $H = \begin{bmatrix} -2.9815 \times 10^{-4} \\ -2.5171 \times 10^{-6} \\ 0.0233 \end{bmatrix}$.

After successful discretization of the chaotic system, the initial value of the given chaotic system is obtained as $x^{(0)} = 5$, $y^{(0)} = 6$, and $z^{(0)} = 14$ through MATLAB simulation. The chaotic signal characteristics of (x, y), (x, z), (y, z), and (x, y, z) are displayed in Figure 1.

Because chaotic systems are susceptible to initial values, if the initial values at the transmitting and the receiving sides differ, accurate decryption depends on the synchronization controller. In this study, the state variables of the chaotic system at the transmitter are defined as $x_m^{(k)}$, $y_m^{(k)}$, and $z_m^{(k)}$ with the initial value $x_m^{(0)} = 5$, $y_m^{(0)} = 6$, and $z_m^{(0)} = 14$, where k is the time index, and the state variables of the chaotic system at the receiver are defined as $x_s^{(k)}$, $y_s^{(k)}$, and $z_s^{(k)}$ with the initial value $x_s^{(0)} = -4$, $y_s^{(0)} = 7$, and $z_s^{(0)} = 3$, for synchronizing both the transmitter and the receiver with different initial values. Since the chaotic system is easily affected by the initial value and causes the system to be unstable, this manuscript selects the abovementioned initial values that can prevent the system from diverging as the simulation parameters. A PID controller is selected because of its simplicity, convenience, and strong robustness. The proportional controller (K_P) can speed up the response speed of the system, improve the accuracy of the system adjustment, and reduce the system response time. This allows the chaotic system to quickly catch up with the master state when the state error between the master and slave is large. The integral controller (K_I) considers the past error and controls the state to eliminate the steady-state error, but because the steady-state error is less than a certain value when synchronizing, it does not affect subsequent decryption. Furthermore, if the integral control is improper, overshoot may occur. Therefore, integral control was not adopted in the synchronous design. The differential controller (K_D) can consider future errors and achieve advanced control, which can improve system stability, reduce synchronization time, and avoid system overshoot. The state error of the master and slave formula is defined as $e^{(k)} = x_m^{(k)} - x_s^{(k)}$, and the PID controller is $u^{(k)} = K_P e^{(k)} + K_I \sum_{i=1}^{k} e^{(i)} + K_D(\Delta e^{(k)})$, where $K_P = -0.05, K_I = 0$, and $K_D = -0.7$. The control input $u^{(k)}$ is applied in the chaotic system at the receiver, which is expressed in (5). Then, some numerical simulations via MATLAB are performed to demonstrate the system performances. The state relations and errors between the transmitter and the receiver without the controller are displayed in Figures 2 and 3. We then apply the PID controller to synchronize the master and slave systems. The state relations and errors between the transmitter and the receiver with the proposed PID controller are displayed depicted in Figures 4 and 5, which verify the chaotic synchronization is obtained:

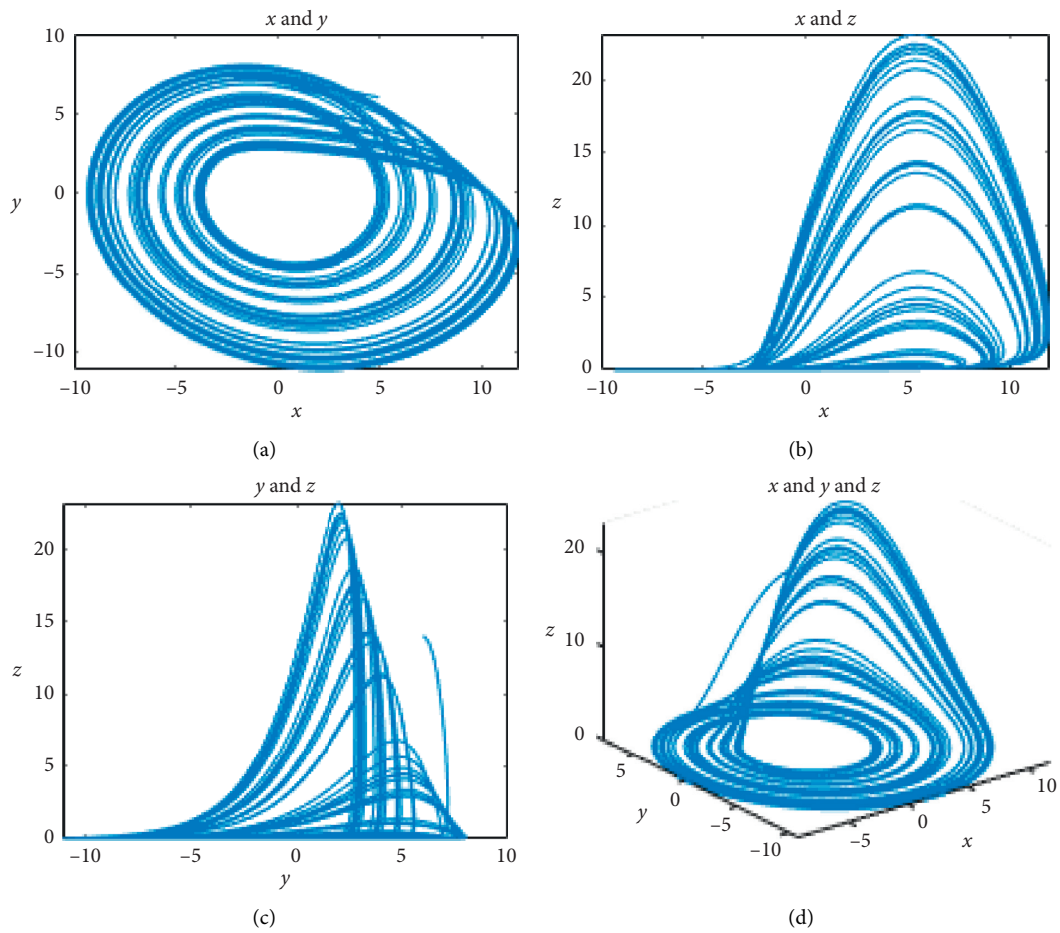

Figure 1: State characteristics of the Rossler chaotic system.

$$\begin{cases} e^{(k)} = x_m^{(k)} - x_s^{(k)}, \\ u^{(k)} = K_P e^{(k)} + K_I \sum_{i=1}^{k} e^{(i)} + K_D\left(\Delta e^{(k)}\right), \\ x_s^{(k+1)} = 0.9997 x_s^{(k)} - 0.0251 y_s^{(k)} - 0.0233 z_s^{(k)} + u^{(k)}. \end{cases} \tag{5}$$

2.2. VLC System Architecture. VLC hardware implementation is divided into two parts: the transmitter and receiver. The Arduino Due microcontroller board is the main control core of the system hardware. As to audio MP3 signals, the sampling frequency should be at least 44.1 MHz. The Arduino Due microcontroller board used in this article has a crystal oscillation frequency of 84 MHz, 12-bit input, high operation speed, and resolution ability, which are sufficient for the audio signal processing. The analog to digital (A/D) and digital to analog (D/A) conversions used in signal processing are processed internally by Arduino Due microcontroller board. The A/D convertor has the fastest conversion rate of 1 MHz, and the D/A processor performance can reach approximately 1.74 MHz, which is sufficient to process and encrypt/decrypt music signals. In the encryption, we add the state of the chaotic system to the audio signal for encryption. In the decryption, after the channel modulation and synchronization, we only need to subtract the state of the chaotic system from the ciphertext, and we can obtain the original signal. To improve the signal strength, the transmitter was combined with PAM8403, and the receiver output was combined with the LM386 amplifier to increase the signal strength. The working voltage of the transmitter is in the range of 2.5–5.5 V. The maximum gain of the system is 24 dB. The working voltage range of the receiver is 4–12 V. A maximum gain of 26 dB can be obtained. The LED is an RGB LED lamp with a diameter of 5 mm with a working voltage range of 2–3.2 V. The power of the LED is 0.06 W. The working voltage of the optical receiver OPT-101 is 2.7–36 V. The receiver converts the intensity of the received light to different voltages. A 1-MΩ feedback resistor with a bandwidth of 14 kHz is placed inside the receiver. The internal resistance of the speaker (horn) is 8 Ω, and its power rating is 0.3 W. System architectures of the transmitter and the receiver of the VLC system are given in Figures 6 and 7, respectively.

3. Experimental Results and Discussion

3.1. Realization of Signal Transmission by Using Visible Light. In this study, an MP3 signal is used as the transmission signal. The transmitter converts the music signal ($m^{(k)}$)

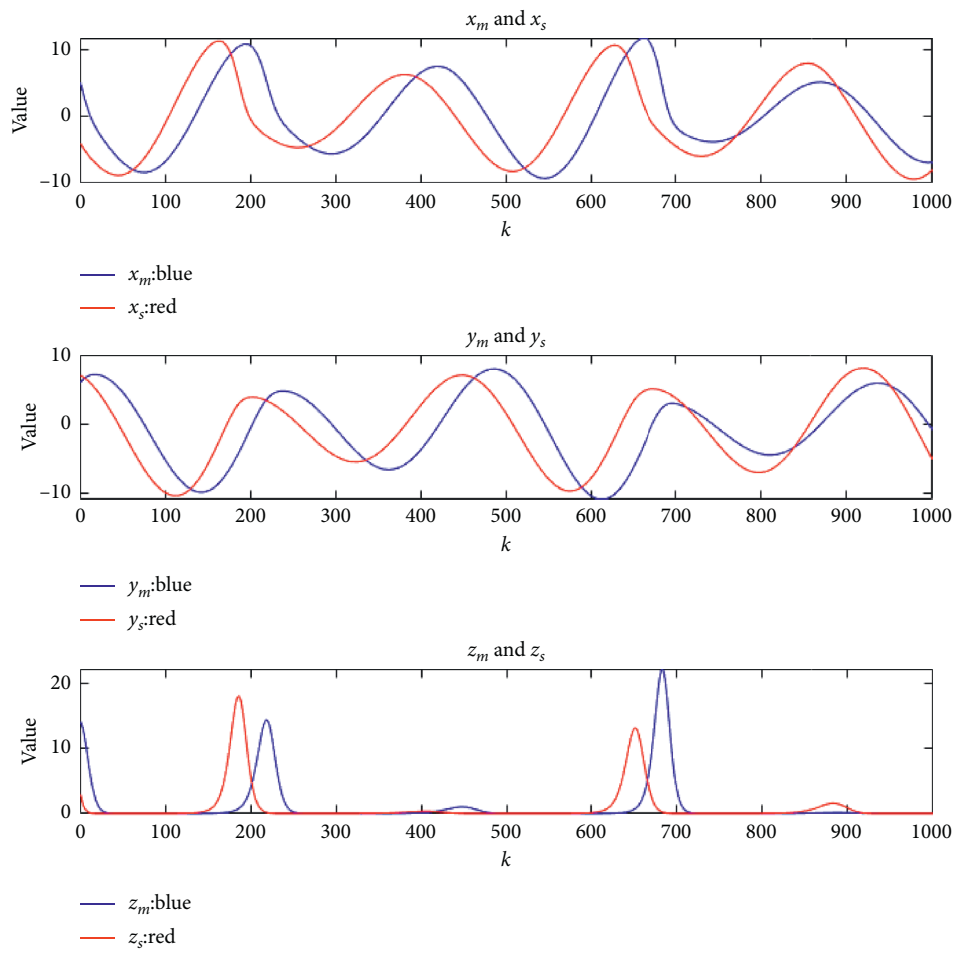

Figure 2: Unsynchronized status at the transmitter and receiver.

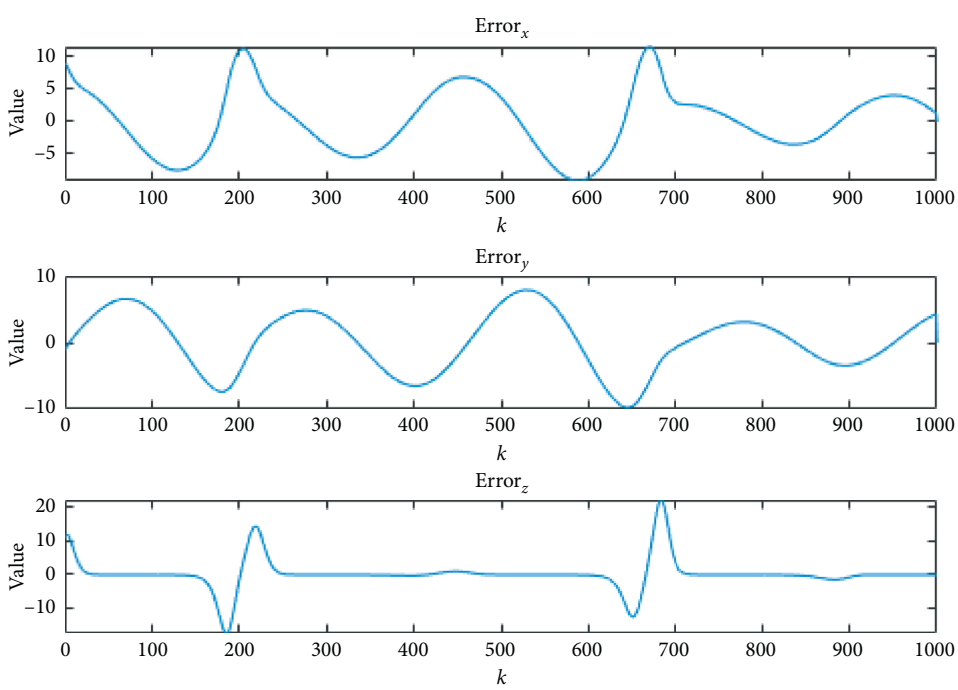

Figure 3: Unsynchronized error of the transmitter and receiver.

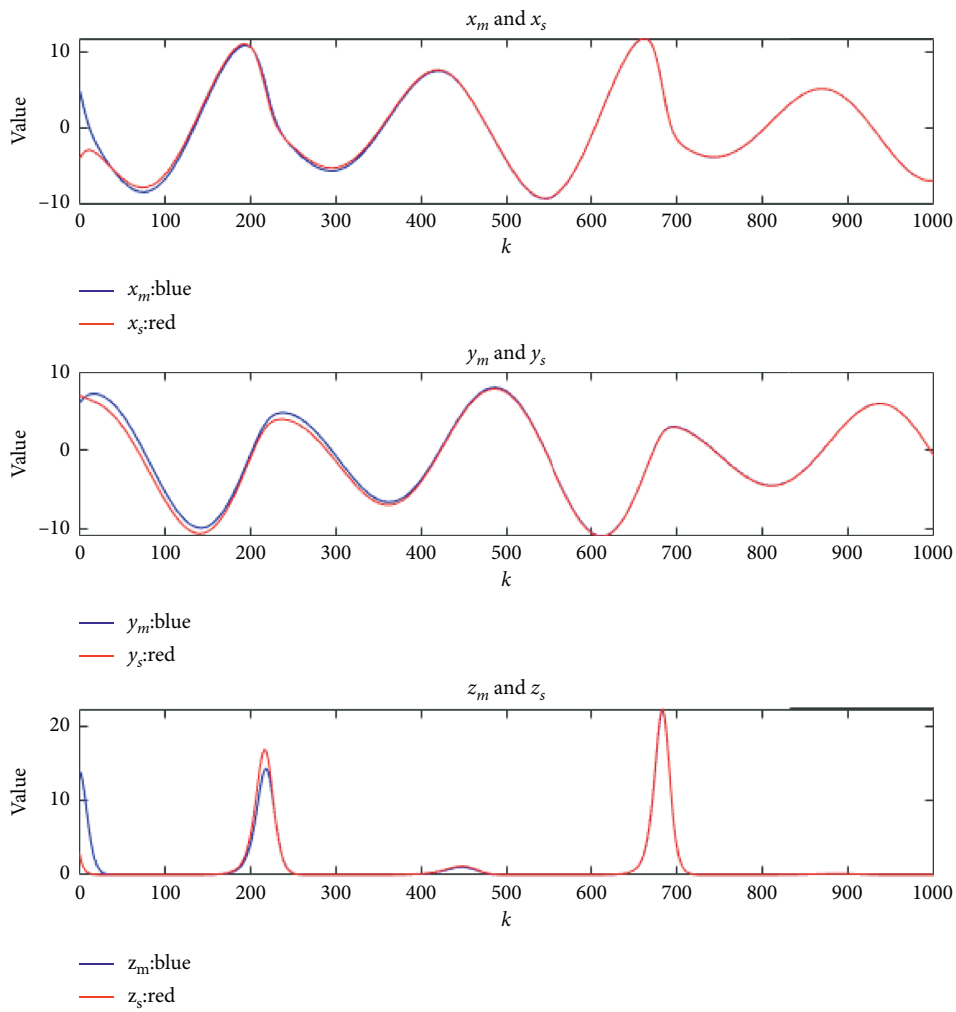

Figure 4: Status of the synchronization process at the transmitter and receiver.

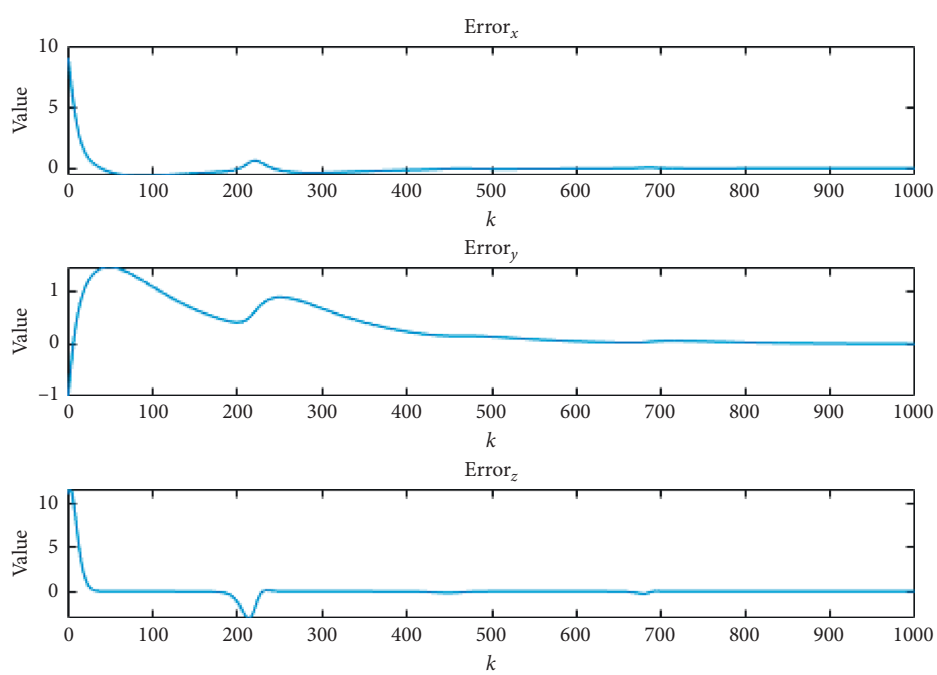

Figure 5: Error trajectory of the synchronization process at the transmitter and receiver.

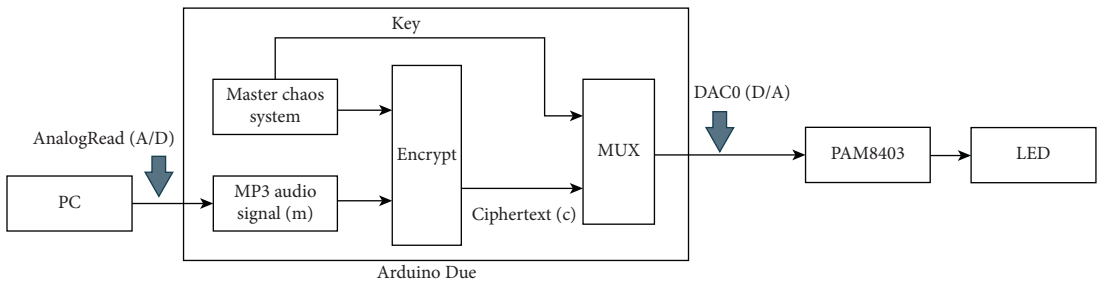

Figure 6: System architecture of the transmitter of the VLC system.

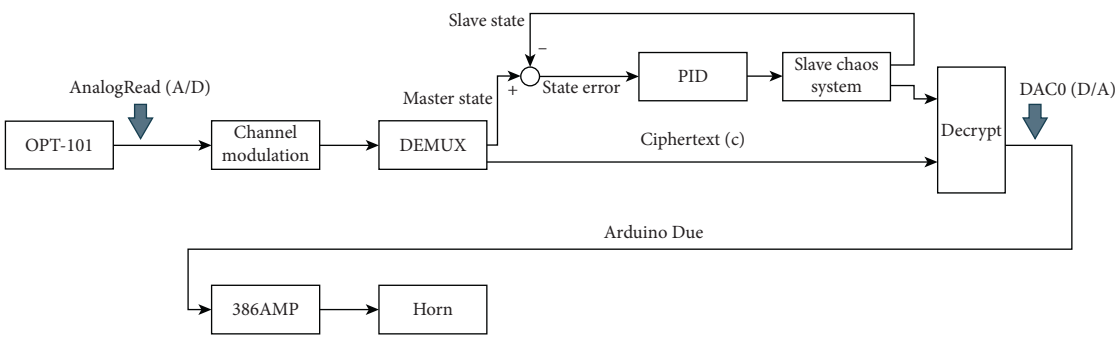

Figure 7: System architecture of the receiver of the VLC system.

played by the computer through the analogRead function of Arduino Due microcontroller board (A/D), where k is the time index. Then, the music signal is converted to an analog signal (D/A) through the analog output pin DAC1. The A/D in Arduino Due microcontroller can withstand a voltage of 5 V and convert it to a 12-bit digital signal, so the numerical resolution range is 0–4095 (unit), and the accuracy of each unit is $5\,\text{V}/4096 = 1.22\,\text{mV}$, and the same is true for D/A. Then, the PAM8403 amplifier is used to drive the LED for transmission, and the MP3 audio signal is transmitted to the receiver, as depicted in Figure 8.

The receiver uses an optical sensor module (OPT-101) to receive the LED signal of the transmitter and then quantize the audio signal. The signal receiver also receives the music signal at the same time through the A/D convertor. After signal processing (as presented in Figure 9), the signal is converted by the D/A convertor, whose output functions as the input to the amplifier (386AMP), and the audio signal is played by the speaker. The actual hardware implementation is displayed in Figure 10. Although VLC was realized using digital signals, the output was analog. At the receiver, the noise caused by external interference factors and channel length modulation can be removed using a filter.

3.2. Ensuring Security of Data Transmission. To ensure the security of data transmission, a chaotic synchronization control system is used to encrypt and decrypt transmitted data. To avoid data breach, the difference between the frequency band of the transmitted data and the frequency band of the chaotic system is minimized. The fast Fourier transform (FFT) is used to observe the frequency band distribution. As displayed in Figure 11, a suitable chaotic system is used to ensure security of transmission data. The fast Fourier analysis of the chaotic signal is displayed in Figure 12. With this design, even if the data are stolen at the transmitter, the data cannot be easily decrypted, which strengthens the system security.

3.3. Function of Audio and Chaotic Signals. The 12-bit ADC resolution from analogRead function between value 0 and 4095 (unit) of Arduino Due microcontroller is used in the signal transmitter to read the audio signal ($m^{(k)}$) played by the computer to complete the A/D conversion, and then, the audio signal is encrypted by the chaotic system into a ciphertext ($c^{(k)}$) according to (6). Figure 13 displays the encrypted signal. Furthermore, the ciphertext is converted from the digital to analog signal, and then the amplifier is used to improve the signal strength to drive the LEDs for transmission. The receiver receives the ciphertext signal ($C^{(k)}$) through the OPT101 module, as displayed in Figure 14. The signal receiver receives the encrypted signal ($C^{(k)}$) through OPT-101 and transmits it to Arduino Due microcontroller through analogRead:

$$c^{(k)} = m^{(k)} + 50x_m^{(k)}. \tag{6}$$

Considering channel modulation, the relationship between the value of the ciphertext at the transmitter ($c^{(k)}$) and the value of the ciphertext signal at the receiver ($C^{(k)}$) is established under conditions to avoid external interference, as displayed in Table 1. To decrypt the received signal, the receiver value is converted into original information:

$$c'^{(k)} = 500 + 2.5\left(C^{(k)} - 2200\right), \tag{7}$$

where $c'^{(k)} = c^{(k)}$.

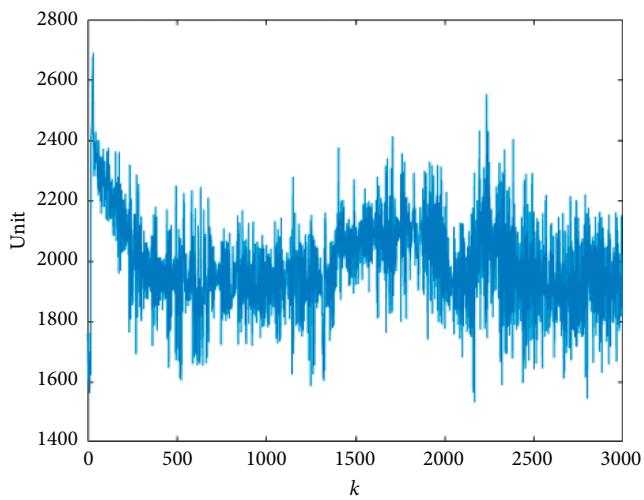

Figure 8: MP3 audio signal processing at the output of the signal transmitter.

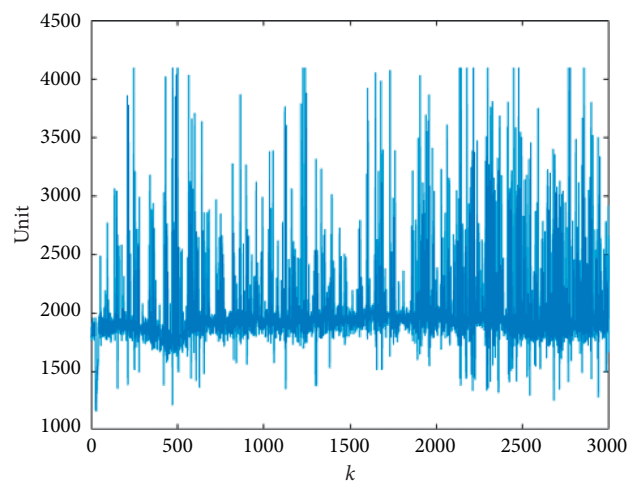

Figure 9: Signal receiver output display.

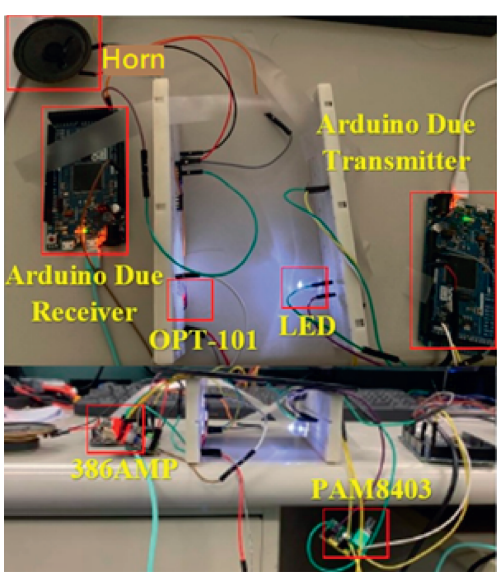

Figure 10: VLC system prototype and hardware.

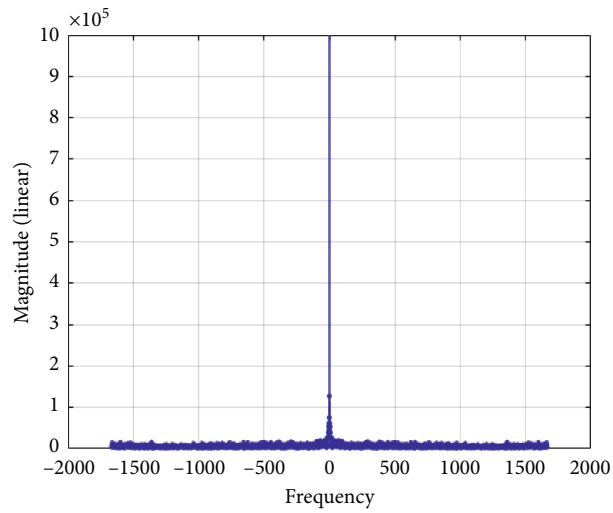

Figure 11: Analysis of audio signals by using FFT.

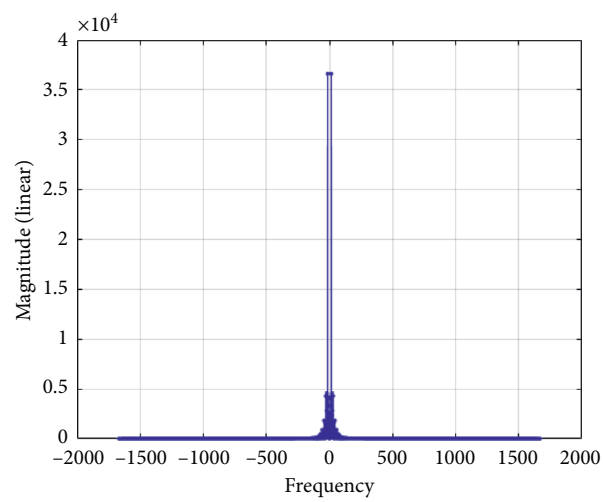

Figure 12: Analysis of chaotic signals by using FFT.

Immediately after converting the value back to the original information, the ciphertext was decrypted using the chaotic signal that is synchronized with the transmitter, as expressed in (8). Thus, the original music is obtained. Figures 15 and 16 display the results of the decryption of the unmodulated signal and the modulated signal, respectively.

To ensure the feasibility of the channel modulation and decryption proposed in this manuscript, we transmit some data through VLC, and the value is shown in Figure 17. And, then, we observe the received data; it can be found in Figure 18 that the value before channel modulation has a large error with the original data. Figure 19 shows that the value after channel modulation is very similar to the original data. The error between the original data and the data before channel modulation is shown in Figure 20. And, the error between the original data and the data after channel modulation is shown in Figure 21:

$$m^{(k)} = c'^{(k)} - 50x_s^{(k)}. \tag{8}$$

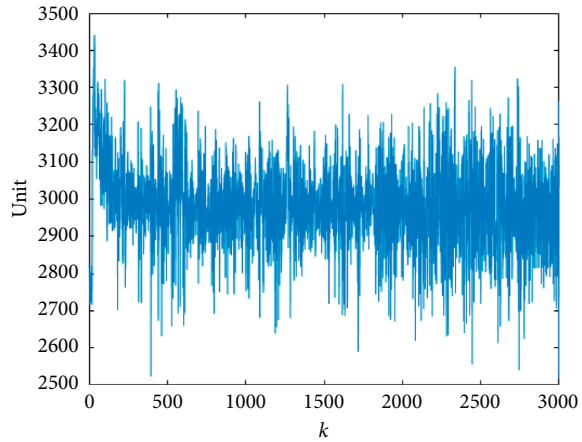

Figure 13: Schematic of the ciphertext signal after the signal transmitter encrypts the audio signal.

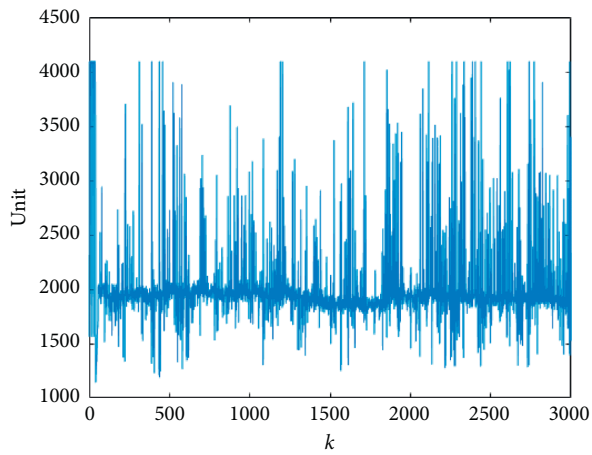

Figure 14: Schematic of the ciphertext signal received by the signal receiver.

Table 1: Numerical relationship between the transmitter and receiver.

Resolution	12-bit ADC values between 0 and 4095 (unit)	
	Transmitter	Receiver
—	100	1900
	500	2200
	1000	2400
	1500	2600

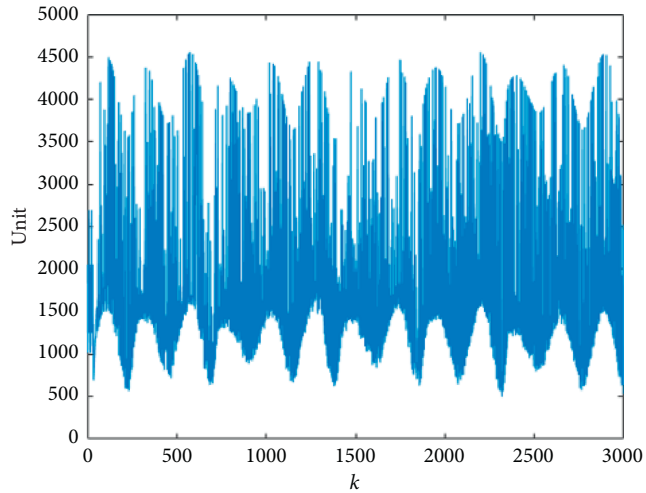

Figure 15: Unmodulated signal decryption results.

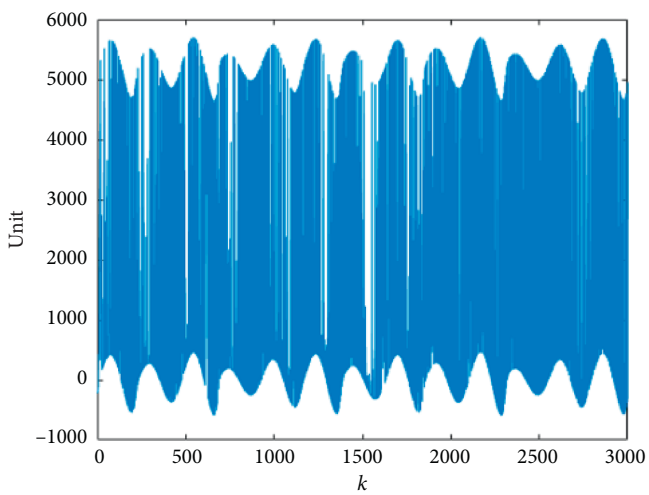

Figure 16: Demodulated signal decryption results.

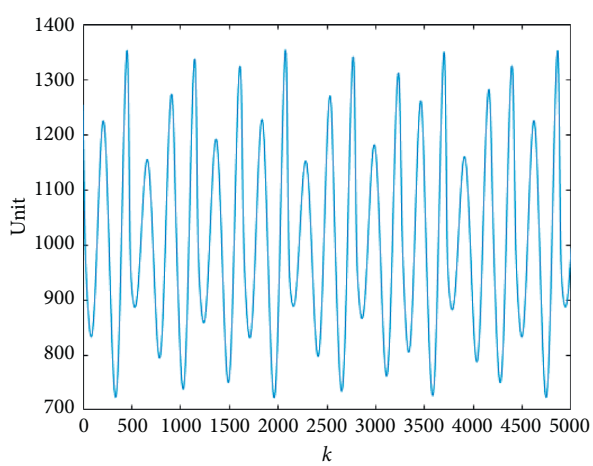

Figure 17: The data of the transmitter.

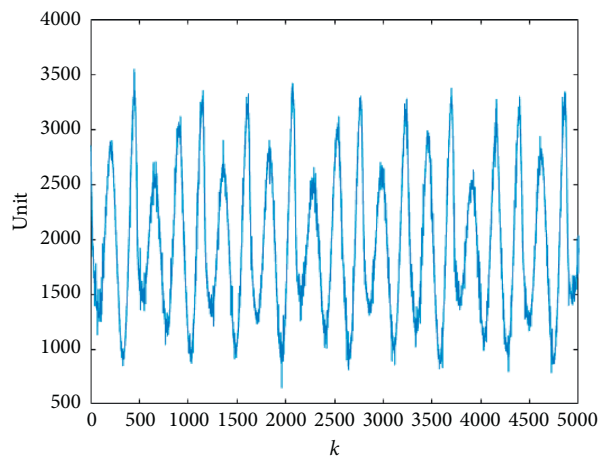

Figure 18: The data of the receiver before channel modulation.

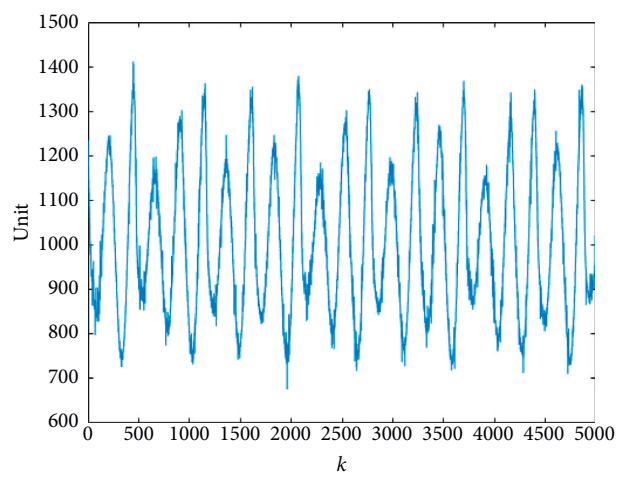

Figure 19: The data of the receiver after channel modulation.

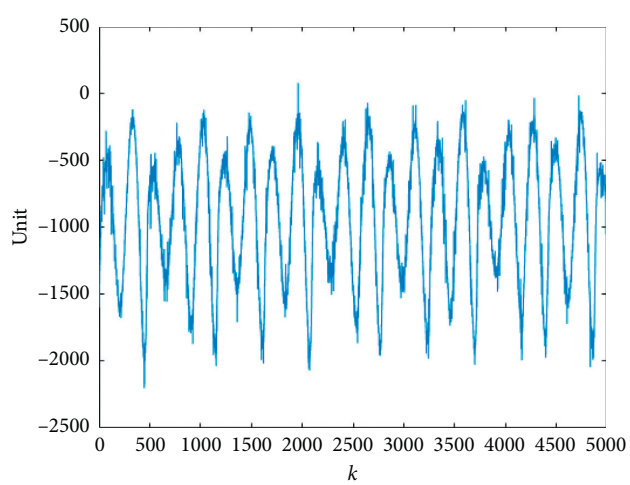

Figure 20: The error between the transmitter and receiver before channel modulation.

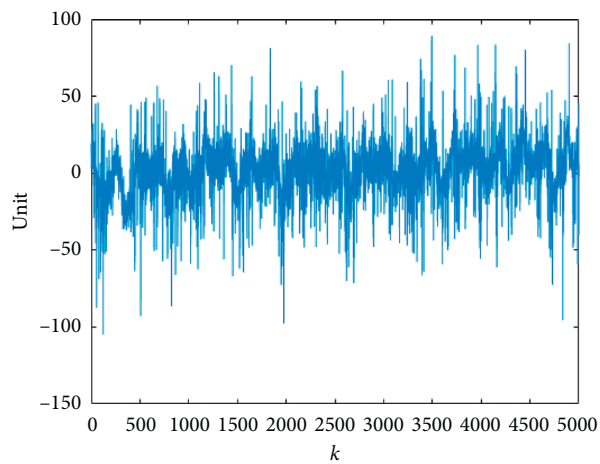

Figure 21: The error between the transmitter and receiver after channel modulation.

4. Conclusion

A novel VLC system integrated with a chaotic system has been proposed in the study to enhance the security of data transmission. The Arduino Due microcontroller is used in the proposed VLC system. LEDs are used as light sources to transmit information, and a light-sensing OPT-101 module is used to receive the light signal. A synchronization controller is used to reduce the state error and synchronize the master and slave mechanism. Some numerical simulations are conducted to verify the effectiveness of the proposed PID controller and analyze the signal. Furthermore, a chaotic system is used for encryption. The design has improved the resolution of optical communication transmission and accelerated the synchronization of the chaotic system. Most of the interference of external light sources was removed using appropriate filters. In addition, this manuscript is different from digital transmission, and we use VLC to transmit data, which proposes channel modulation methods to solve the shortcomings of analog transmission that is susceptible to external environmental interference. The experimental results of the prototype visible light information communication system can be used as the basis for the improvement of the next generation of communication technology.

Data Availability

The data used to support the findings of the study are cited in the references within the article.

Conflicts of Interest

The authors declare no conflicts of interest.

Acknowledgments

This research was supported in part by the Ministry of Science and Technology, Taiwan, under Grant nos. MOST 108-2221-E-992-094, MOST 108-2221-E-006-214-MY2, and MOST 109-2221-E-366-004.

References

[1] M. Calderbank, *The RSA Cryptosystem: History, Algorithm, Primes*, University of Chicago, Chicago, IL, USA, 2007.

[2] P. Paillier, "Public-key cryptosystems based on composite degree residuosity classes," in *Advances in Cryptology-EUROCRYPT'99*, pp. 223–238, Springer, Berlin, Germany, 1999.

[3] B. Paul and F. Marcus, "The rossler attractor in 3D," 2002, http://paulbourke.net/fractals/rossler/.

[4] Y. T. Chang, "A CDMA-based indoor visible light communications system for message broadcasting," Thesis, National Chiao Tung University Institute of Computer Science and Engineering, Hsinchu, Taiwan, 2013.

[5] Z. Y. Chen, "VLC-based indoor positioning system using smartphone," Thesis, National Yunlin University of Science and Technology Electronic Engineering, Douliu, Taiwan, 2017.

[6] C. H. Shih, "Application of remote voice control system for visible light communication," Thesis, National Chung Hsing University Electronic Engineering, Taichung, Taiwan, 2015.

[7] P. C. Chiang, "The electronic circuit realization and nonlinear analysis of synchronization between Lorenz and Rössler chaotic systems," Thesis, Department of Physics National Kaohsiung Normal University, Kaohsiung, Taiwan, 2018.

[8] K. L. Wu, "Synchronization of chaotic systems and its application," Thesis, I-SHOU University Department of Civil and Ecological Engineering, Kaohsiung, Taiwan, 2006.

[9] L. M. Pecora and T. L. Carroll, "Synchronization in chaotic systems," *Physical Review Letters*, vol. 64, no. 8, p. 821, 1990.

[10] C. S. Carroll, "Synchronous control of chaotic systems and its development in wireless digital image/audio secure communication," Thesis, National Kaohsiung Marine University, Kaohsiung, Taiwan, 2015.

[11] A. Ouannas, A. A. Khennaoui, S. Momani, V.-T. Pham, and R. El-Khazali, "Hidden attractors in a new fractional–order discrete system: chaos, complexity, entropy, and control," *Chinese Physics B*, vol. 29, no. 5, Article ID 050504, 2020.

[12] A. Ouannas, A. A. Khennaoui, S. Momani, G. Grassi, and V.-T. Pham, "Chaos and control of a three-dimensional fractional order discrete-time system with no equilibrium and its synchronization," *AIP Advances*, vol. 10, no. 4, Article ID 045310, 2020.

[13] A. Ouannas, A. A. Khennaoui, S. Momani, and V.-T. Pham, "The discrete fractional duffing system: chaos, 0–1 test, C 0 complexity, entropy, and control," *Chaos: An Interdisciplinary Journal of Nonlinear Science*, vol. 30, no. 8, Article ID 083131, 2020.

[14] C. Sánchez-López, "An experimental synthesis methodology of fractional-order chaotic attractors," *Nonlinear Dynamics*, vol. 100, no. 4, pp. 3907–3923, 2020.

[15] A. D. Pano-Azucena, J. de Jesus Rangel-Magdaleno, E. Tlelo-Cuautle, and A. de Jesus Quintas-Valles, "Arduino-based chaotic secure communication system using multi-directional multi-scroll chaotic oscillators," *Nonlinear Dynamics*, vol. 87, no. 4, pp. 2203–2217, 2017.

[16] M. Zapateiro De la Hoz, L. Acho, and Y. Vidal, "An experimental realization of a chaos-based secure communication using arduino microcontrollers," *The Scientific World Journal*, vol. 2015, Article ID 123080, 10 pages, 2015.

[17] M. L. Hung, J. S. Lin, J. J. Yan, and T. L. Liao, "Optimal PID control design for synchronization of delayed discrete chaotic systems," *Chaos, Solitons and Fractals*, vol. 35, no. 4, pp. 781–785, 2008.

[18] G. Wen, Q.-G. Wang, C. Lin, G. Li, and X. Han, "Chaos synchronization via multivariable PID control," *International Journal of Bifurcation and Chaos*, vol. 17, no. 5, pp. 1753–1758, 2007.

Hindawi
Mathematical Problems in Engineering
Volume 2021, Article ID 8887566, 10 pages
https://doi.org/10.1155/2021/8887566

Research Article

On the Approximate Solutions of the Constant Forced (Un) Damping Helmholtz Equation for Arbitrary Initial Conditions

Alvaro H. Salas,[1] **Castillo H. Jairo E**,[2] **and M. R. Alharthi**[3]

[1]*Department of Mathematics, Universidad Nacional de Colombia, Universidad Nacional de Colombia-Nubia Campus, Department of Mathematics and Statistics FIZMAKO Research Group, Manizales, Colombia*
[2]*Grupo FIZMAKO, Universidad Distrital Francisco José de Caldas, Bogotá, Colombia*
[3]*Department of Mathematics and Statistics, College of Science, Taif University, P.O. Box 11099, Taif 21944, Saudi Arabia*

Correspondence should be addressed to Alvaro H. Salas; ahsalass@unal.edu.co

Received 17 September 2020; Revised 7 January 2021; Accepted 20 January 2021; Published 31 January 2021

Academic Editor: Viet-Thanh Pham

This paper presents some novel solutions to the family of the Helmholtz equations (including the constant forced undamping Helmholtz equation (equation (1)) and the constant forced damping Helmholtz equation (equation (2))) which have been reported. In the beginning, equation (1) is solved analytically using two different techniques (direct and indirect solutions): in the first technique (direct solution), a new assumption is introduced to find the analytical solution of equation (1) in the form of the Weierstrass elliptic function with arbitrary initial conditions. In the second case (indirect solution), the solution of the undamping (standard) Duffing equation is devoted to determine the analytical solution to equation (1) in the form of Jacobian elliptic function with arbitrary initial conditions. Moreover, equation (2) is solved using a new ansatz and with the help of equation (1) solutions. Also, the evolution equations (equations (1) and (2)) are solved numerically via the Adomian decomposition method (ADM). Furthermore, a comparison between the approximate analytical solution and approximate numerical solutions using the fourth-order Runge–Kutta method (RK4) and ADM is reported. Furthermore, the maximum distance error for the obtained solutions is estimated. As a practical application, the Helmholtz-type equation will be derived from the fluid governing equations of quantum plasma particles with(out) taking the ionic kinematic viscosity into account for investigating the characteristics of (un)damping oscillations in a degenerate quantum plasma model.

1. Introduction

The ordinary and partial differential equations have played an important role in explaining many natural phenomena, in addition to their applications in many engineering and physical problems. Due to the great role played by these equations, many authors focused their efforts on finding some solutions to these equations [1–10]. The undamping Helmholtz equation ($\ddot{q}(t) + \sum_{i=1}^{n} k_i q^i(t) = 0$, where i is the odd number, i.e., $i = 1, 3, 5, \ldots$) and undamping Duffing equation ($\ddot{q}(t) + \sum_{i=1}^{n} k_i q^i(t) = 0$, where $i = 1, 2, 3, \ldots$) in addition to their family (including friction/damping force in addition to excitation/perturbation force) are among the most famous differential equations in dynamic, electrical, and engineering systems [11–16]. A lot of physical and engineering problems such as the human eardrum oscillations, the dynamics of the ships, the electrical circuits signal oscillations, heavy symmetric gyroscope, and microperforated panel absorber [17–21] have been investigated using different solutions of the Helmholtz-type oscillator. The Helmholtz-type oscillator is a second-order differential equation with a quadratic nonlinear term in addition to some other terms. For realistic physical situations, we cannot ignore both the friction/dissipation force

and excitation/perturbation forcing. Accordingly, the general form of the Helmholtz equation reads [22–24]

$$\left\{ \ddot{q} + 2\gamma\dot{q} + \alpha q + \beta q^2 = F, q(0) = q_0 \,\&\, q'(0) = \dot{q}_0, \right. \quad (1)$$

where q denotes the displacement of the system, α is the natural frequency, β is a nonlinear system parameter, γ represents the damping factor, and F is a constant/excitation force. The first equation in system (1) is called the constant forced damping Helmholtz equation (equation (2)). If the coefficient γ of the damping term $(2\gamma\dot{q})$ is neglected, equation (2) reduces to the constant forced Helmholtz equation $(\ddot{q} + \alpha q + \beta q^2 = F)$ (equation (1)). Also, if both the coefficient γ of the damping term and the constant force F are neglected, the traditional form of Helmholtz equation is covered $(\ddot{q} + \alpha q + \beta q^2 = 0)$. The initial value problem (IVP) (1) and its family have many applications in several fields, starting from analyzing the signals that propagate in electrical circuits, plasma physics, general relativity, betatron oscillations, vibrations of shells, vibrations of the acoustically driven human eardrum, solid-state physics, etc. [26–33].

It is well known that, in the absence of both friction and the excitation forces from the IVP (1), the unforced and undamping Helmholtz equations are covered. The exact analytic solutions to the unforced and undamping Helmholtz equation have been derived in detail in the literature in terms of the Weierstrass elliptic function [34–38] and Jacobi elliptic functions [38–41]. Generally, to solve any quadratic or cubic nonlinear second-order differential equation, firstly, we should transform it to an elliptic integral and then we solve it [24]. It is known that the unforced and undamping Helmholtz equations are completely integrable, so they have exact solutions, but if the friction force (damping term) is included, then the unforced damping Helmholtz equation becomes nonintegrable and cannot support an exact solution for arbitrary values of its coefficients (γ, α, β). Thus, under certain condition, the unforced damping Helmholtz equation has been solved analytically in terms of the Jacobi elliptic functions by Johannessen [24]. Also, Almendral and Sanjuán [27] derived an exact solution to the unforced damping Helmholtz equation using the Lie theory under certain conditions for the coefficients (γ, α, β).

In many realistic physical models, both the damping and the excitation/external terms are very important to be included, and thus the problem becomes more complicated to find its analytical solutions. In this paper, we will derive some analytical solutions to equation (1) in the terms of the Weierstrass and Jacobian elliptic functions. Also, an approximate analytical solution to equation (2) for arbitrary values to the coefficients and the initial conditions will be derived in detail. Moreover, the problem under consideration will be solved numerically via using the RK4 and ADM to make a comparison between the obtained solutions and the approximate numerical solutions. Furthermore, the maximum distance error between the approximate analytical solution and the approximate numerical solutions will be estimated. Also, the dynamics of nonlinear oscillations that can be generated in the RLC electronic circuits and quantum plasma will be investigated using the solution of equation (2).

The rest of this work is organized in the following manner: in Section 2, we will introduce in detail our methodology for solving the family of the Helmholtz-type equations. Also, we will introduce some new approaches for solving equation (1) as well as the exact solution of the undamped and unforced Duffing equation, which will be devoted to finding an approximate analytical solution to equation (2). In Section 3, a comparison between the obtained solutions and the approximate numerical solution using the ADM will be investigated. In Section 4, some realistic applications will be introduced. Finally, our results will be summarized in Section 5.

2. Our Methodology for Solving the Family of the Helmholtz Equations

Before proceeding in solving the IVP (1), it is necessary to refer to two fundamental equations and their solutions: the first one is called the Duffing equation and the other is called the constant forced Helmholtz equation.

2.1. Duffing Equation and Its Solution. The analytical solution to the following IVP, which is called Duffing equation [30],

$$\begin{cases} \eta''(t) + R\eta(t) + S\eta^3(t) = 0, \\ \eta(0) = \eta_0 \,\&\, \eta'(0) = \dot{\eta}_0, \end{cases} \quad (2)$$

is given by the following formula:

$$\eta(t) = c_1 cn\left(\sqrt{R + Sc_1^2}\, t + c_2, m\right). \quad (3)$$

By inserting this relation into the IVP (2) and after several tedious but simple math operations, we finally get the values of c_1 and c_2 as follows:

$$\begin{aligned} c_1 &= \pm\sqrt{\frac{-R + \sqrt{\Delta}}{S}}t, \\ c_2 &= cn^{-1}\left(\frac{\eta_0}{c_1}, \frac{Sc_1^2}{2\left(R + Sc_1^2\right)}\right), \end{aligned} \quad (4)$$

where R, S, η_0, and $\dot{\eta}_0$ are real numbers and Δ is called the discriminant to Duffing (2):

$$\Delta = \left(R + \eta_0^2 S\right)^2 + 2\dot{\eta}_0^2 S > 0. \quad (5)$$

Solution (3) could be expressed as

$$\eta(t) = \frac{\eta_0 cn(\omega t|m) + (\dot{\eta}_0/\omega)\mathrm{d}n(\omega t|m)sn(\omega t|m)}{1 - (1/2)\left(1 - \left(R + S\eta_0^2/\sqrt{\Delta}\right)\right)sn(\omega t|m)^2}, \quad (6)$$

where

$$\omega = \sqrt[4]{\Delta},$$
$$m = \frac{1}{2} - \frac{R}{2\sqrt{\Delta}}. \tag{7}$$

For negative discriminant $(\Delta < 0)$, the solution may be written in the following form:

$$\eta(t) = \rho - \frac{2\rho}{1 + \kappa sc\left(\sqrt{\omega}\, t + sc^{-1}\left(\rho + \eta_0/\kappa(\rho - \eta_0)\right), m\right)}, \tag{8}$$

where

$$m = \frac{4\rho\sqrt{2S}\sqrt{\rho^2 S - R}}{2\rho\sqrt{2S}\sqrt{\rho^2 S - R} + R - 3\rho^2 S},$$
$$\omega = \frac{1}{4}\left(2\rho\sqrt{2S}\sqrt{\rho^2 S - R} + R - 3\rho^2 S\right),$$
$$\kappa = \frac{\sqrt{2\rho\sqrt{2S}\sqrt{\rho^2 S - R} - R + 3\rho^2 S}}{\sqrt{R + \rho^2 S}}, \tag{9}$$
$$\rho = \pm\sqrt[4]{\frac{2R\eta_0^2 + S\eta_0^4 + 2\dot{\eta}_0^2}{-S}}.$$

For a zero discriminant $(\Delta = 0)$, the solution of Duffing equation (2) will be

$$\eta(t) = c_1 \tan h\left(c_1\sqrt{\frac{-S}{2}}\, t + c_2\right), \tag{10}$$

with

$$c_1 = \pm\frac{\sqrt{\sqrt{-S}\eta_0^4 - \sqrt{2}\eta_0^2\dot{\eta}_0}}{\sqrt[4]{-s}S\eta_0},$$
$$c_2 = \frac{1}{2}\log\left(\frac{\dot{\eta}_0 - \sqrt{2}\,\eta_0^2\sqrt{-S} - \sqrt[4]{-S}\sqrt{2\eta_0^4\sqrt{-S} - 2\sqrt{2}\,\eta_0^2\dot{\eta}_0}}{\dot{\eta}_0}\right), \tag{11}$$

where $\dot{\eta}_0\eta_0 \neq 0$.

When $(R + \eta_0^2 S)^2 + 2\dot{\eta}_0^2 S = \eta_0 = 0$, the solution reads

$$\eta(t) = \sqrt{\frac{-S}{2}}\,\dot{\eta}_0 \tan h\left(\sqrt{\frac{-S}{2}}\,\dot{\eta}_0 t\right). \tag{12}$$

In case $(R + \eta_0^2 S)^2 + 2\dot{\eta}_0^2 S = \dot{\eta}_0 = 0$, the solution becomes the constant function $\eta(t) = \eta_0$.

2.2. The Analytical Solution to the Constant Forced Helmholtz Equation. The solution of the constant forced Helmholtz equation

$$\begin{cases} \xi''(t) + a + b\xi(t) + c\xi^2(t) = 0, \\ \xi(0) = \xi_0 \;\&\; \xi'(0) = \dot{\xi}_0, \end{cases} \tag{13}$$

may be expressed in either one of the following forms. Note that $a = -F$.

2.2.1. First Formula. Suppose that the solution of system (13) has the following form:

$$\xi(t) = A + \frac{B}{1 + C\left((1/4)\left(d_2 - \wp'(t; g_2, g_3)/d_1 - \wp(t; g_2, g_3)\right)^2 - d_1 - \wp(t; g_2, g_3)\right)}, \tag{14}$$

as well as

$$\xi(t) = A + \frac{B}{1 + C\wp\left(t \pm \wp^{-1}(d_1; g_2, g_3); g_2, g_3\right)}, \tag{15}$$

where a represents the constant force and $\wp(t)$ gives the Weierstrass elliptic function, which satisfies the following relations:

$$\wp'(x; g_2, g_3)^2 = 4\wp^3(x; g_2, g_3) - g_1\wp(x; g_2, g_3) - g_3,$$
$$\wp''(x; g_2, g_3) = -\frac{g_2}{2} + 6\wp^2(x; g_2, g_3). \tag{16}$$

Inserting equation (14) into system (13) and after tedious straightforward calculations, we can estimate the values of B, C, g_2, g_3, d_1, and d_2 as follows:

$$B = -\frac{6(a + A(Ac + b))}{(2Ac + b)},$$
$$C = \frac{12}{2Ac + b},$$
$$g_2 = \frac{1}{12}\left(b^2 - 4ac\right),$$
$$g_3 = \frac{1}{216}(2Ac + b)\left(b^2 - 2c\left(3a + A^2c\right) - 2Abc\right), \tag{17}$$
$$d_1 = \frac{(A - \xi_0)(2Ac + b)}{6(a + A(Ac + b))},$$
$$d_2 = -\frac{\dot{\xi}_0(2Ac + b)}{6(a + A(Ac + b))}.$$

The value of parameter A represents a root to the following quartic equation:

$$\begin{aligned}
&4a^2b + a^2b^2 - 4a^3c + 4ab^2\xi_0 - 4b^2\xi_0^2 + 4abc\xi_0^2 \\
&\quad -2\begin{pmatrix} 8bc\xi_0^2 - 2ab^2 - ab^3 - 4a^2c + 4a^2bc \\ -4b^2\xi_0 - 2b^3\xi_0 - 4abc\xi_0 - 2b^2c\xi_0^2 - 4ac^2\xi_0^2 \end{pmatrix}A \\
&\quad +\begin{pmatrix} b^4 - 4b^2 + 12abc - 2ab^2c - 8a^2c^2 \\ +32bc\xi_0 + 12b^2c\xi_0 - 16c^2\xi_0^2 + 12bc^2\xi_0^2 \end{pmatrix}A^2 \\
&\quad + 2c\left(b^3 - 8b + 4ac - 4abc + 16c\xi_0 + 4bc\xi_0 + 4c^2\xi_0^2\right)A^3 \\
&\quad - c^2\left(16 - b^2 + 4ac\right)A^4 = 0.
\end{aligned} \tag{18}$$

2.2.2. Second Formula. As another form for the solution of system (13), let us assume that its solution is given by the following relationship:

$$\xi(t) = A + \frac{B}{1 - \eta(t)}, \tag{19}$$

where $\eta = \eta(t)$ is the solution to the following Duffing equation:

$$\begin{cases} \eta''(t) + R\eta(t) + S\eta^3(t) = 0, \\ \eta(0) = \eta_0 \,\&\, \eta'(0) = \dot{\eta}_0. \end{cases} \tag{20}$$

By following the same procedures in the above sections, we finally obtain

$$\begin{aligned}
R &= \frac{3a + b(3A + B) + Ac(3A + 2B)}{B}, \\
S &= -\frac{a + A(Ac + b)}{B}, \\
\eta_0 &= \frac{B}{A - \xi_0} + 1, \\
\dot{\eta}_0 &= \frac{B\dot{\xi}_0}{(A - \xi_0)^2}.
\end{aligned} \tag{21}$$

The value of parameter A is a solution to the following equation:

$$\begin{aligned}
0 &= A^6c^3 + 3bc^2A^5 + 15ac^2A^4 \\
&\quad - 10c^2\left(6a\xi_0 + 3b\xi_0^2 + 2c\xi_0^3 + 3\dot{\xi}_0^2\right)A^3 \\
&\quad - 15c\left(3a^2 + 6ab\xi_0 + 3b^2\xi_0^2 + 2bc\xi_0^3 + 3b\dot{\xi}_0^2\right)A^2 \\
&\quad - 3\begin{pmatrix} 9a^2b + 18ab^2\xi_0 - 12a^2c\xi_0 + 9b^3\xi_0^2 \\ -6abc\xi_0^2 + 6b^2c\xi_0^3 - 4ac^2\xi_0^3 + 9b^2\dot{\xi}_0^2 - 6ac\dot{\xi}_0^2 \end{pmatrix}A \\
&\quad + \begin{pmatrix} -27a^3 - 54a^2b\xi_0 - 27ab^2\xi_0^2 - 72a^2c\xi_0^2 - 90abc\xi_0^3 \\ -18b^2c\xi_0^4 - 48ac^2\xi_0^4 - 24bc^2\xi_0^5 - 8c^3\xi_0^6 - 27ab\dot{\xi}_0^2 \\ -72ac\xi_0\dot{\xi}_0^2 - 36bc\xi_0^2\dot{\xi}_0^2 - 24c^2\xi_0^3\dot{\xi}_0^2 - 18c\dot{\xi}_0^4 \end{pmatrix}.
\end{aligned} \tag{22}$$

Also, the value of parameter B is a solution to the following equation:

$$\begin{aligned}
0 &= c^4B^6 - 9c^2\left(b^2 - 4ac\right)B^4 - \\
&\quad 432\begin{pmatrix} -3a^2b^2 + 16a^3c - 6ab^3\xi_0 + 36a^2bc\xi_0 \\ -3b^4\xi_0^2 + 18ab^2c\xi_0^2 + 36a^2c^2\xi_0^2 - 2b^3c\xi_0^3 \\ +48abc^2\xi_0^3 + 9b^2c^2\xi_0^4 + 24ac^3\xi_0^4 + 12bc^3\xi_0^5 + \\ 4c^4\xi_0^6 - 3b^3\dot{\xi}_0^2 + 18abc\dot{\xi}_0^2 + 36ac^2\xi_0\dot{\xi}_0^2 \\ +18bc^2\xi_0^2\dot{\xi}_0^2 + 12c^3\xi_0^3\dot{\xi}_0^2 + 9c^2\dot{\xi}_0^4 \end{pmatrix}.
\end{aligned} \tag{23}$$

2.3. The Approximate Analytical Solution for the Constant Forced and Damped Helmholtz Equation. Let us rewrite system (1) in the following traditional form:

$$\left\{\ddot{x} + 2\varepsilon\dot{x} + \alpha x + \beta x^2 = F, x(0) = x_0 \;\; x'(0) = \dot{x}_0,\right. \tag{24}$$

with $\beta \neq 0$.

Also, let us assume that

$$\alpha^2 + 4F\beta \geq 0. \tag{25}$$

Now, suppose that the solution of system (24) is given by

$$x(t) = d + \exp(-\varepsilon t)y(t), \tag{26}$$

where $y = y(t)$ is a solution to the following Helmholtz equation:

$$\begin{cases} y'' + py + \beta y^2 = 0, \\ y(0) = y_0 = x_0 - d, \\ y'(0) = \dot{y}_0 = \varepsilon x_0 + \dot{x}_0 - \mathrm{d}\varepsilon. \end{cases} \tag{27}$$

Inserting (26) into the first equation in system (24), $\mathbb{R}(t) \equiv \ddot{x} + 2\varepsilon\dot{x} + \alpha x + \beta x^2 - F = 0$, we obtain

$$\begin{aligned}
\mathbb{R}(t) &= \beta d^2 + \alpha d - F \\
&\quad + e^{-2\varepsilon t}y(t)\left[\beta y(t) - e^{\varepsilon t}\left(-\alpha - 2\beta d + \varepsilon^2 + p + \beta y(t)\right)\right].
\end{aligned} \tag{28}$$

Expression (28) suggests the following choices:

$$\begin{aligned}
-\alpha - 2\beta d + \varepsilon^2 + p &= 0, \\
\beta d^2 + \alpha d - F &= 0,
\end{aligned} \tag{29}$$

giving us the values of p and d as follows:

$$\begin{aligned}
p &== \alpha + 2\beta d - \varepsilon^2, \\
d &= \frac{-\alpha + \sqrt{\alpha^2 + 4F\beta}}{2\beta}.
\end{aligned} \tag{30}$$

The solution to the following IVP,

$$\begin{cases} y'' + \left(\alpha + 2\beta d - \varepsilon^2\right) y + \beta y^2 = 0, \\ y(0) = y_0 = x_0 - d, \\ y'(0) = \dot{y}_0 = \varepsilon x_0 + \dot{x}_0 - \mathrm{d}\varepsilon, \end{cases} \tag{31}$$

may be expressed in different forms as we explained in the previous section.

3. A Comparison between Our Solutions and ADM Solution

There are many numerical methods that could be used to find approximate solutions to IVP (24). Here, we make use of the ADM [42–44] to solve IVP (24) with(out) forcing term (F). According to this method, the first iteration/approximation for the unforced case (F) reads

$$x_{\mathrm{ADM0}}(t) = \left(\frac{e^{-\varepsilon t}}{\mathscr{F}}\right)\left[(\varepsilon x_0 + \dot{x}_0)\Theta_1 + x_0 \mathscr{F} \Theta_2\right], \tag{32}$$

where $\Theta_1 = \sin(t\mathscr{F})$, $\Theta_2 = \cos(t\mathscr{F})$, and $\mathscr{F} = \sqrt{\alpha - \varepsilon^2}$.

For the second iteration/approximation, we have

$$x_{\mathrm{ADM1}}(t) = \beta\left(\frac{e^{-\varepsilon t}}{\alpha\mathscr{F}}\right)^3 \frac{\left(-e^{\varepsilon t}\mathscr{F} + \varepsilon\Theta_1 + \mathscr{F}\Theta_2\right)}{\left[\alpha x_0 \mathscr{F}\Theta_2 + \left(\varepsilon x_0 \mathscr{F}^2 + \dot{x}_0 \mathscr{F}^2 + \varepsilon^3 x_0 + \varepsilon^2 \dot{x}_0\right)\Theta_1\right]^2}. \tag{33}$$

The approximate Adomian approximate solution reads

$$x(t) = x_{\mathrm{ADM0}}(t) + x_{\mathrm{ADM1}}(t) + \cdots. \tag{34}$$

For $(\varepsilon, \alpha, \beta, F) = (0.1, 4, 1, 0)$ and $x(0) = 0$ & $x'(0) = 0.2$, we can compare between the approximate/semi-analytical solution (26) (for $F = 0$) and the ADM approximate numerical solution (34) and the RK4 approximate numerical solution as shown in Figure 1. Also, the maximum distance error according to the formula $L_D = \max_{t_i \le t \le t_f} |x_{\mathrm{RK4}}(t) - x_{\mathrm{method}}(t)|$ has been estimated:

$$\begin{aligned} L_D &= \max_{0 \le t \le 40} \left|x_{\mathrm{RK4}}(t) - x_{\mathrm{semi-analy}}(t)\right| = 0.000504825, \\ L_D &= \max_{0 \le t \le 40} \left|x_{\mathrm{RK4}}(t) - x_{\mathrm{ADM}}(t)\right| = 0.0000997768. \end{aligned} \tag{35}$$

It is clear that the semianalytical solution (26) (for $F = 0$) gives good results as compared to both the RK4 and ADM approximate numerical solutions.

Now, let us find an approximate solution for IVP (24) in the presence of the forcing term, using the ADM. Accordingly, the first approximation is given by

$$x_{\mathrm{ADM0}}(t) = \left(\frac{e^{-\varepsilon t}}{\widetilde{\mathscr{F}}}\right)\left[\left(\varepsilon\left(x_0 - d\right) + \dot{x}_0\right)\widetilde{\Theta}_1 + \left(x_0 - d\right)\widetilde{\mathscr{F}}\widetilde{\Theta}_2\right], \tag{36}$$

where $\widetilde{\Theta}_1 = \sin(t\widetilde{\mathscr{F}})$, $\widetilde{\Theta}_2 = \cos(t\widetilde{\mathscr{F}})$, $\widetilde{\mathscr{F}} = \sqrt{\Lambda - \varepsilon^2}$, $\Lambda = (\alpha + 2\beta d)$, and $d = (-\alpha \pm \sqrt{\alpha^2 + 4F\beta})/(2\beta)$.

The second approximation to IVP (24) according to the ADM reads

$$\begin{aligned} x_{\mathrm{ADM1}}(t) = {} & \left(\frac{\beta e^{-2t\varepsilon}}{2\Lambda\widetilde{\mathscr{F}}^2}\right)\left[\left(d - x_0\right)^2\left(-2d\beta - \alpha\right) + 2\dot{x}_0\varepsilon\left(d - x_0\right) - \dot{x}_0^2\right] \\ & + \left(\frac{\beta e^{-t\varepsilon}}{\Lambda\widetilde{\mathscr{F}}\mathbb{N}}\right)\left[\varepsilon\left(d - x_0\right)^2\left(13\Lambda - 8\varepsilon^2\right) - 6\Lambda\dot{x}_0\left(d - x_0\right) + 2\dot{x}_0^2\varepsilon\right]\widetilde{\Theta}_1 \\ & + \left(\frac{\beta e^{-2t\varepsilon}}{\Lambda\widetilde{\mathscr{F}}\mathbb{N}}\right)\left[\varepsilon\left(d - x_0\right)^2\left(8\varepsilon^2 - 5\Lambda\right) + \dot{x}_0\left(d - x_0\right)\left(3\Lambda - 8\varepsilon^2\right) + 2\dot{x}_0^2\varepsilon\right]\widetilde{\Theta}_1 \\ & - \left(\frac{\beta e^{-t\varepsilon}}{\Lambda\mathbb{N}}\right)\left[\left(d - x_0\right)^2\left(3\Lambda + 8\varepsilon^2\right) + 16\dot{x}_0\varepsilon\left(x_0 - d\right) + 6\dot{x}_0^2\right]\widetilde{\Theta}_2 \\ & - \left(\frac{\beta e^{-2t\varepsilon}}{2\Lambda\mathbb{N}\widetilde{\mathscr{F}}^2}\right)\begin{pmatrix} 2\dot{x}_0\varepsilon\left(d - x_0\right)\left(7\Lambda - 8\varepsilon^2\right) + \dot{x}_0^2\left(-3\Lambda + 4\varepsilon^2\right) + \\ \left(d - x_0\right)^2\left(-18\varepsilon^2\Lambda + 3\Lambda^2 + 16\varepsilon^4\right) \end{pmatrix}\widetilde{\Theta}_2, \end{aligned} \tag{37}$$

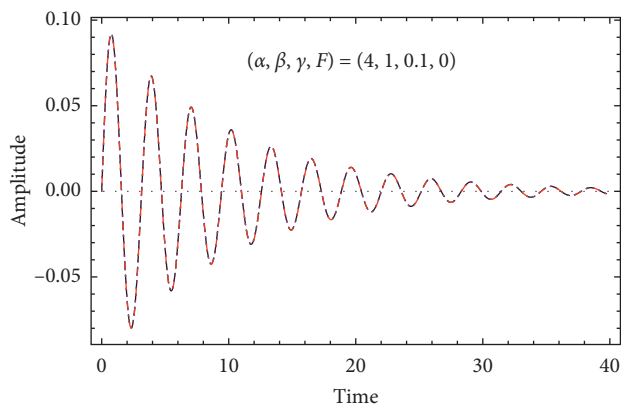

Figure 1: A comparison between approximate analytical solution (26) (dotted curve) for $F = 0$ and both RK4 (dashed curve) and ADM (dashed-dot curve) numerical solutions is plotted against the time.

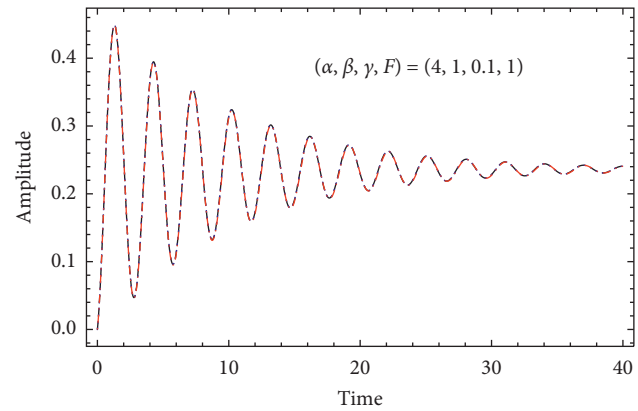

Figure 2: A comparison between approximate analytical solution (26) (dotted curve) for $F \neq 0$ and both RK4 (dashed curve) and ADM (dashed-dot curve) numerical solutions is plotted against the time.

where $\mathbb{N} = (8\varepsilon^2 - 9(2\,d\beta + \alpha))$.

The approximate Adomian approximate solution is given by

$$x(t) = x_{\mathrm{ADM0}}(t) + x_{\mathrm{ADM1}}(t) + \cdots. \tag{38}$$

For $(\varepsilon, \alpha, \beta, F) = (0.1, 2, 1, 1)$ and $x(0) = 0$ & $x'(0) = 0.2$, a comparison between the semianalytical solution (26) (for $F \neq 0$) and the ADM approximate numerical solution (38) and the RK4 approximate numerical solution has been investigated as shown in Figure 2. Furthermore, the maximum distance error has been calculated as follows:

$$\begin{aligned} L_D &= \max_{0\le t\le 40}\left|x_{\mathrm{RK4}}(t) - x_{\mathrm{semi-analy}}(t)\right| = 0.00332902, \\ L_D &= \max_{0\le t\le 40}\left|x_{\mathrm{RK4}}(t) - x_{\mathrm{ADM}}(t)\right| = 0.00132421. \end{aligned} \tag{39}$$

Also, the semianalytical solution (26) for $F = 0$ and $F \neq 0$ gives excellent results as compared to the ADM approximate numerical solution (38).

4. Quantum Plasma Oscillations

In this section, we will reduce the fluid governing equations of a quantum plasma model to an evolution equation using the RPT [45–49]. After a suitable transformation, we will be able to convert the obtained evolution equation to a Helmholtz-type equation in order to investigate the characteristics behavior of the damping oscillations in the model under consideration. Now, let us assume that we have a collisionless and unmagnetized electron-ion quantum plasma consisting of inertialess degenerate trapped electrons which obey the Fermi–Dirac distribution and classical fluid cold positive nondegenerate ion. Thus, the basic normalized fluid equations that govern the nonlinear dynamics of various structures could be presented as [51, 52]

$$\begin{aligned} \partial_t n + \partial_x(nu) &= 0, \\ \partial_t u + u\partial_x u + \partial_x \phi &= \eta \partial_x^2 u, \\ \partial_x^2 \phi &= (n_e - n), \end{aligned} \tag{40}$$

where n_e and n represent the normalized electron and ion number densities, respectively, u gives the normalized ion speed, η is the normalized kinematic viscosity of the ions, and ϕ indicates the normalized electrostatic wave potential. Therefore, we shall adopt the adiabatic trapped degeneracy for electrons, by relying on notations similar to those in [52], wherein the fundamental algebra is expressed in detail. The electron normalized number density according to Fermi–Dirac distribution reads

$$\begin{aligned} n_e &= \sqrt{(1+\phi)^3} + \frac{T^2}{\sqrt{(1+\phi)}} \\ &\approx s_0 + s_1\phi + s_2\phi^2 + s_3\phi^3, \end{aligned} \tag{41}$$

where T expresses the normalized temperature of the degenerate electron, $s_0 = (1 + T^2)$, $s_1 = (3 - T^2)/2$, $s_2 = 3(1 + T^2)/8$, and $s_3 = -(1 + 5T^2)/6$. Note that expression (41) is obtained under the approximation $\phi \ll 1$ for small wave amplitude.

For investigating the nonlinear structures and oscillations in the present model, the RPM will be employed for this purpose. Accordingly, the stretching and expansions for the independent and dependent variables are, respectively, introduced as follows:

$$\begin{aligned} \xi &= \varepsilon^{(1/2)}\left(x - V_{\mathrm{ph}}t\right), \\ \tau &= \varepsilon^{(3/2)}t, \end{aligned} \tag{42}$$

$$\begin{aligned} n(x,t) &= 1 + \varepsilon n^{(1)} + \varepsilon^2 n^{(2)} + \varepsilon^3 n^{(3)} + \cdots, \\ u(x,t) &= \varepsilon u^{(1)} + \varepsilon^2 u^{(2)} + \varepsilon^3 u^{(3)} + \cdots, \\ \phi(x,t) &= \varepsilon \phi^{(1)} + \varepsilon^2 \phi^{(2)} + \varepsilon^3 \phi^{(3)} + \cdots, \end{aligned} \tag{43}$$

where ε is a small ($\varepsilon \ll 1$) and real parameter and V_{ph} represents the normalized phase velocity of the unmodulated structures. It is assumed that the impact of ionic kinematic viscosity is small according to many lab experiments [53, 54]. Thus, we could set $\eta = \varepsilon^{1/2}\tilde{\eta}$, where $\tilde{\eta}$ is $O(1)$. By substituting stretching (42) and expansions (43) into system (40) and by collecting the terms of different powers of ε, we could get a system of reduced equations. Solving the system of reduced equations for the first-two orders of ε by following the same procedures in [46–49], we finally obtain the Korteweg–de Vries Burgers (KdVB) equation [50].

$$\partial_\tau \phi + A_p \phi \partial_\xi \phi + B_p \partial_\xi^3 \phi - C_p \partial_\xi^2 \phi = 0, \tag{44}$$

with

$$\begin{aligned} A_p &= B_p\left(\frac{3}{V_{\text{ph}}^4} - 2s_2\right), \\ B_p &= \frac{V_{\text{ph}}^3}{2}, \\ C_p &= \frac{\tilde{\eta}}{2}, \\ V_{\text{ph}} &= \frac{1}{\sqrt{s_1}}, \end{aligned} \tag{45}$$

where A_p, B_p, and C_p represent the coefficients of the nonlinear, dispersion, and dissipative terms, respectively, and $\phi \equiv \phi^{(1)}$.

Using the traveling wave transformation $\phi(\xi + V_f t) = q(\zeta)$, where $\zeta = \xi + V_f t$ and V_f gives the frame velocity, into the KdVB equation (44) and integrating once over ζ, we get the constant forced and damped Helmholtz equation as follows:

$$q''(\zeta) + 2\gamma q'(\zeta) + \alpha q(\zeta) + \beta q(\zeta)^2 = \mathbb{C}, \tag{46}$$

where $\mathbb{C}$ is the integration constant, $\gamma = -C_p/(2B_p)$, $\alpha = V_f/B_p$, and $\beta = A_p/(2B_p)$. Now, we can apply the above solution of the constant forced and damped Helmholtz equation that is given in equation (26) to equation (46) for investigating the characteristics of the damped oscillations in a quantum plasma.

Note that if the ionic kinematic viscosity is neglected, i.e., $C_p = 0$, then the KdV and undamped Helmholtz equations could be covered. The KdV equation, i.e., equation (44) for $C_p = 0$, is one of the most popular soliton and cnoidal equations and has been extensively investigated. For the soliton solution, the following conditions must be fulfilled: $(q(\zeta), q'(\zeta), q''(\zeta)) \longrightarrow 0$ at $\zeta \longrightarrow \pm\infty$, so the integration constant $\mathbb{C}$ in equation (46) must vanish. Accordingly, equation (46) could be reduced to the undamped Helmholtz equation:

$$q''(\zeta) + \alpha q(\zeta) + \beta q(\zeta)^2 = 0. \tag{47}$$

It is well known that equation (47) supports many solutions such as periodic solution (see the solutions to the constant forced Helmholtz equation above) and solitons. The soliton solution to equation (47) in the form of the Weierstrass elliptic function $\wp$ could be written in the following manner:

$$\phi(x,t) = \frac{2\alpha\beta + \sqrt{\alpha^2\left(\beta^2 + 2\alpha C\right)}}{\alpha^2} - \frac{(9\beta/2\alpha)}{1 + 6\wp\left(x - \left(t\sqrt{\alpha^2\left(\beta^2 + 2C\alpha\right)}/\alpha\right); (1/12), -(1/216)\right)}, \tag{48}$$

where $(x,t) \equiv (\zeta, \tau)$.

Here, the obtained approximate analytical solution (26) to the constant forced and damped Helmholtz equation (46) will be analyzed numerically according to the quantum plasma parameters $(T, \tilde{\eta}) = (0.1, 0.055)$, i.e., $(\alpha, \beta, \gamma, F) = (1.828, 2.98, -0.05, F)$, and $(T, \tilde{\eta}) = (0.9, 0.18)$, i.e., $(\alpha, \beta, \gamma, F) = (1.146, 1.7273, -0.1, F)$. The behavior of the quantum plasma oscillations according to the approximate analytical solution (26) and the approximate numerical solution according to the RK4 method is presented in Figure 3 for different values of quantum plasma parameters. It is clear from Figure 3 that our approximate analytical solution (26) is more accurate than the RK4 numerical solution. On the contrary, the RK4 numerical solution gives poor results and with increasing time this solution becomes unstable.

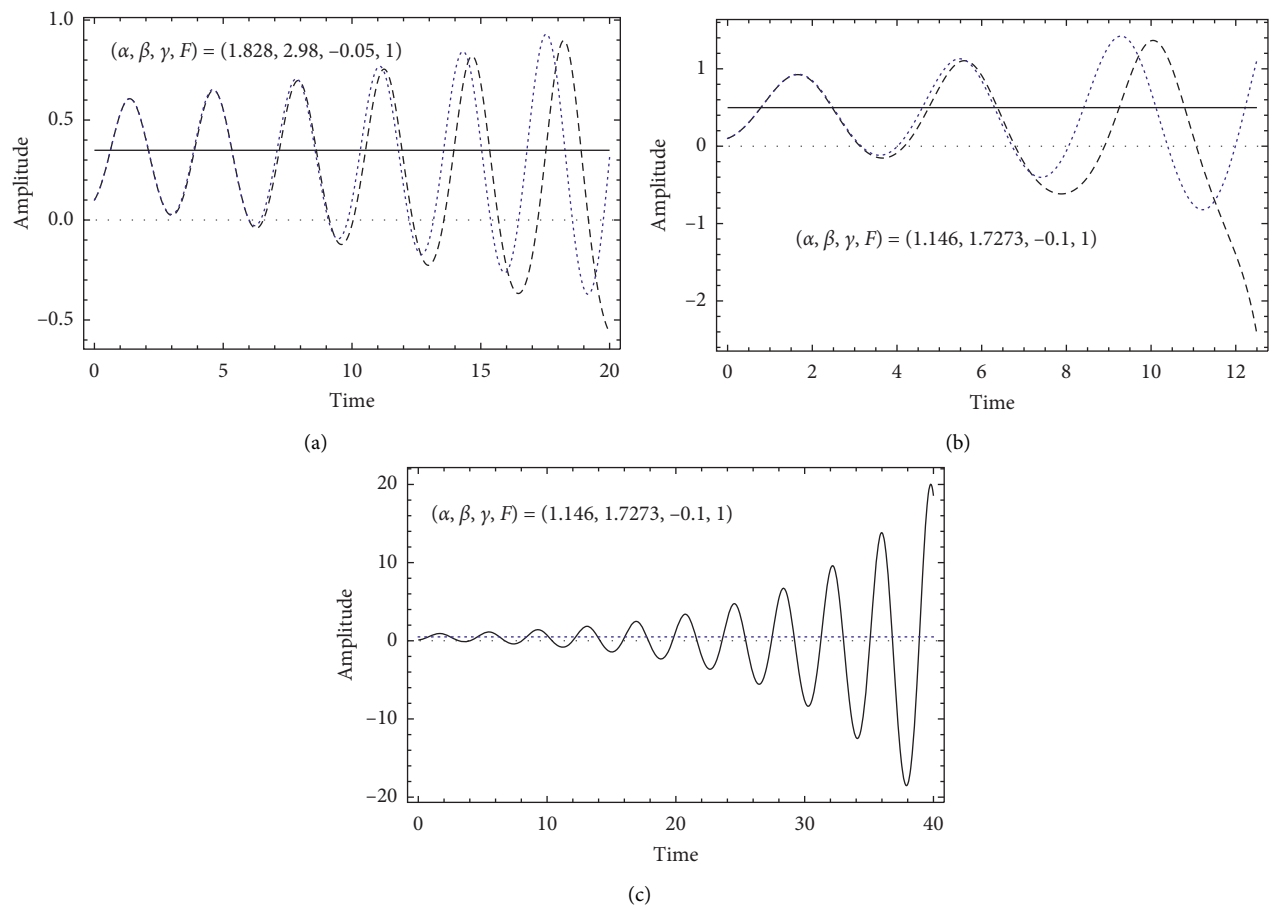

Figure 3: A comparison between the approximate analytical solution (26) (dotted curve) and the RK4 numerical solution (dashed curve) is plotted for different values of quantum plasma parameters $(T, \tilde{\eta})$, i.e., for different values of $(\alpha, \beta, \gamma, F)$. Here, $q_0 = 0.1$, and $\dot{q}_0 = 0.2$.

5. Conclusions

The Helmholtz-type equations including the constant forced undamping Helmholtz equation (equation (1)) and the constant forced damping Helmholtz equation (equation (2)) have been solved analytically and numerically. Two techniques were used to get the analytical solutions to equation (1). In the first technique, we used a new assumption to find an analytical solution to equation (1) in the form of Weierstrass elliptic function. In the second case, the solution of the standard Duffing equation has been utilized to find an analytical solution to equation (1) in the form of Jacobian elliptic function. However, the main goal of this paper is to solve equation (2), using the obtained solutions of equation (1). Moreover, both equation (1) and equation (2) have been solved numerically via the ADM. The analytical and approximate analytical solutions of equations (1) and (2) have been compared to the RK4 and ADM approximate numerical solutions. Furthermore, the maximum distance error between the RK4 approximate numerical solution and the approximate analytical solutions in addition to the approximate numerical solution using the ADM has been estimated. It was found that the obtained solutions are generally consistent with both RK4 and ADM solutions. Moreover, the obtained solutions have been applied for analyzing the oscillations that may arise in the quantum plasma. During the analysis, it was found sometimes that the approximate analytical solution is better than the RK4 numerical solution as shown in the quantum plasma model. Finally, these solutions may help us understand the oscillations that may arise in the different physical and engineering systems.

In future work, the similar approaches could be used for analyzing and solving higher-order nonlinear oscillator equations. Also, a damping Helmholtz–Duffing equation with time-dependent forced term is considered one of the most important and vital problems due to its great role in explaining many natural phenomena in different branches of science. Thus, in the next work, some new approaches will be devoted to find some solutions for these problems.

Data Availability

No data were used to support the findings of this study.

Conflicts of Interest

The authors declare that they have no conflicts of interest.

Acknowledgments

This study was supported by Taif University Researchers Supporting Project (no. TURSP-2020/275), Taif University,

Taif, Saudi Arabia. The authors thank Associate Professor S.A. El-Tantawy, the Chief of Research Center for Physics (RCP), Faculty of Science and Arts, Al-Baha University, Saudi Arabia, and Faculty of Science, Port Said University, Egypt, for fruitful discussions, careful reading, his contributions to applications to plasma physics, and improving their manuscript very well.

References

[1] A. Ouannas, A. A. Khennaoui, X. Wang, V.-T. Pham, S. Boulaaras, and S. Momani, "Bifurcation and chaos in the fractional form of Hénon-Lozi type map," *The European Physical Journal Special Topics*, vol. 229, no. 12-13, pp. 2261–2273, 2020.

[2] A. Ben Dhahbi, Y. Chargui, S. M. Boulaaras, and S. Ben Khalifa, "A one-sided competition mathematical model for the sterile insect technique," *Complexity*, vol. 2020, Article ID 6246808, 12 pages, 2020.

[3] A. M. Wazwaz, *Partial Differential Equations and Solitary Waves Theory*, Higher Education Press, Beijing, China, 2009.

[4] S. A. El-Tantawy, "Nonlinear dynamics of soliton collisions in electronegative plasmas: the phase shifts of the planar KdV- and mkdV-soliton collisions," *Chaos, Solitons & Fractals*, vol. 93, pp. 162–168, 2016.

[5] S. A. El-Tantawy, M. H. Alshehri, F. Z. Duraihem, and L. S. El-Sherif, "Dark soliton collisions and method of lines approach for modeling freak waves in a positron beam plasma having superthermal electrons," *Results in Physics*, vol. 19, pp. 103452–103458, 2020.

[6] S. Boulaaras and M. Haiour, "L^∞-asymptotic behavior for a finite element approximation in parabolic quasi-variational inequalities related to impulse control problem," *Applied Mathematics and Computation*, vol. 217, no. 14, pp. 6443–6450, 2011.

[7] S. Boulaaras and M. Haiour, "The finite element approximation of evolutionary Hamilton-Jacobi-Bellman equations with nonlinear source terms," *Indagationes Mathematicae*, vol. 24, no. 1, pp. 161–173, 2013.

[8] S. Boulaaras, "Some new properties of asynchronous algorithms of theta scheme combined with finite elements methods for an evolutionary implicit 2-sided obstacle problem," *Mathematical Methods in the Applied Sciences*, vol. 40, no. 18, pp. 1–9, 2017.

[9] S. Boulaaras, M. Haiour, and M. A. Bencheick Le hocine, "L^∞-error estimates of discontinuous Galerkin methods with theta time discretization scheme for an evolutionary HJB equations L^∞-error estimates of discontinuous Galerkin methods with theta time discretization scheme for an evolutionary HJB equations"" *Mathematical Methods in the Applied Sciences*, vol. 40, no. 12, p. 4310, 2017.

[10] S. Boulaaras, M. El Amine Bencheikh Le Hocine, and M. Haiour, "A new error estimate on uniform norm of a parabolic variational inequality with nonlinear source terms via the subsolution concepts," *Journal of Inequalities and Applications*, vol. 2020, 2020.

[11] K. Johannessen, "The Duffing oscillator with damping," *European Journal of Physics*, vol. 36, 2015.

[12] K. Johannessen, "The duffing oscillator with damping for a softening potential," *International Journal of Applied and Computational Mathematics*, vol. 3, no. 4, p. 3805, 2017.

[13] A. Elías-Zúñiga, "Exact solution of the quadratic mixed-parity Helmholtz-Duffing oscillator," *Applied Mathematics and Computation*, vol. 218, no. 14, pp. 7590–7594, 2012.

[14] M. Hammad, A. H. Salas, and S. A. El-Tantawy, "New method for solving strong conservative odd parity nonlinear oscillators: applications to plasma physics and rigid rotator," *AIP Advances*, vol. 10, no. 8, pp. 085001–085011, 2020.

[15] A. H. Salas and S. A. El-Tantawy, "On the approximate solutions to a damped harmonic oscillator with higher-order nonlinearities and its application to plasma physics: semi-analytical solution and moving boundary method," *The European Physical Journal-Plus*, vol. 135, pp. 833–917, 2020.

[16] Md.A. Hosen and M. S. H. Chowdhury, "Analytical approximate solutions for the helmholtz-duffing oscillator," *ARPN Journal of Engineering and Applied Sciences*, vol. 10, pp. 17363–17369, 2015.

[17] Y. Geng, "Exact solutions for the quadratic mixed-parity Helmholtz-Duffing oscillator by bifurcation theory of dynamical systems," *Chaos, Solitons & Fractals*, vol. 81, pp. 68–77, 2015.

[18] E. Metter, "Dynamic buckling," in *Handbook of Engineering Mechanics*, W. Flügge, Ed., Wiley, Hoboken, NJ, USA, 1992.

[19] M. Bikdash, B. Balachandran, and A. Nayfeh, "Melnikov analysis for a ship with a general roll-damping model," *Nonlinear Dynamics*, vol. 6, pp. 101–124, 1994.

[20] V. Ajjarapu and B. Lee, "Bifurcation theory and its application to nonlinear dynamical phenomena in an electrical power system," *IEEE Transactions on Power Systems*, vol. 7, no. 1, pp. 424–431, 1992.

[21] I. S. Kang and L. G. Leal, "Bubble dynamics in time-periodic straining flows," *Journal of Fluid Mechanics*, vol. 218, no. 1, pp. 41–69, 1990.

[22] D.-Q. Wei, X.-S. Luo, and S.-Y. Zeng, "Noise-triggered escapes in Helmholtz oscillator," *Modern Physics Letters B*, vol. 28, pp. 1450047-1450048, 2014.

[23] J. A. Almendral, J. M. Seoane, and M. A. F. Sanjúan, "Nonlinear dynamics of the helmholtz oscillator," *Journal of Sound and Vibration*, vol. 2, pp. 115–150, 2004.

[24] K. Johannessen, "The solution to the differential equation with linear damping describing a physical systems governed by a cubic energy potential," http://arxiv.org/abs/1810.10336.

[25] J. M. Seoane, S. Zambrano, S. Euzzor, R. Meucci, F. T. Arecchi, and M. A. F. Sanju, "Avoiding escapes in open dynamical systems using phase control," *Physical Review E*, vol. 75, pp. 16205–16208, 2008.

[26] N. Nayfeth and D. T. Mook, *Non-linear Oscillations*, Wiley, New York, NY, USA, 1973.

[27] J. A. Almendral and M. A. F. Sanjuan, "Integrability and symmetries for the helmholtz oscillator with friction," *Journal of Physics A: Mathematical and General*, vol. 36, no. 3, pp. 695–710, 2003.

[28] S. Morfa and J. C. Comte, "A nonlinear oscillators network devoted to image processing," *International Journal of Bifurcation and Chaos*, vol. 14, pp. 1385–1394, 2009.

[29] Y. Geng, J. Li, and L. Zhang, "Exact explicit traveling wave solutions for two nonlinear Schrödinger type equations," *Applied Mathematics and Computation*, vol. 217, no. 4, pp. 1509–1521, 2010.

[30] A. H. Salas and J. E. Castillo, "Exact solutions to cubic Duffing equation for a nonlinear electrical circuit," *Visión Electrónica: algo más que un Estado Sólido*, vol. 8, pp. 46–53, 2014.

[31] E. Gluskin, "A nonlinear resistor and nonlinear inductor using a nonlinear capacitor," *Journal of the Franklin Institute*, vol. 336, no. 7, pp. 1035–1047, 1999.

[32] A. H. Salas, "Soluciones exactas a la ecuación del oscilador de helmholtz para circuitos eléctricos con no linealidad cuadrática," *Visión Electrónica*, vol. 9, no. 2, pp. 248–252, 2015.

[33] A. H. Salas, E. Jairo, H. Castillo, J. Darin, and P. Mosquera, "A new approach for solving the undamped Helmholtz oscillator for the given arbitrary initial conditions and its physical applications," *Mathematical Problems in Engineering*, vol. 2020, Article ID 7876413, 7 pages, 2020.

[34] K. S. Viswanathan, "The theory of the anharmonic oscillator," *Proceedings of the Indian Academy of Sciences A*, vol. 46, pp. 201–217, 1957.

[35] B. F. Apostol, "On anharmonic oscillators," *Journal of Physics*, vol. 50, pp. 915–918, 2005.

[36] P. Amore and F. M. Fernández, "Exact and approximate expressions for the period of anharmonic oscillators," *European Journal of Physics*, vol. 26, no. 4, pp. 589–601, 2005.

[37] S. Y. Vernov, "Exact solutions of nonlocal nonlinear field equations in cosmology," *Theoretical and Mathematical Physics*, vol. 166, no. 3, pp. 392–402, 2011.

[38] A. J. Brizard, "A primer on elliptic functions with applications in classical mechanics," *European Journal of Physics*, vol. 30, no. 4, pp. 729–750, 2009.

[39] J.-H. He, "Some asymptotic methods for strongly nonlinear equations," *International Journal of Modern Physics B*, vol. 20, no. 10, pp. 1141–1199, 2006.

[40] P. Walker, "The analyticity of Jacobian functions with respect to the parameter k," *Proceedings of the Royal Society of London. Series A: Mathematical, Physical and Engineering Sciences*, vol. 459, no. 2038, pp. 2569–2574, 2003.

[41] A. A. Hussein and S. Al Athel, "A note on the Helmholz oscillator," *Chaos, Solitons & Fractals*, vol. 12, no. 10, pp. 1835–1838, 2001.

[42] G. Adomian, "A review of the decomposition method in applied mathematics," *Journal of Mathematical Analysis and Applications*, vol. 135, no. 2, pp. 501–544, 1988.

[43] A.-M. Wazwaz, "Adomian decomposition method for a reliable treatment of the Bratu-type equations," *Applied Mathematics and Computation*, vol. 166, no. 3, pp. 652–663, 2005.

[44] A. M. Wazwaz, "A new algorithm for calculating Adomian polynomials for nonlinear operators," *Applied Mathematics and Computation*, vol. 111, pp. 53–69, 2000.

[45] H. Washimi and T. Taniuti, "Propagation of ion-acoustic solitary waves of small amplitude," *Physical Review Letters*, vol. 17, no. 19, pp. 996–998, 1966.

[46] N. H. Aljahdaly and S. A. El-Tantawy, "Simulation study on nonlinear structures in nonlinear dispersive media," *Chaos: An Interdisciplinary Journal of Nonlinear Science*, vol. 30, no. 5, pp. 053117–53213, 2020.

[47] B. S. Kashkari, S. A. El-Tantawy, A. H. Salas, and L. S. El-Sherif, "Homotopy perturbation method for studying dissipative nonplanar solitons in an electronegative complex plasma," *Chaos, Solitons & Fractals*, vol. 130, pp. 109457–109510, 2020.

[48] S. A. El-Tantawy, T. Aboelenen, and S. M. E. Ismaeel, "Local discontinuous Galerkin method for modeling the nonplanar structures (solitons and shocks) in an electronegative plasma," *Physics of Plasmas*, vol. 26, no. 2, pp. 022115–22211, 2019.

[49] S. A. El-Tantawy and A. M. Wazwaz, "Anatomy of modified Korteweg–de Vries equation for studying the modulated envelope structures in non-Maxwellian dusty plasmas: freak waves and dark soliton collisions," *Physics of Plasmas*, vol. 25, 2018.

[50] S. A. El-Tantawy, "Effect of ion viscosity on dust ion-acoustic shock waves in a nonextensive magnetoplasma," *Astrophysics and Space Science*, vol. 361, p. 249, 2016.

[51] S. A. El-Tantawy, S. Ali Shan, N. Akhtar, and A. T. Elgendy, "Impact of electron trapping in degenerate quantum plasma on the ion-acoustic breathers and super freak waves," *Chaos, Solitons & Fractals*, vol. 113, pp. 356–364, 2018.

[52] H. A. Shah, M. N. S. Qureshi, and N. Tsintsadze, "Effect of trapping in degenerate quantum plasmas," *Physics of Plasmas*, vol. 17, no. 3, pp. 032312–032316, 2010.

[53] S. A. El-Tantawy, A. H. Salas, M. Abu Hammad, S. M. E. Ismaeel, D. M. Moustafa, and E. I. El-Awady, "Impact of dust kinematic viscosity on the breathers and rogue waves in a complex plasma having kappa distributed particles," *Waves in Random and Complex Media*, 2019.

[54] S. A. El-Tantawy, "Ion-acoustic waves in ultracold neutral plasmas: modulational instability and dissipative rogue waves," *Physics Letters A*, vol. 381, no. 8, pp. 787–791, 2017.

Hindawi
Mathematical Problems in Engineering
Volume 2021, Article ID 6681562, 11 pages
https://doi.org/10.1155/2021/6681562

Research Article

An Improved Linear State Error Feedback Synchronization Control Criteria for a Six-Axis Duffing Chaotic System

Hao Jia[1,2] **and Chen Guo**[1]

[1]*College of Marine Electrical Engineering, Dalian Maritime University, Dalian 116026, China*
[2]*School of Electrical Engineering, Dalian University of Science and Technology, Dalian 116052, China*

Correspondence should be addressed to Hao Jia; haun_jia@dlmu.edu.cn

Received 24 November 2020; Revised 31 December 2020; Accepted 15 January 2021; Published 27 January 2021

Academic Editor: Viet-Thanh Pham

By the employment of an improved linear state error feedback method, the synchronization control of a six-axis Duffing chaotic system was studied. Compared with previous methods, it has two advantages: the nonlinear term of the Duffing chaotic system is reserved in the synchronization error system, and the trajectory bound of the response system is predicted in advance to deduce the synchronization criteria. First, a typical ship parametric excitation roll chaotic system with parametric and forced excitation is taken as the control object to realize chaos synchronization control. Then, the control method is applied to the conventional six-axis Duffing oscillatory chaotic system and the four-axis Duffing oscillatory chaotic system. Finally, three simulation cases are presented to illustrate the validity of the synchronization criteria.

1. Introduction

Some dampers and drive model oscillators have been widely used in ship, machinery, and electrical systems, among which a typical one is the six-axis Duffing oscillator [1–5]. With proper parameters, a Duffing oscillator exhibits chaotic behaviors. Chaos is an important branch of nonlinear science and a complex dynamic behavior. Chaos synchronization has been the focus of present research on chaos. Chaos synchronization has potential applications in many fields, such as secure communication in the field of communication, automatic control in aerospace, roll control in ship navigation, and electrical chaos control in power systems. Many scholars have studied its chaos synchronization through many methods, including adaptive pulse control [6], optimal control [7], back stepping [8], pure finite time control [9], sliding mode control [10, 11], PID control [12], linear state feedback control [13], and fuzzy logic control [14]. In most methods, however, the nonlinear terms intrinsically contained by the system are removed from the controller. For example, in prior studies [4, 5], Njah employed active control to realize master-slave system synchronization.

In the present work, a parametric excitation roll motion system of a ship is first taken as the object to study the synchronization problem of six-axis Duffing chaos systems. The mathematical model of the parametric excitation rolling motion system of ship is a typical six-axis Duffing chaos system. So far, many different synchronization control techniques of chaos systems have been applied to ship roll systems, such as conventional passivity-based control, random Melnikov method [15], negative feedback algorithm [16], and chaos search with ant colony algorithm [17]. Other research on the roll chaos of ship has also been conducted, such as researching a numerical approach of the chaos threshold [18], researching the rolling vibration of a nonlinear semisubmersible system using an improved IHBC algorithm [19], and analyzing the environmental risk and ultimate roll motion of a ship [20]. It should be noted that in six-axis Duffing chaos systems, the chaotic oscillator is a nonlinear system, where nonlinear terms play an important role in the generation of the chaotic attractor, and thus how to use the properties of the nonlinear error system to derive synchronization conditions is very meaningful. Moreover, the trajectory boundary of the drive system and the response

system is broadly applied to the derivation of the criteria of synchronization chaos system (e.g., prior work by authors in [21–24]), but the estimation of the response system boundary is difficult. Therefore, it is more meaningful to solve some (not all) of the bounds of the trajectory of the response system in advance of the drive system and to realize synchronization criteria by the estimated bounds of the response system.

In this work, a synchronization scheme tailored for the parametric excitation roll chaos system of a ship with parametric and forced excitation is constructed, and linear state error feedback control is employed. Firstly, the trajectory bound of the response system is found, and then this is utilized to obtain synchronization conditions while the nonlinear terms of the system are retained in the synchronization scheme to ensure the high efficiency of control criteria. Besides, three typical Duffing oscillatory chaos systems are used to illustrate the applicability of the synchronization criteria.

The remainder of this work is organized as follows: In section 2, relevant issues and concepts are introduced. In section 3, the synchronization criteria tailored for the parametric excitation roll six-axis Duffing chaos system of a ship with parametric and forced excitation are presented. In section 4, the applications of synchronization criteria of a classical six-axis Duffing oscillatory chaos system and a four-axis Duffing oscillatory chaos system are presented. In section 5, the simulation results of the parametric excitation roll Duffing chaos system of a ship with parametric and forced excitation, a classical six-axis Duffing oscillatory chaos system, and a four-axis Duffing oscillatory chaos system are presented. The conclusions and future work are discussed in section 6.

2. Problems Proposed

The nonlinear mathematical model for the roll system of a ship with parametric and forced excitation in a regular longitudinal wave is as follows:

$$\begin{aligned}&\ddot{\phi}(t)+\mu_1\dot{\phi}(t)+\mu_3\dot{\phi}^3(t)\\&\quad+\omega_0^2\left(\phi(t)+\alpha_3\phi^3(t)+\alpha_5\phi^5(t)+h_0\phi(t)\cos(\omega_1 t)\right),\\&=K_e\sin(\omega_1 t+\delta_0),\end{aligned}\tag{1}$$

where $\phi(t)$ is the roll angle; h_0 is the amplitude of parametric excitation; ω_1 is the frequency of metric excitation, which is usually twice that of natural frequency when chaos occurs in the system; μ_1 and μ_3 are the damping factors of the roll; α_3 and α_5 are the dimensionless righting moment coefficients; ω_0 is the natural frequency of the ship roll; and $K_e\sin(\omega_1 t+\delta_0)$ is the forced roll moment in regular waves, where K_e is the amplitude of the forced excitation and δ_0 is encounter location of the ship and regular wave, assigned as 0. The potential term in the solution of the equation above is

$$\begin{aligned}&\frac{1}{2}\omega_0^2\phi^2(t)+\frac{1}{4}\omega_0^2\alpha_3\phi^4(t)\\&\quad+\frac{1}{6}\omega_0^2\alpha_5\phi^6(t),\end{aligned}\tag{2}$$

and hence it is called a six-axis system.

Let $x_1(t)=\phi(t), x_2(t)=\dot{\phi}(t)$, and, by conversion to state equations, it is obtained as follows:

$$\begin{cases}\dot{x}_1(t)=x_2(t),\\ \dot{x}_2(t)=-ax_2(t)-bx_2^3(t)-cx_1(t)\\ +dx_1^3(t)-ex_1^5(t)\\ -fx_1(t)\cos\omega t+g\sin\omega t,\end{cases}\tag{3}$$

where$a=\mu_1, b=\mu_3, c=\omega_0^2, d=-\omega_0^2\alpha_3,\ e=\omega_0^2\alpha_5, f=\omega_0^2 h_0$, $\omega=\omega_1$, and $g=K_e$.

To reflect the actual states more accurately, relevant parameters can be assigned with the reference of a marine patrol vessel as an example as follows:

$$\begin{aligned}a&=0.069,\\ b&=0.5367,\\ c&=1.25,\\ d&=0.9926,\\ e&=0.0998,\\ f&=2.875,\\ \omega&=2.236,\\ g&=0.16.\end{aligned}\tag{4}$$

As the parameters are determined, the nonlinear mathematical model for the parametric excitation roll system of the ship is as follows:

$$\begin{cases}\dot{x}_1(t)=x_2(t),\\ \dot{x}_2(t)=-0.069x_2(t)-0.5367x_2^3(t)\\ -1.25x_1(t)+0.9926x_1^3(t)\\ -0.0998x_1^5(t)\\ -2.875x_1(t)\cos 2.236\,t\\ +0.16\sin 2.236\,t.\end{cases}\tag{5}$$

The parametric excitation roll system of a ship is a chaos system that can be proved by MATLAB simulation results. The history charts of x_1 and x_2 of the parametric excitation roll system of the ship are shown in Figures 1 and 2, respectively, in which it is clear that the system is in chaos. The phase diagram of the parametric excitation roll system of the ship is shown in Figure 3, which further proves that the system is a chaos system and like a Duffing chaos system. Hence, this system is a typical six-axis Duffing chaos system. The next step is to perform synchronization control for system (3).

It is obtained from equation (3) that

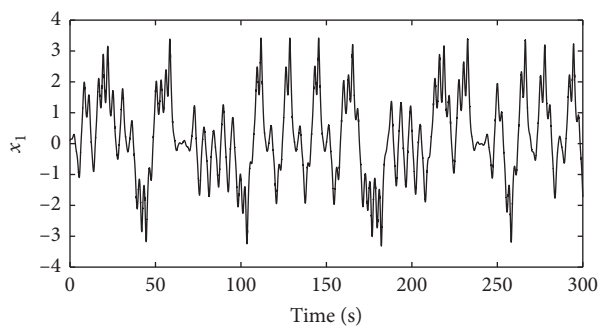

Figure 1: Time response of x_1 for system (5).

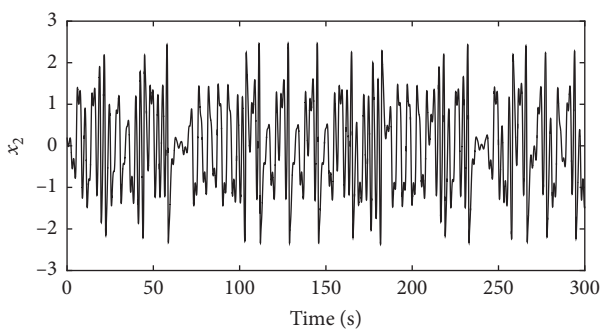

Figure 2: Time response of x_2 for system (5).

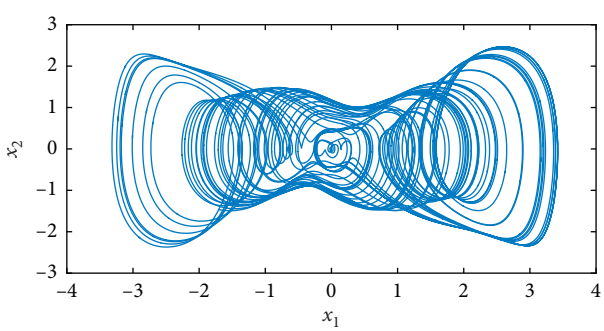

Figure 3: Phase diagram of chaotic system (5).

$$\begin{cases} \dot{x}_1(t) = x_2(t), \\ \dot{x}_2(t) = -(c + f\cos\omega t)x_1(t) - ax_2(t) \\ +i(x_1(t)) + j(x_2(t)) + q(t), \end{cases} \tag{6}$$

where

$$i(x_1(t)) = \mathrm{d}x_1^3(t) - ex_1^5(t), \tag{7}$$

$$j(x_2(t)) = -bx_2^3(t), \tag{8}$$

and

$$q(t) = g\sin\omega t. \tag{9}$$

System (6) is defined as a drive system, and the initial values of variables of system (6) are defined as $x_1(0) = x_{10}, x_2(0) = x_{20}$. The response system is as follows:

$$\begin{cases} \dot{y}_1(t) = y_2(t) + u_1(t), \\ \dot{y}_2(t) = -(c + f\cos\omega t)y_1(t) \\ -ay_2(t) + i(y_1(t)) + j(y_2(t)) \\ +q(t) + u_2(t), \end{cases} \tag{10}$$

where

$$i(y_1(t)) = \mathrm{d}y_1^3(t) - ey_1^5(t), \tag{11}$$

and

$$j(y_2(t)) = -by_2^3(t). \tag{12}$$

The initial values of the variables of system (10) are defined as $y_1(0) = y_{10}, y_2(0) = y_{20}$. The error system is assumed to be

$$\mathbf{e}(\mathbf{t}) = \begin{pmatrix} e_1(t) \\ e_2(t) \end{pmatrix} \in \mathbf{R}^2. \tag{13}$$

In this work, bold type denotes a vector. In the equation above,

$$\begin{cases} e_1(t) = x_1(t) - y_1(t), \\ e_2(t) = x_2(t) - y_2(t). \end{cases} \tag{14}$$

The controller is selected as

$$\begin{cases} u_1(t) = k_1e_1(t) + e_2(t), \\ u_2(t) = k_2e_1(t) + k_3e_2(t), \end{cases} \tag{15}$$

where k_1, k_2, and k_3 are controller gains which can be determined later. According to the method in this paper, k_1, k_2, and k_3 and other system parameters constitute the constraints of system synchronization, and k_1, k_2, and k_3 should ensure that other system parameter values meet the actual situation.

Then, from equations (6), (10), (14), and (15), the following is obtained:

$$\begin{cases} \dot{e}_1(t) = -k_1e_1(t), \\ \dot{e}_2(t) = (-(c + f\cos(\omega t)) - k_2)e_1(t) \\ -(k_3 + a)e_2(t) + i(x_1(t)) - i(y_1(t)) \\ +j(x_2(t)) - j(y_2(t)). \end{cases} \tag{16}$$

With the differential mean value theorem and equations (7) and (11), it is obtained that

$$\begin{aligned} &i(x_1(t)) - i(y_1(t)) \\ &\quad = \dot{i}(\gamma_1(t))(x_1(t) - y_1(t)) \\ &\quad = \dot{i}(\gamma_1(t))e_1(t), \end{aligned} \tag{17}$$

where

$$\begin{aligned} \dot{i}(\gamma_1(t)) &= \frac{\mathrm{d}i(\rho)}{d\rho}\Big|_{\rho=\gamma_1(t)} \\ &= 3\,d\gamma_1^2(t) - 5e\gamma_1^4(t), \end{aligned} \tag{18}$$

and $\gamma_1(t) \in (\min\{x_1(t), y_1(t)\}, \max\{x_1(t), y_1(t)\})$.

Similarly, by deriving from equations (8) and (12), it is obtained that

$$\begin{aligned} & j(x_2(t)) - j(y_2(t)) \\ & \quad = \dot{j}(\gamma_2(t))(x_2(t) - y_2(t)) \\ & \quad = \dot{j}(\gamma_2(t))e_2(t), \end{aligned} \tag{19}$$

where

$$\begin{aligned} \dot{j}(\gamma_2(t)) &= \frac{\mathrm{d}j(\rho)}{d\rho}\Big|_{\rho=\xi_2(t)} \\ &= -3b\gamma_2^2(t), \end{aligned} \tag{20}$$

and $\gamma_2(t) \in (\min\{x_2(t), y_2(t)\}, \max\{x_2(t), y_2(t)\})$.

By substituting equations (17) and (19) into equation (16), it is obtained that

$$\begin{cases} \dot{e}_1(t) = -k_1 e_1(t), \\ \dot{e}_2(t) = (-(c + f\cos(\omega t)) - k_2 \\ +\dot{i}(\gamma_1(t)))e_1(t) + (-(k_3 + a) \\ +\dot{j}(\gamma_2(t)))e_2(t). \end{cases} \tag{21}$$

Then,

$$\dot{e}(\mathbf{t}) = \hat{k}(\mathbf{t})\mathbf{e}(\mathbf{t}), \tag{22}$$

where

$$\begin{aligned} \hat{k}(\mathbf{t}) &= \begin{pmatrix} k_{11} & k_{12} \\ k_{21} & k_{22} \end{pmatrix}, \\ k_{11} &= -k_1, \\ k_{12} &= 0, \\ k_{21} &= -(c + f\cos(\omega t)) - k_2 + \dot{i}(\gamma_1(t)), \\ k_{22} &= -(k_3 + a) + \dot{j}(\gamma_2(t)). \end{aligned} \tag{23}$$

The initial conditions of system (21) are $e_1(0) = x_{10} - y_{10}, e_2(0) = x_{20} - y_{20}$.

Because the drive system described by equation (6) is chaotic, there are two boundary values $n_1 > 0, n_2 > 0$, and for the initial values x_{10}, x_{20} in any chaotic attractor region range formed in Figure 3, the following equation is satisfied:

$$\begin{aligned} & |x_i(t)| \le n_i, \quad i = 1, 2, \forall t > 0, \\ & e_1(t) = (x_{10} - y_{10})\exp(-k_1 t), \\ & y_1(t) = x_1(t) - (x_{10} - y_{10})\exp(-k_1 t), \end{aligned} \tag{24}$$

and, finally,

$$\begin{aligned} y_1(t) &\le |x_1(t)| + |x_{10} - y_{10}| \\ &\le n_1 + |x_{10} - y_{10}|, \quad \forall t > 0. \end{aligned} \tag{25}$$

Similarly,

$$\begin{aligned} y_2(t) &\le |x_2(t)| + |x_{20} - y_{20}| \\ &\le n_2 + |x_{20} - y_{20}|. \end{aligned} \tag{26}$$

It is obtained from equation (11) that

$$\begin{aligned} |\dot{i}(\gamma_1(t))| &= |3d\gamma_1^2(t) - 5e\gamma_1^4(t)| \\ &\le |3d\gamma_1^2(t)| + |5e\gamma_1^4(t)| \le \lambda_1, \end{aligned} \tag{27}$$

where

$$\lambda_1 = (3|d| + 5|e|\alpha_1)\alpha_1, \tag{28}$$

and

$$\alpha_1 = \max\{\gamma_1^2(t)\}. \tag{29}$$

$\forall \gamma_1(t) \in (\min\{x_1(t), y_1(t)\}, \max\{x_1(t), y_1(t)\})$, similarly,

$$|\dot{j}(\gamma_2(t))| \le \lambda_2, \tag{30}$$

where

$$\lambda_2 = 3|b|\alpha_2, \tag{31}$$

and

$$\begin{aligned} & \alpha_2 = \max\{\gamma_2^2(t)\}, \\ & \quad \forall \gamma_2(t) \in (\min\{x_2(t), y_2(t)\}, \max\{x_2(t), y_2(t)\}). \end{aligned} \tag{32}$$

Note 1. As to $\forall t > 0$, the critical values of $y_1(t)$ can be estimated by equation (25) and those of $y_2(t)$ can be estimated by equation (26); the critical values of $|\dot{i}(\gamma_1(t))|$ and λ_1 can be estimated by equations (27), (28), and (29), and those of $|\dot{j}(\gamma_2(t))|$ and λ_2 can be estimated by equations (30), (31), and (32).

The objective of this work is to study the master-slave synchronization of the system described by system (6); solve the gains of controller k_1, k_2, k_3 and make the error system described by equation (21) tend to be globally stable to realize synchronization of the systems described by systems (6) and (10), that is, realize synchronization of the roll six-axis Duffing chaos system of a ship with parametric and forced excitation.

3. Synchronization Criteria

In this section, the stability criteria for error system (16) are given to ensure the synchronization of systems (6) and (10).

Theorem 1. *If the Lyapunov function is selected as follows:*

$$\begin{aligned} \mathbf{V}(\mathbf{t}) &= \mathbf{e}^{\mathbf{T}}(\mathbf{t})\mathbf{Q}\mathbf{e}(\mathbf{t}), \\ \mathbf{Q} &= \begin{pmatrix} q_{11} & q_{12} \\ q_{21} & q_{22} \end{pmatrix} \in \mathbf{R}^{2\times 2}, \end{aligned} \tag{33}$$

and the following criteria are satisfied:

$$\begin{cases} \Phi_1 = -k_1 q_{11} + (-(c + f\cos(\omega t) - k_2)q_{12} + \lambda_1 \cdot |q_{12}| < 0; \\ \Phi_2 = -(k_3 + a)q_{22} + \lambda_2 |q_{22}| < 0 \\ \left(\left|(-k_1 - k_3 - a)q_{12} + (-(c + f\cos(\omega t)) - k_2)q_{22}\right| + \lambda_1 q_{22} + \lambda_2 q_{12}\right)^2 \le 4\Phi_1\Phi_2, \end{cases} \tag{34}$$

then, with the control of error system (16) and controller (15), systems (6) and (10) are synchronized.

Proof.

$$\dot{V}(\mathbf{t}) = \mathbf{e}^{\mathbf{T}}(\mathbf{t})\mathbf{M}(\mathbf{t})\mathbf{e}(\mathbf{t}), \quad \text{Where,}$$
$$\mathbf{M}(\mathbf{t}) = \widehat{k}^{\mathbf{T}}(\mathbf{t})\mathbf{Q} + \mathbf{Q}\widehat{k}(\mathbf{t}) = \begin{pmatrix} m_{11}(t) & m_{12}(t) \\ m_{21}(t) & m_{22}(t) \end{pmatrix}. \tag{35}$$

By substituting $\widehat{\mathbf{k}}(\mathbf{t})$ and $\mathbf{Q}$ into $\mathbf{M}(\mathbf{t})$ in the equation above, the following can be obtained:

$$\begin{cases} m_{11}(t) = 2\big(-k_1 q_{11} + (-(c + f\cos(\omega t)) \\ -k_2 + \dot{i}(\gamma_1(t)))q_{12}\big); \\ m_{12}(t) = -k_1 q_{12} + (-(c + f\cos(\omega t)) \\ -k_2 + \dot{i}(\gamma_1(t)))q_{22} + (-(k_3 + a) \\ +\dot{j}(\gamma_2(t)))q_{12}; \\ m_{22}(t) = 2\big(\big(-(k_3 + a) + \dot{j}(\gamma_2(t))\big)q_{22}\big). \end{cases} \tag{36}$$

If these are satisfied,

$$\begin{cases} m_{11}(t) < 0, \\ m_{22}(t) < 0, \\ m_{12}^2(t) < m_{11}(t)m_{22}(t), \end{cases} \tag{37}$$

then $\dot{V}(t) < 0, \forall e_1(t), e_2(t) \neq 0$, and thus systems (6) and (10) are synchronized, and the conclusion is proved. Next, the relationship between equations (37) and (34) is proved.

From the first equation in equation (36), it is obtained that

$$\begin{aligned} \frac{m_{11}(t)}{2} &= -k_1 q_{11} + (-(c + f\cos(\omega t)) - k_2)q_{12} + \dot{i}(\gamma_1(t))q_{12} \\ &\le -k_1 q_{11} + (-(c + f\cos(\omega t)) - k_2)q_{12} \\ &\quad + |\dot{i}(\gamma_1(t))||q_{12}|. \end{aligned} \tag{38}$$

By substituting equation (27) into the equation above, it is obtained that

$$\frac{m_{11}(t)}{2} \le -k_1 q_{11} + (-(c + f\cos(\omega t)) - k_2)q_{12} + \lambda_1 \cdot |q_{12}| = \Phi_1. \tag{39}$$

The second equation in equation (36) yields

$$\begin{aligned} \frac{m_{22}(t)}{2} &= \big(-(k_3 + a) + \dot{j}(\gamma_2(t))\big)q_{22} \\ &= -(k_3 + a)q_{22} + \dot{j}(\gamma_2(t))q_{22} \\ &\le -(k_3 + a)q_{22} + |\dot{j}(\gamma_2(t))||q_{22}|. \end{aligned} \tag{40}$$

By substituting equation (30) into the equation above, it is obtained that

$$\frac{m_{22}(t)}{2} \le -(k_3 + a)q_{22} + \lambda_2 |q_{22}| = \Phi_2. \tag{41}$$

The third equation in equation (36) yields

$$\begin{aligned} m_{12}^2(t) &= \big(-k_1 q_{12} + \big(-(c + f\cos(\omega t)) - k_2 + \dot{i}(\gamma_1(t))\big)q_{22} + \big(-(k_3 + a) + \dot{j}(\gamma_2(t))\big)q_{12}\big)^2 \\ &= \big(-k_1 q_{12} + (-(c + f\cos(\omega t)) - k_2)q_{22} + \dot{i}(\gamma_1(t))q_{22} + (-(k_3 + a))q_{12} + \dot{j}(\gamma_2(t))q_{12}\big)^2 \\ &= \big((-k_1 - k_3 - a)q_{12} + (-(c + f\cos(\omega t)) - k_2)q_{22} + \dot{i}(\gamma_1(t))q_{22} + \dot{j}(\gamma_2(t))q_{12}\big)^2 \\ &\le \big(\left|(-k_1 - k_3 - a)q_{12} + (-(c + f\cos(\omega t)) - k_2)q_{22}\right| + |\dot{i}(\gamma_1(t))|q_{22} + |\dot{j}(\gamma_2(t))|q_{12}\big)^2. \end{aligned} \tag{42}$$

By substituting equations (27) and (30) into the equation above, the following is obtained:

$$m_{12}^2(t) \le \left(\left|(-k_1 - k_3 - a)q_{12} + \left(-(c + f\cos(\omega t)) - k_2\right)q_{22}\right| + \lambda_1 q_{22} + \lambda_2 q_{12}\right)^2. \tag{43}$$

In sum, if equation (34) is true, then equation (37) can be guaranteed to be true, and, at this point, error system (16) achieves global asymptotic stability, and thus systems (6) and (10) reach synchronization with the control of controller (15). The proof is concluded, that is, the synchronization criteria of equation (34) are obtained for systems (6) and (10) to reach synchronization.

Generally, let $\mathbf{Q} = \begin{pmatrix} 1 & 0 \\ 0 & 1 \end{pmatrix}$, and then, when systems (6) and (10) reach synchronization, the synchronization criteria equations become

$$\begin{cases} k_1 > 0; \\ -k_3 - a + \lambda_2 < 0; \\ 2\sqrt{k_1(k_3 + a - \lambda_2)} \\ > \left|c + f\cos(\omega t) + k_2\right| + \lambda_1. \end{cases} \tag{44}$$

□

Note 1. In prior works [4, 5], Njah established a synchronization scheme for the six-axis Duffing equation and studied the master-slave synchronization criteria with active control, which are as follows:

Controller:

$$\begin{cases} u_1(t) = -\hat{a}e_1(t) - \hat{b}e_2(t), \\ u_2(t) = -a\left(x_1^5(t) - y_1^5(t)\right) - l\left(x_1^3(t) - y_1^3(t)\right) \\ \quad -w_1 e_1(t) - w_2 e_2(t), \end{cases} \tag{45}$$

where $\hat{a}, \hat{b}, w_1, w_2$ are the input parameters of the controller.

Error system:

$$\begin{cases} \dot{e}_1(t) = \hat{a}e_1(t) + (1 + \hat{b})e_2(t), \\ \dot{e}_2(t) = -(d - w_1)e_1(t) - (c - w_2)e_2(t). \end{cases} \tag{46}$$

It is clear that the linear error system described by (46) can be completely derived by controller (45) [4, 5], but all the nonlinear terms of the original six-axis Duffing system are removed, and this error system can be easily acquired. Compared with controller (45) [4, 5], controller (15) and error system (21) in the present work have two merits. The first is the reservation of nonlinear terms in error system (21) instead of linear error system (46). The second is easy preestimation of the bounds of the response systems $y_1(t), y_2(t)$ by equations (24)–(32) and the subsequently obtained stability criteria for the error system described by (16).

4. Applications of the Six-Axis Duffing Oscillatory System and the Four-Axis Duffing Oscillatory System

4.1. Application of the Six-Axis Duffing Oscillatory System. In the previous section, the synchronization criteria for the six-axis Duffing oscillatory system in prior work [4, 5] was compared with that for the parametric excitation roll system of a ship in this work, but the method proposed in this work has not been applied to a conventional six-axis Duffing oscillatory system, which is to be presented here.

The mathematical model of the six-axis Duffing oscillatory system is as follows:

$$\begin{aligned} \ddot{x}(t) &= -c\dot{x}(t) - \mathrm{d}x(t) - lx^3(t) \\ &\quad -ax^5(t) + q\cos\omega t(t). \end{aligned} \tag{47}$$

Let $x_1(t) = x(t), x_2(t) = \dot{x}_1(t)$, then equation (47) becomes

$$\begin{cases} \dot{x}_1(t) = x_2(t), \\ \dot{x}_2(t) = -\mathrm{d}x_1(t) - cx_2(t) + i\left(x_1(t)\right) + q(t), \end{cases} \tag{48}$$

where

$$\begin{aligned} q(t) &= q\cos\omega t, \\ i\left(x_1(t)\right) &= -lx_1^3(t) - ax_1^5(t). \end{aligned} \tag{49}$$

The response system is

$$\begin{cases} \dot{y}_1(t) = y_2(t) + u_1(t), \\ \dot{y}_2(t) = -\mathrm{d}y_1(t) - cy_2(t) + i\left(y_1(t)\right) + q(t) + u_2(t). \end{cases} \tag{50}$$

The controller is

$$\begin{cases} u_1(t) = k_1 e_1(t) + e_2(t), \\ u_2(t) = k_2 e_1(t) + k_3 e_2(t). \end{cases} \tag{51}$$

The error system is defined as

$$\begin{cases} e_1(t) = x_1(t) - y_1(t), \\ e_2(t) = x_2(t) - y_2(t), \end{cases} \tag{52}$$

and then

$$\begin{cases} \dot{e}_1(t) = -k_1 e_1(t), \\ \dot{e}_2(t) = -(k_2 + d)e_1(t) - (k_3 + c)e_2(t) + i\left(x_1(t)\right) - i\left(y_1(t)\right). \end{cases} \tag{53}$$

According to the method proposed in the present work, the synchronization criteria for (48) and (50) can be described as

$$\begin{cases} \Phi_1 = -(k_2 + d)q_{12} - q_{11}k_1 + \lambda|q_{12}| < 0, \\ \Phi_2 = -q_{22}(k_3 + c) < 0(1 - (k_2 + k_3 + c)q_{12} \\ \quad -(k_2 + d)q_{22} + \lambda q_{22})^2 \le 4\Phi_1\Phi_2. \end{cases} \tag{54}$$

Let $\mathbf{Q} = \begin{pmatrix} 1 & 0 \\ 0 & 1 \end{pmatrix}$, and then

$$\begin{cases} k_1 > 0, \\ c + k_3 > 0, \\ 2\sqrt{k_1(c + k_2)} - |d + k_2| > \lambda. \end{cases} \tag{55}$$

The estimation method of system bound values is

$$|x_i(t)| \le n_i, \quad i = 1, 2, \forall t > 0, \tag{56}$$

$$|y_1(t)| \le n_1 + |x_{10} - y_{10}|, \quad \forall t > 0, k_1 > 0 \tag{57}$$

$$\dot{i}(\gamma(t)) = -\left(3\lambda\gamma^2(t) + 5a\gamma^4(t)\right), \tag{58}$$

and

$$|\dot{i}(\gamma(t))| \le \lambda, \tag{59}$$

where

$$\lambda = (3|l| + 5|a|\alpha)\alpha, \tag{60}$$

and

$$\alpha = \max\{\gamma^2(t)\}, \quad \forall\gamma(t) \in (\min\{x_1(t), y_1(t)\}, \max\{x_1(t), y_1(t)\}). \tag{61}$$

The merits of the synchronization criteria referred to in this work can be found. As expected, the nonlinear terms in error system (53) are retained, and the bounds of $y_1(t), y_2(t)$ can be easily estimated by (56)–(61). Thus, the stability criteria of the error system described by (54) required by the derivation of the stability is obtained.

4.2. Application of the Four-Axis Duffing Oscillatory System. Regarding the six-axis Duffing oscillatory system, if $a = 0$, then it is converted to a four-axis Duffing oscillatory system as follows:

$$\ddot{x}(t) = c\dot{x}(t) - \mathrm{d}x(t) - lx^3(t) + q \cdot \cos\omega t. \tag{62}$$

Let $x_1(t) = x(t)$ and $x_2(t) = \dot{x}_1(t)$, and then

$$\begin{cases} \dot{x}_1(t) = x_2(t), \\ \dot{x}_2(t) = -\mathrm{d}x_1(t) - cx_2(t) + i(x_1(t)) + q(t), \end{cases} \tag{63}$$

where

$$\begin{aligned} q(t) &= q \cdot \cos\omega t, \\ g(x_1(t)) &= -lx_1^3(t). \end{aligned} \tag{64}$$

The response system is

$$\begin{cases} \dot{y}_1(t) = y_2(t) + u_1(t), \\ \dot{y}_2(t) = -\mathrm{d}y_1(t) - cy_2(t) \\ +i(y_1(t)) + q(t) + u_2(t). \end{cases} \tag{65}$$

The controller is

$$\begin{cases} u_1(t) = k_1e_1(t) + e_2(t), \\ u_2(t) = k_2e_1(t) + k_3e_2(t). \end{cases} \tag{66}$$

The error is defined as

$$\begin{cases} e_1(t) = x_1(t) - y_1(t), \\ e_2(t) = x_2(t) - y_2(t). \end{cases} \tag{67}$$

The error system is

$$\begin{cases} \dot{e}_1(t) = -k_1e_1(t), \\ \dot{e}_2(t) = -(k_2 + d)e_1(t) - (k_3 + c)e_2(t) + i(x_1(t)) - i(y_1(t)). \end{cases} \tag{68}$$

According to the method of this work, the synchronization criteria for systems (63) and (65) are

$$\begin{cases} \Phi_1 = -(k_2 + d)q_{12} - q_{11}k_1 + \tilde{\lambda}|q_{12}| < 0, \\ \Phi_2 = -q_{22}(k_3 + c) < 0 \\ \left(|-(k_1 + k_3 + c)q_{12} - (k_2 + d)q_{22}| + \tilde{\lambda}q_{22}\right)^2 \\ \le 4\Phi_1\Phi_2. \end{cases} \tag{69}$$

Let $\mathbf{Q} = \begin{pmatrix} 1 & 0 \\ 0 & 1 \end{pmatrix}$, and then

$$\begin{cases} k_1 > 0, \\ c + k_3 > 0, \\ 2\sqrt{k_1(c + k_3)} - |d + k_2| > \tilde{\lambda}. \end{cases} \tag{70}$$

The estimation method for the system bound values is as follows:

$$|x_i(t)| \le n_i, \quad i = 1, 2, \forall t > 0, \tag{71}$$

$$|y_1(t)| \le n_1 + |x_{10} - y_{10}|, \quad \forall t > 0, k_1 > 0, \tag{72}$$

$$\dot{i}(\gamma(t)) = -3l\gamma^2(t), \tag{73}$$

$$|\dot{i}(\gamma(t))| \le \tilde{\lambda}, \tag{74}$$

$$\tilde{\lambda} = 3|l| \cdot \alpha, \tag{75}$$

and

$$\alpha = \max\{\gamma^2(t)\}, \quad \forall\gamma(t) \in (\min\{x_1(t), y_1(t)\}, \max\{x_1(t), y_1(t)\}). \tag{76}$$

Note 2. Han et al. [25], Njah, and Vincent et al. [26] established the synchronization schemes for four-axis Duffing equations and studied the master-slave synchronization criteria under active control. The criteria are as follows:

The controller is

$$\begin{cases} u_1(t) = -y_1(t) + x_1(t) + \breve{k}_1 e_1(t), \\ u_2(t) = \mathrm{d}y_1(t) + cy_2(t) + ly_1^3(t) \\ -\mathrm{d}x_1(t) - cx_2(t) - lx_1^3(t) + \breve{k}_2 e_2(t), \end{cases} \tag{77}$$

where $\breve{k}_1, \breve{k}_2$ are gains of feedback; and the error system is

$$\begin{cases} \dot{e}_1(t) = -\breve{k}_1 e_1(t), \\ \dot{e}_2(t) = -\breve{k}_2 e_2(t). \end{cases} \tag{78}$$

As discussed in Note 2, the error system described by (78) is a linear system. Compared with the control methods of prior studies [25, 26], both linear and nonlinear terms are retained in the present control method, and $-\mathrm{d}x_1(t) - cx_2(t) - lx_1^3(t)$ is fully utilized to derive the synchronization control criteria (69).

5. Simulation Study

5.1. Synchronous Simulation of the Parametric Excitation Roll Chaotic Six-Axis Duffing System of a Ship with Parametric and Forced Excitation. Regarding the parametric excitation roll six-axis Duffing systems (6) and (10) of a ship with parametric and forced excitation, the parameters $a = 0.069$, $b = 0.5367, c = 1.25, d = 0.9926$,

$$\begin{aligned} e &= 0.0998, \\ f &= 2.875, \\ \omega &= 2.236, \\ g &= 0.16 \end{aligned} \tag{79}$$

were selected and the initial values

$$\begin{aligned} x_1(0) &= x_{10} = 0, \\ x_2(0) &= x_{20} = -1, \\ y_1(0) &= y_{10} = 0.1, \\ y_2(0) &= y_{20} = -1.1 \end{aligned} \tag{80}$$

were assigned. The chaotic attractor could be obtained from Figure 3 with a bound of $|x_1| \le 3.5, |x_2| \le 2.5$, and thus $n_1 = 3.5, n_2 = 2.5$. By equation (25), $y_1(t) \le 3.5 + |0 - (-0.1)| = 3.6$ was obtained. By equation (26), $y_2(t) \le 2.5 + |-1 - (-1.1)| = 2.6$ was obtained. By equations (27), (28), and (29), $|\dot{i}(\gamma_1(t))| \le \lambda_1 = 122.44$ was obtained. By equations (30), (31), and (32), $|\dot{j}(\gamma_2(t))| \le \lambda_2 = 10.88$ was obtained. If $k_2 = 0, k_1 = k_3$ was assigned, then $k_1 = k_3 = 69$ could be obtained based on equation (44).

Figures 4–6 present the simulation results. As seen from the error effects shown in Figure 4, it can be observed that when t approximated 0.1 s, errors e_1 and e_2 almost stabilized around the zero point, indicating that system (16) achieved global asymptotic stability. As shown in Figures 5 and 6, when t was close to 0.1 s, x_1 and y_1 of drive system (6) and x_2 and y_2 of response system (10) reached synchronization, indicating that the method proposed in this work was verified.

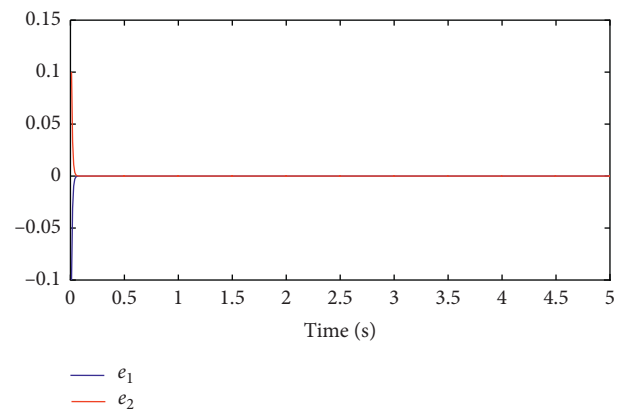

Figure 4: Synchronization error of systems (6) and (10) ($k_2 = 0, k_1 = k_3 = 69$).

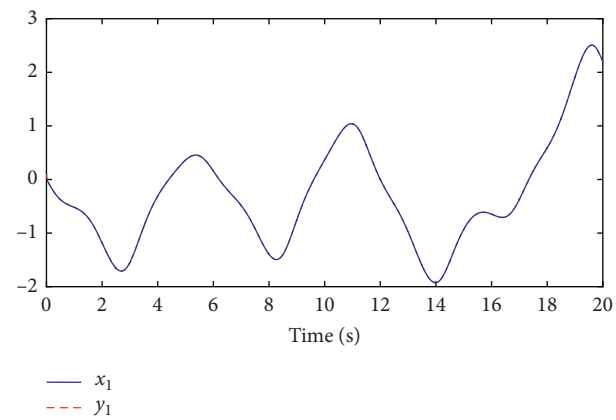

Figure 5: x_1 and y_1 synchronization time response of systems (6) and (10) ($k_2 = 0, k_1 = k_3 = 69$).

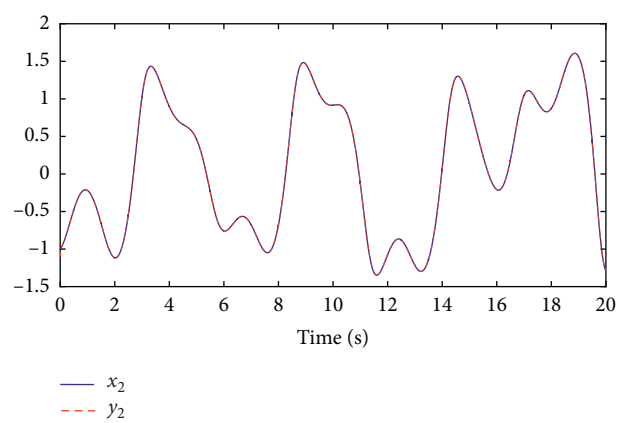

Figure 6: x_2 and y_2 synchronization time response of systems (6) and (10) ($k_2 = 0, k_1 = k_3 = 69$).

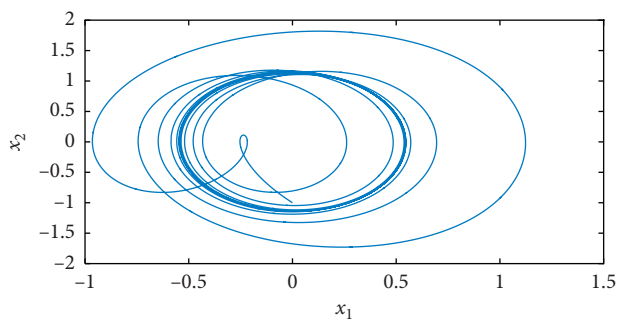

Figure 7: Phase diagram of six-axis Duffing oscillatory chaotic system (48).

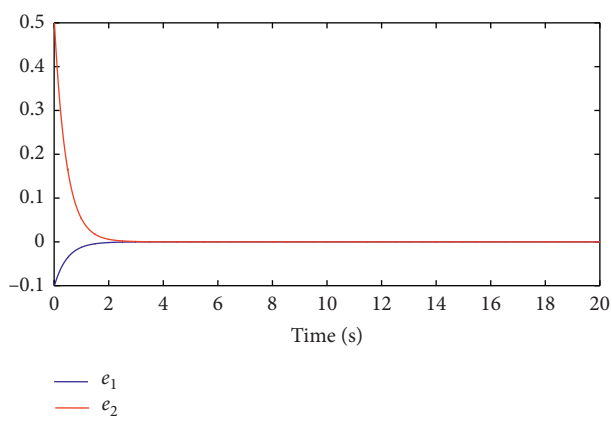

Figure 8: Synchronization error of six-axis Duffing oscillatory chaotic systems (48) and (50) $(k_2 = 0, k_1 = k_3 = 2.09)$.

5.2. Synchronous Simulation of a Six-Axis Duffing Oscillatory Chaotic System. Regarding six-axis Duffing oscillatory chaotic systems (48) and (50), the parameters $a = 0.1, c = 0.4, d = 1.1, l = 0.4, q = 1.8$, and $\omega = 2.1$ were selected, and the initial values $x_1(0) = x_{10} = 0$, $x_2(0) = x_{20} = -1$ and $y_1(0) = y_{10} = 0.1, y_2(0) = y_{20} = -1.5$ were assigned. The chaotic attractor could be derived from Figure 7 with a bound defined by $|x_1| \leq 1.2$, and thus $n_1 = 1.2$. Via equation (57), $y_1(t) \leq 1.2 + |0 - 0.1| = 1.3$ was obtained, and by equations (59), (60), and (61), $|\dot{i}(\gamma(t))| \leq \lambda = 3.45605$ was obtained. If $k_2 = 0, k_1 = k_3$ was assigned, then $k_1 = k_3 = 2.09$ could be obtained based on equation (55).

Figures 8–10 present the simulation results. As shown from the error effects in Figure 8, when t approximated 2 s, errors e_1 and e_2 almost stabilized around the zero point, indicating that error system (53) achieved global asymptotic stability. As shown in Figures 9 and 10, when t was close to 2 s, x_1 and y_1 of drive system (48) and x_2 and y_2 of response system (50) reached synchronization, indicating that the method proposed in this work was verified.

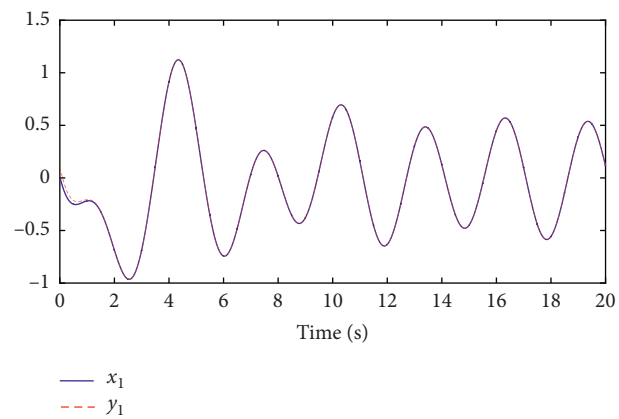

Figure 9: x_1 and y_1 synchronization time response of six-axis Duffing oscillatory chaotic systems (48) and (50) $(k_2 = 0, k_1 = k_3 = 2.09)$.

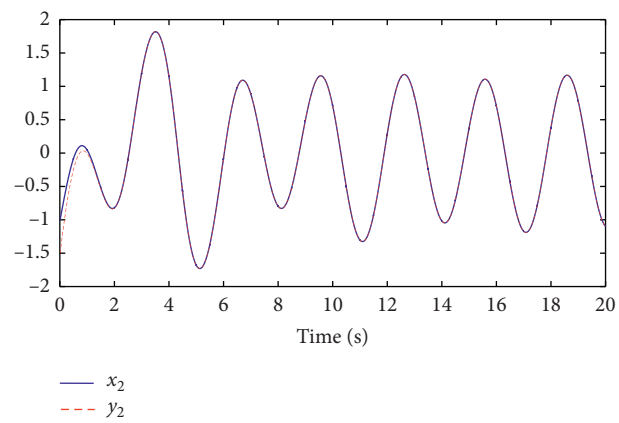

Figure 10: x_2 and y_2 synchronization time response of six-axis Duffing oscillatory chaotic systems (48) and (50) $(k_2 = 0, k_1 = k_3 = 2.09)$.

5.3. Synchronous Simulation of a Four-Axis Duffing Oscillatory Chaotic System. Regarding four-axis Duffing oscillatory chaotic systems (63) and (65), the parameters $a = 0.1, c = 0.4, d = 1.1, l = 0.4, q = 1.8$, and $\omega = 2.1$ were selected and the initial values $x_1(0) = x_{10} = 0, x_2(0) = x_{20} = -1$ and $y_1(0) = y_{10} = 0.1, y_2(0) = y_{20} = 1.5$were assigned. The chaotic attractor could be obtained in Figure 11 with a bound defined by $|x_1| \leq 1.2$, and thus $n_1 = 1.2$. By equation (72), $y_1(t) \leq 1.2 + |0 - 0.1| = 1.3$ was obtained, and by equations (74), (75), and (76), $|\dot{i}(\gamma(t))| \leq \lambda = 2.028$ was obtained. If $k_2 = 0, k_1 = k_3$ was assigned, then $k_1 = k_3 = 1.38$ could be obtained based on equation (70).

Figures 12–14 present the simulation results. As shown from the error effects in Figure 12, when t approximated 3 s, errors e_1 and e_2 almost stabilized around

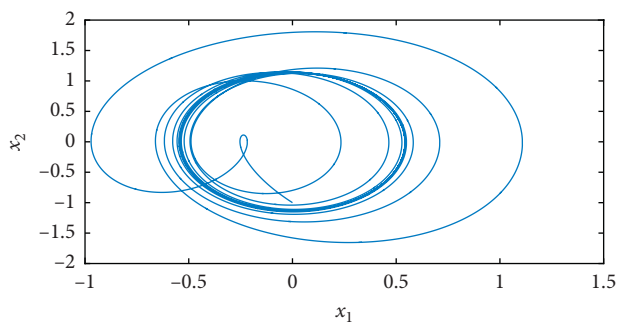

Figure 11: Phase diagram of four-axis Duffing oscillatory chaotic system (63).

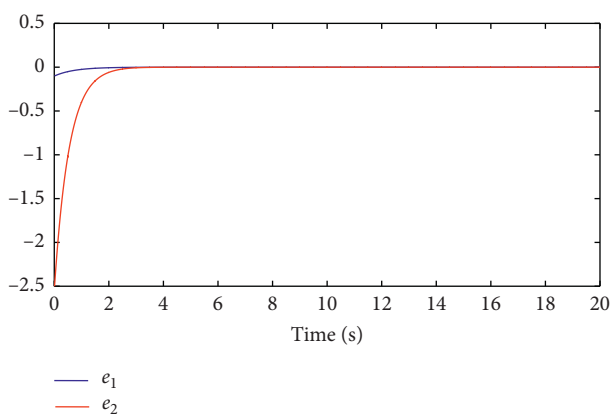

Figure 12: Synchronization error of four-axis Duffing oscillatory chaotic systems (63) and (65) ($k_2 = 0, k_1 = k_3 = 1.38$).

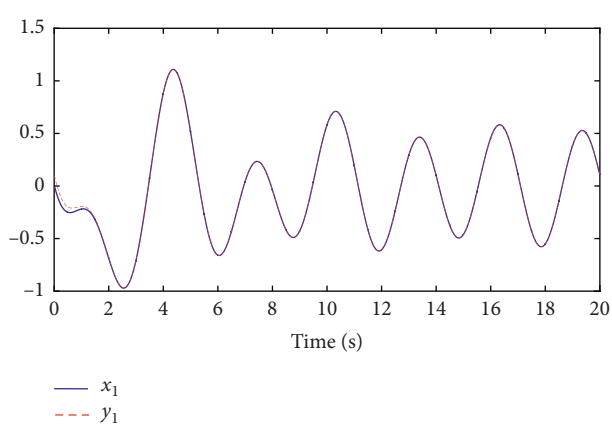

Figure 13: x_1 and y_1 synchronization time response of four-axis Duffing oscillatory chaotic systems (63) and (65) ($k_2 = 0, k_1 = k_3 = 1.38$).

the zero point, indicating that error system (64) achieved global asymptotic stability. As shown in Figures 13 and 14, when t neared 3 s, x_1 and y_1 of drive system (63) and

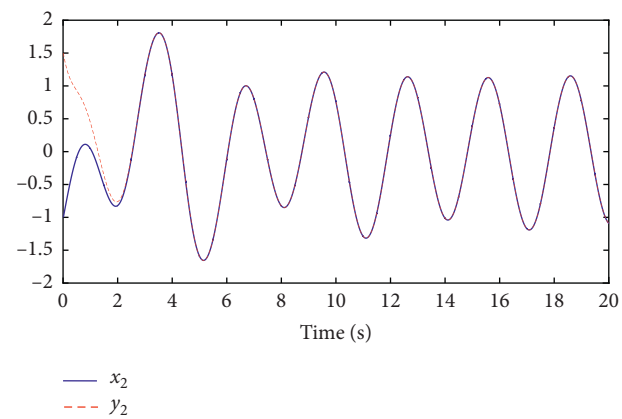

Figure 14: x_2 and y_2 synchronization time response of four-axis Duffing oscillatory chaotic systems (63) and (65) ($k_2 = 0, k_1 = k_3 = 1.38$).

x_2 and y_2 of response system (65) reached synchronization, indicating that the method proposed in this work was verified.

6. Conclusions

A synchronization study was conducted for a six-axis Duffing oscillatory chaotic system. A linear state error feedback method was employed, and the parametric excitation roll chaotic six-axis Duffing system of a ship with parametric and forced excitation was regarded as the main object of study. These were applied to typical six-axis Duffing oscillatory system and four-axis Duffing oscillatory system, and the validity of the synchronization criteria for Duffing oscillators was demonstrated by simulation verification. In the control process, not only are the nonlinear terms of original Duffing system reserved in the error system but the synchronization criteria are derived by the prediction of trajectory bounds of the response system. The synchronized drive system and response system in this work share the same structure, and the synchronization of chaos system of different structures can be regarded as a future research interest.

Data Availability

The data used to support the findings of this study are available from the corresponding author upon request.

Conflicts of Interest

The authors declare that there are no conflicts of interest regarding the publication of this paper.

Acknowledgments

This work was supported by the National Natural Science Foundation of China under Grant nos 51809028, 51579024, and 51879027.

References

[1] A. K. Agrawal, J. N. Yang, and J. C. Wu, "Non-linear control strategies for duffing systems," *International Journal of Non-linear Mechanics*, vol. 33, no. 5, pp. 829–841, 1998.

[2] H. Nijmeijer and H. Berghuis, "On lyapunov control of the duffing equation," *IEEE Transactions on Circuits and Systems I: Fundamental Theory and Applications*, vol. 42, no. 8, pp. 473–477, 1995.

[3] U. E. Vincent, R. K. Odunaike, J. A. Laoye, and A. A. Gbindinninuola, "Adaptive backstepping control and synchronization of a modified and chaotic van der pol-duffing oscillator," *Journal of Control Theory and Applications*, vol. 9, no. 2, pp. 273–277, 2011.

[4] A. N. Njah, "Synchronization via active control of identical and non-identical chaotic oscillators with external excitation," *Journal of Sound and Vibration*, vol. 327, no. 3–5, pp. 322–332, 2009.

[5] A. Njah, "Synchronization via active control of parametrically and externally excited Φ6 van der pol and duffing oscillators and application to secure communications," *Journal of Vibration and Control*, vol. 17, no. 4, pp. 493–504, 2010.

[6] Y.-S. Chen, R. R. Hwang, and C.-C. Chang, "Adaptive impulsive synchronization of uncertain chaotic systems," *Physics Letters A*, vol. 374, no. 22, pp. 2254–2258, 2010.

[7] FV. Panaitescu, M. Panaitescu, D. Deleanu, and I. A. Anton, "Analysis of environmental risk and extreme roll motions for a ship in waves," *Journal of Environmental Protection and Ecology*, vol. 20, no. 3, pp. 1204–1213, 2019.

[8] A. E. Gohary, "Optimal synchronization of Rössler system with complete uncertain parameters," *Chaos Soliton Fract*, vol. 27, pp. 345–355, 2006.

[9] H. Wang, Z.-z. Han, Q.-y. Xie, and W. Zhang, "Finite-time chaos synchronization of unified chaotic system with uncertain parameters," *Communications in Nonlinear Science and Numerical Simulation*, vol. 14, no. 5, pp. 2239–2247, 2009.

[10] Mohanty, N. Prasad, R. Dey, and B. Roy, "Switching synchronisation of a 3-D multi-state-time-delay chaotic system including externally added memristor with hidden attractors and multi-scroll via sliding mode control," *The European Physical Journal Special Topics*, vol. 229, no. 6-7, pp. 1231–1244, 2020.

[11] J. Wang, L. Liu., C. Liu., and X. Li, "Adaptive sliding mode control based on equivalence principle and its application to chaos control in a seven-dimensional power system," *Mathematical Problems in Engineering*, vol. 2020, Article ID 1565460, 13 pages, 2020.

[12] G. Ablay, "Chaos in PID controlled nonlinear systems," *Journal of Electrical Engineering & Technology*, vol. 10, no. 4, pp. 1843–1850, 2015.

[13] Q. Yao, Y.. Su, and L. Li, "Application of Negative Feedback Control Algorithm in Controlling Nonlinear Rolling Motion of Ships," in *Proceedings of the 2018 7th International Conference on Advanced Materials and Computer Science (ICAMCS)*, pp. 88–94, Dalian, China, December 2019.

[14] B Wang and L. L. Chen, "New results on fuzzy synchronization for a kind of disturbed memristive chaotic system," *Complexity*, vol. 2018, Article ID 3079108, 9 pages, 2018.

[15] L. Shenghong and K. Wang., "Chaos analysis of ship rolling motion in stochastic beam seas," *Journal of Ship Mechanics and Journal of Vibro Engineering*, vol. 19, no. 8, pp. 6403–6412, 2017.

[16] Q. Yao, Y. Su, and L. Li, "Application of negative feedback control algorithm in controlling nonlinear rolling motion of ships," in *Proceedings of the 2018 7th International Conference on Advanced Materials and Computer Science (ICAMCS)*, pp. 88–94, Dalian, China, December 2019.

[17] H. Wang, C. Che, L. Yu, S. Liu, and J. You, "Control method for a fin/tank integrated stabilization chaotic system," *CAAI Transactions on Intelligent Systems*, vol. 12, no. 3, pp. 318–324, 2017.

[18] Y Liu, "Research on numerical method of ship-roll chaos threshold," *Journal of Ship Mechanics*, vol. 23, no. 2, 2019.

[19] M. Ranjan Kumar, A. Krishna Banik, T. Kanti Datta, and S. Chatterjee, "Nonlinear roll oscillation of semisubmersible system and its control," *International Journal of Non-linear Mechanics*, vol. 107, pp. 42–55, 2018.

[20] C. Wang and S. S. Ge, "Adaptive synchronization of uncertain chaotic systems via backstepping design," *Chaos, Solitons & Fractals*, vol. 12, no. 7, pp. 1199–1206, 2001.

[21] X. Wu, J. Cai, and M. Wang, "Global chaos synchronization of the parametrically excited Duffing oscillators by linear state error feedback control," *Chaos, Solitons & Fractals*, vol. 36, no. 1, pp. 121–128, 2008.

[22] Y. Lei, K.-L. Yung, and Y. Xu, "Chaos synchronization and parameter estimation of single-degree-of-freedom oscillators via adaptive control," *Journal of Sound and Vibration*, vol. 329, no. 8, pp. 973–979, 2010.

[23] X. Shi. and Z. Wang, "Complete synchronization of delay hyperchaotic Lü system via a single linear input," *Nonlinear Dynamics*, vol. 69, no. 4, pp. 2245–2253, 2012.

[24] Z.-L. Wang and X.-R. Shi, "Chaotic bursting lag synchronization of Hindmarsh-Rose system via a single controller," *Applied Mathematics and Computation*, vol. 215, no. 3, pp. 1091–1097, 2009.

[25] Q. Han, X. Sun., X. Yang, and B. Wen, "External synchronization of a hysteretic system with a duffing system by feedback control strategy," *International Journal of Structural Stability and Dynamics*, vol. 9, no. 3, pp. 461–471, 2009.

[26] A. N. Njah and U. E. Vincent, "Chaos synchronization between single and double wells duffing–van der pol oscillators using active control," *Chaos, Solitons & Fractals*, vol. 37, no. 5, pp. 1356–1361, 2008.

Hindawi
Mathematical Problems in Engineering
Volume 2021, Article ID 6611992, 8 pages
https://doi.org/10.1155/2021/6611992

Research Article

Finite Horizon Robust Nonlinear Model Predictive Control for Wheeled Mobile Robots

Phuong Nam Dao,[1] **Hong Quang Nguyen**,[2] **Thanh Long Nguyen**,[1,3] **and Xuan Sinh Mai**[1]

[1]*School of Electrical Engineering, Hanoi University of Science and Technology, Hanoi, Vietnam*
[2]*Thai Nguyen University of Technology, No. 666 3/2 Street, Thai Nguyen, Vietnam*
[3]*Hung Yen University of Technology and Education, Hung Yen, Vietnam*

Correspondence should be addressed to Hong Quang Nguyen; quang.nguyenhong@tnut.edu.vn

Received 21 October 2020; Revised 28 December 2020; Accepted 31 December 2020; Published 18 January 2021

Academic Editor: Sundarapandian Vaidyanathan

The control of mobile robotic systems with input constraints is still a remarkable problem for many applications. This paper studies the model predictive control-based kinematic control scheme after implementing the decoupling technique of wheeled mobile robots (WMRs). This method enables us to obtain the easier optimization problem with fixed initial state. The finite horizon in cost function of model predictive control (MPC) algorithm requires the appropriate terminal controller as well as the equivalent terminal region. The stability of MPC is determined by feasible control sequence. Finally, offline simulation results validate that the computation load is significantly reduced and also validate trajectory tracking control effectiveness of our proposed control scheme.

1. Introduction

Mobile vehicle systems have a broad application prospective in many important fields (military, industry, and hospital task) and are attractive to researchers throughout the world following several main directions including interaction between chaotic systems and mobile robots [1, 2], multirobot coordination [3], trajectory tracking control, and motion-force control problem. The conventional nonlinear control technique has been mentioned in many works by researchers [4]. The classical sliding mode control (SMC) was considered in the work of [4] based on the computation the control signals in each stages consisting of converging to sliding surface and moving on it. Furthermore, the SMC technique has been implemented for different systems such as bilateral teleoperators, under the consideration of order reduction [5]. Because of the nonholonomic constraints and under-actuated description, it is worth noting that a robotic system can be classified into two subsystems. It leads us to consider a cascade controller and stabilization problem [5–9]. Under the influence of unknown wheel slip, this separation technique can be still considered for robotic systems to develop the back-stepping controller achieving the whole system stability [8]. Moreover, the authors in [7] still employ the back-stepping technique for output feedback problem as well as for tractor-trailer systems in [9].

During the last three decades, the motion-force control design of robotic systems under the effect of underactuated mechanical systems and nonholonomic constraints has been considered as a remarkable challenge. The fact is that the above separation method only depends on the trajectory tracking problem due to the constraint coefficient elimination after the transformation. Therefore, the motion/force controller for robotics has been proposed in [10] after obtaining the equivalent map. On the other hand, the challenge of actuator saturation has been handled by classical nonlinear controllers [6]. However, in general nonlinear systems, it is necessary to consider the model predictive control (MPC) solution because of the advantage in handling the actuator saturation.

Optimal control solution has the remarkable way that can solve the above constraint problems by considering the

constraint-based optimization [11–14], and model predictive control (MPC) is also one of the most effective solutions to handle the constraint in single systems [15, 16] as well as multiagent systems [17]. In the direction of optimal control, finding the explicit solution of Ricatti equation and partial differential HJB (Hamilton–Jacobi–Bellman) equation in general nonlinear systems [11] is necessary. Thanks to the neural network approximation effectiveness, the novel online adaptive dynamic programming (ADP) algorithm which enables to adjust simultaneously both actor and critic terms [11] is proposed. The training technique of the critic neural network (NN) was implemented by the modified Levenberg–Marquardt method to minimize the square residual error. Furthermore, the weight convergence and stability problem were shown by the need of persistence of excitation (PE) condition [11]. Considering the extension of this work, a model-free adaptive reinforcement learning has been proposed via the special cost function without the knowledge of the system dynamics [12]. Moreover, the nonlinear systems were acted by online adaptive reinforcement learning with completely unknown dynamics after implementing the data collection and Kronecker product.

In recent years, the model predictive control (MPC) has been considered as an effective approach to deal with state/input constraints along with guaranteeing many control objectives under choosing the equivalent cost functions [18, 19]. The main difference between MPC and conventional nonlinear control approaches is that we give out the control sequence by solving optimization problem at each sampling time [20, 21]. Moreover, the tracking problem as well as stability effectiveness of closed systems should be mentioned in MPC algorithm after satisfying the optimization problem. A number of two directions are considered in MPC solution to ensure the stability effectiveness of closed systems, including finite horizon [15, 22–24] and infinite horizon cost function [25, 26]. In order to satisfy the feasibility problem in the MPC control system, the linear matrix inequalities (LMIs) were mentioned in the case of infinite horizon cost function [25, 26], and the appropriate terminal cost function, equivalent terminal controller, terminal region were found in the case of finite horizon [15, 22–24]. This method was also considered for active car suspension and linear parameter varying (LPV) systems in the description of discrete time systems by using LMIs technique without finding the terminal controller in the work of [16, 27], respectively.

Furthermore, a different approach to consider the stability of MPC control systems was also investigated by using Lyapunov-based MPC solution [28]. In [22–24], the authors considered the way to handle the disturbance based on nominal systems, which are obtained by eliminating the disturbance, and this technique was extended by an additional disturbance observer [29]. Furthermore, the extension of this method is considered via a cascade controller with different terminal controller [15]. Similar to the work in [22–24, 30], the robust MPC was applied for manipulators based on optimization problem with which the initial state belongs to the region obtained from disturbance influence [31]. The linearization technique was applied for the advantage of obtaining easier optimization problem in manipulator [32] and in mobile robots [33]. Extending the work in [22–24], the event-based model predictive control for tracking of a nonholonomic mobile robot was investigated in [34]. Moreover, the motion-force control objective can be considered after the work in [35] employing nonlinear MPC for chained form systems. In [36], the nonlinear MPC was investigated for autonomous underwater vehicles (AUVs), not only the kinematic subsystem but also dynamic model. Inspired by the above contents and consideration of MPC problem for robotic systems, the work focuses on the MPC-based kinematic control for mobile robots with main contributions listed as follows:

(1) In comparison with the previous papers [15, 22–24, 30], a MPC-based kinematic control scheme with an easier optimization problem considering fixed initial state and eliminating the predicted model in MPC law

(2) The strict proof concerning the new terminal controller as well as the terminal region is given based on the Lyapunov stability theory

The remainder of our paper is organized as follows. The robot mathematical model and problem statements are given in Section 2. The model predictive-based kinematic tracking control design is presented in Section 3. Subsequently, the simulation results are shown in Section 4. Finally, the conclusions are determined in Section 5.

2. Robot Mathematical Model and Problem Statements

In [8, 9], we can establish the Lagrange function after obtaining the kinematic and dynamic energy. Based on Lagrange dynamic equation, the mathematical model of WMRs can be represented in Figure 1 as mentioned in [8, 9]:

$$\begin{cases} M(\eta)\ddot{\eta} + C(\eta,\dot{\eta})\dot{\eta} + B(\eta)\left(F(\dot{\eta}) + \tau_d\right) = B(\eta)\tau + J^T(\eta)\lambda, \\ J(\eta)\dot{\eta} = 0, \end{cases} \tag{1}$$

where $\eta = [x, y, \theta]^T$ is the vector of joint variables. Let us describe in detail about this vector: three variables, namely, x, y, and θ are sequentially denoted by the position coordinates, the orientation angle of the mobile robot with respect to the axis. All the parameters as well as variables are described in Table 1. Moreover, $M(\eta)$ is the symmetric and positive-definite inertia matrix; $C(\eta,\dot{\eta})$ denotes the centripetal and Coriolis matrix; $F(\dot{\eta})$ and τ_d represent the friction term and bounded external disturbances, respectively; $B(\eta)$ denotes the input transformation matrix; $J^T(\eta)$ is the associated constraint matrix; λ is the Lagrange coefficient; and the mobile robot is acted by the input vector $\tau = [\tau_l, \tau_r]^T$ including left and right torques. The nonholonomic description of general mobile robotic systems (1) leads us to obtain many appropriate control designs based on the existence of solutions $S^T(\eta)$ satisfying the equation

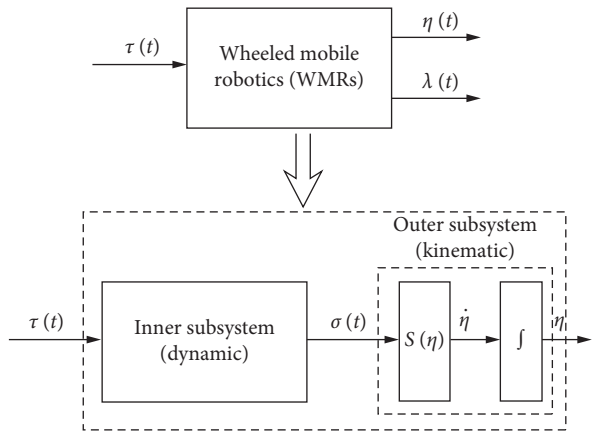

Figure 1: The model of wheeled mobile robotics.

Table 1: Parameters and physical variables of WMRs.

Parameter	Meaning	Unit
b	Half of distance between two wheels	m
r	The wheel's radius	m
r	The wheel's radius	m
m_r	The weight of platform	Kg
I_{rz}	Inertia moment of platform with respect to z-axis	kgm^2
I_{wz}	Inertia moment of wheels with respect to z-axis	kgm^2
I_{wy}	Inertia moment of wheels with respect to wheel axis	kgm^2
x	Projection of the coordinate with respect to x-axis	m
y	Projection of the coordinate with respect to y-axis	m
θ	Heading angle of mobile robots with respect to x-axis	rad
θ_r, θ_l	Angular displacement of each wheel	rad
v	WMR's velocity	m/s

$S^T(\eta)$. $J^T(\eta) = 0$. Consequently, there exists a vector σ such that $\dot{\eta}(t) = S(\eta)\sigma$. Therefore, taking the time derivative of this equation, we obtain that

$$\ddot{\eta} = \dot{S}(\eta)\sigma + S(\eta)\dot{\sigma}. \tag{2}$$

In the case of WMRs, the vector σ was determined as $\sigma = [\vartheta, \omega]^T$, where ϑ and ω are the linear and angular velocities, respectively. It is worth noting that the state variables can be represented by $[\eta^T, \sigma^T]^T = [x, y, \theta, \vartheta, \omega]^T$. By multiplying on both sides of mathematical model (1), we achieve the two connected subsystems of WMRs as follows:

$$\begin{cases} \dot{\eta} = S(\eta)\sigma, \\ D(\eta)S(\eta)\dot{\eta} + C_1(\eta, \dot{\eta})\eta = B(\eta)\tau. \end{cases} \tag{3}$$

Remark 1. It can be verified that the above decoupling technique (3) has the following advantage. The dynamic part (inner subsystem) is a fully actuated subsystem being influenced by unknown parameters and unmodeled disturbances. Meanwhile, the kinematic part, namely, the outer subsystem is the only underactuated system without any uncertain terms.

Remark 2. The decoupling technique was the starting idea of robust adaptive control design in mobile robotic systems [9]. However, it is worth noting that this technique does not guarantee implementing motion/force control objective due to elimination of constraint force factor being the Lagrangian constraint coefficient (3). In order to implement the motion/force control problem, the chain form-based decoupling techniques were mentioned in [25].

The control objective is to find the control signal satisfying the trajectory tracking control problem based on the model predictive control (MPC) algorithm with the advantages not only the optimization problem but also the closed loop stability. Additionally, the purpose of this article is also to reduce the complexity of MPC law by decoupling the WMRs model.

3. Model Predictive-Based Kinematic Tracking Control Design

In this section, we first design the tracking controller using the MPC technique and then analyze the feasibility and closed loop stability of the proposed MPC algorithm. According to (3), in the case of WMRs, the kinematic model can be represented as

$$\begin{bmatrix} \dot{x} \\ \dot{y} \\ \dot{\theta} \end{bmatrix} = \begin{bmatrix} \cos\theta & 0 \\ \sin\theta & 0 \\ 0 & 1 \end{bmatrix} \begin{bmatrix} v \\ \omega \end{bmatrix}. \tag{4}$$

Because of the existence of trigonometric factor in (4), according to the desired trajectory $[x_r, y_r, \theta_r]^T$ and equivalent $[v_r, \omega_r]^T$, the tracking error model of kinematic subsystem should be transformed as follows:

$$\begin{bmatrix} x_e(t) \\ y_e(t) \\ \theta_e(t) \end{bmatrix} = \begin{bmatrix} \cos\theta & \sin\theta & 0 \\ -\sin\theta & \cos\theta & 0 \\ 0 & 0 & 1 \end{bmatrix} \begin{bmatrix} x_r(t) - x(t) \\ y_r(t) - y(t) \\ \theta_r(t) - \theta(t) \end{bmatrix}. \tag{5}$$

Therefore, the tracking error model's dynamic of the kinematic subsystem can be obtained as follows:

$$\frac{\mathrm{d}}{\mathrm{d}t} p_e = \begin{bmatrix} \dot{x}_e \\ \dot{y}_e \\ \dot{\theta}_e \end{bmatrix} = \begin{bmatrix} \omega y_e - v + v_r \cos(\theta_e) \\ -\omega x_e + v_r \sin(\theta_e) \\ \omega_r - \omega \end{bmatrix}, \tag{6}$$

where the modified control inputs:

$$u_e = \begin{bmatrix} u_{1e} \\ u_{2e} \end{bmatrix} = \begin{bmatrix} v_r \cos(\theta_e) - v \\ \omega_r - \omega \end{bmatrix}. \tag{7}$$

Remark 3. The difference in description method in comparison with [15] is described by choosing the equivalent coordinate. In our work, the local coordinate frame of the WMR uses the geometrical center. Meanwhile, the mass

center of WMR was chosen for the local coordinate frame in [15]. It leads us to find the appropriate terminal region, terminal controller. Furthermore, it is obviously different from the existing control methods for WMRs in [4, 6–10]. The proposed robust MPC is first structured to obtain the optimization purpose being the extension of classical trajectory tracking control.

Thanks to the decoupling technique above, the disturbance has been eliminated in the kinematic subsystem (6) and then leads us to present the MPC algorithm with modified optimization problem considering the fixed starting point as follows:

$$\underset{u(\tau|t_k)}{\arg\min}\, J(p_e, u_e) = \int_{t_k}^{t_k+T} L(p_e(\tau|t_k), u_e(\tau|t_k))\mathrm{d}\tau + g(p_e(t_k+T|t_k)), \tag{8}$$

subject to

$$\begin{aligned} \dot{p}_e(\tau|t_k) &= f(x_e(\tau|t_k), u_e(\tau|t_k)), \quad \tau \in [t_k, t_k+T], \\ p_e(t_k|t_k) &= p_e(t_k), \\ u(\tau|t_k) &\in U \\ &= \left\{[v,\omega]^T : 0 \le v \le v_{\max}, -\omega_{\max} \le \omega \le \omega_{\max}\right\}, \\ &\tau \in [t_k, t_k+T], \\ p_e(t_k+T) &\in \Omega, \end{aligned} \tag{9}$$

where

$$\begin{aligned} L(p_e(\tau|t_k), u_e(\tau|t_k)) &= \|p_e(\tau|t_k)\|_Q^2 + \|u_e(\tau|t_k)\|_P^2, \\ g(p_e(t_k+T|t_k) &= \frac{1}{2}\|p_e(t_k+T|t_k)\|^2, \\ Q &= \mathrm{diag}\{q_1, q_2, q_3\}, \\ P &= \mathrm{diag}\{p_1, p_2\}, \\ T &= N\delta; \quad N \in, N > 0, \end{aligned} \tag{10}$$

and Ω is the terminal region, and then it will be defined and found later.

Remark 4. Thanks to the decoupling technique, the kinematic model belongs to certain systems. Therefore, the optimization problem will be considered with the fixed initial state, as described in the following algorithm.

Remark 5. Unlike that the classical MPC needs to employ the predictive model, this above optimization problem can solve directly based on the kinematic model without external disturbances and uncertainties. The modified optimization problem is solved online at each step by consideration of the optimal control problem without implementing the computation of predicted model. It should be noted that, by combining with the consideration of a fixed initial point in optimization problem, it is able to obtain simplicity in implementing the MPC law. Furthermore, the unification of optimization and tracking problem is solved in the Theorem 1.

The following theorem shows the tracking problem of closed systems using the modified optimization-based algorithm (Algorithm 1).

Theorem 1. *Consider the outer loop error system (6) with the above kinematic tracking algorithm. Then, the closed control system is ISS.*

In order to obtain the proof of Theorem 1, several definitions and lemmas are considered as follows.

Definition 1. Consider the tracking error model (6), the terminal region Ω, and the equivalent terminal controller $u^L(.)$ are described that if $p_e(t_k+T|t_k) \in \Omega$, then the closed system with this terminal controller satisfies, for any $\tau \in (t_k+T, t_{k+1}+T]$:

$$\begin{cases} p_e(\tau|t_k) \in \Omega; \\ u(\tau|t_k) \in U; \\ \dfrac{\mathrm{d}g(p_e(\tau|t_k))}{\mathrm{d}\tau} + L(p_e(\tau|t_k), u_e(\tau|t_k)) \le 0. \end{cases} \tag{11}$$

Lemma 1 enables to find the equivalent terminal region for a terminal controller. It leads us to determine the stability of closed system by using the intermediate estimation.

Lemma 1. *For the outer loop error system (6), the following set*

$$\Omega = \left\{ \begin{array}{c} p_e : |x_e| \ge |y_e|, \quad y_e\theta_e < 0, \\ \dfrac{v_r\cos\theta_e - v_{\max}}{k_1} \le x_e \le \dfrac{v_r\cos\theta_e + v_{\max}}{k_1} \\ -\dfrac{(\omega_{\max}+\omega_r)}{k_2} \le \theta_e \le \dfrac{(\omega_{\max}-\omega_r)}{k_2} \end{array} \right\}, \tag{12}$$

is a terminal region for the equivalent terminal controller:

$$u^L(t|t_k) = \begin{bmatrix} -k_1x_e + v_r\cos(\theta_e) \\ k_2\theta_e \end{bmatrix}, \tag{13}$$

for any $\tau \in [t_k+T, t_{k+1}+T)$, where k_1 and k_2 satisfy $k_1 - q_1 - p_1k_1^2 > q_2, k_2 - q_3 - p_2k_2^2 > 0$.

Proof. It can be seen that the terminal controller satisfies $u^L \in U$ if $p_e(t_k|t_k) \in \Omega$.

Taking the time derivative of $p_e(t_k|t_k) \in \Omega$ with respect to τ, we have

$$\begin{aligned} \frac{\mathrm{d}g(p_e(\tau|t_k))}{\mathrm{d}\tau} &= x_e\dot{x}_e + y_e\dot{y}_e + \theta_e\dot{\theta}_e \\ &= -k_1x_e^2 - k_2\theta_e^2 + y_ev_r\sin(\theta_e). \end{aligned} \tag{14}$$

(1) At time t_k, implement the measurement of actual state
(2) Solve the modified optimization problem to obtain the controller $u_e(t)$
(3) Apply the result during the sampling time interval $[t_k, t_k+1)$
(4) Update the time instant $t_k \longrightarrow t_{k+1}$

Algorithm 1: MPC-based kinematic tracking algorithm.

According to (12) and (14), we imply $(\mathrm{d}g(p_e(\tau\mid t_k))/\mathrm{d}\tau) < 0$. Therefore, the first condition in (11) is satisfied. Furthermore, based on $p_e(\tau\mid t_k) \in \Omega$, we obtain the result as follows:

$$\begin{aligned}\frac{\mathrm{d}g(\tilde{p}_e(\tau\mid t_k))}{\mathrm{d}\tau} &+ L(p_e(\tau\mid t_k), u_e(\tau\mid t_k)) \\ &= x_e\dot{x}_e + y_e\dot{y}_e + \theta_e\dot{\theta}_e + q_1x_e^2 + q_2y_e^2 \\ &\quad + q_3\theta_e^2 + p_1u_{1e}^2 + p_2u_{2e}^2 \\ &= -\left(k_1 - q_1 - p_1k_1^2\right)x_e^2 - \left(k_2 - q_3 - p_2k_2^2\right)\theta_e^2 \\ &\quad + y_ev_r\sin(\theta_e) + q_2y_e^2 < 0.\end{aligned} \tag{15}$$

It is obvious that the third condition of (11) is satisfied, which completes Lemma 1. □

Proof. First, it is necessary to consider the feasibility problem of Algorithm 1. Assuming that there exists a feasible solution, an optimal solution $u^*(t_k)$ is obtained at the sampling instant time t_k. Implementing the application of this control sequence $u^*(t_k)$ to (6), the state trajectory is driven into the terminal region Ω, by means that $p_e^*(t_k + T \mid t_k) \in \Omega$. Furthermore, $p_e(t_{k+1}\mid t_k) = p_e^*(t_{k+1})$ is a feasible initial state for the modified optimization problem. Therefore, a feasible control sequence is considered as the intermediate control sequence for estimation in Step 2, which can be established as follows:

$$u(\tau\mid t_{k+1}) = \begin{cases} u^*(\tau\mid t_k), & \tau \in [t_{k+1}, t_k+T), \\ u^L(\tau\mid t_k), & \tau \in [t_k+T, t_{k+1}+T). \end{cases} \tag{16}$$

Secondly, in order to prove the stability of closed system, we choose the Lyapunov function using optimal cost function as $V(t_k) = J(p_e^*(t_k), u_e^*(t_k)), k = \overline{1,\infty}$.

Considering the deviation of the two Lyapunov candidate functions at time t_k and t_k+1,

$$\begin{aligned}\Delta V &= V(t_{k+1}) - V(t_k) \\ &= J(p_e^*(t_{k+1}), u_e^*(t_{k+1})) - J(p_e^*(t_k), u_e^*(t_k)) \\ &\le J(p_e(t_{k+1}), u_e(t_{k+1})) - J(p_e^*(t_k), u_e^*(t_k)) \\ &= -\int_{t_{k+T}}^{t_{k+1}} \left(\|p_e^*(t\mid t_k)\|_Q^2 + \|u_e^*(t\mid t_k)\|_P^2\right)\mathrm{d}t \\ &\quad + \int_t^{t_{k+1}+T} \left(\|p_e(t\mid t_{k1})\|_Q^2 + \|u_e(t\mid t_{k1})\|_P^2\right)\mathrm{d}t \\ &\quad + \frac{1}{2}\|p_e(t_{k+1}+T\mid t_{k+1})\|^2 - \frac{1}{2}\|p_e^*(t_k+T\mid t_k)\|^2.\end{aligned} \tag{17}$$

According to (11), integrating from (t_k+T) to $(t_{k+1}+T)$, we imply that

$$\begin{aligned}&\frac{1}{2}\|p_e(t_{k+1}+T\mid t_{k+1})\|^2 - \frac{1}{2}\|p_e^*(t_k+T\mid t_k)\|^2 \\ &+ \int_t^{t_{k+1}+T} \left(\|p_e(t\mid t_{k+1})\|_Q^2 + \|u_e(t\mid t_{k+1})\|_P^2\right)\mathrm{d}t \le 0.\end{aligned} \tag{18}$$

According to (17) and (18), the following holds:

$$\begin{aligned}\Delta V &= V(t_{k+1}) - V(t_k) \\ &\le -\int_{t_{k+T}}^{t_{k+1}} \left(\|p_e^*(t\mid t_k)\|_Q^2 + \|u_e^*(t\mid t_k)\|_P^2\right)\mathrm{d}t \\ &\le -\int_{t_{k+T}}^{t_{k+1}} \left(\|p_e^*(t\mid t_k)\|_Q^2\right)\mathrm{d}t.\end{aligned} \tag{19}$$

Furthermore, we obtain $V(\infty) - V(0) \le -\int_0^\infty (\|p_e^*(t)\|_Q^2)\mathrm{d}t$. Because $V(\infty) \ge 0$, there exists the finite integral $\int_0^\infty (\|p_e^*(t)\|_Q^2)\mathrm{d}t$. Moreover, according to (19), a finite limitation $\lim_{k\longrightarrow\infty} V(t_k) = \phi < \infty$ exists. It is obvious that

$$\begin{aligned}0 &\le \lim_{k\longrightarrow\infty} \int_{t_k}^{t_{k+1}} \|p_e^*(t)\|_Q^2 \mathrm{d}\tau \\ &\le \lim_{k\longrightarrow\infty} \int_{t_k}^{t_{k+1}} \left(\|p_e^*(t)\|_Q^2 + \|u_e^*(t\mid t_k)\|_P^2\right)\mathrm{d}t \\ &\le \lim_{k\longrightarrow\infty} (V(t_{k+1}) - V(t_k)) \\ &= \phi - \phi = 0.\end{aligned} \tag{20}$$

Therefore, we conclude that $\lim_{k\longrightarrow\infty} \int_{t_k}^{t_{k+1}} \|p_e^*(\tau)\|_Q^2 \mathrm{d}\tau = 0 \Longrightarrow \lim_{t\longrightarrow\infty} \|p_e^*(t)\|_Q^2 = 0$. □

Remark 6. Unlike the proposed solutions in [15, 22–24], the terminal controller and equivalent terminal region in our work are based on the local coordinate frame using the geometrical center.

4. Simulation Results

The offline simulation is implemented by Casadi tool for modified optimization problem with fixed initial state. The trajectory of WMR to be tracked as follows: the desired trajectory $x_r = 0.8\cos(0.5t)$, $y_r = 0.8\sin(0.5t)$ and parameters of the controller are set to be $q_1 = q_2 = q_3 = 0.5$, $r_1 = r_2 = 0.2$, $k_1 = 2$, and $k_2 = 1$. Algorithm 1 is used for the kinematic model of WMR to obtain the tracking trajectory as described in Figure 2. Furthermore, we also present the response of velocities and the joint variable's error in Figures 3 and 4, respectively. The good behaviours in Figures 2–4 validate the

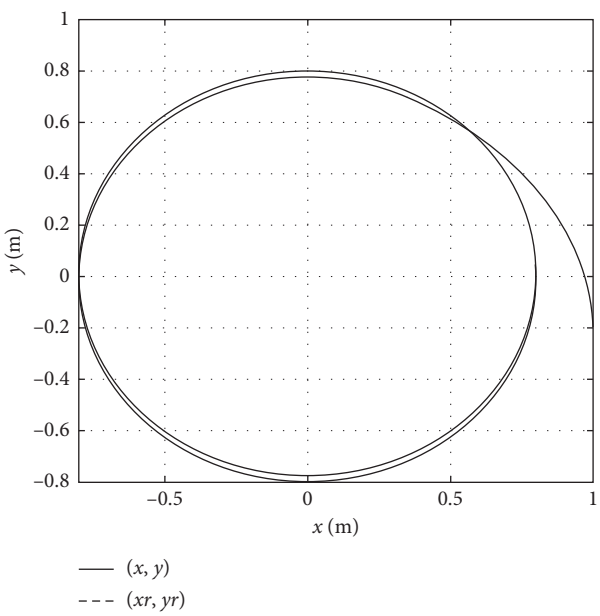

Figure 2: The trajectory response.

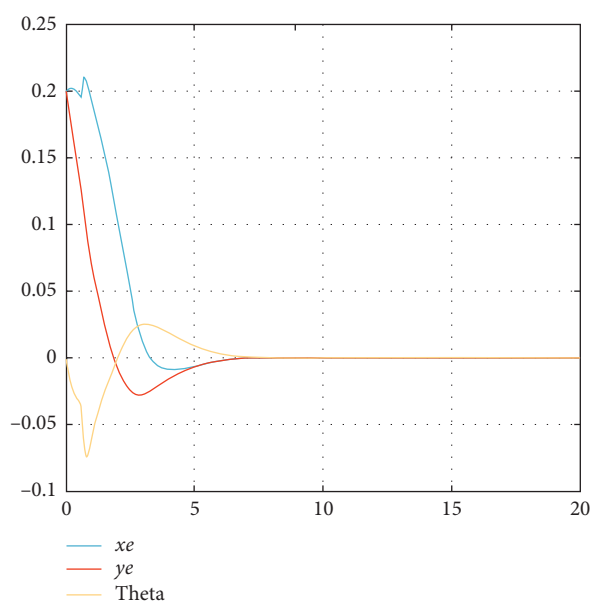

Figure 3: The joint variable's response.

high effectiveness of the proposed solution in paper. Furthermore, the computational complexity is easier than the previous works in [15, 22–24] because of the advantage of the fixed initial state in the modified optimization problem.

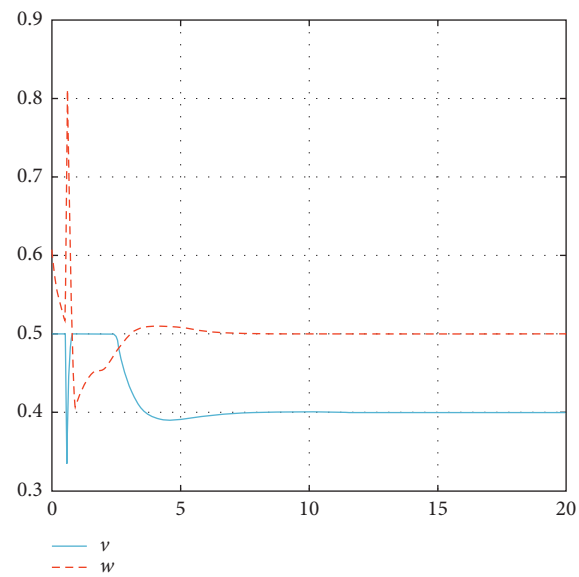

Figure 4: The control signals.

5. Conclusions

In this paper, the MPC-based kinematic control scheme has been developed for WMRs with input constraint and disturbances. The work was implemented under the advantage of decoupling technique of the WMR model based on the nonholonomic property in WMRs. The MPC algorithm, based on modified optimization problem with fixed initial state and eliminating the computation of predicted model, enables us to obtain easier computational complexity. The unification of optimization and tracking problem is handled by considering the feasibility and feasible region, appropriate Lyapunov function candidate. Using the Casadi tool in MATLAB software, simulation results and theoretical analysis demonstrated the effectiveness of the proposed solution. Future work of this research encompasses experimental validation of mobile robotic systems.

Data Availability

The multiple datasets supporting this study are cited in references.

Conflicts of Interest

The authors declare that they have no conflicts of interest.

Acknowledgments

This research was supported by the Ministry of Education and Training, Vietnam, under grant B2020-BKA-05.

References

[1] A. Sambas, S. Vaidyanathan, M. Mamat, W. S. M. Sanjaya, and D. S. Rahayu, "A 3-D novel jerk chaotic system and its application in secure communication system and mobile robot navigation," *Advances and Applications in Chaotic Systems*, vol. 636, pp. 283–310, 2016.

[2] S. Vaidyanathan, A. Sambas, M. Mamat, and M. Sanjaya, "A new three-dimensional chaotic system with a hidden attractor, circuit design and application in wireless mobile robot," *Archives of Control Sciences*, vol. 27, 2017.

[3] P. Paniagua-Contro, Hernandez-Martinez, E. Gamaliel et al., "Extension of leader-follower behaviours for wheeled mobile robots in multirobot coordination," *Mathematical Problems in Engineering*, vol. 2019, pp. 1–16, 2019.

[4] M. Asif, M. J. Khan, and N. Cai, "Adaptive sliding mode dynamic controller with integrator in the loop for nonholonomic wheeled mobile robot trajectory tracking," *International Journal of Control*, vol. 87, no. 5, pp. 964–975, 2013.

[5] Y.-C. Liu, P. N. Dao, and K. Y. Zhao, "On robust control of nonlinear teleoperators under dynamic uncertainties with variable time delays and without relative velocity," *IEEE Transactions on Industrial Informatics*, vol. 16, no. 2, pp. 1272–1280, 2020.

[6] J. Huang, C. Wen, W. Wang, and Z.-P. Jiang, "Adaptive stabilization and tracking control of a nonholonomic mobile robot with input saturation and disturbance," *Systems & Control Letters*, vol. 62, no. 3, pp. 234–241, 2013.

[7] J. Huang, C. Wen, W. Wang, and Z.-P. Jiang, "Adaptive output feedback tracking control of a nonholonomic mobile robot," *Automatica*, vol. 50, no. 3, pp. 821–831, 2014.

[8] T. Nguyena, T. Hoang, M. Pham, and N. Dao, "A Gaussian wavelet network-based robust adaptive tracking controller for a wheeled mobile robot with unknown wheel slips," *International Journal of Control*, vol. 92, no. 11, pp. 2681–2692, 2018.

[9] N. T. Binh, N. A. Tung, D. P. Nam, and N. H. Quang, "An adaptive backstepping trajectory tracking control of a tractor trailer wheeled mobile robot," *International Journal of Control, Automation and Systems*, vol. 17, no. 2, pp. 465–473, 2019.

[10] J. Fu, T. Chai, C.-Y. Su, and Y. Jin, "Motion/force tracking control of nonholonomic mechanical systems via combining cascaded design and backstepping," *Automatica*, vol. 49, no. 12, pp. 3682–3686, 2013.

[11] K. G. Vamvoudakis, D. Vrabie, and F. L. Lewis, "Online adaptive algorithm for optimal control with integral reinforcement learning," *International Journal of Robust and Nonlinear Control*, vol. 24, no. 17, pp. 2686–2710, 2013.

[12] Y. Zhu, D. Zhao, and X. Li, "Using reinforcement learning techniques to solve continuous-time non-linear optimal tracking problem without system dynamics," *IET Control Theory & Applications*, vol. 10, no. 12, pp. 1339–1347, 2016.

[13] Y. Lv, J. Na, Q. Yang, X. Wu, and Y. Guo, "Online adaptive optimal control for continuous-time nonlinear systems with completely unknown dynamics," *International Journal of Control*, vol. 89, no. 1, pp. 99–112, 2015.

[14] S. Li, L. Ding, H. Gao, Y.-J. Liu, L. Huang, and Z. Deng, "ADP-based online tracking control of partially uncertain time-delayed nonlinear system and application to wheeled mobile robots," *IEEE Transactions on Cybernetics*, vol. 50, no. 7, pp. 3182–3194, 2020.

[15] H. Yang, M. Guo, Y. Xia, and Z. Sun, "Dual closed-loop tracking control for wheeled mobile robots via active disturbance rejection control and model predictive control," *International Journal of Robust and Nonlinear Control*, vol. 30, no. 1, pp. 80–99, 2019.

[16] S. Bououden, M. Chadli, L. Zhang, and T. Yang, "Constrained model predictive control for time-varying delay systems: application to an active car suspension," *International Journal of Control, Automation and Systems*, vol. 14, no. 1, pp. 51–58, 2016.

[17] J. Lee, J.-S. Kim, H. Song, and H. Shim, "A constrained consensus problem using MPC," *International Journal of Control, Automation and Systems*, vol. 9, no. 5, pp. 952–957, 2011.

[18] K. Oh, J. Seo, J.-G. Kim, and K. Yi, "MPC-based approach to optimized steering for minimum turning radius and efficient steering of multi-axle crane," *International Journal of Control, Automation and Systems*, vol. 15, no. 4, pp. 1799–1813, 2017.

[19] F. Korkmaz, "Performance improvement of induction motor drives with model-based predictive torque control," *Turkish Journal of Electrical Engineering Computer Sciences*, vol. 28, no. 1, 2020.

[20] G. Bai, Y. Meng, L. Liu, W. Luo, Q. Gu, and L. Liu, "Review and comparison of path tracking based on model predictive control," *ElectronicsMultidisciplinary Digital Publishing Institute (MDIP)*, vol. 8, no. 10, p. 1077, 2019.

[21] T. Nguyen and L. Le, "Neural network-based adaptive tracking control for a nonholonomic wheeled mobile robot with unknown wheel slips, model uncertainties, and unknown bounded disturbances," *Turkish Journal of Electrical Engineering & Computer Sciences*, vol. 26, no. 1, pp. 378–392, 2018.

[22] Z. Sun and Y. Xia, "Receding horizon tracking control of unicycle-type robots based on virtual structure," *International Journal of Robust and Nonlinear Control*, vol. 26, no. 17, pp. 3900–3918, 2016.

[23] Z. Sun, L. Dai, K. Liu, Y. Xia, and K. H. Johansson, "Robust MPC for tracking constrained unicycle robots with additive disturbances," *Automatica*, vol. 90, pp. 172–184, 2018.

[24] P. Wang, X. Feng, W. Li, X. Ping, and W. Yu, "Robust RHC for wheeled vehicles with bounded disturbances," *International Journal of Robust and Nonlinear Control*, vol. 29, no. 7, pp. 2063–2081, 2019.

[25] A. Boccia, L. Grüne, and K. Worthmann, "Stability and feasibility of state constrained MPC without stabilizing terminal constraints," *Systems & Control Letters*, vol. 72, pp. 14–21, 2014.

[26] W. Yang, D. Xu, C. Zhang, and W. Yan, "A novel robust model predictive control approach with pseudo terminal designs," *Information Sciences*, vol. 481, pp. 128–140, 2019.

[27] X. Ping, Z. Li, and A. Al-Ahmari, "Dynamic output feedback robust MPC for LPV systems subject to input saturation and bounded disturbance," *International Journal of Control, Automation and Systems*, vol. 15, no. 3, pp. 976–985, 2017.

[28] Z. Wu, F. Albalawi, Z. Zhang, J. Zhang, H. Durand, and P. D. Christofides, "Control lyapunov-barrier function-based model predictive control of nonlinear systems," *Automatica*, vol. 109, Article ID 108508, 2019.

[29] Z. Sun, Y. Xia, L. Dai, K. Liu, and D. Ma, "Disturbance rejection MPC for tracking of wheeled mobile robot," *IEEE/ASME Transactions on Mechatronics*, vol. 22, no. 6, pp. 2576–2587, 2017.

[30] S. Yu, X. Li, H. Chen, and F. Allgöwer, "Nonlinear model predictive control for path following problems," *International*

Journal of Robust and Nonlinear Control, vol. 25, no. 8, pp. 1168–1182, 2014.

[31] Y. Yu, L. Dai, Z. Sun, and Y. Xia, "Robust nonlinear model predictive control for robot manipulators with disturbances," in *Proceedings of the 37th Chinese Control Conference (CCC)*, pp. 3629–3633, Wuhan, China, July 2018.

[32] T. Sun, Y. Pan, J. Zhang, and H. Yu, "Robust model predictive control for constrained continuous-time nonlinear systems," *International Journal of Control*, vol. 91, no. 2, pp. 359–368, 2017.

[33] H. Yang, M. Guo, Y. Xia, and L. Cheng, "Trajectory tracking for wheeled mobile robots via model predictive control with softening constraints," *IET Control Theory & Applications*, vol. 12, no. 2, pp. 206–214, 2018.

[34] Z. Sun, L. Dai, Y. Xia, and K. Liu, "Event-based model predictive tracking control of nonholonomic systems with coupled input constraint and bounded disturbances," *IEEE Transactions on Automatic Control*, vol. 63, no. 2, pp. 608–615, 2018.

[35] H. Li, W. Yan, and Y. Shi, "A receding horizon stabilization approach to constrained nonholonomic systems in power form," *Systems & Control Letters*, vol. 99, pp. 47–56, 2017.

[36] C. Shen, Y. Shi, and B. Buckham, "Integrated path planning and tracking control of an AUV: a unified receding horizon optimization approach," *IEEE/ASME Transactions on Mechatronics*, vol. 22, no. 3, pp. 1163–1173, 2017.

Hindawi
Mathematical Problems in Engineering
Volume 2021, Article ID 6634762, 9 pages
https://doi.org/10.1155/2021/6634762

Research Article

Solitary Wave Diffraction with a Single and Two Vertical Circular Cylinders

Zouhair Hafsia,[1] Saliha Nouri,[1] Salah Mahmoud Boulaaras,[2] Ali Allahem,[3] Salem Alkhalaf,[4] and Aldo Munoz Vazquez[5]

[1]*Department of Physics, College of Science and Arts at ArRass, Qassim University, Buraydah, Saudi Arabia*
[2]*Department of Mathematics, College of Science and Arts at ArRass, Qassim University, Buraydah, Saudi Arabia*
[3]*Department of Mathematics, College of Science, Qassim University, Buraydah, Saudi Arabia*
[4]*Department of Computer Science, College of Science and Arts at ArRass, Qassim University, Buraydah, Saudi Arabia*
[5]*College of Engineering, Texas A&M University, Higher Education Center at McAllen, 6200 Tres Lagos Blvd, McAllen, TX 78504, USA*

Correspondence should be addressed to Ali Allahem; aallahem@qu.edu.sa

Received 12 December 2020; Revised 28 December 2020; Accepted 5 January 2021; Published 16 January 2021

Academic Editor: Sundarapandian Vaidyanathan

This study investigates the three-dimensional (3-D) solitary wave interaction with two cylinders in tandem and side-by-side arrangements for two wave heights. The solitary wave generation and propagation are predicted using the volume of fluid method (VOF) coupled with the NavierStokes transport equations. The PHOENICS code is used to solve these transport equations. The solitary wave generation based on the source line developed by Hafsia et al. (2009) is extended in three-dimensional wave flow and is firstly validated for solitary waves propagating on a flat bottom. The comparison between numerical results and analytical solution for small wave height $(H/h) = 0.1$ and 0.2 shows good agreements. The wave crest and the pseudo-wavelength are well reproduced. Excellent agreements were found in terms of maximum run-up and wave forces by comparison with the present model and analytical studies. The present model can be tested for the extreme solitary wave to extend its application to a more realistic case study as the solitary wave diffraction with an offshore oil platform.

1. Introduction

To ensure the safety of the offshore oil or airport platform, it is necessary to determine the interaction of the nonlinear waves with single or multiple cylinders structures. The main tasks of the wave structure interaction (WSI) problems are the prediction of the wave run-up, forces, breaking, and flow separation. The wave diffraction near multiple cylinders depended on the interference flow fields following the gap distance between the cylinders.

Different approaches are used to solve the WSI including experimental, analytical, or numerical methods. The interaction of a solitary wave (representing a real tsunami wave) with a single circular cylinder was studied experimentally by Yates and Wang [17] for weak and strong nonlinear waves. The development of a numerical wave tank (NWT) and its implementation on a computational fluid dynamics (CFD) code constitutes an alternative to the experiments (Cao and Wan [1], Windt et al. [2], and Ji et al. [3]). The NWT includes those based on full NavierStokes equations or the depth-average Boussinesq equations the simplified irrotational flow. The diffraction of monochromatic short-crested waves on a single vertical cylinder is studied by Zhu [4]. Based on the irrotational flow assumption, analytical solutions were proposed in this limiting assumption. Lin and Man [5] developed a nonlinear wave interaction around coastal structures by the extended Boussinesq equations of Nowogu. The computed results are compared to the full (3-D) NavierStokes results. Based on the Boussinesq model for wave generation and propagation, Zhao et al. [6] investigate numerically the solitary wave run-up around one, two, and four circular cylinders. The wave diffraction of the cnoidal

wave over two side-by-side or tandem arrangement is studied numerically by Wang and Ren [7] using a generalized Boussinesq model. Ning et al. [8] integrate the cut-cell method in a Boussinesq model to study the solitary wave diffraction in Cartesian grid cells.

The Boussinesq model has the advantage that it can be used for nonlinear wave transformation for large-scale problems. However, the nonlinear effects are not well reproduced due to average operation. Hence, the numerical solution of the complete NavierStokes equations in three-dimensional (3-D) is necessary. Xie et al. [9] used a cut-cell method in a fully (3-D) code to simulate solitary wave interaction with a vertical circular cylinder and a thin horizontal plate. The Smagorinsky subgrid-scale model was used to simulate the turbulence structure. The desired waves are generated by prescribing the analytical solutions at the inlet. The monochromatic wave diffraction through a rectangular cylinder was conducted using a (3-D) free surface model by Li et al. [10]. Zhi and Jie-Min [11] propose to generate a cnoidal wave through the specification of the incident wave characteristics at the inlet (velocity components induced by the desired wave). This three-dimensional model is used to predict the cnoidal wave run-up through a single bottom cylinder. Kriebel [12] presents a theoretical solution of the run-up around a circular cylinder due to regular and nonlinear monochromatic waves. The comparison of experimental and analytical solutions shows that the nonlinear nature of wave propagation has a large effect on wave run-up. A Large Eddy Simulation (LES) to predict turbulence structure is used by Mo et al. [12] for monochromatic wave flow interaction with a single circular cylinder. Kamath et al. [14] developed a full three-dimensional model to study the free surface displacements and wave forces on three and four vertical cylinders. Frantzis et al. [15] analyze numerically the reflection and transmission coefficients induced by a breakwater formed by a single row of vertical circular piles closely spaced. The free surface deformation is simulated using the (VOF) method, and the (LES) model was used to reproduce the small scales of turbulence.

The present study investigates numerically the interaction of solitary wave with a single and twin circular cylinder. The NWT was first validated for solitary wave propagating on a flat bottom and then used to simulate the wave force exerted on a single and twin circular cylinder in tandem and side-by-side arrangements. The source line used by Hafsia et al. [16] in two-dimensional (2-D) NavierStokes model has been extended to generate a nonlinear wave for a three-dimensional (3-D) model.

2. Mathematical Formulation

2.1. Computational Domain. Figure 1 represents the locations of the source line and the different grid regions to control the grid distributions through the computational domain. As shown in this figure, the incident solitary wave propagates along the x-direction and impacts one or two circular cylinders in two arrangements following the angle β: in tandem ($\beta = 0$) and side-by-side ($\beta = 90^\circ$). The ratio of the still water depth to cylinder radius is $(h/a) = 3$. For a given water depth $h = 0.2\,\mathrm{m}$, the cylinder ratio is $a = 0.067\,\mathrm{m}$. The two vertical cylinders are closely separated with $(G/2a) = 2$, where G is the gap distance between two cylinders (center to center). The wave forces are calculated for the tandem and side-by-side arrangements and for the following nondimensional wave heights: $(H/h) = 0.1$ and 0.2. Figure 2 presents the grid structure for two cylinders arranged in tandem with a refinement around the free surface and the circular cylinders. The two circular cylinders are represented using the cut-cell method in a Cartesian grid as shown by Figure 2(b). For all the cylinder arrangements, the grid number along the x-direction is taken equal to $N_x = 190$ and along the z-direction equal to $N_z = 94$. For a single cylinder and the tandem arrangement, the grid number along the y-direction: $N_y = 40$. However, for the side-by-side cylinders: $N_y = 60$. The same time step is adopted for all simulated cases $\Delta t = 0.01\,\mathrm{s}$.

2.2. Governing Transport Equations. The proposed (NWT) was based on the full three-dimensional (3-D) NavierStokes transport equations coupled to the volume of liquid (VOF) convective transport equation to reproduce the water wave interface. For unsteady flow and incompressible fluid, the mass and momentum conservation equations are written as follows:

The mass conservation equation:

$$\frac{\partial \rho}{\partial t} + \frac{\partial u_i}{\partial x_i} = 0. \tag{1}$$

The momentum transport equation:

$$\frac{\partial u_i}{\partial t} + u_j \frac{\partial u_i}{\partial x_j} = -\frac{1}{\rho}\frac{\partial p}{\partial x_i} + \frac{\partial}{\partial x_j}\left[\nu\left(\frac{\partial u_i}{\partial x_j} + \frac{\partial u_j}{\partial x_i}\right)\right] + g_i + s_{d,i}, \tag{2}$$

where x_i the Cartesian coordinates, u_i is the velocity components, ρ is the density of the mixture, p is the pressure, ν is the kinematic viscosity of the mixture, g is the acceleration due to gravity, and $s_{d,z}$ is a momentum source term added to the momentum equation along z-direction to avoid wave reflection at the open boundaries given by

$$s_{d,z} = \gamma\,(x)\,w. \tag{3}$$

where $\gamma(x)$ is a linear damping function and w is the velocity component along the z vertical direction.

2.3. Free Surface Capture. The air-water interface is modeled using the mixture model flow. If α_q denotes the volume fraction of the q th fluid in a cell, then

The density of the mixture is given by

$$\rho = \sum_{q=1}^{2} \rho_q\,\alpha_q. \tag{4}$$

where ρ_q is the density of the water when $(q = 1)$ and air when $(q = 2)$.

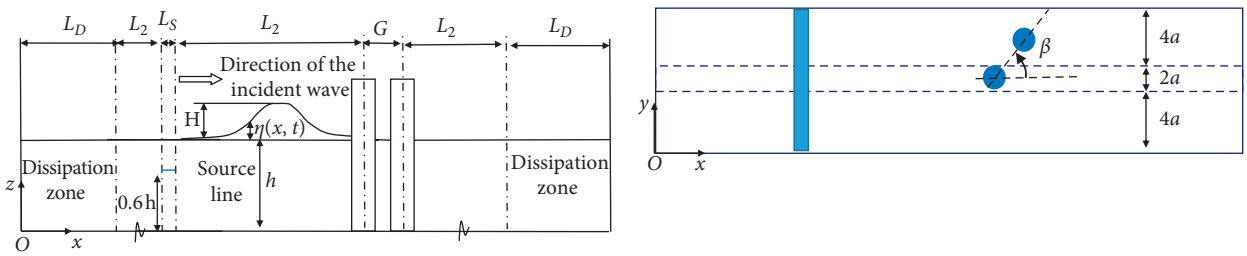

(a) (b)

Figure 1: Grid regions of the computational domain and wave source line location: (a) side view; (b) top view.

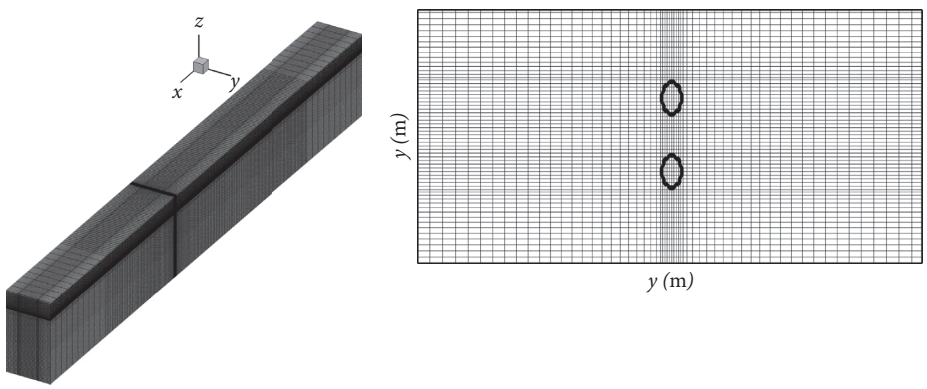

(a) (b)

Figure 2: The grid of computational domain: (a) side view; (b) top view of the grid details around the side-by-side circular cylinders by the cut-cell method.

And, dynamic viscosity of the mixture is

$$\mu = \sum_{q=1}^{2} \mu_q \alpha_q. \tag{5}$$

where μ_q is the dynamic viscosity of the water if $(q = 1)$ and air when $(q = 2)$.

The volume fraction of fluid is determined by the following mass conservation equation for each phase:

$$\frac{\partial \alpha_q}{\partial t} + \frac{\partial(\alpha_q u_i)}{\partial x_i} = 0. \tag{6}$$

When $\alpha_q = 0$, the cell is occupied by air, $\alpha_q = 1$, the cell is occupied by water, and $0 < \alpha_q < 1$, the cell contains the interface (Hirt et al. [18]).

2.4. Wave Generation. The desired solitary wave was generated by an internal source inlet across a source line as proposed by Hafsia et al. [16]. The inlet vertical velocity is prescribed as a time-dependent inlet boundary condition:

$$w^I = \frac{2\, c\, \eta(x_s, t)}{L_s}, \tag{7}$$

where L_s is the length of the internal source line.

The wave celerity is given by Dominguez et al. [19]:

$$c = \sqrt{g\,(H + h)}. \tag{8}$$

The solitary wave surface elevation $\eta(x_s, t)$ is given by the following equation:

$$\eta = H \operatorname{sech}^2 [k\,(x_s - c\,t)], \tag{9}$$

where H is the incident wave height and t is the time. The distance x_s permitting to have a negligible source at $t = 0$ s is determined by the following equation:

$$x_s = \frac{4h}{\sqrt{(H/h)}}. \tag{10}$$

The equivalent wave number k is

$$k = \sqrt{\frac{3\,H}{4h^2\,(H + h)}}. \tag{11}$$

Following this equivalent wave number, the pseudo-wave length can be determined by

$$L = \frac{2\pi}{k}. \tag{12}$$

Table 1 summarizes the wave parameters and the length of the source line L_s for the two considered wave height to water depth ratios. The length L_s and the position of the source line are determined by the calibration procedure as indicated by Hafsia et al. [16].

Table 1: Solitary wave parameters and the length of the source line.

	k (m^{-1})	c (m/s)	x_s (m)	L (m)	L_s (m)
$H/h = 0.1$	1.31	1.47	2.53	4.58	0.120
$H/h = 0.2$	1.77	1.53	1.79	3.24	0.072

2.5. Initial and Boundary Conditions. The following initial and boundaries conditions are adopted for the governing transport equations. The imposed initial condition is still water with a depth h. For the top boundary, the pressure P is set equal to the atmospheric pressure. Two dissipation zones are adopted at the open boundaries (Figure 1). At all the other boundaries of the computational domain, symmetric boundary conditions are imposed.

To solve this proposed model, we adopt the PHOENICS code (Parabolic Hyperbolic or Elliptic Numerical Integration Code Series). In this code, the SIMPLEST iterative algorithm is used to solve the pressure and velocity coupling in the NavierStokes equations (Artemov et al. [20]). The upwind scheme is used for nonlinear convection terms and an implicit formulation for the transient term. The VOF method is used to predict the interface between the water wave and air. For all the presented simulation results, the cut-cell within the PARSOL (PARtial SOLid) treatment is used to detect the solid-fluid interface which is not aligned with the Cartesian grid. The proposed three-dimensional wave generation method is implemented in the PHOENICS code.

3. Numerical Results

3.1. Wave Diffraction by a Single Circular Cylinder. The proposed wave generation method based on an internal source line is validated for two solitary waves having the nondimensional heights $H/h = 0.1$ and 0.2. The simulated results show that, before reaching the vertical cylinder, the wave profile is invariant in the transverse direction and can be represented by two-dimensional profiles in the center of the computational domain. Figure 3 represents the simulated wave profiles at the center of the computational domain before impacting the cylinder. For these two wave heights, the wave is not affected by the cylinder and the free surface profiles agree very well with the analytical one. The wave crests and the pseudo-wave lengths are in accordance with the analytical one. For $(H/h) = 0.1$, the wave is generated after $t = 3$ s. As the wave height increases, the solitary wave is completely generated more rapidly (after $t' = 2.3$ s).

In order to validate the cut-cell method, the maximum run-up is compared to the available literature. The maximum wave run-up is determined from the evolution of the solitary wave profiles along the centerline. In Figure 4, the solitary wave profiles are presented for different times around the maximum run-up which takes place at $t3 = 4.3$ s. For a nondimensional wave height, $H/h = 0.1$; the maximum wave run-up is equal to $R_{\max} = 0.0212$ m $= 1.060$ H which implies that the wave height increased by $(R_{\max} - H/H) * 100 = 6.0\,\%$. There is no significant difference between this value and the maximum run-up found by Domínguez et al. [19] that is equal to 1.065 for the same wave flow parameters. The maximum wave run-up increases when the wave height increases and is equal to $R_{\max} = 0.0466$ m $= 1.165$ H for $(H/h) = 0.2$ which implies that the wave height increased by 16.5 %. Following Domínguez et al. [19], the computed maximum run-up is 1.147 which is almost the same value given by the present study.

The evaluation of the wave forces exerted on the cylinder has great importance on the engineering applications and depends on the wave run-up R at the front of the stagnation point. The wave force $\vec{F}$ acting on the cylinder is computed by integrating the water pressure p and the normal component of the viscous stress tensor τ on the wetted surface of the cylinder S:

$$\vec{F} = \int_S (-\vec{n}\,p + \vec{n}.\tau)\mathrm{d}S, \tag{13}$$

where $\vec{n}$ is the normal unit vector pointing into the water.

The time histories of the computed wave force on the x-direction acting on an isolated cylinder are presented in Figure 5 for two different solitary wave heights. The peak of the in-line force becomes sharper when the solitary wave height increases. The computed forces are in good agreement with other numerical studies and the tested cut-cell method is validated.

3.2. Wave Diffraction by Two Circular Cylinders. Two vertical circular cylinders with the same radius are considered with different arrangements: in tandem ($\beta = 0$) and side-by-side ($\beta = 90°$). The still water depth to the radius ratio is $h/a = 3$. The cylinder and the nondimensional gap distance is $G/2a = 2$. In order to explain the wave diffraction between the two cylinders, Figure 6 illustrates the perspective view of the free surface elevation at different instants for nondimensional wave height: $H/h = 0.2$. The free surface raised at the upstream side of the cylinder and decreases behind it. When the reflected diffracted wave propagates away of the upstream cylinder, the free surface elevation drops significantly. The maximum run-up with partial wave reflection propagating radially occurs at instant $t3 = 4.3$ s for $H/h = 0.1$ and at the instant $t'3 = 3.72$ s $H/h = 0.2$. This radial wave is also observed by Yates and Wang [17]. At the instant $t6 = 5.2$ s, the solitary wave almost passes through the cylinder and the portion of the wave nonblocked by the cylinder is diffracted around the cylinder.

In order to compare the wave forces, Figure 7 represents the evolution of the in-line wave forces on the two vertical cylinders and on the isolated cylinder. The maximum run-up on the upstream cylinder is almost the same as the isolated one. However, due to the wave field interference, the maximum run-up on the downstream cylinder is less than that on the upstream cylinder for tandem arrangement and

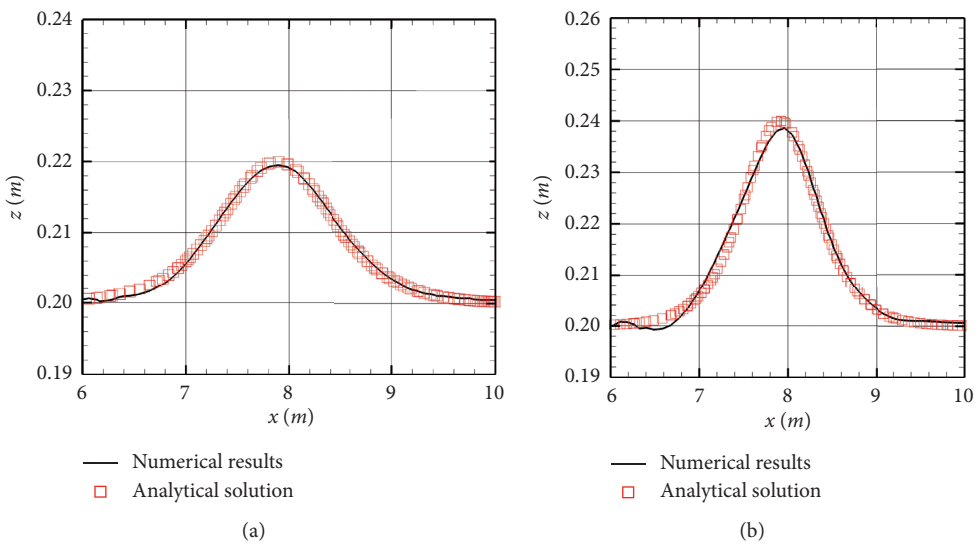

Figure 3: Comparison between the numerical and analytical free surface profiles at the centerline of computational domain: (a) $H/h = 0.1$ at $t = 3$ s and (b) $H/h = 0.2$ at t' = 2.3 s.

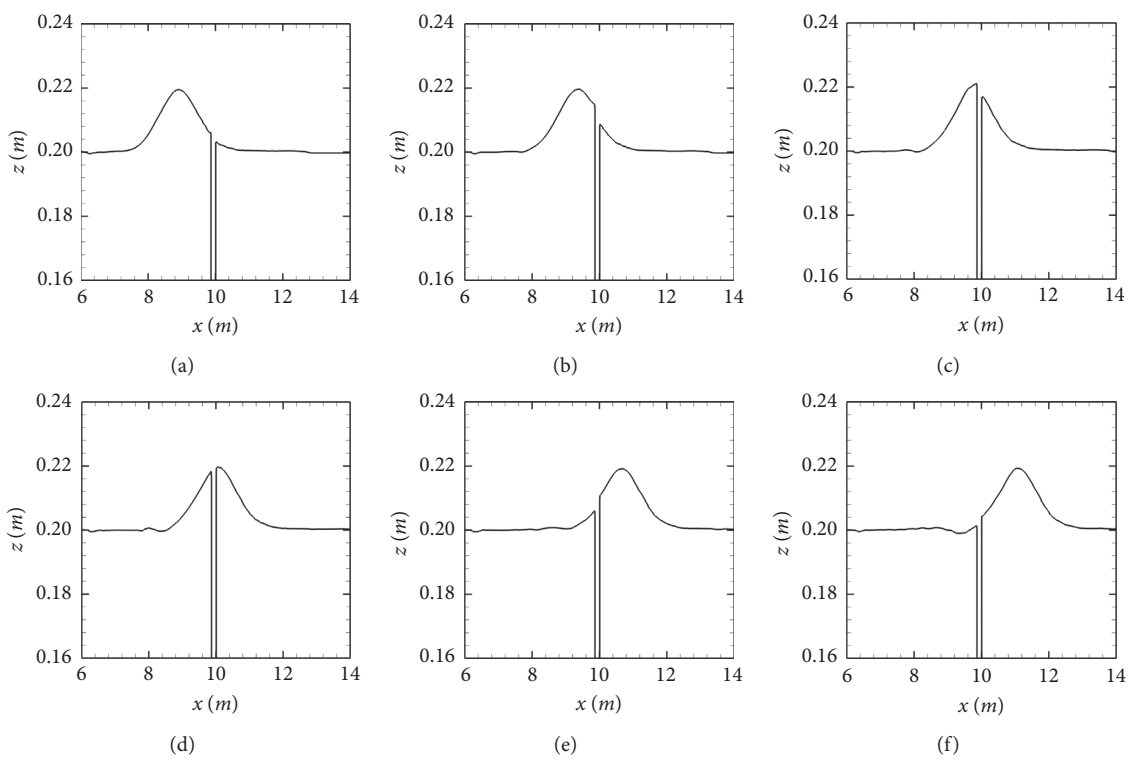

Figure 4: The wave run-up along the centerline of computational domain at different instants for $H/h = 0.1$: (a) $t_1 = 3.7$ s; (b) $t_2 = 4.0$ s; (c) $t_3 = 4.3$ s; (d) $t_4 = 4.5$ s; (e) $t_5 = 4.9$ s; (f) $t_6 = 5.2$ s.

$H/h = 0.1$. Following Yates and Wang [17], this interference effect is known as the shielding effect of the upstream cylinder on the downstream one. This mechanism induces the reduction of the in-line force on the downstream cylinder by 15 % compared to the force on the upstream cylinder (Table 2). The shielding effect is not observed for tandem arrangement and $H/h = 0.2$ where the in-line force on the downstream cylinder is greater than the upstream one (Table 3). For side-by-side arrangement, the wave force on the first cylinder is the same as that on the second cylinder for $H/h = 0.1$ and $H/h = 0.2$. The maximum force is observed at the same time for the two cylinders in side-by-side cylinders for the different wave heights. However, due to the gap distance, the maximum force for the downstream cylinder occurs after some time lag equal to 0.22 s.

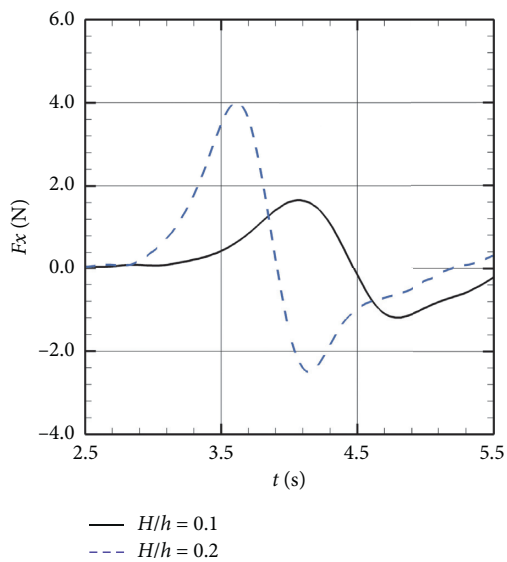

Figure 5: Time evolution of the in-line force on a single cylinder: (a) $H/h = 0.1$; (b) $H/h = 0.2$.

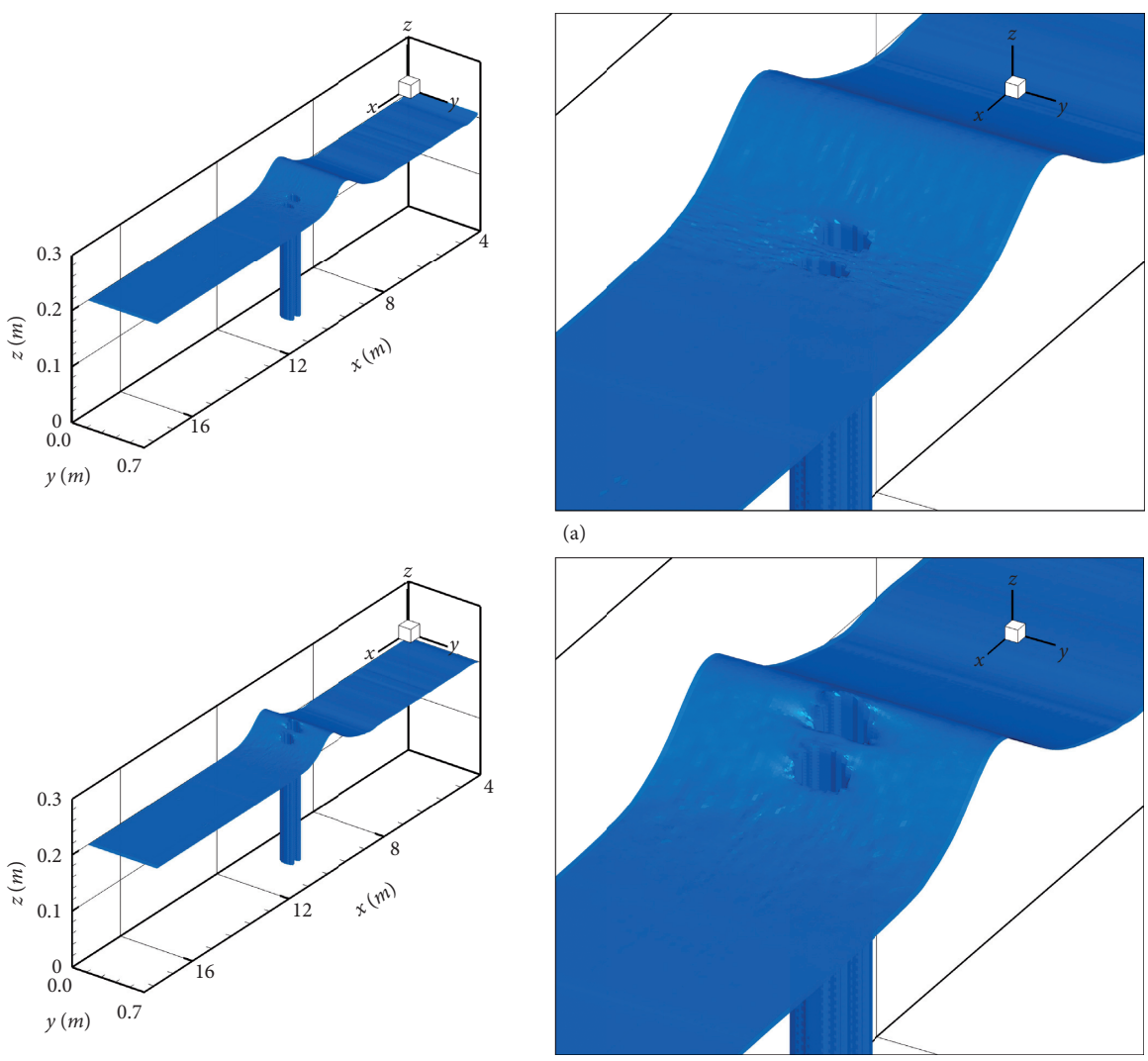

Figure 6: Continued.

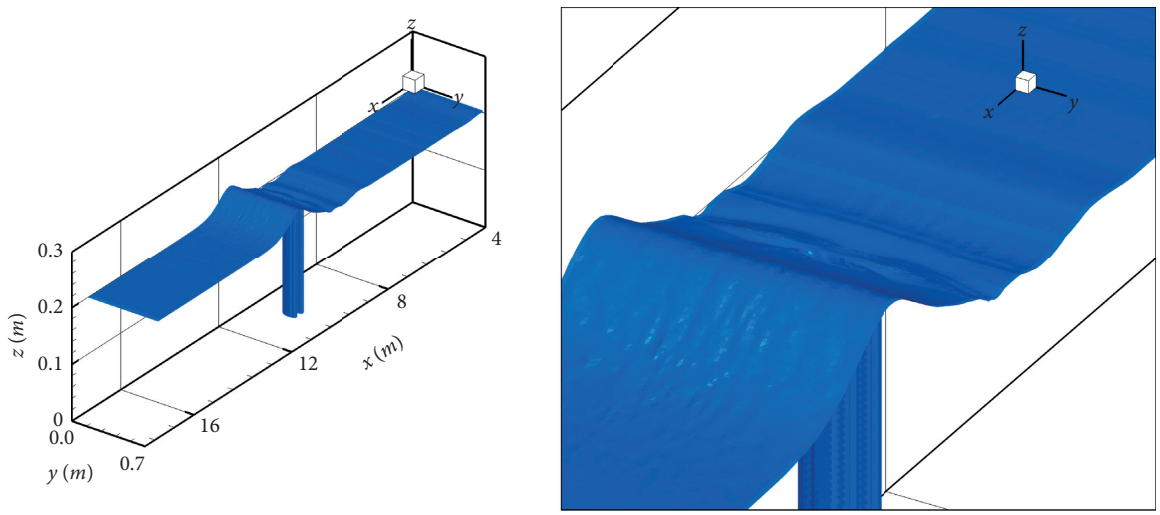

(c)

Figure 6: A three-dimensional free-surface elevation for two tandem circular cylinders ($\beta = 0^{\circ}$) at different times for $H/h = 0.2$: (a) $t_1 = 3.32$ s; (b) $t_2 = 3.72$ s; (c) $t_3 = 4.7$ s.

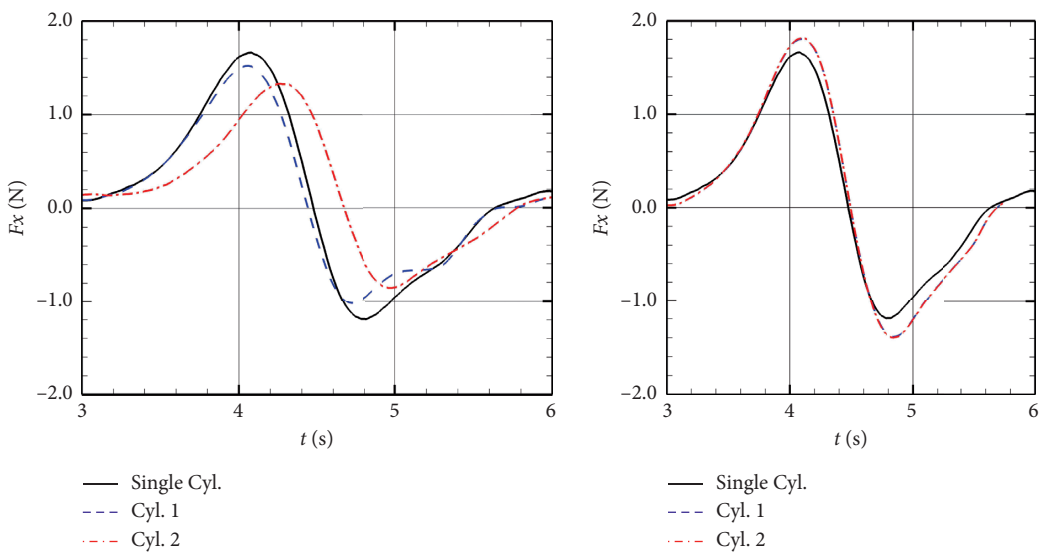

(a) (b)

Figure 7: Continued.

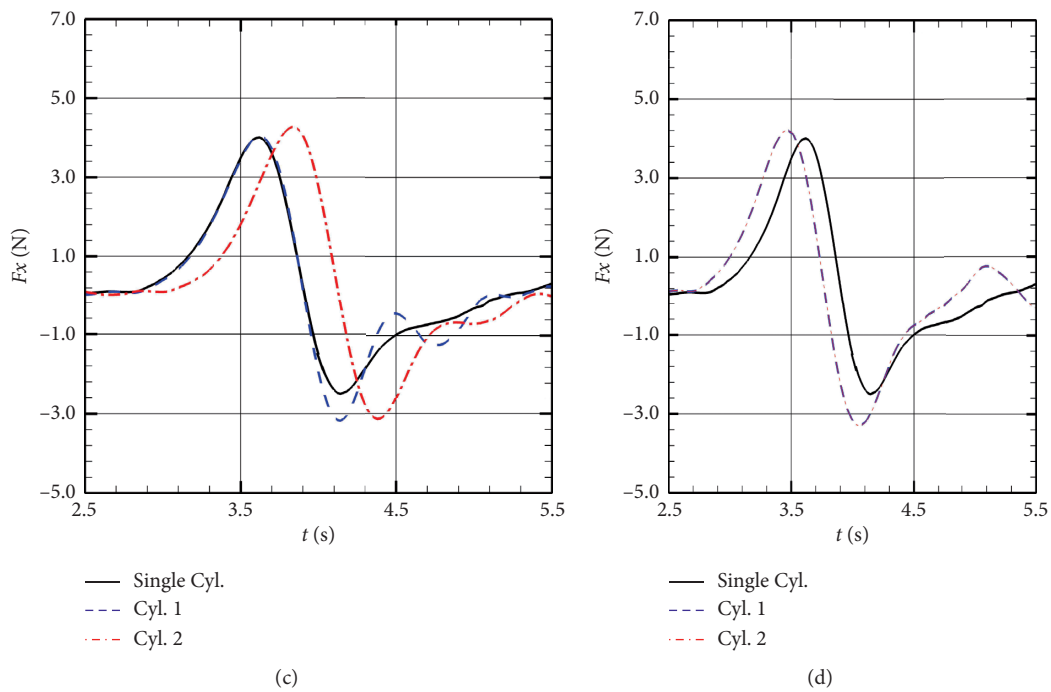

Figure 7: Time evolution of the in-line force on a single cylinder and two cylinders spaced by $G/a = 4$: (a) tandem circular cylinders ($\beta = 0^\circ$) for $H/h = 0.1$; (b) side-by-side circular cylinders ($\beta = 90^\circ$) for $H/h = 0.1$; (c) tandem circular cylinders ($\beta = 0^\circ$) for $H/h = 0.2$; (d) side-by-side circular cylinders ($\beta = 90^\circ$) for $H/h = 0.2$.

Table 2: Maximum and minimum in-line forces (N) for $H/h = 0.1$.

	Single cyl	Tandem arrangement ($\beta = 0$)		Side-by-side arrangement ($\beta = 90^\circ$)	
		Cyl 1	Cyl 2	Cyl 1	Cyl 2
$F_{x,\max}$	1.66	1.52	1.32	1.81	1.81
$F_{x,\min}$	−1.19	−1.02	−0.86	−1.39	−1.39

Table 3: Maximum and minimum in-line forces (N) for $H/h = 0.2$.

	Single cyl	Tandem arrangement ($\beta = 0$)		Side-by-side arrangement ($\beta = 90^\circ$)	
		Cyl 1	Cyl 2	Cyl 1	Cyl 2
$F_{x,\max}$	4.00	4.00	4.27	4.21	4.21
$F_{x,\min}$	−2.49	−3.17	−3.12	−3.29	−3.29

4. Conclusions

The proposed numerical wave tank (NWT) was validated for wave generation and wave diffraction with a single and two vertical circular cylinders for two solitary wave heights. All the simulated results are conducted in the Cartesian coordinates using the cut-cell method to represent the cylinder shape. Numerical results show that the solitary wave and the wave forces on the cylinder are well reproduced for a weak nonlinear wave. In the tandem arrangement and for $H/h = 0.1$, the shielding effect is observed. However, for $H/h = 0.2$, the in-line force for the downstream cylinder is greater than the upstream one. For the side-by-side arrangement, equally aligned, the in-line force for the two cylinders is the same. The diffracted wave affects this force compared to the single cylinder by some time lag.

The present model can be tested for the extreme solitary wave to extend its application to a more realistic case study as the solitary wave diffraction with an offshore oil platform.

Data Availability

No data were used to support the study.

Conflicts of Interest

The authors declare that they have no conflicts of interest regarding this study.

Acknowledgments

The third author would like to thank all the professors of the Mathematics Department at the University of Annaba in Algeria, especially his professors/scientists Pr. Mohamed Haiour, Pr. Ahmed-Salah Chibi, and Pr. Azzedine Benchettah for the important content of masters and PhD courses in pure and applied mathematics that he received during his studies. Moreover, he thanks them for the additional help they provided to him during office hours in their office about the few concepts/difficulties he had encountered, and he appreciates their talent and dedication for their postgraduate students currently and previously. The authors gratefully acknowledge Qassim University, represented by the Deanship of Scientific Research, on the financial support for this research under the number (10261-cos-2020-1-3-I) during the academic year 1442 AH/2020 AD.

References

[1] G. T. Yates and K. H. Wang, "Solitary wave scattering by a vertical cylinder: experimental study," in *Proceedings of the Fourth International Offshore and Polar Engineering Conference*, Osaka, Japan, April 1994.

[2] H. Cao and D. Wan, "Benchmark computations of wave run-up on single cylinder and four cylinders by naoe-FOAM-SJTU solver," *Applied Ocean Research*, vol. 65, p. 327, 2017.

[3] C. Windt, J. Davidson, E. J. Ransley et al., "Validation of a CFD-based numerical wave tank model for the power production assessment of the wavestar ocean wave energy converter," *Renewable Energy*, vol. 146, 2020.

[4] Q. Ji, Y. Wang, and G. Zhang, "Numerical study of solitary wave interaction with a submerged semicircular cylinder," *Mathematical Problems in Engineering*, vol. 2019, pp. 1–15, 2019.

[5] S. Zhu, "Diffraction of short-crested waves around a circular cylinder," *Ocean Engineering*, vol. 20, no. 4, 1993.

[6] P. Lin and C. Man, "A staggered-grid numerical algorithm for the extended Boussinesq equations," *Applied Mathematical Modelling*, vol. 31, no. 2, pp. 349–368, 2007.

[7] M. Zhao, L. Cheng, and B. Teng, "Numerical simulation of solitary wave scattering by a circular cylinder array," *Ocean Engineering*, vol. 34, no. 3-4, pp. 489–499, 2007.

[8] K.-H. Wang and X. Ren, "Interactions of cnoidal waves with cylinder arrays," *Ocean Engineering*, vol. 26, pp. 1–20, 1999.

[9] D. Z. Ning, J. Zang, Q. Liang, P. H. Taylor, and A. G. L. Borthwick, "Boussinesq cut-cell model for non-linear wave interaction with coastal structures," *International Journal for Numerical Methods in Fluids*, vol. 57, no. 10, pp. 1459–1483, 2008.

[10] Z. Xie, T. Stoesser, S. Yan, Q. Ma, and P. Lin, "A Cartesian cut-cell based multiphase flow model for large-eddy simulation of three-dimensional wave-structure interaction," *Computers & Fluids*, vol. 213, no. 15, pp. 1–17, 2020.

[11] Y. S. Li, S.-X. Liu, Y.-X. Yu, and G.-Z. Lai, "Numerical modeling of Boussinesq equations by finite element method," *Coastal Engineering*, vol. 37, no. 2, pp. 97–122, 1999.

[12] D. Zhi and Z. Jie-Min, "Numerical modeling of wave evolution and runup in shallow water," *Journal of Hydrodynamics*, vol. 21, no. 6, pp. 731–738, 2009.

[13] D. L. Kriebel, "Non-linear wave interaction with a vertical cylinder. part II: wave run-up," *Ocean Engineering*, vol. 19, no. 1, pp. 475–499, 1992.

[14] W. Mo, K. Irschik, H. Oumeraci, and P. L.-F. Liu, "A 3D numerical model for computing non-breaking wave forces on slender piles," *Journal of Engineering Mathematics*, vol. 58, no. 1-4, pp. 19–30, 2007.

[15] A. Kamath, H. Bihs, M. A. Chella, and O. A. Arntsen, "Upstream-cylinder and downstream-cylinder influence on the hydrodynamics of a four-cylinder group," *Journal of Waterway, Port, Coastal, and Ocean Engineering*, vol. 142, no. 4, Article ID 04016002, 2016.

[16] C. Frantzis, D. G. E. Grigoriadis, and A. A. Dimas, "Numerical study of solitary waves past slotted breakwaters with a single row of vertical piles: wave processes and flow behavior," *Ocean Engineering*, vol. 211, no. 1, pp. 1–21, 2020.

[17] Z. Hafsia, M. B. Hadj, H. Lamloumi, and K. Maalel, "Internal inlet for wave generation and absorption treatment," *Coastal Engineering*, vol. 56, no. 9, pp. 951–959, 2009.

[18] C. W. Hirt and B. D. Nichols, "Volume of fluid (VOF) method for the dynamics of free boundaries," *Journal of Computational Physics*, vol. 39, no. 1, pp. 201–225, 1981.

[19] J. M. Domínguez, C. Altomare, J. Gonzalez-Caoa, and P. Lomonaco, "Towards a more complete tool for coastal engineering: solitary wave generation, propagation and breaking in an SPH-based model," *Coastal Engineering Journal*, vol. 61, pp. 1–15, 2019.

[20] V. Artemov, S. B. Beale, G. de Vahl Davis et al., "A tribute to D.B. Spalding and his contributions in science and engineering," *International Journal of Heat and Mass Transfer*, vol. 52, no. 17-18, pp. 3884–3905, 2009.

Hindawi
Mathematical Problems in Engineering
Volume 2021, Article ID 8848914, 9 pages
https://doi.org/10.1155/2021/8848914

Research Article

Spiral Waves in a Lattice Array of Josephson Junction Chaotic Oscillators with Flux Effects

Balamurali Ramakrishnan,[1] Ramesh Ramamoorthy,[1] Chunbiao Li,[2,3] Akif Akgul,[4] and Karthikeyan Rajagopal[5]

[1]*Chennai Institute of Technology, Chennai, Tamilnadu, India*
[2]*Jiangsu Collaborative Innovation Center of Atmospheric Environment and Equipment Technology (CICAEET), Nanjing University of Information Science & Technology, Nanjing 210044, China*
[3]*Jiangsu Key Laboratory of Meteorological Observation and Information Processing, Nanjing University of Information Science & Technology, Nanjing, China*
[4]*Department of Electrical and Electronics Engineering, Faculty of Technology, Sakarya University of Applied Sciences, Serdivan 54050, Sakarya, Turkey*
[5]*Nonlinear Systems and Applications, Faculty of Electrical and Electronics Engineering, Ton Duc Thang University, Ho Chi Minh City, Vietnam*

Correspondence should be addressed to Karthikeyan Rajagopal; karthikeyan.rajagopal@tdtu.edu.vn

Received 8 September 2020; Accepted 31 December 2020; Published 13 January 2021

Academic Editor: Adel Ouannas

Josephson junction devices play a significant role in various physical nonlinear systems because of their complex characteristics. Chaotic phenomenon in various types of Josephson junction devices has been widely reported, but many of those literature studies exempted the analysis into multistability and megastability features of the device. In this work, we investigate the network behaviour using a type of Josephson junction-memristor (JJM) device considering the feedback flux effects while modelling. We have considered both AC- and DC-type external excitation currents, and while considering the AC excitation, the system shows megastability (Ramakrishnan et al. 2020). When analysing the lattice layer network constructed with JJM excited by DC bias current, the network shows a turbulent behaviour thus forming spiral waves. This was not the case when we applied AC bias current for which the network showed a much pattern-like formation confirming localised areas of energy distribution. This energy distribution is due to the homogeneous states of the local nodes which are correlated by the respective periodicity plots. When we apply AC bias current with very low frequency, the network shows small areas of local spirals which are soon dissipated by the inhomogeneous nodes nearby. Thus, we could show that the external bias current plays an important role in the collective performance of the Josephson junction devices.

1. Introduction

A mathematical model of a superconducting Josephson junction finds its attraction among nonlinear dynamical studies because of its rich variety of characteristics. Mostly, the nonlinear dynamical systems, nonlinearity, and the corresponding parameter region are significant to reveal chaotic behaviour [1, 2]. Chaotic systems are more sensitive to the initial condition for particular parameter values. Negative resistor, nonlinear capacitor, and inductor could be used to induce nonlinearity [3]. Indeed, prologue of the memristor in the Josephson junction circuit engendered the nonlinear behaviour [1, 3], that is, the dependency of memductance on input current and memory effect enhance the transition between different modes of oscillations in the circuit [4]. Resetting initial values of the states may lead to different attractor profiles and results in transition from periodic to complex chaotic oscillation [4, 5].

In biological systems such as neuronal activity in the neocortex [6, 7], cardiac tissue [8, 9], and pancreatic beta cells [10], reaction-diffusion systems [11, 12], and a network of coupled oscillators [13, 14], an interesting phenomenon is observed and identified as spatiotemporal patterns. Spiral waves represent remarkable spatiotemporal structures, and they appear while the spatiotemporal system is not in a thermodynamically equilibrium state. The collective behaviour and pattern formation in a spatiotemporal system caused by the network topology depend on the dynamics of a single building block in the network [15]. On the contrary, the topological defect can be identified with the movement of the spiral wave tip (singularity in the core) [16]. Coexistence of synchronization and nonsynchronization is another significant property studied in spatiotemporal systems. Spiral waves can be caused in a subexcitable medium, while the plane waves are interrupted with the electric field [15–20]. Spiral waves can be ascribed by calculating the spatial distribution [21]. Dynamics of spiral waves in an excitable medium is more related to the interaction of different boundaries [22]. In [23], the shape and the rotation frequency of spiral waves and, more importantly, the algorithm for selection with suitable excitation are discussed. The same concepts are experimentally studied in [24, 25].

Memory properties of the memristor (exponential flux) in the Josephson junction induce spiral wave formation because of the high nonlinear relation between charge and magnetic flux [15]. Already, we investigated the local dynamics of the Josephson junction-memristor (JJM) oscillator with exponential flux and reported spiking behaviour. Now, in this paper, our investigation focused on network behaviours.

The paper summarises the collective dynamics of the Josephson junction with exponential flux memristor. Firstly, we considered the JJM with static bias current and investigated the wave propagation in the network. In the next section, we considered a time-varying bias current and investigated the wave propagation in the JJM network. In every section, corresponding spatiotemporal plots are presented.

2. Collective Dynamics of JJM

In [26], the Josephson junction with magnetic effects is modelled using an exponential flux-controlled memristor along with a Josephson junction device [27] whose circuit model is given as in Figure 1.

Various dynamical properties are discussed in [26], where the authors showed infinite coexisting attractors when the excitation current is a periodic force. The mathematical model of the circuit in Figure 1 proposed by [26] is given by

$$\begin{aligned}
\dot{x} &= \frac{1}{\beta_C}\left(I_{\text{Bias}} - Gx - \sin(y)\right) - z - k_0 x W(\phi),\\
\dot{y} &= x,\\
\dot{z} &= \frac{1}{\beta_L}(x - z),\\
\dot{\phi} &= k_1 x - k_2 \phi,\\
W(\phi) &= \alpha^{\beta\phi} k\beta \ln(\alpha),
\end{aligned} \tag{1}$$

where the dimensionless state variables are $x = V/I_J R_1$, $y = \gamma/I_L R_1$, and $z = I_L/I_{jJ}$. For the details about the parameters and the detailed derivation of the mathematical model, the readers are encouraged to refer [26]. As we have already investigated the local dynamics of the Josephson junction-memristor (JJM) circuit in [26], our interest is now to analyse the network performance of the JJM. Hence, we construct the 2D lattice network of the JJM whose mathematical model is defined by

$$\begin{aligned}
\dot{x}_{ij} &= \frac{1}{\beta_C}\left(I_{\text{Bias}} - Gx_{ij} - \sin\left(y_{ij}\right) - z - k_0 x_{ij} W\left(\phi_{ij}\right)\right.\\
&\quad + D\left(x_{i+1j} + x_{i-1j} + x_{ij+1} + x_{ij-1} - 4x_{ij}\right) + F(t)\beta_{i\delta_1}\beta_{j\delta_2},\\
\dot{y}_{ij} &= x_{ij},\\
\dot{z}_{ij} &= \frac{1}{\beta_L}\left(x_{ij} - z_{ij}\right),\\
\dot{\phi}_{ij} &= k_1 x_{ij} - k_2 \phi_{ij},\\
W\left(\phi_{ij}\right) &= \alpha^{\beta\phi_{ij}} k\beta \ln(\alpha).
\end{aligned} \tag{2}$$

In model (2), we considered the 2D network with $i, j = 1{:}\ N$, where $N = 150$, and the external force (stimuli) applied to the network is considered to be a sinusoid defined as $F(t) = A\sin(\Omega t)$. The external force is applied to the centre of the network by choosing $i = \theta_1 = 75$ and $j = \theta_2 = 75$ for which $\beta_{i\theta_1} = \beta_{j\theta_2} = 1$. We have considered no-flux boundary conditions for the analysis, and the initial conditions for the nodes in the network are [0.1, 0.1, 0.1]. The parameters for the simulation are taken from [26], and the source current is the control variable for our discussion. We have considered two different cases of source current, and when $I_{\text{Bias}} = 1.26$, it is considered a DC-excited JJM, and for $I_{\text{Bias}} = I\sin(\omega t)$ with $I = 2.5$ and $\omega = 1.2$, the model is considered an AC-excited JJM.

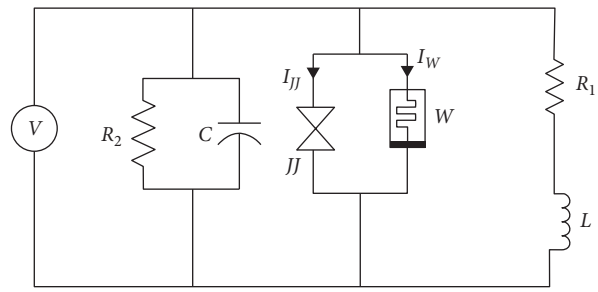

Figure 1: The Josephson junction with magnetic effects modelled using an exponential flux-controlled memristor [26].

2.1. Considering DC Bias Current. In the earlier work in [26], the JJM with DC bias current does not have complex behaviours such as multistability and coexistence, but it shows spiking behaviour for certain values of the bias current (I_{Bias}), and hence, we started our discussion by studying the behaviour of JJM network (2) for various values of I_{Bias}. The applied external force is considered to be applied to the centre of the network, and the amplitude and frequency of the force are $A = 1$ and $\Omega = 0.01$. For values of $I_{\text{Bias}} < 1$, the network goes unbounded, and we could not identify the wave propagation or pattern formation in the network, but for $I_{\text{Bias}} = 1$, the network shows signs of spiral waves propagating to all corners of the network. This is because the periodic behaviour of the node changes drastically with the applied force which makes certain nodes to have chaotic oscillations while some to have transient-like behaviour which soon becomes periodic. To show this, we have shown the spatiotemporal dynamics of the state as well as their periods in Figure 2. The upper plots in Figure 2 show the dynamics of the network, while the lower plots show their periodic behaviours. When we increased I_{Bias} to 1.2, the spiral waves and the ring-like circular cluster formed earlier (for $I_{\text{Bias}} = 1$) are now dissipated, and the clusters are converted into pools of incoherent nodes which are initially influenced by the external force at the entry point of the stimulus but soon the network dissipates them due to high periodicity of the nodes. This can be seen from Figure 2 for $I_{\text{Bias}} = 1.2$, where the petal-like waves formed by the network show red (closer red) colour showing high period due to the high-amplitude nodes, whereas the entry being affected by the external force and amplitudes are now reduced thus showing less periods of oscillations. For $I_{\text{Bias}} = 1.3$, the network is influenced fully by the external force, but the chaotic nodes are in random coherency which obstructs the wave propagation, and the network shows complete more of synchronous behaviour which can also be seen from the periodic plot (max and min period difference reduces). The centre of the periodic plot is having high periods of oscillation confirming complex chaos, whereas the boundaries show low periods which confirms complete incoherency. Finally, for $I_{\text{Bias}} = 1.4$, the network nodes are coherent, and hence, the wave propagation is not supported by the nodes as they are in complete synchronisation. This makes the external force to get dissipated in the centre of the network with only few nodes disturbed.

Now, to study the influence of the applied periodic force on the network, we consider different amplitudes of the force, while the bias current $I_{\text{Bias}} = 1$, and the frequency of the periodic force is $\Omega = 0.0001$. We divide the discussion into two sets, wherein in the first set, we consider higher amplitudes, and in the second set, we consider lower amplitudes. When the applied force amplitude is $A = 1$, the network shows multiple small-amplitude spiral waves which are largely affected by the lower periods of oscillations in the nodes as in Figure 3. This can be seen from the periodic plot shown. When the amplitude is increased further, the low periodic oscillations of the nodes (yellow-red in the periodic plot) reduce, and for $A = 7$, they completely disappear showing only complex chaotic oscillations (magenta-blue in the periodic plot). The respective spatiotemporal behaviour is now showing predominant spiral waves with much stronger amplitude features.

In the second set, lower amplitudes of periodic force are considered. For the amplitude $A = 0.1$, the applied force travels through the network without much obstructions, and thus, no spiral seeds are seen, but we could see regions of cripples between $i \in (60, 80)$ and $j \in (60, 80)$, and these cripples are because of the low periodicity of the nodes which can be seen from the periodicity plots shown in Figure 4. When we decrease the amplitude to $A = 0.01$, the propagation frequency of the target wave decreases, and we could see larger bandwidth of periods in the network. While most of the nodes remain in periods around 250 (green), the wave-captured nodes are with much higher periods around 400. This larger difference in the periods obstructs the target wave to propagate in higher velocities and thus eliminates the spiral wave transformations in the network. This can be concluded by further reducing the amplitude to $A = 0.001$, where the target wave is now reduced to only two regions and the period bandwidth now increases further.

2.2. Considering AC Bias Current. After showing that the JJM network with static (DC) bias current shows spiral wave turbulence, our interest now falls on the dynamic bias current (AC). For this, we consider the bias current as a periodic sinusoid defined by $I_{\text{Bias}} = I\sin(\omega t)$. For this discussion, we consider the bias current amplitude (I) and frequency (ω) as the control parameters. Firstly, we consider two values of frequency (ω): one as low as $\omega = 0.0001$ and the other to be $\omega = 1.3$. For both these cases, we vary the amplitude of bias current and study the network behaviours as shown in Figures 5 and 6.

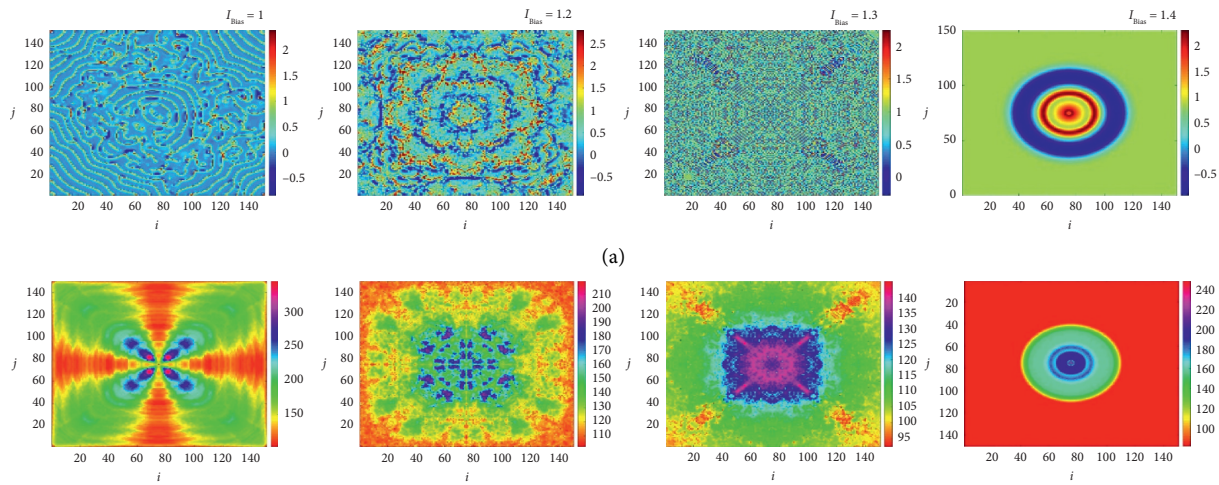

(a)

(b)

Figure 2: (a) The spatiotemporal plots of the nodes (i vs. j) for different values of I_{Bias}. (b) The periodicity of each node plotted for respective I_{Bias} values.

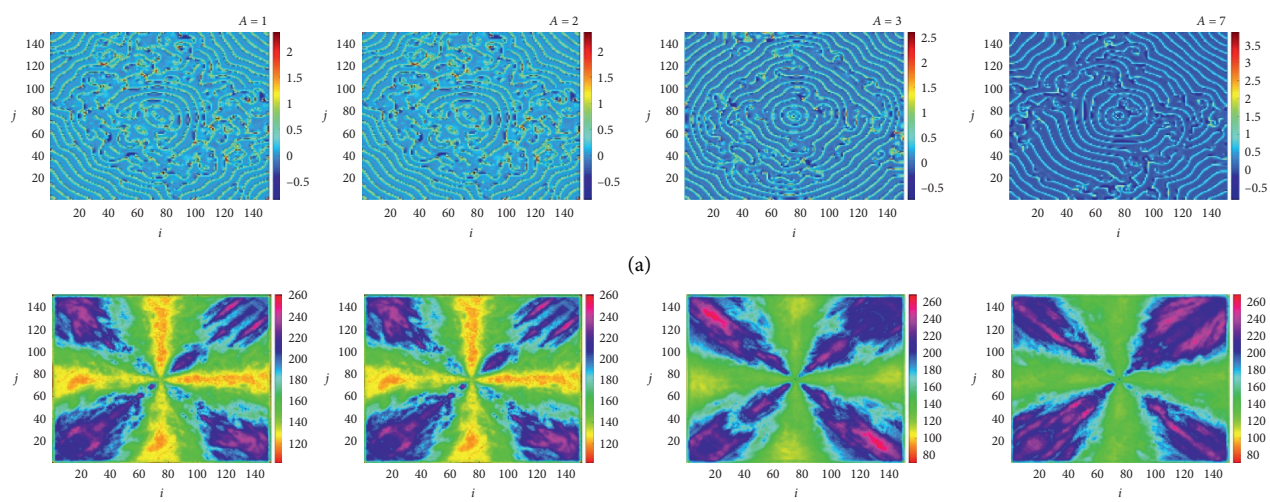

(a)

(b)

Figure 3: (a) The spatiotemporal plots of the nodes (i vs. j) for different values of periodic force amplitude A. (b) The periodicity of each node plotted for respective A values.

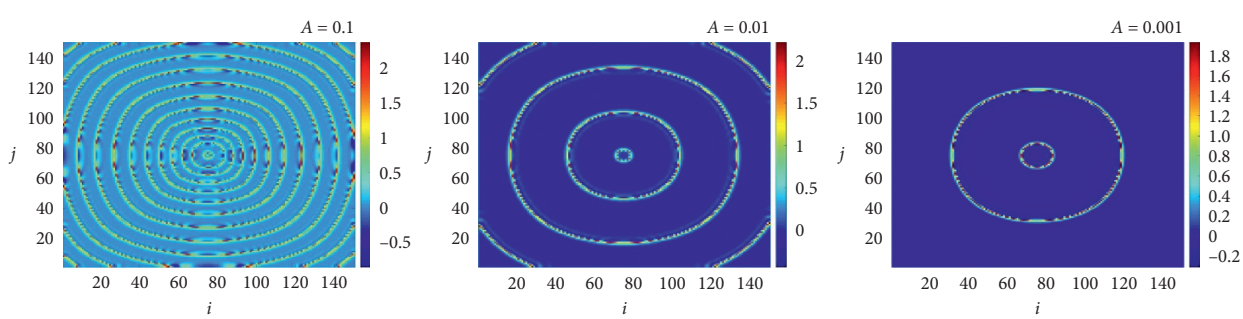

(a)

Figure 4: Continued.

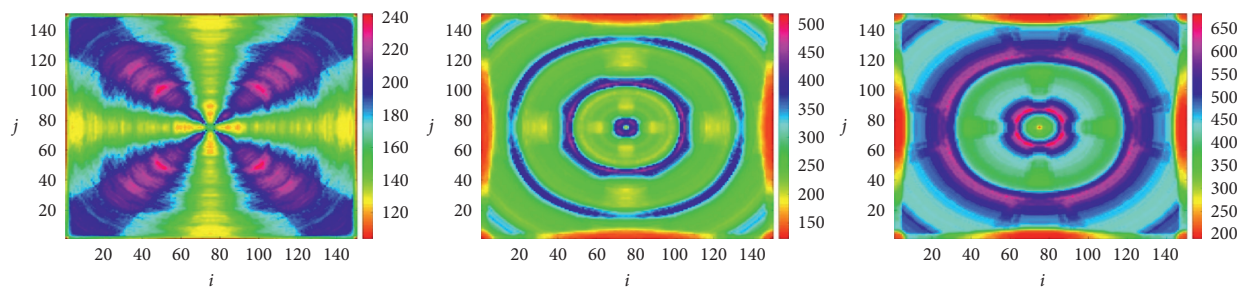

(b)

Figure 4: (a) The spatiotemporal plots of the nodes (i vs. j) for different values of periodic force amplitude A. (b) The periodicity of each node plotted for respective A values.

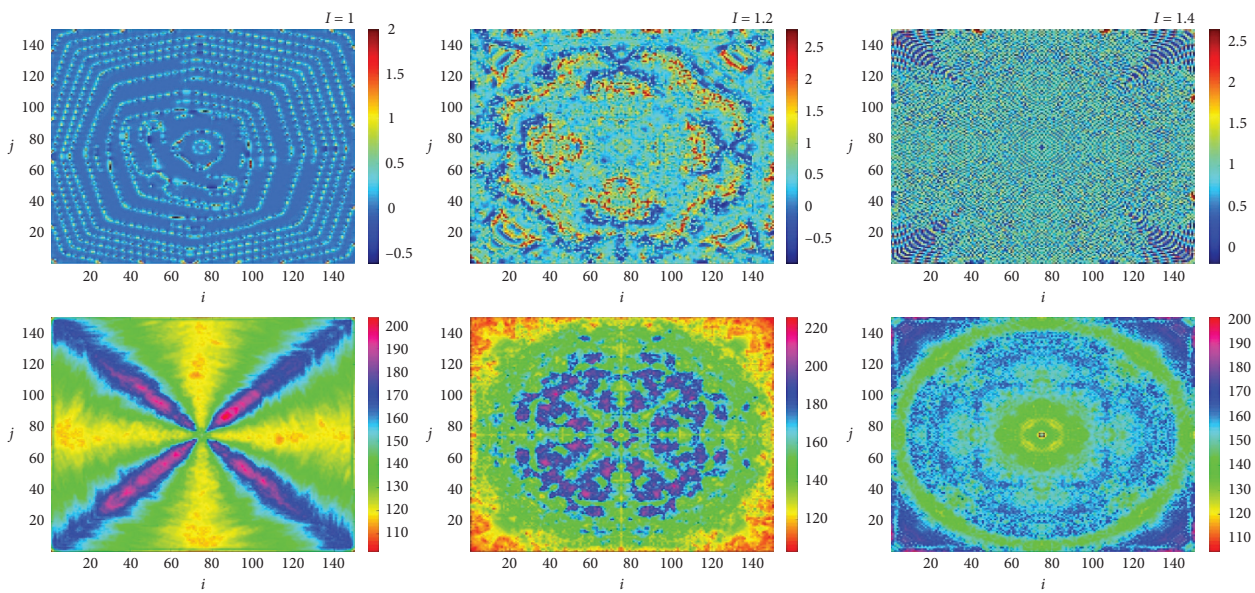

(a)

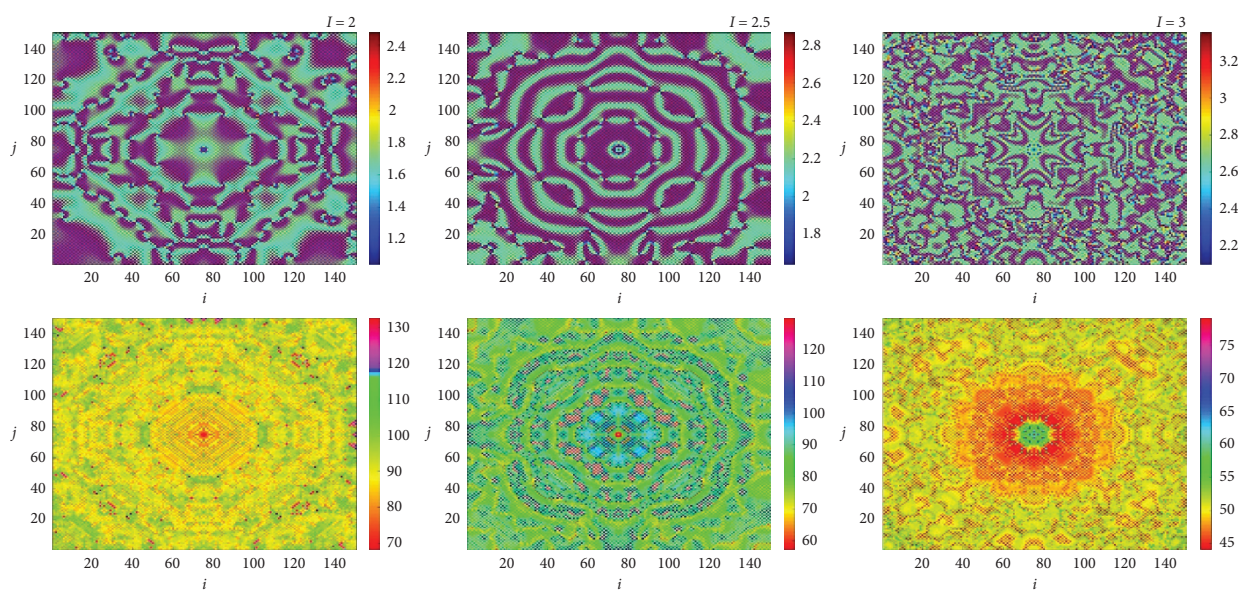

(b)

Figure 5: (a) Dynamics of the network for various values of the bias current amplitude (I). (b) The corresponding periodicity of each node for different I. The bias current frequency is kept as $\omega = 0.0001$.

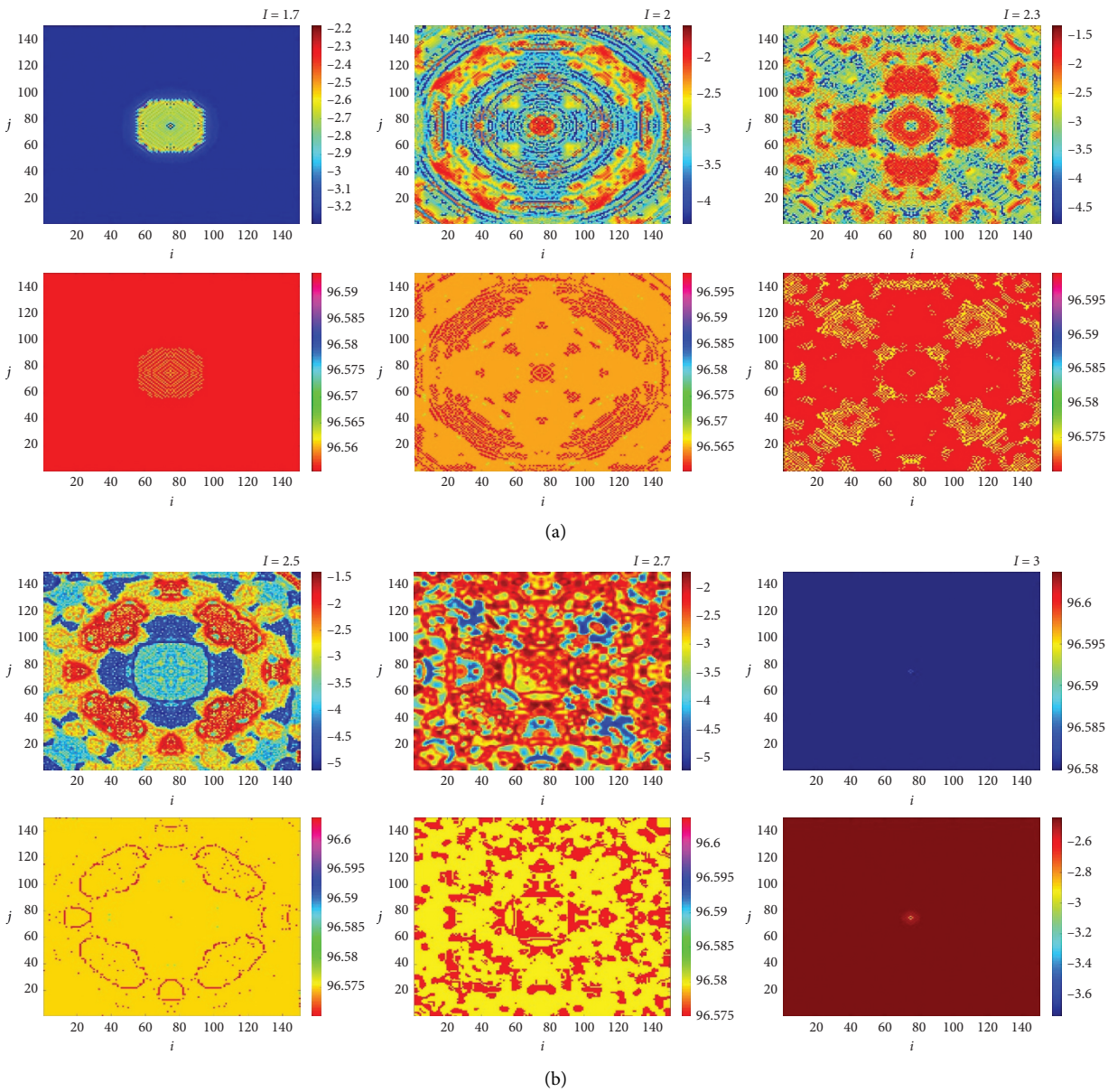

Figure 6: (a) Dynamics of the network for various values of the bias current amplitude (I). (b) The corresponding periodicity of each node for different I. The bias current frequency is kept as $\omega = 1.3$.

In Figure 5, we consider the frequency of bias current to be $\omega = 0.0001$, and we vary the amplitude of the bias current. For $I < 1$, the network goes unbounded, and hence, we have not showed those snapshots. For $I = 1$, the network shows broken target waves which are obstructed by the low periodic nodes shown by the yellow-red regions in Figure 5(b). As the bias current is time-varying, the spiral waves seen in Figure 2 for $I = 1$ are partially destroyed when a time-varying bias current is applied even though the frequency of bias current is as low as $\omega = 0.0001$. This is because that the JJM shows infinite coexisting attractors when a AC bias current is applied [26]. Furthermore, as we have chosen random initial conditions for the network ranging between [0, 5], the possibility of coexistence is more considering there exist multiple attractors in this range as shown in [26]. When we increase I further, the nodes are highly incoherent with different periods of oscillations as shown in Figure 5. Hence, uniform pattern formation is now seen for the range $1.2 \leq I \leq 1.9$, but for $I = 2$, a symmetric pattern exists which is due to the individual nodes with low period oscillations which confirms that the JJM is exiting the complex chaotic phenomenon. Further increasing I shows that the period bandwidth (refer to the colour bar in Figure 5(b)) keeps reducing and finally reaches a bandwidth of 35 confirming that the nodes are coming into synchrony. This partial coherency is shown with the patterns containing multiple small pools of incoherent nodes and coherent nodes.

For the bias current frequency $\omega = 1.3$, the network goes unbounded for values of bias current amplitude $I < 1.7$, and this confirms that the periodic bias current plays a vital role

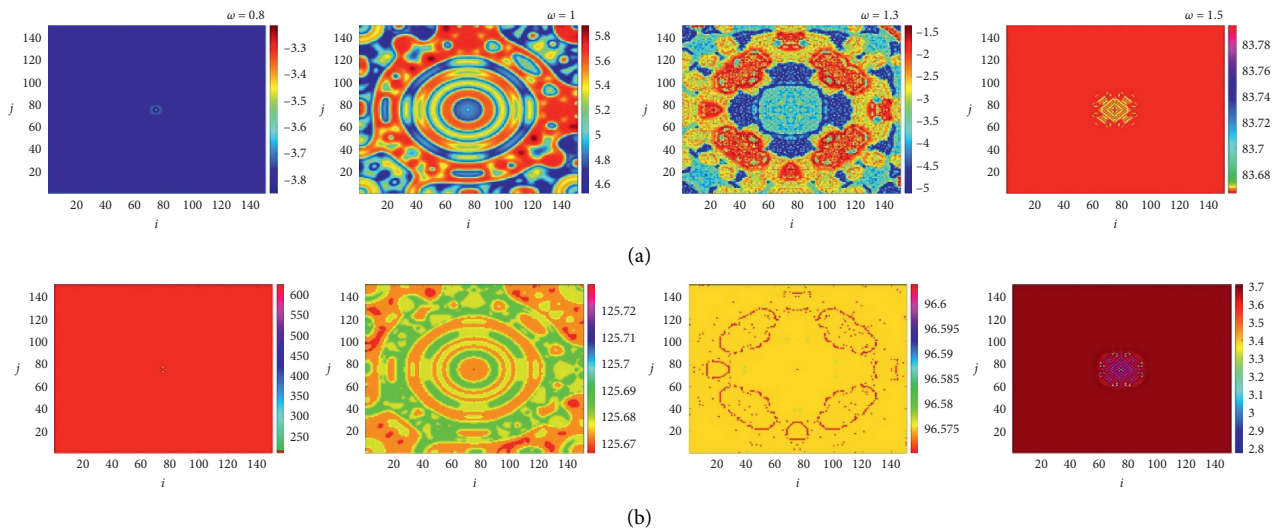

Figure 7: (a) Dynamics of the network for various values of the bias current frequency (ω). (b) The corresponding periodicity of each node for different ω. The bias current frequency is kept as $I = 2.5$.

in determining the dynamical properties of the JJM [26]. For $I = 1.7$, there are no oscillations in the network as can be seen from the period plot in Figure 6 which shows a total period bandwidth of 0.03. The applied stimulus tried to excite the local nodes around the centre, but due to the lack of self-excited oscillations in the nodes due to the current amplitude, the wave propagation diminishes. Hence, we increase the value of I to see the network behaviour. For $I = 2$, the nodes are now excited to show periodic bursting which now encourages the wave propagation. This can be seen by the formation of local pools of low period oscillations shown in red in both the spatiotemporal snapshot and the periodic plot. Having low period of oscillation means that the nodes are in chaotic regions and thus show self-excited oscillations. The local nodes forming small groups are due to the coherency behaviour between them which are shown by similar colour in Figure 6. For $I = 2.5$, we could see a perfect correlation between the snapshots and the periodicity plots confirming the pattern formations are due to the high-amplitude spiking of the nodes. Further increasing the current amplitude results in diving of these large-amplitude groups which are soon driven unbounded by the bias current amplitude. This confirms that the periodic bias current plays a significant role in the network performance of the JJM.

In the second part of our investigation, we keep the amplitude of the bias current fixed and vary the frequency of the bias current (ω) and capture the wave propagation of the applied stimulus as in Figure 7. We could show that the pattern formations in the network are largely due to the grouping of similar period nodes or in other works' coherent nodes. These coherent nodes are excited by the applied stimulus to different amplitudes and hence have different patterns (colours) as confirmed from the periodicity plots (Figure 7(b)). Increasing ω after 1.3 results in the nodes being completely synchronised and thus does not have irregular or complex bursting which results in the nodes being unsupportive or nonreactive to the stimulus. Hence, the excitation of the nodes is only seen near the centre where the stimulus is applied. We could also correlate this with the discussion in [26], where it was shown that, for $\omega > 1.3$, the JJM exits bursting oscillations.

3. Conclusion

The collective dynamics of a Josephson junction chaotic oscillator considering feedback flux coupling is investigated. A simple lattice array of the JJM-based oscillator is constructed, and we have assumed no-flux boundary conditions. We first applied a DC bias current, and a sinusoidal stimulus is applied to the centre of the network. The network shows nodal spiral waves which are seen for larger amplitudes of the stimuli. Comparing the network snapshots with the periodicity plots, we could see that the spiral waves are exhibited when the period difference between the nodes is less or, in other words, when most of the nodes are in the homogeneous state. When we applied very low-amplitude stimuli, the period difference increases and obstructs the target wave to propagate in higher velocities and thus eliminates the spiral wave transformations in the network. Hence, we could show that low-amplitude stimulus force eliminates the spiral waves, while the high-amplitude stimuli induce them. Now, in the second discussion, we have considered AC bias current (sinusoidal). For high frequency of the bias current, the network forms unique patterns which can be compared with the respective periodic plots, and we could say that the boundaries of the formed patterns are defined by low period nodes. These low period nodes split the networks into pools of small energy areas which collectively defined the local performance. In other words, the network forms multiple smaller areas of homogeneous nodes. When we decrease the bias current frequency to low (0.0001), the network shows small turbulent areas which are soon destroyed by the medium

oscillations. When the nodes are in the chaotic state, the network shows patterned areas confirming pooled oscillations, whereas when the nodes are in the periodic state, the wave propagation is completely terminated. This was not the case in DC bias as when the nodes are in the periodic state, the network shows spiral waves which convert into unique patterns when the nodes enter chaos. As we mentioned, the JJM shows infinite coexisting attractors when excited by AC bias current, and to understand the influence of different attractors (initialised by different initial conditions), we studied the network behaviour for various values of initial conditions. To our surprise, the network behaviour does not change and remains in the same pattern. This confirms that the nodes synchronise and form a homogeneous medium whatever be the attractor type. Hence, the wave propagation behaviour of the network rather depends on the overall synchronisation but not the local coupling alone.

Data Availability

No data were used to support this study.

Conflicts of Interest

The authors declare that there are no conflicts of interest regarding the publication of this paper.

References

[1] G. Zhang, J. Ma, A. Alsaedi, B. Ahmad, and F. Alzahrani, "Dynamical behavior and application in Josephson Junction coupled by memristor," *Applied Mathematics and Computation*, vol. 321, pp. 290–299, 2018.

[2] A. A. Elsadany, A. M. Yousef, and A. Elsonbaty, "Further analytical bifurcation analysis and applications of coupled logistic maps," *Applied Mathematics and Computation*, vol. 338, pp. 314–336, 2018.

[3] T. Hongray, J. Balakrishnan, and S. K. Dana, "Bursting behaviour in coupled Josephson junctions," *Chaos: An Interdisciplinary Journal of Nonlinear Science*, vol. 25, no. 12, Article ID 123104, 2015.

[4] Y. Liu, G. Ren, P. Zhou, T. Hayat, and J. Ma, "Synchronization in networks of initially independent dynamical systems," *Physica A: Statistical Mechanics and Its Applications*, vol. 520, pp. 370–380, 2019.

[5] F. Wu, P. Zhou, A. Alsaedi, T. Hayat, and J. Ma, "Synchronization dependence on initial setting of chaotic systems without equilibria," *Chaos, Solitons & Fractals*, vol. 110, pp. 124–132, 2018.

[6] L. Pivik, "Autowaves and spatial-temporal chaos in CNNs–Part I: a tutorial," *IEEE Transactions on Circuits and Systems I*, vol. 42, no. 12, pp. 638–649, 1995.

[7] G. Hu, J. Xiao, L. O. Chua, and L. Pivka, "Controlling spiral waves in a model of two-dimensional arrays of chua's circuits," *Physical Review Letters*, vol. 80, no. 9, p. 1884, 1998.

[8] F. H. Samie, R. Mandapati, R. A. Gray et al., "A mechanism of transition from ventricular fibrillation to tachycardia," *Circulation Research*, vol. 86, no. 6, pp. 684–691, 2000.

[9] F. Samie and J. Jalife, "Mechanisms underlying ventricular tachycardia and its transition to ventricular fibrillation in the structurally normal heart," *Cardiovascular Research*, vol. 50, no. 2, pp. 242–250, 2001.

[10] K. Rajagopal, Z. Wei, I. Moroz, A. Karthikeyan, and P. Duraisamy, "Elimination of spiral waves in a one-layer and two-layer network of pancreatic beta cells using a periodic stimuli," *Chaos, Solitons & Fractals*, vol. 139, Article ID 110093, 2020.

[11] P. S. Hagan, "Spiral waves in reaction-Diffusion Equations," *SIAM Journal on Applied Mathematics*, vol. 42, no. 4, pp. 762–786, 1982.

[12] M. C. Cross and P. C. Hohenberg, "Pattern formation outside of equilibrium," *Reviews of Modern Physics*, vol. 65, no. 3, pp. 851–1112, 1993.

[13] S. Sinha, J. Saramaki, and K. Kaski, "Emergence of self-sustained patterns in small-world excitable media," *Physical Review E*, vol. 76, Article ID 015101, 2007.

[14] Q. Wang, M. Perc, Z. Duan, and G. Chen, "Delay-enhanced coherence of spiral waves in noisy Hodgkin-Huxley neuronal networks," *Physics Letters A*, vol. 372, no. 35, pp. 5681–5687, 2008.

[15] K. Rajagopal, F. Parastesh, H. Azarnoush, B. Hatef, S. Jafari, and V. Berec, "Spiral waves in externally excited neuronal network: solvable model with a monotonically differentiable magnetic flux," *Chaos: An Interdisciplinary Journal of Nonlinear Science*, vol. 29, no. 4, Article ID 043109, 2019.

[16] B. Hu, J. Ma, and J. Tang, "Selection of multiarmed spiral waves in a regular network of neurons," *PLoS One*, vol. 8, no. 7, Article ID e69251, 2013.

[17] X. Wu and J. Ma, "The formation mechanism of defects, spiral wave in the network of neurons," *PLoS One*, vol. 8, no. 1, Article ID e55403, 2013.

[18] G. Zhang, F. Wu, T. Hayat, and J. Ma, "Selection of spatial pattern on resonant network of coupled memristor and Josephson junction," *Communications in Nonlinear Science and Numerical Simulation*, vol. 65, pp. 79–90, 2018.

[19] H. Li, Y. Yang, Li Wen, S. He, and C. Li, "Extremely rich dynamics in a memristor-based chaotic system," *The European Physical Journal—Plus*, vol. 135, p. 579, 2020.

[20] K. Rohlf, L. Glass, and R. Kapral, "Spiral wave dynamics in excitable media with spherical geometries," *Chaos: An Interdisciplinary Journal of Nonlinear Science*, vol. 16, no. 3, Article ID 037115, 2006.

[21] D. Gonze, S. Bernard, C. Waltermann, A. Kramer, and H. Herzel, "Spontaneous synchronization of coupled circadian oscillators," *Biophysical Journal*, vol. 89, no. 1, pp. 120–129, 2005.

[22] I. Aranson, D. Kessler, and I. Mitkov, "Drift of spiral waves in excitable media," *Physica D: Nonlinear Phenomena*, vol. 85, no. 1-2, pp. 142–155, 1995.

[23] V. S. Zykov, "Kinematics of rigidly rotating spiral waves," *Physica D: Nonlinear Phenomena*, vol. 238, no. 11-12, pp. 931–940, 2009.

[24] X. Huang, W. C. Troy, Q. Yang, H. T. Ma, C. R. Laing et al., "Spiral waves in disinhibited mammalian neocortex," *Journal of Neuroscience*, vol. 24, no. 44, pp. 9897–9902, 2004.

[25] X. Huang, W. Xu, J. Liang, K. Takagaki, X. Gao, and J.-Y. Wu, "Spiral wave dynamics in neocortex," *Neuron*, vol. 68, no. 5, pp. 978–990, 2010.

[26] B. Ramakrishnan, D. Ali, K. Rajagopal, and A. Akgul, "Infinite attractors in a chaotic circuit with exponential memristor and Josephson junction resonator," *AEU—International Journal of Electronics and Communications*, vol. 123, Article ID 153319, 2020.

[27] W. G. Choe and S. Kim, "Spatiotemporal dynamics of domain-wall solitons in the fully frustrated Josephson-junction ladder arrays," *Physical Review B*, vol. 53, p. R502, 1996.

[28] F. Xie and A. Hilda, "Cerdeira, clustering bifurcation and spatiotemporal intermittency in RF-driven Josephson junction series arrays," *International Journal of Bifurcation and Chaos*, vol. 8, no. 8, pp. 1713–1718, 1998.

Hindawi
Mathematical Problems in Engineering
Volume 2020, Article ID 8849283, 15 pages
https://doi.org/10.1155/2020/8849283

Research Article

Analysis of a New Hidden Attractor Coupled Chaotic System and Application of Its Weak Signal Detection

Wenhui Luo,[1] **Qingli Ou**,[1] **Fei Yu**,[2] **Li Cui**,[1] **and Jie Jin**[1,3]

[1]*Hunan University of Science and Technology, Xiangtan 411201, Hunan, China*
[2]*School of Computer and Communication Engineering, Changsha University of Science and Technology, Changsha 410114, China*
[3]*College of Information Science and Engineering, Jishou University, Jishou 416000, China*

Correspondence should be addressed to Wenhui Luo; wenhuiluo@mail.hnust.edu.cn

Received 1 October 2020; Revised 4 November 2020; Accepted 10 December 2020; Published 23 December 2020

Academic Editor: Viet-Thanh Pham

In order to improve the complexity of the chaotic system and the accuracy of the weak signal detection, this paper propose a new hidden attractor coupled chaotic system and a corresponding weak signal detection system, which can be used to obtain the phase diagram of the proposed system using the fourth order of the Runge-Kutta method. The dynamic behavior of the chaotic system is analyzed through the bifurcation diagram, Lyapunov exponent, and power spectrum. The Lyapunov exponent is used to depict the basins of attraction for the system. After research, it is discovered that symmetry exists in the system. Comparative analysis has demonstrated that the system has higher detection accuracy and excellent antinoise performance. Finally, the circuit simulation and FPGA realization of the system indicated that the numerical simulation results are consistent with the FPGA implementation results, proving the theoretical analysis to be correct and the accuracy of the detection results.

1. Introduction

After Lorenz introduced the Lorenz system [1] in 1963, the chaos theory has become a hot spot of nonlinear field research. With the deepening of theoretical research, researchers have conducted a lot of analysis into the attractor and basins of attraction of the chaotic system. In [2], after an investigation into the basins of attraction of coexistence attractors in the coupled Duffing system, the riddled basins of attraction of the Chen system are studied, and the riddled basins of attraction have a positive repulsive set of Lebesgue measures via mathematical proofs. It is found in [3] that the number of coexisting attractors is different when the initial values are different. A numerical method for estimating the shortening calculation time of the relative area of the basins of attraction is proposed in [4], and its application scope is verified. In [5], the mixed basins of attraction formed when multiple attractors coexist in a chaotic system are analyzed, and the research shows that the basins of attraction have a fractal regular structure. In addition, the hidden attractors [6] and hidden bifurcations in the system have also attracted extensive attention of researchers. For example, the phenomenon of hidden attractor and hidden bifurcation in multiscroll Chua chaotic system is studied in [7]. The dynamic characteristics of multistable chaotic systems with hidden attractors are studied in [8]. A four-wing hidden attractor chaos is studied in [9]. In [10], a three-dimensional hidden attractor chaotic system with Lyapunov dimension of 2.9075 is studied, and a Bluetooth device for autonomous wireless mobile robot based on chaotic motion controller is proposed. At the same time, as a special state of chaotic system, multistability has been widely studied. The chaotic system with multiple attractors coexisting and multistability are analyzed in [11, 12]. Reference [13] analyzed the multistability of a chaotic system with two circles of equilibrium points and implemented the system using FPGA technology. With the research of electronic components, the realization of memristors provides a new method for the construction of

chaotic systems. Nowadays, chaotic systems based on memristors [14–16] and chaotic neural networks [17–19] have received great attention from researchers.

With the in-depth theoretical research of chaotic systems, their engineering application has become more mature. In recent years, the application of chaotic systems has spread throughout many fields including electronic circuit [20–24], image processing [25–30], secure communication [31–34], complex networks [35–38], and random signal generation [39–41]. Traditional stochastic resonance [42], wavelet transform [43], and empirical mode decomposition [44] are widely used in early fault signal detection. The stochastic resonance method enhances the signal utilizing noise, destroying the original information of the signal. Immune to certain noises and sensitive to specific signals, the chaotic system is featured by simple detection methods and retention of the original signal information. In 1992, Birx and Pipenberg first proposed detecting weak signals by using chaotic oscillators [45], and, since then, the chaotic systems have been represented by the Duffing system and the van der Pol system [46, 47] began to be widely applied in weak signal detection. This research, based on the time domain and frequency domain detection methods for weak signals [48, 49] and the antinoise of chaotic system [50], enables chaotic system detection methods to be more mature. The criteria for judging the state of chaotic systems will directly affect the accuracy of detection; thus, scholars have also conducted in-depth studies on the calculation of the threshold of chaotic systems. In [51], Melnikov method is used to identify chaotic features. In [52], the threshold of the system is determined by solving the Lyapunov exponent. At present, most of the researches on weak signals based on chaos theory use a single chaotic system for detection. The system proposed in [53] can only detect signals with a size of 0.01 and the SNR can only reach −45.85 dB. The system in [54] can detect signals with a size of 1×10^{-9}, but a noise signal that can be immune to it can only reach the order of 1×10^{-9}. The system in [55] can detect a signal with a wider frequency range, but the detection range of the initial phase angle of the signal is too large and thus is unfavorable for determining the signal parameters. At present, most of the researches on weak signals based on chaos theory use a single chaotic system for detection. Compared with the single chaotic system, the coupled system has excellent stability, high antinoise performance, and low detection threshold. Therefore, the coupled chaotic system has high theoretical research value and practical application value.

To improve the chaotic system complexity and the accuracy of signal detection, this paper proposes a new hidden attractor coupled chaotic system. Through an analysis of the system's phase diagram, the Lyapunov index, and so forth, the complex dynamic behavior of the system is explained in detail. Moreover, the basins of attraction for the system are drawn using the Lyapunov index to study the characteristics of the system's attractor. Theoretical analysis indicates that the system is sensitive to initial values and immune to noise, and the coupled chaotic system is applied to weak signal detection. Finally, through OrCAD circuit simulation and FPGA implementation, the correctness of the theoretical analysis and the accuracy of signal detection are verified. Through data analysis and experimental data, the system proposed in this paper can detect signals sized 1×10^{-6}, and the signal-to-noise ratio reaches −73.892 dB. Moreover, the immune signal reached the order of 3.5×10^{-3}, and the error range of the initial phase angle is ± 0.09. Therefore, the detection performance of the coupled system proposed in this paper is better than the single chaotic system proposed in [45, 46, 53–55].

2. Coupled Chaotic System Model and Dynamic Analysis

2.1. Coupled Chaotic System Model. Through [45–47], a single chaotic system with different nonlinear terms is analyzed, and the limitations of signal detection performance detection are studied at the same time. For example, [53] can detect low signal amplitude, and [54] can be immune. The noise is small, and [55] detects that the initial phase angle error of the signal is too large. Based on the above reasons, this paper proposes a new system:

$$\begin{cases} \ddot{x} + c_1\dot{x} - x + c_2x^5 + k(x-y) = f\cos(\omega t + \theta), \\ \ddot{y} + c_3\left(1-y^3\right)\dot{y} + y + y^3 + k(y-x) = f\cos(\omega t + \theta), \end{cases} \tag{1}$$

where k is the linear coupling coefficient of system (1). The larger the coefficient, the higher the degree of coupling; $c1$, $c2$, and $c3$, respectively, represent the coefficients of the nonlinear terms. $f\cos(\omega t + \theta)$ is the driving force of the system, and f, ω, and θ represent the amplitude, frequency, and initial phase angle of the driving force, respectively.

2.2. Analysis of the Equilibrium Point and Lyapunov Exponent of a Coupled Chaotic System. We obtained system (2) by coupling system (1) and taking the coefficients $c1 = 0.5$, $c2 = 0.2$, $c3 = 0.8$, and $k = 0.4$, with the state space model expression of system (2) shown in the following equation:

$$\begin{cases} \dot{x} = z, \\ \dot{y} = q, \\ \dot{z} = -c_1z + x - c_2x^5 - k(x-y) + f\cos(\omega t + \theta), \\ \dot{q} = -c_3\left(1-y^2\right)q - y - y^3 - k(y-x) + f\cos(\omega t + \theta). \end{cases} \tag{2}$$

To simulate the coupled chaotic system (2), take the frequency $\omega = 1$ and the initial phase angle $\theta = 0$. The system's initial value is (−1, −1, 0, 0). When the magnitude f of the driving force takes 0.3, 0.46, 0.8, and 1.2, the homoclinic orbit, the period-doubling bifurcation, chaotic state, and periodic state will appear in system (2). The driving signal of system (2) is defined as H, and the signal as a whole system (2) is analyzed. Let the left side of the equation be equal to 0; then,

$$\begin{cases} z = 0, \\ q = 0, \\ -0.5z + x - 0.2x^5 - 0.4(x - y) + H = 0, \\ -0.8\left(1 - y^2\right)q - y - y^3 - 0.4(y - x) + H = 0. \end{cases} \tag{3}$$

When $H = 1$, equation (3) has a real number solution $x1 = 1.6299$, $y1 = 0.8060$, $z1 = q1 = 0$, and fourteen complex number solutions. With the changes of H, equation (3) will have an infinite number of equilibrium points, so system (2) is a hidden attractor coupled chaotic system. The Jacobian matrix of system (2) at the equilibrium point $M(x_1, y_1, z_1, q_1)$ is

$$J = \begin{bmatrix} 0 & 0 & 1 & 0 \\ 0 & 0 & 0 & 1 \\ 1 - x_1^4 - 0.4 & 0.4 & -0.5 & 0 \\ 0.4 & -1.4 - 3y_1^2 & 0 & -0.8\left(1 - y_1^2\right) \end{bmatrix}. \tag{4}$$

Let $|J - \lambda I| = 0$; its characteristic values $\lambda_1 = -0.2486 + 2.5373i$, $\lambda_1 = -0.2486 - 2.5373i$, $\lambda_3 = -0.1415 + 1.6983i$, and $\lambda_4 = -0.1415 - 1.6983i$ can be obtained. According to the Routh-Hurwitz criterion, the real parts of the eigenvalues are all less than 0, so system (2) is stable at the equilibrium point (x_1, y_1, z_1, q_1). When $H = 1$, the waveform diagram of each state variable phase changing over time and phase diagram within system (2) are shown in Figure 1.

Derivation of equation (2) can achieve

$$\begin{aligned} \nabla V &= \frac{\partial \dot{x}}{\partial x} + \frac{\partial \dot{y}}{\partial y} + \frac{\partial \dot{z}}{\partial z} + \frac{\partial \dot{q}}{\partial q} \\ &= -1.3 + 0.8y^2. \end{aligned} \tag{5}$$

When $y \in [-1.2748, 1.2748]$, $\nabla V < 0$, and system (2) is a dissipative system.

Let $\beta = \omega t$ and take $\omega = 1$ and $\theta = 0$. Convert system (2) into the form shown in the following equation:

$$\begin{cases} \dot{x} = z, \\ \dot{y} = q, \\ \dot{z} = -0.5z + x - 0.2x^5 - 0.4(x - y) + f\cos\beta, \\ \dot{q} = -0.8\left(1 - y^2\right)q - y - y^3 - 0.4(y - x) + f\cos\beta, \\ \dot{\beta} = 1, \end{cases} \tag{6}$$

and the previous equation can be expressed by vector method as

$$\dot{X}(t) = w(X(t); \eta). \tag{7}$$

The state space variable $X(t) = [x(t), y(t), z(t), q(t), \beta(t)]^T$, $w = [w_1, w_2, w_3, w_4, w_5]^T$, η represents the parameter set, and $[\cdots]^T$ represents the transposed matrix. The deviation δX equation from orbit X (t) can be expressed as $\delta\dot{X}(t) = L_{ij}(X(t); \eta)\delta X$, $i, j = 1, 2, ..., 5$. $L_{ij} = (\partial w_i / \partial x_j)$ and the Jacobian matrix form is

$$J = \begin{bmatrix} 0 & 0 & 1 & 0 & 0 \\ 0 & 0 & 0 & 1 & 0 \\ 1 - x^4 - 0.4 & 0.4 & -0.5 & 0 & -f\sin\beta \\ 0.4 & 1.6qy - 3y^2 - 1.4 & 0 & -0.8\left(1 - y^2\right) & -f\sin\beta \\ 0 & 0 & 0 & 0 & 0 \end{bmatrix}. \tag{8}$$

When $f = 0.8$, the Lyapunov exponents are $L_{E1} = 0.184134$, $L_{E2} = 0$, $L_{E3} = -0.305903$, $L_{E4} = -0.312796$, and $L_{E5} = -0.697360$, respectively. The value of L_{E1} is greater than 0, and system (2) is in a chaotic state. The sum of Lyapunov exponents is less than 0, and system (2) is in a dissipative system, which is consistent with the previous results. In a chaotic state, the phase diagram of system (2) and the cross section diagram of Poincare are shown in Figure 2.

3. Bifurcation of the Driving Force Parameters and Lyapunov Exponent Spectrum Analysis

As the various parameters of the driving force have a very significant impact on the dynamics of the system, focus on the analysis of the parameters f, ω, and θ was implemented, and the initial values of system (2) take (−1, −1, 0, 0) on a uniform basis. When $\omega = 1$, $\theta = 0$. When the amplitude f changes within the interval [0, 2], the bifurcation diagram and Lyapunov exponent spectrum of system (2) are shown in the following diagrams 3(a) and 3(b). As shown in Figure 3(a), system (2) enters chaos from the period-doubling bifurcation, the chaotic state interval is approximately [0.41, 0.88], and the system is in a periodic state in the subsequent interval. According to the comparison between Figures 3(a) and 3(b), the intervals of the chaotic and periodic states of the system are consistent.

When $f = 0.8$, $\theta = 0$, and when the frequency ω changes in the interval [0, 3], the bifurcation diagram and Lyapunov exponent spectrum of system (2) are shown in Figures 4(a) and 4(b). As shown in Figure 4(a), the system enters a chaotic state from a period-doubling bifurcation. As seen from Figures 4(a) and 4(b), the change of frequency ω has a more significant impact on the system than the amplitude f. The bifurcation diagram of ω in the interval in [0, 0.8] and [1, 2] is shown in Figures 4(c) and 4(d). As seen from the

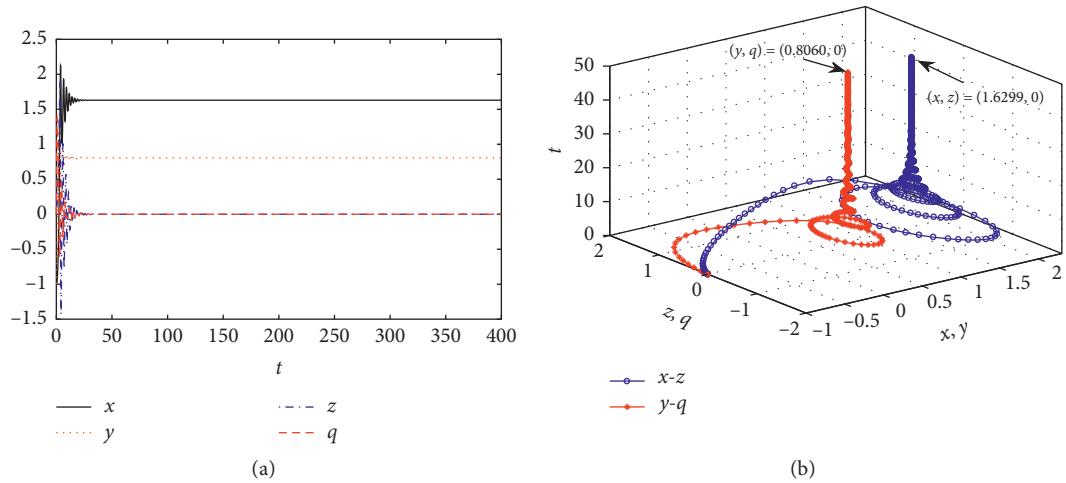

Figure 1: (a) When $H = 1$, system (2) state variables are x, (y) z, q, and the waveform diagram. (b) When (H) = 1, system (2) $x - y$ and $z - q$ phase diagram.

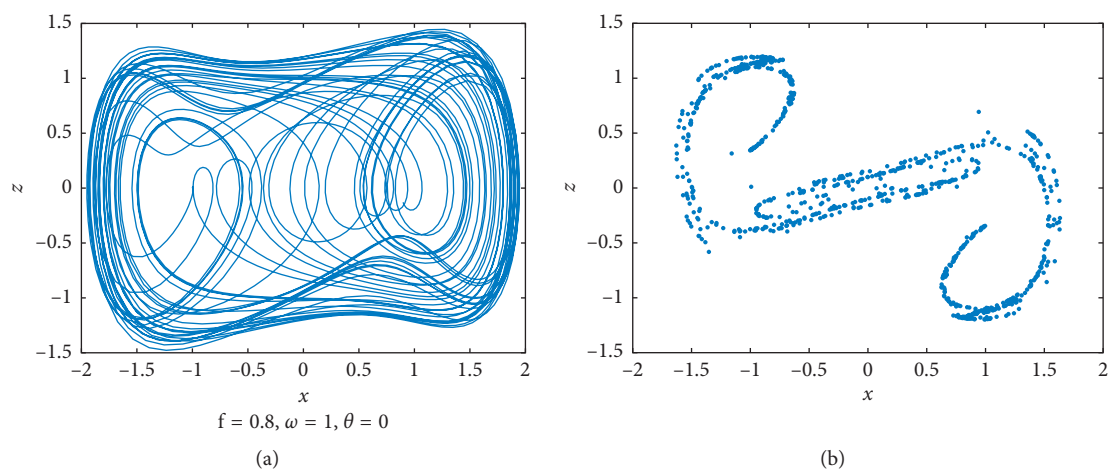

Figure 2: (a) X-y phase diagram of system (2). (b) Poincare section view of the x-z plane.

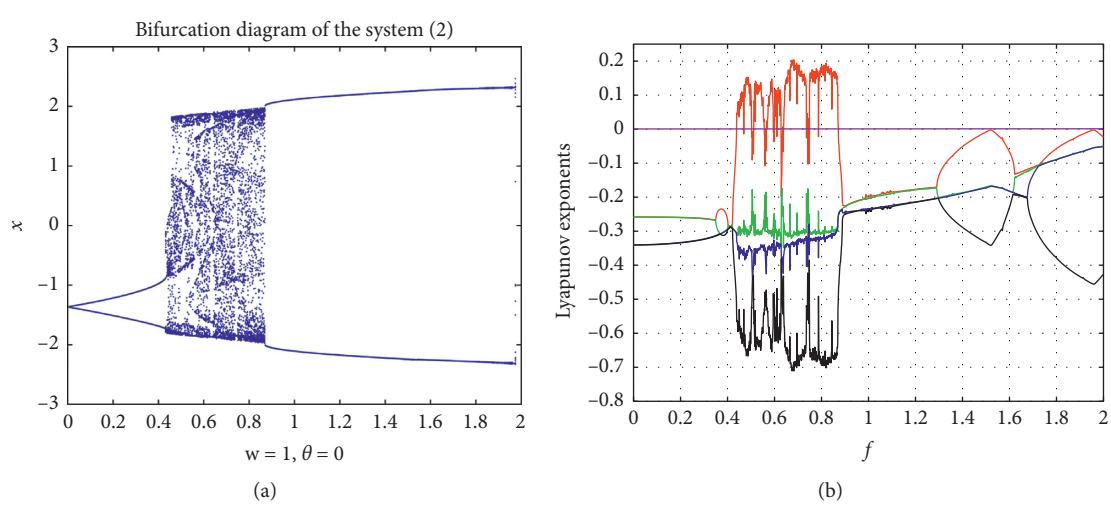

Figure 3: (a) The bifurcation diagram of (f) for system (2). (b) The lyapunov exponent diagram of (f).

local bifurcation diagram, a chaotic state occurs in system (2) within a small range of about $\omega = 0.5$, and a periodic state appears within a small range of about $\omega = 1.3$.

When $\omega = 1$, f becomes 0.8 and 1, respectively. According to the above analysis, when $\omega = 1$ and $f = 0.8$, system (2) is in a chaotic state. When $\omega = 1$ and $f = 1$, system (2) is in a periodic state. In the two different kinetic states of system (2), the initial phase angle θ is made to change at an interval $[0, 2\pi]$, and the bifurcation diagram and Lyapunov exponent diagram are shown in Figure 5. As seen from the analysis in Figure 5, when system (2) is in a chaotic state, with a change to the initial phase angle θ, the dynamic state of system (2) does not change. This is also the case when system (2) is in a periodic state. Therefore, the change of the initial phase angle θ of the driving force will not cause a change in the dynamic state of system (2).

4. Basins of Attraction

According to the set limit of system dynamics, the phase space formed by all possible initial points is divided into several disjoint subsets of the same dimension, and these subsets are called the basins of attraction. When a system with complex dynamics has multiple attractors, the boundary of the basins of attraction may have fractal characteristics. Within a certain time range, we compare the transverse maximum Lyapunov index of system (2) to the Lyapunov index of a particular track and further obtain the image of the basins of attraction for x (0) – y (0) and x (0) – z) (0) for system (2). The initial values are set to [x (0), y (0), 0, 0], $x(0) \in [-5, 5]$, $y(0) \in [-5, 5]$ and [x (0), −1, z (0), 0], $x(0) \in [-5, 5]$, $z(0) \in [-5, 5]$, respectively. As shown in Figure 6, the basins of attraction formed by the attractor in system (2) have a complex basins structure, including both riddled basins of attraction and mixed basins of attraction. In Figure 7, the basins of attraction are featured by an overall symmetry and global mixing. In Figures 6 and 7, the red area represents the basins of attraction of the attractor at infinity, that is, the point set where the trajectory of the system diverges. The yellow area represents the basins of attraction of the chaotic attractor; that is, the overall system is stable and multiple attractors coexist. The blue area represents the transition state.

As far as current research is concerned [56, 57], the conditions for the existence of basins of attraction in an attractor are as follows:

(i) There is a smooth and invariant subspace containing chaotic attractors

(ii) There is another asymptotic final state outside the invariant subspace (not necessarily chaotic)

(iii) The horizontal Lyapunov exponent of the invariant subspace is negative

(iv) The positive finite time change is associated with the lateral stability of the unstable periodic orbit of the attractor

According to research in [58], the area of the basins of attraction will change with the initial value. The research in [5] shows that when a sieve shape appears in the basins of attraction for the Chen system, the existence of a repulsive set of positive Lebesgue measures is obtained through mathematical justification. As seen in Figure 6, the change of the basins of attraction is affected by the initial value, and the area of $|y| > 2$ will show riddled basins of attraction, indicating that the attractor contains the repulsive set of the positive Lebesgue measures in the neighborhood of this area. The overall symmetry of the basins of attraction also manifests the synchronization of the system. Further research shows that it is impossible to predict the asymptotic attractor of the complex basins of attraction. The basins of attraction are shown in Figure 6; when y is in the intervals [−1.5, 5] and [2, 5], the initial value of the attractor will be unpredictable. There are six attractors in a coupled system in [6], wherein the basins of attraction of two attractors are not connected, and basins of attraction of the remaining two synchronous attractors and two asynchronous attractors constitute a basin of attraction with a symmetrical mixing distribution. When $3.5 > |y| > 2$, there will be a yellow area not connected to the left and right, and there is also a very narrow blue area. In this paper, whether the basins of attraction of different connected states represent the basins of attraction of different attractors, the relationship between the characteristics of the sieve shape of the connected area and the state changes of coexisting attractors should be further studied. The above analysis proves that there are mathematical conditions for the existence of hidden attractors and riddled basins of attraction in system (2). We also show that the horizontal Lyapunov exponents of hidden attractors are locally unstable.

As seen from Figure 7, the basins of attraction are a symmetrical figure and based on fractal theory are self-similar. According to Milnor's generalization of the classic definition of attractors, assuming that D is a smooth compact manifold and bounded, η represents the Lebesgue measure. The compact invariant set A on D satisfies the following conditions:

(1) Basins of attraction $\sigma(A) = \{x\colon x \in d, \omega(x) \subset A\}$, with a positive measure $((A)) > 0$

(2) There is no set A', making $A'A, \eta(\sigma(A')) - \eta(\sigma(A)) = 0$

A is called an attractor. That is, when A has an attraction set of positive Lebesgue measures, the attractor will have an attractive neighborhood. Based on studies of attractors, if all $x\sigma(A)$ and $\delta > 0$, it was discovered that when attractor A has riddled basins of attraction Φ (A), it satisfies

$$\eta(\sigma_\delta(x) \cap \sigma(A))\eta(\sigma_\delta(x) \cap \sigma(A)^c) > 0, \tag{9}$$

where $\sigma_\delta(x)$ is the δ neighborhood of x. As seen from this, when the basin of attraction formed by the attractor has a sieve-shaped characteristic, any neighborhood of the attractor contains the attraction set of the positive Lebesgue measures and the repulsive set of positive Lebesgue measures. In the riddled basins of attraction, there are points that are attracted by the attractor as well as points that diverge.

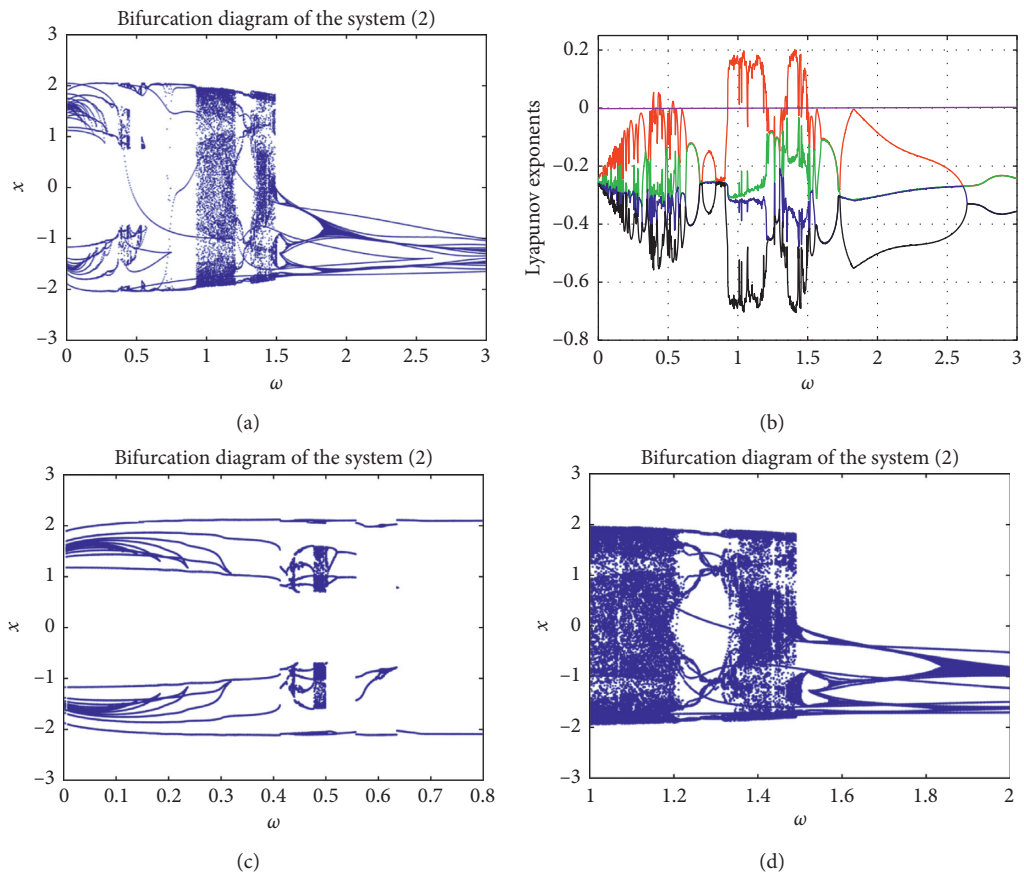

Figure 4: (a) The ω bifurcation diagram of system (2). (b) The Lyapunov exponent diagram of ω. (c) The partially enlarged diagram of bifurcation of ω in the interval [0, 0.8]. (d) The partially enlarged diagram of bifurcation of ω in the interval [1, 2].

Our research from [6] shows that when the system coexistence attractor exhibits synchronous changes, the attraction basins' structure is symmetrical. The research from [59] on the basins of attraction of coexistence attractors shows that when the system has multiple attractors, the basins of attraction formed by attractors will develop a mixing condition. The basins of attraction shown in Figure 7 also manifest with the characteristics of mixing and symmetry simultaneously. The study of the two subsystems in this system in this paper shows that the attractors of the two subsystems maintain synchronization between chaos periods. Based on the above references and the research in this paper, the structure of the basins of attraction in the coupled system can reflect a synchronization of the system to a certain extent. Furthermore, the structure of the attractor and the structure of the basins of attraction can also be mapped to each other under certain circumstances; that is, the symmetry of the basins of attraction can reflect the changing features of the system, and vice versa.

5. Application of Coupled System in Weak Signal Detection

According to the analysis in Figure 3, when the driving force frequency ω is a constant value, the state of system (2) will change from a chaotic state to a periodic state as the amplitude f changes. Weak signals can be detected by using the change to system (2) state. Therefore, this paper proposes a detection system corresponding to system (2), as shown in the following equation:

$$\begin{cases} \dot{x} = z, \\ \dot{y} = q, \\ \dot{z} = -0.5z + x - 0.2x^5 - 0.4(x - y) + f_0 \cos(\omega_0 t + \theta_0) + [b\cos(\omega t + \theta) + S(t)], \\ \dot{q} = -0.8\left(1 - y^2\right)q - y - y^3 - 0.4(y - x) + f_0 \cos(\omega_0 t + \theta_0) + [b\cos(\omega t + \theta) + S(t)]. \end{cases} \tag{10}$$

In system (10), $b\cos(\omega t+\theta)$ represents a weak signal, and $S(t)$ represents a noise signal. $f_0 \cos(\omega_0 t + \theta_0)$ represents the driving force of the system. First, the driving force amplitude f_0 is adjusted so that the system is at a critical

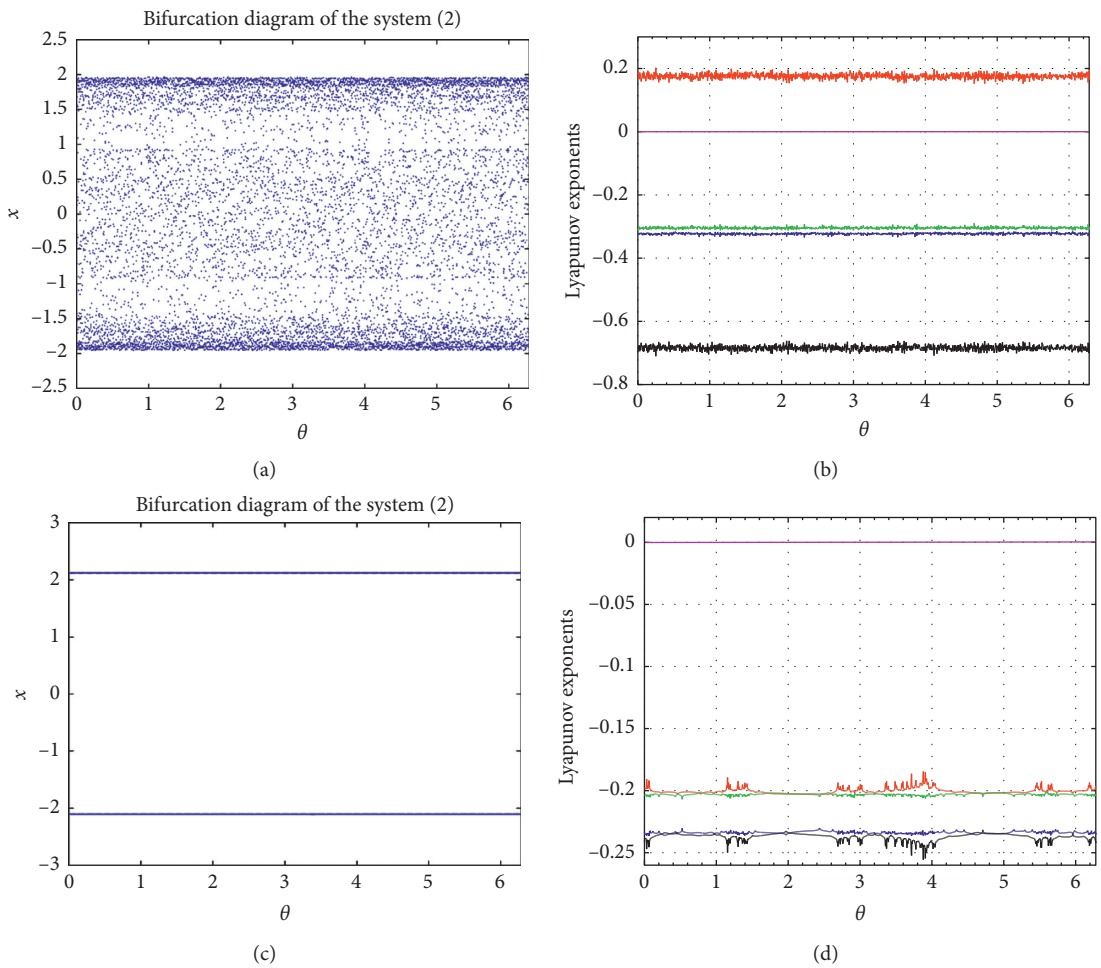

FIGURE 5: (a) The bifurcation diagram of θ when $f = 0.8$ and $\omega = 1$. (b) The Lyapunov exponent diagram of θ when $f = 0.8$ and $\omega = 1$. (c) The bifurcation diagram of θ when $f = 1$ and $\omega = 1$. (d) The Lyapunov exponent diagram of θ when $f = 1$ and $\omega = 1$.

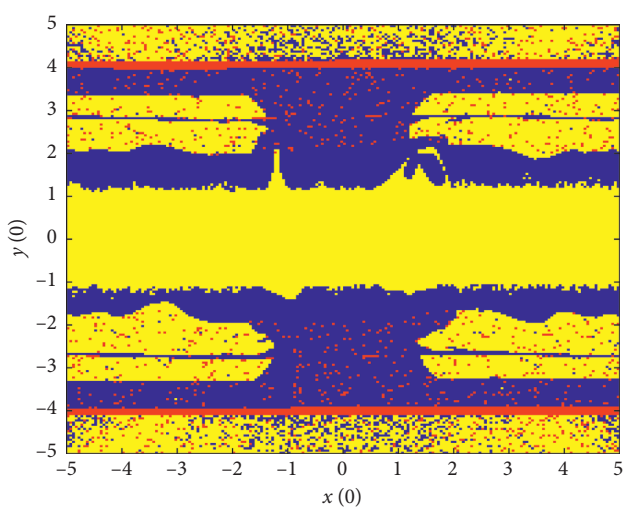

FIGURE 6: Diagram of x (0) – y (0) basins of attraction for system (2).

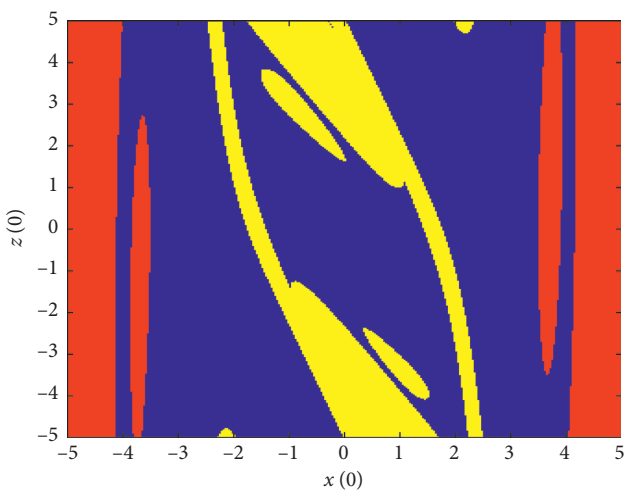

Figure 7: The x (0)–z (0) basins of attraction diagram for system (2).

point of state transition, and, at this time, f_0 is called the system threshold. When the driving force amplitude $f_0 = 0.8747909$, system (10) is in a critical state.

5.1. Research on the Influence of Weak Signal Parameters on the System. When the frequency $\omega_0 = 1$ of system (10) is taken, the initial phase angle $\theta_0 = 0$. When amplitude $f0 = 0.8747909$, Lyapunov exponent values $L_{E1} = 0.026845$, $L_{E2} = 0$, $L_{E3} = -0.256585$, $L_{E4} = -0.256435$, and $L_{E5} = -0.508001$. At this time, the phase diagram and the power spectrum of system (10) are shown in Figure 8. Research shows that the power spectrum of the periodic signals is a discrete spectrum. The power spectrum of nonperiodic signals is a continuous spectrum. The chaotic signal is a nonperiodic signal, and the power spectrum is a continuous spectrum. Therefore, the state of system (10) may be determined based on the power spectrum. When the amplitude $f0$ is adjusted to 0.8747909, the phase diagram and power spectrum of system (10) are shown in Figure 8. According to Figure 8, the x-z phase diagram of system (10) is in a chaotic state and the power spectrum is continuous; therefore, system (10) is in a chaotic state.

At this time, after a weak signal with a frequency $\omega = 1$, initial phase angle $\theta = 0$, and amplitude $b = 1 \times 10^{-6}$ is added to system (10), Lyapunov index values of the system are $L_{E1} = -0.014575$, $L_{E2} = 0$, $L_{E3} = -0.251969$, $L_{E4} = -0.253323$, and $L_{E5} = -0.490388$. The phase diagram and the power spectrum for system (10) are shown in Figure 9. As seen from Figure 9, when a weak signal with an amplitude 1×10^{-6} is added to system (10), the x-z phase diagram of system (10) is in a periodic state and the power spectrum is a discrete spectrum, and the state of system (10) becomes periodic.

Because system (10) can only detect weak signals in the same or similar interval as the driving force frequency and initial phase angle, the research system can detect the frequency range of the weak signal and take the driving force frequency $\omega_0 = 1$ and the initial phase angle $\theta_0 = 0$; the initial phase angle of the weak signal $\theta = 0$, and the amplitude $b = 1 \times 10^{-6}$. By calculating ω in [0.6, 1.3], we get system (10) Lyapunov exponent data when the frequency ω changes in Table 1. As seen in Table 1, when the frequency ω of the weak signal is within [0.8, 1.1], the dynamic state of system (10) will change.

The studied system (10) can detect the range of the initial phase angle θ of a weak signal, taking the system's driving force frequency $\omega_0 = 1$, the initial phase angle $\theta_0 = 0$, the weak signal frequency $\omega = 1$, and the amplitude $b = 1 \times 10^{-6}$. The driving force f_0 of the system and the weak signal b are to be measured as a whole; when A is input into the system,

$$\begin{aligned} A(t) &= f_0 \cos(\omega_0 t + \theta_0) + b\cos(\omega t + \theta) \\ &= f_0 \cos\omega_0 t \cos\theta_0 - f_0 \sin\omega_0 t \sin\theta_0 + b\cos\omega t \cos\theta \\ &\quad - b\sin\omega t \sin\theta. \end{aligned} \tag{11}$$

When $\omega_0 = \omega$,

$$\begin{aligned} A(t) &= (f_0 \cos\theta_0 + b\cos\theta)\cos\omega t \\ &\quad - (f_0 \sin\theta_0 + b\sin\theta)\sin\omega t \\ &= F(t)\cos(\omega t + \varphi(t)). \end{aligned} \tag{12}$$

In equation (10), $F(t) = \sqrt{f_0^2 + 2f_0 b\cos(\theta_0 - \theta) + b^2}$ $\varphi(t) = \arctan((f_0 \sin\theta_0 + b\sin\theta)/(f_0 \cos\theta_0 + b\cos\theta))$.

When $F(t) \geq 0.8747919$, the state of system (10) will change from a chaotic state to a periodic state. When $b = 1 \times 10^{-6}$, the frequency of the driving force $\omega = 1$, and the initial phase angle $\theta_0 = 1^\circ$ to obtain $0.91^\circ \leq \theta \leq = 1.09^\circ$. As seen from the research conclusion of the initial phase angle of the driving force of system (2), the threshold of system $f0$ does not change when the initial phase angle changes and the weak signals of different initial phase angles can be detected by adjusting the initial phase angle of the system's driving force. According to the above analysis, the system has a higher detection accuracy for the unknown weak signal, and, at the moment, the relative error of the initial phase angle measurement does not exceed ±0.09.

5.2. Research on the Antinoise Performance of System (10). The antinoise performance of system (10) was studied by adding Gaussian white noise. When excessive noise was added, the phase diagram of system (10) converging in the periodic state will also become disorderly. Therefore, the antinoise performance of system (10) can be studied by drawing the phase diagram of system (10) under noise conditions. The regulation system is in a critical state. After Gaussian white noise power $p_{s(t)} = 0.0035$ was added to system (10), the system dynamic state did not change, as shown in Figure 10(a). Then a weak signal was added to system (10), and the state of the system changes at this time, as shown in Figure 10(b). As seen in Figure 10(b), the added noise has no relevant impact on the stability of the system. Therefore, the system signal-to-noise ratio SRN is

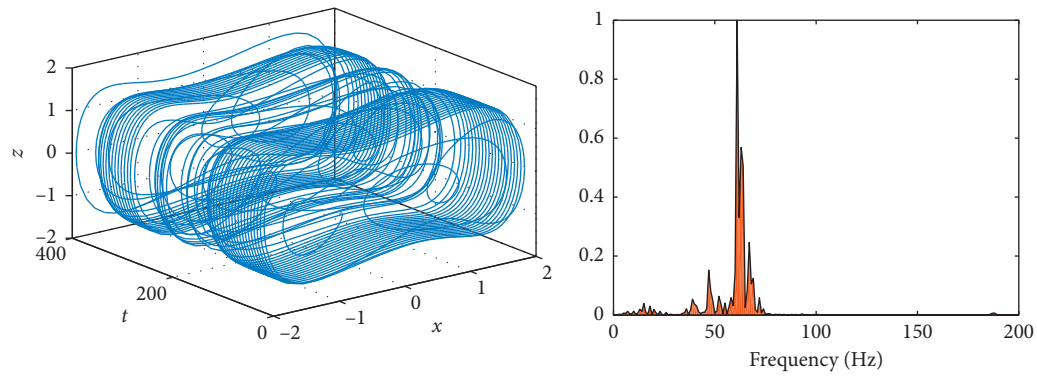

(a) (b)

Figure 8: (a) Phase diagram of system (10) when a weak signal is not added. (b) Power spectrum diagram of system (10) when a weak signal is not added.

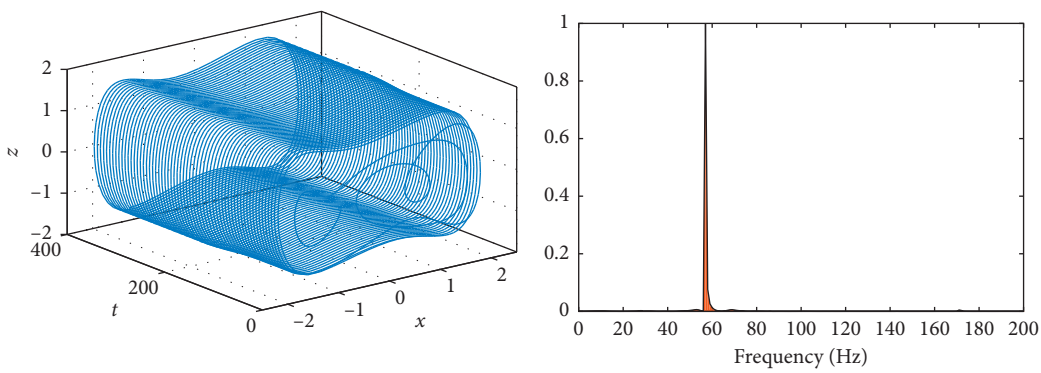

(a) (b)

Figure 9: (a) Phase diagram of system (10) after a weak signal was added. (b) Power spectrum of system (10) after a weak signal is added.

Table 1: Lyapunov exponent statistics table of frequency ω withing the interval [0.7, 1.3].

ω	L_{E1}	L_{E2}	L_{E3}	L_{E4}	L_{E5}	System state
0.6	0.054782	0	−0.253654	−0.264728	−0.542015	Chaotic state
0.7	0.001082	0	−0.253727	−0.259955	−0.506094	Chaotic state
0.8	0	−0.010830	−0.254174	−0.253927	−0.493878	Periodic state
0.9	0	−0.025991	−0.250020	−0.251349	−0.478236	Periodic state
1.1	0	−0.029113	−0.251380	−0.250912	−0.474047	Periodic state
1.2	0.069098	0	−0.272891	−0.274010	−0.577603	Chaotic state
1.3	0.015809	0	−0.259136	−0.261232	−0.521500	Chaotic state

$$SRN = 10\lg\left(\frac{p_b}{p_{S(t)}}\right) = 10\lg\left[0.5\frac{\left(1\times10^{-6}\right)^2}{(0.0035)^2}\right] \approx -73.892\,dB \tag{13}$$

In [53], only a signal with a size of 0.01 can be detected and the signal-to-noise ratio can only reach −45.85 dB. The system in [54] can detect signals with the size of 1×10^{-9}, but the noise signal that the system can be immune to can only reach a size of 1×10^{-9}. The system in [55] can detect signals of a larger frequency range, but the fluctuation range of the initial phase angle from the measured signal is too large, and the error range is ±60.6, which is not conducive to confirmation of signal parameters. The system proposed in this paper can detect signals sized 1×10^{-6}, and the signal-to-noise ratio reaches -73.892 dB. Moreover, the immune signal reached the order of 3.5×10^{-3}, and the error range of the initial phase angle is ±0.09. In summary, the system introduced in this paper has superior detection performance.

6. Circuit Design and Realization of System

6.1. Circuit Design of System. According to the circuit principle and the characteristics of electronic components,

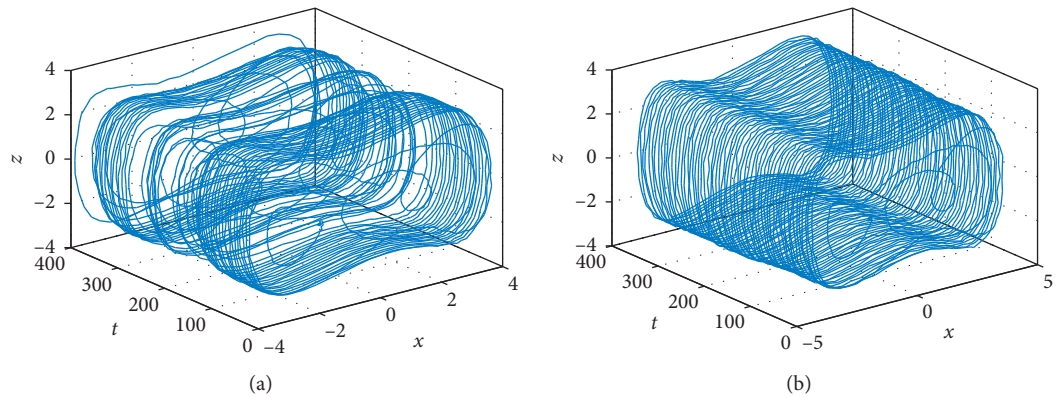

Figure 10: (a) Phase diagram of system (10) after adding Gaussian white noise. (b) Phase diagram of system (10) after adding a weak signal in the presence of Gaussian white noise.

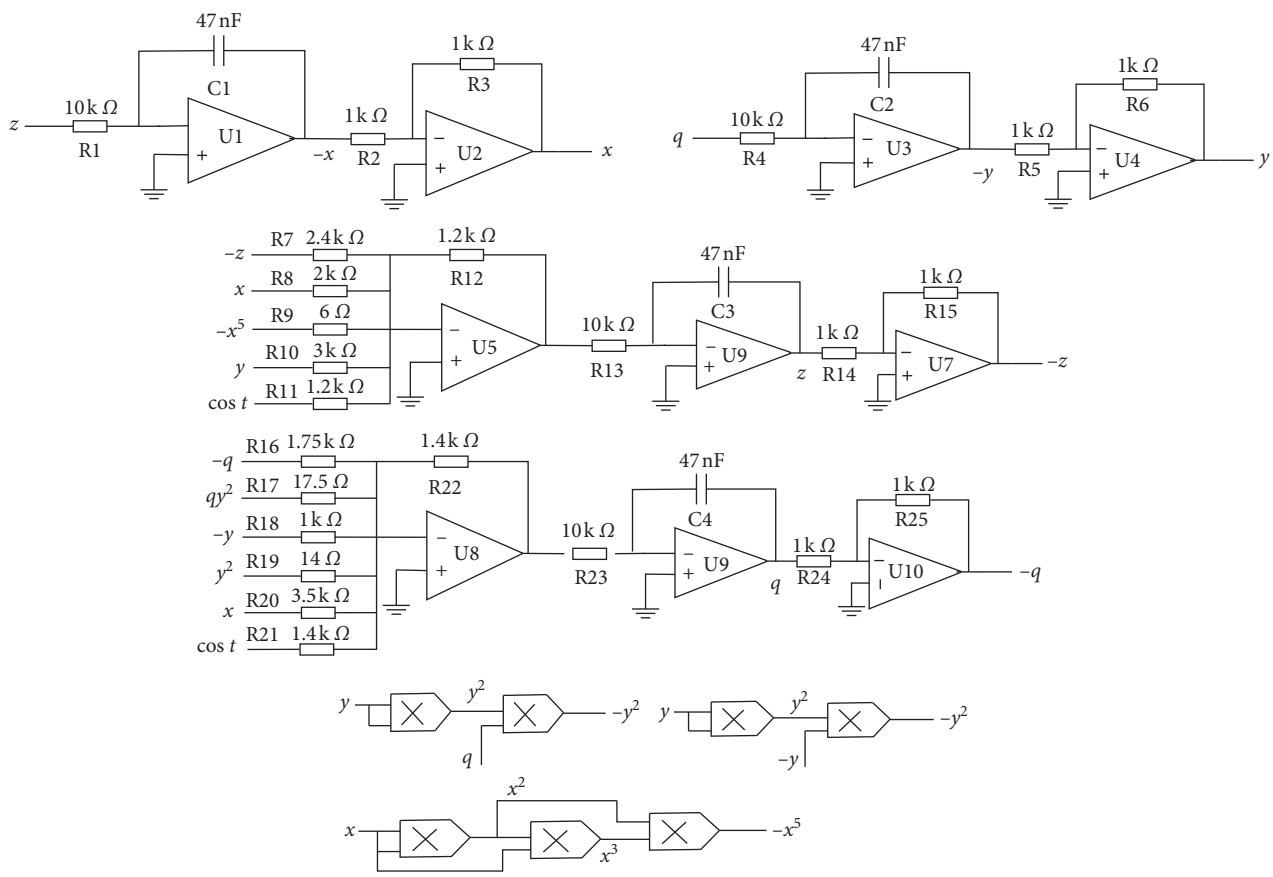

Figure 11: Circuit diagram schematic for system (2).

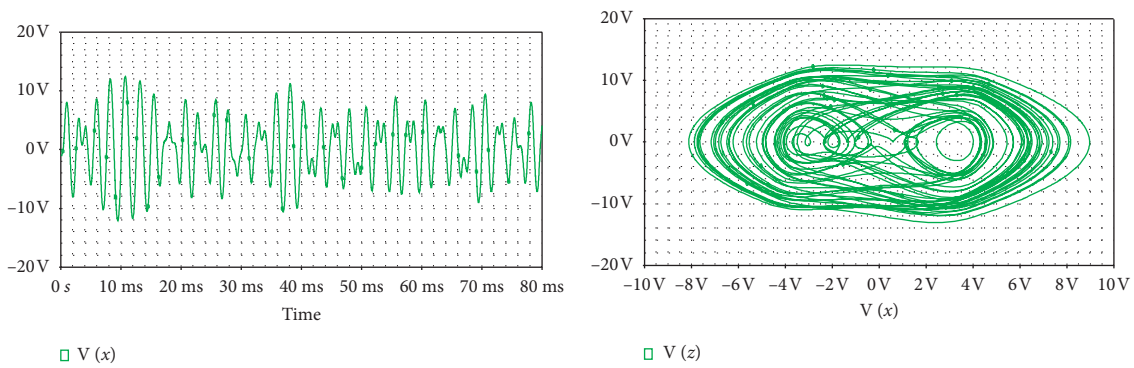

Figure 12: (a) Oscillogram of system (2) variable x; (b) x-z phase diagram of system (2).

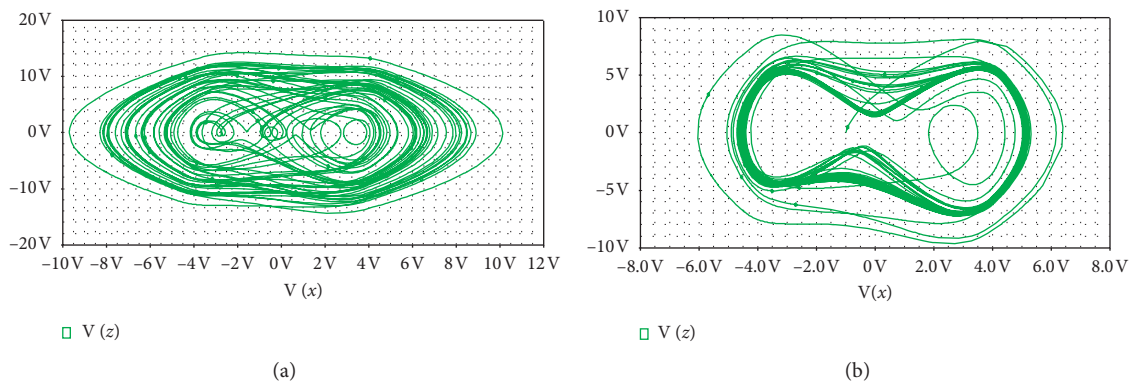

Figure 13: (a) x-z phase diagram of (10) without a weak signal; (b) x-z phase diagram of system (10) with a weak signal.

the circuit equation (14) as shown in system (2) can be obtained as follows:

$$\begin{cases} \dfrac{dV_x}{dt} = -\dfrac{1}{R_1C_1}V_z, \\ \dfrac{dV_y}{dt} = -\dfrac{1}{R_2C_2}V_q, \\ \dfrac{dV_z}{dt} = -\dfrac{1}{R_{13}C_3}\left(-\dfrac{R_{12}}{R_7}V_z + \dfrac{R_{12}}{R_8}V_x - \dfrac{R_{12}}{R_9}V_{x^5} + \dfrac{R_{12}}{R_{10}}V_y + \dfrac{R_{12}}{R_{11}}V_{\cos t}\right), \\ \dfrac{dV_q}{dt} = -\dfrac{1}{R_{23}C_4}\left(-\dfrac{R_{22}}{R_{16}}V_q + \dfrac{R_{22}}{R_{17}}V_{qy^2} - \dfrac{R_{22}}{R_{18}}V_y - \dfrac{R_{22}}{R_{19}}V_{y^3} + \dfrac{R_{22}}{R_{20}}V_x + \dfrac{R_{22}}{R_{21}}V_{\cos t}\right). \end{cases} \tag{14}$$

The circuit for equation (14) is shown in Figure 11. System (2) is compared with equation (14) to make their coefficients equal, and the selected device parameters $C_1 = C_2 = C_3 = C_4 = 47\text{nF}$, $R_2 = R_3 = R_5 = R_6 = R_{14} = R_{15} = R_{18} = R_{24} = R_{25} = 1k\Omega$, $R_1 = R_4 = R_{13} = R_{23} = 10k\Omega$, $R_{11} = R_{12} = 1.2k\Omega$, $R_{21} = R_{22} = 1.4k\Omega$, $R_7 = 2.4k\Omega$, $R_8 = 2k\Omega$, $R_9 = 6\Omega$, $R_{10} = 3k\Omega$, $R_{16} = 1.75K\Omega$, $R_{17} = 17.5\Omega$, $R_{19} = 14\Omega$, and $R_{20} = 3.5k\Omega$. The operational amplifier

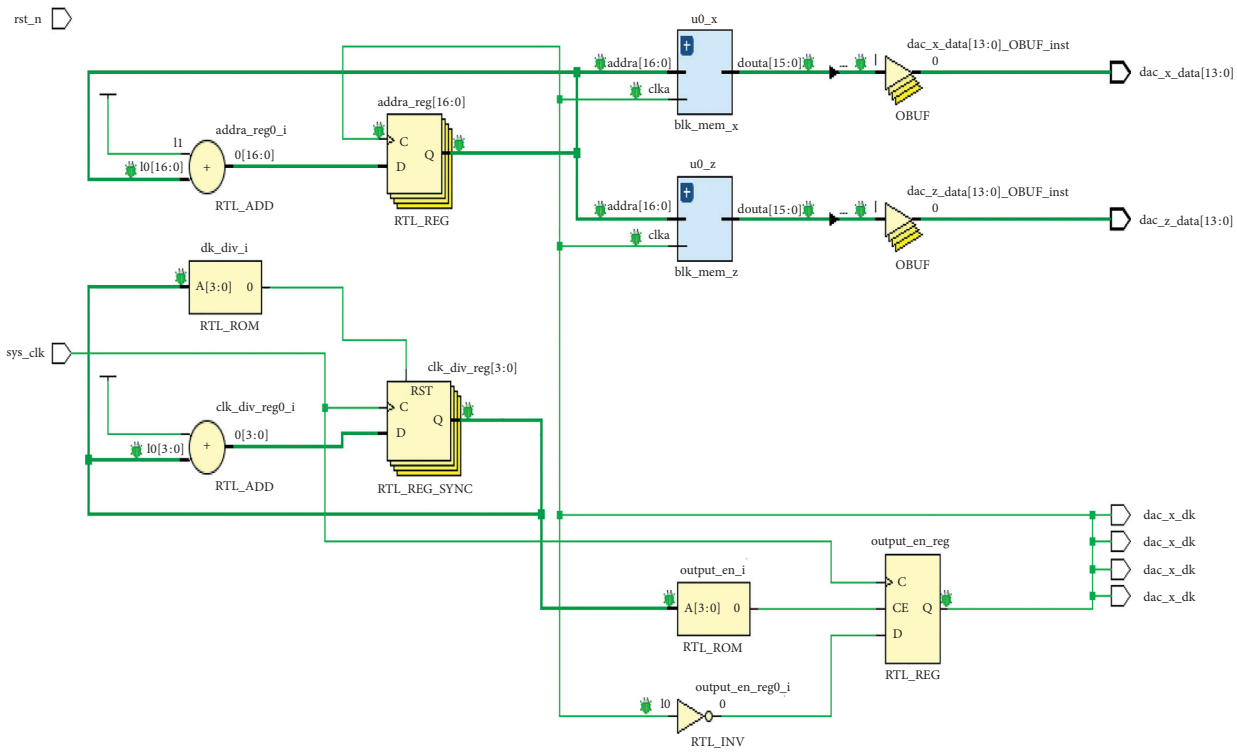

Figure 14: RTL view based on FPGA implementation.

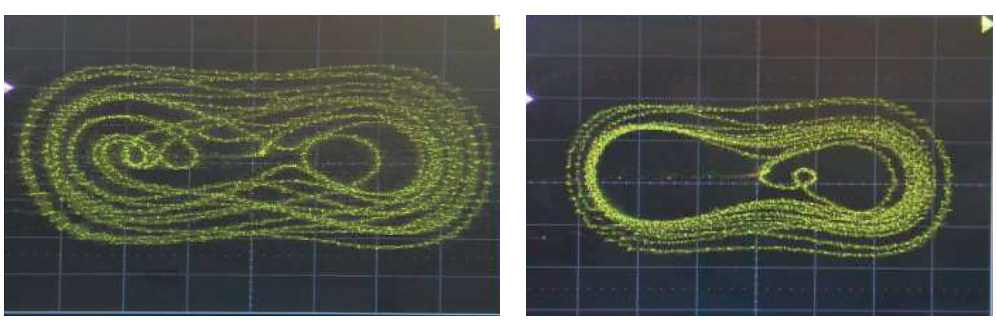

(a) (b)

Figure 15: (a) x-z phase diagram of system (10) before adding a weak signal; (b) x-z phase diagram of system (10) after adding a weak signal.

model selected by the circuit is TL082, and the multiplier model is AD633.

6.2. System Circuit Simulation and FPGA Implementation. In this paper, OrCAD was used to simulate the system circuit, the amplitude was set as $f = 8$ V, and the frequency $\varphi = 400$ Hz, with the waveform diagram of the state variable x and the phase diagram of x-z shown in Figure 12.

Test the detection performance of system (10), take the frequency $\varphi = 400$ Hz, and adjust the amplitude $f = 13.5664362$ V, with system (10) in a chaotic state as shown in Figure 13(a). When the driving force amplitude $f = 13.5664372$ is adjusted, the state of system (10) changes to a periodic state, as shown in Figure 13(b). Therefore, system (10) can effectively detect the sine signal with an amplitude of 1×10^{-6} V.

Based on FPGA technology and fixed-point number method, hardware experiment is carried out on system (10). We use Xilinx zynq-7000 XC7Z020 FPGA chip and AD9767 dual-port parallel 14-bit A/D module with the highest conversion rate of 125 MHz. The software used is Vivado 17.4 and system generator compiler is used to realize the joint debugging of MATLAB and FPGA. In addition, we also use SIGLENT 1202X digital oscilloscope to visualize analog output. After compiling, the automatically generated RTL view is shown in Figure 14.

The regulation system was in a critical state, as shown in Figure 15(a). After adding a weak signal, the phase diagram of system (10) is shown in Figure 15(b), and the state of system (10) changes. Therefore, system (10) can effectively detect weak signals.

7. Conclusion

Through calculation, this paper concludes that system (2) has an infinite number of equilibrium points, and there is a Lyapunov exponent greater than 0. Therefore, system (2) is a hidden attractor coupled chaotic system. The analysis of the basins of attraction shows that system (2) has the characteristics of structural symmetry, and the state of the attractor changes synchronously. Further research finds that the Lyapunov exponent of the hidden attractor is locally unstable. The research on the Lyapunov indexes of all parameters of system (10) driving force has proved that system (10) can more accurately detect signals with a size of 1×10^{-6}, and the research on system (10) with noise shows that system (10) has excellent antinoise performance. Finally, circuit simulation and FPGA implementation have demonstrated the theoretical analysis and the accuracy of weak signal detection to be correct.

In future research, the focus will be on how to detect different types of signals, how to improve the system's antinoise performance, and identifying the system's state. As there is no unified conclusion on the structure of the basins of attraction, the research results should be further verified. Moreover, no unified results have been achieved in the theoretical research on the structure of the basins of attraction, and thus the research on the basins of attraction will also be a hot spot in the future.

Data Availability

The data used to support the findings of this study are included within the article.

Conflicts of Interest

The authors declare that they have no conflicts of interest.

Acknowledgments

This work was supported by the National Natural Science Foundation of China under Grants 61504013 and 61561022, the Natural Science Foundation of Hunan Province under Grants 2019JJ50648, 2020JJ4315, and 2017JJ3254, and Hunan Provincial Education Department under Grant 20B216.

References

[1] E. N. Lorenz, "Deterministic nonperiodic flow," *Journal of the Atmospheric Sciences*, vol. 20, no. 2, pp. 130–141, 1963.

[2] Z. Liu, Y. Li, and G. Chen, "The basin of attraction of the Chen attractor," *Chaos, Solitons & Fractals*, vol. 34, no. 5, pp. 1696–1703, 2007.

[3] S. P. Raj, S. Rajasekar, and K. Murali, "Coexisting chaotic attractors, their basin of attractions and synchronization of chaos in two coupled Duffing oscillators," *Physics Letters A*, vol. 264, no. 4, pp. 283–288, 1999.

[4] J. A. Wright, J. H. B. Deane, M. Bartuccelli et al., "Basins of attraction in forced systems with time-varying dissipation," *Communications in Nonlinear Science and Numerical Simulation*, vol. 29, no. 1-3, pp. 72–87, 2015.

[5] G. Wang, F. Yuan, G. Chen et al., "Coexisting multiple attractors and riddled basins of a memristive system," *Chaos: An Interdisciplinary Journal of Nonlinear Science*, vol. 28, no. 1, Article ID 013125, 2018.

[6] A. Bayani, K. Rajagopal, A. J. M. Khalaf, S. Jafari, G. D. Leutcho, and J. Kengne, "Dynamical analysis of a new multistable chaotic system with hidden attractor: antimonotonicity, coexisting multiple attractors, and offset boosting," *Physics Letters A*, vol. 383, no. 13, pp. 1450–1456, 2019.

[7] L. Xiong, S. Zhang, Y. Zeng, and B. Liu, "Dynamics of a new composite four-Scroll chaotic system," *Chinese Journal of Physics*, vol. 56, no. 5, pp. 2381–2394, 2018.

[8] H. Jahanshahi, A. Yousefpour, J. M. Munoz-Pacheco, I. Moroz, Z. Wei, and O. Castillo, "A new multi-stable fractional-order four-dimensional system with self-excited and hidden chaotic attractors: dynamic analysis and adaptive synchronization using a novel fuzzy adaptive sliding mode control method," *Applied Soft Computing*, vol. 87, p. 105943, 2020.

[9] Q. Deng, C. Wang, and L. Yang, "Four-wing hidden attractors with one stable equilibrium point," *International Journal of Bifurcation and Chaos*, vol. 30, no. 06, p. 2050086, 2020.

[10] Sundarapandian Vaidyanathan, Aceng Sambas, Mustafa Mamat, and W. S. Mada Sanjaya, "A new three-dimensional chaotic system with a hidden attractor, circuit design and application in wireless mobile robot," *Archives of Control Sciences*, vol. 27, no. LXIII, pp. 541–554, 2017.

[11] Yu Fei, Li Liu, H. Shen et al., "Dynamic analysis, Circuit design and Synchronization of a novel 6D memristiv four-wing hyperchaotic system with multiple coexisting attractors," *Complexity*, vol. 2020, Article ID 5904607, , 2020.

[12] F. Yu, L. Liu, H. Shen et al., "Multistability analysis, coexisting multiple attractors and FPGA implementation of Yu-Wang four-wing chaotic system," *Mathematical Problems in Engineering*, vol. 2020, Article ID 7530976, , 2020.

[13] A. Sambas, S. Vaidyanathan, E Tlelo-Cuautle et al., "A novel chaotic system with two circles of equilibrium points: multistability, electronic circuit and FPGA realization," *Electronics*, vol. 8, no. 11, Article ID 1211, 2019.

[14] C. Wang, H. Xia, and L. Zhou, "A memristive hyperchaotic multiscroll jerk system with controllable scroll numbers," *International Journal of Bifurcation and Chaos*, vol. 27, no. 06, Article ID 1750091, 2017.

[15] R. Wu and C. Wang, "A new simple chaotic circuit based on memristor," *International Journal of Bifurcation and Chaos*, vol. 26, no. 09, Article ID 1650145, 2016.

[16] C. Wang, X. Hu, and L. Zhou, "Implementation of a new memristor-based multiscroll hyperchaotic system," *Pramana*, vol. 88, no. 2, p. 34, 2017.

[17] H. Lin, C. Wang, W. Yao, and Y. Tan, "Chaotic dynamics in a neural network with different types of external stimuli," *Communications in Nonlinear Science and Numerical Simulation*, vol. 90, Article ID 105390, 2020.

[18] W. Yao, C. Wang, Y. Sun, C. Zhou, and H. Lin, "Exponential multistability of memristive Cohen-Grossberg neural networks with stochastic parameter perturbations," *Applied Mathematics and Computation*, vol. 386, p. 125483, 2020.

[19] H. Lin, C. Wang, and Y. Tan, "Hidden extreme multistability with hyperchaos and transient chaos in a Hopfield neural network affected by electromagnetic radiation," *Nonlinear Dynamics*, vol. 99, pp. 2369–2386, 2020.

[20] V. T. Pham, D. S. Ali, N. M. G. Al-Saidi, K. Rajagopal, F. E. Alsaadi, and S. Jafari, "A novel mega-stable chaotic circuit," *Radioengineering*, vol. 29, no. 1, pp. 140–146, 2020.

[21] V. -T. Pham, S. Vaidyanathan, C. Volos, S. Jafari, and T. Kapitaniak, "A new multi-stable chaotic hyperjerk system, its special features, circuit realization, control and synchronization," *Archives of Control Sciences*, vol. 30, no. 1, pp. 23–45, 2020.

[22] J. Jin and L. Cui, "Fully integrated memristor and its application on the scroll-controllable hyperchaotic system," *Complexity*, vol. 2019, Article ID 4106398, 2020.

[23] J. Jin, "Programmable multi-direction fully integrated chaotic oscillator," *Microelectronics Journal*, vol. 75, pp. 27–34, 2018.

[24] J. Jin and L. Zhao, "Low voltage low power fully integrated chaos generator," *Journal of Circuits, Systems and Computers*, vol. 27, no. 10, Article ID 1850155, 2018.

[25] J. Sun, Mu Peng, F. Liu, and C. Tang, "Protecting compressive ghost imaging with hyper-chaotic system and DNA encoding," *Complexity*, vol. 2020, Article ID 8815315, 2020.

[26] C. Xu, J. Sun, and C. Wang, "A novel image encryption algorithm based on bit-plane matrix rotation and hyper chaotic systems," *Multimedia Tools and Applications*, vol. 79, no. 9-10, pp. 5573–5593, 2020.

[27] Xi Chen, S. Qian, Yu Fei et al., "Pseudorandom number generator based on three kinds of four-wing memristive hyperchaotic system and its application in image encryption," *Complexity*, vol. 2020, Article ID 8274685, 2020.

[28] S. Wang, C. Wang, and C. Xu, "An image encryption algorithm based on a hidden attractor chaos system and the Knuth-Durstenfeld algorithm," *Optics and Lasers in Engineering*, vol. 128, p. 105995, 2020.

[29] A. Sambas, S. Vaidyanathan, E. Tlelo-Cuautle et al., "A 3-D multi-stable system with a peanut-shaped equilibrium curve: circuit design, FPGA realization, and an application to image encryption," *The Institute of Electrical and Electronics Engineers Access*, vol. 8, pp. 137116–137132, 2020.

[30] Y. Huang, L. Huang, Y. Wang, Y. Peng, and F. Yu, "Shape synchronization in driver-response of 4-D chaotic system and its application in image encryption," *The Institute of Electrical and Electronics Engineers Access*, vol. 8, pp. 135308–135319, 2020.

[31] L. Zhou, F. Tan, and F. Yu, "A robust synchronization-based chaotic secure communication scheme with double-layered and multiple hybrid networks," *The Institute of Electrical and Electronics Engineers Systems Journal*, vol. 14, no. 2, pp. 2508–2519, 2020.

[32] L. Zhou, F. Tan, F. Yu, and W. Liu, "Cluster synchronization of two-layer nonlinearly coupled multiplex networks with multi-links and time-delays," *Neurocomputing*, vol. 359, pp. 264–275, 2019.

[33] F. Peng, X. Zhu, and M. Long, "An ROI privacy protection scheme for H. 264 video based on FMO and chaos," *The Institute of Electrical and Electronics Engineers Transactions on Information Forensics and Security*, vol. 8, no. 10, pp. 1688–1699, 2013.

[34] F. Yu, S. Qian, X. Chen et al., "A new 4D four-wing memristive hyperchaotic system: dynamical analysis, electronic circuit design, shape synchronization and secure communication," *International Journal of Bifurcation and Chaos*, vol. 30, no. 10, Article ID 2050147, 2020.

[35] J. Jin, L. Zhao, M. Li, F. Yu, and Z. Xi, "Improved zeroing neural networks for finite time solving nonlinear equations," *Neural Computing and Applications*, vol. 32, no. 9, pp. 4151–4160, 2020.

[36] F. Yu, L. Liu, L. Xiao, K. Li, and S. Cai, "A robust and fixed-time zeroing neural dynamics for computing time-variant nonlinear equation using a novel nonlinear activation function," *Neurocomputing*, vol. 350, pp. 108–116, 2019.

[37] J. Jin, "A robust zeroing neural network for solving dynamic nonlinear equations and its application to kinematic control of mobile manipulator," *Complex & Intelligent Systems*, 2020.

[38] J. Jin and J. Gong, "An interference-tolerant fast convergence zeroing neural network for dynamic matrix inversion and its application to mobile manipulator path tracking," *Alexandria Engineering Journal*, 2020.

[39] F. Yu, L. Liu, S. Qian et al., "Chaos-based application of a novel multistable 5D memristive hyperchaotic system with coexisting multiple attractors," *Complexity*, vol. 2020, Article ID 8034196, 2020.

[40] F. Yu, Q. Wan, J. Jin et al., "Design and FPGA implementation of a pseudorandom number generator based on a four-wing memristive hyperchaotic system and Bernoulli map," *The Institute of Electrical and Electronics Engineers Access*, vol. 7, pp. 181884–181898, 2019.

[41] F. Yu, L. Li, Q. Tang et al., "A survey on true random number generators based on chaos," *Discrete Dynamics in Nature and Society*, vol. 2019, Article ID 2545123, 2019.

[42] J. Yan and L. Lu, "Improved Hilbert-Huang transform based weak signal detection methodology and its application on incipient fault diagnosis and ECG signal analysis," *Signal Processing*, vol. 98, pp. 74–87, 2014.

[43] Y. Wang, G. Xu, L. Liang, and K. Jiang, "Detection of weak transient signals based on wavelet packet transform and manifold learning for rolling element bearing fault diagnosis," *Mechanical Systems and Signal Processing*, vol. 54-55, pp. 259–276, 2015.

[44] L. Lu, J. Yan, and C. W. de Silva, "Dominant feature selection for the fault diagnosis of rotary machines using modified genetic algorithm and empirical mode decomposition," *Journal of Sound and Vibration*, vol. 344, pp. 464–483, 2015.

[45] D. L. Birx and S. J. Pipenberg, "Chaotic oscillators and complex mapping feed forward networks (CMFFNS) for signal detection in noisy environments," *The Institute of Electrical and Electronics Engineers* in *Proceedings 1992] IJCNN International Joint Conference on Neural Networks*, vol. 2, pp. 881–888, Baltimore, MD, USA, January 1992.

[46] Z.-H. Lai and Y.-G. Leng, "Weak-signal detection based on the stochastic resonance of bistable Duffing oscillator and its application in incipient fault diagnosis," *Mechanical Systems and Signal Processing*, vol. 81, pp. 60–74, 2016.

[47] Y. Jiang, H. Zhu, and Z. Li, "A new compound faults detection method for rolling bearings based on empirical wavelet transform and chaotic oscillator," *Chaos, Solitons & Fractals*, vol. 89, pp. 8–19, 2016.

[48] X. Liu and X. Liu, "Weak signal detection research based on duffing oscillator used for downhole communication," *Journal of Computers*, vol. 6, no. 2, pp. 359–367, 2011.

[49] F. Yang, L. Jing, W. Zhang, Y. Yan, and H. Ma, "Experimental and numerical studies of the oblique defects in the pipes using a chaotic oscillator based on ultrasonic guided waves," *Journal of Sound and Vibration*, vol. 347, pp. 218–231, 2015.

[50] P. Kumar, S. Narayanan, and S. Gupta, "Investigations on the bifurcation of a noisy Duffing-van der Pol oscillator," *Probabilistic Engineering Mechanics*, vol. 45, pp. 70–86, 2016.

[51] N. Chunyan and S. Yaowu, "The research of Chaotic characteristic identification base on weak signal detection," *ACTA Metrological Sinica*, vol. 10, no. 4, pp. 308–313, 2000.

[52] T. Xie, X. Wei, and R. Yu, "Noise immunity analysis in external excitation chaotic oscillator detecting system[C]//2010 International Conference on Intelligent System Design and Engineering Application," *The Institute of Electrical and Electronics Engineers*, vol. 1, pp. 1013–1016, 2010.

[53] Z. Zhao and S. Yang, "Application of vanderPol-Duffing oscillator in weak signal Detection," *Computers and Electrical Engineering*, vol. 41, pp. 1–8, 2015.

[54] A. Gokyildirim, Y. Uyaroglu, and I. Pehlivan, "A novel chaotic attractor and its weak signal detection application," *Optik*, vol. 127, no. 19, pp. 7889–7895, 2016.

[55] Y. Zhang, H. Mao, H. Mao, and Z. Huang, "Detection the nonlinear ultrasonic signals based on modified Duffing equations," *Results in Physics*, vol. 7, pp. 3243–3250, 2017.

[56] U. Chaudhuri and A. Prasad, "Complicated basins and the phenomenon of amplitude death in coupled hidden attractors," *Physics Letters A*, vol. 378, no. 9, pp. 713–718, 2014.

[57] S. Camargo, R. L. Viana, and C. Anteneodo, "Intermingled basins in coupled Lorenz systems," *Physical Review E*, vol. 85, no. 3, Article ID 036207, 2012.

[58] B. L. Lan and C. Yapp, "Dissipative relativistic standard map: periodic attractors and basins of attraction," *Chaos, Solitons & Fractals*, vol. 37, no. 5, pp. 1300–1304, 2008.

[59] C. Chen, J. Chen, H. Bao, M. Chen, and B. Bao, "Coexisting multi-stable patterns in memristor synapse-coupled Hopfield neural network with two neurons," *Nonlinear Dynamics*, vol. 95, no. 4, pp. 3385–3399, 2019.

Hindawi
Mathematical Problems in Engineering
Volume 2020, Article ID 6677084, 12 pages
https://doi.org/10.1155/2020/6677084

Research Article

Stability, Chaos Detection, and Quenching Chaos in the Swing Equation System

Shun-Chang Chang

Department of Mechanical and Automation Engineering, Da-Yeh University, No. 168 University Road, Dacun, Changhua 51591, Taiwan

Correspondence should be addressed to Shun-Chang Chang; changsc@mail.dyu.edu.tw

Received 31 October 2020; Revised 21 November 2020; Accepted 5 December 2020; Published 23 December 2020

Academic Editor: Viet-Thanh Pham

The main objective of this study is to explore the complex nonlinear dynamics and chaos control in power systems. The rich dynamics of power systems were observed over a range of parameter values in the bifurcation diagram. Also, a variety of periodic solutions and nonlinear phenomena could be expressed using various numerical skills, such as time responses, phase portraits, Poincaré maps, and frequency spectra. They have also shown that power systems can undergo a cascade of period-doubling bifurcations prior to the onset of chaos. In this study, the Lyapunov exponent and Lyapunov dimension were employed to identify the onset of chaotic motion. Also, state feedback control and dither signal control were applied to quench the chaotic behavior of power systems. Some simulation results were shown to demonstrate the effectiveness of these proposed control approaches.

1. Introduction

The characteristics of power systems are well known to be inherently nonlinear owing to the nonlinearity of synchronous generators. The most important issue in power system operation is the prevention of voltage collapse. Various works have already studied the voltage collapse in electric power systems [1–4]. A power system is typically described by a nonlinear dynamical system of equations, including system parameters. Altering one of these parameters changes the power system dynamics that exhibit chaos motion, leading to voltage collapse. However, the chaotic motion in a power system may destabilize it, leading to voltage collapses and even catastrophic blackouts. Modern nonlinear theories of bifurcation and chaos are widely adopted in the studies of nonlinear systems, and chaos dynamics in power systems have been widely studied [5–14]. This work presents several numerical schemes, including bifurcation diagrams, phase portraits, Poincaré maps, and frequency spectra, to clearly explain the rich nonlinear dynamics in power systems. Additionally, the Lyapunov exponents of smooth dynamical systems were calculated using highly developed algorithms [15–17] with the objective of determining whether a system exhibits chaos or not.

Chaotic behaviors in power systems are considered undesirable due to the restrictions they impose on the operating ranges of electrical and mechanical devices. The dynamics of a power system become unstable when they exhibit chaotic motions. If instability is not properly controlled, it causes voltage collapse, eventually leading to blackouts [12]. Hence, in many engineering applications, control approaches are developed to convert chaotic motions into periodic orbits or steady states. Since the pioneering work of Ott et al. [18] in controlling chaos, many modified methods and other approaches have been successively proposed [19–26]. Various control algorithms have also been presented to control the chaos of power systems [8, 27–30]. This work proposed converting chaotic behaviors into periodic motions to improve the performance of system dynamics with multiple machine power system chaotic behaviors. Also, chaotic motions in a power system were inhibited using state feedback control [21, 31] and dither signal control [32], and the simulation results were

presented to confirm the feasibility and efficacy of the proposed control approaches.

2. The Problem Description and Modeling of Special Swing Equations for Three Machines

A power system model of three synchronous generators with a resistive load configuration was considered, as shown in Figure 1. Synchronous generators are the most important energy source for power systems. The study of interconnected power systems with synchronous motors as significant equipment is the key to studying the dynamic characteristics of power systems. The governing differential equations of the power system in Figure 1 can be expressed as follows [33, 34]:

$$\dot{\delta}_1 = \dot{\omega}_1, \tag{1a}$$

$$M_1\dot{\omega}_1 = -D_1\omega_1 + P_1 - F_{12}\sin(\delta_1 - \delta_2) - F_{13}\sin(\delta_1 - \delta_3), \tag{1b}$$

$$\dot{\delta}_2 = \dot{\omega}_2, \tag{1c}$$

$$M_2\dot{\omega}_2 = -D_2\omega_2 + P_2 - F_{21}\sin(\delta_2 - \delta_1) - F_{23}\sin(\delta_2 - \delta_3), \tag{1d}$$

$$\dot{\delta}_3 = \dot{\omega}_3, \tag{1e}$$

$$M_3\dot{\omega}_3 = -D_3\omega_3 + P_3 - F_{31}\sin(\delta_3 - \delta_1) - F_{32}\sin(\delta_3 - \delta_2). \tag{1f}$$

A special case of the swing equations was considered for three machines. It was assumed that machine 1 has a large inertia, i.e., $M_1 = (\overline{M}_1/\varepsilon)$ and $\varepsilon \ll 1$. The transmission line joining machines 2 and 3 is shorter than that of the other lines. Similarly, the external power P_1 is proportionally larger: $P_1 = (\overline{P}_1/\varepsilon)$. With these assumptions, the conservative swing equations for the three machines are

$$\dot{\delta}_1 = \dot{\omega}_1, \tag{2a}$$

$$\overline{M}_1\dot{\omega}_1 = -\varepsilon D_1\omega_1 + \overline{P}_1 - \varepsilon F_{12}\sin(\delta_1 - \delta_2) - \varepsilon F_{13}\sin(\delta_1 - \delta_3), \tag{2b}$$

$$\dot{\delta}_2 = \dot{\omega}_2, \tag{2c}$$

$$M_2\dot{\omega}_2 = -D_2\omega_2 + P_2 - F_{21}\sin(\delta_2 - \delta_1) - F_{23}\sin(\delta_2 - \delta_3), \tag{2d}$$

$$\dot{\delta}_3 = \dot{\omega}_3, \tag{2e}$$

$$M_3\dot{\omega}_3 = -D_3\omega_3 + P_3 - F_{31}\sin(\delta_3 - \delta_1) - F_{32}(\delta_3 - \delta_2). \tag{2f}$$

From [33, 34], δ_1 can be expressed as follows:

$$\delta_1 = -\varepsilon\mu_2\delta_2 - \varepsilon\mu_3\delta_3, \tag{3}$$

where $\mu_2 = (M_2/\overline{M}_1)$ and $\mu_3 = (M_3/\overline{M}_1)$.

By substituting equation (3) in equations (2a)–(2f), write an autonomous differential equation for δ_2, δ_3, ω_2, and ω_3 and eliminate δ_1 and ω_1 as follows:

$$\dot{\delta}_2 = \dot{\omega}_2, \tag{4a}$$

$$\begin{aligned}\dot{\omega}_2 = {} & -D_2\omega_2 + \overline{\alpha}_2 - \beta_{21}\sin[\delta_2(1 + \varepsilon\mu_2) + \varepsilon\mu_3\delta_3] \\ & - \beta_{23}\sin(\delta_2 - \delta_3),\end{aligned} \tag{4b}$$

$$\dot{\delta}_3 = \dot{\omega}_3, \tag{4c}$$

$$\begin{aligned}\dot{\omega}_3 = {} & -D_3\omega_3 + \overline{\alpha}_3 - \beta_{31}\sin[\delta_2(1 + \varepsilon\mu_2) + \varepsilon\mu_3\delta_3] \\ & - \beta_{32}\sin(\delta_3 - \delta_2),\end{aligned} \tag{4d}$$

where $\overline{\alpha}_2 = (P_2/M_2)$, $\beta_{21} = (F_{21}/M_2)$, $\beta_{23} = (F_{23}/M_2)$, $\overline{\alpha}_3 = (P_3/M_3)$, $\beta_{31} = (F_{31}/M_3)$, and $\beta_{32} = (F_{32}/M_3)$.

For convenience, let $\varepsilon = 0$, and simplify equations (4a)–(4d) into

$$\dot{\delta}_2 = \dot{\omega}_2, \tag{5a}$$

$$\dot{\omega}_2 = -D_2\omega_2 + \overline{\alpha}_2 - \beta_{21}\sin(\delta_2) - \beta_{23}\sin(\delta_2 - \delta_3), \tag{5b}$$

$$\dot{\delta}_3 = \dot{\omega}_3, \tag{5c}$$

$$\dot{\omega}_3 = -D_3\omega_3 + \overline{\alpha}_3 - \beta_{31}\sin(\delta_3) - \beta_{32}\sin(\delta_3 - \delta_2). \tag{5d}$$

From [33, 34], express $\overline{\alpha}_k$ as follows:

$$\overline{\alpha}_k = \overline{P}_k - K_f\omega_k, \quad k = 2, 3, \tag{6}$$

where P_k is a constant real power and $K_f = L_k/M_k$. L_k is a load-frequency coefficient. By substituting equation (6) in (5a)–(5d),

$$\dot{\delta}_2 = \dot{\omega}_2, \tag{7a}$$

$$\dot{\omega}_2 = -D_2\omega_2 + \overline{P}_2 - K_f\omega_2 - \beta_{21}\sin(\delta_2) - \beta_{23}\sin(\delta_2 - \delta_3), \tag{7b}$$

$$\dot{\delta}_3 = \dot{\omega}_3, \tag{7c}$$

$$\dot{\omega}_3 = -D_3\omega_3 + \overline{P}_3 - K_f\omega_3 - \beta_{31}\sin(\delta_3) - \beta_{32}\sin(\delta_3 - \delta_2). \tag{7d}$$

With $y_1 = \delta_2$, $y_2 = \omega_2$, $y_3 = \delta_3$, and $y_4 = \omega_3$ as the state variables, the state equations of the swing equation can be written as follows:

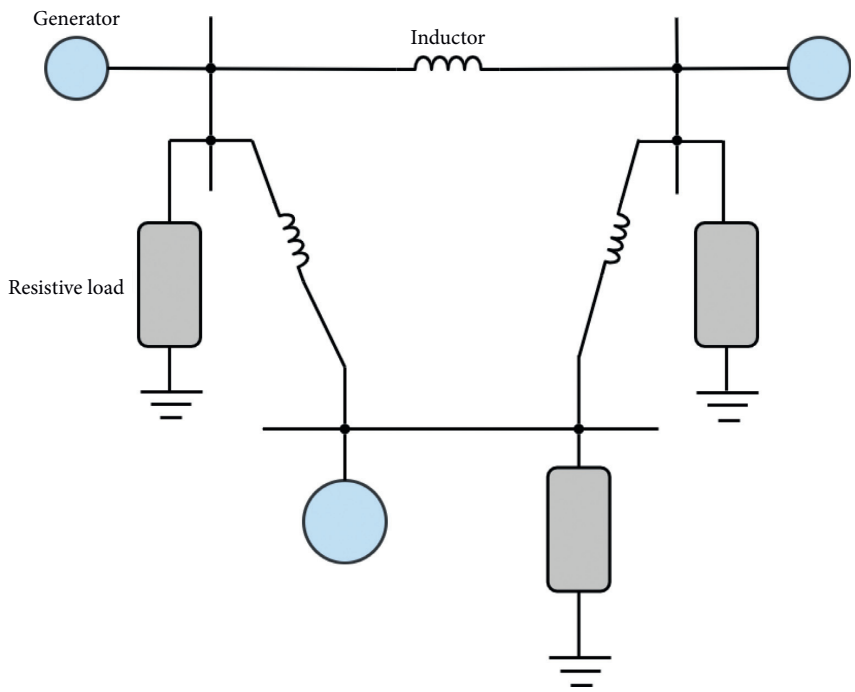

Figure 1: Schematic of a power system.

$$\dot{y}_1 = y_2, \tag{8a}$$

$$\dot{y}_2 = \overline{P}_2 - \left(D_2 + K_f\right)y_2 - \beta_{21}\sin\left(y_1\right) - \beta_{23}\sin\left(y_1 - y_3\right), \tag{8b}$$

$$\dot{y}_3 = y_4, \tag{8c}$$

$$\dot{y}_4 = \overline{P}_3 - \left(D_3 + K_f\right)y_4 - \beta_{31}\sin\left(y_3\right) - \beta_{32}\sin\left(y_3 - y_1\right). \tag{8d}$$

Table 1 [31] lists the numerical values for all the parameters in equations (8a)–(8d).

3. Overall Characteristics of the Power System: Simulation Results and Discussion

Numerical simulations were executed based on equations (8a)–(8d) to clearly understand the overall characteristics of the power system. The commercial package DIVPRK of IMSL in the FORTRAN subroutines was utilized for the mathematic applications to solve the ordinary differential equation problems [35]. Figure 2 presents the resulting bifurcation diagram, which clearly reveals that the first period-doubling bifurcation occurred at about $K_f = 0.078$ and that a chaotic motion appeared approximately below $K_f = 0.0109$. Figures 3–6 display various responses exhibited by this system in detail, where each type of response was characterized in detail using a phase portrait, a Poincaré map, and a frequency spectrum. The equilibrium point of equations (8a)–(8d) was stable with $K_f > 0.078$, revealing that no chatter vibration occurred. Figures 3(a)–3(d) show the period-1 motion. Also, Figures 4(a)–4(d) show a cascade of period-doubling bifurcations with new frequency components at $\Omega/2$, $3\Omega/2$, $5\Omega/2$. . ., causing a series of subharmonic components. Figures 5(a)–5(d) depict the first period-four bifurcation, which occurred when K_f fell below $K_f \approx 0.0275$. A cascade of chaos-inducing period-doubling bifurcations then appeared as K_f continued to fall in Figure 2, resulting in a chatter vibration that could cause a voltage collapse, thereby significantly reducing the power system performance and possibly causing catastrophic blackouts. Two descriptors, the Poincaré map and frequency spectrum, could be utilized to characterize the essence of the chaotic behavior. The Poincaré map shows an infinite set of points called a strange attractor. Simultaneously, the frequency spectrum of the chaotic motion is a continuous broad spectrum. These two main features, strange attractors and continuous-type Fourier spectrum, are strong indicators of chaos. Figures 6(a)–6(d) clearly reveal the chaotic behavior in detail.

4. Lyapunov Exponent and Lyapunov Dimension for Analyzing the Chaos in the Power System

As described in Section 3, the chaotic motion in power systems is difficult to identify using traditional approaches. This section describes the use of Lyapunov exponents to verify the occurrence of chaos in power systems. Every dynamic system involves a spectrum of Lyapunov exponents (λ) [15], indicating changes in the length, area, and volume within a phase space. To determine whether a system exhibits the characteristics of chaos, only the largest Lyapunov exponent needs to be calculated to determine

Table 1: Physical parameters of a power system.

Parameter	Value
β_{21}	−2
β_{23}	−1
β_{31}	−1
β_{32}	−1
D_2	0.2
D_3	0.5
$\overline{P}_2$	0.3
$\overline{P}_3$	0.5

whether nearby trajectories diverge ($\lambda > 0$) or converge ($\lambda < 0$) on average. Any bounded motion in a system with at least one positive Lyapunov exponent is defined as chaotic, whereas periodic motions exhibit no positive Lyapunov exponents.

Figure 7 plots the evolutions of the largest Lyapunov exponent in the power system, as computed using the algorithm proposed by Wolf et al. [15]. This figure reveals that the onset of the chaotic motion occurred at approximately $K_f = 0.0109$. At point $\mathbf{P_3}$, the sign of the largest Lyapunov exponent changed from negative to positive as the parameter K_f slowly decreased. At points $\mathbf{P_1}$ and $\mathbf{P_2}$, the largest Lyapunov exponents approached zero, which is beyond the point at which the system can undergo bifurcation. Nonetheless, the Lyapunov exponent at that point provided no indication of the involved bifurcation type, thereby necessitating the application of a bifurcation diagram, as shown in Figure 2. A conducted comparison of Figures 7 and 2 indicated the occurrence of period-2 bifurcation at $\mathbf{P_1}$ and period-4 bifurcation at $\mathbf{P_2}$. When $K_f = 0.09$, the Lyapunov exponents obtained using equations (8a)–(8d) were $\lambda_1 = -0.000084$, $\lambda_2 = -0.0157341$, $\lambda_3 = -0.5120906$, and $\lambda_4 = -0.5977934$, and their sum was $\lambda_1 + \lambda_2 + \lambda_3 + \lambda_4 = -1.1257021$, which is negative, indicating that the power system had stable periodic motion. By denoting $\lambda_1 \geq \cdots \geq \lambda_n$ as the Lyapunov exponents of a dynamical system, Kaplan and Yorke [36] expressed the estimate of the Lyapunov dimension d_L as

$$d_L = j + \frac{1}{\left|\lambda_{j+1}\right|} \sum_{i=1}^{j} \lambda_i, \quad \text{where} \sum_{i=1}^{j} \lambda_i > 0 \text{ and} \sum_{i=1}^{j+1} \lambda_i < 0. \tag{9}$$

Thus, the Lyapunov dimension is an integer for periodic orbits and a noninteger for chaotic motion. Using equations (8a)–(8d) with $K_f = 0.09$, this calculation yielded a Lyapunov dimension of $d_L = 1$. Therefore, this system exhibited periodic motion, as the Lyapunov dimension was an integer. When the parameter K_f continuously decreased across bifurcation point $\mathbf{P_3}$, for example, $K_f = 0.009$, the Lyapunov exponents were $\lambda_1 = 0.0340716$, $\lambda_2 = -0.0000068$, $\lambda_3 = -0.3985904$, and $\lambda_4 = -0.5270599$, and the Lyapunov dimension was $d_L = 2.0854$. Obviously, the power system could be demonstrated to exhibit chaotic motion, as the largest Lyapunov exponent was positive and the Lyapunov dimension was a noninteger.

5. Quenching Chaos in the Power System

Analyzing and predicting the behaviors of chaotic systems are beneficial, but a system needs to be controlled to maximize its benefits. Improving the performance of a dynamic system and avoiding chaotic motion both require periodic motion, which is more important when working under specific conditions. This section presents two control methods, state feedback control [21, 31] and dither control [32], to suppress the chaos in the used power system in this study.

5.1. State Feedback Control. Cai et al. [21, 31] proposed a simple and effective method for converting chaos into periodic motion at a steady state using the linear-state feedback of an available system variable. For an n-dimensional dynamic system, this method can be briefly summarized as follows:

$$\dot{x} = f(x, t), \tag{10}$$

where $x(t) \in R^n$ is the state vector and $f = (f_1, \ldots, f_i, \ldots, f_n)$, where f_i is a linear or nonlinear function and f includes at least one nonlinear function. If $f_k(x, t)$ is the key nonlinear function that leads to chaotic motion in equation (10), only one term of the state feedback of an available system variable x_m was added to the equation that includes $f_k(x, t)$ as follows:

$$\dot{x}_k = f_k(x, t) + Kx_m, \quad k, m \in \{1, 2, \ldots, n\}, \tag{11}$$

where K is the feedback gain, and the other functions keep their original forms.

Equations (8a)–(8d) can be rewritten as follows with the state feedback control:

$$\dot{y}_1 = y_2, \tag{12a}$$

$$\dot{y}_2 = \overline{P}_2 - \left(D_2 + K_f\right) y_2 - \beta_{21} \sin\left(y_1\right) - \beta_{23} \sin\left(y_1 - y_3\right) + K y_2, \tag{12b}$$

$$\dot{y}_3 = y_4, \tag{12c}$$

$$\dot{y}_4 = \overline{P}_3 - \left(D_3 + K_f\right) y_4 - \beta_{31} \sin\left(y_3\right) - \beta_{32} \sin\left(y_3 - y_1\right) + K y_4. \tag{12d}$$

Without the state feedback control, equations (8a)–(8d) exhibited chaotic behavior under the parameter $K_f = 0.009$. Considering that the effect of the state feedback control was

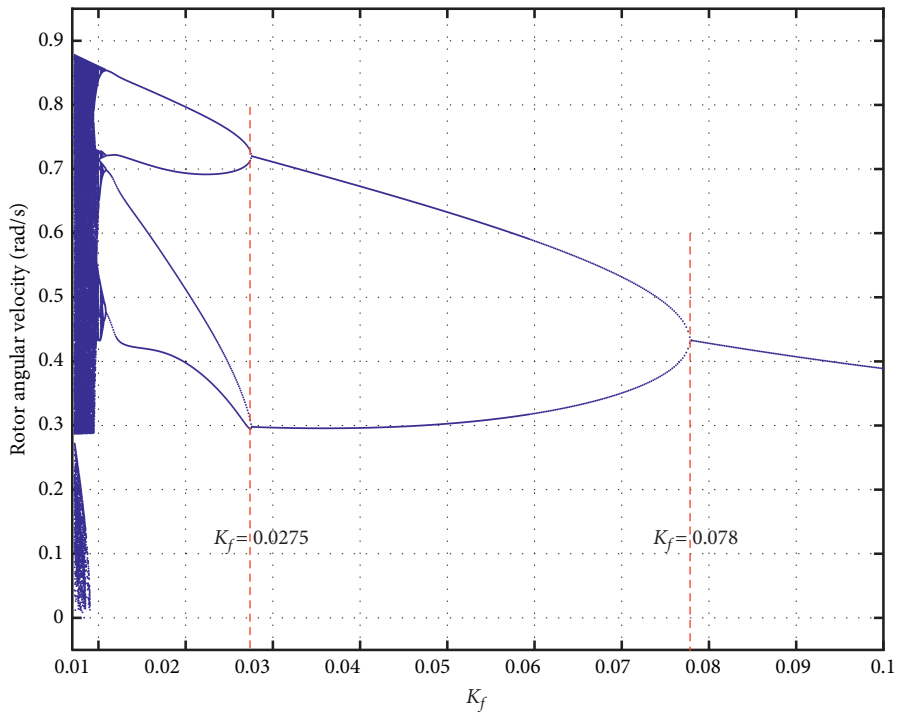

Figure 2: Bifurcation diagram of the rotor angular velocity against K_f.

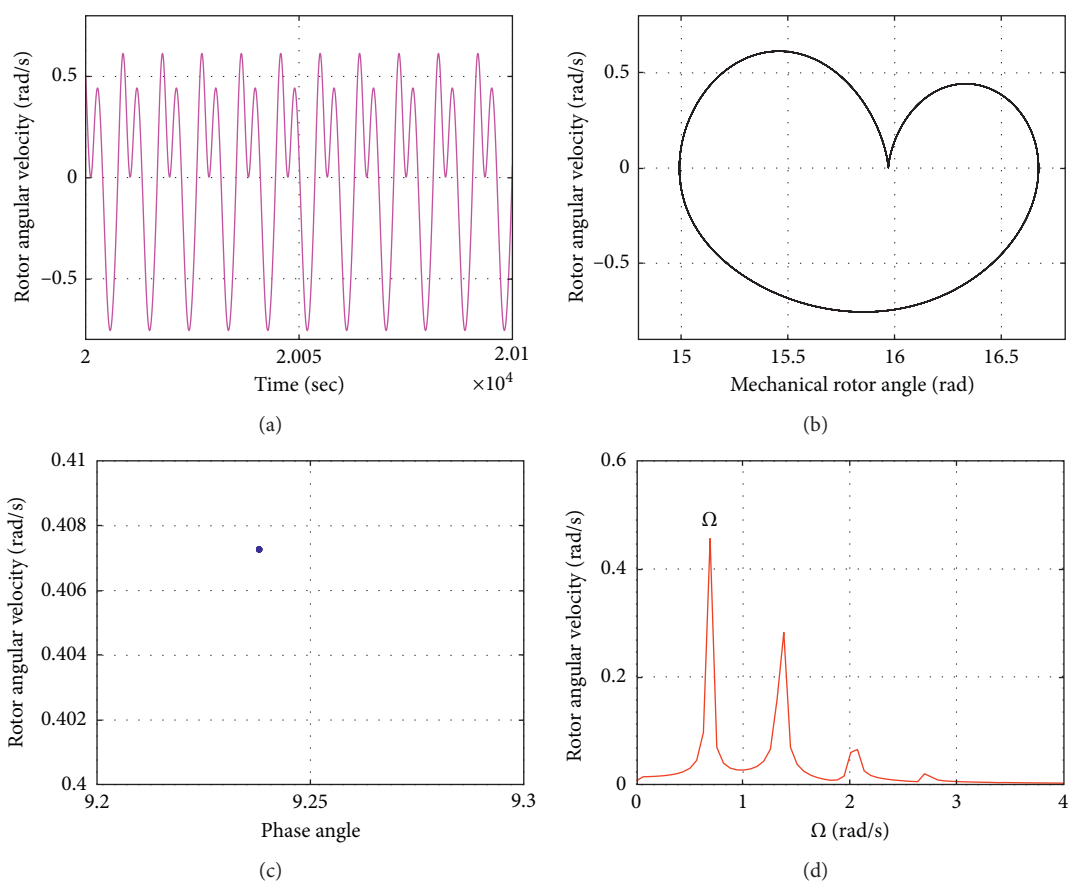

Figure 3: Period-1 orbit of the numerical simulation results for $K_f = 0.09$: (a) time responses; (b) phase portrait; (c) Poincaré map; (d) frequency spectrum.

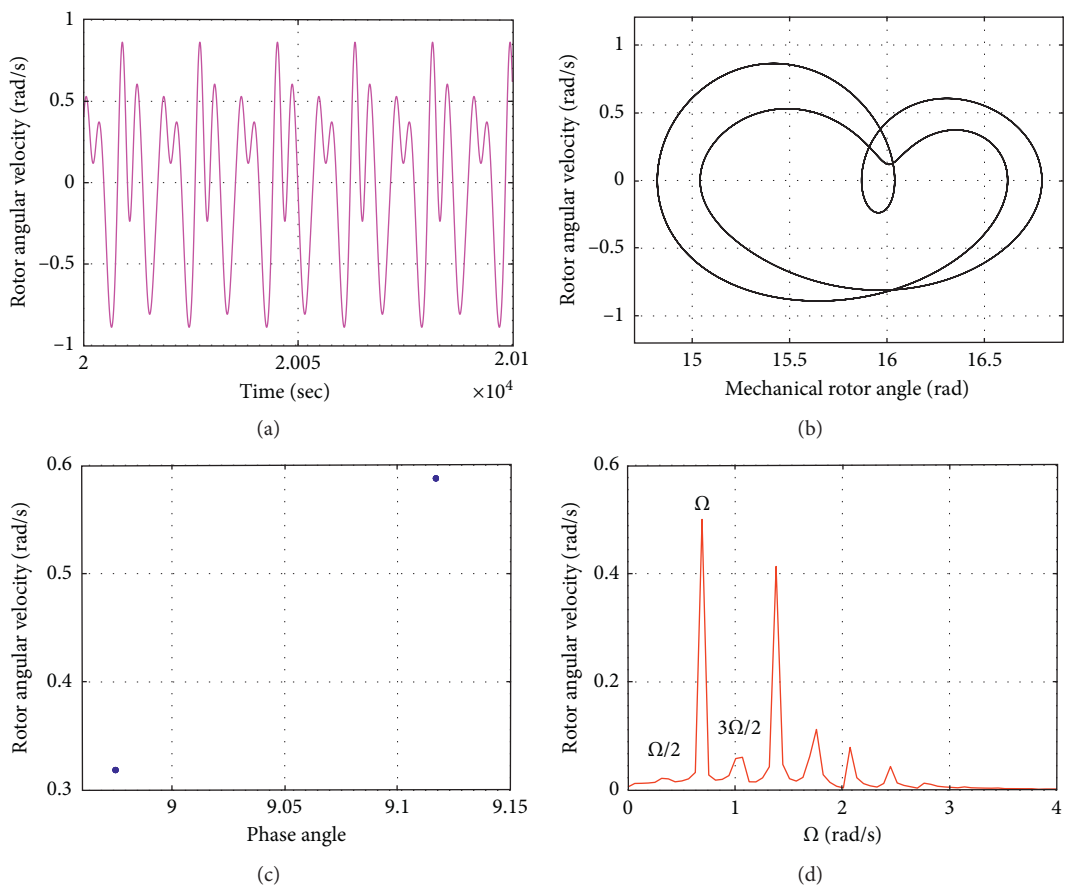

FIGURE 4: Period-2 orbit of the numerical simulation results for $K_f = 0.06$: (a) time responses; (b) phase portrait; (c) Poincaré map; (d) frequency spectrum.

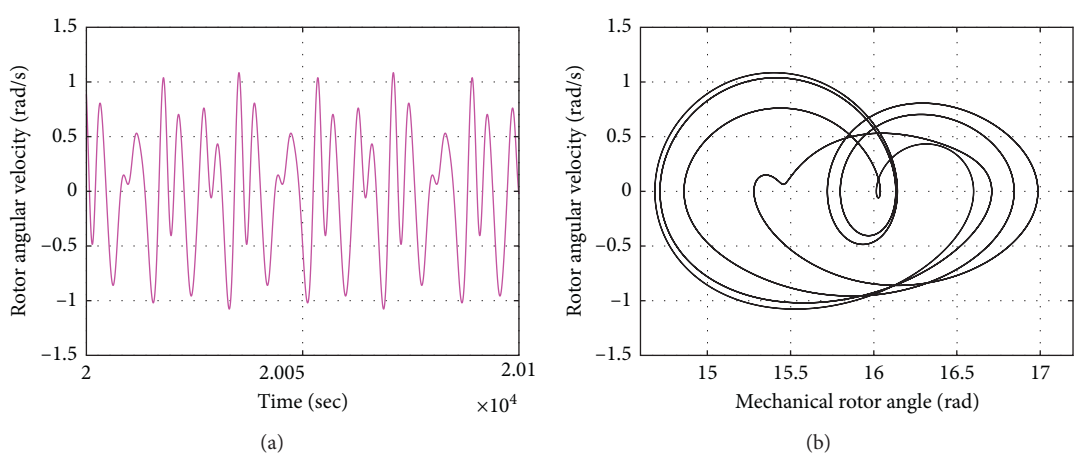

FIGURE 5: Continued.

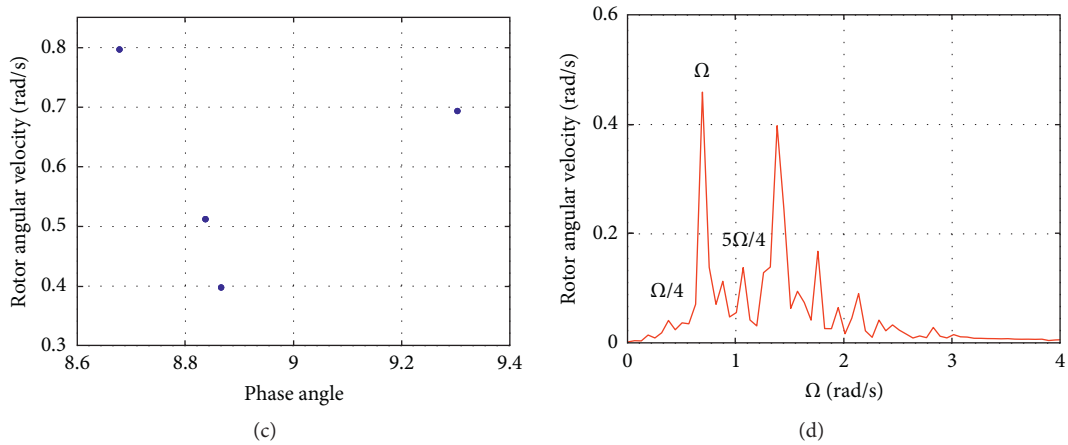

FIGURE 5: Period-4 orbit of the numerical simulation results $K_f = 0.02$: (a) time responses; (b) phase portrait; (c) Poincaré map; (d) frequency spectrum.

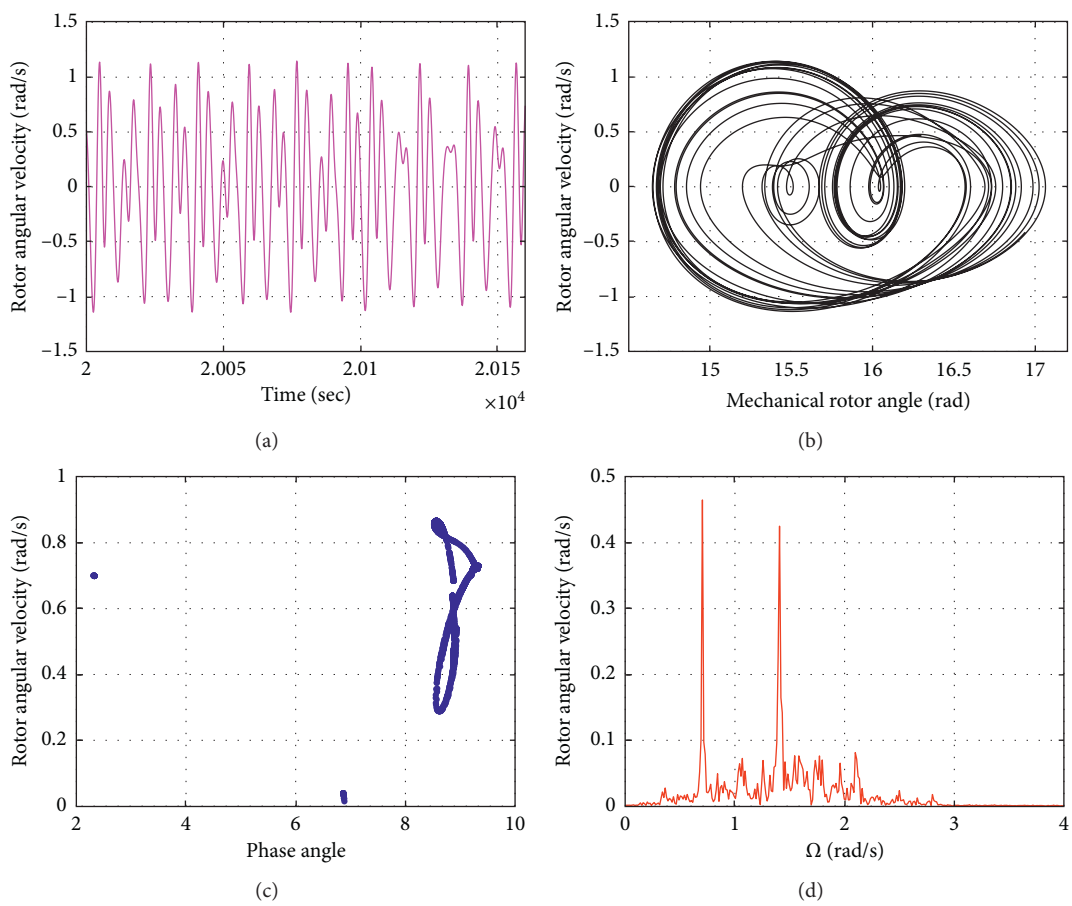

FIGURE 6: Chaotic motion of the numerical simulation results for $K_f = 0.009$: (a) time responses; (b) phase portrait; (c) Poincaré map; (d) frequency spectrum.

added to the right-hand side of equations (8a)–(8d), by decreasing the feedback gain K from 0 to −0.1, the chaotic behavior disappeared at certain feedback gains. Figure 8 presents the resulting bifurcation diagram, which comprehensively explains the dynamic behavior of the controlled power system over a range of feedback gains. Chaotic motion appeared when $K < -0.0008$, and stable periodic motion appeared when K decreased beyond −0.0008. Period-doubling bifurcations

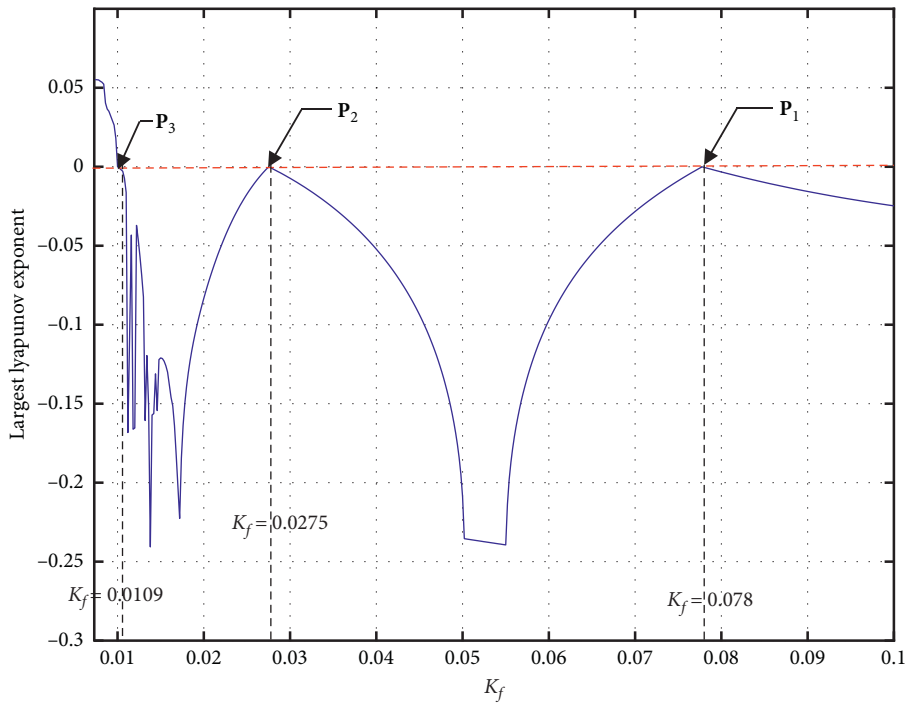

Figure 7: Evolutions of the largest Lyapunov exponent versus K_f.

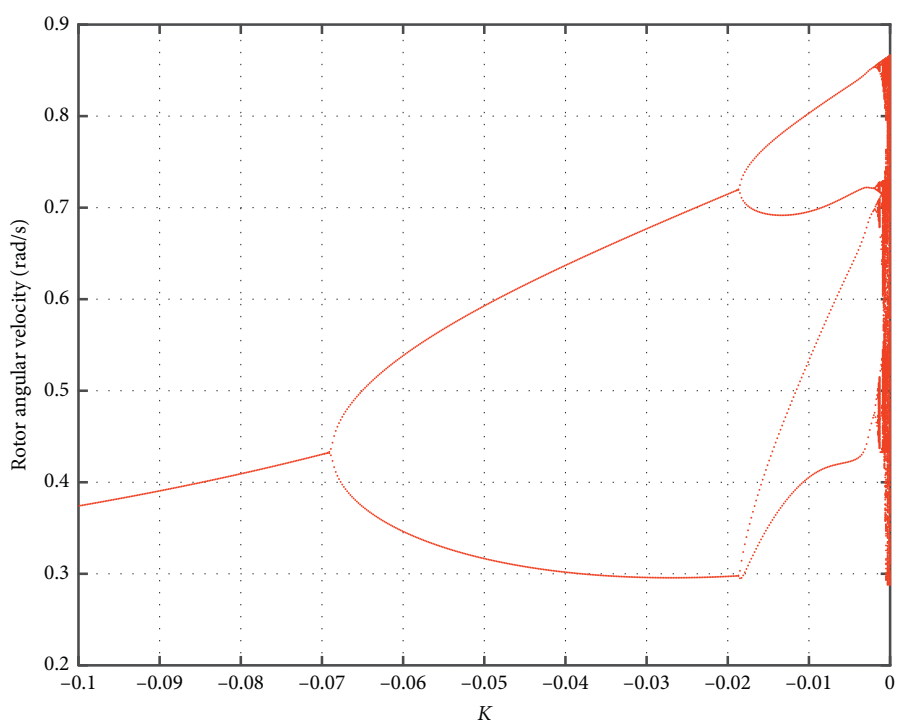

Figure 8: Bifurcation diagram of the rotor angular velocity against K for the power system with the state feedback control, where K indicates the feedback gain.

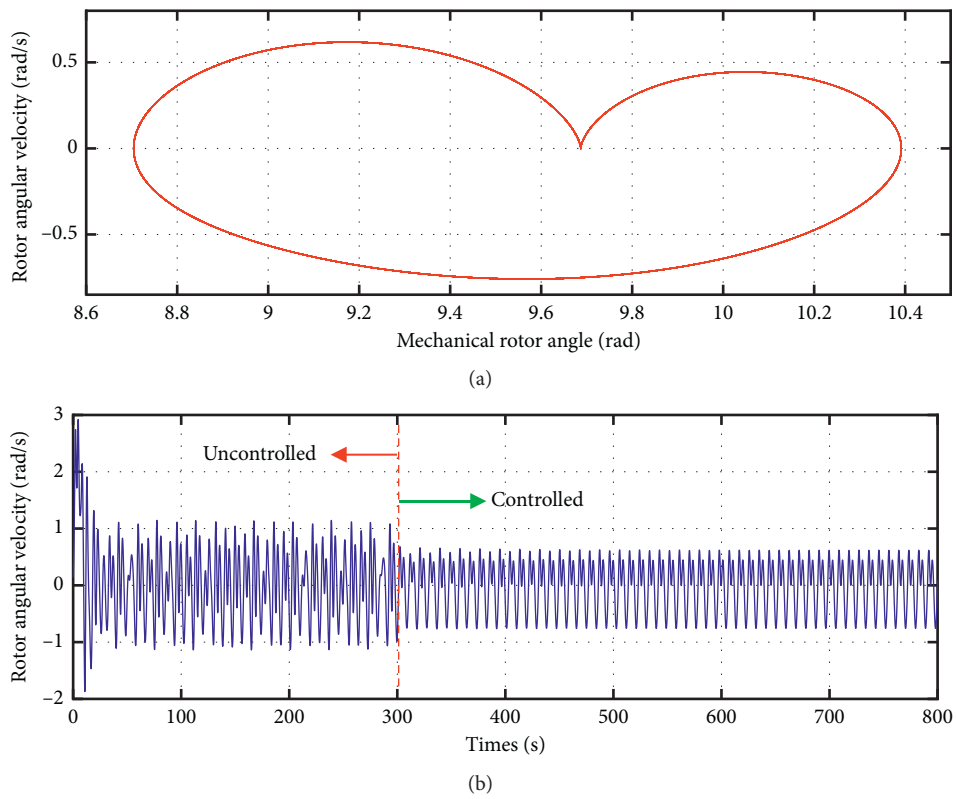

Figure 9: Transforming chaotic motion into a period-1 orbit for $K = -0.08$ and $K_f = 0.009$: (a) phase portrait of the controlled system; (b) time responses of the controlled system. A state feedback control signal was introduced after 300 s.

appeared when K decreased to between about −0.0699 and −0.0008. A further decrease in K beyond −0.0699 resulted in a period-1 motion. The efficacy of the proposed system in controlling chaos was demonstrated by applying a control signal after 300 seconds, as shown in Figure 9. Therefore, to suppress the occurrence of chaos, the simple state feedback of an available system variable can be sufficient to disturb the balance of dynamic behaviors in a chaotic system.

5.2. Dither Control. This section describes how to control motion in a chaotic system by injecting another external input dither signal to only modify nonlinear terms. A dither signal averages nonlinearity due to its high frequency and periodic nature. Researchers have developed dither smoothing methods [32, 37] to stabilize chaotic systems, and popular dither signals were proposed in [38]. The simplest dither signal is a square-wave dither signal in which the frequency and amplitude are 2000 rad/s and W, respectively, in front of the nonlinearity $f(.)$. Therefore, the effective value of μ and the output of the nonlinear element can be expressed as

$$\mu = \frac{1}{2}\left[f(y+W) + f(y-W)\right]. \tag{13}$$

Consequently, the system equation can be expressed as

$$\dot{y} = \mu. \tag{14}$$

Considering the influence of the dither signal control added to systems (8a)–(8d) under the parameter $K_f = 0.009$, by raising the amplitude of the square-wave dither signal from $W = 0$ to $W = 0.5$, the dynamics changed from chaotic behaviors to periodic motions. Figure 10 displays the evolution of the bifurcation diagram. Figure 11(a) depicts the time response of the displacement with the amplitude of the square-wave dither signal $W = 0.2$. The chaotic behavior system was transformed into a period-1 orbit. Figure 11(b) illustrates the phase portrait of the controlled system. Notably, the system exhibited a chaotic behavior before dither was introduced but exhibited a periodic motion afterward.

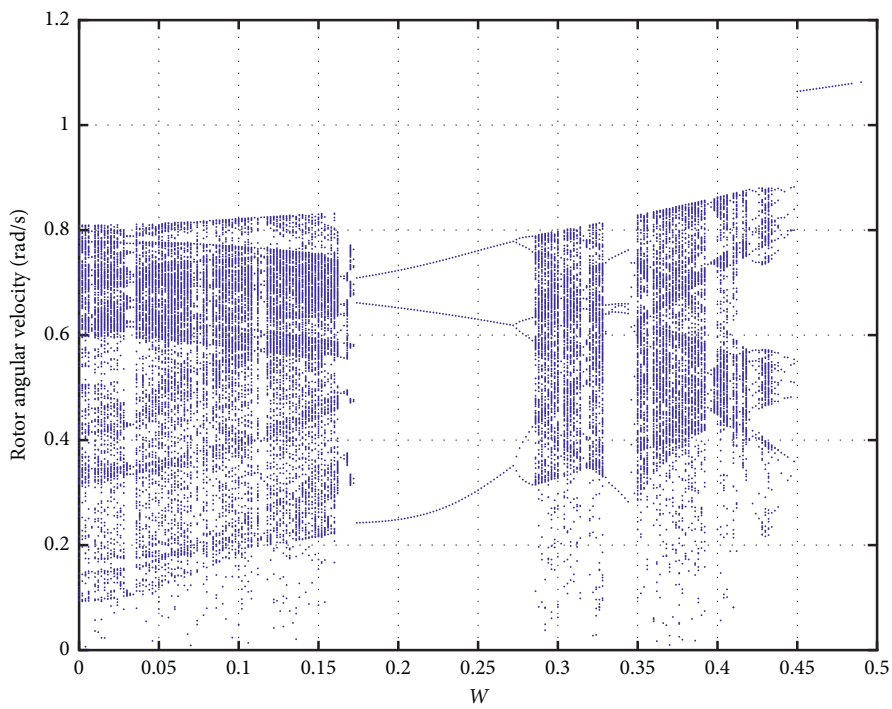

Figure 10: Bifurcation diagram of the rotor angular velocity against W for the power system with square-wave dither, where W represents the dither amplitude.

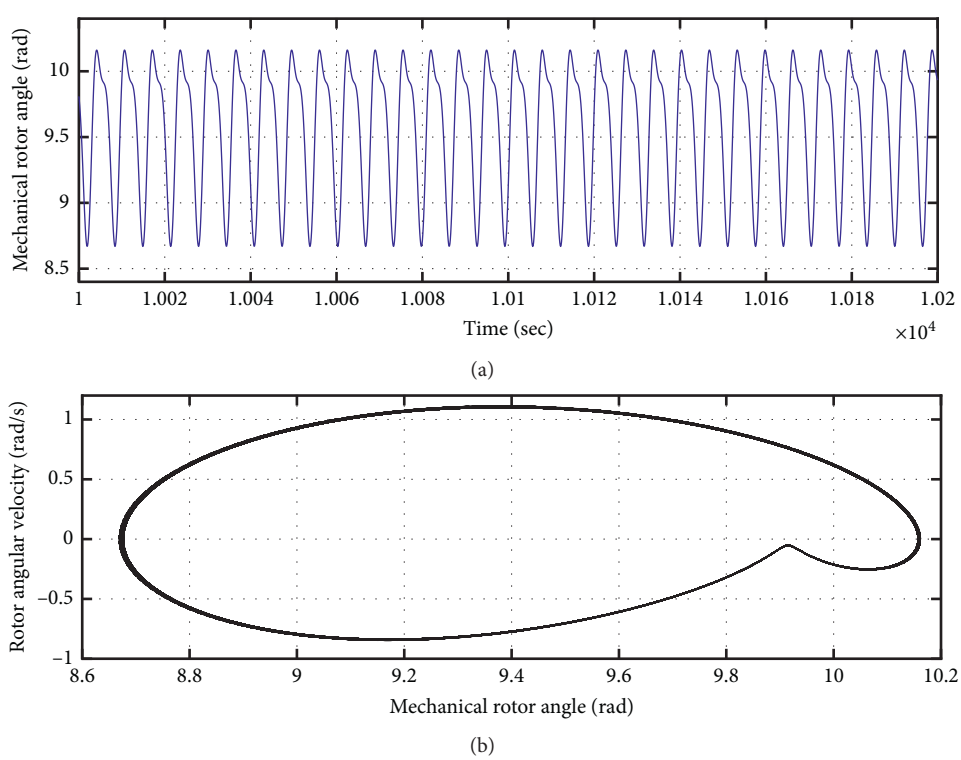

Figure 11: A square-wave dither signal was injected to control the chaotic motion of the power system for $W = 0.2$ and $K_f = 0.009$: (a) time responses of the controlled system; (b) phase portrait of the controlled system.

6. Conclusions

This work addressed the rich nonlinear dynamics and chaos control in power systems. The resulting bifurcation diagram showed many nonlinear behaviors, indicating that the tested power system exhibited chaotic motion at lower K_f, meaning that the system could undergo a cascade of period-doubling bifurcations prior to the onset of chaos. Numerical approaches, including phase portraits, Poincaré maps, and frequency spectra, were employed to explore the dynamics of the used power system. The most powerful algorithm to determine whether a power system is in chaotic motion or not is to use the Lyapunov exponent and Lyapunov dimension. The presence of a chaotic behavior was generic for certain nonlinearities, parameter ranges, and external forces, and it may need to be avoided or controlled to improve the performance of the power system. The state feedback control scheme was simple and effective for chaos suppression, and it can be implemented by adding the feedback of suitable variables to the original system with sufficient control gain to quench chaos development. Additionally, the square wave of the dither signal can be applied to efficiently convert a chaotic motion into a periodic orbit by injecting a dither signal in front of the nonlinearity of the power system. We believe that studying the nonlinear dynamics and chaos control in power systems will help prevent voltage collapses and advance the development of smart power systems.

Other numerous methods for chaos control have been devised, such as synchronization control, time-delayed feedback control, neurofuzzy control, adaptive control, and bang-bang control. In this study, two chaos control strategies, state feedback control and dither control, were implemented to control the chaotic behavior of a power system. The effectiveness of these proposed chaos control strategies was illustrated through numerical simulations. Also, a simple control method was presented to convert chaos into periodic motion using the linear-state feedback of an available system variable. Overall, it was found that compared with other chaos control methods, the state feedback control technique is simple and can be easily implemented in chaos suppression. Finally, the robustness of the parametric perturbation on a chaotic system with various chaos control methods will be studied in my future work.

Data Availability

No experimental data are used to support this study.

Conflicts of Interest

The author declares that there are no conflicts of interest regarding the publication of this paper.

Acknowledgments

The author would like to thank the Ministry of Science and Technology in Taiwan, Republic of China, for financially supporting this research under Contract No. MOST 108-2221-E-212 -010 -MY3.

References

[1] H. O. Wang, E. H. Abed, and A. M. A. Hamdan, "Bifurcations, chaos, and crises in voltage collapse of a model power system," *IEEE Transactions on Circuits and Systems I: Fundamental Theory and Applications*, vol. 41, no. 3, pp. 294–302, 1994.

[2] I. G. Adebayo and Y. Sun, "Performance evaluation of voltage stability indices for a static voltage collapse prediction," in *Proceedings of the 2020 IEEE PES/IAS PowerAfrica*, October 2020.

[3] R. Tiwari, K. R. Niazi, and V. Gupta, "Line collapse proximity index for prediction of voltage collapse in power systems," *International Journal of Electrical Power & Energy Systems*, vol. 41, no. 1, pp. 105–111, 2012.

[4] R. M. M. Pereira, C. M. M. Ferreira, and F. P. M. Barbosa, "Comparative study of STATCOM and SVC performance on dynamic voltage collapse of an electric power system with wind generation," *IEEE Latin America Transactions*, vol. 12, no. 2, pp. 138–145, 2014.

[5] U. G. Vaidya, R. N. Banavar, and N. M. Singh, "A chaotic phenomenon in the damped power swing equation," in *Proceedings of the 38th IEEE Conference on Decision and Control*, pp. 4650–4655, Phoenix, AZ, USA, August 1999.

[6] Y. Yu, H. Jia, P. Li, and J. Su, "Power system instability and chaos," *Electric Power Systems Research*, vol. 65, no. 3, pp. 187–195, 2003.

[7] L. Kuru, E. Kuru, and M. A. Yalcin, "An application of chaos and bifurcation in nonlinear dynamical power systems," in *Proceedings of the 2nd International IEEE Conference on Intelligent Systems*, Varna, Bulgaria, June 2004.

[8] H. Gholizadeh, A. Hassannia, and A. Azarfar, "Chaos detection and control in a typical power system," *Chinese Physics B*, vol. 22, no. 1, 2013.

[9] X. Wang, Y. Chen, G. Han, and C. Song, "Nonlinear dynamic analysis of a single-machine infinite-bus power system," *Applied Mathematical Modelling*, vol. 39, no. 10-11, pp. 2951–2961, 2015.

[10] P. M. Vahdati and A. Kazemi, "Bifurcations and chaos in nonlinear dynamics of power systems," in *Proceedings of the 24th Iranian Conference on Electrical Engineering (ICEE)*, pp. 1706–1711, Shiraz, Iran, May 2016.

[11] K. Rajagopal, A. Karthikeyan, P. Duraisamy, R. Weldegiorgis, and G. Tadesse, "Bifurcation, chaos and its control in a fractional order power system model with uncertainties," *Asian Journal of Control*, vol. 21, no. 1, pp. 184–193, 2019.

[12] H. Ma, F. Min, and Y. Wang, "Nonlinear dynamic analysis and surface sliding mode controller based on low pass filter for chaotic oscillation in power system with power disturbance," *Chinese Journal of Physics*, vol. 56, no. 5, pp. 2488–2499, 2018.

[13] L. Zhou and F. Chen, "Chaotic dynamics for a class of single-machine-infinite bus power system," *Journal of Vibration and Control*, vol. 24, no. 3, pp. 582–587, 2018.

[14] X. Wang, Z. Lu, and C. Song, "Chaotic threshold for a class of power system model," *Shock and Vibration*, vol. 2019, Article ID 3479239, 7 pages, 2019.

[15] A. Wolf, J. B. Swift, H. L. Swinney, and J. A. Vastano, "Determining Lyapunov exponents from a time series," *Physica D: Nonlinear Phenomena*, vol. 16, no. 3, pp. 285–317, 1985.

[16] G. Benettin, L. Galgani, A. Giorgilli, and J.-M. Strelcyn, "Lyapunov Characteristic Exponents for smooth dynamical systems and for Hamiltonian systems; a method for computing all of them. Part 1: Theory," *Meccanica*, vol. 15, no. 1, pp. 9–20, 1980.

[17] G. Benettin, L. Galgani, A. Giorgilli, and J.-M. Strelcyn, "Lyapunov Characteristic Exponents for smooth dynamical systems and for Hamiltonian systems; A method for computing all of them. Part 2: numerical application," *Meccanica*, vol. 15, no. 1, pp. 21–30, 1980.

[18] E. Ott, C. Grebogi, and J. A. Yorke, "Controlling chaos," *Physical Review Letters*, vol. 64, no. 11, pp. 1196–1199, 1990.

[19] W. L. Ditto, S. N. Rauseo, and M. L. Spano, "Experimental control of chaos," *Physical Review Letters*, vol. 65, no. 26, pp. 3211–3214, 1990.

[20] E. R. Hunt, "Stabilizing high-period orbits in a chaotic system: the diode resonator," *Physical Review Letters*, vol. 67, no. 15, pp. 1953–1955, 1991.

[21] C. Cai, Z. Xu, W. Xu, and B. Feng, "Notch filter feedback control in a class of chaotic systems," *Automatica*, vol. 38, no. 4, pp. 695–701, 2002.

[22] S. C. Chang and Y. F. Lue, "A study of the nonlinear response and chaos suppression in a magnetically levitated system," *Australian Journal of Mechanical Engineering*, vol. 18, no. 1, pp. 94–105, 2020.

[23] D. D. A. Costa and M. A. Savi, "Chaos control of an SMA-pendulum system using thermal actuation with extended time-delayed feedback approach," *Nonlinear Dynamics*, vol. 93, no. 2, pp. 571–583, 2018.

[24] P. Tooranjipour and R. Vatankhah, "Adaptive critic-based quaternion neuro-fuzzy controller design with application to chaos control," *Applied Soft Computing*, vol. 70, pp. 622–632, 2018.

[25] O. I. Tacha, C. K. Volos, I. M. Kyprianidis, I. N. Stouboulos, S. Vaidyanathan, and V.-T. Pham, "Analysis, adaptive control and circuit simulation of a novel nonlinear finance system," *Applied Mathematics and Computation*, vol. 276, no. 5, pp. 200–217, 2016.

[26] O. Tutsoy and M. Brown, "Chaotic dynamics and convergence analysis of temporal difference algorithms with bang-bang control," *Optimal Control Applications and Methods*, vol. 37, no. 1, pp. 108–126, 2016.

[27] M. J. Liu and Z. L. Piao, "Study on chaos control for nonlinear power system," in *Proceedings of the IEEE International Workshop on Intelligent Systems and Applications*, Wuhan, China, May 2009.

[28] M. Kumar and P. P. Singh, "Chaos control of an extended four dimensional fundamental power system using sliding mode control," in *Proceedings of the 5th IEEE Uttar Pradesh Section International Conference on Electrical, Electronics and Computer Engineering (UPCON)*, November 2018.

[29] C. Wang, H. L. Zhang, W. H. Fan, and P. Ma, "Finite-time function projective synchronization control method for chaotic wind power systems," *Chaos, Solitons and Fractals*, vol. 135, pp. 1–12, 2020.

[30] J. Wang, L. Liu, C. Liu, and X. Li, "Adaptive sliding mode control based on equivalence principle and its application to chaos control in a seven-dimensional power system," *Mathematical Problems in Engineering*, vol. 2020, Article ID 1565460, 13 pages, 2020.

[31] C. Cai, Z. Xu, and W. Xu, "Converting chaos into periodic motion by state feedback control," *Automatica*, vol. 38, no. 11, pp. 1927–1933, 2002.

[32] C. C. Fun and P. C. Tung, "Experimental and analytical study of dither signals in a class of chaotic system," *Physics Letters A*, vol. 229, no. 4, pp. 228–234, 1997.

[33] N. Kopell and R. Washburn, "Chaotic motions in the two-degree-of-freedom swing equations," *IEEE Transactions on Circuits and Systems*, vol. 29, no. 11, pp. 738–746, 1982.

[34] S. C. Chang, "*Study of Structural Stability for Power System*," M.S. thesis, National Central University, Taoyuan City, Taiwan, 1992.

[35] IMSL, Inc User's Manual–IMSL MATH/LIBRARY, 1989.

[36] J. L. Kaplan and L. A. York, "Chaotic behavior of multidimensional difference equations," *Lecture Notes in Mathematics*, Springer, New York, NY, USA, 1979.

[37] Y. M. Liaw and P. C. Tung, "Application of the differential geometric method to control a noisy chaotic system via dither smoothing," *Physics Letters A*, vol. 239, no. 1-2, pp. 51–58, 1998.

[38] P. A. Cook, *Nonlinear Dynamical Systems*, Prentice-Hall, Upper Saddle River, NY, USA, 1994.

Hindawi
Mathematical Problems in Engineering
Volume 2020, Article ID 6620570, 12 pages
https://doi.org/10.1155/2020/6620570

Research Article

Asymmetric Information on Price Can Affect Bertrand Duopoly Players with the Gradient-Based Mechanism

S. S. Askar [1,2]

[1]*Department of Statistics and Operations Research, College of Science, King Saud University, Riyadh 11451, Saudi Arabia*
[2]*Department of Mathematics, Faculty of Science, Mansoura University, Mansoura 35516, Egypt*

Correspondence should be addressed to S. S. Askar; s.e.a.askar@hotmail.co.uk

Received 26 October 2020; Revised 22 November 2020; Accepted 24 November 2020; Published 10 December 2020

Academic Editor: Adel Ouannas

We study a Bertrand duopoly game in which firms adopt a gradient-based mechanism to update their prices. In this competition, one of the firms knows somehow the price adopted by the other firm next time step. Such asymmetric information of the market price possessed by one firm gives interesting results about its stability in the market. Under such information, we use the bounded rationality mechanism to build the model describing the game at hand. We calculate the equilibrium points of the game and study their stabilities. Using different sets of parameter values, we show that the interior equilibrium point can be destabilized through flip and Neimark–Sacker bifurcations. We compare the region of stability of the proposed model with a classical Bertrand model without asymmetric information. The results show that the proposed game's map is noninvertible with type $Z_0 - Z_2$ or $Z_1 - Z_3$, while the classical model is of type $Z_0 - Z_2$ only. This explains the quite complicated basins of attraction given for the proposed map.

1. Introduction

The Bertrand competition was introduced as a model describing an economic game by the famous scientist Joseph Louis François Bertrand [1]. Such game was used in the literature to simulate interactions among firms (players) who set prices as their strategies. Bertrand claimed but not formalized that firms set prices than quantities as their outputs in the competition would take place with prices and marginal costs that are equal. Comparing Cournot games (on where players set quantities as their strategies) with Bertrand, we report few studies on Bertrand games in the literature. For instance, the minimal differentiation principle was tested in a Bertrand competition in [2], and it was found that it was applied to spatial competition. The capacity precommitment as an entry-deterring device was reexamined in [3] on the price competition of Bertrand–Edgeworth model. In [4], a repeated game of price was studied to detect that when the number of competing firms increased above two competitive players, the outcomes become less likely. For the case of spatial discrimination, a comparison between Bertrand and Cournot in the context of spatial duopoly was analyzed in [5]. In [6], a Bertrand game with an uncertain number of active firms was analyzed. In the case of differentiated quantities, a price setting game has been analyzed in a continuous time scale with random demands [7].

All the above reported studies handled the price setting game statically. There are few studies of Bertrand games about the complex dynamic characteristics of their equilibrium points. We report some of them from the literature as follows. In [8], a Bertrand game whose players adopted the bounded rationality mechanism to update their prices investigated that bifurcation and chaos may occur when the speed of adjustment of players also increases. Ma and Wu [9] introduced the game of Bertrand triopoly with bounded rational players and investigated that the time delay may not improve the stability region of the game. Ma and Sun studied the multiteam Bertrand game in [10]. In [11], a Bertrand game with delayed bounded rational players was considered. In that study, it was pointed out that lagged structure may affect the stable region of the stable state. For substitutable

products in a supply chain [12], the game of price setting analyzed the influences of different competitive strategies on optimum decisions of prices. In [13], an advertising cost-dependent demand for a two-echelon supply chain was investigated, and the obtained results showed that it was beneficial for the firms to use different wholesale pricing strategies. With differentiated products, the complex dynamic characteristics of a Bertrand game were discussed by Fanti et al. in [14]. They have deduced that the interior fixed point can be destabilized when differentiation between firms increased, and therefore, chaotic attractors with complicated structure may arise. Other studies on Bertrand and Cournot–Bertrand games and more information on their complex dynamic behaviors have been reported in the literature [15, 16]. We should also highlight some recent studies on the Bertrand game. For instance, in [17], the bounded rationality and naive expectation mechanisms were used to study a dynamic model of the quantum Bertrand game with differentiated products. In [18], a Bertrand game in the downstream market was investigated. A triopoly Bertrand game based on differentiated products was investigated in [19]. A Cournot–Bertrand game was introduced and studied in [20]. In [21], necessary and sufficient conditions for a unique Nash equilibrium in a standard Bertrand duopoly game based on homogeneous products were analyzed.

There are different types of adjustment mechanisms that have been adopted to model the maps describing such games. For instance, there are the gradient-based mechanisms such as bounded rationality. Bounded rationality has been intensively used for this purpose in the literature [22–27]. This mechanism depends on the estimation of players' profits for updating their outputs. If the profits are increased (or decreased), this will affect the prices whether they will be increased (or decreased). There are also other mechanisms that have been used to formulate the Bertrand and Cournot games such as the local monopolistic approximation (LMA) mechanism [28] and tit-for-tat approach [29]. In the paper at hand, we recall the bounded rationality mechanism to formulate our Bertrand game.

The current paper belongs to the research direction of the Bertrand game with players adopting the bounded rationality, and one of the players possesses information about the price its opponent adopts. We model the game by introducing a discrete-time dynamical map whose variables are prices, and it is nonlinear. The main results in this paper focus on many things. We concern with the destabilization of the interior equilibrium and the routes responsible for that. We investigate the flip and Neimark–Sacker bifurcations under different types of parameter sets causing chaotic behavior of the game's map. Depending on a rich numerical analysis, we show different types of quite complicated attractive basins of periodic cycles. Furthermore, the noninvertibility aspect is numerically discussed for the map.

The paper presents the map describing the game in Section 2. In Section 3, we discuss the main results which include investigation of the stability of the equilibrium points of the map. It also gives local and global analyses about the interior equilibrium point and the routes by which it can be destabilized. This section includes numerical simulation about the basins of attraction and their complicated structure. We also prove in the same section that the game's map is a noninvertible map of type $Z_0 - Z_2$ or $Z_1 - Z_3$ depending on the nature of preimages coexisted. Furthermore, in this section, we compare the influences of asymmetric price information with the classical model without such information. Finally, the obtained results are concluded in Section 4.

2. The Model

The model in this paper consists of two firms (players) whose products are differentiated, and their prices are derived from the utility function introduced by Singh and Vives [30] as follows:

$$U(q_1, q_2) = a(q_1 + q_2) - \frac{1}{2}\left(q_1^2 + q_2^2 + 2bq_1q_2\right), \quad q_1, q_2 > 0, \tag{1}$$

where a is a constant and b is restricted in the interval $(-1, 1)$. Both q_1 and q_2 are the quantities produced by each firm. The following characterize this utility:

(1) U is concave which means $(\partial^2 U/\partial q_i^2) = -1 < 0$; $i = 1, 2$. Economically, the marginal utility of each quantity is decreasing.

(2) $(\partial^2 U/\partial q_1 q_2) = -b \neq 0$. This means that the marginal utility of quantity depends on the other.

(3) $U(\theta q_1, \theta q_2) \neq \theta U(q_1, q_2)$. This means it is not homogeneous.

(4) Using a budget constraint $\sum_{i=1}^{2} p_i q_i \leq m$, we get

$$\begin{aligned} &\mathrm{Max} U(q_1, q_2), \\ &s.t. \quad \sum_{i=1}^{2} p_i q_i \leq m. \end{aligned} \tag{2}$$

Problem (2) is a maximization problem with a consumer's budget constraint. p_i denotes the price of quantity q_i, and m is a constant. Solving (2) gives the following demand functions:

$$\begin{aligned} q_1 &= \frac{a}{1+b} - \frac{p_1}{1-b^2} + \frac{bp_2}{1-b^2}, \\ q_2 &= \frac{a}{1+b} - + \frac{bp_1}{1-b^2} - \frac{p_2}{1-b^2}. \end{aligned} \tag{3}$$

We should mention here that b denotes the horizontal differentiation degree. If $b = 0$, we have two monopolistic firms, and $b = 1$ represents two identical firms. Negative values for b refer to complementarity between the firms. Assuming linear costs, $C_i(q_i) = c_1 q_i$, where $(\partial C_i/\partial q_i) = c_i$ is a constant marginal cost. Now, the profit of each firm becomes

$$\pi_1 = (p_1 - c_1)q_1 = (p_1 - c_1)\left(\frac{a}{1+b} - \frac{p_1}{1-b^2} + \frac{bp_2}{1-b^2}\right),$$
$$\pi_2 = (p_2 - c_2)q_1 = (p_1 - c_1)\left(\frac{a}{1+b} - +\frac{bp_1}{1-b^2} - \frac{p_2}{1-b^2}\right). \tag{4}$$

Now, we consider a Bertrand game whose players adopt a gradient-based mechanism in order to update their prices according to the following discrete dynamical map:

$$p_{1,t+1} = p_{1,t} + kp_{1,t}\frac{\partial \pi_1(p_{1,t}, p_{2,t})}{\partial p_1},$$
$$p_{2,t+1} = p_{2,t} + kp_{2,t}\frac{\partial \pi_2(p_{1,t+1}, p_{2,t})}{\partial p_2}. \tag{5}$$

It should be noted that the second equation in (5) differs from the first because the second player in the game has some advantages. He knows by some way the price of the first player next time step. This kind of asymmetric information gives with (4) and (5) the following discrete time map:

$$T(p_1, p_2): \begin{cases} p_{1,t+1} = p_{1,t} + \dfrac{kp_{1,t}}{1-b^2}\left[a(1-b) + c_1 - 2p_{1,t} + bp_{2,t}\right], \\ p_{2,t+1} = p_{2,t} + \dfrac{kp_{2,t}}{1-b^2}\left[a(1-b) + c_2 + bp_{1,t} - 2p_{2,t}\right] \\ +\dfrac{k^2 bp_{1,t}p_{2,t}}{(1-b^2)^2}\left[a(1-b) + c_1 - bc_2 - 2p_{1,t} + 2bp_{2,t}\right]. \end{cases} \tag{6}$$

Map (6) is nonlinear, and due to the asymmetric information possessed by the second firm, it becomes more complex. Without this asymmetric information, we get the following map:

$$T_1(p_1, p_2): \begin{cases} p_{1,t+1} = p_{1,t} + \dfrac{kp_{1,t}}{1-b^2}\left[a(1-b) + c_1 - 2p_{1,t} + bp_{2,t}\right], \\ p_{2,t+1} = p_{2,t} + \dfrac{kp_{2,t}}{1-b^2}\left[a(1-b) + c_2 + bp_{1,t} - 2p_{2,t}\right]. \end{cases} \tag{7}$$

In this paper, we will compare between maps (6) and (7) in order to see the influences of asymmetric information on the complex dynamic characteristics of the game's equilibrium points.

3. Main Results of Map (6)

3.1. Fixed Points and Stability. Map (6) has four fixed points:

$$E_0 = (0, 0),$$
$$E_1 = \left(0, \frac{a(1-b) + c_2}{2}\right),$$
$$E_2 = \left(\frac{a(1-b) + c_1}{2}, 0\right),$$
$$E_3 = (\widehat{p}_1, \widehat{p}_2), \tag{8}$$

where

$$\widehat{p}_1 = \frac{1}{4kb^2}\left[A - B_1 k + \sqrt{B_1^2 k^2 + Dk + A^2}\right],$$
$$\widehat{p}_2 = \frac{1}{4kb^2}\left[A + B_2 k + \sqrt{B_1^2 k^2 + Dk + A^2}\right],$$
$$A = (1-b^2)(4-b^2),$$
$$B_1 = b^2[(a-c_2)b - a - c_1],$$
$$B_2 = b^2[(a+c_2)b - a - c_1],$$
$$D = 2b^2(1-b^2)\left[ab^3 - c_2 b^3 + 3ab^2 - c_1 b^2 - 4a - 4c_1\right]. \tag{9}$$

The points E_0, E_1, and E_2 are called corner fixed points, while E_3 is an interior fixed point. It is clear that E_0, E_1, and E_2 are positive since $-1 < b < 1$. Due to the complicated form of the interior point, we will discuss its positivity and stability by assuming values for the parameters a, b, c_1, c_2, and k. The Jacobian of map (6) becomes

$$J_m = \begin{pmatrix} J_{11} & J_{12} \\ J_{21} & J_{22} \end{pmatrix}, \tag{10}$$

where

$$J_{11} = 1 + \frac{k[a(1-b) + c_1 - 4p_1 + bp_2]}{1-b^2},$$
$$J_{12} = \frac{bkp_1}{1-b^2},$$
$$J_{21} = \frac{kbp_2(1-b^2) + bk^2 p_2[a(1-b) + c_1 - bc_2 + 2bp_2 - 4bp_1]}{[1-b^2]^2},$$
$$J_{22} = 1 + \frac{k[a(1-b) + c_2 + bp_1 - 4p_2]}{1-b^2} + \frac{bp_1[a(1-b) + c_2 + bp_1 - 4p_2]k^2}{[1-b^2]^2}. \tag{11}$$

The stability of the above fixed points depends on the eigenvalues λ_1 and λ_2 of the Jacobian (10). These eigenvalues have the following properties:

(1) A fixed point is a locally stable attracting node if its eigenvalues satisfy $|\lambda_{1,2}| < 1$

(2) A fixed point is an unstable repelling node if its eigenvalues satisfy $|\lambda_{1,2}| > 1$

(3) A fixed point is a saddle point if its eigenvalues satisfy $|\lambda_1| < 1$ and $|\lambda_2| > 1$ (or $|\lambda_1| > 1$ and $|\lambda_2| < 1$)

(4) A fixed point is a nonhyperbolic point if its eigenvalues satisfy $|\lambda_1| = 1$ and $|\lambda_2| \neq 1$ (or $|\lambda_1| \neq 1$ and $|\lambda_2| = 1$)

Proposition 1. *The fixed point E_0 is an unstable repelling point.*

Proof. The Jacobian at this point becomes

$$J_{E_0} = \begin{pmatrix} 1 + \dfrac{k[a(1-b)+c_1]}{1-b^2}, & 0, \\ 0, & 1 + \dfrac{k[a(1-b)+c_2]}{1-b^2}, \end{pmatrix} \tag{12}$$

whose eigenvalues are $\lambda_i = 1 + ((k[a(1-b)+c_i])/(1-b^2)), i = 1, 2$. Since $|b| < 1$ and $c_i > 0$, we have $|\lambda_i| > 1$. This completes the proof.

Proposition 2. *The point E_1 is a stable point provided that $0 < ((k[a(1-b)+c_2])/(1-b^2)) < 2$ and $0 < ((k[a(1-b)(2+b)+2c_1+bc_2])/(1-b^2)) < 4$.*

Proof. The Jacobian at E_1

$$J_{E_1} = \begin{pmatrix} 1 + \dfrac{k[a(1-b)(2+b)+2c_1+bc_2]}{2[1-b^2]}, & 0, \\ \dfrac{bk[a(1-b)+c_2][(1-b^2)+k(a+c_1)-ab^2k]}{2[1-b^2]^2}, & 1 - \dfrac{k[a(1-b)+c_2]}{1-b^2}, \end{pmatrix} \tag{13}$$

has two real eigenvalues

$$\lambda_1 = 1 - \frac{k[a(1-b)+c_2]}{1-b^2},$$
$$\lambda_2 = 1 - \frac{k[a(1-b)(2+b)+2c_1+bc_2]}{2(1-b^2)}. \tag{14}$$

The conditions $|\lambda_1| < 1$ and $|\lambda_2| < 1$ complete the proof. The same proof is for E_2.

Proposition 3. *At $a = 2$, $b = 0.2$, $c_1 = 1$, $c_2 = 0.3$, and $k = 0.5$, we have $E_3 = (1.41028, 1.10282)$. It is locally asymptotically stable.*

Proof. The Jacobian at those parameters and E_3 is

$$J_{E_3} = \begin{pmatrix} -0.46904 & 0.14690 \\ -0.044276 & -0.11502 \end{pmatrix}, \tag{15}$$

and the eigenvalues are $\lambda_1 \approx -0.4496$ and $\lambda_2 \approx -0.13446$ with $|\lambda_{1,2}| < 1$, and then E_3 is stable. It is easy to see that the determinant of J_{E_3} equals $\delta = 0.060454 < 1$ which means that map (6) is dissipative. This numerical proof of the stability of E_3 gives rise to more studies in order to investigate and get more insights on the regions on where this fixed point can be destabilized. This will be discussed in the simulation given in the next section.

3.2. Dynamic Analysis via Numerical Simulation. Here, we investigate the influences of parameter k on the dynamics of map (6). This makes us to assume different sets of parameter values as follows.

3.2.1. Set 1. In this set, we assume the following values: $a = 2$, $b = 0.2$, $c_1 = 1$, $c_2 = 0.3$, and $k = 0.5$. This set indicates that we have two firms with different marginal costs ($c_1 > c_2$). In this set, we have $E_3 = (1.41028, 1.10282)$. This requires to investigate the impact of one parameter of those parameters on the stability of this point. Let us assume that parameter k will be taken as the bifurcation parameter. The first numerical experiment displayed in Figure 1(a) shows the effect of bifurcation parameter k on the stability of E_3. One can see that it is locally stable for all the values of k except for $k \approx 0.704$ on which the first period-2 cycle is born. Periodic cycles may possess complicated basins of attraction, and this makes us to analyze these basins for cycles. At $k = 0.88$, a period 2 with its basins is given in Figure 1(b) with the fixed point E_3. From now on, we will fix the colors as follows. The grey color denotes the divergent and nonconvergent points, while the other two colors refer to the basins of the plotted cycle. Increasing k further to 0.915 of a period-4 cycle rises with quite complicated basins of attraction than those of period-2 cycle. Figure 1(d) shows complicated basins for period-8 cycle at $k = 0.924$. Further increase in the parameter gives rise to more complicated attractive basins of higher periodic cycles, for instance, at $k = 0.95$, the dynamic changes into two disconnected chaotic areas which gather together to become one chaotic attractor at $k = 0.995$. Figures 1(e) and 1(f) present those chaotic behaviors of map (6).

Using the parameter values in set 1, it is observed through numerical experiments that when the marginal costs are equal ($c_1 = c_2$), another dynamic behavior is emerged. At $c_1 = c_2 = 1$, the fixed point E_3 can be destabilized via Neimark–Sacker bifurcation. The Jacobian (10) at these parameter values becomes

$$J_{E_3} = \begin{pmatrix} -0.80659 & 0.18066 \\ -0.13619 & -0.75027 \end{pmatrix}, \tag{16}$$

with complex eigenvalues $\lambda_{1,2} = -0.77843 \pm 0.15431i$ and $|\lambda_{1,2}| = 0.79358 < 1$, and then E_3 is locally stable. It is easy to see that the determinant of J_{E_3} equals $\delta = 0.62976 < 1$ which means that map (6) is also dissipative. Now, we analyze the influence of k on the stability of this point. When we increase k further, dynamic behaviors arise such as spiral and

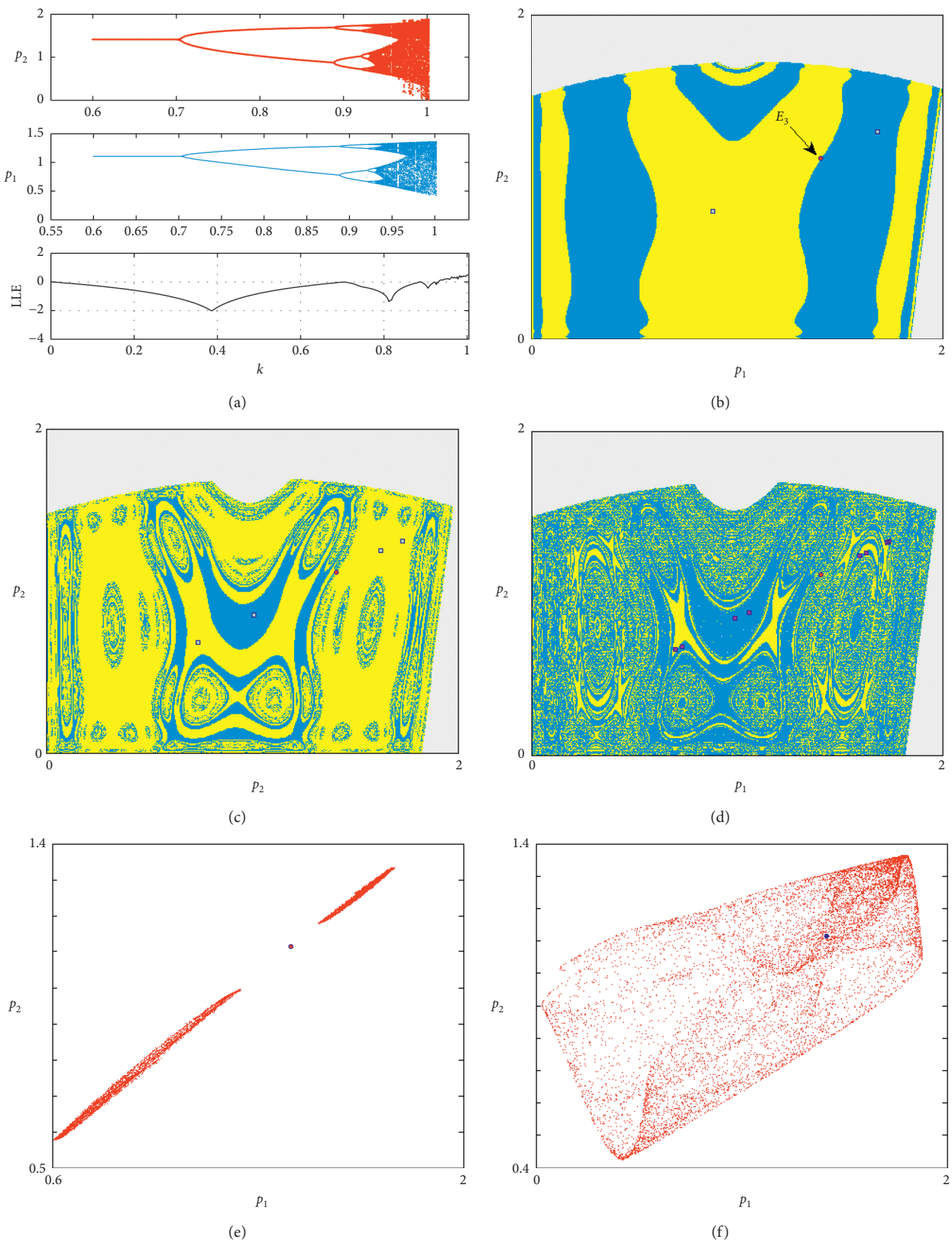

FIGURE 1: (a) Flip bifurcation diagram on varying k. (b) Basins of attraction of the period-2 cycle at $k = 0.88$. (c) Basins of attraction of the period-4 cycle at $k = 0.915$. (d) Basins of attraction of the period-8 cycle at $k = 0.924$. (e) The phase plane of the two chaotic attractors at $k = 0.95$. (f) The phase plane of the chaotic attractor at $k = 0.995$. Other parameter values are $a = 2$, $b = 0.2$, $c_1 = 1$, and $c_2 = 0.3$.

closed curves around the fixed point. Figure 2(b) gives those behaviors for different values of k. When k reaches 0.774, a period-17 cycle appears with quite complicated basins of attraction as given in Figure 2(c). As k increases further, high-periodic cycles coexist with complicated basins until the dynamic turns into a closed chaotic attractor. This chaotic attractor is born at $k = 0.79$, and its phase plane is displayed in Figure 2(d). This chaotic attractor becomes very complicated as k increases to 0.818, and its phase plane is shown in Figure 3(a). This unexpected dynamic gives no predictions about the evolution of map (6) and makes the price game with asymmetric information more complicated. The asymmetry and nonlinearity of this map give more complicated behaviors that we should report here. At $k = 0.827$, a six-piece chaotic attractor is emerged. The phase plane of this dynamic behavior around the fixed point is given in Figure 3(b). In this figure, we enlarge one piece of this chaotic behavior. These six pieces are gathered together as k increases further to form one chaotic and complicated attractor in Figure 3(c). At $k = 0.877$, a period-7 cycle coexists. As given in Figure 3(d), it has very complicated attractive basins. Increasing k to 0.88, another period cycle is raised. This period is of cycle 14, and its basins are plotted in Figure 3(e). Finally, for any other increase for k, the dynamic behavior of map (6) turns to one chaotic attractor. Figure 3(f) displays the phase plane of this chaotic attractor.

3.2.2. Set 2. In this set, we assume the following values: $a = b = c_1 = c_2 = 0.5$ and $k = 1.6$. The fixed point at set 2 becomes $E_3 = (0.5, 0.5)$, and its Jacobian is

$$J_{E_3} = \begin{pmatrix} -1.1333 & 0.53333 \\ -0.60444 & -0.56444 \end{pmatrix}, \tag{17}$$

with complex eigenvalues $\lambda_{1,2} = -0.84889 \pm 0.49139i$ and $|\lambda_{1,2}| = 0.98086 < 1$, and then E_3 is locally stable. It is easy to see that the determinant of J_{E_3} equals $\delta = 0.96207 < 1$ which means that map (6) is again dissipative. As previously stated, we study the effects of k on the stability of the fixed point. It is not a repeated analysis for the above simulation; it gives other interesting and hidden dynamics of map (6). Increasing k makes the fixed point unstable due to Neimark–Sacker bifurcation. For instance, at different values of k, we give in Figure 4(a) different closed curves around the fixed point. Those closed invariant curves are changed to a period-5 cycle as parameter k increases to 1.83. It is plotted in Figure 4(b) with its attractive basins. Another interesting observation is the coexistence of period-5 and period-10 cycles together at $k = 1.9$. They have quite complicated basins of attraction which are given in Figure 4(c). Increasing k further makes those cycles convert into five unconnected and complicated chaotic areas. The phase plane of these chaotic areas is given in Figure 4(d) with the fixed point. These chaotic areas become larger and more complicated as k increases to 1.95. They are displayed in Figure 4(e). After that, the dynamic behavior of map (6) becomes chaotic as k increases to 1.97, as given in Figure 4(f).

We should highlight here that the role of parameter k is affected by parameter b. Figure 5(a) shows that the fixed point can be destabilized due to flip bifurcation on varying parameter k and for the same set of parameter values except for $b = -0.55$. We give some numerical simulations of the dynamic behavior of k at negative values for b. At $k = 1.51$, Figure 5(b) shows the coexistence of unconnected period-3 cycles. It has an attractive basins given in Figure 5(b) which are more complicated than those obtained previously. At $b = -0.5$, the effect of k on the fixed point makes it unstable due to flip bifurcation. Figure 5(c) shows a stable fixed point for all k until the coexistence of the unconnected period-6 cycle. This cycle has basins of attraction which are given in Figure 5(d).

3.3. Map (6) versus Map (7). Here, we compare the two models in order to investigate the influences of asymmetric information in their dynamics. Assuming that $a = 2$, $b = 0.2$, $c_1 = 1$, and $c_2 = 0.3$, Figure 6(a) shows the impact of k on map (7). Comparing Figure 1(a) with Figure 6(a), we see that the asymmetric information possessed by the second firm broadens the stability region for both players simultaneously. Numerical experiments show that the basins of attraction detected for map (6) are quite complicated than those of map (7). Furthermore, we show by experiments that, at sets 1 and 2, the stability region of the fixed point for map (5) is bigger than that detected for the fixed point of map (7). For more details about the properties of classic model (7), refer [31]. In Figure 6(b), we present the attractive basins of the period-4 cycle for map (7). Comparing these basins with others given in Figure 1(c), we get that the dynamics of map (6) are more complex than those of map (7). Therefore, the future prediction for map (6) becomes more complicated.

The previous analysis shows that the structure of basins is quite complicated, and this requires to study extra characteristics of these maps. Setting $p_{1,t+1} = p_1$ and $p_{2,t+1} = p_2$ in (6), where t refers to the time evolution, we get

$$T(p_1, p_2): \begin{cases} \acute{p}_1 = p_1 + \dfrac{kp_1}{1-b^2}\left[a(1-b) + c_1 - 2p_1 + bp_2\right], \\ \acute{p}_2 = p_2 + \dfrac{kp_2}{1-b^2}\left[a(1-b) + c_2 + bp_1 - 2p_2\right] \\ \qquad + \dfrac{k^2 bp_1p_2}{\left(1-b^2\right)^2}\left[a(1-b) + c_1 - bc_2 - 2p_1 + 2bp_2\right]. \end{cases} \tag{18}$$

Complicated nonlinear map (18) makes us to study its noninvertibility characteristic by substituting $a = 2, b = 0.2, c_1 = 1, c_2 = 0.3$, and $k = 0.88$ in (18) as follows:

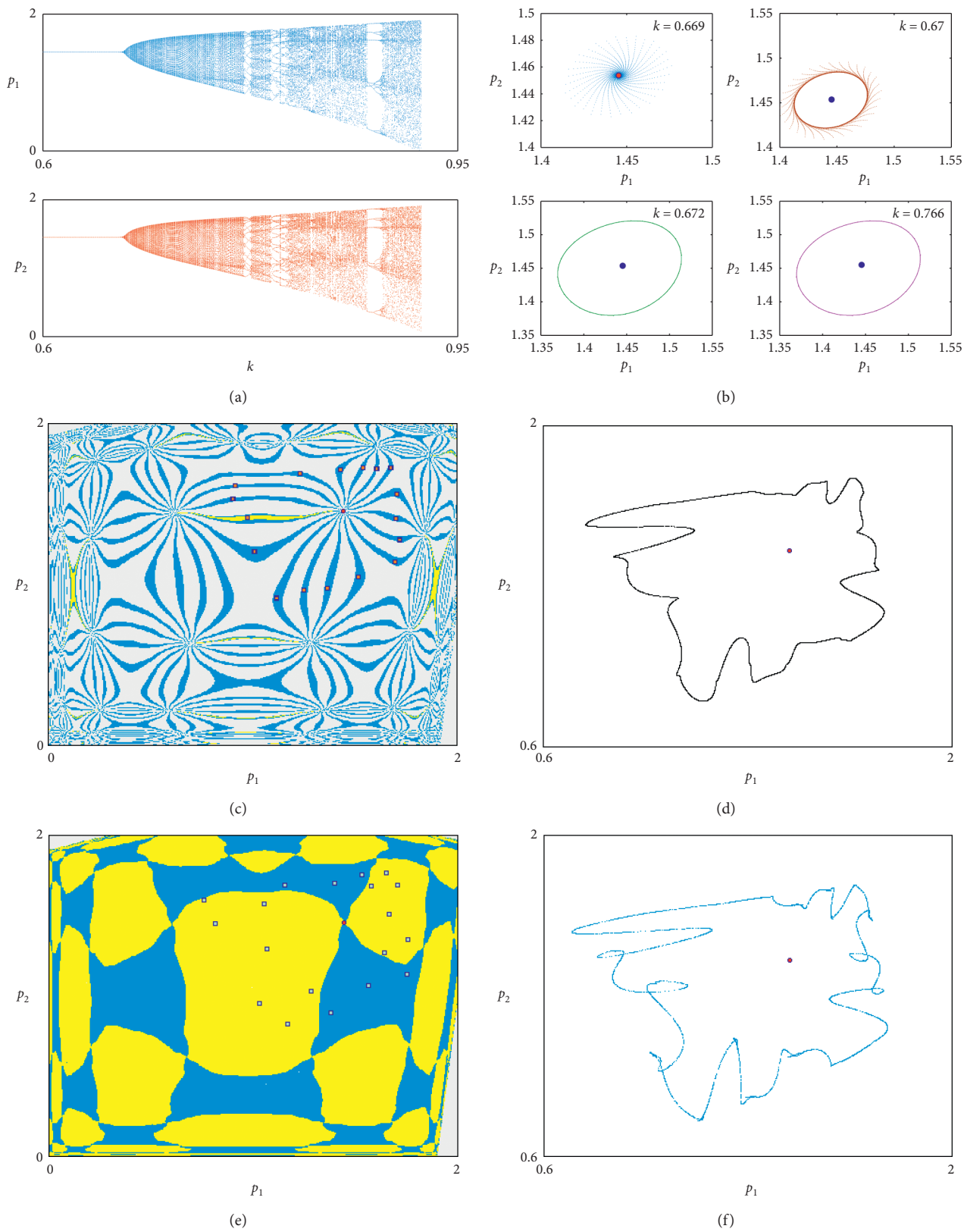

Figure 2: (a) Neimark–Sacker bifurcation diagram on varying k. (b) The phase plane of spiral and closed curves around the fixed point for different values of k. (c) Basins of attraction of the period-17 cycle at $k = 0.774$. (d) The phase plane of the chaotic attractor at $k = 0.79$. (e) Basins of attraction of the period-19 cycle at $k = 0.795$. (f) The phase plane of the chaotic attractor at $k = 0.8$. Other parameter values are $a = 2$, $b = 0.2$, $c_1 = 1$, and $c_2 = 1$.

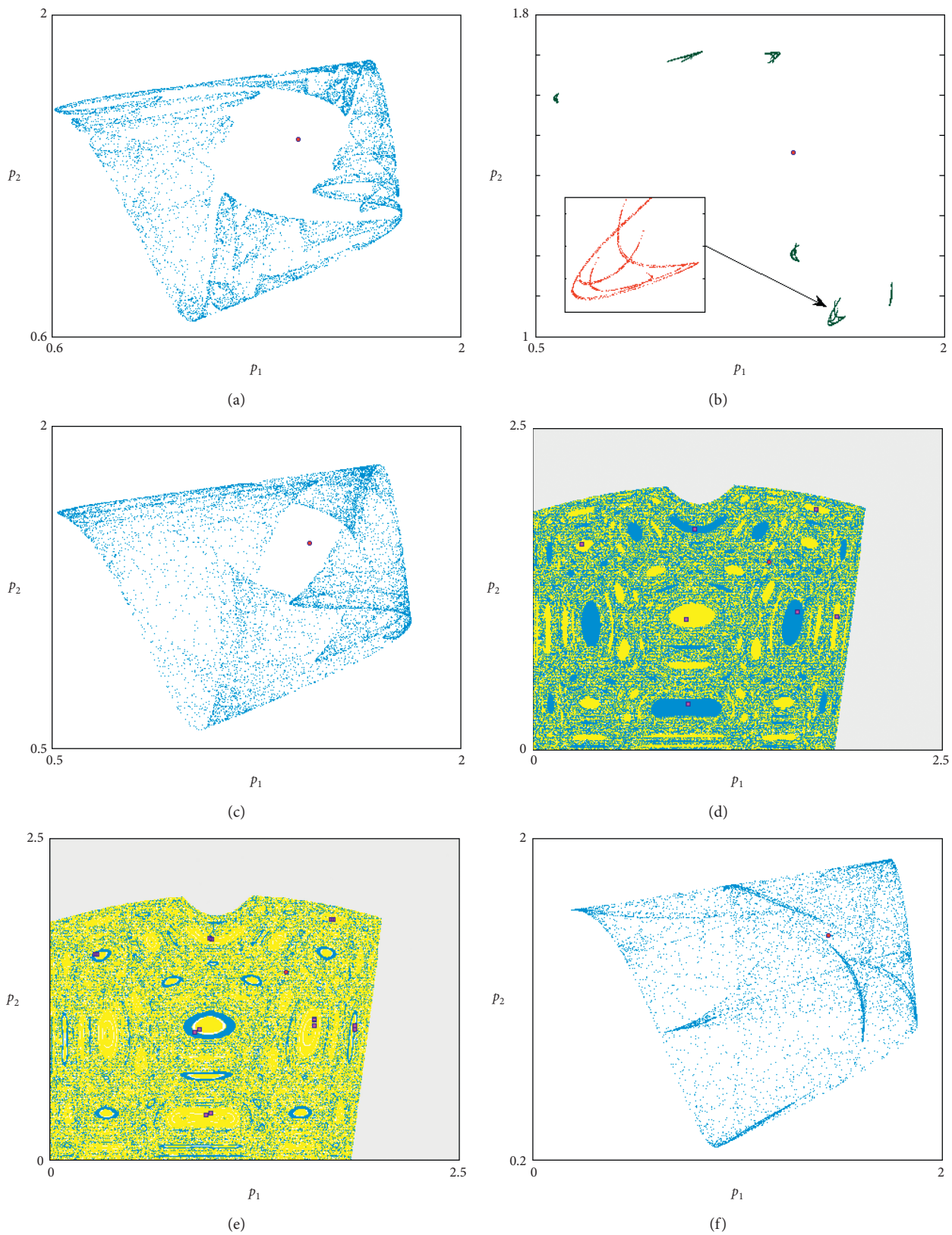

FIGURE 3: (a) The phase plane of the chaotic attractor at $k = 0.818$. (b) The phase plane of six-piece chaotic attractors at $k = 0.827$. (c) The phase plane of the chaotic attractor at $k = 0.835$. (d) Basins of attraction of the period-7 cycle at $k = 0.877$. (e) Basins of attraction of the period-14 cycle at $k = 0.88$. (f) The phase plane of the chaotic attractor at $k = 0.89$. Other parameter values are $a = 2$, $b = 0.2$, $c_1 = 1$, and $c_2 = 1$.

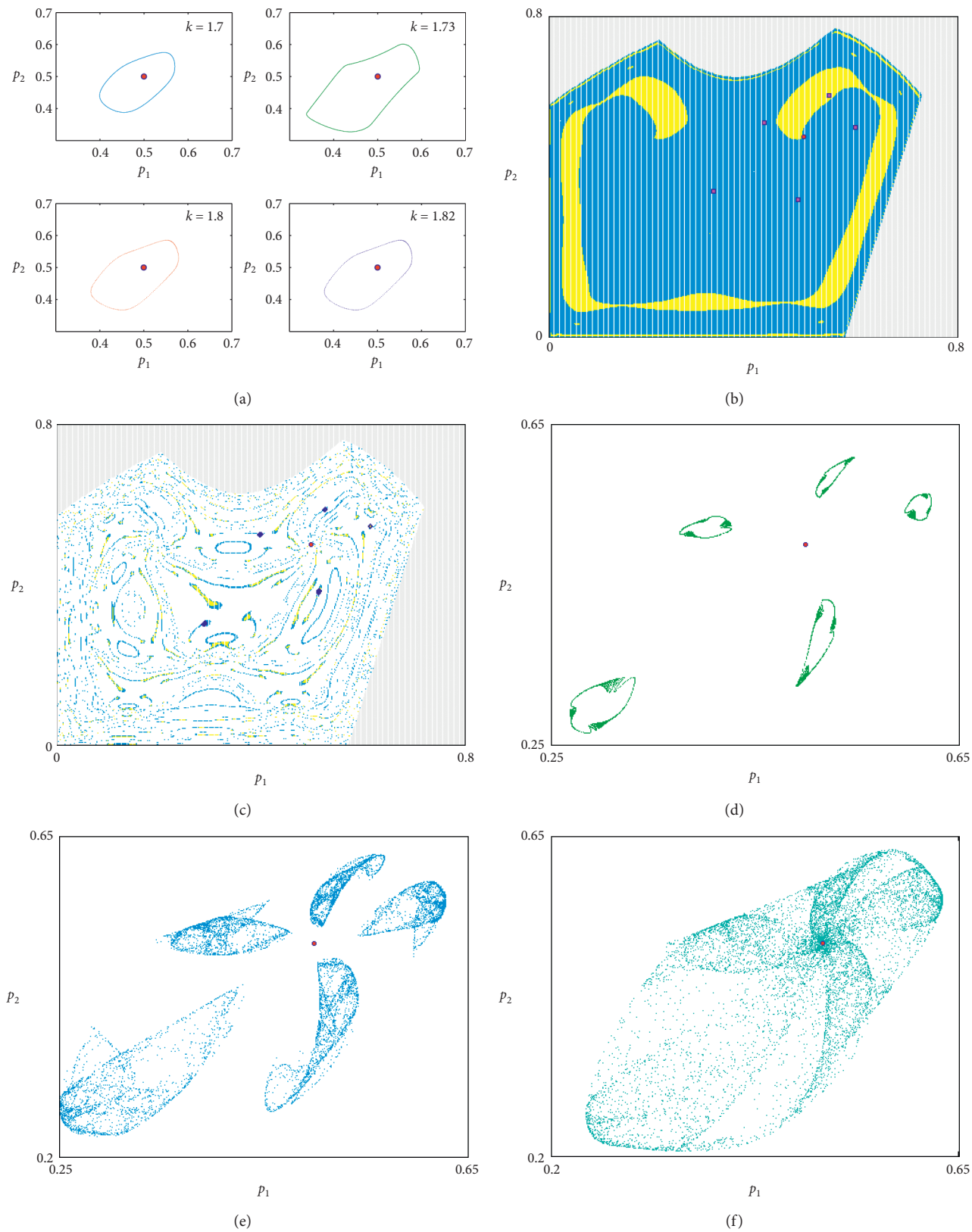

FIGURE 4: (a) The phase plane of closed invariant curves at different values of $k = 0.818$. (b) Basins of attraction of the period-5 cycle at $k = 1.83$. (c) Basins of attraction of period-5 and period-10 cycles at $k = 1.9$. (d) The phase plane of five-piece chaotic attractors at $k = 1.92$. (e) The phase plane of five-piece chaotic attractors at $k = 1.95$. (f) The phase plane of the chaotic attractor at $k = 1.97$. Other parameter values are $a = 0.5$, $b = 0.5$, $c_1 = 0.5$, and $c_2 = 0.5$.

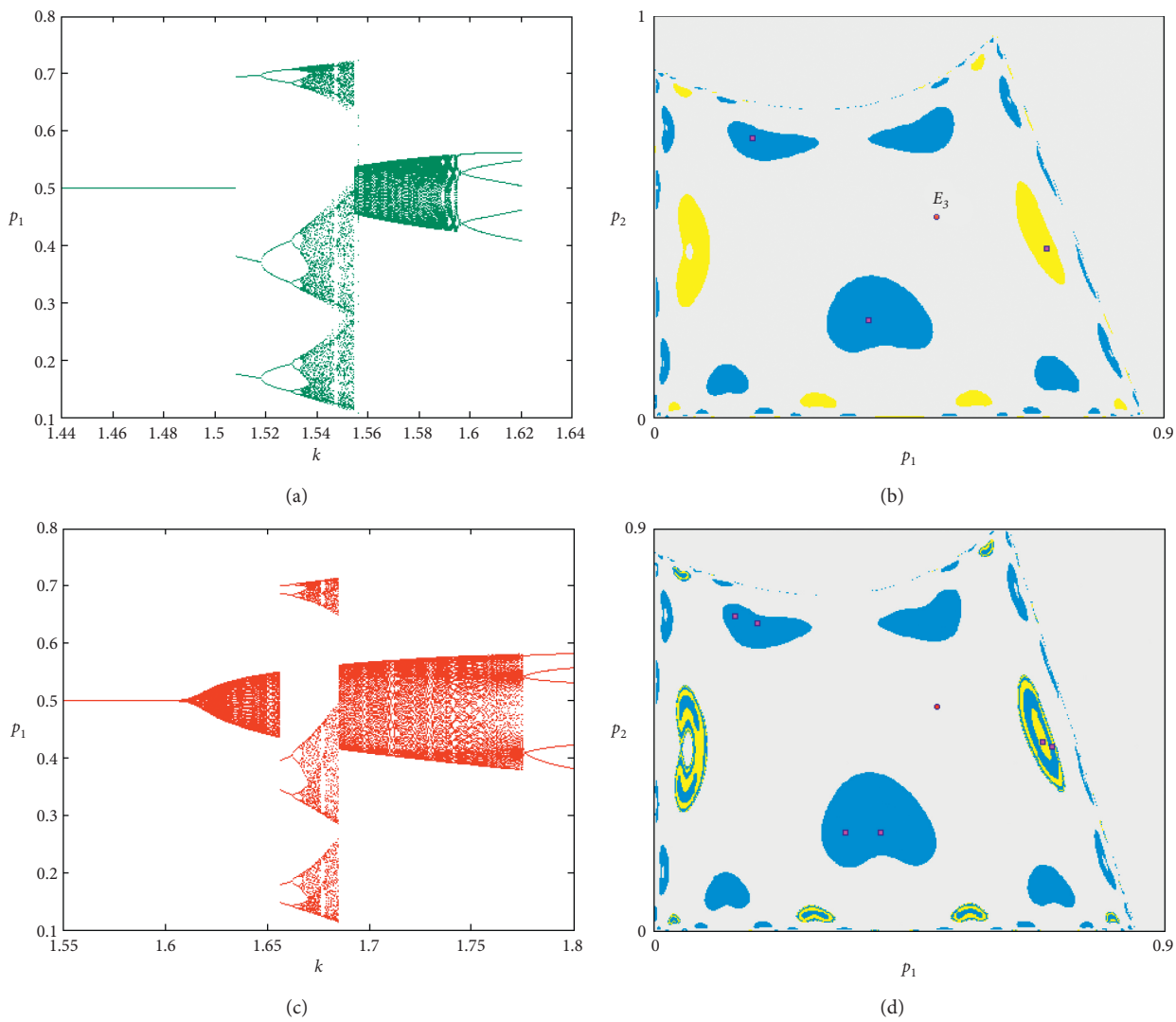

FIGURE 5: (a) The flip bifurcation on varying k at $b = -0.55$. (b) The basins of attraction of the period-3 cycle at $k = 1.51$ and $b = -0.55$. (c) The flip bifurcation on varying k at $b = -0.5$. (d) The basins of attraction of the period-6 cycle at $k = 1.66$ and $b = -0.5$. The other parameter values are $a = 0.5, c_1 = 0.5$, and $c_2 = 0.5$.

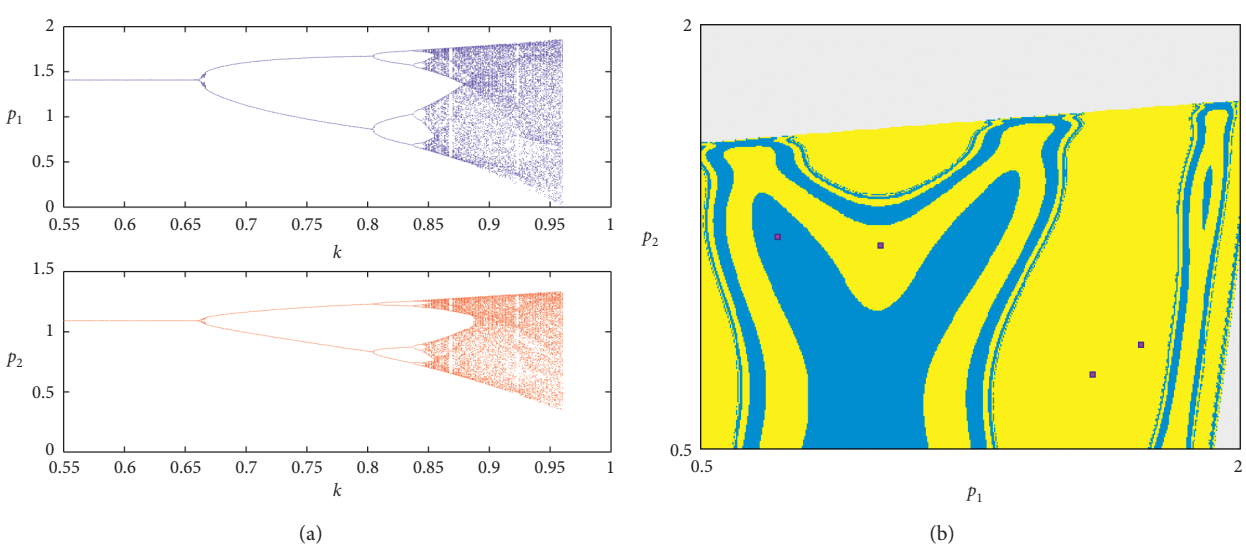

FIGURE 6: (a) Bifurcation diagram for map (7) on varying k. (b) The basins of attraction for the period-4 cycle of map (7) at $k = 0.70$. Other parameters are $a = 2$, $b = 0.2, c_1 = 1$, and $c_2 = 0.3$.

$$T(p_1, p_2): \begin{cases} \acute{p}_1 = p_1(2.2833 - 1.8333p_1 + 0.18333p_2), \\ \acute{p}_2 = p_2(1.6417 + 0.40853p_1 + 0.067222p_1p_2 \\ \qquad -1.8333p_2 - 0.33611p_1^2). \end{cases} \tag{19}$$

This means that a point (p_1, p_2) can be characterized by many rank-1 preimages. Those preimages are mapped in (p_1, p_2) in one iteration. Still, map (19) is in a complicated form to solve it algebraically with respect to the variables p_1 and p_2. Here, we follow the same procedure carried out in [28] by calculating the number of preimages of points belonging to the vertical axis ($p_1 = 0$). Therefore, substituting the point $(0, p_2)$ in (13), we get

$$p_1 = 0 \text{ or } p_1 = 1.245459 + 0.1p_2. \tag{20}$$

This means if we substitute $p_1 = 0$ in the second part of (13), we get two real preimages for the point $(0, p_2)$ provided that $p_2 \in (-\infty, 0.36753)$; otherwise, we have no preimages. This concludes that T is a noninvertible map of type $Z_0 - Z_2$, and hence, the phase plane is divided into two regions that are Z_0 and Z_2. On the contrary, substituting $p_1 = 1.245459 + 0.1p_2$ in the second part gives that the point $(0, p_2)$ has three real preimages provided that $p_2 \in (0.37050, \infty)$; otherwise, we have only one real preimage. This means the preimages of the point in this case divide the phase plane into two regions Z_1 and Z_3, and hence, the map T is of type $Z_1 - Z_3$. The same procedure can be used for the points belonging to the horizontal axis ($p_2 = 0$) and take the form $(p_1, 0)$. It is worth to mention here that both critical lines LC and LC_{-1} are obtained at those parameter values, but they have long forms to be written here or even to be plotted. We have performed the same procedure for map T_1 for the points $(0, p_2)$ and $(p_1, 0)$. The results show that map T_1 is of type $Z_0 - Z_2$ only.

4. Conclusion

The current paper has introduced and studied a Bertrand duopoly game with asymmetric price information. A gradient-based mechanism that is the bounded rationality has been adopted by game's players to update their prices in the next time step. The interior equilibrium point of the proposed game has been calculated, and its stability conditions have been discussed. We have compared our model with the classical Bertrand model without asymmetric information as both players in the two models use the same gradient-based mechanism. Our contributions have shown that the asymmetric price information has broadened the stability region of the interior point. Furthermore, the structure of basins of attraction for periodic cycles due to this information has shown quite complicated structure for those basins in comparison with those obtained for classical Bertrand. Moreover, the local and global analysis performed have shown that the proposed game's map is noninvertible and belongs to the type of $Z_0 - Z_2$ or $Z_1 - Z_3$ depending on the parameter value sets, while the model of classical Bertrand belongs to the type $Z_0 - Z_2$ only.

Data Availability

The data used to support the findings of this study are included within the article.

Conflicts of Interest

The author declares that there are no conflicts of interest.

Acknowledgments

This work was supported by the Research Supporting Project Number (RSP-2020/167), King Saud University, Riyadh, Saudi Arabia.

References

[1] https://en.wikipedia.org/wiki/Bertrand_competition.
[2] C. D' Aspremont, J. J. Gabszewicz, and J. F. Thisse, "On Hotelling's stability in competition," *Econometrica*, vol. 47, no. 5, pp. 1145–1150, 1979.
[3] B. Allen, R. Deneckere, T. Faith, and D. Kovenock, "Capacity precommitment as a barrier to entry: a Bertrand-Edgeworth approach," *Economic Theory*, vol. 15, no. 3, pp. 501–530, 2000.
[4] W. Elberfeld and E. Wolfstetter, "A dynamic model of Bertrand competition with entry," *International Journal of Industrial Organization*, vol. 17, no. 4, pp. 513–525, 1999.
[5] J. H. Hamilton, J.-F. Thisse, and A. Weskamp, "Spatial discrimination," *Regional Science and Urban Economics*, vol. 19, no. 1, pp. 87–102, 1989.
[6] M. Janssen and E. Rasmusen, "Bertrand competition under uncertainty," *The Journal of Industrial Economics*, vol. 50, no. 1, pp. 11–21, 2003.
[7] A. Ledvina and R. Sircar, "Dynamic Bertrand oligopoly," *Applied Mathematics & Optimization*, vol. 63, no. 1, pp. 11–44, 2010.
[8] J. Zhang, Q. Da, and Y. Wang, "The dynamics of Bertrand model with bounded rationality," *Chaos, Solitons & Fractals*, vol. 39, no. 5, pp. 2048–2055, 2009.
[9] J. Ma and K. Wu, "Complex system and influence of delayed decision on the stability of a triopoly price game model," *Nonlinear Dynamics*, vol. 73, no. 3, pp. 1741–1751, 2013.
[10] J. H. Ma and L. Sun, "Study and simulation on discrete dynamics of Bertrand triopoly team-game," *Mathematical Problems in Engineering*, vol. 2015, Article ID 960380, 12 pages, 2015.
[11] J. Peng, Z. Miao, and f. Peng, "Study on a 3-dimensional game model with delayed bounded rationality," *Applied Mathematics and Computation*, vol. 218, no. 5, pp. 1568–1576, 2011.
[12] J. Zhao, J. Wei, and Y. Li, "Pricing decisions for substitutable products in a two-echelon supply chain with firms' different channel powers," *International Journal of Production Economics*, vol. 153, pp. 243–252, 2014.
[13] B. C. Giri and S. Sharma, "Manufacturer's pricing strategy in a two-level supply chain with competing retailers and advertising cost dependent demand," *Economic Modelling*, vol. 38, pp. 102–111, 2014.
[14] L. Fanti, L. Gori, C. Mammana, and E. Michetti, "The dynamics of a Bertrand duopoly with differentiated products:

synchronization, intermittency and global dynamics," *Chaos, Solitons & Fractals*, vol. 52, no. 1, pp. 73–86, 2013.

[15] S. S. Askar, "On Cournot-Bertrand competition with differentiated products," *Annals of Operations Research*, vol. 223, no. 1, pp. 81–93, 2014.

[16] S. S. Askar and M. Abouhawwash, "Quantity and price competition in a differentiated triopoly: static and dynamic investigations," *Nonlinear Dynamics*, vol. 91, no. 3, pp. 1963–1975, 2018.

[17] X. Zhang, D. Sun, S. Ma, and S. Zhang, "The dynamics of a quantum Bertrand duopoly with differentiated products and heterogeneous expectations," *Physica A: Statistical Mechanics and Its Applications*, vol. 557, Article ID 124878, 2020.

[18] M. Alipranti and E. Petrakis, "Fixed fee discounts and Bertrand competition in vertically related markets," *Mathematical Social Sciences*, vol. 106, pp. 19–26, 2020.

[19] J. Andaluz, A. A. Elsadany, and G. Jarne, "Nonlinear Cournot and Bertrand-type dynamic triopoly with differentiated products and heterogeneous expectations," *Mathematics and Computers in Simulation*, vol. 132, pp. 86–99, 2017.

[20] A. Semenov and J.-B. Tondji, "On the dynamic analysis of Cournot-Bertrand Equilibria," *Economics Letters*, vol. 183, Article ID 10854, 2019.

[21] R. Amir and I. V. Evstigneev, "A new look at the classical Bertrand duopoly," *Games and Economic Behavior*, vol. 109, pp. 99–103, 2018.

[22] E. Ahmed, A. S. Hegazi, M. F. Elettreby, and S. S. Askar, "On multi-team games," *Physica A: Statistical Mechanics and Its Applications*, vol. 369, no. 2, pp. 809–816, 2006.

[23] Y. Peng and Q. Lu, "Complex dynamics analysis for a duopoly Stackelberg game model with bounded rationality," *Applied Mathematics and Computation*, vol. 271, pp. 259–268, 2015.

[24] A. K. Naimzada and R. Raimondo, "Chaotic congestion games," *Applied Mathematics and Computation*, vol. 321, pp. 333–348, 2018.

[25] J. Ma, L. Sun, S. Hou, and X. Zhan, "Complexity study on the Cournot-Bertrand mixed duopoly game model with market share preference," *Chaos*, vol. 28, Article ID 023101, 2018.

[26] E. Ahmed and M. F. Elettreby, "Controls of the complex dynamics of a multi-market Cournot model," *Economic Modelling*, vol. 37, pp. 251–254, 2014.

[27] S. S. Askar, "Tripoly Stackelberg game model: one leader versus two followers," *Applied Mathematics and Computation*, vol. 328, pp. 301–311, 2018.

[28] F. Cavalli, A. Naimzada, and F. Tramontana, "Nonlinear dynamics and global analysis of a heterogeneous Cournot duopoly with a local monopolistic approach versus a gradient rule with endogenous reactivity," *Communications in Nonlinear Science and Numerical Simulation*, vol. 23, no. 1–3, pp. 245–262, 2015.

[29] S. S. Askar and K. Alnowibet, "Cooperation versus noncooperation: Cournot duopolistic game based on delay and time-dependent parameters," *Chaos, Solitons & Fractals*, vol. 91, pp. 580–584, 2016.

[30] N. Singh and X. Vives, "Price and quantity competition in a differentiated duopoly," *The RAND Journal of Economics*, vol. 15, no. 4, pp. 546–554, 1984.

[31] S. S. Askar and A. Al-khedhairi, "Dynamic investigations in a duopoly game with price competition based on relative profit and profit maximization," *Journal of Computational and Applied Mathematics*, vol. 367, Article ID 112464, 2020.

Hindawi
Mathematical Problems in Engineering
Volume 2020, Article ID 2640629, 18 pages
https://doi.org/10.1155/2020/2640629

Research Article

New Chaotic Oscillator Derived from Class C Single Transistor-Based Amplifier

Jiri Petrzela

Department of Radio Electronics, Faculty of Electrical Engineering and Communications, Brno University of Technology, Brno 616 00, Czech Republic

Correspondence should be addressed to Jiri Petrzela; petrzelj@feec.vutbr.cz

Received 28 June 2020; Revised 20 October 2020; Accepted 31 October 2020; Published 11 November 2020

Academic Editor: Adel Ouannas

This paper describes a new autonomous deterministic chaotic dynamical system having a single unstable saddle-spiral fixed point. A mathematical model originates in the fundamental structure of the class C amplifier. Evolution of robust strange attractors is conditioned by a bilateral nature of bipolar transistor with local polynomial or piecewise linear feedforward transconductance and high frequency of operation. Numerical analysis is supported by experimental verification and both results prove that chaos is neither a numerical artifact nor a long transient behaviour. Also, good accordance between theory and measurement has been observed.

1. Introduction

Heretofore, formation of the strange attractors was reported in many lumped electronic circuits, both isolated and driven. Chaotic waveforms have several fundamental properties: wideband and continuous frequency spectrum, sensitivity to small changes of initial conditions, dense state attractors with (unlike noise) non-integer metric dimension, and absence of closed-form analytic solution. Because of these features, especially presence of dominant harmonics in frequency spectrum, chaos can be observed in general models of all types of lumped analogue harmonic oscillators, regardless of type of active element used as energy source. For example, paper [1] describes a long-term unpredictable motion of the well-known Colpitts oscillator. Work [2] demonstrates existence of robust strange attractors unfolded during study of motion of the Hartley oscillator. Both oscillators require only single transistor and three accumulation elements for generation of the stable sinusoidal output voltages. Some interesting papers [3, 4] introduce a methodology on how to transform very popular Wien-bridge network configuration into chaotic oscillator. It turns out that simple mechanism dedicated to amplitude stabilization can cause both vector field stretching and folding required for the chaos evolution. In fact, the most famous chaotic electronic system, Chua's oscillator, can be considered as connection of LC parallel resonant tank, timing network, and nonlinear resistor. This nonlinear element can be either polynomial [5] or piecewise linear [6]. Both types of nonlinearities are practically implemented using several commercially available devices and are the only active components in designed chaotic circuits. Study [7] proves that pair of coupled accumulation elements can be substituted by a single higher-order element such as the frequency dependent negative resistor. Single third-order immittance element can be used to create linear part of the vector field as it is demonstrated in paper [8]. Systematic design procedure leading to robust chaotic oscillators with the passive only nonlinear elements is provided in a couple of cookbooks [9, 10]. In these articles, nonlinear resistors have the ampere-voltage curve with single breakpoint and therefore serves as energy valve. Several papers utilize proposed approach to construct original structures of chaotic oscillators [11, 12].

Besides oscillators, unpredictable motion was detected in other naturally non-chaotic analogue building blocks. Recently, in the modern complex electronic systems, chance to observe robust chaos is strengthened because of high frequencies and

amplitudes of useful processed signals. In such cases, parasitic properties (especially input and output impedances) of active elements necessarily introduce error terms in describing set of differential equations, lead to unexpected couplings between independent nodes, change values of working accumulation elements and increase mathematical order of circuit, cause additional functional nonlinearities or hysteresis effects on existing nonlinear transfer curves, etc. Let us provide a few examples of such systems. Presence of structurally stable strange attractors was confirmed in standard topologies of DC-DC converters, namely, buck [13], cuk [14], and boost [15, 16]. Very interesting reading about irregular behaviour in general class of DC-DC converters and its properties, including possible control mechanism, can be found in papers [17, 18]. Another transparent example of chaotic system based on switched power converter is described in study [19]. Impulsive chaos can be observed in switched capacitor circuits as well; see papers [20, 21] for details. Several research papers were dedicated to describing chaos in phase-locked loops: for details, consult several examples provided in papers [22, 23]. Recently, single-spiral as well as double-scroll attractors were detected within high frequency mathematical models of multistate static memory cells composed of the resonant tunnelling diodes; the number of these diodes determines total amount of fixed points. Chaos can be observed if ampere-voltage characteristic is considered piecewise linear [24] as well as cubic polynomial [25]. An interesting consequence coming from these studies is that there is a direct correlation between number of equilibria and complexity of generated chaotic attractors. Very complex vector field and geometric patterns of basins of attraction [26] suggest possible evolution of multiscroll chaotic attractors. Fingerprints of chaos can be observed in very simple networks that contain recently developed memory circuit elements: memristors [27, 28] or mem-elements in general [29, 30], both with integer and fractional order [31]. To end this, very brief, list of chaotic analogue building blocks, we can mention frequency filters as good candidates to exhibit chaotic solution. These filtering sections can be of different topologies, such as the state variable filters [32] or passive ladder filters with active nonlinear feedback. This active nonlinear feedback can be implemented by either two-terminal [5, 33, 34] or two-port [35] device. There, existence of chaos is conditioned by small system dissipation, i.e., filters with high quality factor. Speaking in terms of lumped chaotic circuit with minimum number of elements, it seems that driven R-L-diode circuit is the simplest one [36].

Searching for the most trivial algebraic description of continuous time chaotic flow was started by fundamental question raised in [37]. To date, this problem still represents up-to-date topic.

Existence of robust chaotic waveforms within very simple lumped electronic systems having one or two transistors is old but still an up-to-date problem. Some recent examples of transistor-based chaotic oscillators can be found in paper [38]. Circuits discussed here clearly belong to the simplest cases exhibiting chaotic dynamics because, apart from the transistor used, some comprise only three accumulation elements. A slightly more complicated chaotic network having two standard bipolar transistors is discussed in research work [39].

The main purpose of upcoming sections of this paper is to prove that chaos can be observed, under very specific conditions, in the fundamental cell of class C amplifier comprising single bipolar transistor. This fact has been already mentioned in a very recent publication [40]. Unlike this research, where both backward and forward transconductances of bipolar transistor two-port are considered as polynomial nonlinearity, this work assumes a case much closer to physical reality. In addition, two differently shaped strange attractors instead of one are presented and thoroughly analysed. Although describing mathematical model that gives basis to this work and corresponding circuit realization is not the simplest one, it still represents interesting chaotic dynamical system that belongs to class of systems having a single unstable equilibrium.

This paper is organized as follows. The next section provides a brief mathematical description of autonomous deterministic dynamical system to be analysed. The third section of this paper numerically quantifies chaotic motion produced by analysed system. The fourth section describes two flow-equivalent circuit designs based on class C amplifier cell with polynomial nonlinearity. The fifth section of this manuscript is dedicated to experimental verification of constructed chaotic oscillators. Finally, concluding remarks and future possible topics are revealed.

2. Mathematical Background

The principal structure of class C single transistor-based amplifier is given in Figure 1(a). For useful signals, this network can be redrawn as computational model shown in Figure 1(b). In its basic form, both circuits are linear and valid for small useful signals. Without input waveform, the resulting dynamical system can be described by the following set of ordinary differential equations:

$$\begin{aligned} C_{\mathrm{be}}\frac{\mathrm{d}}{\mathrm{d}t}v_1 &= -y_{11}\cdot v_1 - y_{12}\cdot v_2,\\ (C+C_{\mathrm{ce}})\frac{\mathrm{d}}{\mathrm{d}t}v_2 &= -y_{21}(v_1) - y_{22}\cdot v_2 - i_L,\\ L\frac{\mathrm{d}}{\mathrm{d}t}i_L &= v_2. \end{aligned} \tag{1}$$

Note that admittance parameters of bipolar transistor y_{11}, y_{12}, and y_{22} are considered constant. This represents common situation in many practical applications. Forward transconductance is supposed to be nonlinear, characterized by curve approximated by cubic polynomial of form $y_{21}(v_1) = a\cdot v_1^3 + b\cdot v_1$. Symbolic form of Jacobi matrix is

$$\mathbf{J} = \begin{pmatrix} -\dfrac{y_{11}}{C_{\mathrm{be}}} & -\dfrac{y_{12}}{C_{\mathrm{be}}} & 0\\ -\dfrac{b}{(C+C_{\mathrm{ce}})} & -\dfrac{y_{22}}{(C+C_{\mathrm{ce}})} & -\dfrac{1}{(C+C_{\mathrm{ce}})}\\ 0 & \dfrac{1}{L} & 0 \end{pmatrix}, \tag{2}$$

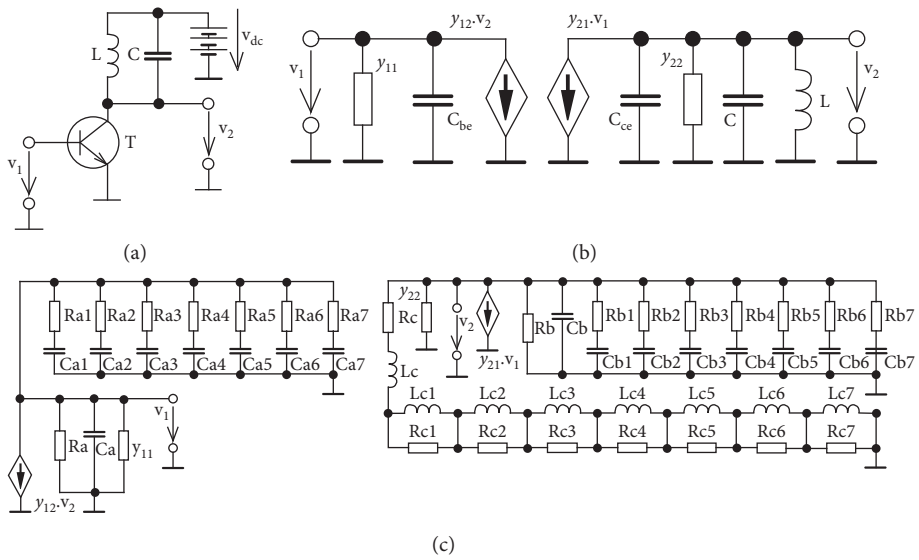

Figure 1: Class C amplifier with single bipolar transistor: (a) conventional simplifier connection, (b) concept considering transistor as two-port described by scalar linear admittance parameters, (c) equivalent circuit for non-integer-order accumulation elements in class C amplifier.

and characteristic polynomial calculated for single fixed point located at origin is

$$\det(\lambda \cdot \mathbf{E} - \mathbf{J}) = \lambda^3 + \left(\frac{y_{11}}{C_{be}} + \frac{y_{22}}{C + C_{ce}}\right)\lambda^2 + \left(\frac{1}{(C + C_{ce})L} + \frac{y_{11} \cdot y_{22} - b \cdot y_{12}}{C_{be}(C + C_{ce})}\right)\lambda + \frac{y_{11}}{C_{be}(C + C_{ce})L} = 0. \tag{3}$$

In further text, let us assume that biasing point forces transistor to work in a regime of constant current source; i.e., $y_{22} = 0$ S. Also, suppose that normalized values of accumulation elements are $C_{ce} = 0$ F, $C_{be} = C = 1$ F, $L = 1$ H and backward transconductance is linear; i.e., $y_{12} = 1$ S. Considering this, characteristic polynomial simplifies into

$$\gamma\colon \lambda^3 + y_{11} \cdot \lambda^2 + (1 - b)\lambda + y_{11} = 0. \tag{4}$$

For the purpose of the upcoming optimization, namely, to reduce size of hyperspace of parameters that undergoes search, limit cases for sought parameters become important

$$\begin{aligned} \lim_{y_{11} \longrightarrow 0} \operatorname{roots}(\gamma)&: \ \lambda_{1,2} = \mp\sqrt{b-1}, \quad \lambda_3 = 0, \\ \lim_{b \longrightarrow 0} \operatorname{roots}(\gamma)&: \ \lambda_{1,2} = \mp j, \quad \lambda_3 = y_{11}. \end{aligned} \tag{5}$$

3. Numerical Analysis

All numerical integration results presented in this paper were achieved by using four-order Runge–Kutta method with fixed step size. This routine was also used as core for calculation of the largest Lyapunov exponent (LLE) [41] together with Gram–Smith orthogonalization. LLE as the flow quantifier forms one fitness function for non-gradient optimization as admitted in papers [42, 43]. In fact, searching for chaotic solution of dynamical system is a multi-objective optimization problem. Firstly, chaotic behaviour should not be interchanged with long transient motion. Therefore, LLE needs to be calculated on the attractor. Also, slowly divergent motion needs to be removed from interesting solution. These potentially useful results are stored and finally verified by handmade analysis and attractor visualization. Boundedness of numerically integrated ω-limit set is verified via inside-sphere condition. Whole optimization routine was implemented in MATLAB. Since evaluation of individual objective functions is not mutually connected, searching process could be significantly accelerated by employing CUDA-based parallel processing. Nevertheless, searching within three-dimensional space of internal system parameters is still a very demanding operation.

Note that the optimization procedure described above and its results, i.e., numerical values of input admittance of transistor and shape of the cubic polynomial forward transconductance, do not have direct correlation with physical nature of one stage class C amplifier. However, admittance is a scalable network quantity (via impedance norm) and, for the large processed amplitudes of useful signal, saturation-type amplification property of bipolar transistor is mild hypothesis. Of course, normalized value of $y_{12} = 1$ S indicates strongly non-unilateral bipolar transistor stage.

Two sets of internal parameters leading to different shapes of strange attractors and associated non-integer

Kaplan–Yorke dimension D_{KY} have been discovered, namely,

$$\begin{aligned} y_{11} &= 0.2, \\ a &= -0.8, \\ b &= 2.56, \\ \mathrm{LE}_{\max} &= 0.061, \\ D_{\mathrm{KY}} &= 2.234, \end{aligned} \tag{6}$$

$$\begin{aligned} y_{11} &= 0.2, \\ a &= -0.8, \\ b &= 3.5, \\ \mathrm{LE}_{\max} &= 0.072, \\ D_{\mathrm{KY}} &= 2.127. \end{aligned} \tag{7}$$

Eigenvalues associated with fixed point for dynamical system with (6) are

$$\begin{aligned} \lambda_1 &= -1.408, \\ \lambda_2 &= 1.077, \\ \lambda_3 &= 0.132, \end{aligned} \tag{8}$$

and for set (7) we get

$$\begin{aligned} \lambda_1 &= -1.721, \\ \lambda_2 &= 1.44, \\ \lambda_3 &= 0.081. \end{aligned} \tag{9}$$

Therefore, origin is saddle-node equilibrium point with stability index 1.

Figure 2 demonstrates shapes of typical strange attractors generated by dynamical system (1) with parameters (6). Numerical integration was calculated with final time 300 s and time step 10 ms. Because of vector field symmetry with respect to the horizontal plane $z = 0$, there are two mirrored strange attractors with the same geometric structure. Figure 2 also shows sensitivity to the small deviations in the initial conditions and vector field near fixed point $\mathbf{x_e} = (0, 0, 0)^T$. For this analysis, final time and time step were kept the same. Figure 3 is a visualization of LLE as two-dimensional function of shape of forward transconductance function $y_{21}(v_1)$. For values of input admittance y_{11} bigger than 0.6, chaos disappears, and class C amplifier produces various limit cycles. Order in circuit is restored thanks to the significant system dissipation. Of course, cases with $y_{11} \leq 0$ are out of the question because of the physical essence of the input admittance. Note that hidden attractors including those with fractal geometric dimension are not excluded by investigations presented in this paper. Figure 4 shows distribution of dynamic energy over state space volume occupied by strange attractor. To visualize the local dynamics calculated at each point in 510×610 grid, numerical integration was up to final time 1 s with time step 10 ms. Value ranges for individual edges are uniform: $v_1 \in (-2.5, 2.5)$ and $v_2 \in (-3, 3)$.

Figure 5 provides information about shape of the strange attractor if dynamical system (1) has the internal parameters (7). It strongly resembles the so-called double hook attractor that can be generated by Chua's circuit with three real eigenvalues associated with fixed point located at origin [44]. Unlike Chua's circuit, there are two coexisting double hooks. Also note evolution of two neighbouring orbits plotted with respect to time: difference is visible after quite a long time; about 120 s lapses to phase shift and 170 s expires to observe exponential divergence.

3.1. Fractional-Order Case. Recently, discovery and presentation of new chaotic dynamical system are usually supported by numerical analysis of describing mathematical model under condition of fractionality; that is, one or all differential equations are of non-integer order. Such investigation could be performed on three levels. The first level is pure mathematical and involves discretization of ordinary [45] or partial [46] differential equations and performing iterations. This numerical approach is well suited for chaotic [47–49] as well as hyperchaotic [50, 51] dynamics. The second level is to model fractional-order (FO) circuit element in the form of two-terminal or two-port using suitable circuit-oriented software such as OrCAD PSpice or Multisim. Both classes of FO elements (often called constant phase elements due to their fundamental properties keeping constant phase shift between response and driving force) could be considered either ideal or approximated in the frequency domain. To reach precise approximation of FO two-terminal fully passive circuit element, paper [52] could be consulted. Design procedure toward approximated FO two-port element is provided in a comprehensive study [53]. Since chaotic signal is wideband, the mentioned approximations should be valid, at least, within the same frequency range. To avoid laborious calculations, passive ladder FO capacitors of different math orders can be found in [54].

Because of practically oriented concluding remarks coming from this research study, the last method dedicated for modelling non-integer nature of accumulation elements associated with class C amplifier has been adopted. New circuit structure to be analysed is provided in Figure 1(c). Note that FO nature of accumulation elements is modelled by fully passive ladder networks having seven sections. This number turns to be enough, from the viewpoint of both required frequency range (five decades) and maximal allowed phase error (that is lower than 1 degree). To increase universality, let us denote mathematical order of the approximation associated with capacitor C_{be} by k, sum of capacitors $C + C_{\mathrm{ce}}$ by letter m, and math order of inductor by n. State vector changes into a more complex form

$$x = \left(v_1, v_{a1}, \ldots, v_{ak}, v_2, v_{b1}, \ldots, v_{bm}, i_L, i_{c1}, \ldots, i_{cn}\right)^T. \tag{10}$$

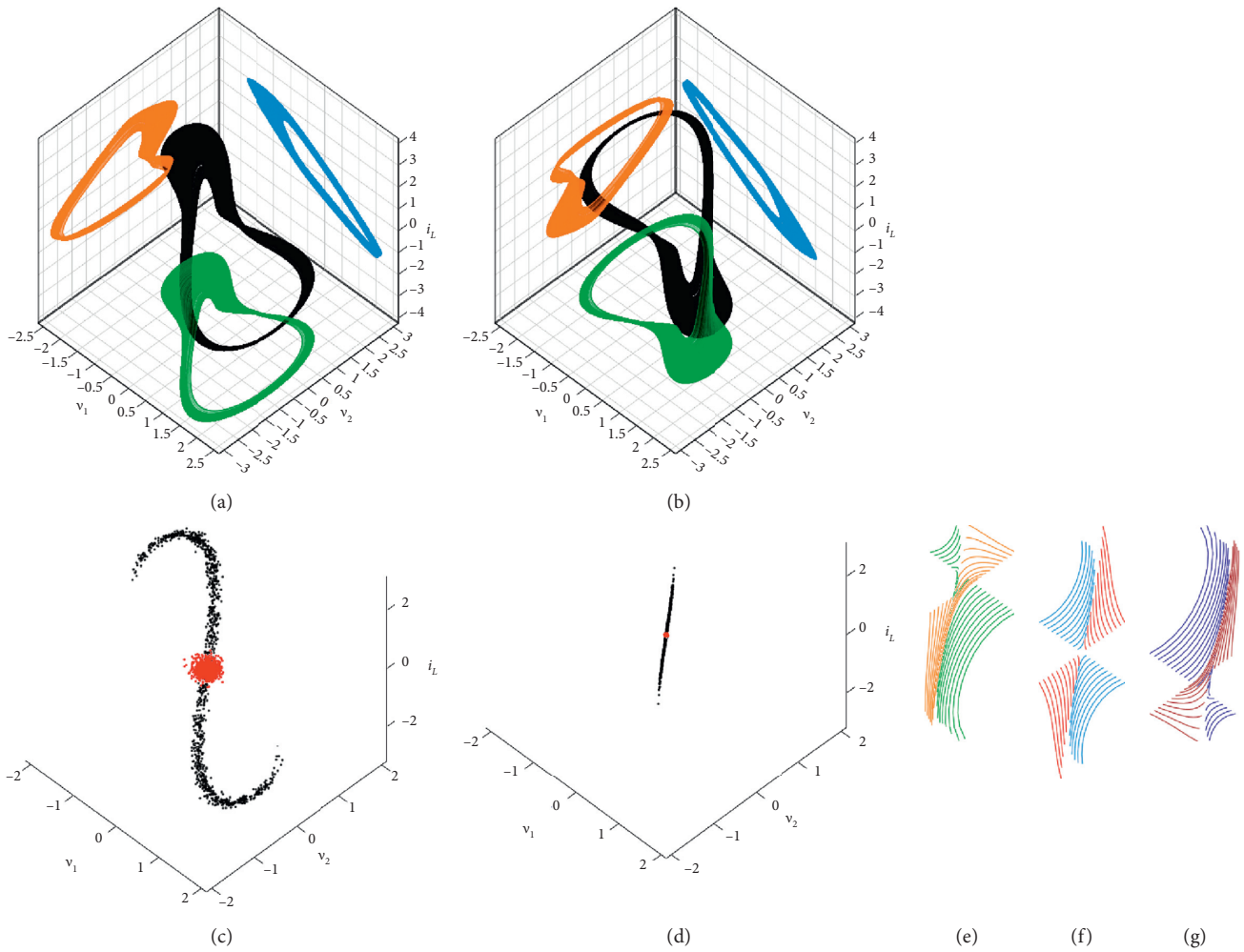

Figure 2: Numerical integration leading to typical chaotic attractors generated by fundamental class C amplifier: (a) $x_0 = (0, 0.5, 0)^T$, and (b) $x_0 = (0, -0.5, 0)^T$. Final states (black dots) that represent sensitivity to changes of initial conditions (red dots), normal distribution of the initial states around $x_0 = (0, 0.5, 0)^T$ with the standard deviation: (c) $\sigma = 0.01$, and (d) $\sigma = 0.1$. Local behaviour close to fixed point: (e) plane $z_0 = 1$, line $y_0 = 0$ (green) and line $x_0 = 0$ (orange), (f) plane $z_0 = 0$, line $y_0 = 0$ (blue), line $x_0 = 0$ (red), and (g) plane $z_0 = -1$, line $x_0 = 0$ (dark blue), line $x_0 = 0$ (brown).

Behaviour of this lumped electronic system is uniquely determined by the following set of ordinary differential equations:

$$\frac{\mathrm{d}}{\mathrm{d}t}v_1 = -\frac{1}{C_a}\left(\frac{1}{R_a} + y_{11}\right)v_1 - \frac{y_{12}}{C_a}v_2 + \frac{1}{C_a}\sum_{j=1}^{k}\frac{1}{R_{aj}}\left(v_{aj} - v_1\right), \tag{11a}$$

$$x = 1, 2, \ldots, k: \frac{\mathrm{d}}{\mathrm{d}t}v_{ax} = \frac{1}{C_{ax}R_{ax}}\left(v_1 - v_{ax}\right), \tag{11b}$$

$$\frac{\mathrm{d}}{\mathrm{d}t}v_2 = -\frac{1}{C_b}\left(\frac{1}{R_b} + y_{22}\right)v_2 - \frac{y_{21}(v_1)}{C_b} + \frac{1}{C_b}\sum_{j=1}^{m}\frac{1}{R_{aj}}\left(v_{bj} - v_2\right), \tag{11c}$$

$$x = 1, 2, \ldots, m: \frac{\mathrm{d}}{\mathrm{d}t}v_{ax} = \frac{1}{C_{ax}R_{ax}}\left(v_2 - v_{ax}\right), \tag{11d}$$

$$\frac{\mathrm{d}}{\mathrm{d}t}i_{L_c} = \frac{v_2}{L_c} - \frac{R_c}{L_c} - \frac{1}{L_c}\sum_{j=1}^{n}R_{cj}\left(i_{L_c} - i_{cj}\right), \tag{11e}$$

$$x = 1, 2, \ldots, n: \frac{\mathrm{d}}{\mathrm{d}t}i_{cx} = \frac{R_{cx}}{L_{cx}}\left(i_{L_c} - i_{cx}\right), \tag{11f}$$

where v_{aj} and v_{bj} stand for voltage across j^{th} capacitor in approximation of C_{be} and $C + C_{\text{ce}}$ FO capacitor, respectively. Similarly, symbol i_{cj} represents current flowing through j^{th} inductor. Note that second, fourth, and sixth differential equation are presented in our system k^{th}, m^{th}, and n^{th} times, respectively. Obviously, we are experiencing system of $3 + k + m + n$ first-order ordinary differential equations. Thus, instead of calculation of the binomial coefficients and discretization of differential equations, we can follow the standard way of numerical integration process. Some numerical results are graphically demonstrated via Figure 6. For mathematical orders of the approximated constant

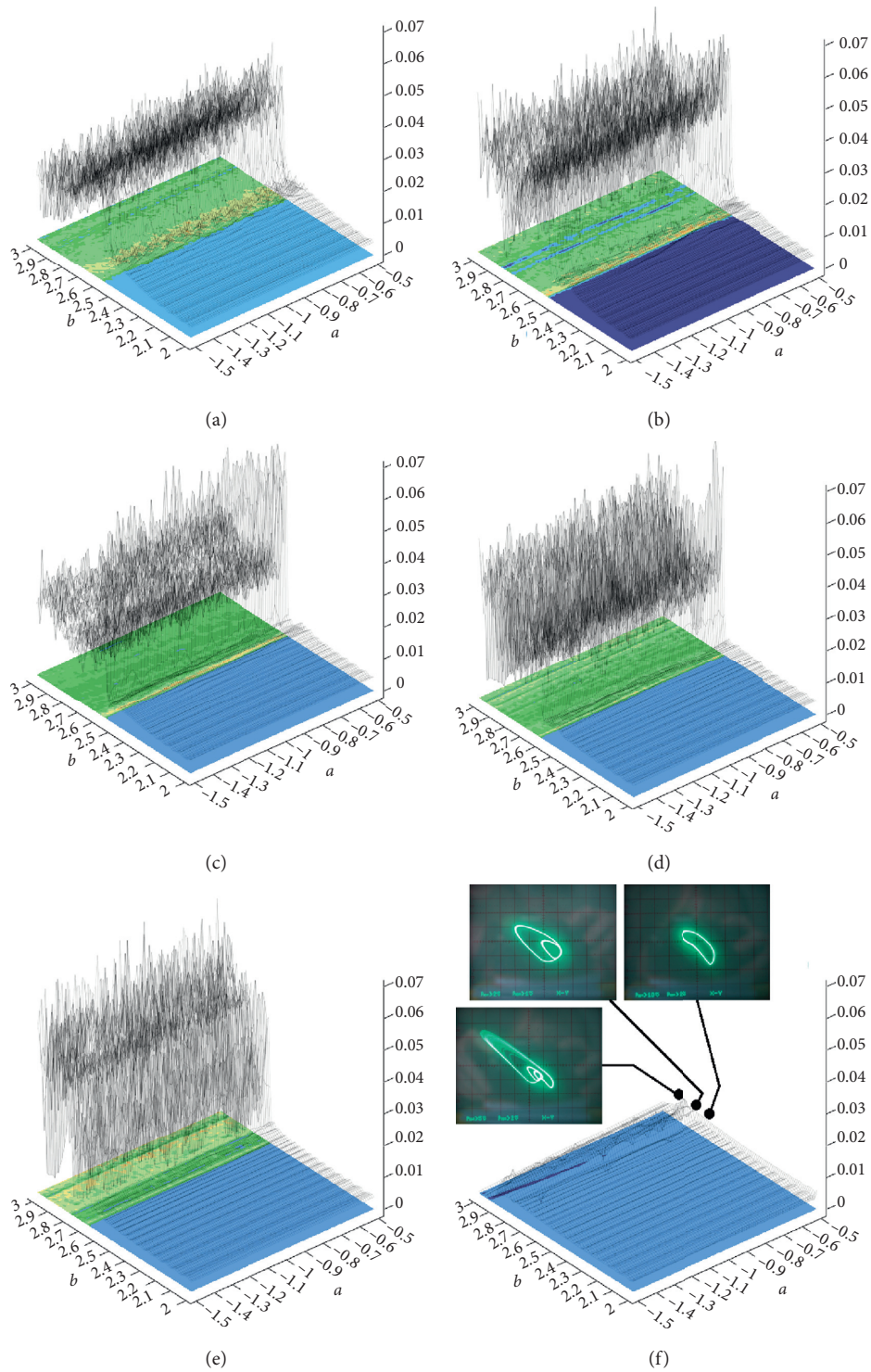

Figure 3: Topographically scaled surface-contour plot of LLE as a function of polynomial coefficients for different values of system dissipation: (a) $y_{11} = 0.1$, (b) $y_{11} = 0.2$, (c) $y_{11} = 0.3$, (d) $y_{11} = 0.4$, (e) $y_{11} = 0.5$, and (f) $y_{11} = 0.6$. Oscilloscope screenshots provided here demonstrate route-to-chaos scenario via period doubling sequence associated with class C amplifier having the largest system dissipation considered in this manuscript.

phase elements below 0.9, chaotic behaviour of class C amplifier disappears and for very low total orders of circuit only limit cycles were observed. Symbols α, β, and δ used in Figure 6 represent FO of first, second, and third differential equation, respectively. Let us discuss a specific FO case where orders of individual differential equations equal 0.9.

By adopting numerical values provided in paper [54] for mathematical order 0.9, frequency range of constant phase

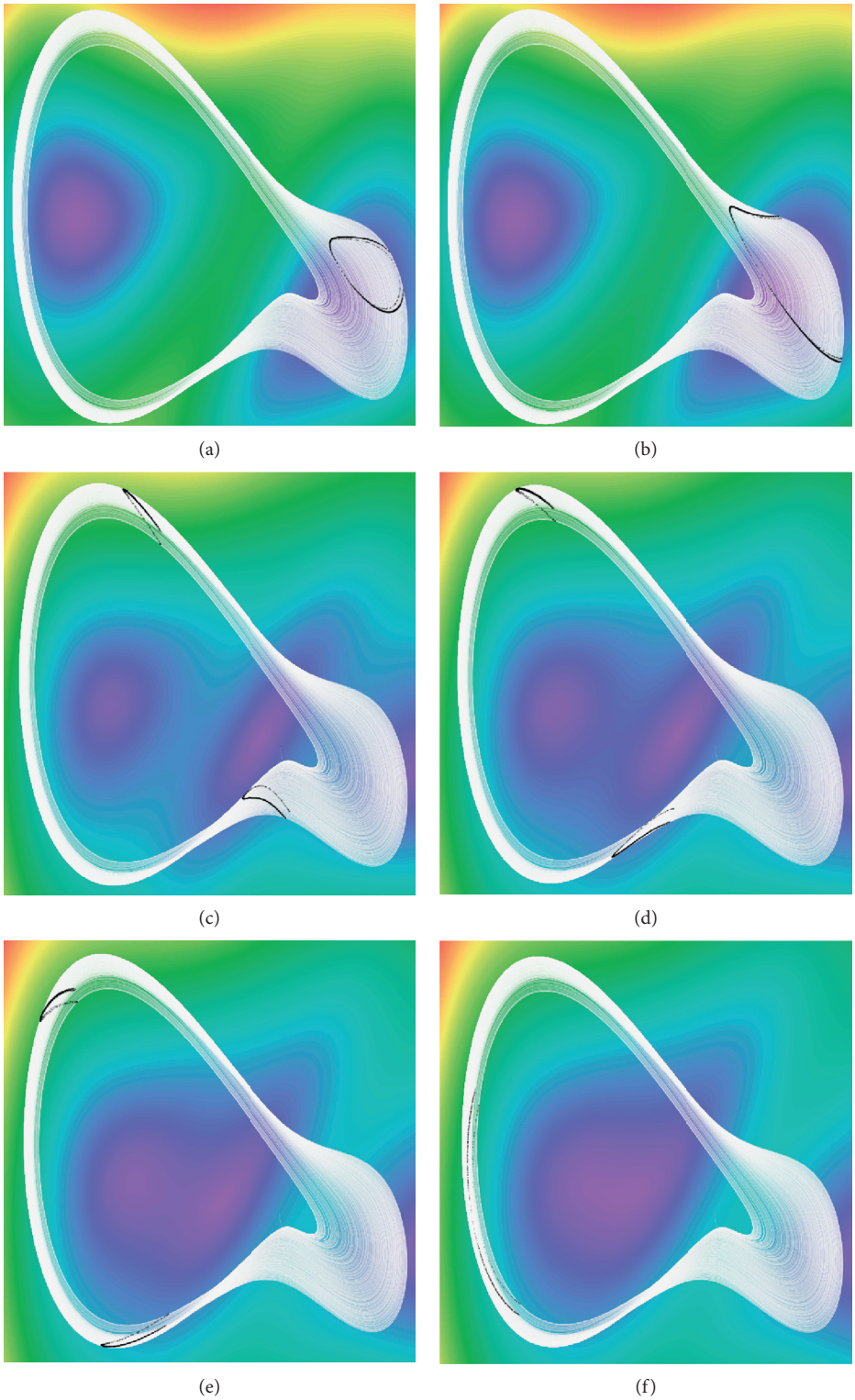

Figure 4: Rainbow scaled plots showing distribution of the kinetic energy over the state space, horizontal slices: (a) $z_0 = -2.3$, (b) $z_0 = -2$, (c) $z_0 = 0$, (d) $z_0 = 0.5$, (e) $z_0 = 1$, and (f) $z_0 = 1.5$. Colour scale is as follows: very high energy (red), high energy (yellow), average energy (green), low energy (blue), very low energy (purple). Black dots represent return maps for the Poincaré sections equivalent to horizontal slices mentioned above.

element can be downscaled from original interval 10 Hz up to 1 MHz. To analyse normalized circuit, pseudo-capacitance of the constant phase element will be $1\,\mathrm{s}^{0.1}/\mathrm{F}$ (FO capacitor) and pseudo-inductance approximately equals $1\,\mathrm{s}^{0.1}/\mathrm{F}$ (FO inductor). For the first case, resulting numerical values of resistors and capacitors will be

$$\begin{aligned} R_a &= 1.19\,\Omega, \\ R_{a1} &= 0.21\,\Omega, \\ R_{a2} &= 0.031\,\Omega, \\ R_{a3} &= 4.579\cdot 10^{-3}\,\Omega, \\ R_{a4} &= 6.79\cdot 10^{-4}\,\Omega, \\ R_{a5} &= 1.008\cdot 10^{-4}\,\Omega, \\ R_{a6} &= 1.498\cdot 10^{-5}\,\Omega, \\ R_{a7} &= 2.24\cdot 10^{-6}\,\Omega, \\ C_a &= 0.206\,\mathrm{F}, \\ C_{a1} &= 0.171\,\mathrm{F}, \\ C_{a2} &= 0.14\,\mathrm{F}, \\ C_{a3} &= 0.113\,\mathrm{F}, \\ C_{a4} &= 0.091\,\mathrm{F}, \\ C_{a5} &= 0.074\,\mathrm{F}, \\ C_{a6} &= 0.06\,\mathrm{F}, \\ C_{a7} &= 0.053\,\mathrm{F}. \end{aligned} \tag{12}$$

Of course, these values hold for second FO capacitor as well; i.e., index a can be replaced by b. FO inductor can be modelled by values

$$\begin{aligned} R_c &= 2.4\,\Omega, \\ R_{a1} &= 12\,\Omega, \\ R_{a2} &= 63\,\Omega, \\ R_{a3} &= 333.6\,\Omega, \\ R_{a4} &= 1716\,\Omega, \\ R_{a5} &= 8850\,\Omega, \\ R_{a6} &= 4.62\cdot 10^{4}\,\Omega, \\ R_{a7} &= 8.4\cdot 10^{4}\,\Omega, \\ L_c &= 0.198\,H, \\ L_{c1} &= 0.12\,H, \\ L_{c2} &= 0.102\,H, \\ L_{c3} &= 0.084\,H, \\ L_{c4} &= 0.072\,H, \\ L_{c5} &= 0.058\,H, \\ L_{c6} &= 0.048\,H, \\ L_{c7} &= 0.04\,\mathrm{H}. \end{aligned} \tag{13}$$

LLE can be utilized to obtain piecewise linear approximation of a smooth polynomial vector field [55]. In our case, transconductance $y_{21}(v)$ could be substituted by the three-segment odd-symmetrical function with parameters

$$\begin{aligned} |v_1| \le V_{\mathrm{BP}}&: \; y_{21}(v_1) = g_{\mathrm{in}}\cdot v_1, \\ v_1 > V_{\mathrm{BP}}&: \; y_{21}(v_1) = g_{\mathrm{out}}(v_1 - V_{\mathrm{BP}}) + g_{\mathrm{in}}\cdot V_{\mathrm{BP}}, \\ v_1 < -V_{\mathrm{BP}}&: \; y_{21}(v_1) = g_{\mathrm{out}}(v_1 + V_{\mathrm{BP}}) - g_{\mathrm{in}}\cdot V_{\mathrm{BP}}. \end{aligned} \tag{14}$$

For the first discovered set of "chaotic" parameters (6), piecewise linear approximation can be adopted with

$$\begin{aligned} V_{\mathrm{BP}} &= 1.2, \\ g_{\mathrm{in}} &= 1.9, \\ g_{\mathrm{out}} &= -6, \end{aligned} \tag{15}$$

while for the second set of parameters (7) leading to evolution of robust chaos optimal piecewise linear approximation is

$$\begin{aligned} V_{\mathrm{BP}} &= 1.3, \\ g_{\mathrm{in}} &= 2.2, \\ g_{\mathrm{out}} &= -7. \end{aligned} \tag{16}$$

The corresponding strange attractor is provided in Figure 7 together with the plot of dynamic energy distribution over three horizontal planes of state space. Note the high degree of attractor similarity with the results provided in Figure 5.

An interesting question that could be raised here is the possibility to generate the so-called multi-scroll [56] or multi-grid [57] strange attractors. This kind of complex behaviour is associated with specific geometry of vector field. State space can be divided into "periodic" formation of the affine segments with the same properties: existence of single fixed point with saddle-spiral local geometry with stability index 1. In each mentioned segment, state trajectory is attracted toward eigen-plane and spirals away to another segment. Famous double-scroll attractor observed in Chua's oscillator can be considered as ancestor for this kind of motion and special type of multi-spiral attractor. However, eigenvalues associated with parameter sets (15) are

$$\begin{aligned} \lambda_1 &= -1.142, \\ \lambda_2 &= 0.687, \\ \lambda_3 &= 0.255, \end{aligned} \tag{17}$$

and for set (16) we obtain

$$\begin{aligned} \lambda_1 &= -1.269, \\ \lambda_2 &= 0.893, \\ \lambda_3 &= 0.176. \end{aligned} \tag{18}$$

These eigenvalues do not lead to vector field configuration promising from the viewpoint of generation of multi-spiral attractor. Also, numerical investigation does not reveal such kind of dynamical motion. In outer regions of the state space, i.e., if $v_1 < -V_{\mathrm{BP}}$ or $v_1 > V_{\mathrm{BP}}$, dynamical system exhibits strong dissipation along all directions and state orbit is pushed toward inner segment as demonstrated by means of Figure 8.

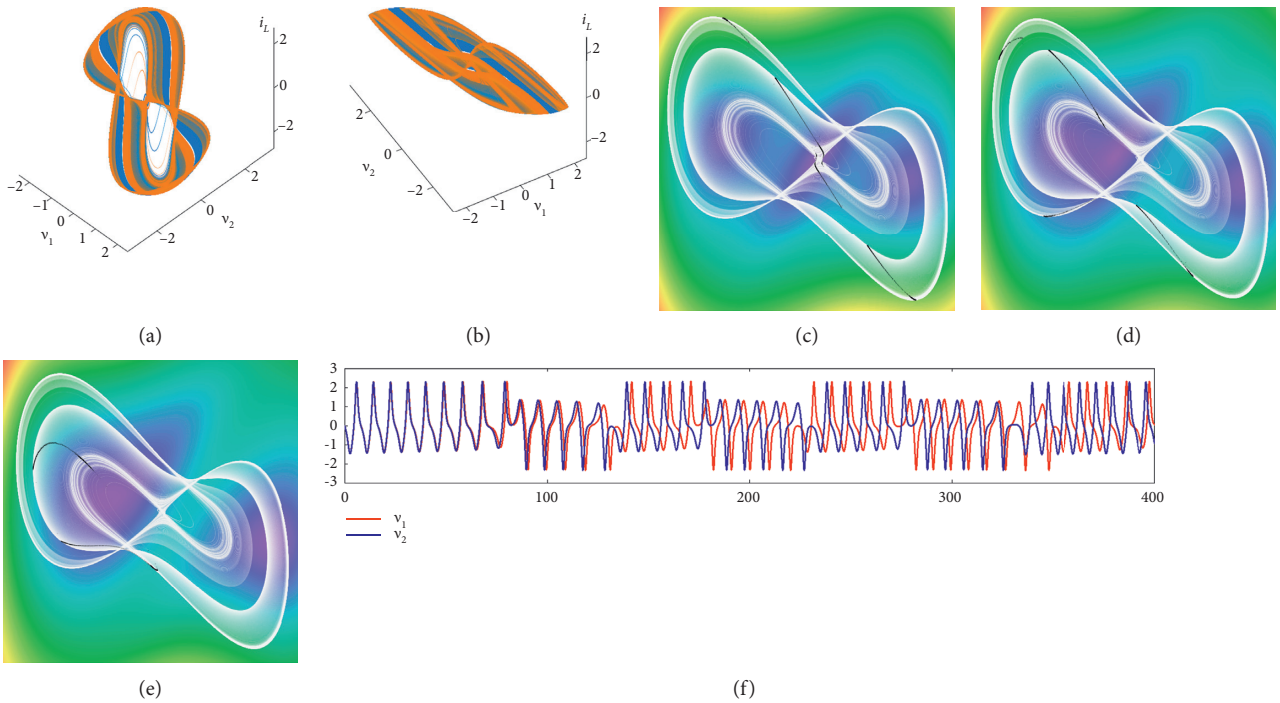

Figure 5: Brief numerical analysis of chaotic system (1) considering second discovered set of parameters (7): (a) (b) perspective visualization of generated strange attractor. Rainbow scaled distribution of kinetic energy measured in plane: (c) $z = 0$, (d) $z = 1$, and (e) $z = 2$. Black dots are return maps plotted at the corresponding planes. Generated waveforms in time domain (f): red curve for $x_0 = (0, 0.5, 0)^T$ and blue curve for $x_0 = (0, 0.51, 0)^T$.

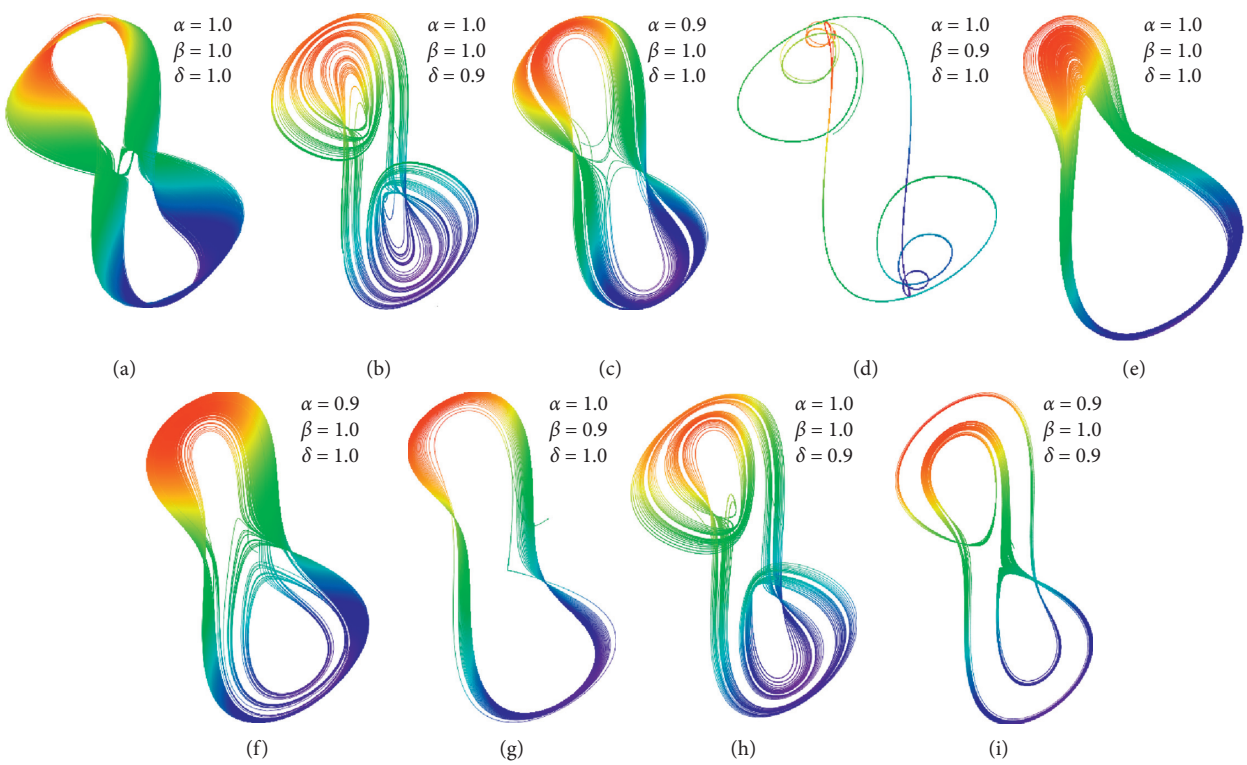

Figure 6: Numerical investigation of class C amplifier with constant phase elements, selected Mathcad-based results: for (a), (b), (c), (d), parameter set (6) was adopted, and plots (e) (f), (g), (h), (i) are bounded to parameter group (7).

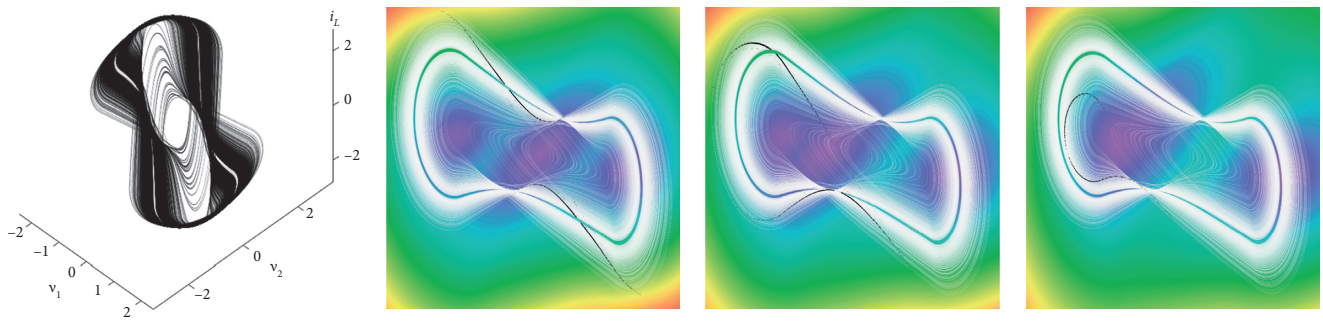

(a) (b) (c) (d)

Figure 7: Brief numerical analysis of the piecewise linear case of the chaotic system: (a) perspective visualization of generated strange attractor. Rainbow scaled distribution of kinetic energy measured in plane: (b) $z = 0$, (c) $z = 1$, and (d) $z = 2$. Black dots are return maps plotted at the corresponding planes.

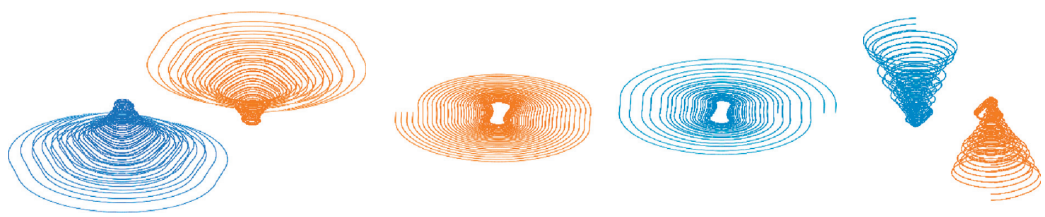

(a) (b) (c)

Figure 8: Convergency of state trajectory toward inner segment of vector field with positive (orange) and negative (blue) displacement of initial conditions in direction of (a) voltage v_1, (b) voltage v_2, and (c) current i_L.

Figure 9 demonstrates complex nature of basins of attraction calculated for dynamical system (1) with parameter group (6). Individual colours distinguish between three ω-limit sets: chaotic attractor (red), solution close to limit cycle (green), and fixed point (black). Due to vector field symmetry, only horizontal state space slices having $z \geq 0$ are provided. Figure 10 represents the same plots but related to parameter set (7).

By introducing constant term to polynomial function $y_{21}(v_1) = a \cdot v_1^3 + b \cdot v_1 + c$, fixed point located at the origin turns into virtual. For small values of parameter c, this equilibrium with less dynamical system still generates strange attractors like the original. Thus, there is the overlap of discovered chaotic dynamical system into quite rare cases without equilibrium.

4. Circuit Design

To meet the basic criteria for presentation of new chaotic system [58], structural stability of desired strange attractor needs to be proven. Because of limited capability of human eye to catch short time transient movement, practical construction and laboratory verification of chaotic oscillator is the best way how to demonstrate such stability.

If a set of ordinary differential equations and numerical values of internal parameters is known, the problem of circuit synthesis belongs to simple and straightforward task with multiple correct solutions. If minimization of circuits elements is not design priority, we can follow the concept of analogue computers. Only three building blocks are required: inverting integrators, differential amplifiers, and two-ports with a nonlinear transfer characteristic. Final network can work in either voltage [59, 60] or current mode [61]. Under specific circumstances, resulting circuit can be simplified by substitution of passive two-ports [62]. More complex nonlinear transfer curves can be implemented by digital subcircuits [63]. The method leading to full on-chip implementation of chaotic oscillator can be found in an example in paper [64]. Circuity realization of chaotic oscillator based on model (1) is shown by means of Figure 11(a). It contains two voltage-feedback operational amplifiers TL082, current feedback operational amplifier with the frequency compensation node (TZ) AD844, and two four quadrant analogue multipliers AD633 with versatile voltage transfer function $V_W = K \cdot (V_{X1} - V_{X2})\,(V_{Y1} - V_{Y2})$. All state variables can be easily measured as voltages at output of inverting integrators. Circuit is fed by symmetrical $\pm 15\,\mathrm{V}$ voltage supply. Dynamical behaviour of this network is described by the following set of ordinary differential equations:

$$\begin{aligned} C\frac{\mathrm{d}}{\mathrm{d}t}v_1 &= -\frac{v_1}{R_1} - \frac{v_2}{R_2}, \\ C\frac{\mathrm{d}}{\mathrm{d}t}v_2 &= -\frac{v_1}{R_3} - \frac{v_3}{R_4} + \frac{K^2}{R_5}v_1^3, \\ C\frac{\mathrm{d}}{\mathrm{d}t}v_3 &= \frac{v_2}{R_6}, \end{aligned} \tag{19}$$

where $K = 0.1$ represents internally trimmed transfer constant of multiplier.

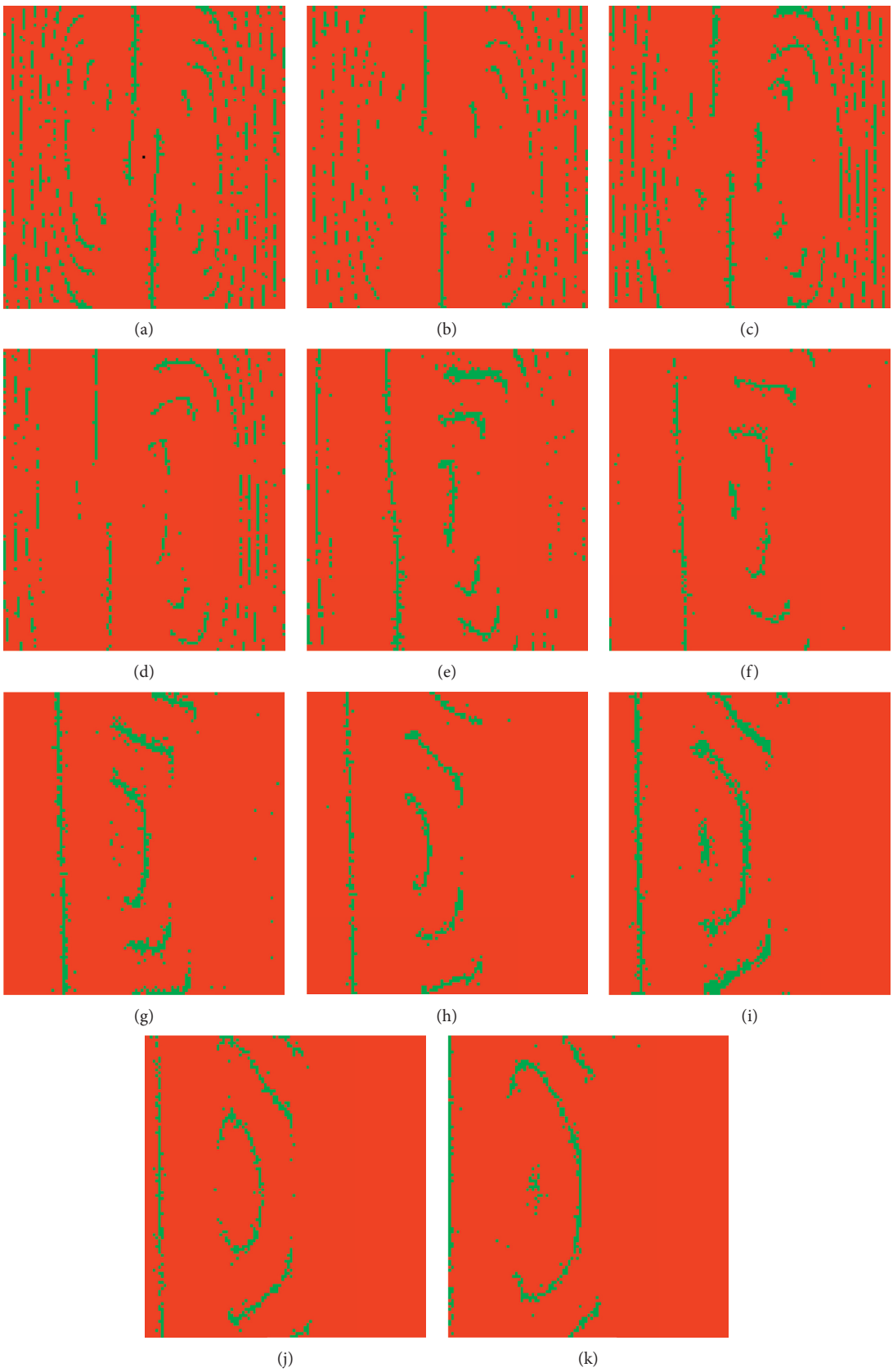

Figure 9: Basins of attraction visualized for list of horizontal planes: (a) $z_0 = 0$, (b) $z_0 = 0.5$, (c) $z_0 = 1$, (d) $z_0 = 1.5$, (e) $z_0 = 2$, (f) $z_0 = 2.5$, (g) $z_0 = 3$, (h) $z_0 = 3.5$, (i) $z_0 = 4$, (j) $z_0 = 4.5$, (k) $z_0 = 5$.

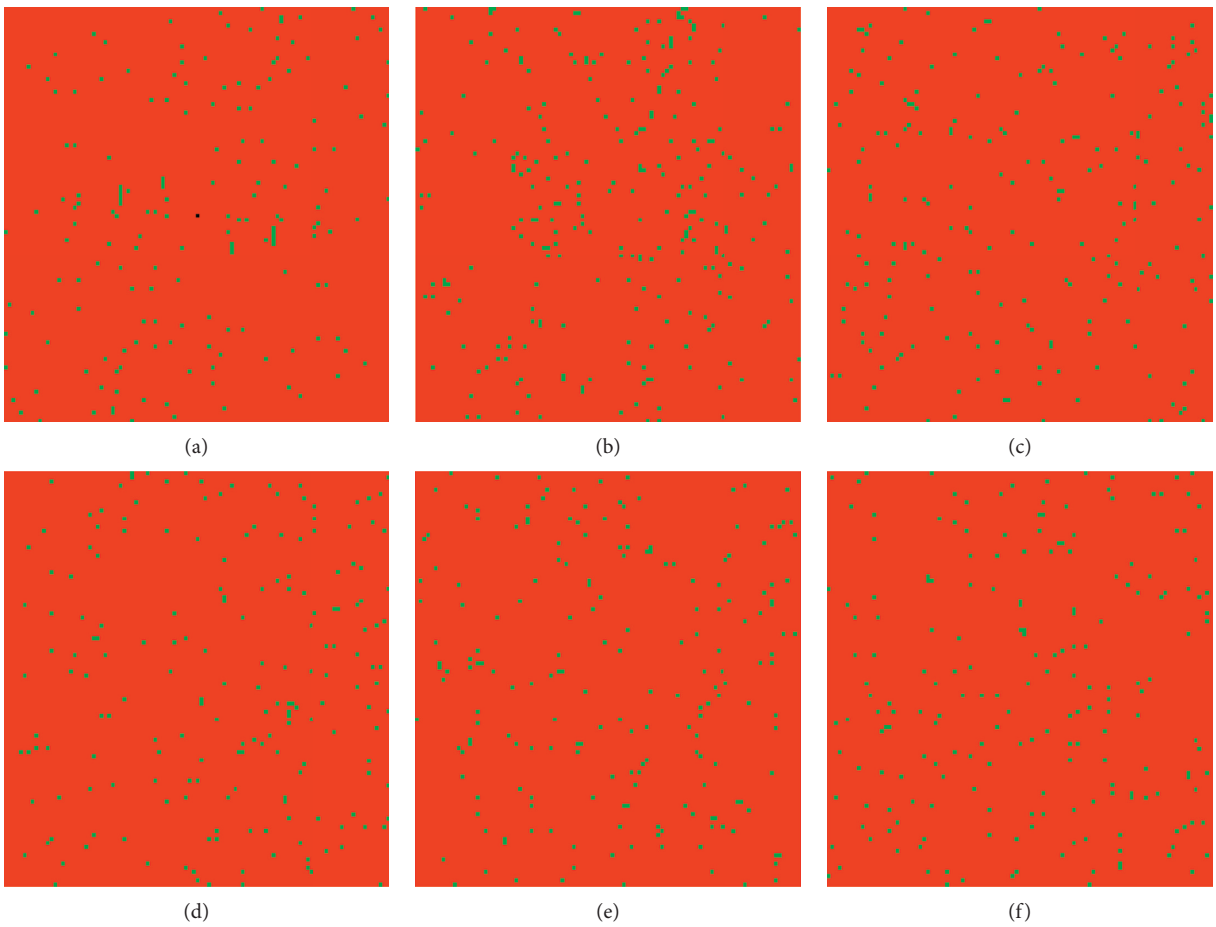

Figure 10: Basins of attraction visualized for list of horizontal planes: (a) $z_0 = 0$, (b) $z_0 = 1$, (c) $z_0 = 2$, (d) $z_0 = 3$, (e) $z_0 = 4$, (f) $z_0 = 5$.

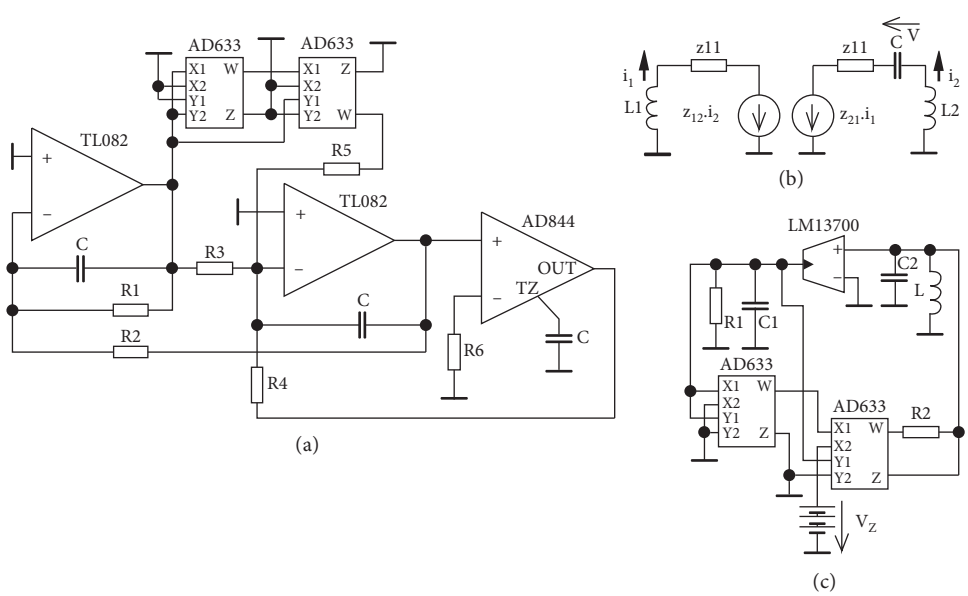

Figure 11: Two flow equivalent circuitry realizations of chaotic dynamical system: (a) voltage mode implementation of dynamical system (1), (b) principal schematic of dual circuit.

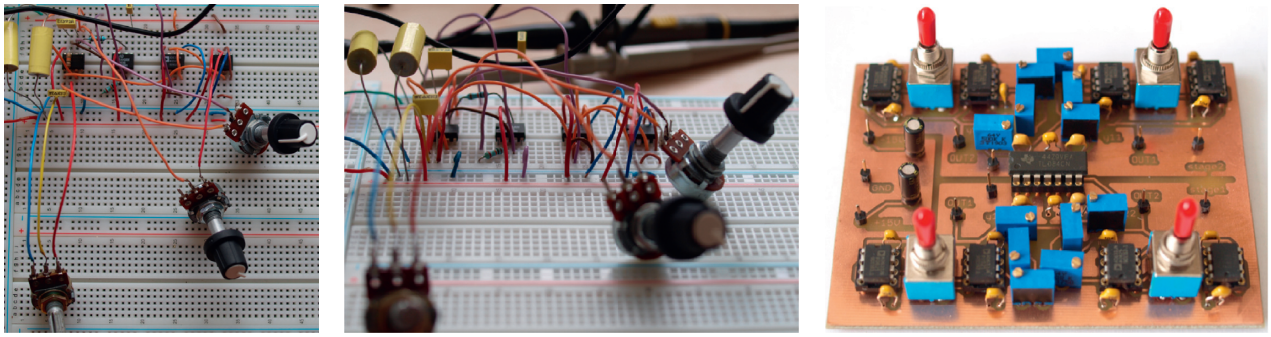

(a) (b) (c)

Figure 12: Experimental verification of discovered new chaotic oscillator: (a) (b) bread board circuit realization, (c) realization of single bipolar transistor-based class C amplifier cell with nonlinear transconductances.

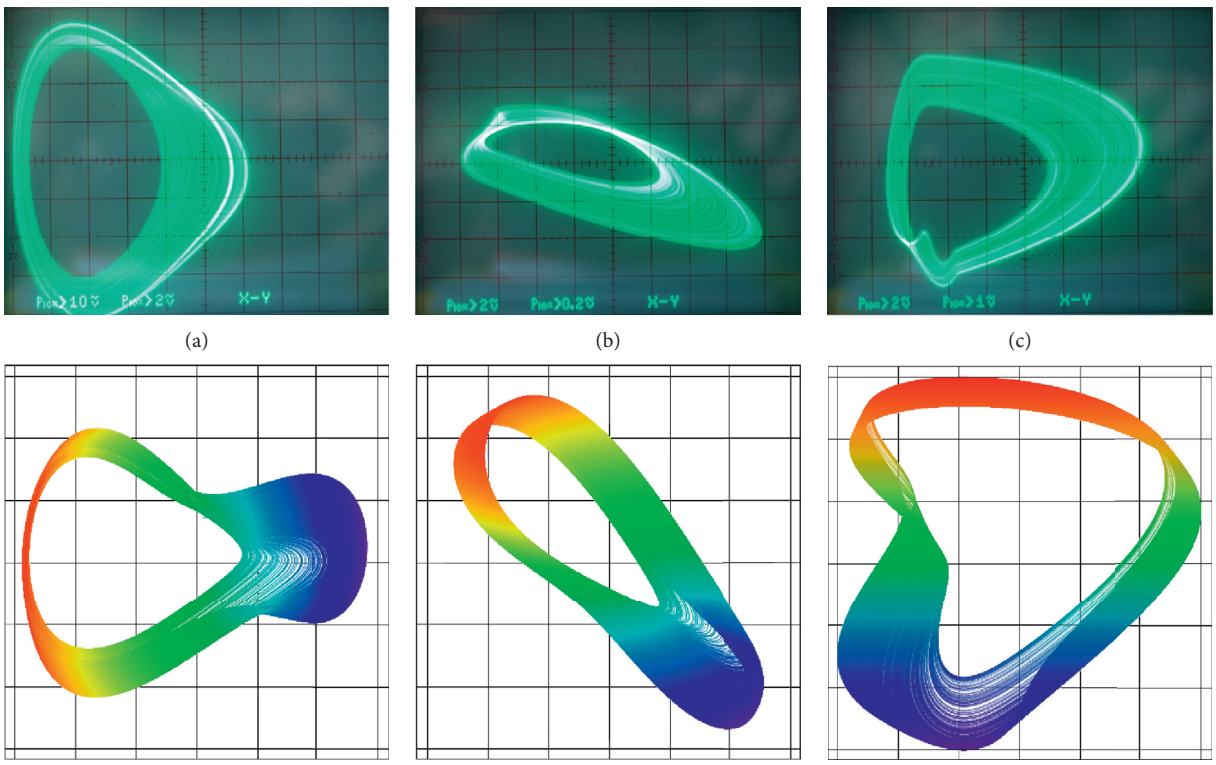

(a) (b) (c)

(d) (e) (f)

Figure 13: Experimental verification of designed circuit representation of class C amplifier, measured strange attractors in different plane projections: (a) v_2 vs v_1, (b) v_3 vs v_1, (c) v_3 vs v_2, and numerically integrated trajectories: (d) v_2 vs v_1 plane, (e) v_3 vs v_1 plane, (f) v_3 vs v_1 plotted with uniform voltage range ± 3 V.

Nonideal and parasitic properties of used active devices clearly limit the frequency spectrum of generated signal. This could be especially important in the case of oscillators where output waveforms (state variables) are the broad-band noise-like chaotic signals. Fortunately, time constant of designed chaotic oscillator can be shortened and resulting waveforms judged, both using suitable circuit simulator or laboratory measurement. Because of better correspondence between theoretical expectations and circuit analysis, OrCAD PSpice program has been utilized for this purpose. Individual active elements were modelled using third level of abstraction and influential parasitic properties swept parametrically. From the viewpoint of designed circuit, the most problematic part is AD633 exhibiting heavily distorted input-output characteristics for time constant of chaotic oscillator shorter than 1 μs. Further interesting reading about this topic can be found in [65].

Figure 11(b) recalls duality principle and construct circuit that is dual to Figure 1(b). It comprises two current-controlled voltage sources, but only z_{21} (i_1) is nonlinear. This circuit is described by the same differential equations as (1)

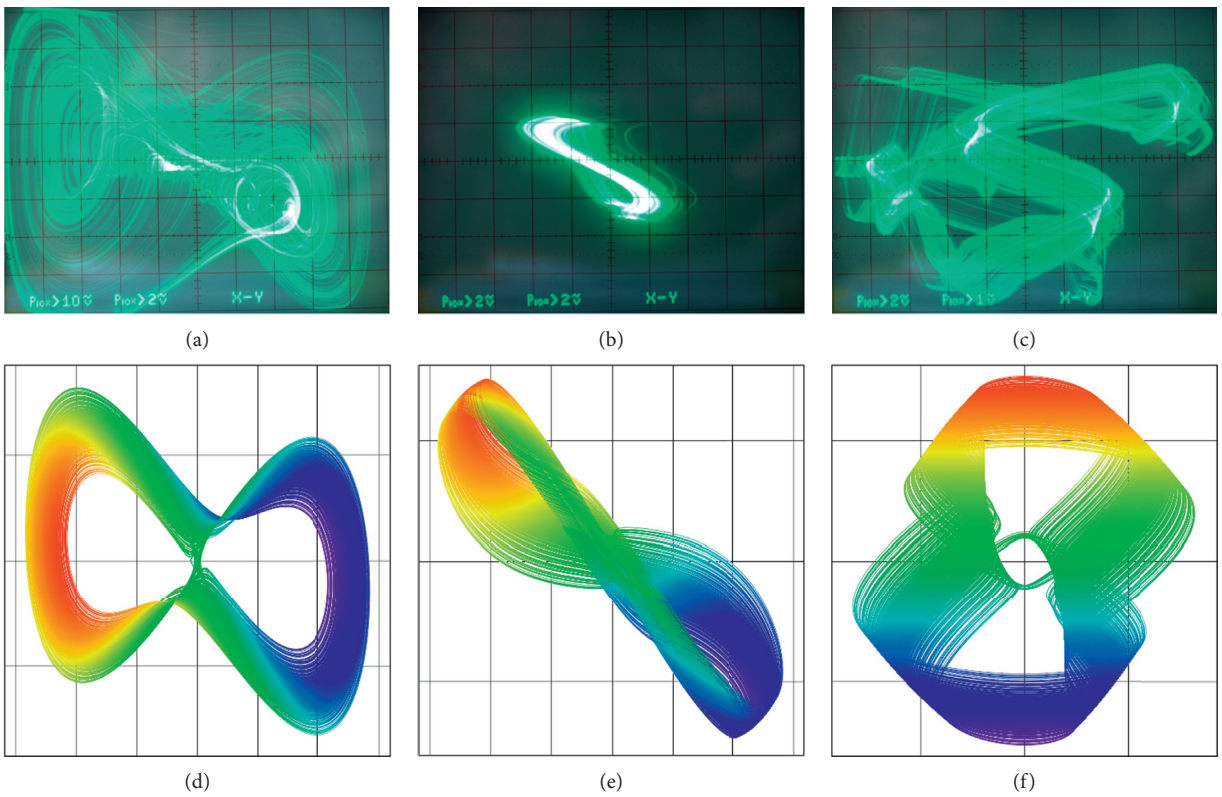

Figure 14: Experimental verification of designed circuit representation of class C amplifier, measured strange attractors in different plane projections: (a) v_2 vs v_1, (b) v_3 vs v_1, (c) v_3 vs v_2, and numerically integrated trajectories: (d) v_2 vs v_1 plane, (e) v_3 vs v_1 plane, (f) v_3 vs v_1 plotted with uniform voltage range ±3 V.

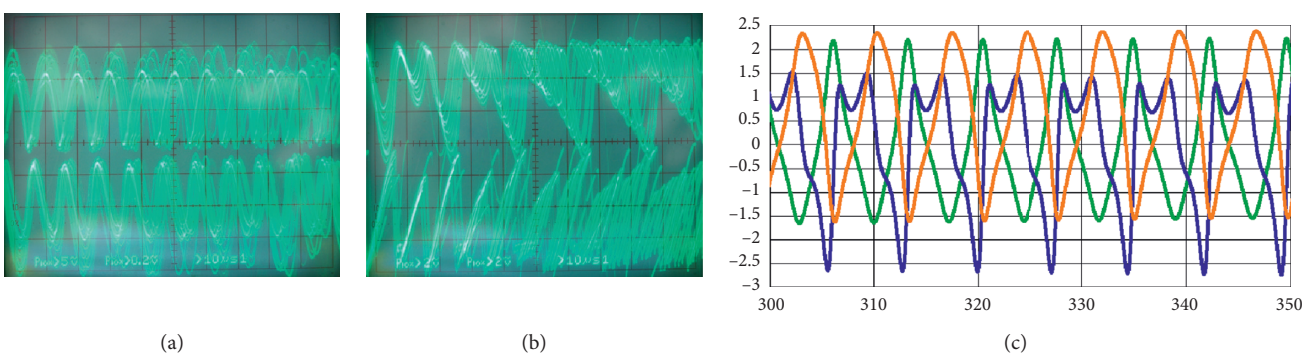

Figure 15: Chaotic waveforms in time domain captured by oscilloscope: (a) $v_3(t)$ and $v_1(t)$, (b) $v_2(t)$ and $v_1(t)$, numerically integrated orbits (c) $v_1(t)$ green, $v_2(t)$ blue, and $v_3(t)$ orange.

but after considering dual variables (voltages/currents) and parameters (admittances/impedances). In detail,

$$\begin{aligned} L_1\frac{\mathrm{d}}{\mathrm{d}t}i_1 &= -z_{11}\cdot i_1 - z_{12}\cdot i_2, \\ L_2\frac{\mathrm{d}}{\mathrm{d}t}i_2 &= -z_{21}\cdot i_1 - z_{22}\cdot i_2 - v, \\ C\frac{\mathrm{d}}{\mathrm{d}t}v &= i_2, \end{aligned} \tag{20}$$

where state vector becomes $x=(i_1,\ i_2,\ v)^T$. Direct circuitry realization of the state description of class C amplifier (1) can be found in Figure 11(c). The corresponding set of the ordinary differential equations are

$$\begin{aligned} C_1\frac{\mathrm{d}}{\mathrm{d}t}v_1 &= -\frac{v_1}{R_1} - g_T\cdot v_2, \\ C_2\frac{\mathrm{d}}{\mathrm{d}t}v_2 &= \frac{1}{R_2}\left(K^2\cdot v_1^3 - K\cdot V_Z\cdot v_1\right) - i_L, \\ L\frac{\mathrm{d}}{\mathrm{d}t}i_L &= v_2, \end{aligned} \tag{21}$$

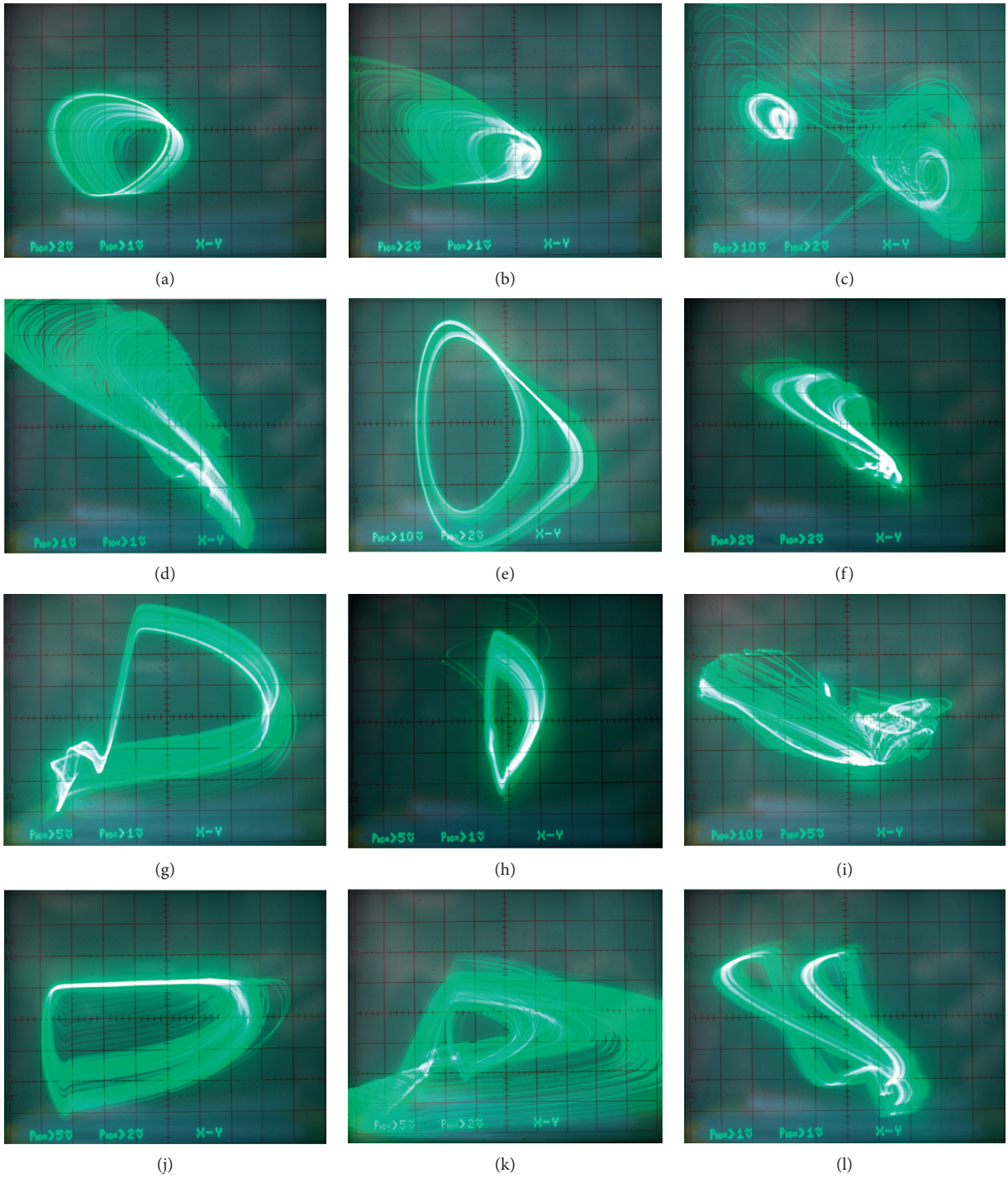

Figure 16: Geometrically interesting, strange attractors observed during experimental measurement but unnoticed in the frame of numerical analysis, different plane projections (not specified).

where g_T is transconductance of operational transconductance amplifier LM13700 precisely adjusted by external DC current. Because the desired strange attractors are located inside a cube with edges ± 3 V, dynamical range of integrated circuit LM13700 does not present a problem. The whole chaotic circuit can be supplied by symmetrical ± 15 V. To turn around output current of LM13700, input voltage nodes should be swapped.

5. Experimental Verification

The chaotic oscillator proposed in the previous section was constructed using breadboard; see Figure 12. For experimental verification, time constant was set to $\tau = 10\,\mu$s. This fact leads to choosing all capacitors 10 nF and, using basic calculations, values of remaining passive circuit components: $R_1 = 50\,\text{k}\Omega$, $R_2 = 10\,\text{k}\Omega$, $R_3 = 3.9\,\text{k}\Omega$, $R_4 = 10\,\text{k}\Omega$,

$R_5 = 127\,\Omega$, and $R_6 = 10\,\mathrm{k}\Omega$. To trace evolution of chaos, two resistors are considered variable, namely, R_3 (parameter b) and R_5 (parameter a). Figure 12 also shows realization of printed circuit board of two-port described by admittance parameters with fully adjustable transconductances; i.e., shapes of both $y_{12}(v_1)$ and $y_{21}(v_1)$ can be adjusted independently. Individual measurement results are provided by means of Figures 13–16.

6. Conclusion

Starting with a very simple mathematical model of class C amplifier with single bipolar transistor, two geometrically distinct strange attractors have been discovered. There are two conditions for chaos evolution: non-unilaterality and nonlinear forward transconductance of transistor. Numerical analysis includes calculation of LLE, energy distributions, and basins of attraction.

Based on this finding, a robust chaos generator is designed and experimentally verified within this paper. Circuitry realization follows analogue computer concept and utilizes cheap and commercially available active elements. Several different shapes of the self-excited strange attractors were observed during experimental verification.

The problem solved in this work opens new topics for future research. For example, existence of chaos in common building blocks dedicated for analogue signal processing such as multi-stage amplifiers, cascodes, current mirrors, and differential amplifiers could be proven via the same fully numerical approach as proposed in this paper. Also, staying focused on topology of class C amplifier, "chaotic" configurations of internal parameters that are closely related to standard operational regime could be localized. Particular attention should be paid to the promising cases where backward transconductance is very low. Finally, input signal as a driving force acts as an additional degree of freedom that can increase the overall probability of chaotic solution.

Data Availability

There are two groups of results (data outputs) presented in this manuscript. 1. Those coming from numerical routines used for mathematical analysis of investigated dynamical system (integration of state trajectories, sensitivity properties, calculation of the largest Lyapunov exponent, and visualization of basins of attraction). 2. Experimental verification of designed chaotic oscillator. This type of output can be re-simulated by using OrCAD PSpice circuit simulator. In both cases, source files, schematics, and simulation profiles can be forwarded to candidates based on the e-mail request submitted to the author of this paper, that is, petrzelj@feec.vutbr.cz. Please do not hesitate to contact the author also in the case of some questions, suggestions, and comments. Details about input parameters for numerical procedures can be found in the main body of the paper.

Conflicts of Interest

The author declares that there are no conflicts of interest regarding the publication of this paper.

Acknowledgments

The author would like to thank Dr. Tomas Gotthans for his long-time support, much useful advice, and recommendations about the concept of this paper. The research described in this paper was financed by Grant Agency of Czech Republic under project no. 19-22248S. For research, the infrastructure of the SIX Center was used.

References

[1] M. P. Kennedy, "Chaos in the colpitts oscillator," *IEEE Transactions on Circuits and Systems I: Fundamental Theory and Applications*, vol. 41, no. 11, pp. 771–774, 1994.

[2] P. Kvarda, "Chaos in hartley's oscillator," *International Journal of Bifurcation and Chaos*, vol. 12, no. 10, pp. 2229–2232, 2002.

[3] R. Kiliç and F. Yildirim, "A survey of wien bridge-based chaotic oscillators: design and experimental issues," *Chaos, Solitons & Fractals*, vol. 38, no. 5, pp. 1394–1410, 2008.

[4] Ö. Morgül, "Wien bridge based RC chaos generator," *Electronics Letters*, vol. 31, no. 24, pp. 2058-2059, 1995.

[5] G.-Q. Zhong, "Implementation of chua's circuit with a cubic nonlinearity," *IEEE Transactions on Circuit and Systems I: Fundamental Theory and Applications*, vol. 41, no. 12, pp. 934–941, 1994.

[6] L. O. Chua and G.-N. Lin, "Canonical realization of chua's circuit family," *IEEE Transactions on Circuits and Systems*, vol. 37, no. 7, pp. 885–902, 1990.

[7] A. S. Elwakil and M. P. Kennedy, "Chaotic oscillator configuration using a frequency dependent negative resistor," *Journal of Circuits, Systems and Computers*, vol. 9, pp. 229–242, 1999.

[8] J. Petrzela, Z. Kolka, and S. Hanus, "Simple chaotic oscillator: from mathematical model to practical experiment," *Radioengineering*, vol. 15, no. 1, pp. 6–12, 2006.

[9] A. S. Elwakil and M. P. Kennedy, "A semi-systematic procedure for producing chaos from sinusoidal oscillators using diode-inductor and FET-capacitor composites," *IEEE Transactions on Circuits and Systems I: Fundamental Theory and Applications*, vol. 47, no. 4, pp. 582–590, 2000.

[10] A. S. Elwakil and M. P. Kennedy, "Novel chaotic oscillator configuration using a diode-inductor composite," *International Journal of Electronics*, vol. 87, no. 4, pp. 397–406, 2010.

[11] P. Bernat and I. Balaz, "RC autonomous circuits with chaotic behavior," *Radioengineering*, vol. 11, no. 2, pp. 1–5, 2002.

[12] A. S. Elwakil and M. P. Kennedy, "Chaotic oscillators derived from sinusoidal oscillators based on the current feedback op amp," *Analog Integrated Circuits and Signal Processing*, vol. 24, no. 3, pp. 239–251, 2000.

[13] E. Fossas and G. Olivar, "Study of chaos in the buck converter," *IEEE Transactions on Circuits and Systems I: Fundamental Theory and Applications*, vol. 43, no. 1, pp. 13–25, 1996.

[14] C. K. Tse and W. C. Y. Chan, "Chaos from a current-programmed ćuk converter," *International Journal of Circuit Theory and Applications*, vol. 23, no. 3, pp. 217–225, 1995.

[15] J. H. B. Deane, "Chaos in a current-mode controlled boost DC-DC converter," *IEEE Transactions on Circuits and Systems I: Fundamental Theory and Applications*, vol. 39, no. 8, pp. 680–683, 1992.

[16] C. K. Tse, "Flip bifurcation and chaos in three-state boost switching regulators," *IEEE Transactions on Circuits and*

Systems I: Fundamental Theory and Applications, vol. 41, no. 1, pp. 16–23, 1994.

[17] X. Zhou, J. Li, and Y. M, "Chaos phenomena in DC-DC converter and chaos control," *Procedia Engineering*, vol. 29, no. 12, pp. 470–473, 2012.

[18] M. Di Bernardo, F. Garefalo, L. Glielmo, and F. Vasca, "Switchings, bifurcations, and chaos in DC/DC converters," *IEEE Transactions on Circuits and Systems I: Fundamental Theory and Applications*, vol. 45, no. 2, pp. 133–141, 1998.

[19] D. C. Hamill and D. J. Jeffries, "Subharmonics and chaos in a controlled switched-mode power converter," *IEEE Transactions on Circuits and Systems*, vol. 35, no. 8, pp. 1059–1061, 1988.

[20] A. Rodriguez-Vazquez, J. Huertas, and L. Chua, "Chaos in switched-capacitor circuit," *IEEE Transactions on Circuits and Systems*, vol. 32, no. 10, pp. 1083–1085, 1985.

[21] M. Drutarovsky and P. Galajda, "A robust chaos-based true random number generator embedded in reconfigurable switched-capacitor hardware," *Radioengineering*, vol. 16, no. 3, pp. 120–127, 2007.

[22] T. Endo and L. O. Chua, "Chaos from phase-locked loops," *IEEE Transactions on Circuits and Systems*, vol. 35, no. 8, pp. 987–1003, 1988.

[23] T. Endo, "A review of chaos and nonlinear dynamics in phase-locked loops," *Journal of the Franklin Institute*, vol. 331, no. 6, pp. 859–902, 1994.

[24] J. Petrzela, "Multi-valued static memory with resonant tunneling diodes as natural source of chaos," *Nonlinear Dynamics*, vol. 94, no. 3, pp. 1867–1887, 2018.

[25] J. Petrzela, "Strange attractors generated by multiple-valued static memory cell with polynomial approximation of resonant tunneling diodes," *Entropy*, vol. 20, no. 9, pp. 697–719, 2018.

[26] P. Galajda, M. Guzan, and V. Spany, "The state space mystery with negative load in multiple-valued logic," *Radioengineering*, vol. 8, no. 2, pp. 2–7, 1999.

[27] S. C. Yener and H. H. Kuntman, "Fully CMOS memristor based chaotic circuit," *Radioengineering*, vol. 23, no. 4, pp. 1140–1149, 2014.

[28] B. Muthuswamy and L. O. Chua, "Simplest chaotic circuit," *International Journal of Bifurcation and Chaos*, vol. 20, no. 5, pp. 1567–1580, 2010.

[29] Z. Biolek, D. Biolek, and V. Biolkova, "Differential equations of ideal memristors," *Radioengineering*, vol. 24, no. 2, pp. 369–377, 2015.

[30] Z. Biolek and D. Biolek, "Euler-lagrange equations of networks with higher-order elements," *Radioengineering*, vol. 26, no. 2, pp. 397–405, 2017.

[31] K. Rajagopal, C. Li, F. Nazarimehr, A. Karthikeyan, P. Duraisamy, and S. Jafari, "Chaotic dynamics of modified wien bridge oscillator with fractional order memristor," *Radioengineering*, vol. 27, no. 1, pp. 165–174, 2019.

[32] J. Petrzela, "On the existence of chaos in the electronically adjustable structures of the state variable filters," *International Journal of Circuit Theory and Applications*, vol. 44, no. 10, pp. 1779–1797, 2016.

[33] M. J. Ogorzalek, "Order and chaos in a third-order RC ladder network with nonlinear feedback," *IEEE Transactions on Circuits and Systems*, vol. 36, no. 9, pp. 1221–1230, 1989.

[34] G.-Q. Zhong, K.-T. Ko, K.-F. Man, and K.-S. Tang, "A systematic procedure for synthesizing two-terminal devices with polynomial non-linearity," *International Journal of Circuit Theory and Applications*, vol. 29, no. 2, pp. 241–249, 2001.

[35] J. Petrzela and L. Polak, "Minimal realizations of autonomous chaotic oscillators based on trans-immittance filters," *IEEE Access*, vol. 7, no. 1, pp. 17561–17577, 2019.

[36] T. Matsumoto, "Chaos in electronic circuits," *Proceedings of the IEEE*, vol. 75, no. 8, pp. 1033–1057, 1987.

[37] H. P. W. Gottlieb, "What is the simplest jerk function that gives chaos?" *American Journal of Physics*, vol. 64, no. 5, p. 525, 1996.

[38] L. Minati, M. Frasca, P. Oświ□cimka, L. Faes, and S. Drożdż, "Atypical transistor-based chaotic oscillators: design, realization, and diversity," *Chaos: An Interdisciplinary Journal of Nonlinear Science*, vol. 27, no. 7, Article ID 73113, 2017.

[39] L. Keuninckx, G. Van der Sande, and J. Danckaert, "Simple two-transistor single-supply resistor-capacitor chaotic oscillator," *IEEE Transactions on Circuits and Systems II: Express Briefs*, vol. 62, no. 9, pp. 891–895, 2015.

[40] J. Petrzela, "Generalized single stage class c amplifier: analysis from the viewpoint of chaotic behavior," *Applied Sciences*, vol. 10, no. 15, p. 5025, 2020.

[41] K. Grygiel and P. Szlachetka, "Lyapunov exponents analysis of autonomous and nonautonomous sets of ordinary differential equations," *Acta Physica Polonica Series B*, vol. 26, no. 8, pp. 1321–1331, 1995.

[42] S. Jafari, J. C. Sprott, V.-T. Pham, and S. M. R. H. Golpayegani, "A new cost function for parameter estimation of chaotic systems using return maps as fingerprints," *International Journal of Bifurcation and Chaos*, vol. 24, no. 10, pp. 1567–1580, 2014.

[43] S. Panahi, S. Jafari, V.-T. Pham, S. T. Kingni, A. Zahedi, and S. H. Sedighy, "Parameter identification of a chaotic circuit with a hidden attractor using krill herd optimization," *International Journal of Bifurcation and Chaos*, vol. 26, no. 13, Article ID 1650221, 2016.

[44] P. Bartissol and L. O. Chua, "The double hook (nonlinear chaotic circuits)," *IEEE Transactions on Circuits and Systems*, vol. 35, no. 12, pp. 1512–1522, 1988.

[45] I. Podlubny, "Matrix approach to discrete fractional calculus," *Fractional Calculus and Applied Analysis*, vol. 3, no. 4, pp. 359–386, 2000.

[46] I. Podlubny, A. Chechkin, T. Skovranek, Y. Chen, and B. M. Vinagre Jara, "Matrix approach to discrete fractional calculus II: partial fractional differential equations," *Journal of Computational Physics*, vol. 228, no. 8, pp. 3137–3153, 2009.

[47] H. Lu, J. Petrzela, T. Gotthans, K. Rajagopal, S. Jafari, and I. Hussain, "Fracmemristor chaotic oscillator with multistable and antimonotonicity properties," *Journal of Advanced Research*, vol. 25, pp. 137–145, 2020.

[48] J. M. Muñoz-Pacheco, "Infinitely many hidden attractors in a new fractional-order chaotic system based on a fracmemristor," *The European Physical Journal Special Topics*, vol. 228, no. 10, pp. 2185–2196, 2019.

[49] J. Munoz-Pacheco, E. Zambrano-Serrano, C. Volos, S. Jafari, J. Kengne, and K. Rajagopal, "A new fractional-order chaotic system with different families of hidden and self-excited attractors," *Entropy*, vol. 20, no. 8, p. 564, 2018.

[50] C. Volos, V.-T. Pham, E. Zambrano-Serrano, J. M. Munoz-Pacheco, S. Vaidyanathan, and E. Tlelo-Cuautle, "Analysis of a 4-D hyperchaotic fractional-order memristive system with hidden attractors," *Advances in Memristors, Memristive Devices and Systems*, vol. 701, pp. 207–235, 2017.

[51] J. Mou, K. Sun, H. Wang, and J. Ruan, "Characteristic analysis of fractional-order 4D hyperchaotic memristive circuit," *Mathematical Problems in Engineering*, vol. 2017, Article ID 2313768, 13 pages, 2017.

[52] A. Kartci, N. Herencsar, J. T. Machado, and L. Brancik, "History and progress of fractional-order element passive emulators: a review," *Radioengineering*, vol. 29, no. 2, pp. 296–304, 2020.
[53] I. Podlubny, I. Petráš, B. M. Vinagre, P. O'Leary, and L. Dorčák, "Analogue realizations of fractional-order controllers," *Nonlinear Dynamics*, vol. 29, no. 1, pp. 281–296, 2002.
[54] J. Petrzela, "Fractional-order chaotic memory with wideband constant phase elements," *Entropy*, vol. 22, no. 4, p. 422, 2020.
[55] J. Petrzela, "Optimal piecewise-linear approximation of quadratic chaotic dynamics," *Radioengineering*, vol. 21, no. 1, pp. 20–28, 2012.
[56] J. Lü and G. Chen, "Generating multiscroll chaotic attractors: theories, methods and applications," *International Journal of Bifurcation and Chaos*, vol. 16, no. 04, pp. 775–858, 2006.
[57] W. Deng and J. Lü, "Generating multi-directional multi-scroll chaotic attractors via a fractional differential hysteresis system," *Physics Letters A*, vol. 369, no. 5, pp. 438–443, 2007.
[58] J. C. Sprott, "A proposed standard for the publication of new chaotic systems," *International Journal of Bifurcation and Chaos*, vol. 21, no. 9, pp. 2391–2394, 2011.
[59] J. Petrzela, Z. Hrubos, and T. Gotthans, "Modeling deterministic chaos using electronic circuits," *Radioengineering*, vol. 20, no. 2, pp. 438–444, 2011.
[60] M. Itoh, "Synthesis of electronic circuits for simulating nonlinear dynamics," *International Journal of Bifurcation and Chaos*, vol. 11, no. 3, pp. 605–653, 2001.
[61] J. Petrzela, T. Gotthans, and M. Guzan, "Current-mode network structures dedicated for simulation of dynamical systems with plane continuum of equilibrium," *Journal of Circuits, Systems and Computers*, vol. 27, no. 9, Article ID 1830004, 2018.
[62] J. C. Sprott, "A new class of chaotic circuit," *Physics Letters A*, vol. 266, no. 1, pp. 19–23, 2000.
[63] T. Gotthans and J. Petrzela, "Experimental study of the sampled labyrinth chaos," *Radioengineering*, vol. 20, no. 4, pp. 873–879, 2011.
[64] R. Trejo-Guerra, E. Tlelo-Cuautle, V. H. Carbajal-Gómez, and G. Rodriguez-Gómez, "A survey on the integrated design of chaotic oscillators," *Applied Mathematics and Computation*, vol. 219, no. 10, pp. 5113–5122, 2013.
[65] J. M. Muñoz-Pacheco, E. Tlelo-Cuautle, I. Toxqui-Toxqui, C. Sánchez-López, and R. Trejo-Guerra, "Frequency limitations in generating multi-scroll chaotic attractors using CFOAs," *International Journal of Electronics*, vol. 101, no. 11, pp. 1559–1569, 2014.

Hindawi
Mathematical Problems in Engineering
Volume 2020, Article ID 8896566, 9 pages
https://doi.org/10.1155/2020/8896566

Research Article

Mathematical Modelling of the Sterile Insect Technique Using Different Release Strategies

Anis Ben Dhahbi,[1,2] Yassine Chargui,[1,2] Salah Mahmoud Boulaaras,[3,4] Sana Ben Khalifa,[1,5] Waleed Koko,[6] and Faisal Alresheedi[7]

[1]*Physics Department, College of Science and Arts at Ar Rass, Qassim University, PO Box 53, Ar Rass 51921, Saudi Arabia*
[2]*University of Tunis El Manar, Faculty of Sciences of Tunis, Nuclear Physics and High Energy Physics Research Unit, Tunis 2092, Tunisia*
[3]*Department of Mathematics, College of Science and Arts at Ar Rass, Qassim University, P. O. Box 53, Ar Rass 51921, Saudi Arabia*
[4]*Laboratory of Fundamental and Applied Mathematics of Oran (LMFAO), University of Oran Ahmed Benbella, Oran, Algeria*
[5]*Laboratory of Energy and Materials (LabEM), ESSTHS, University of Sousse, 4011 H., Sousse, Tunisia*
[6]*Biology Department, College of Science and Arts at ArRass, Qassim University, P. O. Box 53, ArRass 51921, Saudi Arabia*
[7]*Department of Physics, College of Sciences, Qassim University, P.O. 6644, Buryadh 51452, Saudi Arabia*

Correspondence should be addressed to Sana Ben Khalifa; sana.benkhalifa19@gmail.com

Received 25 September 2020; Revised 22 October 2020; Accepted 27 October 2020; Published 7 November 2020

Academic Editor: Sundarapandian Vaidyanathan

We study simple mathematical models for the dynamics of interactive wild and sterile insect populations. As well as being mathematically tractable, these models can be used as first approximations to real situations occurring with the Sterile Insect Technique (SIT) in which sterile males are released to reduce or eradicate a pest population. This is a method of biological control which can effectively help contain the spread of many pest insects such as the Red Palm Weevil (RPW). Models formulated in this paper are continuous-time, include a strong Allee effect that captures extinction events, and incorporate different strategies of releasing sterile insects. We perform basic studies of dynamical features of these models, with an emphasis on the condition of excitation, and the impact of the different release methods is investigated. Our findings are also demonstrated with some numerical examples.

1. Introduction

In recent years, there has been a rapid rise in the use of biological methods for the control of insect pests. One tool, which has proved effective in the area-wide control of various insects, is the SIT. This method, introduced initially by Knipling [1], consists in releasing high numbers of sterilized males into the environment. Such a technique constitutes a biological control process that disturbs the natural reproduction of the insect pests. This is carried out by using chemical or physical or other radical procedures to treat male insect pests to make them infertile, so they become unable to reproduce regardless of their sex drive. The infertile males are then introduced to the environment and compete for mates with fertile males, such that interaction between sterilized males and any female wild insect pests will not lead to any insect reproduction, thereby disrupting the natural reproductive process of the population. Despite the fact that frequent release of treated insect pests in large amounts will eventually eradicate the wild pest population completely, it is more practical to control the wild insect pest population instead of eliminating it completely. Then, if the number of released sterile males is high enough and is repeated over a sufficient period of time, the average fertility of the target population could be reduced leading to the control or even the eradication of the pest population from large

areas. The first successful SIT operation was against the screwworm population in Florida in the late 1950s. Later, this technique has been applied to combat a number of pests and disease vectors, such as the Mediterranean fruit fly (medfly), the RPW in coconut and date palm gardens, and the tsetse fly in Africa (see [2] for an overall review of the SIT and its applications). Moreover, diseases like dengue fever and malaria that are transmitted to humans by blood-feeding mosquitoes present a significant health concern for people. Roughly around one to three million people every year succumb to malaria as indicated by the World Health Organization (WHO). Malaria vastly hits Africa and South America, majorly taking the lives of children and pregnant women. As there are no vaccines available to prevent mosquito-borne diseases, the only way to prevent these diseases is to control the mosquitoes.

On the other hand, for vector control in particular, new approaches with similar working principles as the SIT have been developed. Those include, on the one hand, genetically modified control methods, such as the RIDL (Release of Insects with Dominant Lethality) technique, and, on the other hand, the *Wolbachia* technique. The former involve the release of genetically engineered insects (that have a lethal gene in their genome in the RIDL strategy), while the latter utilizes the Cytoplasmic Incompatibility (CI) property of the *Wolbachia* bacterium [3–5]. Indeed, these bacteria have the property to alter the sperm of infected males making it unable to fertilize uninfected eggs. This is the principle of the Incompatible Insect Technique (IIT) [6–11]. Moreover, the CI property raises considerably the progeny of infected females. And since *Wolbachia* is maternally inherited, releasing high numbers of W-females into a target population may lead to a Population Replacement (PR) by *Wolbachia*-infected insects and eventually to the elimination of the wild population (see, for example, [12] for a recent review of the *Wolbachia*-based PR strategy). Note that PRs and invasions have been observed in natural populations, such as with the Californian *Culex pipiens* [13] and the Australian *Aedes aegypti* [14].

Motivated by the issue of controlling a pest population by means of an SIT-like method, numerous theoretical studies, especially on the mathematical modelling of the classical SIT, the IIT, and the *Wolbachia*-PR, have been conducted (see, for example, [15–26] for SIT/IIT and [27–30] for PR and references therein). As a matter of fact, mathematical models have proven valuable in understanding various important issues in population dynamics, such as suppression mechanisms and the success or failure of different strategies. Thus, various classes of models have been formulated, including deterministic, stochastic, continuous-time, discrete-time, hybrid approaches, and temporal and spatiotemporal models.

In this paper, we study the dynamics of the interactive wild and sterile insects with a particular focus on the impact of the strategy adopted in releasing sterile individuals. Three release methods are then incorporated based on works [25, 31, 32]. The sterile-fertile interaction is assumed to be a one-sided competition that affects only the wild-type population. To reflect the need of a critical threshold density for the persistence of the wild population, a strong Allee effect is included. Moreover, to keep the model reasonably simple, we consider homogeneous insect populations such that no male-female or stage distinction is made and death rates for sterile and fertile insects are assumed to be density-independent and equal.

The paper is organized as follows. In Section 2, we present our general modelling assumptions. In Sections 3, 4, and 5, respectively, we consider three submodels, each with a different strategy of release: the first involves a constant release rate, the second assumes a release rate proportional to the size of the wild population, and the third uses a release rate of Holling-II type. We carry out detailed mathematical analysis of these models and discuss their dynamical features, especially the existence of equilibria and their stability. We also illustrate our analytical findings with numerical calculations. In the final section, we give a brief conclusion.

2. The General Model

We consider a two-dimensional one-stage model that involves density dependence solely in the growth term of pest insects. We assume that the birth rate of the sterile insects is their release rate and that the sterile-fertile competition affects only the wild population.

Let $N(t)$ be the number of wild insects at time t. In the absence of sterile insects, $N(t)$ is assumed to evolve according to the following equation:

$$\frac{\mathrm{d}N}{\mathrm{d}t} = G(N) - \mu N, \quad t \geq 0, \tag{1}$$

where $G(N)$ is the growth function of the wild population and μ is its death rate taken to be density independent. Furthermore, considering that the subsistence of the wild population requires some critical threshold density, we assume an Allee effect such that the birth function takes the form [33, 34]

$$G(N) = \alpha r N (K - N)(N - \varepsilon), \tag{2}$$

where K is the carrying capacity of the niche and ϵ is the Allee effect parameter ($\epsilon < K$), and we have set $\alpha = 4/(K-\epsilon)^2$, so that the parameter r is the maximum value of the growth rate as in the usual logistic model. Note that the Allee effect has been attracting a lot of interest recently due to its strong potential impact on population dynamics (see, for instance, [35]). This effect may arise from different causes, but the most obvious of them is the difficulty of finding mates at low population sizes [36].

$$\frac{\mathrm{d}N}{\mathrm{d}t} = \alpha r N (K - N)(N - \varepsilon) - \mu N. \tag{3}$$

This equation has a trivial equilibrium point at $N_0^* = 0$, which is locally asymptotically stable. A positive equilibrium of equation (3) should be a zero of the function $Q(N)$ defined by

$$Q(N) := (K - N)(N - \varepsilon) - \tilde{\mu}, \tag{4}$$

with $\tilde{\mu} = \mu/\alpha r$. This function has two roots:

$$N^*_{\pm} = \frac{K + \varepsilon \pm (K - \varepsilon)\sqrt{1 - \mu/r}}{2}, \tag{5}$$

which are real under the condition $r > \mu$, i.e., provided that the mortality rate remains below the maximum growth rate. Hence, the model given by equation (3) may have no, one, or two positive equilibria depending on whether $r > \mu$, $\mu = r$, or $r < \mu$, respectively.

In the case when the condition $r > \mu$ is fulfilled, at a positive equilibrium N^* we have

$$\begin{aligned} &\frac{\mathrm{d}}{\mathrm{d}N}\left[\alpha r N (K - N)(N - \varepsilon) - \mu N\right](N^*) \\ &= \alpha r N^* (K + \varepsilon - 2N^*). \end{aligned} \tag{6}$$

Thus,

$$\begin{aligned} &\frac{\mathrm{d}}{\mathrm{d}N}\left[\alpha r N (K - N)(N - \varepsilon) - \mu N\right](N^*_{\pm}) \\ &= \mp N^*_{\pm} (K - \varepsilon)\sqrt{\frac{1 - \mu}{r}}, \end{aligned} \tag{7}$$

which means that the equilibrium N^*_- is unstable, whereas the equilibrium N^*_+ is asymptotically stable. From now, we assume that the condition $r > \mu$ is satisfied.

Now, after sterile insects are released throughout the wild population, its reproductive success will be reduced. We shall assume that the birth rate of wild insects is affected so that it follows the harmonic mean. On the other hand, as the sterile-fertile interaction is admitted to be a one-sided competition (for mates), sterile insects are not affected by the presence of fertile individuals. Thus, if we denote by $M(t)$ the number of sterile insects at time t, the interactive dynamics are then governed by the following system:

$$\begin{aligned} \frac{\mathrm{d}N}{\mathrm{d}t} &= \alpha r \frac{N^2}{N + M}(K - N)(N - \varepsilon) - \mu N, \\ \frac{\mathrm{d}M}{\mathrm{d}t} &= R(N) - \mu M, \end{aligned} \tag{8}$$

where we have assumed that sterile insects have the same survivability as wild insects. $R(N)$ is a functional characterizing the release strategy, assumed to be independent of t. Subsequently, we will be considering three different forms of $R(N)$, along with the assumption $r > \mu$.

3. Constant Release Rate

We consider here the situation where sterile insects are constantly released so that $R(N) = \gamma$, with γ, a positive constant. Then, system (8) takes the form

$$\begin{aligned} \frac{\mathrm{d}N}{\mathrm{d}t} &= \alpha r \frac{N^2}{N + M}(K - N)(N - \varepsilon) - \mu N, \\ \frac{\mathrm{d}M}{\mathrm{d}t} &= \gamma - \mu M. \end{aligned} \tag{9}$$

For this model, it is easy to check that the rectangle of the phase plane

$$\Omega_1 := \left\{(N, M) \in \mathbb{R}^2 \colon 0 \le N \le N^*_+, \quad 0 \le M \le \eta\right\}, \tag{10}$$

with $\eta := \gamma/\mu$, is a positive invariant, and we assume in this section that $(N, M) \in \Omega_1$.

System (9) has a first equilibrium $E^c_0 := (0, \eta)$ lying on the boundary of Ω_1. It corresponds to the situation of no wild insects, but only a constant population of sterile individuals is present. Besides that, if it exists, a positive equilibrium should be a solution of the cubic equation:

$$NQ(N) - \tilde{\gamma} = 0, \tag{11}$$

with $\tilde{\gamma} = \gamma/\alpha r$. By Descartes' rule of signs, this equation has always one real negative solution (that we will disregard) and either no, one, or two real positive solutions. And one or two positive roots occur if the curve of the function $W(N) := NQ(N)$ intercepts the $\tilde{\gamma}$-axis once or twice, respectively. Furthermore, an elementary study of the variations of $W(N)$ shows that $W(N) < 0$ for $N < N^*_-$. Then, as N increases from N^*_-, this function also increases from zero to attain a certain maximum at the point

$$N_h := \frac{K + \varepsilon + \sqrt{K\varepsilon + (K - \varepsilon)^2 (1 - 3\mu/4r)}}{3}, \tag{12}$$

before lowering indefinitely. Note here that N_h is always real and positive as we have presumed that $r > \mu$. We then deduce that the condition for the existence of two positive solutions for equation (11) is

$$N_h Q(N_h) > \tilde{\gamma}. \tag{13}$$

This defines a threshold value of the release rate γ as

$$\gamma^c_c := \alpha r N_h Q(N_h), \tag{14}$$

at which equation (11) admits a unique positive root. Note that this definition of γ^c_c tacitly requires that $Q(N_h)$ be positive, and we can easily show that this is still the case as $r > \mu$.

Thus, we infer that the model given by equation (9) will have no, one, or two positive equilibria if $\gamma > \gamma^c_c$, $\gamma = \gamma^c_c$, or $\gamma < \gamma^c_c$, respectively. Note also that all the equilibria of the model lie on the border of the rectangle Ω_1 at which $M = \eta$.

Next, we address the stability of the equilibria. The Jacobian matrix at an equilibrium point (N^*, η) has the form

$$J^c := \begin{pmatrix} J^c_{11}, & -\dfrac{\mu N^*}{(N^* + \eta)}, \\ 0, & -\mu. \end{pmatrix} \tag{15}$$

At the boundary equilibrium E^c_0, we have $J^c_{11} = -\mu$; therefore, E^c_0 is always asymptotically stable. Moreover, in the case where no positive equilibrium exists as Ω_1 is a positive invariant set, we conclude by the Poincaré–Bendixson theorem that E^c_0 is globally asymptotically stable. Thus, for a release rate of sterile insects $\gamma > \gamma^c_c$, the wild population evolves to extinction whatever its initial number is. This is a very important outcome of the model since estimating the optimal number of sterile insects to be

released in order to eradicate the pest population remains one of the ultimate goals of the SIT modelling.

At a positive equilibrium (N^*, η), the matrix element J_{11}^c can be written as

$$J_{11}^c = \frac{\mathrm{d}}{\mathrm{d}N}\left\{\frac{\alpha r N}{(N+\eta)}\left[W(N) - \tilde{\gamma}\right]\right\}(N^*). \tag{16}$$

Then, keeping in mind that $W(N^*) = \tilde{\gamma}$, we can re-express J_{11} as

$$J_{11}^c = \frac{\alpha r N^*}{(N^* + \eta)} W'(N^*), \tag{17}$$

with $W' = \mathrm{d}W/\mathrm{d}N$. On the other hand, if we denote by $N_1^{*,c}$ and $N_2^{*,c}$ the two positive equilibria of the model (with $N_2^{*,c} > N_1^{*,c}$), we can deduce from the aforesaid behavior of the function $W(N)$ that $N_-^0 < N_1^{*,c} < N_h$ and $N_2^{*,c} > N_h$. Moreover, since $W(N)$ is strictly increasing over (N_-^0, N_h), then, in particular, $W'(N_1^{*,c})$ is strictly positive and thus $J_{11}(N_1^{*,c}) > 0$. Similarly, as $W(N)$ is strictly decreasing for $N > N_h$, it follows that, in particular, $W'(N_2^{*,c})$ is strictly negative and so $J_{11}(N_2^{*,c}) < 0$. This eventually implies that the equilibrium $E_1^c := (N_1^{*,c}, \eta)$ is a saddle point and that $E_2^c := (N_2^{*,c}, \eta)$ is a locally asymptotically stable node.

The above results are summed up in the following theorem.

Theorem 1. *Assume that $\mu < r$; then, system (9) possesses a boundary equilibrium $E_0^c := (0, \eta)$, which is globally asymptotically stable if no positive equilibrium occurs and locally asymptotically stable if it is not the case. System (9) has either no, one, or two positive equilibria depending on whether $\gamma > \gamma_c^c$, $\gamma = \gamma_c^c$, or $\gamma < \gamma_c^c$, respectively, where γ_c^c is defined by equation (14). In that case where two positive equilibria exist, $E_1^c := (N_1^{*,c}, \eta)$ and $E_2^c := (N_2^{*,c}, \eta)$ with $N_-^* < N_1^{*,c} < N_h$ and $N_2^{*,c} > N_h$, E_1^c is a saddle point, and E_2^c is locally asymptotically stable node.*

These results are illustrated with numerical examples presented in Figure 1.

4. Release Rate Proportional to the Wild Population

In general, a constant release rate of sterile insects is not optimal and better strategies can be adopted by adjusting the release rate to the size of the wild population [37–39]. One choice is to let the release rate be proportional to the number of pest insects if the latter is relatively small [25, 31]. Of course, a close monitoring of the pest population will be required, and particularly, its smallness remains critical for the economy of this choice. Within this strategy, the release function is given by $R(N) = \gamma N$, where γ is a positive constant (hereafter referred to as the relative release rate). Then, system (8) takes the form

$$\begin{aligned} \frac{\mathrm{d}N}{\mathrm{d}t} &= \alpha r \frac{N^2}{N+M}(K-N)(N-\varepsilon) - \mu N, \\ \frac{\mathrm{d}M}{\mathrm{d}t} &= \gamma N - \mu M. \end{aligned} \tag{18}$$

Define the region of the phase plan Ω_2 as

$$\Omega_2 := \left\{(N, M) \in \mathbb{R}^2 \colon 0 \le N \le N_+^*, \quad 0 \le M \le \eta N_+^*\right\}, \tag{19}$$

and then we can easily verify that Ω_2 is a positive invariant set for system (18), and we only consider $(N, M) \in \Omega_2$ in this section.

The model (18) has a trivial equilibrium at the origin $(0, 0)$, and it is always locally asymptotically stable. A possible positive equilibrium verifies the quadratic equation

$$(K-N)(N-\varepsilon) - (\tilde{\mu} + \tilde{\gamma}) = 0. \tag{20}$$

It is worth noting that equation (20) is completely similar to the equation $Q(N) = 0$, giving the positive equilibria of the model in the absence of sterile insects, but with $\tilde{\mu}$ substituted now by $\tilde{\mu}_e := \tilde{\mu} + \tilde{\gamma}$. This term highlights the effect of the sterile-fertile interactivity within the present model and may be seen as the effective death rate after sterile insects are released. Then, equation (4) has two roots:

$$N_\pm^{*,p} := \frac{K + \varepsilon \pm (K-\varepsilon)\sqrt{1 - \tilde{\mu}_e/r}}{2}. \tag{21}$$

Thus, if $\tilde{\mu}_e < r$, both solutions $N_{p,\pm}^*$ are real and system (18) has two positive equilibria. But if $\tilde{\mu}_e > r$, that is, the effective mortality rate exceeds the maximum growth rate, no positive equilibrium occurs. This clearly defines a threshold value of the relative release rate: $\gamma_c^p := r - \mu$, such that the model (18) has either no, one, or two positive equilibria if either $\gamma > \gamma_c^p$, $\gamma = \gamma_c^p$, or $\gamma < \gamma_c^p$, respectively.

Moreover, for $\gamma > \gamma_c^p$ the unique equilibrium $(0, 0)$ is globally asymptotically stable since Ω_2 is a positive invariant set for system (18). Thus, if the relative release rate of sterile insects is greater than $\gamma > \gamma_c^p$, the wild population ends up being eradicated whatever its initial size is.

In the case where $\gamma < \gamma_c^p$, the equilibria are given by $E_-^p := (N_-^{*,p}, \eta N_-^{*,p})$ and $E_+^p := (N_+^{*,p}, \eta N_+^{*,p})$. The stability of these equilibria is investigated below.

The general form of the Jacobian matrix at an equilibrium is

$$J^p := \begin{pmatrix} J_{11}^p, & J_{12}^p, \\ \gamma, & -\mu. \end{pmatrix}. \tag{22}$$

At a positive equilibrium $(N^*, \gamma N^*/\mu)$, the matrix element J_{11}^c can be written as

$$J_{11}^p = \frac{\partial}{\partial N}\left\{\frac{\alpha r N}{(N+M)}\left[W(N) - \tilde{\mu} M\right]\right\}\left(\frac{N^*, \gamma N^*}{\mu}\right). \tag{23}$$

Then, since $W(N^*) = \tilde{\gamma} N^*$, we readily find

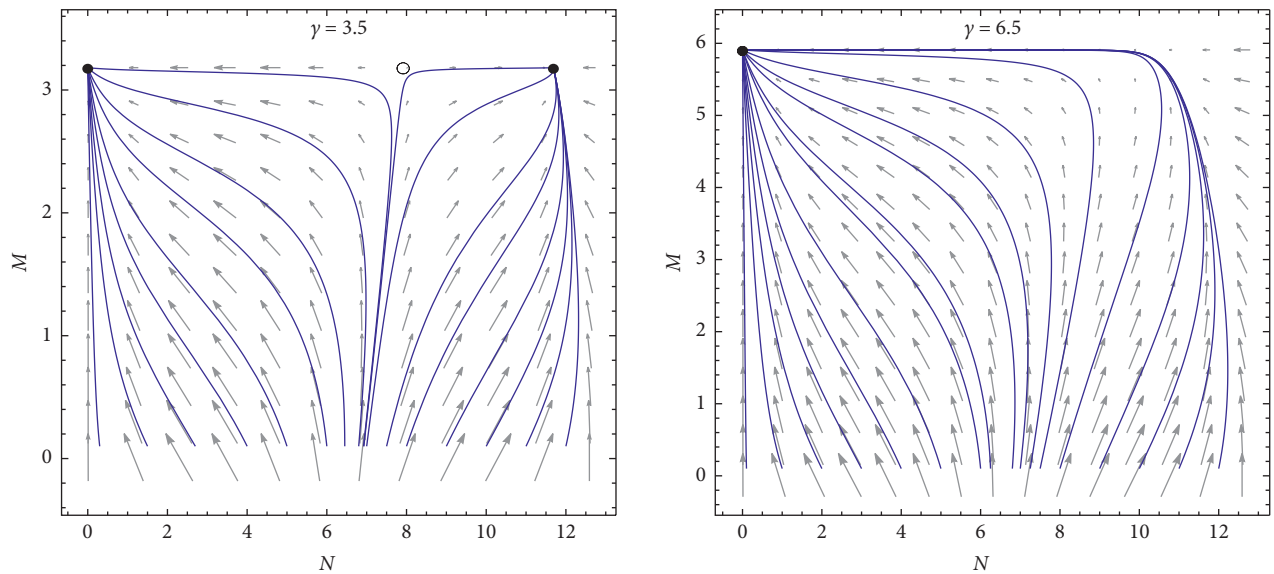

Figure 1: Trajectories and equilibria of system (9) for parameters values chosen as $K = 14.7$, $\epsilon = 4.3$, $r = 1.7$, and $\mu = 1.1$. The release threshold is $\gamma_c^c = 5.843$. For $\gamma = 6.5 > \gamma_c^c$, the unique equilibrium is $E_0^c = (0, 5.91)$ and it is globally stable (all solutions approach this point). For $\gamma = 3.5 < \gamma_c^c$, two positive equilibria occur: $E_1^c = (7.915, 3.182)$ and $E_2^c = (11.686, 5.909)$, with E_1^c a saddle point and E_2^c a stable node.

$$J_{11}^p = \frac{\alpha r}{1+\eta}\left[\widetilde{\gamma} + N^* Q'(N^*)\right] = \frac{\alpha r}{1+\eta}\left[\widetilde{\gamma} + N^*(K + \varepsilon - 2N^*)\right]. \tag{24}$$

The calculation of the element J_{12}^p is also straightforward and gives

$$J_{12}^p = -\frac{\mu}{1+\eta}. \tag{25}$$

This leads to

$$\det J^p = -\frac{\alpha r \mu}{1+\eta} N^*(K + \varepsilon - 2N^*), \tag{26}$$

wherein N^* is either $N_-^{*,p}$ or $N_+^{*,p}$. It follows from equation (26) that

$$\det J^p\left(N_\pm^{*,p}\right) = \mp\frac{\alpha r \mu}{1+\eta} N_\pm^{*,p}(K - \varepsilon)\sqrt{\frac{1-\widetilde{\mu}_e}{r}}. \tag{27}$$

This means firstly that the equilibrium E_-^p is a saddle point. For the equilibrium E_+^p, we need once more to see the sign of trJ^p. Then, we easily verify that

$$trJ^p\left(N_+^{*,p}\right) = -\frac{\alpha r \mu}{1+\eta} N_+^{*,p}\left[\widetilde{\mu} + (K - \varepsilon)\sqrt{\frac{1-\widetilde{\mu}_e}{r}}\right] < 0. \tag{28}$$

Equation (27) and equation (28) allow concluding that E_+^p is a locally asymptotically stable node or spiral.

We sum up the results of this section in the following theorem.

Theorem 2. *The origin $(0,0)$ is a locally asymptotically stable node for system (18). Furthermore, assume that $\mu < r$; if $\gamma > \gamma_c^p$ where $\gamma_c^p = r - \mu$, the origin is the unique equilibrium and it is globally asymptotically stable. And if $\gamma < \gamma_c^p$, system (9) possesses two positive equilibria, $E_-^p = (N_-^{*,p}, \eta N_-^{*,p})$ and $E_+^p = (N_+^{*,p}, \eta N_+^{*,p})$, with $N_+^{*,p}$ given by equation (21). Moreover, E_-^p is a saddle point and E_+^p is a locally asymptotically stable node or spiral.*

We illustrate the above results with numerical examples as given in Figure 2.

5. Saturating Proportional Release Rate

As noted in the previous section, the proportional release rate may turn out to be a very costly process if the wild population becomes big sized, since the number of releases should be great as well. Then, a new strategy, compromising the two previous strategies, has been proposed in [31]. It consists in adjusting the release rate so that it is proportional to N for a small N but tends towards saturation for sufficiently large N. Following [31], in this section we consider a release function of Holling-II type: $R(N) = \gamma N/(1+N)$ with γ a positive constant. Then, system (8) takes the form

$$\begin{aligned} \frac{dN}{dt} &= \alpha r \frac{N^2}{N+M}(K-N)(N-\varepsilon) - \mu N, \\ \frac{dM}{dt} &= \frac{\gamma N}{1+N} - \mu M. \end{aligned} \tag{29}$$

Then, it can be easily checked that Ω_1 defined in equation (19) is a positive invariant set for system (29), and we assume $(N, M) \in \Omega_1$ in this section.

The model (29) has a trivial equilibrium at the origin $(0,0)$, which is always locally asymptotically stable. For a

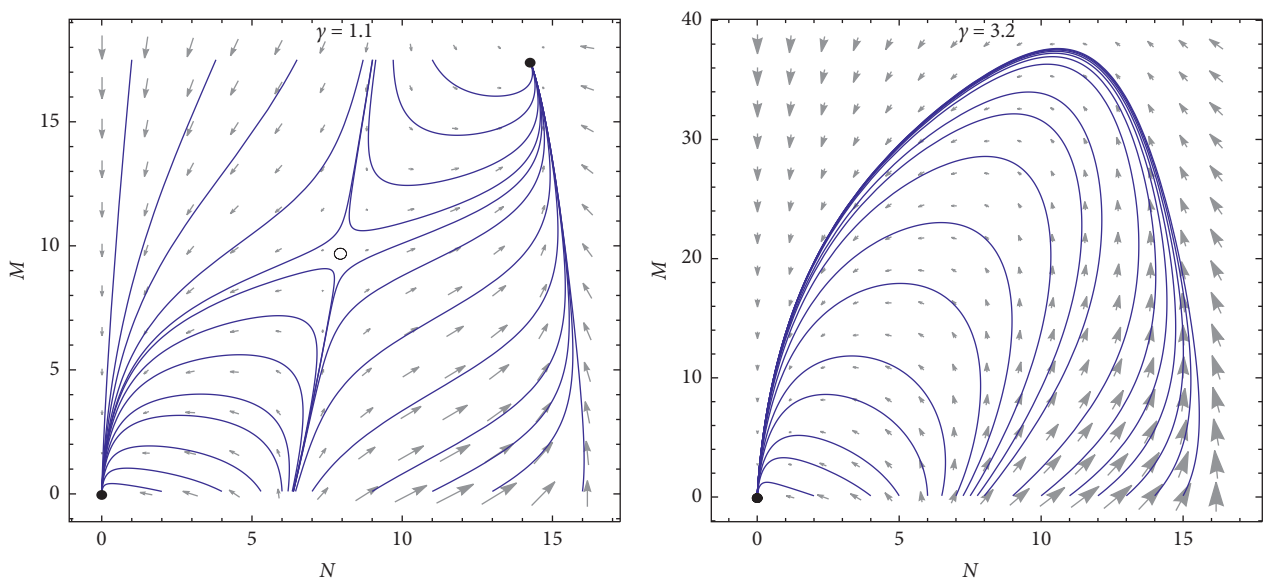

Figure 2: Trajectories and equilibria of system (18) for parameters values chosen as $K = 17.3$, $\epsilon = 4.9$, $r = 2.7$, and $\mu = 0.9$. The release threshold is $\gamma_c^c = 1.9$. For $\gamma = 3.2 > \gamma_c^c$, the unique equilibrium is the origin $(0,0)$ and it is globally stable (all solutions approach the origin). For $\gamma = 1.1 < \gamma_c^c$, there are two positive equilibria: $E_-^p = (7.943, 9.708)$ and $E_+^p = (14.257, 17.425)$, where E_-^p is a saddle point and E_+^p is a stable node.

positive equilibrium, the following cubic equation should be satisfied:

$$(N+1)Q(N) - \tilde{\gamma} = 0, \tag{30}$$

or equivalently

$$\begin{aligned} &N^3 - (K+\varepsilon-1)N^2 - (K+\varepsilon-K\varepsilon-\tilde{\mu}) \\ &N - (K\varepsilon+\tilde{\mu}+\tilde{\gamma}) = 0. \end{aligned} \tag{31}$$

The situation here is very similar to that of constant release rate. According to Descartes' rule of signs, equation (31) may have either no, one, or two real positive solutions. Note that the non-existence of positive roots requires both conditions $K+\epsilon<1$ and $K+\epsilon-K\epsilon<\tilde{\mu}$, which cannot be fulfilled simultaneously because $r>\mu$. Furthermore, a positive root occurs when the curve of the function $P(N) := (N+1)Q(N)$ intercepts the $\tilde{\gamma}$-axis. Furthermore, the study of the variations of $P(N)$ shows that $P(N)<0$ for $N<N_-^*$. Then, as N increases from N_-^*, the function $P(N)$ rises to reach a maximum at the point

$$N_h' := \frac{K+\varepsilon-1+\sqrt{(K+1)(\varepsilon+1)+(K-\varepsilon)^2(1-3\mu/4r)}}{3}, \tag{32}$$

with N_h' always real and positive since $r>\mu$. And for $r>\mu$, $P(N)$ is strictly decreasing. Hence, the condition for the occurrence of two positive solutions for equation (30) is

$$(N_h{}'+1)Q(N_h') > \tilde{\gamma}. \tag{33}$$

This clearly defines a threshold value of γ as

$$\gamma_c^s := \alpha r(N_h{}'+1)Q(N_h{}'), \tag{34}$$

such that equation (30) admits only one positive root if $\gamma = \gamma_c^s$. Therefore, we conclude that system (29) has no, one, or two positive equilibria if $\gamma>\gamma_c^s$, $\gamma=\gamma_c^s$, or $\gamma<\gamma_c^s$, respectively. Moreover, for $\gamma>\gamma_c^s$ the origin $(0,0)$ is globally asymptotically stable as Ω_1 is a positive invariant set for system (29). For $\gamma<\gamma_c^s$, the additional positive equilibria of the model are given by $E_1^s := [N_1^{*,s}, \eta N_1^{*,s}/(1+N_1^{*,s})]$ and $E_2^s := [N_2^{*,s}, \eta N_2^{*,s}/(1+N_2^{*,s})]$, where $N_1^{*,s}$ and $N_2^{*,s}$ are positive solutions of equation (30).

Next, we investigate the stability of the equilibria E_1^s and E_2^s. The Jacobian matrix at an equilibrium point has the form

$$J^s := \begin{pmatrix} J_{11}^s, & -\dfrac{\mu(1+N^*)}{N^*+1+\eta}, \\ \dfrac{\gamma}{(1+N^*)^2}, & -\mu, \end{pmatrix}, \tag{35}$$

wherein N^* is either $N_1^{*,s}$ or $N_2^{*,s}$. In addition, using the relation $W(N^*) = \tilde{\gamma}N^*/(N^*+1)$, J_{11}^s can be written as

$$J_{11}^s = \frac{\alpha r(N^*+1)}{N^*+1+\eta}W'(N^*). \tag{36}$$

This entails

$$\det J^s = -\frac{\mu\alpha r}{N^*+1+\eta}\left[(N^*+1)^2 W'(N^*) - \tilde{\gamma}\right]. \tag{37}$$

On the other hand, it follows from the relation $W(N) = NP(N)/N+1$ and the fact that $P(N^*) = \tilde{\gamma}$ that

$$W'(N^*) = \frac{N^*}{N^*+1}P'(N^*) + \frac{\tilde{\gamma}}{(N^*+1)^2}. \tag{38}$$

This leads to

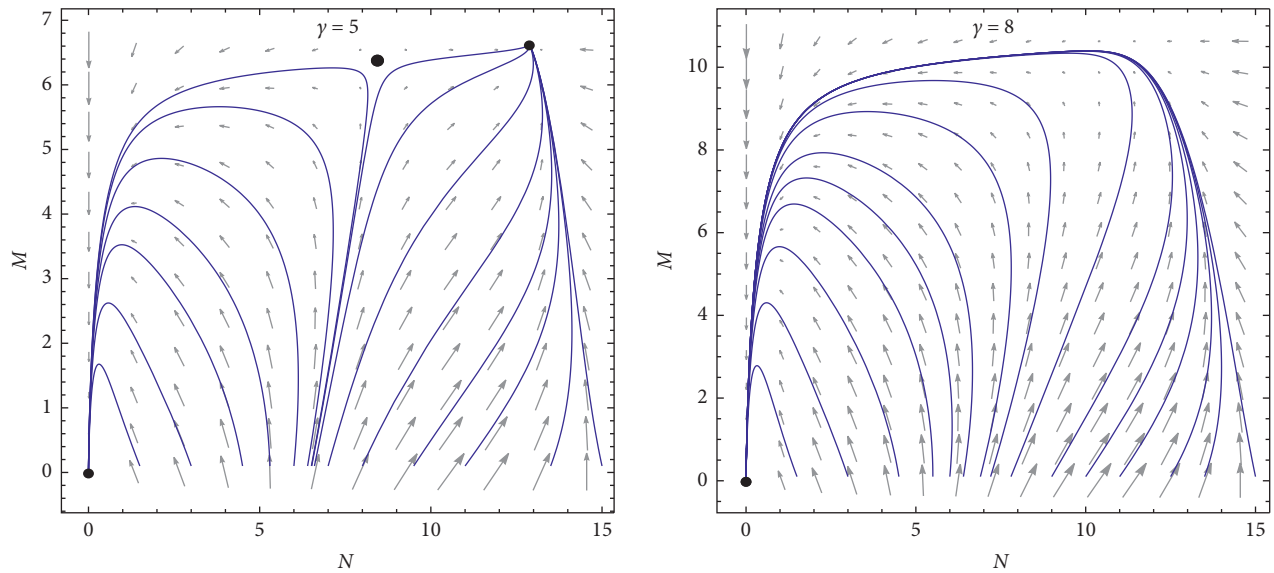

Figure 3: Trajectories and equilibria of system (29) for parameters values chosen as $K = 16.7$, $\epsilon = 3.7$, $r = 1.3$, and $\mu = 0.7$. The release threshold is $\gamma_c^s = 6.862$. For $\gamma = 8 > \gamma_c^s$, the origin $E_0^c = (0,0)$ is the unique equilibrium and it is globally stable (all solutions approach this point). For $\gamma = 5 < \gamma_c^s$, two positive equilibria occur: $E_1^s = (8.441, 6.386)$ and $E_2^c = (12.877, 6.628)$, with E_1^s a saddle point and E_2^s a stable node.

$$\det J^s = -\mu\alpha r \frac{N^*(N^*+1)}{N^*+1+\eta} P'(N^*). \tag{39}$$

Furthermore, from the variations of the function $P(N)$, we can infer that $N_-^0 < N_1^{*,s} < N_h$ and $N_2^{*,s} > N_h$. Subsequently, as $P(N)$ is strictly increasing over (N_-^0, N_h), then $P'(N_1^{*,s})$ is certainly strictly positive and thus $\det J^s(N_1^{*,s}) > 0$. Similarly, as $P(N)$ is strictly decreasing for $N > N_h$, $P'(N_2^{*,s})$ is consequently strictly negative and thus $\det J^s(N_2^{*,s}) < 0$. This implies firstly that the equilibrium E_1^s is a saddle point. Next, to identify the nature of the equilibrium E_2^s let us write $\mathrm{tr}J^s$. We have

$$trJ^s = \alpha r \frac{N^*+1}{N^*+1+\eta}\left[W'(N^*) - \tilde{\mu} - \frac{\tilde{\gamma}}{N^*+1}\right]. \tag{40}$$

Then, using equation (38) we find

$$\mathrm{tr}J^s = \alpha r \frac{N^*}{N^*+1+\eta}\left[P'(N^*) - \frac{\tilde{\mu}(N^*+1)}{N^*} - \frac{\tilde{\gamma}}{N^*+1}\right], \tag{41}$$

And since $P'(N_2^{*,s}) < 0$, we conclude that E_2^s is a locally asymptotically stable node.

The results of this section are summed up in the following theorem.

Theorem 3. *System (29) has a locally asymptotically stable node at the origin* $(0,0)$. *Moreover, assume that* $\mu < r$, *if* $\gamma > \gamma_c^s$ *where* γ_c^s *is given in equation (34), the origin is the unique equilibrium and it is globally asymptotically stable. And if* $\gamma < \gamma_c^s$ *system two positive equilibria occur for (29):* $E_1^s := [N_1^{*,s}, \eta N_1^{*,s}/(1+N_1^{*,s})]$ *and* $E_2^s := [N_2^{*,s}, \eta N_2^{*,s}/(1+N_2^{*,s})]$, *with* $N_-^* < N_1^{*,s} < N_h$ *and* $N_2^{*,s} > N_h$. *In addition,* E_1^s *is a saddle point and* E_2^s *is a locally asymptotically stable node.*

The results for this model are illustrated with numerical examples shown in Figure 3.

6. Conclusion

In summary, this work studies relatively simple mathematical models describing the dynamics of interactive wild and sterile insect populations, occurring within the SIT. The latter is a method of biological control, in which sterile males are released to reduce or eradicate a pest population, which can effectively help contain the spread of many pest insects such as the Red Palm Weevil (RPW). Modelling assumptions adopted in this paper allow for substantial simplifications of the SIT dynamics but in the meantime yield a model that can bias the results in comparison with real biological situations. As a matter of fact, we assumed homogeneous insect populations such that no male-female or stage distinction has been made. Here, we note that a recent comparison made between stage structured models and homogeneous models revealed that they share very similar dynamical features [25]. Moreover, death rates for sterile and fertile insects are assumed density-independent and equal. This seems reasonable since released insects are all adults so that the competition between them for natural resources is relatively weak. On the other hand, the competition for mates is the mechanism emphasised by SIT. Such competition obviously does not affect the sterile population. The sterile-fertile interaction is then assumed to be a one-sided competition that affects only the wild-type population. Moreover, to account for the need of a critical

threshold density in order that the wild population could persist, a strong Allee effect has been included in the growth term of the wild population. Subsequently, we considered three submodels, each characterized by a different strategy of release: the first involves a constant release rate, the second assumes a release rate proportional to the size of the wild population, and the third uses a release rate of Holling-II type. We have carried out complete mathematical analysis of these submodels and discussed their dynamical features, especially the existence of equilibria and their stability. In particular, we demonstrated the existence of release threshold for all the three strategies. Thus, if the release rate is below the threshold value, each submodel admits two positive interior equilibria: a saddle point and a stable node (or spiral for the second submodel). However, as soon as the release rate exceeds the threshold value, positive equilibria no longer exist. Each of the three submodels possesses a unique equilibrium with a vanishing number of wild insects. In this situation, the wild population evolves to extinction whatever its initial number is. Finally, our analytical findings for all submodels have been illustrated with numerical examples.

Data Availability

No data were used to support this study.

Conflicts of Interest

The authors declare that there are no conflicts of interest regarding the publication of this paper.

Authors' Contributions

The study was carried out in collaboration among all authors. All authors read and approved the final manuscript.

Acknowledgments

The third author would like to thank his Professors/Scientists Prof. Mohamed Haiour, Prof. Ahmed-Salah Chibi, and Prof. Azzedine Benchettah at Annaba University in Algeria for the important content of Master's and PhD courses in pure and applied mathematics which he received during his studies. Moreover, he thanks them for the additional help they provided to him during office hours in their office about the few concepts/difficulties he had encountered, and he appreciates their talent and dedication for their postgraduate students currently and previously. In addition, the authors gratefully acknowledge Qassim University, represented by the Deanship of Scientific Research, on the material support for this research under the number 6766-alrasscac-bs-2019-2-2-I during the academic year 1441 AH/2019 AD.

References

[1] E. F. Knipling, "Possibilities of insect control or eradication through the use of sexually sterile Males1," *Journal of Economic Entomology*, vol. 48, no. 4, pp. 459–462, 1955.

[2] V. A. Dyck, J. Hendrichs, and A. S. Robinson, *The Sterile Insect Technique, Principles and Practice in Area-wide Integrated Pest Management*, Springer, Dordrecht, Netherlands, 2006.

[3] K. Bourtzis, *Wolbachia-based Technologies for Insect Pest Population Control: Advances in Experimental Medicine and Biology*, Springer, New York, NY, USA, 2008.

[4] S. P. Sinkins, "Wolbachia and cytoplasmic incompatibility in mosquitoes," *Insect Biochemistry and Molecular Biology*, vol. 34, no. 7, pp. 723–729, 2004.

[5] S. Zabalou, M. Riegler, M. Theodorakopoulou, C. Savakis, and K. Bourtzis, "Wolbachia-induced cytoplasmic incompatibility as a means for insect pest population control," *Proceedings of the National Academy of Sciences*, vol. 101, no. 42, pp. 15042–15045, 2004.

[6] M. Marranzano, R. Ragusa, M. Platania, G. Faro, and M. A. Coniglio, "Knowledge, attitudes and practices towards patients with HIV/AIDS in staff Nurses in one university hospital in Sicily," *Ital. Journal of Public Health*, vol. 10, no. 1, pp. 1–23, 2013.

[7] K. Nikolouli, F. Sassù, L. Mouton, C. Stauffer, and K. Bourtzis, "Combining sterile and incompatible insect techniques for the population suppression of Drosophila suzukii," *Journal of Pest Science*, vol. 93, no. 2, pp. 647–661, 2020.

[8] R. Ragusa, S. Russo, L. Villari, and G. Schilirò, "Hodgkin's disease as a second malignant neoplasm in childhood: report of a case and review of the literature," *Pediatric Hematology and Oncology*, vol. 18, no. 6, pp. 407–414, 2001.

[9] G. Reale, G. I. Russo, M. Di Mauro et al., "Association between dietary flavonoids intake and prostate cancer risk: a case-control study in Sicily," *Complementary Therapies in Medicine*, vol. 39, pp. 14–18, 2018.

[10] D. Stauffer, R. S. Lees, Z. Xi et al., "Combining the sterile insect technique with Wolbachia-based approaches: II a safer approach to *Aedes albopictus* population suppression programmes, designed to minimize the consequences of inadvertent female release," *PLoS One*, vol. 10, no. 8, pp. 1–26, 2015.

[11] D. Zhang, X. Zheng, Z. Xi, K. Bourtzis, and J. R. Gilles, "Combining the sterile insect technique with the incompatible insect technique: I-impact of wolbachia infection on the ftness of triple- and double-infected strains of *Aedes albopictus*," *PLoS One*, vol. 10, no. 4, pp. 1–15, 2015a.

[12] P.-S. Yen and A.-B. Failloux, "A review: wolbachia-based population replacement for mosquito control shares common points with genetically modified control approaches," *Pathogens*, vol. 9, no. 5, pp. 404–421, 2020.

[13] J. L. Rasgon and T. W. Scott, "Wolbachia and cytoplasmic incompatibility in the California culex pipiens mosquito species complex: parameter estimates and infection dynamics in natural populations," *Genetics*, vol. 165, no. 4, pp. 2029–2038, 2003.

[14] A. A. Hoffmann, B. L. Montgomery, J. Popovici et al., "Successful establishment of wolbachia in aedes populations to suppress dengue transmission," *Nature*, vol. 476, no. 7361, pp. 454–457, 2011.

[15] S. Boulaaras and M. Haiour, "The finite element approximation of evolutionary Hamilton-Jacobi-Bellman equations with nonlinear source terms," *Indagationes Mathematicae*, vol. 24, no. 1, pp. 161–173, 2013.

[16] S. Boulaaras and M. Haiour, "L∞-asymptotic behavior for a finite element approximation in parabolic quasi-variational inequalities related to impulse control problem," *Applied Mathematics and Computation*, vol. 217, no. 14, pp. 6443–6450, 2011.

[17] S. Boulaaras, "Some existence results for a new class of elliptic kirchhoff equation with logarithmic source terms," *Journal of Intelligent & Fuzzy Systems*, vol. 37, no. 6, pp. 8335–8344, 2019.

[18] S. Boulaaras, "Some new properties of asynchronous algorithms of theta scheme combined with finite elements methods for an evolutionary implicit 2-sided obstacle problem," *Mathematical Methods in the Applied Sciences*, vol. 40, no. 18, pp. 7231–7239, 2017.

[19] S. Boulaaras, "An optimal error estimate of finite element method for parabolic quasi-variational inequalities with non linear source terms," *Asymptotic Analysis*, vol. 100, no. 3-4, pp. 193–208, 2016.

[20] S. Boulaaras, "Existence of positive solutions for a new class of Kirchhoff parabolic systems," *Rocky Mountain Journal of Mathematics*, vol. 50, no. 2, pp. 445–454, 2020.

[21] C. Dufourd and Y. Dumont, "Modeling and simulations of mosquito dispersal. the case of *Aedes albopictus*," *Biomath*, vol. 1, no. 2, 7 pages, Article ID 1209262, 2012.

[22] C. Dufourd and Y. Dumont, "Impact of environmental factors on mosquito dispersal in the prospect of sterile insect technique control," *Computers & Mathematics with Applications*, vol. 66, no. 9, pp. 1695–1715, 2013.

[23] Y. Dumont and J. M. Tchuenche, "Mathematical studies on the sterile insect technique for the chikungunya disease and *Aedes albopictus*," *Journal of Mathematical Biology*, vol. 65, no. 5, pp. 809–855, 2012.

[24] M. Huang, X. Song, and J. Li, "Modelling and analysis of impulsive releases of sterile mosquitoes," *Journal of Biological Dynamics*, vol. 11, no. 1, pp. 147–171, 2017.

[25] J. Li, L. Cai, and Y. Li, "Stage-structured wild and sterile mosquito population models and their dynamics," *Journal of Biological Dynamics*, vol. 11, no. 1, pp. 79–101, 2017.

[26] J. Li and Z. Yuan, "Modelling releases of sterile mosquitoes with different strategies," *Journal of Biological Dynamics*, vol. 9, no. 1, pp. 1–14, 2015.

[27] J. Z. Farkas and P. Hinow, "Structured and unstructured continuous models for wolbachia infections," *Bulletin of Mathematical Biology*, vol. 72, no. 8, pp. 2067–2088, 2010.

[28] A. Fenton, K. N. Johnson, J. C. Brownlie, and G. D. D. Hurst, "Solving the wolbachia paradox: modeling the tripartite interaction between host, wolbachia, and a natural enemy," *The American Naturalist*, vol. 178, no. 3, pp. 333–342, 2011.

[29] J. Z. Farkas, S. A. Gourley, R. Liu, and A.-A. Yakubu, "Modelling Wolbachia infection in a sex-structured mosquito population carrying west nile virus," *Journal of Mathematical Biology*, vol. 75, no. 3, pp. 621–647, 2017.

[30] G. Nadin, M. Strugarek, and N. Vauchelet, "Hindrances to bistable front propagation: application to wolbachia invasion," *Journal of Mathematical Biology*, vol. 76, no. 6, pp. 1489–1533, 2018.

[31] A. Bendhahbi, Y. Chargui, S. Boulaaras, and S. Ben Khalifa, "A one-sided competition mathematical model for the sterile insect technique," *Complexity*, vol. 2020, Article ID 6246808, 12 pages, 2020.

[32] J. Li, "New revised simple models for interactive wild and sterile mosquito populations and their dynamics," *Journal of Biological Dynamics*, vol. 11, no. 2, pp. 316–333, 2017.

[33] F. Courchamp, T. Clutton-Brock, and B. Grenfell, "Inverse density dependence and the Allee effect," *Trends in Ecology & Evolution*, vol. 14, no. 10, pp. 405–410, 1999.

[34] Y. Gruntfest, R. Arditi, and Y. Dombrovsky, "A fragmented population in a varying environment," *Journal of Theoretical Biology*, vol. 185, no. 4, pp. 539–547, 1997.

[35] J. A. Walter, K. L. Grayson, and D. M. Johnson, "Variation in allee effects: evidence, unknowns, and directions forward," *Population Ecology*, vol. 59, no. 2, pp. 99–107, 2017.

[36] F. Courchamp, L. Berec, and J. Gascoigne, *Allee Effects in Ecology and Conservation*, Oxford University Press, Oxford, UK, 2008.

[37] C. P. Ferreira, H. M. Yang, and L. Esteva, "Assessing the suitability of sterile insect technique applied toaedes aegypti," *Journal of Biological Systems*, vol. 16, no. 04, pp. 565–577, 2008.

[38] J. Kim, H. Lee, C. Lee, and S. Lee, "Assessment of optimal strategies in a two-patch dengue transmission model with seasonality," *PLoS One*, vol. 12, no. 3, pp. 1–21, 2017.

[39] L. Multerer, T. Smith, and N. Chitnis, "Modeling the impact of sterile males on an *Aedes aegypti* population with optimal control," *Mathematical Biosciences*, vol. 311, pp. 91–102, 2019.

Hindawi
Mathematical Problems in Engineering
Volume 2020, Article ID 8813736, 4 pages
https://doi.org/10.1155/2020/8813736

Research Article

Synchronized Chaos of a Three-Dimensional System with Quadratic Terms

Ali Allahem

Department of Mathematics, College Of Science, Qassim University, Buraydah, Saudi Arabia

Correspondence should be addressed to Ali Allahem; aallahem@qu.edu.sa

Received 28 August 2020; Revised 1 October 2020; Accepted 6 October 2020; Published 19 October 2020

Academic Editor: Sundarapandian Vaidyanathan

In this paper, a novel chaotic new three-dimensional system has been studied by Zhang et al. in 2012. In the system, there are three control parameters and three different nonlinear terms which governed equations. Zhang et al. studied elementary (preliminary) dynamic properties of the chaotic new three-dimensional system by means of bifurcation diagram, maximum Lyapunov exponent, phase portraits, dynamics behaviors by changing some parameters etc., using all possible theoretical analysis and numerical simulation. In this paper, we have demonstrated its complete synchronization. The proposed results are verified by numerical simulations.

1. Introduction

Since the first chaotic attractor in a three-dimensional autonomous system was found by Loranz in 1963 [1], many researchers and groups have concentrated in these three-dimensional systems recently. After the Loranz chaotic system, several chaotic systems have been found in the past few decades, for example, the Rösslor system [2], Lü and Chen system [3], Chua et al.'s system [4], Chen and Ueta system [5], and many others. Some proposed systems have studied by adding a nonlinear term in each equation (see [6], for more details). Zhang et al. [7] set up a novel three-dimensional autonomous system. In this system, they added to the second equation of the Rucklidge system [8] one cross-product nonlinear term only. The additional term created complex dynamics behaviors that can be shown in the numerical simulation. Zhang et al.'s system shows similar behavior as the Lorenz chaotic system by varying the control parameters. The study of the system covers most of the elementary dynamic properties, including phase portraits, Lyapunov exponent spectra, and bifurcation diagram, in each study cases.

In this paper, the synchronized chaos of Zhang et al.'s system has been provided which can finish the dynamical study of the system. Chaotic behaviors are very sensitive to initial conditions. If the nearby trajectories start, then we may have a huge difference in the future. We can synchronize the evolution of two nearby trajectories using a suitable control with the presence of a time lag. Literature reviews about synchronization schemes exist in numerous applications such as [9–12]. As pointed by [13], the concomitant unpredictability along with chaos poses certain difficulties in decoding the chaotic systems. Successful chaos synchronisation schemes can be found such as adaptive control [14], back stepping design [15], active control [16, 17], and nonlinear control [18, 19]. We herewith present a chaotic three-dimensional system, brief previous results from [7], and demonstrate how the active control can be employed to synchronize Zhang et al.'s system.

2. Preliminary Results

The new chaotic attractor proposed in this article is motivated by Zhang et al.'s system. It is given by the following system of ordinary differential equations:

$$\begin{aligned} \dot{x} &= -ax + by - yz, \\ \dot{y} &= x + xz, \\ \dot{z} &= -cz + y^2, \end{aligned} \tag{1}$$

where $\dot{x} = \mathrm{d}x/\mathrm{d}\tau$, x, y, and z are state of three variables, and a, b, and c are control parameters of system (1). In the topological point of view, Zhang et al. show that system (1) is not equivalent to the original Lorenz chaotic system or others similar to the Lorenz system. It has been presented using the effort of Ćelikovský and Chen [20–23] to the evident that system (1) is not topologically equivalent to the Lorenz chaotic system.

Preliminary results have been calculated. Equilibrium points can be obtained by setting $\dot{x} = \dot{y} = \dot{z} = 0$. Thus, we have

$$\begin{aligned} S_1 &= (0, 0, 0), \\ S_{2,3} &= (0, \pm\sqrt{bc}, b). \end{aligned} \tag{2}$$

The equilibrium point S_1 represents two eigenvalues with negative real part (stable) and one eigenvalue with non-negative real part (unstable) which is so-called saddle points of index one. However, the equilibrium point $S_{2,3}$ represent one eigenvalue with negative real part (stable) and two becoming a pair of complex conjugate eigenvalues with positive real parts which is so-called saddle points of index two.

System (1) is clearly dissipative. We have three Lyapunov exponents, and the divergence of the system is

$$f = \Delta V = \sum_{i=1}^{3} \mathrm{LE}_i = \frac{\partial \dot{x}}{\partial x} + \frac{\partial \dot{y}}{\partial y} + \frac{\partial \dot{z}}{\partial z} = -(a + c), \tag{3}$$

where LE_i denotes the three Lyapunov exponents of the system. It is negative when $a, c \geq 0$. The exponent rate is

$$\frac{\mathrm{d}V}{\mathrm{d}t} = e^f = e^{-(a+c)}. \tag{4}$$

From (4), it can be seen that a volume element V_0 is deceased by the flow into a volume element $V_0 e^{-\mathrm{ft}}$ in time t. This means that each volume containing the system trajectory tends to zero as $t \longrightarrow \infty$ at an exponential rate of $-f$.

The Lyapunov exponent is defined as the rate of divergence and convergence of nearby trajectories in the phase space [24,25]. According to the Jacobian method, the Lyapunov exponent can be calculated and presented. In system (1), we have seen one positive, one negative, and zero Lyapunov exponent for certain initial conditions, namely, $(x_0 = 7.2, y_0 = 7.8, z_0 = 2.3)$. Therefore, system (1) can be defined to be chaotic because we have at least one positive Lyapunov exponent, namely, we have $(l_1 = 2.46, l_2 = 0, l_3 = -14.45)$. In addition, the Lyapunov exponent dimension of system (1) is obtained by

$$D_l = j + \frac{\sum_{i=1}^{j} l_i}{\left|j_{j+1}\right|} = 2 + \frac{l_1 + l_2}{\left|l_3\right|} = 2.17. \tag{5}$$

Since the Lyapunov exponent dimension is fractal in system (1) and the system is dissipated, then a strange attractor is observed.

The dynamical studies of system (1) and the observation of the chaotic complex dynamics are well explained in [7], including the phase portrait, calculation of the maximum Lyapunov exponent, as well as the bifurcation diagram. All these dynamic properties are computed by fixing two control parameters and varying the third one. Thus, three complete cases have been studied.

3. Synchronization of the Chaotic System

In this section, we present synchronization of system (1). Consider the master system as

$$\begin{aligned} \dot{x_1} &= -ax_1 + by_1 - y_1 z_1, \\ \dot{y_1} &= x_1 + x_1 z_1, \\ \dot{z_1} &= -cz_1 + y_1^2, \end{aligned} \tag{6}$$

and the slave system as

$$\begin{aligned} \dot{x_2} &= -ax_2 + by_2 - y_2 z_2 + u_1, \\ \dot{y_2} &= x_2 + x_2 z_2 + u_2, \\ \dot{z_2} &= -cz_2 + y_2^2 + u_3, \end{aligned} \tag{7}$$

where $a = 4, b = 28$, and $c = 2$ and u_1, u_2, and u_3 are control terms to be determined. The initial conditions are chosen to be

$$x_1(0), y_1(0), z_1(0), x_2(0), y_2(0), z_2(0) = (0, -12, 33, -3, -14, 30). \tag{8}$$

Let us define the error functions as follows:

$$\begin{aligned} e_1 &= x_2 - x_1, \\ e_2 &= y_2 - y_1, \\ e_3 &= z_2 - z_1. \end{aligned} \tag{9}$$

The error system can be obtained by substituting equation (9) into systems (6) and (7) as follows:

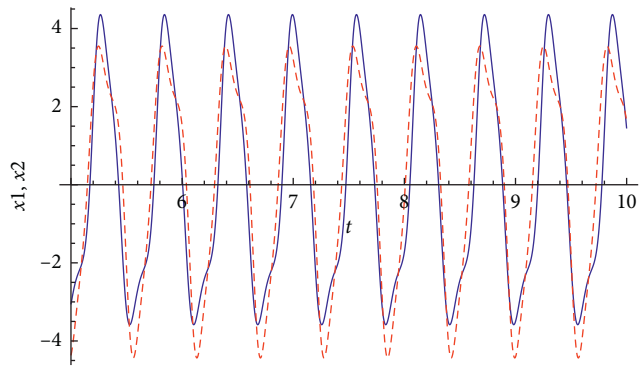

FIGURE 1: Time series of x_1 and x_2. The solid blue line represents x_1, and the dashed red line represents x_2.

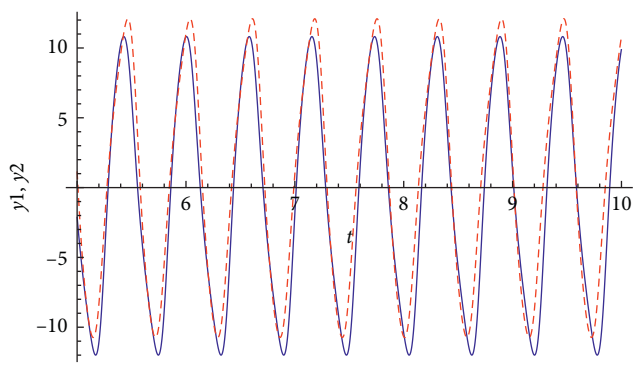

FIGURE 2: Time series of y_1 and y_2. The solid blue line represents y_1, and the dashed red line represents y_2.

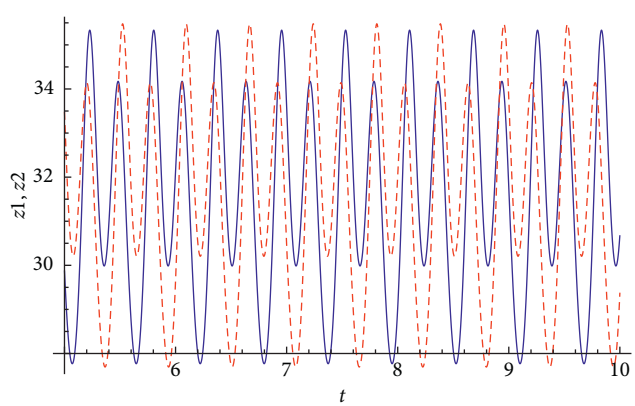

FIGURE 3: Time series of z_1 and z_2. The solid blue line represents z_1, and the dashed red line representsz_2.

$$\begin{aligned} \dot{e_1} &= -ae_1 + be_2 + (y_2z_2 - y_1z_1) + u_1, \\ \dot{e_2} &= e_1 + (x_2z_2 - x_1z_1) + u_2, \\ \dot{e_3} &= -ce_3 + \left(y_2^2 - y_1^2\right) + u_3, \end{aligned} \tag{10}$$

with some choice of initial conditions $e_1(0), e_2(0)$, and $e_3(0)$.

The control functions u_i have been chosen to be stable system (10) which means that $\lim_{t\longrightarrow\infty} e_i(t) = 0$. Suppose

$$\begin{aligned} u_1 &= y_1z_1 - y_2z_2, \\ u_2 &= x_1z_1 - x_2z_2, \\ u_3 &= y_1^2 - y_2^2, \end{aligned} \tag{11}$$

System (10) can be written as

$$\begin{bmatrix} \dot{e_1} \\ \dot{e_2} \\ \dot{e_3} \end{bmatrix} = \begin{bmatrix} -a & b & 0 \\ 1 & 0 & 0 \\ 0 & 0 & -c \end{bmatrix} \begin{bmatrix} e_1 \\ e_2 \\ e_3 \end{bmatrix}. \tag{12}$$

From the coefficient matrix of error system (12), we can calculate the eigenvalues which are

$$\begin{aligned} \lambda_{1,2} &= \frac{1}{2}\left(\pm \sqrt{a^2 + 4b} - a \right), \\ \lambda_3 &= -c. \end{aligned} \tag{13}$$

The system is stable as all the eigenvalues are negative, and synchronization is achieved when $b = 0$ and $a \geq 0$. From Figures 1–3, we show the synchronization for $x(t)$, $y(t)$, and $z(t)$, respectively. A solid blue line represents the response system and red lines represent to the drive system.

4. Conclusion

To sum up, a new chaotic system by Zhang et al. [7] presented a three-dimensional autonomous chaotic system with quadratic terms. The basic properties of the system have been already investigated in more detail by using the method of fixing the parameters and varying only one. We have observed the dynamic behavior for the system and calculated the preliminary dynamical studies, including bifurcation diagram, maximum Lyapunov exponent, and phase portraits. Since we have the chaotic attractors which are very important in some applications and some related areas, we have provided synchronization of the chaotic system using the active control method. On the other hand, we hope the synchronization of the chaotic system finds some interesting problems to apply.

Data Availability

No data were used to support this study.

Conflicts of Interest

The author declares that there are no conflicts of interest regarding the publication of this manuscript.

References

[1] E. N. Lorenz, "Deterministic nonperiodic flow," *Journal of the Atmospheric Sciences*, vol. 20, no. 2, p. 130, 1963.

[2] O. E. Rössler, "An equation for continuous chaos," *Physics Letters A*, vol. 57, no. 5, pp. 397-398, 1976.

[3] J. Lü and G. Chen, "A new chaotic attractor coined," *International Journal of Bifurcation and Chaos*, vol. 12, no. 03, pp. 659–661, 2002.

[4] L. Chua, M. Komuro, and T. Matsumoto, "The double scroll family," *IEEE Transactions on Circuits and Systems*, vol. 33, pp. 1073–1118, 1986.

[5] G. Chen and T. Ueta, "Yet another chaotic attractor," *International Journal of Bifurcation and Chaos*, vol. 09, no. 07, pp. 1465-1466, 1999.

[6] G. Qi, G. Chen, S. Du, Z. Chen, and Z. Yuan, "Analysis of a new chaotic system," *Physica A: Statistical Mechanics and Its Applications*, vol. 352, no. 2-4, pp. 295–308, 2005.

[7] X. Zhang, H. Zhu, and H. Yao, "Analysis of a new three-dimensional chaotic system," *Nonlinear Dynamics*, vol. 67, no. 1, pp. 335–343, 2012.

[8] A. M. Rucklidge, "Chaos in models of double convection," *Journal of Fluid Mechanics*, vol. 237, pp. 209–229, 1992.

[9] E. Mosekilde, Y. Maistrenko, and D. Postnov, *Chaotic Synchronization: Applications to Living Systems*, World Scientific, Singapore, 2002.

[10] L. M. Pecora and T. L. Carroll, "Synchronization in chaotic systems," *Physical Review Letters*, vol. 64, no. 8, p. 821, 1990.

[11] L. M. Pecora and T. L. Carroll, "Driving systems with chaotic signals," *Physical Review A*, vol. 44, no. 4, p. 2374, 1991.

[12] R. He and P. G. Vaidya, "Implementation of chaotic cryptography with chaotic synchronization," *Physical Review E*, vol. 57, no. 2, pp. 1532–1535, 1998.

[13] S. Boccaletti, J. Kurths, G. Osipov, D. L. Valladares, and C. S. Zhou, "The synchronization of chaotic systems," *Physics Reports*, vol. 366, no. 1-2, pp. 1–101, 2002.

[14] S. Chen and J. Lü, "Synchronization of an uncertain unified chaotic system via adaptive control," *Chaos, Solitons & Fractals*, vol. 14, no. 4, pp. 643–647, 2002.

[15] X. Tan, J. Zhang, and Y. Yang, "Synchronizing chaotic systems using backstepping design," *Chaos, Solitons & Fractals*, vol. 16, no. 1, pp. 37–45, 2003.

[16] M.-C. Ho and Y.-C. Hung, "Synchronization of two different systems by using generalized active control," *Physics Letters A*, vol. 301, no. 5-6, pp. 424–428, 2002.

[17] M. T. Yassen, "Chaos synchronization between two different chaotic systems using active control," *Chaos, Solitons & Fractals*, vol. 23, no. 1, pp. 131–140, 2005.

[18] L. Huang, R. Feng, and M. Wang, "Synchronization of chaotic systems via nonlinear control," *Physics Letters A*, vol. 320, no. 4, pp. 271–275, 2004.

[19] H. Chen, "Global chaos synchronization of new chaotic systems via nonlinear control," *Chaos, Solitons & Fractals*, vol. 23, no. 4, pp. 1245–1251, 2005.

[20] S. Ćelikovský and G. Chen, "On a generalized Lorenz canonical form of chaotic systems," *International Journal of Bifurcationand Chaos*, vol. 12, pp. 1789–1812, 2002.

[21] S. Ćelikovský and G. Chen, "Hyperbolic-type generalized Lorenz system and its canonical form," in *Proceedings of the 15th Triennial World Congress of IFAC*, Barcelona, Spain, July 2002.

[22] S. Ćelikovský and G. Chen, "On the generalized Lorenz canonical form," *Chaos Solitons Fractals*, vol. 26, pp. 1271–1276, 2005.

[23] H.-K. Chen, "Synchronization of two different chaotic systems: a new system and each of the dynamical systems Lorenz, Chen and Lü," *Chaos, Solitons & Fractals*, vol. 25, no. 5, pp. 1049–1056, 2005.

[24] A. Allahem and T. Bartsch, "Chaotic dynamics in multidimensional transition states," *Journal of Chemical Physics*, vol. 137, no. 21, Article ID 214310, 2012.

[25] A. Allahem, "Analytical solution to normal forms of Hamiltonian systems," *Mathematical and Computational Applications*, vol. 22, no. 3, p. 37, 2017.

Hindawi
Mathematical Problems in Engineering
Volume 2020, Article ID 8218740, 12 pages
https://doi.org/10.1155/2020/8218740

Research Article

Synchronous Behavior for Memristive Synapse-Connected Chay Twin-Neuron Network and Hardware Implementation

Quan Xu, Xiao Tan, Dong Zhu, Mo Chen, Jie Zhou, and Huagan Wu

School of Information Science and Engineering, Changzhou University, Changzhou 213164, China

Correspondence should be addressed to Huagan Wu; wuhg@cczu.edu.cn

Received 11 July 2020; Accepted 17 August 2020; Published 11 September 2020

Guest Editor: Viet-Thanh Pham

Synchronous behavior can be responsible for the function or dysfunction of a neural network. To employ a memristor with threshold memductance as a bidirectional synapse, a memristive synapse-connected Chay twin-neuron network is constructed. This paper numerically presents the synchronous behavior for four representative firing activities in the memristive twin-neuron network by utilizing time-domain waveforms, synchronized transition states (STSs), and mean synchronization errors (MSEs). Indeed, the synchronous behaviors are truly related to the coupling strength and initial condition of the memristor. Besides, utilizing the powerful XC7Z020 FPGA, a digitally circuit-implemented electro-neuron and the memristive synapse-connected Chay twin-neuron network are made. Thereafter, the four representative firing activities and their STSs are experimentally captured to further confirm the numerical simulations.

1. Introduction

Biological system propagates and handles neural signal via abundant collective behaviors [1–5]. As one of the most outstanding collective behaviors in neuronal network, synchronous behavior is important for the realization of signal propagation, information handling, and other activities [6–8]. Synchronous behavior for neuron-coupled models abstracted from the biological system has attracted much interest due to their simplicity and without loss of generality [9–15]. Numerous investigations of synchronous behavior in gap junction-coupled Huber–Braun neurons [9], gap junction-coupled or noise-sustained FitzHugh–Nagumo neurons [10–12], feedback unidirectional-coupled Hindmarsh–Rose neurons [7, 13], and chemical synaptic-coupled Hindmarsh–Rose neurons [14] have been explored in theoretical and numerical levels. Besides, excessive synchronization can be achieved through stimulating neuron by external control signal, which can be employed to cure some disorder diseases of Alzheimer's, epilepsy, Parkinson's, and hand shaking [15–17].

Based on the law of electromagnetic induction theory, Lv et al. have come up with the idea that the memristor can be employed as a connected synapse to describe transmembrane current generated by the membrane potentials' difference between two coupled neurons [18, 19]. When two coupled neurons own different initial conditions, i.e., different neuron membrane potentials, electromagnetic induction current can be generated to exchange the charged ions across the membrane. In this way, the neuron membrane potentials are altered and synchronization could be achieved [7]. The memristor is a novel circuit device with its memductance really depending on the input and with memory effect [20], which is regarded as a valid candidate for neuronal synapse [21]. Thus, it is interesting to find the emergence of synchronous behavior for memristor synapse-coupled two neurons having different membrane potentials between them [22–25]. The coexisting firing activities and synchronous behaviors associated to initial condition of the memristor in a memristive synapse-connected Morris–Lecar double neurons' network are explored [22]. Besides, the coexisting firing activities and initial-associating bifurcation behaviors, as well as the extreme events are disclosed in two adjacent Hindmarsh–Rose neurons connected by flux-controlled memristor [26]. However, the memristor initial condition-associated synchronous behavior still needs further investigation.

Three-dimensional (3D) Chay neuron model is a more physiologically excitable three-variable neuron model with simple mathematical form and rich essential features of electrical activities [27]. In essence, the 3D Chay neuron

model has the feature of a fast-slow structure to represent the membrane potential and ionic events in excitable membranes as in [28]. The 3D Chay neuron model can give birth to abundant firing activities of periodic and chaotic bursting/spiking behaviors [29], as well as the bifurcation scenarios for stochastic resonance are disclosed [30]. Besides, GWN and magnetro-acoustical simulation-induced multiple firing activities are explored by numerical simulations [31–33]. From the viewpoint of ions' effect mechanisms in biological neuron, the outward current carried by K^+ ions and the inward one by Na^+ and Ca^{2+} ions play key role in living biological activities. Thus, beyond all these investigations, by selecting four sets of the maximal conductances for the two ions currents, four representative firing activities are revealed. Besides, the synchronization for these four representative firing activities in coupled Chay neuron models are barely disclosed, which hinders the process of unveiling living biological activities.

The theoretical explorations and numerical simulations are classical methods to investigate neural dynamics, but hardware implementations and experimental measurements have become increasingly promising for diverse neuron-based engineering applications [34–43]. To date, on the benefit of real-time modification, easy software control, and adjustment, field programmable gate array (FPGA) has been employed to verify the dynamical behaviors of Hindmarsh–Rose neuron model [35, 36], Wilson neuron model [37], Morris–Lecar neuron model [38], and FitzHugh–Nagumo neuron model [39] in the hardware level. One of another remarkable benefit is that the FPGA-based experiments can assign the desired initial conditions in software accurately and easily, which is conducive to investigate initial condition-associated electrical activities in the hardware level [40]. To consider the virtue of FPGA-based realization method, there should be important significance to develop various digital electronic neurons for utilizing in hardware level synthesizers for large-scale neuromprphic circuits. Besides, the digitally circuit-implemented neuron network can effectively imitate the synchronous behavior in the network, which can promote the integrated circuit design and diverse neuron-based engineering applications [22]. To our best knowledge, there is no comprehensive exploration about the Chay neuron model in this valuable approach.

The arrangement of this paper is well designed as follows. The representative firing activities in a 3D Chay neuron model are briefly reviewed by employing numerical plots of phase trajectories and time-domain waveforms. Besides, a memristive synapse-connected Chay twin-neuron network is built in Section 2. Section 3 explores synchronous behavior in the memristive Chay twin-neuron network by utilizing time-domain waveforms, STSs, and MSEs. A FPGA-based electronic neuron and the memristive synapse-connected Chay twin-neuron network are realized and the hardware tests are executed to verify the numerically simulated ones in Section 4. Eventually, the conclusion is drawn.

2. Memristive Synapse-Connected Chay Twin-Neuron Network

2.1. Minireview for 3D Chay Neuron Model. The 3D Chay neuron model is an effective candidate in the numerical simulation for electrical activities in single biological neuron [27], which is described as

$$\begin{aligned}
\frac{\mathrm{d}V}{\mathrm{d}t} &= g_1 m_\infty^3 h_\infty (V_I - V) + g_{K,V} n^4 (V_K - V) + g_{K,C} \frac{C}{1+C} (V_K - V) + g_L (V_L - V), \\
\frac{\mathrm{d}n}{\mathrm{d}t} &= \frac{(n_\infty - n)}{\tau_n}, \\
\frac{\mathrm{d}C}{\mathrm{d}t} &= \rho \left[m_\infty^3 h_\infty (V_C - V) - k_C C \right],
\end{aligned} \tag{1}$$

where the three dynamic variables V, n, and C correspond to the membrane potential, open probability of the voltage-sensitive potassium ions channel, and intracellular concentration of calcium ions, respectively. The model parameter in (1) is assigned and shown in Table 1. Besides, $y_\infty = \alpha_y/(\alpha_y + \beta_y)$ is unified to the expressions of m_∞, h_∞, and n_∞, in which y presents the alphabets m, h, and n. Herein, the expression formats for α_m, β_m, α_h, β_h, α_n, β_n, and τ_n are

$$\alpha_m = \frac{0.1(25+V)}{\left(1-e^{-(V+25/10)}\right)},$$
$$\beta_m = 4e^{-(V+50/18)},$$
$$\alpha_h = 0.07e^{-(V+50/20)},$$
$$\beta_h = \frac{1}{\left(1+e^{-(V+20/10)}\right)}, \tag{2}$$
$$\alpha_n = \frac{0.01(20+V)}{\left(1-e^{-(V+20/10)}\right)},$$
$$\beta_n = 0.125e^{-(V+30/80)},$$
$$\tau_n = \frac{1}{[r_n(\alpha_n+\beta_n)]}.$$

On account of the fast-slow effect, the bursting and spiking behaviors are two representative firing activities generated in this neuron model [27]. By using MATLAB ODE45-based method with time step 10^{-3} s, fixing the initial conditions (0.1 mV, 0.1, 0.1 nmol/L), and employing the model parameters in Table 1, note that "MaxStep" and "RelTol" in MATLAB-based ODE45 algorithm should be assigned as 10^{-3} s and 10^{-4} s, respectively.

The firing activities related to the reversal potentials [30, 32], external stimulus [31, 33], and time kinetic constant [41] have been investigated in numerical survey. Differently, by selecting four sets of model parameters for the maximal conductance g_{I} of mixed Na^+-Ca^{2+} channel and maximal conductance $g_{\mathrm{K,V}}$ of potassium ions channel, four representative types of firing activities including periodic and chaotic bursting and chaotic spiking behaviors are revealed by utilizing the trajectories in the C-V plane and the time-domain waveforms of the membrane potential V and intracellular concentration C of calcium ions, as shown in Figure 1. Figures 1(a) and 1(d) exhibit two kinds of periodic bursting behaviors, Figure 1(b) demonstrates chaotic bursting behavior with disordered spikes, and Figure 1(c) illustrates conventional chaotic spiking behavior. The bifurcation mechanisms for the two kinds of periodic bursting behaviors are different. Those are periodic fold/fold bursting in Figure 1(a) and periodic fold/homoclinic bursting in Figure 1(d) [42, 43]. Figure 2(b) shows the chaotic fold/homoclinic bursting behaviors, and Figure 1(c) denotes the chaotic spiking activity. The synchronous behaviors in a memristive synapse-connected Chay twin-neuron network under the four sets of model parameters will be disclosed in the next sections, respectively.

2.2. Modeling for Memristive Synapse-Connected Twin-Neuron Network. Support two identical neurons are bidirectionally coupled by memristor synapse to represent the electromagnetic induction effect induced with the membrane potential differences between them. Herein, the memristor with threshold memductance $W(\varphi) = \tan\mathrm{h}(\varphi)$ and the membrane potential difference $V_M = V_1 - V_2$ are employed [26], so the inducted current I_M and memristor synapse characteristic model can be described as

$$\begin{aligned} I_M &= W(\varphi)V_M = \tanh(\varphi)(V_1 - V_2), \\ \dot{\varphi} &= V_M = V_1 - V_2, \end{aligned} \tag{3}$$

with two identical Chay neurons coupled by the threshold memristor, and a memristive synapse-connected Chay twin-neuron network can be described as

$$\begin{aligned}
\frac{\mathrm{d}V_1}{\mathrm{d}t} &= g_{\mathrm{I}} m_{1\infty}^3 h_{1\infty}(V_{\mathrm{I}} - V_1) + g_{\mathrm{K,V}} n_1^4 (V_{\mathrm{K}} - V_1) + g_{\mathrm{K,C}} \frac{C_1}{1+C_1}(V_{\mathrm{K}} - V_1) + g_{\mathrm{L}}(V_{\mathrm{L}} - V_1) + k\tanh\varphi(V_1 - V_2), \\
\frac{\mathrm{d}n_1}{\mathrm{d}t} &= \frac{(n_{1\infty} - n_1)}{\tau_{1n}}, \\
\frac{\mathrm{d}C_1}{\mathrm{d}t} &= \rho\left[m_{1\infty}^3 h_{1\infty}(V_{\mathrm{C}} - V_1) - k_{\mathrm{C}} C_1\right], \\
\frac{\mathrm{d}V_2}{\mathrm{d}t} &= g_{\mathrm{I}} m_{2\infty}^3 h_{2\infty}(V_{\mathrm{I}} - V_2) + g_{\mathrm{K,V}} n_2^4 (V_{\mathrm{K}} - V_2) + g_{\mathrm{K,C}} \frac{C_2}{1+C_2}(V_{\mathrm{K}} - V_2) + g_{\mathrm{L}}(V_{\mathrm{L}} - V_2) - k\tanh\varphi(V_1 - V_2), \\
\frac{\mathrm{d}n_2}{\mathrm{d}t} &= \frac{(n_{2\infty} - n_2)}{\tau_{2n}}, \\
\frac{\mathrm{d}C_2}{\mathrm{d}t} &= \rho\left[m_{2\infty}^3 h_{2\infty}(V_{\mathrm{C}} - V_2) - k_{\mathrm{C}} C_2\right], \\
\frac{\mathrm{d}\varphi}{\mathrm{d}t} &= V_1 - V_2,
\end{aligned} \tag{4}$$

Table 1: Parameters' values and significations of the 3D Chay neuron model.

Parameters	Significations	Values
V_{I}	Reversal potentials for mixed Na^+-Ca^{2+} ions	100 mV
V_{K}	Reversal potentials for K^+ ions	−75 mV
V_{L}	Reversal potentials for leakage ions	−40 mV
V_{C}	Reversal potentials for Ca^{2+} ions	100 mV
g_{I}	Maximal conductance of mixed Na^+-Ca^{2+} channel	1925 mS/cm^2
$g_{\mathrm{K,V}}$	Maximal conductance of K^+ channel	1700 mS/cm^2
$g_{\mathrm{K,C}}$	Maximal conductance of Ca^{2+}-sensitive K^+ channel	12 mS/cm^2
g_{L}	Maximal conductance of leakage channel	7 mS/cm^2
r_n	Time kinetic constant of the fast variable	230 ms
k_{C}	Rate constant for the efflux of intracellular Ca^{2+} ions	3.3/18 ms^{-1}
ρ	Time constant determines the changing rate C	0.27 ms

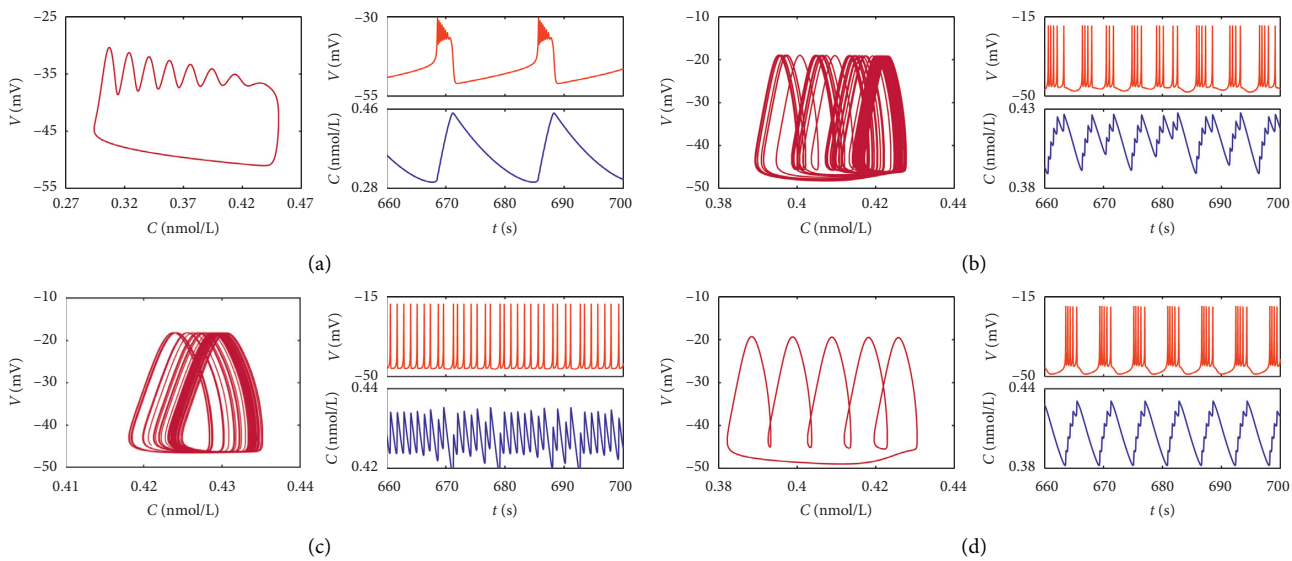

Figure 1: Trajectories in the $C-V$ plane and time-domain waveforms of V and C for different g_{I} and $g_{\mathrm{K,V}}$. (a) Periodic bursting behavior for $g_{\mathrm{I}} = 1250$ mS/cm^2 and $g_{\mathrm{K,V}} = 1700$ mS/cm^2; (b) chaotic bursting behavior for $g_{\mathrm{I}} = 1850$ mS/cm^2 and $g_{\mathrm{K,V}} = 1700$ mS/cm^2; (c) chaotic spiking behavior for $g_{\mathrm{I}} = 1925$ mS/cm^2 and $g_{\mathrm{K,V}} = 1700$ mS/cm^2; (d) periodic bursting behavior with 5 spikes per burst for $g_{\mathrm{I}} = 1800$ mS/cm^2 and $g_{\mathrm{K,V}} = 1650$ mS/cm^2.

where V_1 and V_2 are the membrane potential, n_1 and n_2 are probability of the voltage-sensitive K^+ channel for the two identical Chay neuron models, C_1 and C_2 are the intracellular concentration of calcium ions for them, respectively, and $k\tan\mathrm{h}\varphi(V_1 - V_2)$ stands for the memristor synapse-coupled item with k as positive to feature the coupling strength. In (4), the coupling strength k can control the effect of memristor synapse. Actually, the memristor synapse-connected item just inputs additive current leading to that the membrane potentials which can be regulated. Also, (4) explained the mechanism for memristive feedback control. Besides, $y_{i\infty} = \alpha_{iy}/(\alpha_{iy} + \beta_{iy})$ can be unified to the explications of $m_{i\infty}$, $h_{i\infty}$, and $n_{i\infty}$, in which y stands for m, h, and n and $i = 1, 2$. The explicit expressions for α_{im}, β_{im}, α_{ih}, β_{ih}, α_{in}, β_{in}, and τ_{in} are

$$\begin{aligned}
\alpha_{im} &= \frac{0.1(25 + V_i)}{\left(1 - e^{-(V_i+25/10)}\right)}, \quad \beta_{im} = 4e^{-(V_i+50/18)}, \\
\alpha_{ih} &= 0.07e^{-(V_i+50/20)}, \quad \beta_{ih} = \frac{1}{\left(1 + e^{-(V_i+20/10)}\right)}, \\
\alpha_{in} &= \frac{0.01(20 + V_i)}{\left(1 - e^{-(V_i+20/10)}\right)}, \quad \beta_{in} = 0.125e^{-(V_i+30/80)}, \\
\tau_{in} &= \frac{1}{[r_n(\alpha_{in} + \beta_{in})]}.
\end{aligned} \tag{5}$$

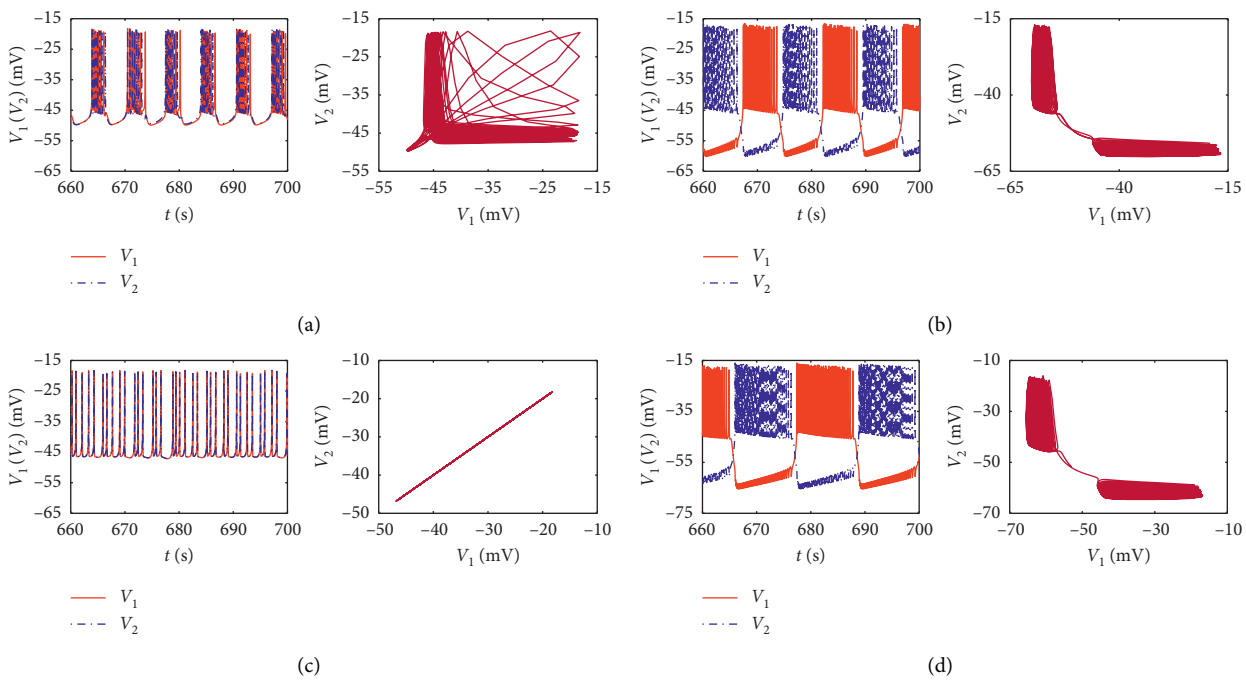

FIGURE 2: Synchronous behavior for the memristive twin-neuron network with various k and φ_0, where the lefts are time-domain waveforms and the rights are STSs. (a) $k = 1$ and $\varphi_0 = -2$ mWb; (b) $k = 3$ and $\varphi_0 = -2$ mWb; (c) $k = 4$ and $\varphi_0 = -2$ mWb; (d) $k = 4$ and $\varphi_0 = 1$ mWb.

Thus, the synchronous behaviors for the memristive synapse-connected Chay twin-neuron network can be disclosed by system (4). Following on this, we mainly focus on exploring the memristor initial condition and coupling strength associated synchronous behaviors in the proposed memristive network.

3. Synchronous Behaviors for the Chay Twin-Neuron Network

The exploration of synchronous behaviors for the Chay twin-neuron network is performed by MATLAB numerical simulations. Herein, we mainly focus on the two coupled neurons with only difference initial membrane potentials between them. Thus, the Chay twin-neuron network is triggered by initial conditions (0.1 mV, 0, 0.1 nmol/L, 1 mV, 0, 0.1 nmol/L, φ_0) without loss of the generality, within which the memristor initial condition φ_0 is tunable.

The electrical activity is chaotic spiking under the model parameters in Table 1, for each neuron in the memristive synapse-connected Chay twin-neuron network. The synchronized transition states (STSs) are plotted at the right in Figures 2(a)–2(d). There exist no errors between the two membrane potentials with a line in the V_1-V_2 plane, which means that the two neurons are in sync. Otherwise, the relatively large errors between the two membrane potentials indicate the two neurons out of synchronization. When $\varphi_0 = -2$ mWb, the difference between the two membrane potentials become smaller with $k = 1$ and 3 increasingly and disappear with $k = 4$, as shown in Figures 2(a)–2(c). This manifests that the two coupled neurons are asymptotically synchronized with increasing k. However, when $k = 4$ with increasing φ_0 as −2 mWb and 1 mWb, the difference between the two membrane potentials become larger, as shown in Figures 2(c) and 2(d). It is indicated that the two coupled neurons are loose their synchronization. Summarily, by increasing the coupling strength k or decreasing memristor initial condition φ_0, the synchronization can be realized and the difference between the two membrane potentials is becoming smaller in the memristive synapse-connected Chay twin-neuron network. The mechanism for this process is that the coupling memristor exchanges the magnetic flux. Thus, the induced current is the carrier to drive the two Chay neurons in sync. Otherwise, the two connected Chay neurons are loss synchronization under tiny electromagnetic induction outputs.

To fully explore the synchronous behavior associated to the coupling strength k and initial condition φ_0 of the memristor synapse simultaneously, mean synchronization error (MSE) E is employed and defined as

$$E = \frac{1}{N}\sum_{j=1}^{N}\frac{\sqrt{[V_1(j)-V_2(j)]^2+[n_1(j)-n_2(j)]^2+[C_1(j)-C_2(j)]^2}}{\sqrt{V_1(j)^2+V_2(j)^2+n_1(j)^2+n_2(j)^2+C_1(j)^2+C_2(j)^2}}, \tag{6}$$

where $V_i(j)$, $n_i(j)$, and $C_i(j)$ $(i = 1, 2)$ are the jth sampling values and N is the number of total samples. The normalized MSE of the Chay twin-neuron network is becoming zero for synchronous state and nonzero for out of synchronization.

Herein, the time sequence interval (600 s and 700 s) and the time step 0.01 s are selected. Thus, the number of total samples is $N = 10000$. The normalized MSEs for different coupling strength k and initial condition φ_0, as well as different g_I and $g_{K,V}$ are given in the $\varphi_0 - k$ plane, as plotted

in Figure 3. The regions padded by red indicate the two connected Chay neurons in sync with $E = 0$, whereas the regions padded by other colors denote the two connected Chay neurons loss synchronization with $E > 0$. In general, as coupling strength k becoming larger and more negative initial condition φ_0, the normalized MSEs E drops near zero. Thus, the two connected Chay neurons become sync. Contrarily, the two connected Chay neurons are in asynchronous state with k becoming smaller and small negative or positive φ_0.

The normalized MSEs is given in Figure 3. The results show that the synchronous behaviors for the memristive synapse-connected Chay twin-neuron network are really associated with the memristor synapse coupling strength and the initial condition. Such an initial condition related synchronous behavior has been rarely reported in previous literature [22].

4. FPGA-Based Hardware Implementation

It is more complex to physically realize the memristive synapse-connected Chay twin-neuron network than a single 3D Chay neuron model by FPGA. Thus, only the memristive synapse-connected Chay twin-neuron model by the digital electronic platform is demonstrated with representativeness. For this aim, fourth-order Runge–Kutta algorithm is utilized to obtain the discrete-time form for model (4) and given as

$$\begin{aligned}
(V_1)_N &= (V_1)_{N-1} + \frac{l\left[D_1 k_{(V_1)1} + D_2 k_{(V_1)2} + D_3 k_{(V_3)3} + D_4 k_{(V_4)4}\right]}{D_1 + D_2 + D_3 + D_4},\\
(n_1)_N &= (n_1)_{N-1} + \frac{l\left[D_1 k_{(n_1)1} + D_2 k_{(n_1)2} + D_3 k_{(n_3)3} + D_4 k_{(n_1)4}\right]}{D_1 + D_2 + D_3 + D_4},\\
(C_1)_N &= (C_1)_{N-1} + \frac{l\left[D_1 k_{(C_1)1} + D_2 k_{(C_1)2} + D_3 k_{(C_1)3} + D_4 k_{(C_1)4}\right]}{D_1 + D_2 + D_3 + D_4},\\
(V_2)_N &= (V_2)_{N-1} + \frac{l\left[D_1 k_{(V_2)1} + D_2 k_{(V_2)2} + D_3 k_{(V_2)3} + D_4 k_{(V_2)4}\right]}{D_1 + D_2 + D_3 + D_4},\\
(n_2)_N &= (n_2)_{N-1} + \frac{l\left[D_1 k_{(n_2)1} + D_2 k_{(n_2)2} + D_3 k_{(n_2)3} + D_4 k_{(n_2)4}\right]}{D_1 + D_2 + D_3 + D_4},\\
(C_2)_N &= (C_2)_{N-1} + \frac{l\left[D_1 k_{(C_2)1} + D_2 k_{(C_2)2} + D_3 k_{(C_2)3} + D_4 k_{(C_2)4}\right]}{D_1 + D_2 + D_3 + D_4},\\
\varphi_N &= \varphi_{N-1} + \frac{l\left[D_1 k_{\varphi 1} + D_2 k_{\varphi 2} + D_3 k_{\varphi 3} + D_4 k_{\varphi 4}\right]}{D_1 + D_2 + D_3 + D_4},
\end{aligned} \tag{7}$$

where i is the sampling interval, N is the total number of iterations, and D_q ($q = 1, 2, 3, 4$) denotes the coefficient of variation. To achieve the unique expression of intermediate vector $k_{(V_i)q}, k_{(n_i)q}, k_{(C_i)q}$, and $k_{\varphi q}$ ($i = 1, 2$ and $q = 1, 2, 3, 4$), the assumption of $k_{(V_i)0} = k_{(n_i)0} = k_{(C_i)q} = k_{\varphi 0} = 0$ is applied. Then, one yields

$$\begin{aligned}
K_{(V_1)q} &= g_1 m_N^3 h_N \left[V_I - \left((V_1)_{N-1} + \frac{l k_{(V_1)q-1}}{D_q}\right)\right]\\
&\quad + g_{K,V} n_{1\,N-1}^4 \left[V_K - \left((V_1)_{N-1} + \frac{l k_{(V_1)q-1}}{D_q}\right)\right]\\
&\quad + g_{K,C} \frac{(C_1)_{N-1}}{1 + (C_1)_{N-1}}\\
&\quad \cdot \left[V_K - \left((V_1)_{N-1} + \frac{l k_{(V_1)q-1}}{D_q}\right)\right]\\
&\quad + g_L \left[V_L - \left((V_1)_{N-1} + \frac{l k_{(V_1)q-1}}{D_q}\right)\right]\\
&\quad + k \tan \varphi_{N-1} \left((V_1)_{N-1} + \frac{l k_{(V_1)q-1}}{D_q} - (V_2)_{N-1}\right),\\
K_{(n_1)q} &= \frac{d_N - \left((n_1)_{N-1} + \left(l k_{(n_1)q-1}/D_q\right)\right)}{\tau_N},\\
K_{(C_1)q} &= \rho\left[m_N^3 h_N (V_C - (V_1)_{N-1}) - K_C\left((C_1)_{N-1} + \frac{l k_{(C_1)q-1}}{D_q}\right)\right],\\
K_{(V_2)q} &= g_I m_N^3 h_N \left[V_I - \left((V_2)_{N-1} + \frac{l k_{(V_2)q-1}}{D_q}\right)\right]\\
&\quad + g_{K,V} n_{2\,N-1}^4 \left[V_K - \left((V_2)_{N-1} + \frac{l k_{(V_2)q-1}}{D_q}\right)\right]\\
&\quad + g_{K,C} \frac{(C_2)_{N-1}}{1 + (C_2)_{N-1}}\\
&\quad \cdot \left[V_K - \left((V_2)_{N-1} + \frac{l k_{(V_2)q-1}}{D_q}\right)\right]\\
&\quad + g_L \left[V_L - \left((V_2)_{N-1} + \frac{l k_{(V_2)q-1}}{D_q}\right)\right]\\
&\quad - k \tan \varphi_{N-1} \left((V_1)_{N-1} - (V_2)_{N-1} - \frac{l k_{(V_2)q-1}}{D_q}\right),\\
K_{(n_2)q} &= \frac{d_N - \left((n_2)_{N-1} + \left(l k_{(n_2)q-1}/D_q\right)\right)}{\tau_N},\\
K_{(C_2)q} &= \rho\left[m_N^3 h_N (V_C - (V_2)_{N-1}) - K_C\left((C_2)_{N-1}\right) + \frac{l k_{(C_2)q-1}}{D_q}\right],\\
K_{\varphi q} &= (V_1)_{N-1} - (V_2)_{N-1},
\end{aligned} \tag{8}$$

in which $q = 1, 2, 3, 4$, and

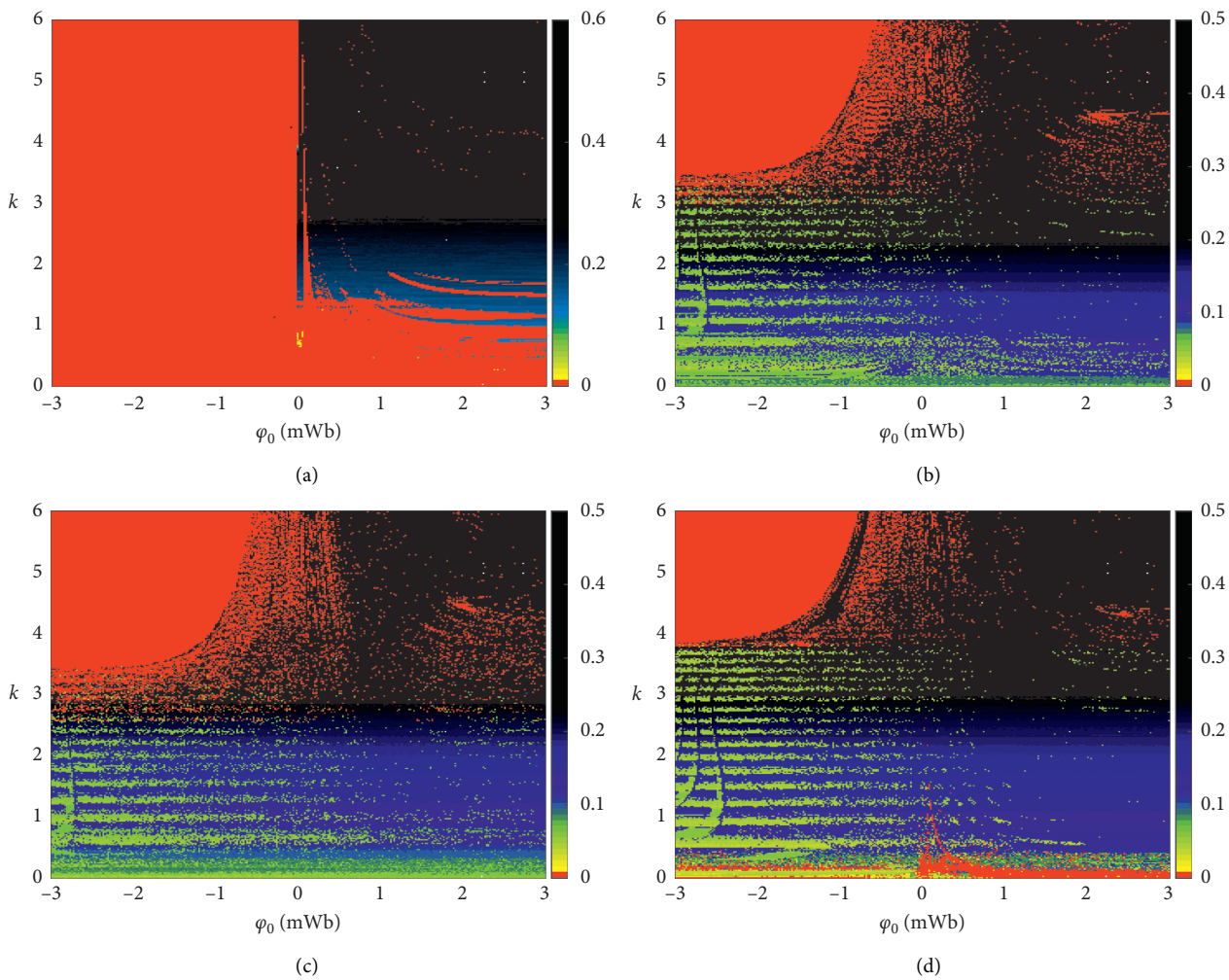

FIGURE 3: Normalized MSEs of the memristive synapse-connected Chay twin-neuron network in the $\varphi_0 - k$ plane. (a) $g_I = 1250\ \mathrm{mS/cm^2}$ and $g_{K,V} = 1700\ \mathrm{mS/cm^2}$; (b) $g_I = 1850\ \mathrm{mS/cm^2}$ and $g_{K,V} = 1700\ \mathrm{mS/cm^2}$; (c) $g_I = 1925\ \mathrm{mS/cm^2}$ and $g_{K,V} = 1700\ \mathrm{mS/cm^2}$; (d) $g_I = 1800\ \mathrm{mS/cm^2}$ and $g_{K,V} = 1650\ \mathrm{mS/cm^2}$.

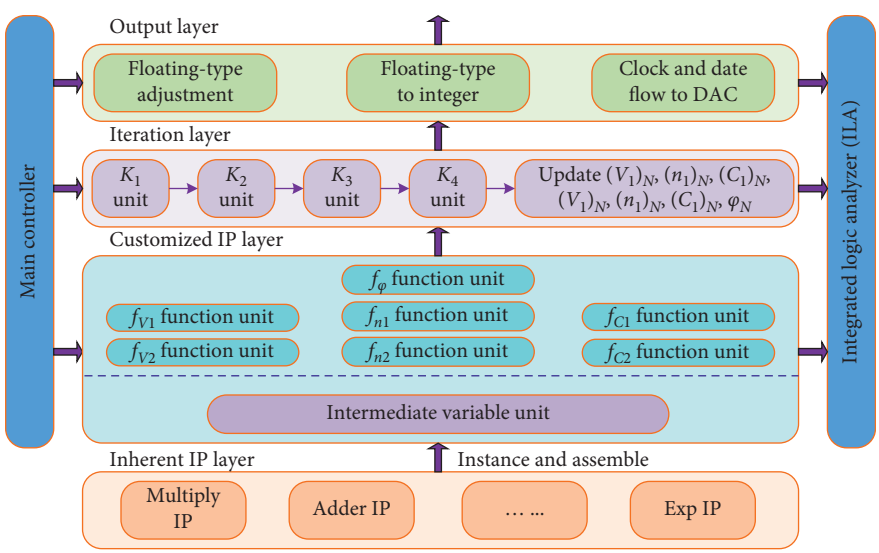

FIGURE 4: Hierarchical structure of the Verilog HDL program for the memristive synapse-connected Chay twin-neuron model.

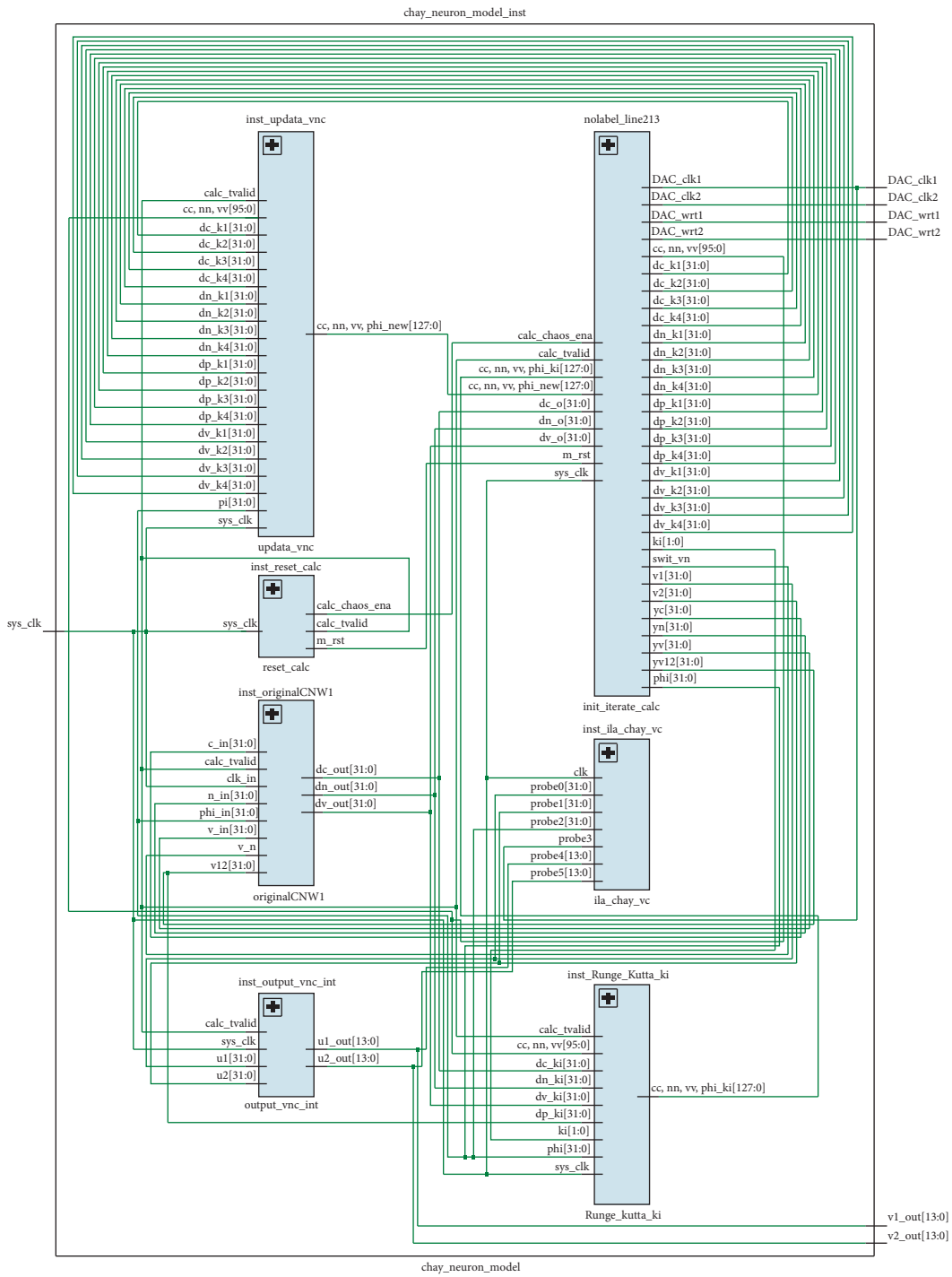

Figure 5: RTL schematics of the discrete-time memristive synapse-connected Chay twin-neuron model executed on XC7Z020 FPGA.

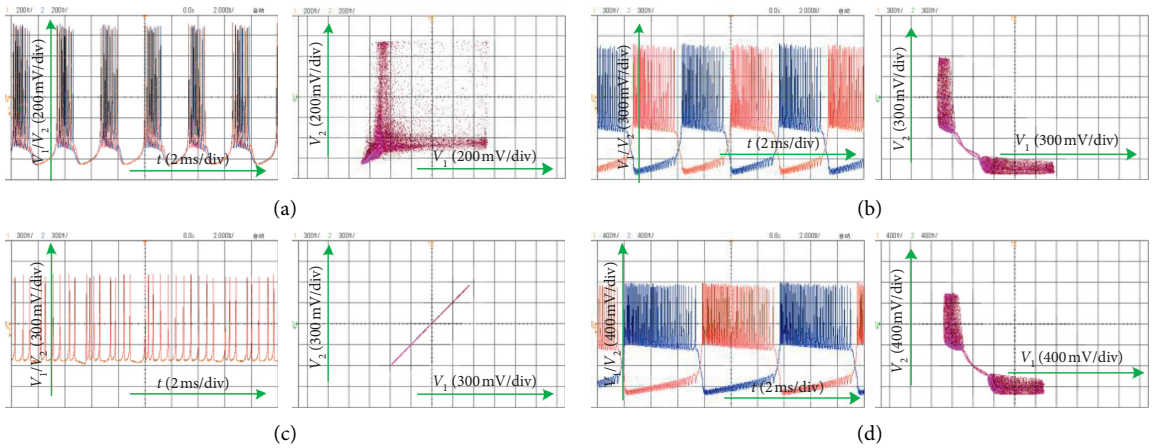

Figure 6: Hardware measured time-domain waveforms and synchronous transition states with different coupling strength k and initial condition $\varphi 0$. (a) $k=1$ and $\varphi 0=-2$ mWb; (b) $k=3$ and $\varphi 0=-2$ mWb; (c) $k=4$ and $\varphi 0=-2$ mWb; (d) $k=4$ and $\varphi 0=1$ mWb.

$$
\begin{aligned}
(m_i)_N &= \frac{25+(V_1)_{N-1}}{25+(V_1)_{N-1}+40\left(1-e^{-0.1(V_i)_{N-1}-2.5}\right)e^{-((V_i)_{N-1}+50)/80}},\\
(h_i)_N &= \frac{7\left(1+^{e-0.1(V_i)_{N-1}-2}\right)e^{-0.05(V_i)_{N-1}-2.5}}{7\left(1+e^{-0.1(V_i)_{N-1}-2}\right)e^{-0.05(V_i)_{N-1}-2.5}+100},\\
(d_i)_N &= \frac{20+(V_i)_{N-1}}{20+(V_1)_{N-1}+12.5\left(1-e^{-0.1(V_i)_{N-1}-2}\right)e^{-((V_i)_{N-1}+30)/80}},\\
(\tau_i)_N &= \frac{100\left(1+e^{-0.1(V_i)_{N-1}-2}\right)}{r_n\left[(20+(V_i)_{N-1})+12.5e^{-((V_i)_{N-1}+30)/80}\left(1+e^{-0.1(V_i)_{N-1}-2}\right)\right]}.
\end{aligned}
\tag{9}
$$

To achieve the discrete-time memristive synapse-connected Chay twin-neuron model (7), we employ a low-cost yet powerful XC7Z020 FPGA to execute the model for the first time. The FPGA software program using Verilog language is coded, within which the number of iteration $N=150000$, the sampled interval $i=0.001$, and the coefficients of variation $D_1=D_4=1$ and $D_2=D_4=2$ are set up. The parameters g_I, $g_{K,V}$, k, and φ_0, which impact the firing activities and synchronous behaviors, are changed by the software program to capture the four typical firing activities, time-domain waveforms, and STSs corresponding to the numerical simulations.

The hierarchical structure of the Verilog HDL program is illustrated in Figure 4. A main controller is set to reset the electro-neuron and to start the iteration form of initial conditions for V_i, n_i, C_i, and φ while the power is on. The floating-type operation IPs are contained in the lowest inherent IP layer, which can be instanced to construct our own customized IP. In the customized IP layer, add-, subtract-, multiply-, divide-, and exponent-operators are instanced to construct each function of the right side of continuous-time model (4) (expressed as f_{V1}, f_{n1}, $f_{C1}f_{V2}$, f_{n2}, f_{C2}, and f_φ). The intermediate variables $m_{1\infty}$, $h_{1\infty}$, $n_{1\infty}$, $m_{2\infty}$, $h_{2\infty}$, and $n_{2\infty}$ have to be calculated before the calculations of f_V, f_n, and f_C; thus, a sublayer for intermediate variables is hired in this layer. In the iteration layer, the functions f_{V1}, f_{n1}, $f_{C1}f_{V2}$, f_{n2}, f_{C2}, and f_φ are transmitted by time multiplex way to compute the intermediate vectors $k_{(V_i)q}$, $k_{(n_i)q}$, $k_{(C_i)q}$, and $k_{\varphi q}$ ($i=1,2$ and $q=1,2,3,4$) (marked as K_1, K_2, K_3, and K_4) in (8), and then the $(V_1)_N$, $(n_1)_N$, $(C_1)_N$, $(V_2)_N$, $(n_2)_N$, $(C_2)_N$, and φ_N are updated. Finally, an output layer is employed to adjust the output signal for visualizing expediently. The RTL schematic for the digitally electronic twin-neuron network is generated, as shown in Figure 5.

Since the outputs of a FPGA are digital, they are fed to a two-channel 14 bit D/A converter (AD9767) combined with the peripheral circuit to convert the digital outputs into analog ones. Herein, an oscilloscope Agilent DSO-X 3012A is employed to display the output analog signals. Note that, all variables are in the single-precision floating-type during the computation process, so they must be converted into integers and enlarged to the range of [−8192, 8191] to take full use of 14 bits of the DAC digital input ports. The time-domain waveforms of V_1 and V_2 and

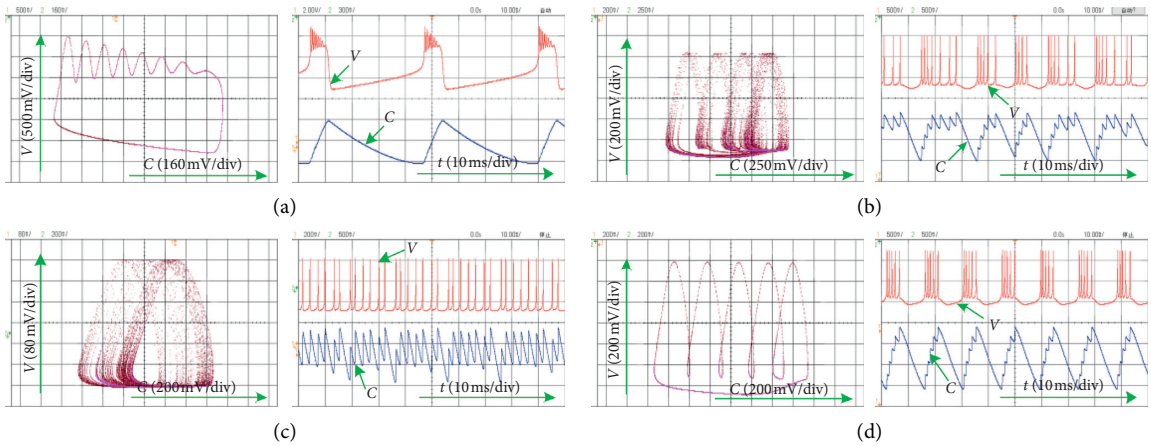

Figure 7: Experimentally captured trajectories in the C-V phase plane and time-domain waveforms. (a) Periodic bursting behavior for $g_I = 1250\ \mathrm{mS/cm^2}$ and $g_{K,V} = 1700\ \mathrm{mS/cm^2}$; (b) chaotic bursting behavior for $g_I = 1850\ \mathrm{mS/cm^2}$ and $g_{K,V} = 1700\ \mathrm{mS/cm^2}$; (c) chaotic spiking behavior for $g_I = 1925\ \mathrm{mS/cm^2}$and $g_{K,V} = 1700\ \mathrm{mS/cm^2}$; (d) periodic bursting behavior with burster-5 for $g_I = 1800\ \mathrm{mS/cm^2}$ and $g_{K,V} = 1650\ \mathrm{mS/cm^2}$.

synchronous transition states in the $V_1 - V_2$ plane for different coupling strength k and initial condition φ_0 in the Chay bi-neuron network are captured and displayed in Figure 6. The amplitudes of V_1 and V_2 on the oscilloscope are differed from that of MATLAB simulations in Figure 2, but they are proportional with each other due to the same enlargement. It is clearly shown that the proposed FPGA-based digital hardware can verify the synchronous behavior for the memristive synapse-connected Chay twin-neuron network. Note that the initial states in our digital circuit experiment are accurately assigned in the software [44]. This is very different from the randomly sensed way of acquiring initial states by repeatedly switching on and off the power supply in an analog circuit experiment [45]. Hence, the initial states are determined in the digital circuits but undetermined in the analog ones.

Besides, a FPGA-based digital hardware electronic neuron is simply realized to confirm the four representative firing activities in the 3D Chay neuron model. The trajectories in the $V_1 - V_2$ phase plane and time sequences of V_1 and V_2 are captured and displayed in Figure 7. The model parameters are selected the same as these utilized in Figure 1.

5. Conclusion

Four kinds of representative firing activities classified on the dependence of two maximal conductances in a 3D Chay neuron model are briefly reviewed. Then, a memristive synapse-connected Chay twin-neuron network is built, upon which synchronous behaviors are explored by utilizing time-domain waveforms, STSs, and MSEs. The numerical simulations demonstrated the success and effectiveness of employing the memristor synapse to achieve synchronization. It is found that, associating with the large coupling strength and more negative initial condition of the memristor, synchronous behaviors are achieved. An effective approach to implement the electronic neuron and the Chay twin-neuron network via FPGA are employed, from which the four kinds of representative firing activities of chaotic and periodic bursting/spiking behaviors, as well as the STSs are experimentally captured to confirm the correctness of the numerical ones. Synchronous behavior disclosed in neuronal network can well reveal the benefit for understanding the dynamical intricacy in the biological neurons and reflect the feasibility of diverse neuron-based applications.

Data Availability

The data used to support the findings of this study are available from the corresponding author upon request.

Conflicts of Interest

The authors declare that they have no conflicts of interest.

Acknowledgments

This work was supported by the National Natural Science Foundation of China under Grant nos. 61801054 and 51777016, Natural Science Foundations of Jiangsu Province, China, under Grant nos. BK20160282 and BK20191451, and Postgraduate Research and Practice Innovation Program of Jiangsu Province, China, under Grant nos. KYCX19_1768 and KYCX20_2550.

References

[1] F. Parastesh, K. Rajagopal, F. E. Alsaadi, T. Hayat, V.-T. Pham, and I. Hussain, "Birth and death of spiral waves in a network of hindmarsh-rose neurons with exponential magnetic flux and excitable media," *Applied Mathematics and Computation*, vol. 354, pp. 377–384, 2019.

[2] A. Mauroy and R. Sepulchre, "Clustering behaviors in networks of integrate-and-fire oscillators," *Chaos*, vol. 18, no. 3, Article ID 037122, 2008.

[3] K. Wu, T. Wang, C. Wang, T. Du, and H. Lu, "Study on electrical synapse coupling synchronization of hindmarsh-rose

neurons under Gaussian white noise," *Neural Computing and Applications*, vol. 30, no. 2, pp. 551–561, 2018.

[4] S. Mostaghimi, F. Nazarimehr, S. Jafari, and J. Ma, "Chemical and electrical synapse-modulated dynamical properties of coupled neurons under magnetic flow," *Applied Mathematics and Computation*, vol. 348, pp. 42–56, 2019.

[5] J. Ma and J. Tang, "A review for dynamics of collective behaviors of network of neurons," *Science China Technological Sciences*, vol. 58, no. 12, pp. 2038–2045, 2015.

[6] R. D. Pinto, P. Varona, A. R. Volkovskii, A. Szücs, H. D. I. Abarbanel, and M. I. Rabinovich, "Synchronous behavior of two coupled electronic neurons," *Physical Review E*, vol. 62, no. 2, pp. 2644–2656, 2000.

[7] G. Ren, Y. Xu, and C. Wang, "Synchronization behavior of coupled neuron circuits composed of memristors," *Nonlinear Dynamics*, vol. 88, no. 2, pp. 893–901, 2017.

[8] Z. T. Njitache, I. S. Doubla, J. Kengne, and A. Cheukem, "Coexistence of firing patterns and its control in two neurons coupled through an asymmetric electrical synapse," *Chaos: An Interdisciplinary Journal of Nonlinear Science*, vol. 30, no. 2, Article ID 023101, 2020.

[9] A. Tchaptchet, "Activity patterns with silent states in a heterogeneous network of gap-junction coupled huber-braun model neurons," *Chaos: An Interdisciplinary Journal of Nonlinear Science*, vol. 28, no. 10, Article ID 106327, 2018.

[10] A. Muhammad, K. S. Hong, and M. Y. Jeong, "Synchronization of coupled chaotic fitHugh-nagumo systems," *Communications in Nonlinear Science and Numerical Simulation*, vol. 17, no. 4, pp. 1615–1627, 2012.

[11] M. Rehan, K.-S. Hong, and M. Aqil, "Synchronization of multiple chaotic FitzHugh-Nagumo neurons with gap junctions under external electrical stimulation," *Neurocomputing*, vol. 74, no. 17, pp. 3296–3304, 2011.

[12] D. S. Alejandro and G. I. Gonzalo, "Noise-sustained synchronization of electrically coupled FitzHugh-Nagumo networks under counterphase external forcing," *Physics Letters A*, vol. 380, no. 22–23, pp. 1964–1970, 2016.

[13] H. Dalibor, "Synchronization of two Hindmarsh-Rose neurons with unidirectional coupling," *Neural Networks*, vol. 40, pp. 73–79, 2013.

[14] J. Juang and Y. H. Liang, "Cluster synchronization in networks of neurons with chemical synapses," *Chaos*, vol. 24, no. 1, Article ID 013110, 2014.

[15] F. Mormann, T. Kreuz, R. G. Andrzejak, P. David, K. Lehnertz, and C. E. Elger, "Epileptic seizures are preceded by a decrease in synchronization," *Epilepsy Research*, vol. 53, no. 3, pp. 173–185, 2003.

[16] S. J. G. Lewis and R. A. Barker, "Understanding the dopaminergic deficits in Parkinson's disease: insights into disease heterogeneity," *Journal of Clinical Neuroscience*, vol. 16, no. 5, pp. 620–625, 2009.

[17] P. J. Uhlhaas and W. Singer, "Neural synchrony in brain disorders: relevance for cognitive dysfunctions and pathophysiology," *Neuron*, vol. 52, no. 1, pp. 155–168, 2006.

[18] M. Lv, C. Wang, G. Ren, J. Ma, and X. Song, "Model of electrical activity in a neuron under magnetic flow effect," *Nonlinear Dynamics*, vol. 85, no. 3, pp. 1479–1490, 2016.

[19] M. Lv and J. Ma, "Multiple modes of electrical activities in a new neuron model under electromagnetic radiation," *Neurocomputing*, vol. 205, pp. 375–381, 2016.

[20] L. Chua, "Everything you wish to know about memristors but are afraid to ask," *Radioengineering*, vol. 24, no. 2, pp. 319–367, 2015.

[21] L. O. Chua, V. Sbitnev, and H. Kim, "Hodgkin-Huxley axon is made of memristors," *International Journal of Bifurcation and Chaos*, vol. 22, no. 3, Article ID 1230011, 2012.

[22] B. Bao, Q. Yang, D. Zhu, Y. Zhang, Q. Xu, and M. Chen, "Initial-induced coexisting and synchronous firing activities in memristor synapse-coupled Morris-Lecar bi-neuron network," *Nonlinear Dynamics*, vol. 99, no. 3, pp. 2339–2354, 2020.

[23] Y. Xu, Y. Jia, J. Ma, A. Alsaedi, and B. Ahmad, "Synchronization between neurons coupled by memristor," *Chaos, Solitons & Fractals*, vol. 104, pp. 435–442, 2017.

[24] J. Ma, L. Mi, P. Zhou, Y. Xu, and T. Hayat, "Phase synchronization between two neurons induced by coupling of electromagnetic field," *Applied Mathematics and Computation*, vol. 307, pp. 321–328, 2017.

[25] F. Xu, J. Zhang, T. Fang, S. Huang, and M. Wang, "Synchronous dynamics in neural system coupled with memristive synapse," *Nonlinear Dynamics*, vol. 92, no. 3, pp. 1395–1402, 2018.

[26] H. Bao, W. Liu, and A. Hu, "Coexisting multiple firing patterns in two adjacent neurons coupled by memristive electromagnetic induction," *Nonlinear Dynamics*, vol. 95, no. 1, pp. 43–56, 2019.

[27] T. R. Chay, "Chaos in a three-variable model of an excitable cell," *Physica D: Nonlinear Phenomena*, vol. 16, no. 2, pp. 233–242, 1985.

[28] A. L. Hodgkin and A. F. Huxley, "A quantitative description of membrane current and its application to conduction and excitation in nerve," *Bulletin of Mathematical Biology*, vol. 52, no. 1-2, pp. 25–71, 1990.

[29] Z. Yang, Q. Lu, H. Gu, and W. Ren, "Integer multiple spiking in the stochastic Chay model and its dynamical generation mechanism," *Physics Letters A*, vol. 299, no. 5-6, pp. 499–506, 2002.

[30] H. Gu, M. Yang, L. Li, Z. Liu, and W. Ren, "Dynamics of autonomous stochastic resonance in neural period adding bifurcation scenarios," *Physics Letters A*, vol. 319, no. 1-2, pp. 89–96, 2003.

[31] Z. Yang, Q. Lu, H. Gu, and W. Ren, "Gwn-induced bursting, spiking, and random subthreshold impulsing oscillation before hopf bifurcations in the Chay model," *International Journal of Bifurcation and Chaos*, vol. 14, no. 12, pp. 4143–4159, 2004.

[32] L. Duan, Q. Lu, and Q. Wang, "Two-parameter bifurcation analysis of firing activities in the Chay neuronal model," *Neurocomputing*, vol. 72, no. 1-3, pp. 341–351, 2008.

[33] Y. Yuan, N. Pang, Y. D. Chen, Y. Wang, and X. L. Li, "Theoretical analysis of the effects of transcranial magnetroacoustical simulation on neuronal firing rhythm and Ca^{2+} concentration with Chay neuron model," *Biomedical Physics & Engineering Express*, vol. 3, Article ID 055006, 2017.

[34] B. C. Bao, A. H. Hu, H. Bao, Q. Xu, M. Chen, and H. G. Wu, "Three-dimensional memristive Hindmarsh-Rose neuron model with hidden coexisting asymmetric behaviors," *Complexity*, vol. 2018, Article ID 3872573, 11 pages, 2018.

[35] N. Dahasert, İ. Öztürk, and R. Kiliç, "Experimental realizations of the HR neuron model with programmable hardware and synchronization applications," *Nonlinear Dynamics*, vol. 70, no. 4, pp. 2343–2358, 2012.

[36] H. Soleimani and E. M. Drakakise, "An efficient and reconfigurable synchronous neuron model," *IEEE Transactions on Circuits and Systems II: Express Briefs*, vol. 65, no. 1, pp. 91–95, 2018.

[37] M. Nouri, M. Hayati, T. Serrano-Gotarredona, and D. Abbott, "A digital neuromorphic realization of the 2-D Wilson neuron model," *IEEE Transactions on Circuits and Systems II: Express Briefs*, vol. 66, no. 1, pp. 136–140, 2019.

[38] M. Hayati, M. Nouri, S. Haghiri, and D. Abbott, "Digital multiplierless realization of two coupled biological Morris-Lecar neuron model," *IEEE Transactions on Circuits and Systems I: Regular Papers*, vol. 62, no. 7, pp. 1805–1814, 2015.

[39] M. Nouri, G. R. Karimi, A. Ahmadi, and D. Abbott, "Digital multiplierless implementation of the biological FitzHugh-Nagumo model," *Neurocomputing*, vol. 165, pp. 468–476, 2015.

[40] V. Ntinas, I. Vourkas, A. Abusleme, G. C. Sirakoulis, and A. Rubio, "Experimental study of artificial neural networks using a digital memristor simulator," *IEEE Transactions on Neural Networks and Learning Systems*, vol. 29, no. 10, pp. 5098–5110, 2018.

[41] Y.-S. Fan and T. R. Chay, "Generation of periodic and chaotic bursting in an excitable cell model," *Biological Cybernetics*, vol. 71, no. 5, pp. 417–431, 1994.

[42] Y. Li, H. Gu, and X. Ding, "Bifurcations of enhanced neuronal bursting activities induced by the negative current mediated by inhibitory autapse," *Nonlinear Dynamics*, vol. 97, no. 4, pp. 2091–2105, 2019.

[43] H. G. Gu and W. W. Xiao, "Different between intermittent chaotic bursting and spiking of nural firing patterns," *International Journal of Bifurcation and Chaos*, vol. 24, no. 6, Article ID 1450082, 2014.

[44] F. Yu, L. Liu, B. He et al., "Analysis and FPGA realization of a novel 5D hyperchaotic four-wing memristive system, active control synchronization, and secure communication application," *Complexity*, vol. 2019, Article ID 4047957, 18 pages, 2019.

[45] Q. Xu, Q. L. Zhang, N. Wang, H. G. Wu, and B. C. Bao, "An improved memristive diode bridge-based band pass filter chaotic circuit," *Mathematical Problems in Engineering*, vol. 2017, Article ID 2461964, 11 pages, 2017.

Hindawi
Mathematical Problems in Engineering
Volume 2020, Article ID 7530976, 16 pages
https://doi.org/10.1155/2020/7530976

Research Article

Multistability Analysis, Coexisting Multiple Attractors, and FPGA Implementation of Yu–Wang Four-Wing Chaotic System

Fei Yu,[1,2] **Li Liu**,[1] **Hui Shen**,[1] **Zinan Zhang**,[1] **Yuanyuan Huang**,[1] **Shuo Cai**,[1] **Zelin Deng**,[1] **and Qiuzhen Wan**[3]

[1]*School of Computer and Communication Engineering, Changsha University of Science and Technology, Changsha 410114, China*
[2]*Guangxi Key Laboratory of Cryptography and Information Security, Guilin University of Electronic Technology, Guilin 541004, China*
[3]*Hunan Provincial Key Laboratory of Intelligent Computing and Language Information Processing, Hunan Normal University, Changsha 410081, China*

Correspondence should be addressed to Fei Yu; yufeiyfyf@csust.edu.cn and Qiuzhen Wan; wanqiuzhen@sina.com

Received 15 June 2020; Revised 10 July 2020; Accepted 13 July 2020; Published 29 August 2020

Guest Editor: Viet-Thanh Pham

In this paper, we further study the dynamic characteristics of the Yu–Wang chaotic system obtained by Yu and Wang in 2012. The system can show a four-wing chaotic attractor in any direction, including all 3D spaces and 2D planes. For this reason, our interest is focused on multistability generation and chaotic FPGA implementation. The stability analysis, bifurcation diagram, basin of attraction, and Lyapunov exponent spectrum are given as the methods to analyze the dynamic behavior of this system. The analyses show that each system parameter has different coexistence phenomena including coexisting chaotic, coexisting stable node, and coexisting limit cycle. Some remarkable features of the system are that it can generate transient one-wing chaos, transient two-wing chaos, and offset boosting. These phenomena have not been found in previous studies of the Yu–Wang chaotic system, so they are worth sharing. Then, the RK4 algorithm of the Verilog 32-bit floating-point standard format is used to realize the autonomous multistable 4D Yu–Wang chaotic system on FPGA, so that it can be applied in embedded engineering based on chaos. Experiments show that the maximum operating frequency of the Yu–Wang chaotic oscillator designed based on FPGA is 161.212 MHz.

1. Introduction

Due to the extreme sensitivity of chaos to initial conditions and parameters and the characteristics of the generated chaotic sequence such as aperiodicity and pseudo-randomicity, chaos has been widely used in memristors [1–4], random number generators [5–7], electronic circuits [8–10], image encryption [11–14], complex networks [15–19], synchronization [20–23], and secure communication [24–28] in the past two decades. Up to now, numerous various chaotic systems have been extensively studied, including multiwing chaotic systems [29, 30], multiscroll chaotic systems [31–34], hyperchaotic systems [35–38], and chaotic systems with hidden attractors [39–42].

A class of chaotic systems are characterized by the coexistence of many different types of attractors, a phenomenon referred to as multistability which has become a very important research topic and received much attention recently [43–46]. In [44], a smooth piecewise quadratic nonlinear four-wing chaotic system is proposed. When the appropriate parameters including a two-wing and four-wing chaotic attractor are selected, the system can observe four kinds of unconnected coexisting stable states under different initial values and show rich dynamic behaviors. In [45], a 4D chaotic system with planar equilibrium is introduced. Through dynamic analysis, it is revealed that the chaotic system has three different types of coexisting attractors in a certain parameter range: chaotic attractors, stable node

attractors, and limit cycle attractors. In addition, when the initial conditions of a state variable change and the number of attractors approaches infinity, this phenomenon is called extreme multistability [47–50]. More and more attention has been paid to the research related to extreme multistability. In [47], the flux-controlled memristor model is introduced into the existing 5D hyperchaotic autonomous system, and a 6D autonomous system is obtained. By analyzing the dynamics of the system, it is found that the system has the characteristics of extreme multistability, bursting, transient chaos, and offset boosting phenomenon.

Chaos generator is one of the most basic structures of chaos in practical application. Chaos generator is mainly realized by analog and digital methods. The method to realize a chaotic system in the analog circuit is mainly by using discrete components on the combined bread board [30, 32, 42]. The chaotic signal realized by this method is unstable, and its portability is very poor. Secondly, the integrated circuit (IC) chaos generator chip is designed by the CMOS technology, and the chaos generator based on IC can achieve the highest performance [51–53]. However, the implementation based on IC is not easy to realize the frequency tunability of the chaotic oscillator, and there are some problems such as a long design period and a high cost of the tape [54–56]. Compared with analog generators, chaos generators based on digital circuits have comparative advantages. Digital chaos generators are implemented by the digital signal processor (DSP) [57, 58] and the field programmable gate array (FPGA) [59–65]. In complex mathematical operations, DSP chips generally perform operations sequentially, so it takes a long time to calculate output values sequentially using DSP-based chaos generators. On the contrary, FPGA chips have a relatively flexible architecture that allows simultaneous computation, and FPGA chip design and test cycle costs are particularly low [66–68]. Through the numerical and reconfigurable characteristics of FPGA, the FPGA-based chaos generator and its application can be more flexible.

In this study, we consider the dynamics of a relatively simple chaotic system with a fully qualified four-wing chaotic attractor introduced by Yu et al. [69], with particular emphasis on the chaos mechanism and the possibility of multiple coexisting attractors varying with five system parameters. Chaotic systems with coexisting attractors have great potential for engineering applications. The research on the multistability of the Yu–Wang system has not been fully discussed, which is worthy of further study. In this paper, we find and focus on the multistability window. Secondly, some remarkable characteristics of the system such as transient chaos and offset boosting can be generated under certain conditions.

The rest of this paper is organized as follows. The mathematical model of the Yu–Wang chaotic system is described and analyzed in Section 2. In Section 3, we analyze the dynamic characteristics of the system in detail. The complex dynamics of the system is analyzed from five aspects: coexistence of attractors with different parameters, multistability, basin of attraction, transient chaos, and offset boosting. In Section 4, we use the RK4 algorithm and the Verilog language to design a Yu–Wang chaotic oscillator based on FPGA on Vivado 2018.3. Then, by analyzing the statistical data of the FPGA chip, the simulation results and the phase diagram of the oscilloscope output are obtained. Finally, some conclusions are given in Section 5.

2. Description and Analysis of the Model of Yu–Wang Chaotic System

The Yu–Wang chaotic system, which was proposed by Yu et al. [69], is described by the following simple 4D autonomous system with four quadratic nonlinear terms:

$$\begin{cases} \dot{x} = -ax + yz + bw, \\ \dot{y} = cy - xz, \\ \dot{z} = xy - dz, \\ \dot{w} = xz - ew, \end{cases} \tag{1}$$

where x, y, z, and w are the state variables of the system and a, b, c, d, and e are the system parameters. When $a = 8$, $b = 5, c = 12, d = 60$, and $e = 4$ and the initial conditions are $[2, 1, 1, 2]$, the system is a fully four-wing chaotic system. It is very interesting that the attractors of the system can exhibit a four-wing form in any direction of any phase plane, including all 3D spaces and 2D planes as shown in Figure 1. The four Lyapunov exponents (LEs) of system (1) are LE1 = 1.4247, LE2 = 0.0014, LE3 = −6.4991, and LE4 = −54.9120, respectively, and the system has positive Lyapunov exponents, so the system has a very interesting dynamic behavior. The Yu–Wang system is symmetric about the z axis; that is, it remains unchanged under the coordinate transformation $(x, y, z, w) \longrightarrow (-x, -y, z, -w)$.

The equilibrium point of system (1) can be obtained by solving the following equations:

$$\begin{cases} -ax + yz + bw = 0, \\ cy - xz = 0, \\ xy - dz = 0, \\ xz - ew = 0. \end{cases} \tag{2}$$

On the basis of equation (2), it is easy to get $x = \pm\sqrt{cd}$. The following two cases are discussed:

(i) When $x = \sqrt{cd}$, substituting x into equation (2), we get

$$\begin{cases} -a\sqrt{cd} + yz + bw = 0, \\ cy - \sqrt{cd}\, z = 0, \\ \sqrt{cd}\, y - dz = 0, \\ \sqrt{cd}\, z - ew = 0, \end{cases} \tag{3}$$

and according to equation (3), we obtain the following equation:

$$z_{1,2} = \frac{-(bc/e) \pm \sqrt{\left(b^2c^2/e^2\right) + 4ac}}{2}, \tag{4}$$

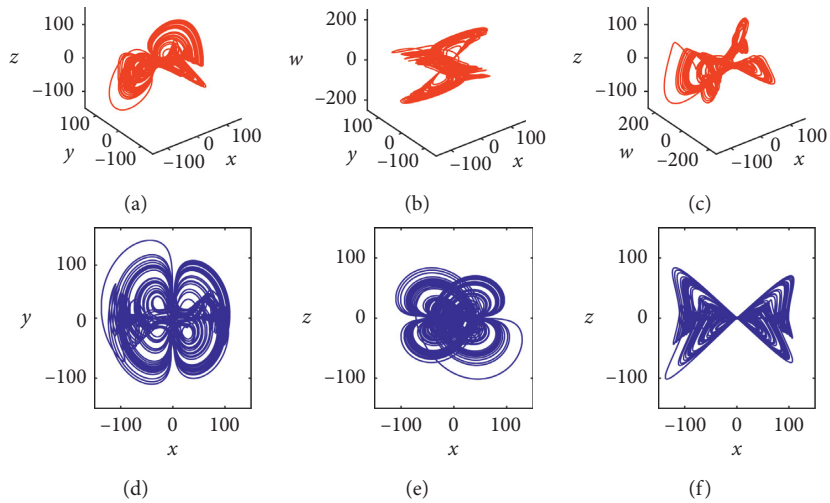

Figure 1: The four-wing chaotic attractor of system (1) in 3D spaces and 2D planes: (a) in the $x-y-z$ space, (b) in the $x-y-w$ space, (c) in the $x-w-z$ space, (d) in the $x-y$ plane, (e) in the $y-z$ plane, and (f) in the $x-z$ plane.

and because $y=\sqrt{(d/c)}z$ and $w=(\sqrt{cd}/e)z$, we can get

$$y_{1,2}=\frac{-(bc/e)\pm\sqrt{\left(b^2c^2/e^2\right)+4ac}}{2\sqrt{c/d}},$$
$$w_{1,2}=\frac{-(bc/e)\pm\sqrt{\left(b^2c^2/e^2\right)+4ac}}{2e/\sqrt{cd}}. \tag{5}$$

(ii) When $x=-\sqrt{c\,d}$, substituting x into equation (2), we get

$$\begin{cases} a\sqrt{cd}+yz+bw=0,\\ cy+\sqrt{cd}\,z=0,\\ -\sqrt{cd}\,y-dz=0,\\ -\sqrt{cd}\,z-ew=0,\end{cases} \tag{6}$$

and based on equation (6), we can obtain

$$z_{3,4}=-\frac{-(bc/e)\pm\sqrt{\left(b^2c^2/e^2\right)+4ac}}{2},$$
$$y_{3,4}=-\frac{-(bc/e)\pm\sqrt{\left(b^2c^2/e^2\right)+4ac}}{2\sqrt{(c/d)}}, \tag{7}$$
$$w_{3,4}=-\frac{-(bc/e)\pm\sqrt{\left(b^2c^2/e^2\right)+4ac}}{2\left(e/\sqrt{cd}\right)}.$$

According to the above analysis, the five equilibrium points of system (1) are $S_0=[0,0,0,0]$, $S_{1,2}=[\sqrt{cd},y_{1,2},z_{1,2},w_{1,2}]$, and $S_{3,4}=[-\sqrt{cd},y_{3,4},z_{3,4},w_{3,4}]$ when $a=8$, $b=5$, $c=12$, $d=60$, and $e=4$. The five equilibrium points of system (1) can be calculated as $S_0=[0,0,0,0]$, $S_{1,3}=[\pm26.83,\pm10.82,4.84,\pm32.47]$, and $S_{2,4}=[\pm26.84,\mp44.36,-19.84,\mp133.09]$.

The Jacobian matrix of system (1) can be described as

$$\mathrm{JO}=\begin{bmatrix}-a & z & y & b\\ -z & c & -x & 0\\ y & x & -d & 0\\ z & 0 & x & -e\end{bmatrix}. \tag{8}$$

In order to consider the stability of the system, each equilibrium point is considered to calculate the corresponding eigenvalue according to the Jacobian matrix, and the eigenvalues are, respectively, obtained as $(-8,12,-60,-4)$, $(-51.65,-11.54,1.60+9.67i,1.60-9.67i)$, $(-88.54,15.39+65.61i,15.39-65.61i,-2.25)$, $(-51.65,-11.54,1.60+9.67i,1.60-9.67i)$, and $(-88.54,15.39+65.61i,15.39-65.61i,-2.25)$. According to the five eigenvalues, it can be judged that system (1) has an unstable saddle focal equilibrium point, which will lead to chaos.

The dissipativity of system (1) is described as

$$\nabla V=\frac{\mathrm{d}\dot{x}}{\mathrm{d}x}+\frac{\mathrm{d}\dot{y}}{\mathrm{d}y}+\frac{\mathrm{d}\dot{z}}{\mathrm{d}z}+\frac{\mathrm{d}\dot{w}}{\mathrm{d}w}=-a+c-d-e=-60. \tag{9}$$

Equation (9) shows that the divergence is negative. Consequently, the general condition of dissipativity associated with the existence of attractive sets in system (1) is fulfilled.

3. Dynamic Characteristic Analysis of System (1)

In this section, complex dynamics of the Yu–Wang autonomous chaotic system is numerically investigated with the help of various tools. These include the bifurcation diagram, Lyapunov exponents, phase portraits, and attraction basins. All numerical simulations are based on the resolution of system (1) using the fourth-order Runge–Kutta method. For the computation of Lyapunov exponents, the algorithm proposed by Wolf et al. [70] is used.

3.1. Dynamic Analysis of Different System Parameters. The dynamic behaviors of the parameters in system (1) are analyzed. It is found that there are many kinds of attractors coexisting in system (1). Table 1 shows the dynamic behavior of different parameters of the system.

3.1.1. Case 1. Fixing the parameters $b = 5, c = 12, d = 60$, and $e = 4$, we make the parameter a change in the range of $(0, 40]$. Figure 2(a) is the bifurcation diagram of the system in the initial conditions $[2, 1, 1, 2]$ and $[-2, -1, 1, -2]$, and Figure 2(b) is the largest LE spectrum. From Figure 2, we can see that the dynamic characteristics of the system are very complex, and there are many coexisting attractors. When the parameter $a \in (0, 11.1)$, system (1) shows a chaotic state. When $a \in [11.1, 12.6]$, system (1) is in a periodic state, and when $a = 11.5, a = 12.3$, and $a = 12.5$, the attractors of system (1) are, respectively, represented by the one-wing period-1, one-wing period-2, and one-wing period-4, and the phase portraits of the coexisting attractors are shown in Figures 3(a)–3(c). When $a \in (12.6, 19]$, the system behaves as a chaotic state. Especially when $a = 12.6$, system (1) presents the one-wing chaotic state, and its coexisting attractor is shown in Figure 3(d). When $a = 15.8$, the system is in the three-wing period state, and its coexisting attractor is shown in Figure 3(e). When $a \in (19, 23.8)$, the inverse period bifurcations and period bifurcation occur in this system, which are generally consistent with $a \in [11.1, 12.6]$. Therefore, the same phenomenon is not shown in Figure 3. When $a = 20$, system (1) is in the four-wing period-1 state, and its coexistence attractor is shown in Figure 3(f). When $a = 19.1$, system (1) is in the four-wing period-4 state, and its coexistence attractor is shown in Figure 3(g). When $a \in [23.8, 31.5)$, the system shows a new chaotic state. When $a = 28$, system (1) is a four-wing chaotic attractor, and its coexisting attractor is shown in Figure 3(h). When $a \in [31.5, 40]$, the system is in a stable state, and when $a = 31.6$, system (1) is in a stable state, and the phase portrait of its coexistence point attractor is shown in Figure 3(i).

3.1.2. Case 2. Fixing the parameters $a = 8, c = 12, d = 60$, and $e = 4$, we make the parameter b change in the range of $[-20, 20]$. Figure 4(a) shows the bifurcation diagram of the system in the initial conditions $[2, 1, 1, 2]$ and $[-2, -1, 1, -2]$, and Figure 4(b) shows the largest LE spectrum. From Figure 4, the system is completely symmetric with respect to the dynamic characteristics of parameter b. When parameter $b \in [0, 2.3]$, system (1) has an inverse period bifurcation, in which when $b = 0, b = 0.5$, and $b = 0.58$, system (1) is displayed as the one-wing period-1, one-wing period-2, and one-wing period-4, respectively, and the phase portraits of their coexisting attractors are shown in Figures 5(a)–5(c); when $b \in (2.3, 20]$, the system (1) state is mostly chaotic, and some periodic windows are included; especially when $b = 19.35$, the system is a two-wing period phenomenon, and its coexistence attractor is shown in Figure 5(d). When $b = 17.8$, the system is in the three-wing periodic state, and its coexistence attractor is shown in Figure 5(e). When $b = 15$, the system is in four-wing chaos, and its coexistence attractor is shown in Figure 5(f).

3.1.3. Case 3. Fixing the parameters $a = 8, b = 5, d = 60$, and $e = 4$, let the parameter c change in the range of $[0, 50]$. Figure 6(a) shows the bifurcation diagram of the system under two different initial conditions (the blue region represents the initial conditions of $[2, 1, 1, 2]$ and the red region represents the initial conditions of $[-2, -1, 1, -2]$). Figure 6(b) shows the largest LE exponent spectrum of Figure 6(a). According to Figure 6, the system has experienced the process from periodic state to chaos to periodic state to chaos to period doubling bifurcation to chaos. In the interval $c \in [0, 10.4]$, system (1) is in the periodic state. When $c = 0.06, c = 0.1$, and $c = 0.2$, the system is in the one-wing period-1, one-wing period-3, and two-wing period-3, respectively, and their coexisting attractor phase portraits are shown in Figures 7(a)–7(c). Figures 7(d) and 7(e) are the phase portraits of the coexistence of attractors in two different states when the system changes from two-wing multiperiod to two-wing period-1 state. In the interval $c \in (10.4, 14.9)$, the system is in a chaotic state. When $c = 10.6$, the system has a four-wing chaotic attractor, and its coexisting attractor is shown in Figure 7(f); in $c \in [14.9, 15.2)$, the system is in the periodic state. When $c = 15$, the system is in the two-wing period-1 state, and its coexisting attractor is shown in Figure 7(g); the system is chaotic in the interval $c \in [15.2, 29.4)$. When $c = 15.32$, the system has a two-wing chaotic attractor, and its coexisting attractor is shown in Figure 7(h); in the interval $c \in [29.4, 32.1)$, system (1) experiences period doubling bifurcation, in which when $c = 31, c = 31.8$, and $c = 31.9$, the system is in the one-wing period-1, one-wing period-2, and one-wing period-4 states, respectively, and the phase portraits of their coexisting attractors are shown in Figures 7(i)–7(k). In the interval $c \in [32.1, 50]$, the system is in a chaotic state. When $c = 32.5$, the system has a one-wing chaotic attractor, and its coexisting attractor is shown in Figure 7(l).

3.1.4. Case 4. For the given parameters $a = 8, b = 5, c = 12$, and $e = 4$, let parameter d vary within the range of $[16, 100]$. Figure 8(a) is the bifurcation diagram of the system under two different initial conditions (the blue region is the initial conditions of $[2, 1, 1, 2]$ and the red region is the initial conditions of $[-2, -1, 1, -2]$). Figure 8(b) is the largest LE spectrum of Figure 8(a). As can be seen from Figure 8, the system dynamics is very complex, with period doubling bifurcation, inverse period bifurcation, and chaotic states. When $d = 16$, the system is in the period-1 state; when $d = 17$, the system is in the period-2 state; when $d = 17.2$, the system is in the period-4 state; when $d = 17.8$, the system has one-wing chaotic attractors; when $d = 25$, the system has four-wing chaotic attractors; when $d = 42$, the system is in a multiperiod state; when $d = 50$, the system is in a multiperiod state; when $d = 68$, the system is in the two-wing period-1 state; when $d = 70$, the system is in the two-wing multiperiod state. The phase portrait of coexisting attractors

Table 1: Dynamic behavior under different parameters.

Case	Parameter value	Dynamic behavior
Case 1	$b = 5, c = 12, d = 60, e = 4, a \in (0, 40]$	Three kinds of periodic phenomena, two kinds of chaotic attractors with different wings and point attractor
Case 2	$a = 8, c = 12, d = 60, e = 4, b \in [-20, 20]$	Three different types of periodic phenomena and four-wing chaotic attractors
Case 3	$a = 8, b = 5, d = 60, e = 4, c \in [0, 50]$	Seven kinds of periodic phenomena, two kinds of quasiperiodic attractors, and two kinds of chaotic attractors
Case 4	$a = 8, b = 5, c = 12, e = 4, d \in [16, 100]$	Three different types of periodic phenomena and two different types of chaotic attractors
Case 5	$a = 8, b = 5, c = 12, d = 60, e \in [0, 44]$	Two kinds of periodic phenomena and two kinds of chaotic attractors with different wings

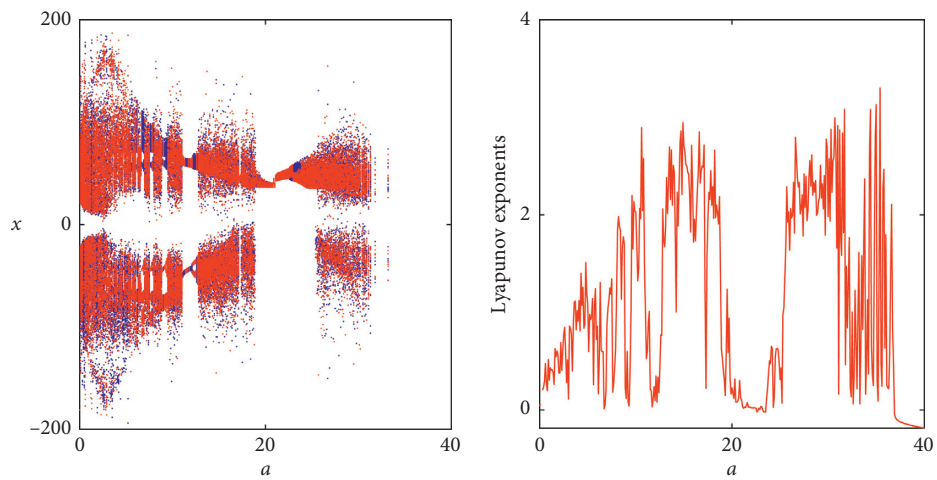

Figure 2: The bifurcation diagram and the largest LE for increasing parameter $a \in (0, 40]$. (a) The bifurcation diagram with initial conditions $[2, 1, 1, 2]$ (blue) and $[-2, -1, 1, -2]$ (red). (b) The largest LE.

of the above analyzed states under two initial conditions is shown in Figures 9(a)–9(i), respectively.

3.1.5. Case 5. For the given parameters $a = 8, b = 5, c = 12$, and $d = 60$, the parameter e changes in the range of $[0, 44]$. Figure 10(a) shows the bifurcation of the system under two different initial conditions (the blue indicates that the initial condition is $[2, 1, 1, 2]$ and red indicates that the initial condition is $[-2, -1, 1, -2]$). Figure 10(b) shows the largest LE spectrum of Figure 10(a). As can be seen from Figure 10, the system undergoes the process of period doubling bifurcation to chaos to period doubling bifurcation to chaos to periodic state. In the interval $e \in [0, 2.5]$, system (1) experiences period doubling bifurcation. When $e = 0.2$, the system is in the four-wing periodic state, and Figure 11(a) is the phase portrait of its coexisting attractor. When $e = 1.5, e = 2$, and $e = 2.1$, the system presents the one-wing period-1, one-wing period-2, and one-wing period-4, respectively, and the phase portraits of their coexisting attractors are shown in Figures 11(b)–11(d); in $e \in (2.5, 11.6]$, the system is in a chaotic state. Figure 11(e) shows the phase portraits of the coexistence attractor when $e = 5$; in the interval $e \in (11.6, 15.2)$, the system experiences period doubling bifurcation, and its phase portrait is the same as that of the previous period doubling bifurcation; in $e \in [15.2, 42.3]$, the system is in a chaotic state. When $e = 17$, the system has a two-wing chaotic attractor, whose coexisting attractor is shown in Figure 11(f).

3.2. Multistability. Coexistence of multiple attractors is a very interesting phenomenon in nonlinear systems. It only changes the initial conditions, and the system can produce multiple attractor coexistence. Multistability is the inherent property of many nonlinear dynamical systems and is the result of coexistence of many attractors. In short, a system is multistable if it has multiple attractors, and the external excitation is strong enough to switch between stable states. In this section, we will study the multistability of the 4D Yu–Wang chaotic system.

Figure 12(a) is the phase portrait when parameters $a = 8, b = 5, c = 3.4, d = 60$, and $e = 4$ and initial conditions $y(0) = 1, z(0) = 1$, and $w(0) = 2$ are given. It can be seen from the figure that the system has the coexistence of one-wing period-1, two-wing multiperiod, and four-wing multiperiod phenomena. Figure 12(b) is the phase portrait with the given parameters $a = 8, b = 5, c = 15.32, d = 60$, and $e = 4$ and initial conditions $x(0) = 1, z(0) = 1$, and $w(0) = 2$. It can be seen from the figure that the system has

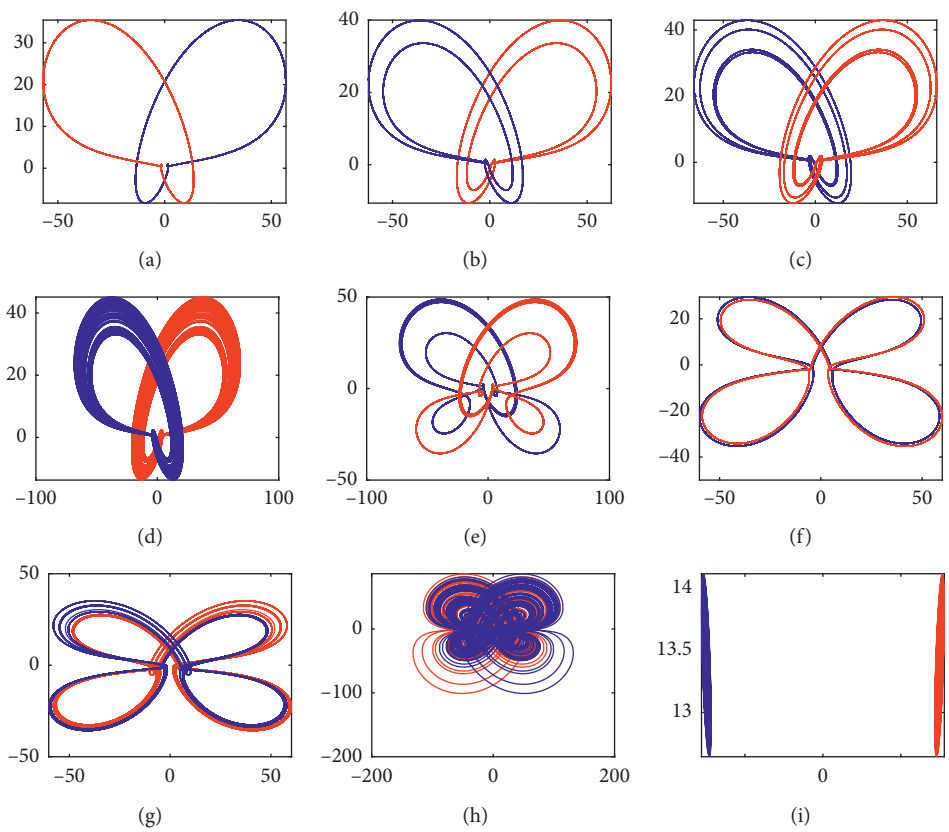

Figure 3: Various coexisting attractors with different values of parameter a in the $y-z$ plane: (a) $a = 11.5$, (b) $a = 12.3$, (c) $a = 12.5$, (d) $a = 12.6$, (e) $a = 15.8$, (f) $a = 20$, (g) $a = 19.1$, (h) $a = 28$, and (i) $a = 31.6$. The blue one is from the initial values $[2, 1, 1, 2]$ and the other from $[-2, -1, 1, -2]$.

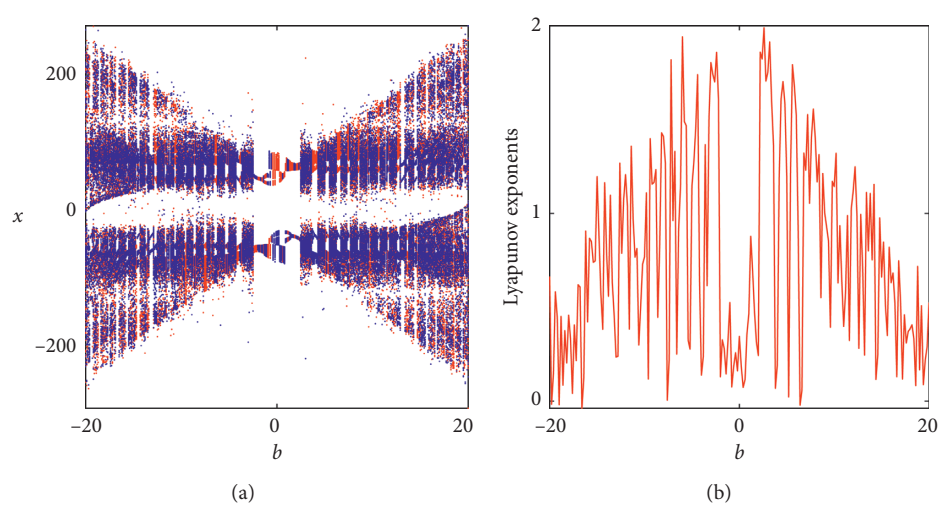

Figure 4: Bifurcation diagram and the largest LE for increasing parameter $b \in [-20, 20]$. (a) The bifurcation diagram with initial conditions $[2, 1, 1, 2]$ (blue) and $[-2, -1, 1, -2]$ (red). (b) The largest LE.

the coexistence phenomenon of four-wing chaotic attractors and two two-wing chaotic attractors of different directions. It is worth pointing out that the phenomenon of the coexistence polyattractor is very important in cryptography, information security, and secure communication.

3.3. Basin of Attraction. If the attractive regions of chaotic attractors are riddled with each other, a kind of intermittence phenomenon of continuous communication between chaotic attractors will occur when the cross-section Lyapunov exponent is slightly greater than 0. After the orbit

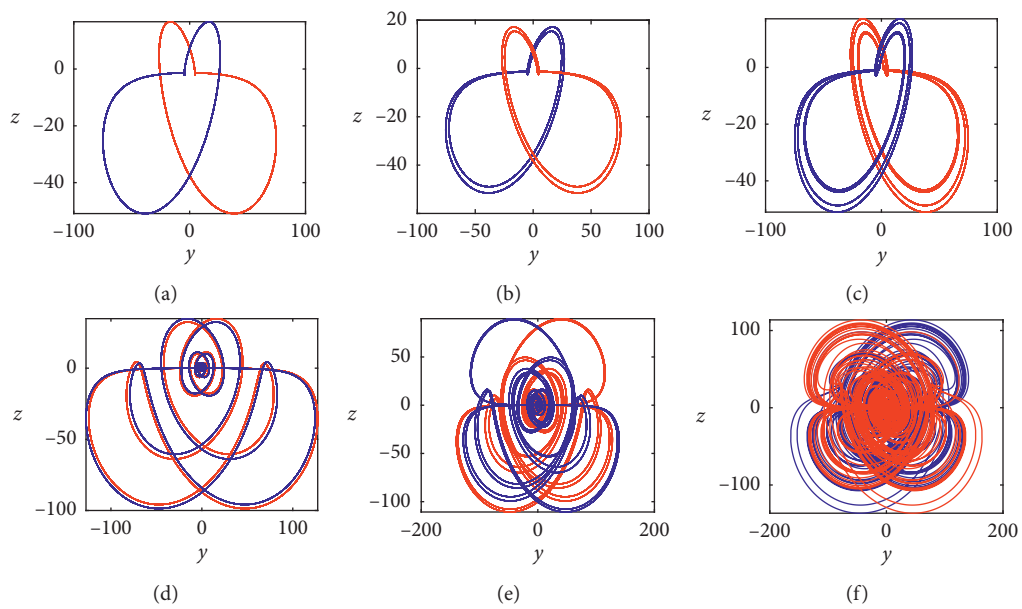

Figure 5: Various coexisting attractors with different values of parameter b in the $y-z$ plane: (a) $b = 0$, (b) $b = 0.5$, (c) $b = 0.58$, (d) $b = 19.35$, (e) $b = 17.8$, and (f) $b = 15$. The blue one is from the initial values $[2, 1, 1, 2]$ and the other from $[-2, -1, 1, -2]$.

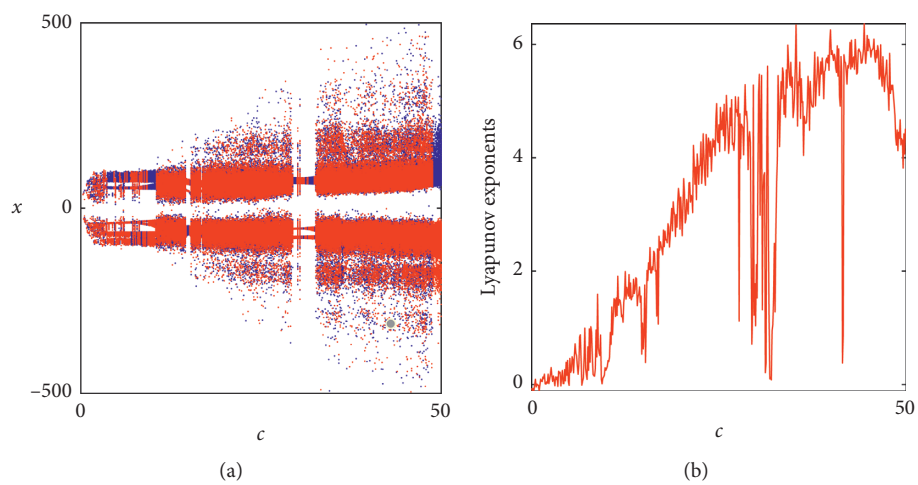

Figure 6: Bifurcation diagram and the largest LE for increasing parameter $c \in [0, 50]$. (a) The bifurcation diagram with initial conditions $[2, 1, 1, 2]$ (blue) and $[-2, -1, 1, -2]$ (red). (b) The largest LE.

stays near one chaotic attractor for a period of time, it jumps to another chaotic attractor and stays for a period of time, and then repeats the above process [71]. In order to verify whether the sieve domains of the system are mutually riddled, we not only observe the graph directly, but also use the Lyapunov index to judge; for example, according to the parameters and initial conditions of the four-wing chaotic system (1), we calculate that the second Lyapunov exponent is $\lambda_2 = 0.0014$, indicating that the system is mutually riddled.

The Wada domain is possible when the system has three or more attractors [72, 73]. When studying the formation mechanism of the Wada domain, Nusse and Yorke introduced the concept of the trap region and the domain cell [74]. There are domain cells in the Wada domain, but there are no trap regions and domain cells in the global sieve domain of this system because every point in the global sieve domain has points in its neighborhood that belong to other attractive domains [75]. Figure 13 is the basin of attraction of system (1) with respect to $x(0) - y(0)$ and $z(0) - w(0)$ planes, respectively. It can be shown that there is no open set in this sieve domain. Therefore, we believe that the sieve domain of the system is formed by the local-global bifurcation of the sieve domain.

3.4. Transient Chaos. Transient chaos is a very common phenomenon in nonlinear dynamic systems. When unattractive saddle points appear in the phase space, the system will be chaotic within a certain time range. With the development of time, the system will eventually become

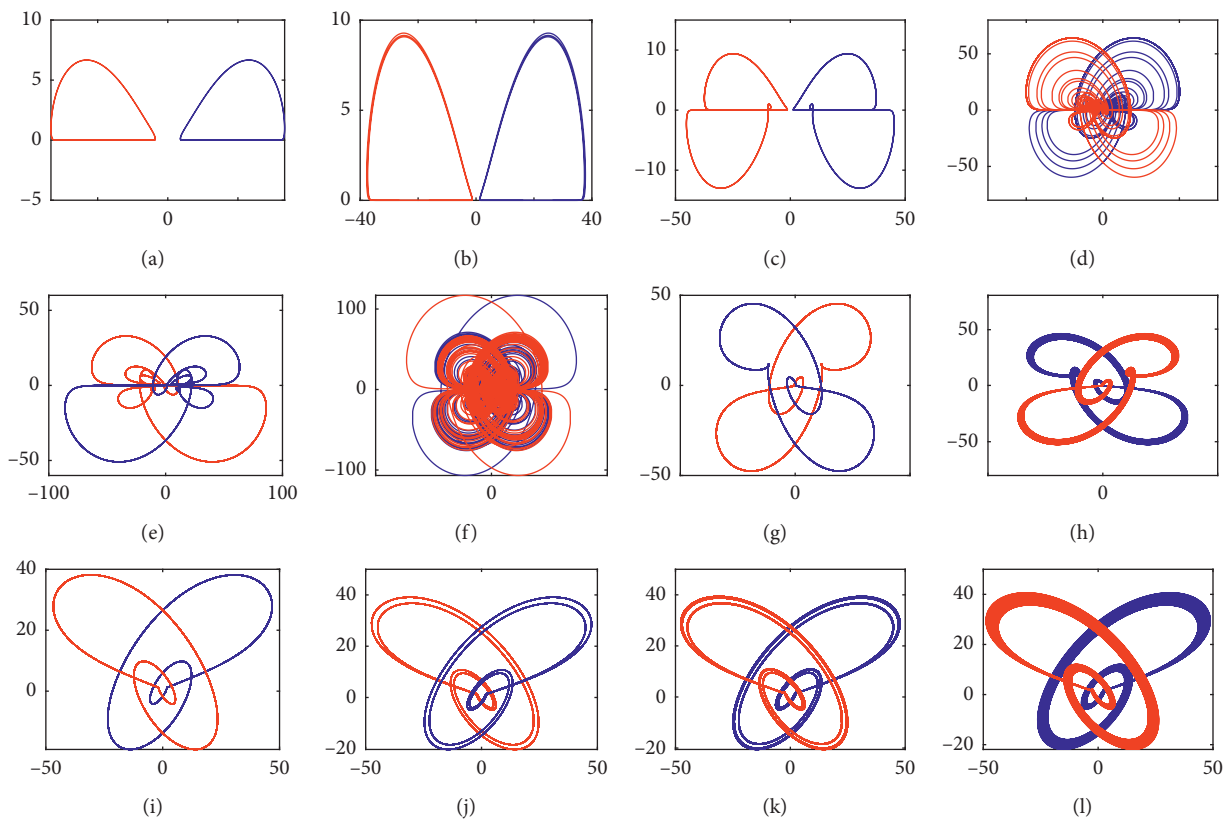

FIGURE 7: Various coexisting attractors with different values of parameter c in the $y-z$ plane: (a) $c = 0.06$, (b) $c = 0.1$, (c) $c = 0.2$, (d) $c = 3.4$, (e) $c = 3.5$, (f) $c = 10.6$, (g) $c = 15$, (h) $c = 15.32$, (i) $c = 31$, (j) $c = 31.8$, (k) $c = 31.9$, and (l) $c = 32.5$. The blue one is from the initial values $[2, 1, 1, 2]$ and the other from $[-2, -1, 1, -2]$.

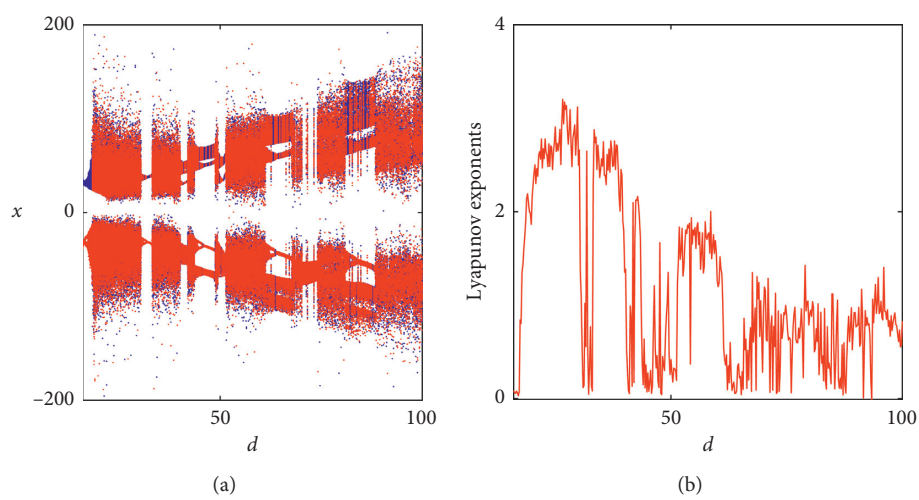

FIGURE 8: Bifurcation diagram and the largest LE for increasing parameter $d \in [16, 100]$. (a) The bifurcation diagram with initial conditions $[2, 1, 1, 2]$ (blue) and $[-2, -1, 1, -2]$ (red). (b) The largest LE.

nonchaotic, which is called transient chaos [40]. As shown in Figure 14, under parameters $a = 8, b = 5, c = 12, d = 17.5$, and $e = 4$ and initial values $[2, 1, 1, 2]$, the transient chaos phenomenon is generated in system (1), and the trajectory of the system evolves over time from transient chaos to steady-state multiperiod behavior. Figure 14(a) is the time-domain waveform of $t \in [0, 200]$. It can be seen from Figure 14(a) that the system is in a chaotic state in $t \in [0, 100]$ and a periodic state in $t \in [100, 200]$. Figures 14(b) and 14(c) are the phase portraits of transient chaotic and steady-state periodic states, respectively. Figure 15 is the transient chaos phenomenon under the parameters $a = 8, b = 5, c = 12, d = 60$, and $e = 11.8$ and the initial values $[2, 1, 1, 2]$. Different from Figure 14, the system

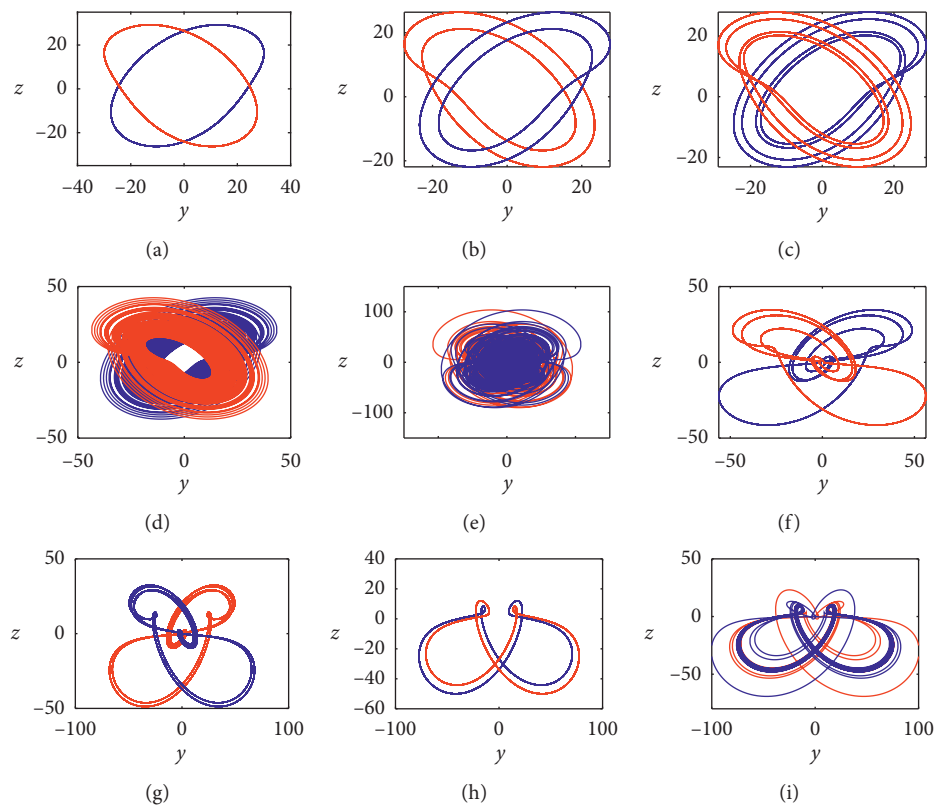

Figure 9: Various coexisting attractors with different values of parameter d in the $y-z$ plane, (a) $d = 16$, (b) $d = 17$, (c) $d = 17.2$, (d) $d = 17.8$, (e) $d = 25$, (f) $d = 42$, (g) $d = 50$, (h) $d = 68$, and (i) $d = 70$. The blue one is from the initial values $[2, 1, 1, 2]$ and the other from $[-2, -1, 1, -2]$.

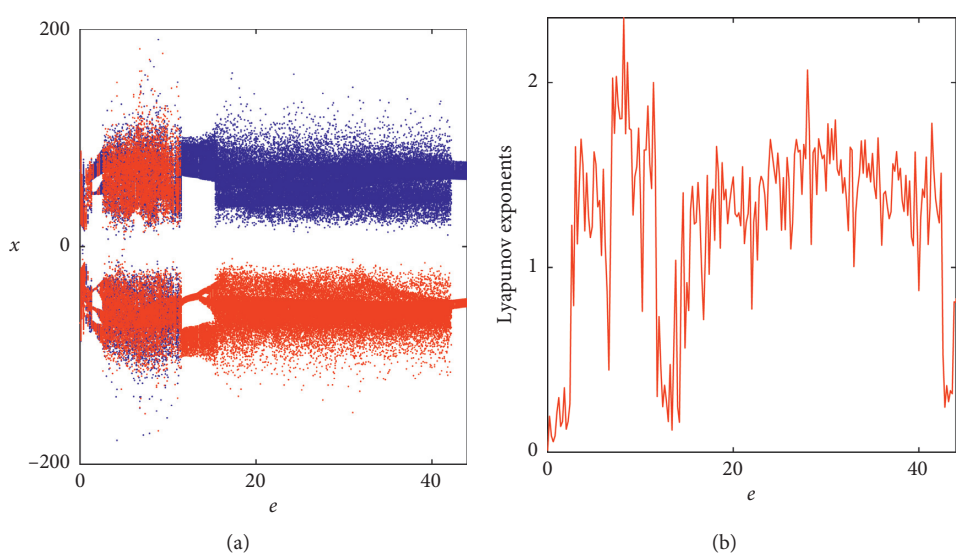

Figure 10: Bifurcation diagram and the largest LE for increasing parameter $e \in [0, 44]$. (a) The bifurcation diagram with initial conditions $[2, 1, 1, 2]$ (blue) and $[-2, -1, 1, -2]$ (red). (b) The largest LE.

has two different transient chaos states with the evolution of time, as shown in Figures 15(b) and 15(c). These two transient chaos states are both two-wing chaotic attractors, but the direction track of entering chaos is different. Figure 15(d) is the phase portrait of the steady-state period-1.

3.5. Offset Boosting. In this section, we will discuss the offset boosting control. There are generally two ways to construct offset boosting: (1) when a variable appears only once in a nonlinear system, adding a constant to the variable will produce an offset; (2) if every variable in a nonlinear system occurs more than once, it is necessary to construct a variable

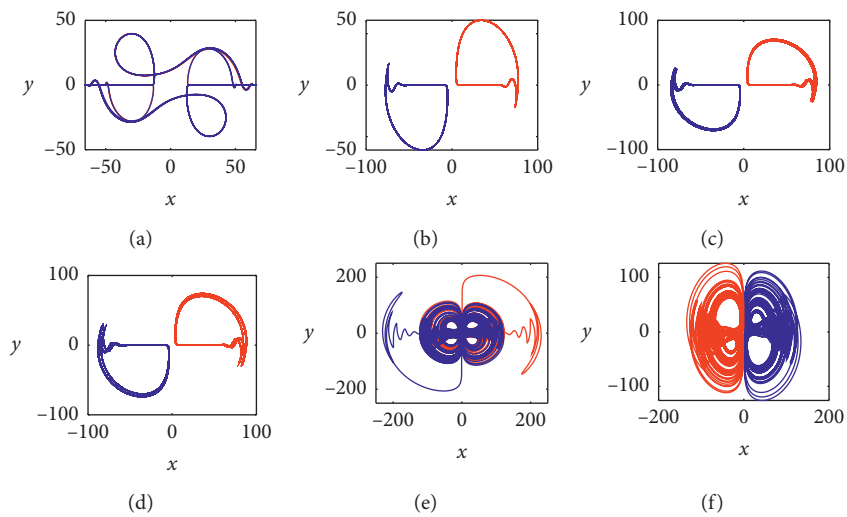

Figure 11: Various coexisting attractors with different values of parameter e in the $x - y$ plane, (a) $e = 0.2$, (b) $e = 1.5$, (c)$e = 2$, (d)$e = 2.1$, (e) $e = 5$, and (f) $e = 17$. The blue one is from the initial values $[2, 1, 1, 2]$ and the other from $[-2, -1, 1, -2]$.

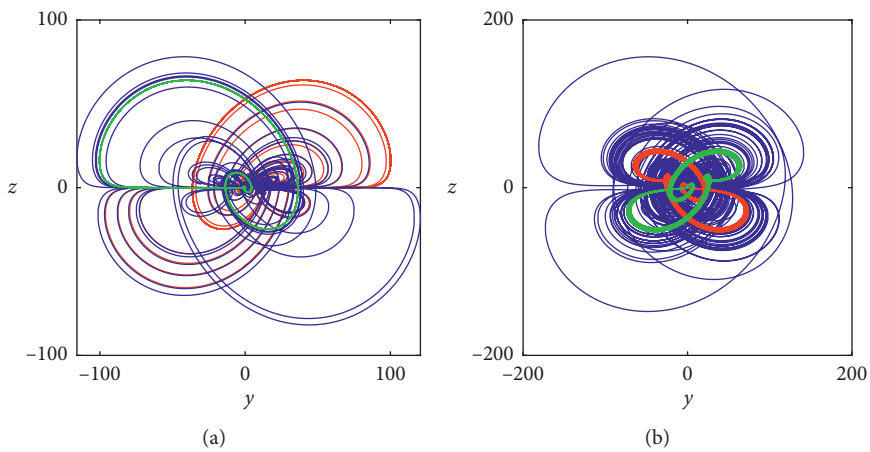

Figure 12: Phase portraits of coexisting multiple attractors. (a) $x(0) = 2$ (red), $x(0) = 0.2$ (green), and $x(0) = 6.5$ (blue); (b) $y(0) = 0.0001$ (blue), $y(0) = 1$ (red), and $y(0) = 8$ (green).

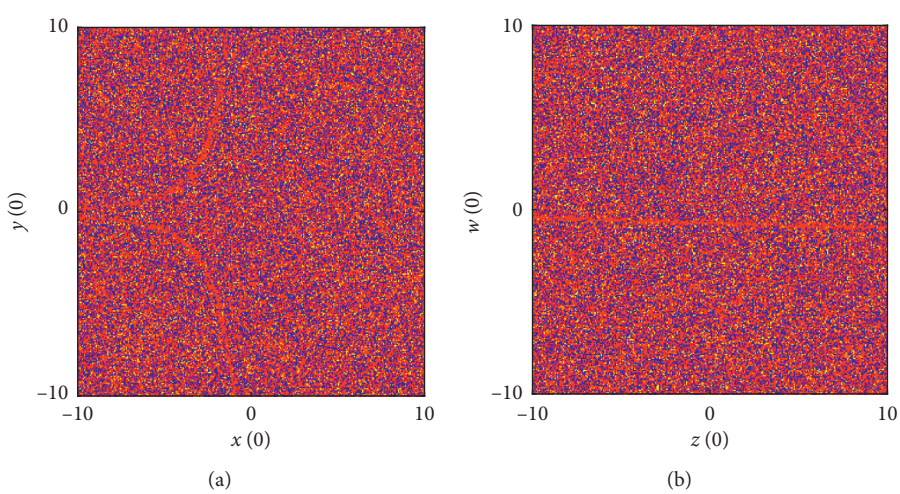

Figure 13: The basin of attraction of system (1): (a) in the $x(0) - y(0)$ plane for $z(0) = 1$ and $w(0) = 2$; (b) in the $z(0) - w(0)$ plane for $x(0) = 2$ and $y(0) = 1$.

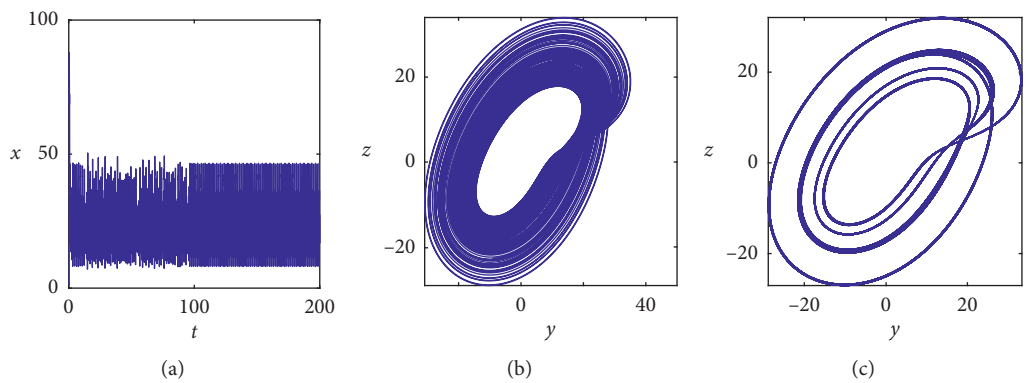

Figure 14: Transient chaos and steady-state multiperiod. (a) Time-domain waveform of x in the time interval $[0, 200]$. (b) Phase portrait of the transient single-wing chaotic attractor in the time interval $[0, 100]$. (c) Phase portrait of the steady-state multiperiod in the time interval $[100, 200]$.

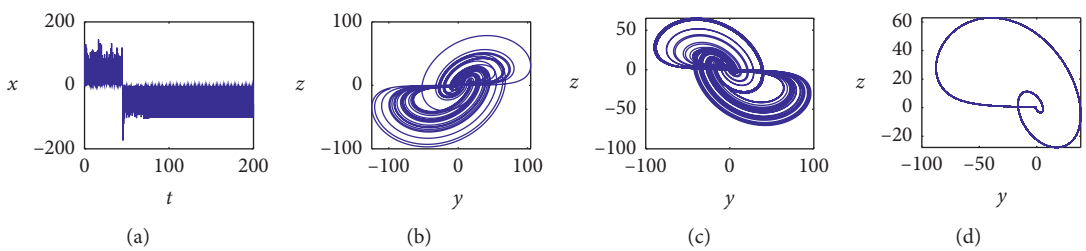

Figure 15: Transient chaos and steady-state period-1. (a) Time-domain waveform of x in the time interval $[0, 200]$. (b) Phase portrait of the transient two-wing chaotic attractor in the time interval $[0, 45)$. (c) Phase portrait of the transient two-wing chaotic attractor in the time interval $[45, 700]$. (d) Phase portrait of the steady-state period-1 in the time interval $[70, 200]$.

that occurs once by some means [45]. Since every variable in system (1) appears more than once, by making the parameter $b = 0$ in the first equation, the variable w appears only once in the system, and then the constant term is added after the variable g, as shown in the following equation:

$$\begin{cases} \dot{x} = -ax + yz, \\ \dot{y} = cy - xz, \\ \dot{z} = xy - dz, \\ \dot{w} = xz - e(w + g). \end{cases} \tag{10}$$

Figure 16(a) is the simulation result of phase portraits when system parameters are $a = 8, c = 12, d = 60$, and $e = 4$, initial conditions are set as $[2, 1, 1, 2]$, and three different control parameters are $g = -50, 0$, and 50. Figure 16(b) is the simulation result of the phase portraits when system parameters are $a = 8, c = 12, d = 30$, and $e = 4$, initial conditions are set as $[2, 1, 1, 2]$, and three different control parameters are $g = -70, 0$, and 70. Figure 16 shows that the variable w can be moved from a bipolar signal to a unipolar signal when the control parameter g is changed.

4. FPGA Implementation of Yu–Wang Chaotic System

In this section, we implement the 4D Yu–Wang four-wing chaotic system on FPGA using the RK4 algorithm and the 32-bit IEEE 754 floating-point standard. The core idea of designing a chaotic signal generator with FPGA is to divide the whole system into several functional modules, which contain many computing units, including multiplier, adder, and subtracter [76]. These running units are created in cooperation with IP core generators and should follow the IEEE 754 standard. The chaotic system design based on the RK4 algorithm is mainly divided into three modules: data selection module, chaotic oscillation module, and data processing module. Data selection module is to obtain the initial conditions of the system. The initial conditions of the first run of the system are defined by the designer himself. The chaotic oscillation module mainly uses the parallel pipeline structure to calculate the RK4 algorithm to generate the output value within a certain clock period and then feeds back the output value to the data selector as the initial value of the next operation. The data processing module converts 32-bit floating-point signals to 14-bit fixed-point signals. The 14-bit output signal is then downloaded to the FPGA development board for synthesis. Finally, the 14-bit digital signal is converted into an analog signal through a digital-analog converter and displayed on an oscilloscope.

On the Xilinx ZYNQ-XC7Z020 FPGA chip and the digital-to-analog converter AN9767, the digital hardware implementation of the 4D Yu–Wang four-wing oscillator based on the RK4 algorithm is synthesized. The whole design process is calculated, synthesized, and implemented by Vivado 2018.3, synthesized on the FPGA chip, and outputs

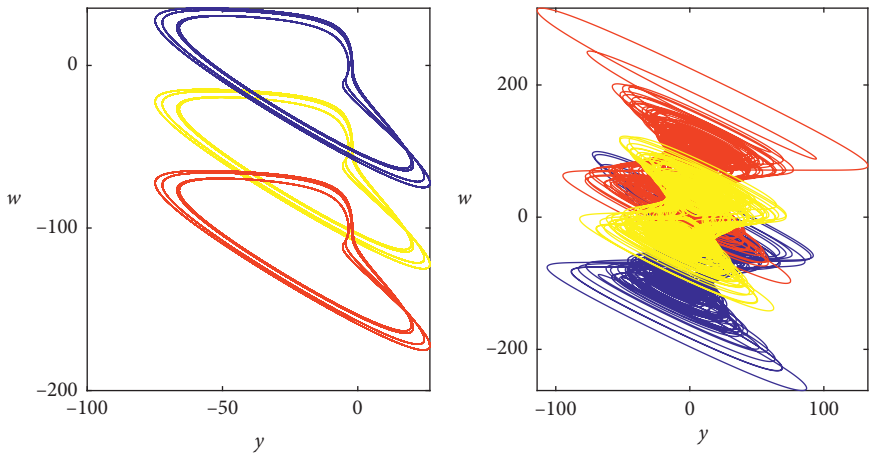

(a) (b)

Figure 16: Offset boosting with control parameter g. (a) In the $y - w$ plane for $g = 0$ (yellow), $g = 50$ (red), and $g = -50$ (blue). (b) In the $y - w$ plane for $g = 0$ (yellow), $g = 70$ (red), and $g = -70$ (blue).

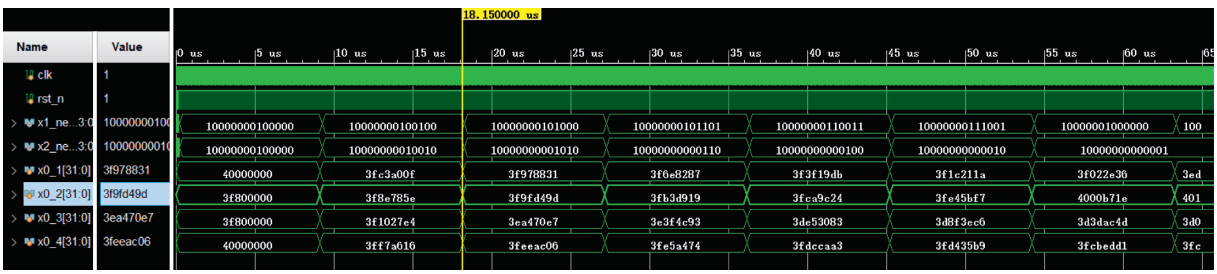

Figure 17: Simulation results of the FPGA-based chaotic system with the RK4 algorithm.

Table 2: Xilinx ZYNQ-XC7Z020 FPGA chip resource usage.

Resource	Used	Available	Utilization (%)
Slice register	20842	106400	19.60
Number of slice LUTs	15931	53200	29.99
Number of bonded IOBs	34	125	27.2
Number of BUFG	1	32	3.13
Max. clock frequency	161.212 MHz	—	—

(a) (b) (c)

Figure 18: Continued.

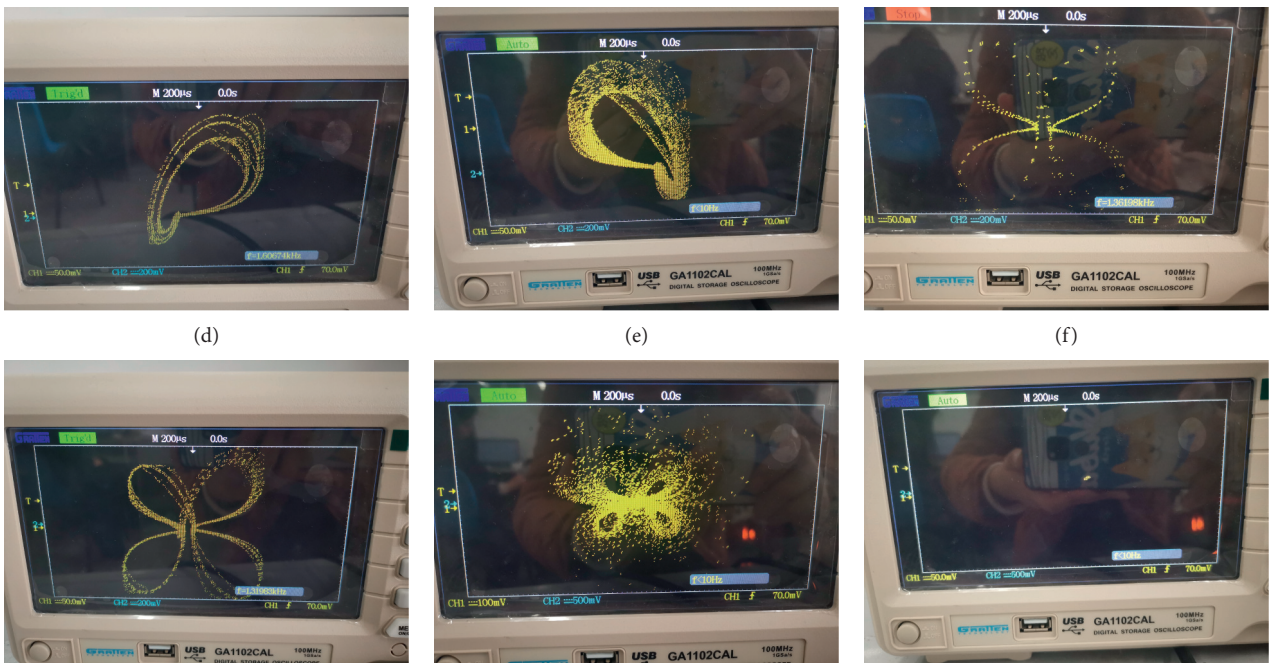

Figure 18: The phase diagrams of the 4D Yu–Wang four-wing chaotic system realized on FPGA based on the RK4 algorithm. (a) Simulation panorama; (b) one-wing period-1; (c) one-wing period-2; (d) one-wing period-4; (e) one-wing chaotic attractor; (f) four-wing period-1; (g) four-wing period-4; (h) four-wing chaotic attractor; (i) stable state.

the analog signal through the digital-to-analog converter and displayed on an oscilloscope. In the design process, the 32-bit IEEE 754 floating-point standard is adopted, but in order to better analyze the experimental results, we convert 32-bit data into 16-bit data. Figure 17 is the discrete sequence generated by the chaos oscillator based on FPGA. Table 2 shows the statistical data of the Yu–Wang system implemented on the Xilinx ZYNQ-XC7Z020 FPGA chip. It can be seen from the table that the maximum operating frequency of the designed chaotic oscillator based on FPGA is 161.212 MHz. Figure 18 shows the phase diagrams of the 4D Yu–Wang four-wing chaotic system displayed on the oscilloscope, which are consistent with the attractor phase portraits shown in MATLAB simulation of Figure 3, which proves that the method of realizing the chaotic system with FPGA is reliable.

5. Conclusion

Our objective is to further study the 4D Yu–Wang four-wing chaotic system using standard nonlinear analysis tools such as Lyapunov exponential spectrum, bifurcation diagram, basin of attraction, and phase portraits. The simulation results show that the system has very complex dynamical behaviors, including coexistence attractor, multistability, transient chaos, and offset boosting. It is worth noting that different system parameters have different coexistence multiple attractors. At the same time, it can also generate transient one-wing chaotic attractors and transient two-wing chaotic attractors. Secondly, using the Xilinx ZYNQ-XC7Z020 FPGA chip and the digital-to-analog converter AN9767, the phase diagram of the Yu–Wang chaotic system was displayed on the oscilloscope, including one-wing period-1, one-wing period-2, one-wing period-4, one-wing chaotic attractor, four-wing period-1, four-wing period-4, four-wing chaotic attractor, and steady state. This paper proves that the 4D Yu–Wang four-wing chaotic system based on the FPGA design can be applied to various embedded engineering system applications based on chaos, including cryptographic system, secure communication, and chaotic random number generator.

Data Availability

All data used to support the findings of this study are available from the corresponding author upon request.

Conflicts of Interest

The authors declare that they have no conflicts of interest.

Acknowledgments

This work was supported by the National Natural Science Foundation of China, under Grants 61504013, 61702052, and 61901169, the Natural Science Foundation of Hunan Province, under Grants 2019JJ50648, 2020JJ4622, and 2019JJ40190, the Guangxi Key Laboratory of Cryptography and Information Security, under Grant GCIS201919, the Postgraduate Training Innovation Base Construction Project of Hunan Province, under Grant 2020-172-48, the Postgraduate Scientific Research Innovation Project of Hunan

Province, under Grant CX20200884, the Scientific Research Fund of Hunan Provincial Education Department, under grant 18A137, and the young teacher development program project of the Changsha University of Science and Technology, under grant 2019QJCZ013.

References

[1] C. Wang, L. Xiong, J. Sun, and W. Yao, "Memristor-based neural networks with weight simultaneous perturbation training," *Nonlinear Dynamics*, vol. 95, no. 4, pp. 2893–2906, 2019.

[2] W. Yao, C. Wang, J. Cao, Y. Sun, and C. Zhou, "Hybrid multisynchronization of coupled multistable memristive neural networks with time delays," *Neurocomputing*, vol. 363, pp. 281–294, 2019.

[3] X. Ma, J. Mou, J. Liu, C. Ma, F. Yang, and X. Zhao, "A novel simple chaotic circuit based on memristor-memcapacitor," *Nonlinear Dynamics*, vol. 100, no. 3, pp. 2859–2876, 2020.

[4] Y. M. Tan and C. H. Wang, "A simple locally active memristor and its application in HR neurons," *Chaos*, vol. 30, no. 5, Article ID 053118, 2020.

[5] F. Yu, Q. Wan, J. Jin et al., "Design and FPGA implementation of a pseudorandom number generator based on a four-wing memristive hyperchaotic system and Bernoulli map," *IEEE Access*, vol. 7, pp. 181884–181898, 2019.

[6] F. Yu, L. Li, Q. Tang, S. Cai, Y. Song, and Q. Xu, "A survey on true random number generators based on chaos," *Discrete Dynamics in Nature and Society*, vol. 2019, Article ID 2545123, 10 pages, 2019.

[7] F. Yu, L. Liu, S. Qian et al., "Chaos-based application of a novel multistable 5D memristive hyperchaotic system with coexisting multiple attractors," *Complexity*, vol. 2020, Article ID 8034196, 19 pages, 2020.

[8] Q. Zhao, C. H. Wang, and X. Zhang, "A universal emulator for memristor, memcapacitor, and meminductor and its chaotic circuit," *Chaos*, vol. 29, Article ID 013141, 2019.

[9] F. Yu, H. Shen, L. Liu et al., "CCII and FPGA realization: a multistable modified fourth-order autonomous chua's chaotic system with coexisting multiple attractors," *Complexity*, vol. 2020, Article ID 5212601, 17 pages, 2020.

[10] F. Yu, L. Liu, H. Shen et al., "Dynamic analysis, circuit design and synchronization of a novel 6D memristive four-wing hyperchaotic system with multiple coexisting attractors," *Complexity*, vol. 2020, Article ID 5904607, 17 pages, 2020.

[11] G. F. Cheng, C. H. Wang, and H. A. Chen, "Novel color image encryption algorithm based on hyperchaotic system and permutation-diffusion architecture," *International Journal of Bifurcation and Chaos*, vol. 29, Article ID 1950115, 2019.

[12] Y. Chen, W. Xu, J. Zuo, and K. Yang, "The fire recognition algorithm using dynamic feature fusion and IV-SVM classifier," *Cluster Computing*, vol. 22, no. S3, pp. 7665–7675, 2019.

[13] F. Peng, X. W. Zhu, and M. Long, "An ROI privacy protection scheme for H.264 video based on FMO and chaos," *IEEE Transactions on Information Forensics and Security*, vol. 8, no. 10, pp. 1688–1699, 2013.

[14] S. Wang, C. Wang, and C. Xu, "An image encryption algorithm based on a hidden attractor chaos system and the Knuth-Durstenfeld algorithm," *Optics and Lasers in Engineering*, vol. 128, Article ID 105995, 2020.

[15] F. Yu, L. Liu, L. Xiao, K. Li, and S. Cai, "A robust and fixed-time zeroing neural dynamics for computing time-variant nonlinear equation using a novel nonlinear activation function," *Neurocomputing*, vol. 350, pp. 108–116, 2019.

[16] J. Jin, L. Zhao, M. Li, F. Yu, and Z. Xi, "Improved zeroing neural networks for finite time solving nonlinear equations," *Neural Computing and Applications*, vol. 32, no. 9, pp. 4151–4160, 2020.

[17] L. Zhou, F. Tan, F. Yu, and W. Liu, "Cluster synchronization of two-layer nonlinearly coupled multiplex networks with multi-links and time-delays," *Neurocomputing*, vol. 359, pp. 264–275, 2019.

[18] H. R. Lin and C. H. Wang, "Influences of electromagnetic radiation distribution on chaotic dynamics of a neural network," *Applied Mathematics and Computation*, vol. 369, Article ID 124840, 2020.

[19] Y. Sun, C. Zhou , H. Lin et al., "Synchronization of inertial memristive neural networks with time-varying delays via static or dynamic event-triggered control," *Neurocomputing*, vol. 404, pp. 367–380, 2020.

[20] F. Yu, L. Gao, K. Gu, B. Yin, Q. Wan, and Z. Zhou, "A fully qualified four-wing four-dimensional autonomous chaotic system and its synchronization," *Optik*, vol. 131, pp. 79–88, 2017.

[21] Y. Huang, L. Huang, Y. Wang, Y. Peng, and F. Yu, "Shape synchronization in driver-response of 4-D chaotic system and its application in image encryption," *IEEE Access*, vol. 8, pp. 135308–135319, 2020.

[22] C. Zhou, C. H. Wang, Y. C. Sun, and W. Yao, "Weighted sum synchronization of memristive coupled neural networks," *Neurocomputing*, vol. 403, pp. 225–232, 2020.

[23] F. Yu and Y. Song, "Complete switched generalized function projective synchronization of a class of hyperchaotic systems with unknown parameters and disturbance inputs," *Journal of Dynamic Systems, Measurement, and Control-Transactions of the ASME*, vol. 136, no. 1, Article ID 014505, 2014.

[24] M. Long, Y. Chen, and F. Peng, "Simple and accurate analysis of BER performance for DCSK chaotic communication," *IEEE Communications Letters*, vol. 15, no. 11, pp. 1175–1177, 2011.

[25] F. Yu, S. Qian, X. Chen et al., "A new 4D four-wing memristive hyperchaotic system: dynamical analysis, electronic circuit design, shape synchronization and secure communication," *International Journal of Bifurcation and Chaos*, vol. 30, no. 10, Article ID 2050147, 2020.

[26] F. Yu, L. Liu, B. He et al., "Analysis and FPGA realization of a novel 5D hyperchaotic four-wing memristive system, active control synchronization, and secure communication application," *Complexity*, vol. 2019, Article ID 4047957, 18 pages, 2019.

[27] F. Yu, Z. Zhang, L. Liu et al., "Secure communication scheme based on a new 5D multistable four-wing memristive hyperchaotic system with disturbance inputs," *Complexity*, vol. 2020, Article ID 5859273, 16 pages, 2020.

[28] L. Zhou, F. Tan, and F. Yu, "A robust synchronization-based chaotic secure communication scheme with double-layered and multiple hybrid networks," *IEEE Systems Journal*, vol. 14, no. 2, pp. 2508–2519, 2020.

[29] Q. L. Deng, C. H. Wang, and L. Yang, "Four-wing hidden attractors with one stable equilibrium point," *International Journal of Bifurcation and Chaos*, vol. 30, no. 6, Article ID 2050086, 2020.

[30] L. Zhou, C. Wang, and L. Zhou, "Generating hyperchaotic multi-wing attractor in a 4D memristive circuit," *Nonlinear Dynamics*, vol. 85, no. 4, pp. 2653–2663, 2016.

[31] F. Yu, P. Li, K. Gu, and B. Yin, "Research progress of multi-scroll chaotic oscillators based on current-mode devices," *Optik*, vol. 127, no. 13, pp. 5486–5490, 2016.

[32] F. Yu, C. Wang, and H. He, "Grid multiscroll hyperchaotic attractors based on colpitts oscillator mode with controllable grid gradient and scroll numbers," *Journal of Applied Research and Technology*, vol. 11, no. 3, pp. 371–380, 2013.

[33] Q. L. Deng and C. H. Wang, "Multi-scroll hidden attractors with two stable equilibrium points," *Chaos: An Interdisciplinary Journal of Nonlinear Science*, vol. 29, no. 9, Article ID 093112, 2019.

[34] X. Zhang, C. Wang, W. Yao, and H. Lin, "Chaotic system with bondorbital attractors," *Nonlinear Dynamics*, vol. 97, no. 4, pp. 2159–2174, 2019.

[35] F. Yang, J. Mou, J. Liu et al., "Characteristic analysis of the fractional-order hyperchaotic complex system and its image encryption application," *Signal Processing*, vol. 169, Article ID 107373, 2020.

[36] X. Ye, J. Mou, C. Luo, and Z. Wang, "Dynamics analysis of Wien-bridge hyperchaotic memristive circuit system," *Nonlinear Dynamics*, vol. 92, no. 3, pp. 923–933, 2018.

[37] C. Xu, J. Sun, and C. Wang, "An image encryption algorithm based on random walk and hyperchaotic systems," *International Journal of Bifurcation and Chaos*, vol. 30, no. 4, Article ID 2050060, 2020.

[38] M. Zhou and C. Wang, "A novel image encryption scheme based on conservative hyperchaotic system and closed-loop diffusion between blocks," *Signal Processing*, vol. 171, Article ID 107484, 2020.

[39] X. Zhang and C. H. Wang, "Multiscroll hyperchaotic system with hidden attractors and its circuit implementation," *International Journal of Bifurcation and Chaos*, vol. 29, Article ID 1950117, 2019.

[40] H. Lin, C. Wang, and Y. Tan, "Hidden extreme multistability with hyperchaos and transient chaos in a Hopfield neural network affected by electromagnetic radiation," *Nonlinear Dynamics*, vol. 99, no. 3, pp. 2369–2386, 2020.

[41] B. Bao, A. Hu, H. Bao, Q. Xu, M. Chen, and H. Wu, "Three-dimensional memristive hindmarsh-rose neuron model with hidden coexisting asymmetric behaviors," *Complexity*, vol. 2018, Article ID 3872573, 11 pages, 2018.

[42] L. Cui, M. Lu, Q. Ou et al., "Analysis and circuit implementation of fractional order multi-wing hidden attractors," *Chaos, Solitons & Fractals*, vol. 138, Article ID 109894, 2020.

[43] H. Lin, C. Wang, Y. Sun, and W. Yao, "Firing multistability in a locally active memristive neuron model," *Nonlinear Dynamics*, vol. 100, pp. 3667–3683, 2020.

[44] V. R. Folifack Signing, J. Kengne, and L. K. Kana, "Dynamic analysis and multistability of a novel four-wing chaotic system with smooth piecewise quadratic nonlinearity," *Chaos, Solitons & Fractals*, vol. 113, pp. 263–274, 2018.

[45] A. Bayani, K. Rajagopal, A. J. M. Khalaf, S. Jafari, G. D. Leutcho, and J. Kengne, "Dynamical analysis of a new multistable chaotic system with hidden attractor: anti-monotonicity, coexisting multiple attractors, and offset boosting," *Physics Letters A*, vol. 383, no. 13, pp. 1450–1456, 2019.

[46] A. T. Azar, N. M. Adele, K. S. T. Alain, R. Kengne, and F. H. Bertrand, "Multistability analysis and function projective synchronization in relay coupled oscillators," *Complexity*, vol. 2018, Article ID 3286070, 12 pages, 2018.

[47] B. A. Mezatio, M. T. Motchongom, B. R. Wafo Tekam, R. Kengne, R. Tchitnga, and A. Fomethe, "A novel memristive 6D hyperchaotic autonomous system with hidden extreme multistability," *Chaos, Solitons & Fractals*, vol. 120, pp. 100–115, 2019.

[48] H. Bao, T. Jiang, K. Chu et al., "Memristor-based canonical chua's circuit: extreme multistability in voltage-current domain and its controllability in flux-charge domain," *Complexity*, vol. 2018, Article ID 5935637, 13 pages, 2018.

[49] X. Zhang and Z. Li, "Hidden extreme multistability in a novel 4D fractional-order chaotic system," *International Journal of Non-linear Mechanics*, vol. 111, pp. 14–27, 2019.

[50] H. Lin, C. Wang, and Y. Tan, "Hidden extreme multistability with hyperchaos and transient chaos in a Hopfield neural network affected by electromagnetic radiation," *Nonlinear Dynamics*, vol. 99, pp. 2369–2386, 2020.

[51] J. Jin, "Programmable multi-direction fully integrated chaotic oscillator," *Microelectronics Journal*, vol. 75, pp. 27–34, 2018.

[52] J. Jin and L. V. Zhao, "Low voltage low power fully integrated chaos generator," *Journal of Circuits, Systems and Computers*, vol. 27, Article ID 1850155, 2018.

[53] J. Jin and L. Cui, "Fully integrated memristor and its application on the scroll-controllable hyperchaotic system," *Complexity*, vol. 2019, Article ID 4106398, 8 pages, 2019.

[54] F. Yu, L. Gao, L. Liu, S. Qian, S. Cai, and Y. Song, "A 1 V, 0.53 ns, 59 μW current comparator using standard 0.18 μm CMOS technology," *Wireless Personal Communications*, vol. 111, no. 2, pp. 843–851, 2020.

[55] F. Yu, Q. Tang, W. Wang, and H. Wu, "A. 2.A 2.7 GHz low-phase-noise LC-QVCO using the gate-modulated coupling technique," *Wireless Personal Communications*, vol. 86, no. 2, pp. 671–681, 2016.

[56] F. Yu, "A low-voltage and low-power 3-GHz CMOS LC VCO for S-band wireless applications," *Wireless Personal Communications*, vol. 78, no. 2, pp. 905–914, 2014.

[57] X. Wu, W. Tan, and H. Wang, "Initial value determination of chua system with hidden attractors and its DSP implementation," *Complexity*, vol. 2020, Article ID 7638243, 9 pages, 2020.

[58] S. He, K. Sun, H. Wang, X. Mei, and Y. Sun, "Generalized synchronization of fractional-order hyperchaotic systems and its DSP implementation," *Nonlinear Dynamics*, vol. 92, no. 1, pp. 85–96, 2018.

[59] M. S. Azzaz, C. Tanougast, S. Sadoudi, R. Fellah, and A. Dandache, "A new auto-switched chaotic system and its FPGA implementation," *Communications in Nonlinear Science and Numerical Simulation*, vol. 18, no. 7, pp. 1792–1804, 2013.

[60] E. Tlelo-Cuautle, L. G. de la Fraga, V.-T. Pham, C. Volos, S. Jafari, and A. d. J. Quintas-Valles, "Dynamics, FPGA realization and application of a chaotic system with an infinite number of equilibrium points," *Nonlinear Dynamics*, vol. 89, no. 2, pp. 1129–1139, 2017.

[61] B. Atiyeh, J. M. Ali, and R. Karthikeyan, "A novel fractional-order chaotic system with specific topology: from proposing to FPGA implementation," *The European Physical Journal Special Topics*, vol. 226, pp. 3729–3745, 2017.

[62] J. X. Yong, X. Cheng, and G. Tao-Tao, "Dynamical analysis and FPGA implementation of a large range chaotic system with coexisting attractors," *Results in Physics*, vol. 11, pp. 368–376, 2018.

[63] A. Karthikeyan and K. Rajagopal, "FPGA implementation of fractional-order discrete memristor chaotic system and its commensurate and incommensurate synchronisations," *Pramana*, vol. 90, no. 1, 2018.

[64] Y. W. Guang, L. B. Xu, and L. W. Zhong, "Design and FPGA Implementation of a new hyperchaotic system," *Chinese Physics B*, vol. 17, pp. 3596–3602, 2018.

[65] D. Enzeng, Y. Mingfeng, and Z. Cong, "Dynamics, topological horseshoe analysis, ultimate boundary estimations of a new 4D hyperchaotic system and its FPGA implementation," *International Journal of Bifurcation and Chaos*, vol. 28, Article ID 1850081, 2018.

[66] J.-L. Zhang, W.-Z. Wang, X.-W. Wang, and Z.-H. Xia, "Enhancing security of FPGA-based embedded systems with combinational logic binding," *Journal of Computer Science and Technology*, vol. 32, no. 2, pp. 329–339, 2017.

[67] R. Karthikeyan, K. Anitha, and S. A. Kuma, "FPGA implementation of novel fractional-order chaotic systems with two equilibriums and no equilibrium and its adaptive sliding mode synchronization," *Nonlinear Dynamics*, vol. 87, no. 4, pp. 2281–2304, 2017.

[68] S. Cai, B. He, W. Wang et al., "Soft error reliability evaluation of nanoscale logic circuits in the presence of multiple transient faults," *Journal of Electronic Testing*, vol. 36, pp. 469–483, 2020.

[69] F. Yu, C. H. Wang, and J. W. Yin, "A 4-D chaos with fully qualified four-wing type," *Acta Physica Sinica*, vol. 61, Article ID 020506, 2012.

[70] A. Wolf, J. B. Swift, H. L. Swinney, and J. A. Vastano, "Determining Lyapunov exponents from a time series," *Physica D: Nonlinear Phenomena*, vol. 16, no. 3, pp. 285–317, 1985.

[71] J. Dai, D.-R. He, X.-L. Xu, and C.-K. Hu, "A riddled basin escaping crisis and the universality in an integrate-and-fire circuit," *Physica A: Statistical Mechanics and Its Applications*, vol. 500, pp. 72–79, 2018.

[72] E. Ott, *Chaos in Dynamical Systems*, Cambridge University Press, Cambridge, UK, 1993.

[73] H. E. Nusse and J. A. Yorke, "Border-collision bifurcations including "period two to period three" for piecewise smooth systems," *Physica D: Nonlinear Phenomena*, vol. 57, no. 1-2, pp. 39–57, 1992.

[74] Y. Cao, "A note about Milnor attractor and riddled basin," *Chaos, Solitons & Fractals*, vol. 19, no. 4, pp. 759–764, 2004.

[75] K. Sathiyadevi, S. Karthiga, V. K. Chandrasekar, D. V. Senthilkumar, and M. Lakshmanan, "Frustration induced transient chaos, fractal and riddled basins in coupled limit cycle oscillators," *Communications in Nonlinear Science and Numerical Simulation*, vol. 72, pp. 586–599, 2019.

[76] M. Tuna, M. Alçın, İ. Koyuncu, C. B. Fidan, and İ. Pehlivan, "High speed FPGA-based chaotic oscillator design," *Microprocessors and Microsystems*, vol. 66, pp. 72–80, 2019.